CRANFIELD UNIVERSITY

Francisco Sánchez Moreno

Nacelle aerodynamic design and optimisation

School of Aerospace, Transport and Manufacturing
Centre For Propulsion and Thermal Power Engineering

Ph.D. Thesis
Academic Year: 2023
Supervisor: Prof. D. G. MacManus
Associate supervisor: Dr F. Tejero

January 2023

© Cranfield University 2023. All rights reserved. No part of this publication may be reproduced without the written permission of the copyright owner.

Abstract

For a required thrust level, the reduction of the specific fuel consumption of an aero-engine can be achieved through an improvement of the propulsive efficiency. This is typically enabled by higher bypass ratios and lower fan pressure ratios. This may result in a larger fan diameter that increases the overall aircraft drag and weight as well as the interference effects between the engine and the airframe. Additionally, the next generation of Ultra-High Bypass Ratio (UHBPR) aero-engines are expected to be installed in a more close-coupled position with the airframe due to multi-disciplinary constraints such as structural loads or ground clearance. Consequently, the aerodynamic interference effects of the installation further increase and the potential benefits of the new UHBPR aero-engine cycles might be eroded. As a result, new design technologies that consider the engine coupled with the airframe have to be developed.

The main focus of this project is on the aerodynamic shape design of compact nacelles in an airframe-installed configuration. This is a challenging design problem governed by computationally expensive numerical simulations, transonic non-linear flow physics and a high dimensional design space. Moreover, this design problem is typically subjected to computational constraints to meet industrial time scales. Therefore, surrogate modelling techniques to accelerate the optimisation process are a key aspect of the work. Single-fidelity and multi-fidelity surrogate models based on Artificial Neural Networks and Kriging interpolation were assessed. While a Reynolds-Averaged Navier-Stokes (RANS) Computational Fluid Dynamics (CFD) method was used as high-fidelity, an inviscid CFD model was used as a low-cost, low-fidelity method.

The research quantified the effect of key aspects in the installed nacelle design problem such as the design variables considered, the surrogate modelling technique, the

sampling size of the design space and the CFD fidelity. From the traditional Euler-based method to assess the aerodynamic integration of the aero-engine in the airframe, a key novel contribution of this research is a systematic evaluation of different modelling approaches to quantify trades between aerodynamic performance and computational effort. The work showed that the size of the design space population for the surrogate models used, even with lower fidelity data, was the most important parameter to determine the design space gradients and identify the optimum design. At the same computational cost, the added complexity of multi-fidelity methods provided no benefits. Overall, for the first time this research established that for installed nacelle configurations, the industrial design problem is best addressed using single-fidelity Kriging models based on Euler CFD data with a posteriori RANS CFD evaluation of the optimal design. It was successfully shown that using this novel approach the installed nacelle design could be improved to provide a 0.6% reduction in cruise fuel burn, while also providing the design space maps to enable trade studies on key nacelle geometric parameters.

Keywords

Nacelle aerodynamics; propulsion system integration; multi-point optimisation; computational fluid dynamics; surrogate model; multi-fidelity method.

Acknowledgements

The doctoral studies have been the greatest academic challenge that I have undertaken until today. It has pushed me towards my limits in many senses. But at the same time, it has made me grow as a researcher, as an engineer and mostly as a person. Although the common thing is to be proud of your parents or your children, today I can say that I am proud of myself.

There are many people that I want to thank. Undoubtedly, the first person is my supervisor Professor David MacManus. Thanks for all the support and guidance throughout this journey. Aside from your incredible technical knowledge, you take care of your students. You truly want to teach us as much as possible and contribute to our growth and I have seen that many times in these years. For all of this, thank you David. Of course, I also want to thank my co-supervisor Dr Fernando Tejero. I have really learnt a lot from you, not only technical aspects but also proper work practices in academia. You have pushed and encouraged me to publish as much as possible and I appreciate it a lot. You are one of the most eager and ambitious professional I have met and that, together with the high quality work you do, will lead you very far in your career. Finally, I would also like to thank my industrial supervisor Mr Chris Sheaf from Rolls-Royce. Always willing to kindly provide very useful feedback. Your massive knowledge and industrial experience has enriched my learning during these years. I am also grateful to other colleagues at Cranfield University for their help and contribution whenever it was needed: Dr Neys Schreiner, Dr Robert Christie, Dr Ioannis Goulos and Dr Alex Heidebretch.

I feel and I want to specially recognise Dr Josep Hueso Rebassa, although for me you will always be Pepo. Only I know how invaluable all your help has been for me to be writing this today. More than a colleague, a real friend. Thank you also for all the support you gave me in the darkest moments, no matter what the reason was. I truly know we will always be in touch. There is no way I can forget about

my ”little menaras”: Pepo, Avery and Jesús (Dr Jesús Matesanz García formally speaking). It has been great sharing with you all this time and experiences. I will never forget our deep conversations. You were always a support in any matter and I am sure we will be in contact throughout the years. A big thank also to my ”annoying catalana” Marta. Although the communication between us was always a problem, the fun moments and laughs were countless. And last but not least, I feel incredibly fortunate for the rest of the ”gang” that I found in Cranfield. After all, Cranfield is special for the links that creates between people. I will never forget those kitchen and living room parties, dinners, CSA nights, boxing classes... In no particular order: Dario (vuyardo), Alex, Dr Luca, Dr Hanah, Dr Pavlos, Raul, Nico, Dani, Marco, Lapo, Claudia, Dr Christos, Priya, Sophie, Ngoni, Dr Ferran, Tom, Dr Matteo, the twins Dimitris and Ioannis, Dr Eva, Dr Dimitris (Dlogo) and Dr Tala.

Dejando la magra para el final, no consigo ordenar las ideas en mi cabeza para escribir algo con sentido y agradecerle a mi familia. A mis padres, Loli y Juan Antonio, y a mis hermanos, Lola y Cristóbal. Un apoyo incondicional sea cual sea el barco al que me suba. Casi siempre lejos de vosotros, pero eso da igual. Gracias por vuestra fuerza cuando en mi ha flaqueado. Esto, sin ninguna duda, va por vosotros.

Por último, quiero acordarme del resto de personas que han formado parte de mi vida, apoyado y guiado hasta este momento. Hoy consigo entregar mi tesis por ser quien soy, y soy quien soy por todos vosotros. Gracias Ana por motivarme en su día a empezar esta aventura, y por supuesto por todo tu apoyo siempre, hasta el último día literalmente. Gracias a la pandilla del pueblo. Y gracias a don Luis Armand Moya, que desde que me cogiste en el colegio del Campillo con 2 años me inculcaste grandes valores como si fueses un padre.

Fran

Contents

Abstract . . . iv
Acknowledgements . . . vi
List of Contents . . . xiii
List of Figures . . . xxv
List of Tables . . . xxix
Nomenclature . . . xxxv

1 Introduction **1**
1.1 Background . . . 1
1.2 Research aim and objectives . . . 3
1.2.1 Overall aim . . . 3
1.2.2 Objectives . . . 4

2 Literature review **5**
2.1 Aerodynamics and performance of nacelles . . . 5
2.1.1 Nacelle aerodynamics and drag . . . 6
2.1.2 Drag extraction methods . . . 9
2.1.3 Nacelle design philosophies . . . 11
2.2 Propulsion system integration . . . 14
2.2.1 Key aerodynamic installation effects . . . 15
2.2.2 Methods for engine integration studies . . . 18
2.2.2.1 Computational methods of different fidelity . . . 20
2.2.3 Performance of the overall engine-airframe system . . . 23
2.2.3.1 Accounting method . . . 23
2.2.3.2 Impact of the engine size and installation position . . . 25
2.2.3.3 Impact of the pylon . . . 28
2.3 Aerodynamic shape design and optimisation . . . 31
2.3.1 Key challenges . . . 31
2.3.2 Optimisation approaches . . . 32
2.3.3 Surrogate models and multi-fidelity techniques for aerodynamic applications . . . 34
2.3.3.1 Single-fidelity surrogate models . . . 34
2.3.3.2 Multi-fidelity surrogate models . . . 36
2.3.4 Nacelle aerodynamic design and optimisation . . . 39
2.3.4.1 Isolated configuration . . . 39

2.3.4.2 Installed configuration . . . 51
2.4 Computational methods for off-design conditions . . . 57
2.4.1 Computational methods . . . 58
2.4.1.1 Hybrid RANS/LES method . . . 59
2.4.2 Aerodynamic applications . . . 60

3 Scope of the project 63
3.1 Research gaps and novel contributions . . . 63
3.2 Results overview . . . 65

4 Methodology 69
4.1 Geometry definition of the different models . . . 69
4.1.1 Isolated engine . . . 70
4.1.2 Airframe and engine installation . . . 74
4.1.2.1 Pylon . . . 76
4.1.3 Wind tunnel configuration . . . 78
4.2 Operating conditions . . . 79
4.3 Computational fluid dynamics methods . . . 81
4.3.1 RANS models . . . 83
4.3.1.1 RANS . . . 83
4.3.1.2 RANS wall functions . . . 92
4.3.1.3 Unsteady RANS . . . 93
4.3.2 Euler models . . . 94
4.3.3 DDES models . . . 96
4.4 Thrust and drag accounting method . . . 99
4.4.1 Nearfield method . . . 99
4.4.1.1 Uncertainty estimate in NVF . . . 104
4.4.2 Farfield method for wind tunnel configuration . . . 104
4.5 Nacelle design and optimisation methods . . . 107
4.5.1 Design space exploration . . . 107
4.5.1.1 Sampling technique . . . 108
4.5.2 Optimisation approaches . . . 109
4.5.2.1 Optimisation algorithm . . . 110
4.5.2.2 Isolated nacelle optimisation method . . . 112
4.5.2.3 Airframe-installed nacelle optimisation method . . . 114
4.6 Surrogate modelling techniques . . . 118
4.6.1 Single-fidelity approaches . . . 118
4.6.1.1 Gaussian Process Regression . . . 118
4.6.1.2 Artificial Neural Networks . . . 120
4.6.2 Multi-fidelity approaches . . . 122
4.6.2.1 Variable Complexity Models . . . 122
4.6.2.2 Multi-Fidelity Neural Networks . . . 123
4.6.3 Verification of surrogate models . . . 124

5 Assessment of CFD methods for isolated nacelle aerodynamics 127

5.1 Nacelle design down selection . . . 128
5.2 Experimental description . . . 129
5.2.1 Wind tunnel test matrix . . . 129
5.2.2 Measurements and instrumentation . . . 130
5.3 Nacelle aerodynamics in the cruise segment . . . 135
5.4 Off-design nacelle aerodynamics . . . 138
5.4.1 Windmilling end-of-runway condition . . . 140
5.4.2 Windmilling diversion condition . . . 142

6 Aerodynamics of engine-aircraft integration 147
6.1 Analysis at cruise condition . . . 147
6.1.1 Impact on the nacelle aerodynamics . . . 147
6.1.2 Impact of the aero-engine installation position . . . 148
6.1.3 Impact of the aero-engine nacelle compactness . . . 154
6.2 Analysis at windmilling diversion . . . 156
6.2.1 Impact of the mass flow capture ratio . . . 159

7 Assessment of different CFD fidelities 163
7.1 Aerodynamic prediction of the installation . . . 163
7.2 Optimal design space of the 2D axi-symmetric configuration . . . 168
7.3 Selection of the low-fidelity model . . . 172

8 Nacelle aerodynamic design and optimisation 175
8.1 2D axi-symmetric isolated configuration . . . 175
8.1.1 CFD-in-the-loop optimisation . . . 176
8.1.2 Multi-fidelity surrogate-based optimisations . . . 177
8.1.2.1 Tuning of the hyperparameters of the models . . . 178
8.1.2.2 Impact of the number of samples . . . 183
8.1.2.3 Down selected design and benefits . . . 186
8.2 Installed non-axisymmetric configuration . . . 189
8.2.1 Exploration of the design space . . . 191
8.2.1.1 Impact of the number of samples . . . 192
8.2.1.2 Impact of the CFD fidelity . . . 194
8.2.2 Surrogate modelling and optimisation . . . 198
8.2.2.1 Single-fidelity Euler-based models . . . 198
8.2.2.2 Single-fidelity RANS-based models . . . 206
8.2.2.3 Multi-fidelity models . . . 208
8.3 Synthesis and discussion . . . 211

9 Conclusions and future work 213
9.1 Conclusions . . . 213
9.2 Future work . . . 215

References 217

A Governing equations **233**
A.1 Fluid properties . . . 233
A.2 Navier-Stokes equations . . . 234
A.2.1 Favre-Averaged Navier-Stokes formulation . . . 235
A.2.1.1 $\kappa - \omega$ SST turbulence model . . . 236
A.2.1.2 Wall functions for the $\kappa - \omega$ SST turbulence model . . . 237
A.2.2 DDES formulation . . . 238
A.2.3 Euler equations . . . 238

B Grid sensitivity studies **241**
B.1 Grid Convergence Index (GCI) . . . 241
B.2 RANS models . . . 243
B.2.1 2D isolated configuration . . . 243
B.2.2 3D isolated configuration . . . 243
B.2.3 3D airframe-installed configuration . . . 244
B.2.4 3D test rig-installed configuration . . . 245
B.3 Euler models . . . 246
B.3.1 2D isolated configuration . . . 246
B.3.2 3D airframe-installed configuration . . . 247
B.4 RANS with wall function models . . . 251
B.4.1 2D isolated configuration . . . 251
B.4.2 3D airframe-installed configuration . . . 251

C Unsteady CFD methods **255**
C.1 URANS . . . 255
C.1.1 Time step study . . . 255
C.1.1.1 End-of-runway condition . . . 256
C.1.1.2 Windmilling diversion condition . . . 258
C.1.2 Statistical convergence . . . 260
C.1.2.1 End-of-runway condition . . . 260
C.1.2.2 Windmilling diversion condition . . . 260
C.2 DDES . . . 261
C.2.1 Statistical convergence . . . 261
C.2.2 Blending functions . . . 262
C.3 Fourier analysis . . . 263

D Verification of the MFNN method **265**
D.1 One-dimensional verification . . . 266
D.1.1 Linear correlation . . . 266
D.1.2 Non-linear correlation . . . 267
D.2 Multi-dimensional verification . . . 268
D.2.1 Linear correlation . . . 268
D.2.2 Non-linear correlation . . . 270

E Evolutionary algorithms for nacelle optimisations **273**

E.1 Algorithms assessed 274
E.1.1 NSGA-II 274
E.1.2 IBEA 275
E.1.3 OMOPSO 276
E.2 Statistical comparison for transonic nacelle optimisations 276
E.2.1 Optimal design space 276
E.2.2 Down selected designs 280
E.2.3 Convergence rate 281
E.2.4 Conclusion 282

List of Figures

1.1 Trend of aero-engine fan size[11]. 2
1.2 Fuel and noise efficiency against fan size of the aero-engine[12]. 3

2.1 Definition of the nacelle geometry within the power plant system. . . 6
2.2 Definition of the aero-engine thrust and drag domains and nacelle main geometrical parameters. 10
2.3 Impact of the nacelle length over the maximum diameter ratio (L_{nac}/d_{max}) on the total nacelle drag at cruise. From Daggett et al.[8]. 13
2.4 Impact of installation on the reduction of fuel consumption with by-pass ratio. Based on Rudnik et al.[65]. 14
2.5 Components of the aircraft model. 15
2.6 Summary of aerodynamic installation effects. 17
2.7 Propulsion system modelling through Through-Flow Nacelles and Turbine-Powered Simulators. 19
2.8 Different aircraft models used for propulsion system integration studies installed in the wind tunnel. 20
2.9 Distribution of pressure coefficient for a wing section of the DLR-F6 at a location inboard of the nacelle and at the cruise condition ($M_\infty = 0.75$ and $C_L = 0.5$). Comparison of different CFD models: Euler solver on the left, Euler solver coupled with 3D boundary layer correction code on the middle, RANS solver on the right. Taken from Rudnik et al[65]. 22
2.10 Comparison between RANS and experiments of (left)[97] the distribution of the pressure coefficient for a wing section of the NASA CRM at a location inboard of the nacelle and at the cruise condition ($M_\infty = 0.85$ and $C_L = 0.5$), and (right)[98] the installation drag with changes in the lift coefficient for $M_\infty = 0.85$. 23
2.11 Method for aero-engine installation. Based on Goulos et al.[98]. 27
2.12 Distribution of NVF in the investigated installation map. Based on Goulos et al.[98]. 27
2.13 Normalised static pressure distributions for the baseline position, axially and vertically close-coupled positions and uninstalled configuration. 27

2.14 Contours of Mach number for the engine-airframe configurations based on the E1 and E2 engines. NASA CRM at $M_\infty = 0.82$, $\alpha_{a/c} = 2.5°$ and $Re = 45\text{x}10^6$. Forward installation position given by $dx/c = -0.05$ and $dz/c = 0.15$. Based on Stańkowski[10]. 28
2.15 Impact of the pylon on the installation aerodynamics of the nacelle and the suction side of the wing. Engine of BPR ≈ 18 installed in the NASA CRM at a typical installation position ($dx/C = 0$ and $dz/C = 0.09$) at cruise condition ($M_\infty = 0.85$ and $C_L = 0.5$). Based on Otter[113]. 30
2.16 Overview of the approach followed by Gradient-Free Methods and Gradient-Based Methods within an optimisation. Figure generated by the author for illustration purposes. 32
2.17 Definition of the geometry of a nacelle and the trend towards compact aero-engine nacelle technologies. 40
2.18 Design space for current and novel compact nacelle configurations based on L_{nac}/r_{hi}, r_{max}/r_{hi} and r_{te}/r_{hi} for long-range applications of Mach number around 0.85. Based on Robinson[183]. 41
2.19 Pareto data sets resulting from 2D axisymmetric nacelle optimisations for different nacelle lengths and trailing edge radius. Results shown based on the performance metrics: cruise drag, drag-rise Mach number and spillage drag. Based on Robinson[183]. 43
2.20 Pareto data sets resulting from 2D axisymmetric nacelle optimisations for different nacelle lengths and trailing edge radius. Results shown based on distributions of the geometrical parameters. The dashed line represents the median while the dotted line indicates the quartiles. Based on Robinson[183]. 44
2.21 Optimal design space shown in terms of geometric parameters for 2D axisymmetric nacelles of different lengths and trailing edge radius. Parallel coordinate plot coloured by cruise drag. Based on Tejero et al.[16]. 45
2.22 Distribution of cruise drag in the space L_{nac}/r_{hi} and r_{te}/r_{hi} for the selected designs with minimum cruise drag from each multi-objective optimisation. Based on Tejero et al.[16]. 46
2.23 Impact of off-design conditions in MOO of different nacelle lengths. Based on Schreiner et al.[18]. 46
2.24 Comparison of CFD and surrogate model prediction for nacelle drag in the as function of Mach number and MFCR. Two different nacelles geometries are shown. Solid and dashed lines represent the M_{DR}. A positive error of the surrogate prediction relative to the CFD data indicates an over-prediction of the surrogate model. Based on Heidebrecht et al.[184]. 47
2.25 Box plots showing the optimal design space for the design variables f_{max}, r_{max}/r_{hi} and f_{if} with the three MOO optimisation strategies compared: CFD-in-the-loop and both TM and AM surrogate-based approaches. Based on Tejero et al.[185]. 48

2.26 Pressure distribution for the initial design and the optimised non-axisymmetric nacelle design. $M_\infty = 0.8$, $MFCR = 0.75$ and $\alpha = 4°$. Based on Fang et al.[186]. 48
2.27 Mach number distribution (top) and axial Mach number distribution (bottom) at cruise condition ($M = 0.8$ and $\alpha = 5°$) for the baseline (left), candidate 1 for $L_{intk}/D_{fan} = 0.25$ (middle) and candidate 2 for $L_{intk}/D_{fan} = 0.19$ (right). Based on Peters et al.[189]. 50
2.28 Mach number distribution (top) and axial Mach number distribution (bottom) at maximum wing lift coefficient condition ($M = 0.25$ and $\alpha = 29°$) for the baseline (left), candidate 1 for $L_{intk}/D_{fan} = 0.25$ (middle) and candidate 2 for $L_{intk}/D_{fan} = 0.19$ (right). Based on Peters et al.[189]. 51
2.29 Mach contours for baseline and optimised designs at cruise and low lift conditions. Based on Saitoh et al.[192]. 53
2.30 Mach contours for baseline and optimised designs at cruise condition. and low lift conditions. Based on Saitoh et al.[192]. 54
2.31 Contours of pressure coefficient for baseline and optimised designs at cruise condition ($M = 0.785$ and $C_L = 0.52$). Inviscid CFD solutions. Based on Smith et al.[193]. 56
2.32 Comparison of distributions of pressure coefficient for the wing-body-nacelle-pylon optimised design between viscous CFD calculations and experimental PSP measurements at the cruise point ($M = 0.785$ and $C_L = 0.52$). Based on Smith et al.[193]. 57
2.33 Turbulent energy cascade and resolution levels with different CFD strategies. Based on Sagaut et al.[196]. 58
2.34 Challenges of the DES computational method. 60
2.35 Co-flow jet aerofoil technology. Based on Wang et al.[207]. 61
2.36 C_L against incidence for the CFJ0025-065-196 aerofoil between experiments and DES and RANS CFD calculations. Based on Wang et al.[207]. 61

3.1 Results overview. 67

4.1 Nacelle configurations assessed in this project. 70
4.2 Definition of the main components of an aero-engine. 71
4.3 Geometry definition of a non-axisymmetric nacelle in isolated configuration with left-right symmetry. 73
4.4 Definition of the installation position of the aero-engine in the NASA CRM airframe. 75
4.5 Definition of the installation angles of the aero-engine in the NASA CRM airframe. 76
4.6 Pylon design method and parameterisation. 77
4.7 Final pylon geometry (red) after a sectional trimming with the wing, the engine and the heatshield. 78
4.8 Nacelle installed in the Z30 rig in the ARA Transonic Wind Tunnel. Courtesy of ARA. 79

4.9 Schematic of the different computational fluid dynamics models used for each nacelle configuration. . . . 82
4.10 Schematics of the fluid domain and boundary conditions of the RANS CFD model for the 2D axi-symmetric nacelle in isolated configuration. 84
4.11 RANS mesh for the 3D isolated model and volumetric mesh refinements. . . . 85
4.12 Contours of y^+ on every wall surface for the RANS CFD model of the 3D isolated configuration. . . . 86
4.13 Schematics of the fluid domain and boundary conditions of the RANS CFD model for the 3D nacelle in isolated configuration. . . . 86
4.14 Schematics of the fluid domain and boundary conditions of the RANS CFD model for the nacelle in the configuration installed with the airframe. . . . 88
4.15 Contours of y^+ on every wall surface for the RANS CFD model of the 3D airframe-installed configuration. . . . 88
4.16 Surface mesh refinements for the RANS model of the 3D airframe-installed configuration. . . . 89
4.17 Volumetric mesh refinements for the RANS model of the 3D airframe-installed configuration. . . . 89
4.18 Schematics of the fluid domain and boundary conditions of the RANS CFD model for the nacelle in the configuration installed with the test rig. . . . 91
4.19 Details of the grid of the RANS CFD model for the nacelle in the configuration installed with the test rig. . . . 92
4.20 Details of the grid of the DDES CFD model for the nacelle in the configuration installed with the test rig. . . . 98
4.21 Turbulent energy cascade and tabulated grid sizes. Based on Gerasimov[224]. . . . 99
4.22 Schematic of the thrust and drag accounting method for an installed aero-engine with a separated-jet exhaust. . . . 100
4.23 Schematic of the farfield method for the drag extraction of the nacelle installed in the test rig. . . . 107
4.24 Schematic of the different optimisation approaches. . . . 110
4.25 Design variables used in the optimisation for the 2D axi-symmetric nacelle in isolated configuration. . . . 112
4.26 Schematics of hypervolume for a two-dimensional application. Based on Deb et al.[236]. . . . 114
4.27 Installed nacelle parameterisation. Design variables selected for nacelle design and optimisation marked in red. . . . 116
4.28 Comparison of isentropic Mach number (M_{is}) distributions between isolated and installed configuration for the different aero-lines. . . . 117
4.29 Artificial neural network model. . . . 121
4.30 Multi-fidelity neural network architecture. . . . 124

5.1 Nacelle installed in the Z30 rig in the ARA Transonic Wind Tunnel. Image courtesy of ARA. . . . 129

5.2 Coverage of experimental test points on the M - MFCR plane for the ANACO experimental campaign. While the black dots represent the operating points tested for the compact nacelle, the red dots denote the conditions measured for the conventional design. Fewer conditions were tested for the conventional nacelle due to budgetary constraints in the project. 130
5.3 Schematic of the different types of data measured on the ANACO experimental campaign. Based on Schreiner[247]. 131
5.4 Instrumentation on the ANACO compact nacelle installed in the Z30 test rig for the ANACO experimental campaign. Images courtesy of ARA. 133
5.5 Radial ($\hat{u}_r$) and azimuthal ($\hat{u}_\Psi$) experimental discretisation of the rakes for the farfield drag calculation. 134
5.6 Location of the 4 Kulites on the ANACO compact nacelle for the ANACO experimental campaign. Nacelle surface represented in an unwrapped manner. 134
5.7 Comparison of the nacelle drag coefficient as a function of the Mach number at the fixed cruise $\text{MFCR}_{cruise} = 0.7$ and incidence $\alpha_{eng} = 4.5°$ between RANS CFD and experiments for the ANACO compact and ANACO conventional nacelles. Based on Tejero et al.[246]. 136
5.8 Comparison of boundary layer profiles for rake arm aligned with the nacelle top aero-line between RANS CFD and experiments. Sensitivity to changes in the Mach number at the fixed cruise $\text{MFCR}_{cruise} = 0.7$ and incidence $\alpha_{eng} = 4.5°$. Based on Tejero et al.[246]. 136
5.9 Comparison of M_{is} distributions along the top aero-line of the nacelle between RANS CFD and experiments. Based on Tejero et al.[246]. . . . 137
5.10 RANS prediction of the ANACO compact nacelle aerodynamics for the windmilling end-of-runway-type of condition at $\alpha_{eng}^{crit} = 17.5°$, M = 0.25 and MFCR = 0.32. Fully separated flow represented through contours of pressure coefficient, a detached streamline and iso-surface of axial velocity (V_x) equal to 0 that shows the approximate boundary of separated flow. 139
5.11 DDES prediction of the ANACO compact nacelle aerodynamics for the windmilling diversion condition (M = 0.65, MFCR = 0.33 and $\alpha_{eng} = 4.5°$). Surface streamlines are used to identify the onset of the flow separation and iso-surfaces of Q-criterion represent the turbulent structures that appear in the flow. 139
5.12 Experimental measurements of the peak M_{is} in the top aero-line ($\Psi = 0°$) as a function of the nacelle incidence α_{eng} for the ANACO compact nacelle at the end-of-runway-type of condition (M = 0.25 and MFCR = 0.32). Effect of increasing and decreasing the incidence. 140
5.13 M_{is} distributions in the top aero-line ($\Psi = 0°$) of the ANACO compact nacelle at the end-of-runway-type of condition (M = 0.25 and MFCR = 0.32). Experimental measurements and RANS CFD predictions. The incidence is increased until flow separation at $\alpha_{eng}^{Exp.\ crit}$ (ramp-up). 141

5.14 Nacelle drag coefficient ($C_{D\,nac}$) as a function of the nacelle incidence (α_{eng}) for the ANACO compact nacelle at the end-of-runway-type of condition (M = 0.25 and MFCR = 0.32). Effect of increasing and decreasing the incidence. 142
5.15 Comparison between experiments and RANS CFD prediction of the M_{is} distribution on the top aero-line of the ANACO compact nacelle for the windmilling diversion condition measured in the test campaign (M = 0.64, MFCR = 0.35 and $\alpha_{eng} = 4.5°$). 143
5.16 Comparison of isentropic Mach number (M_{is}) distributions on the top and top-control aero-lines between steady/unsteady experiments and computational methods. Windmilling diversion condition: M = 0.64, MFCR = 0.35 and $\alpha_{eng} = 4.5°$ in experiments and M = 0.65, MFCR = 0.33 and $\alpha_{eng} = 4.5°$ in CFD. 144
5.17 Snapshots of axial component of wall shear stress on the surface of the ANACO compact nacelle predicted using the DDES CFD model for the windmilling diversion condition (M = 0.65, MFCR = 0.33 and $\alpha_{eng} = 4.5°$). 145
5.18 Sensitivity of nacelle drag coefficient and axial flow separation to changes in MFCR at windmilling diviersion-type of conditions (M = 0.65 and $\alpha_{eng} = 4.5°$). Comparison of RANS, URANS and DDES CFD predictions. 146

6.1 Aerodynamic comparison at cruise condition ($M = 0.85$, $MFCR = 0.7$, $C_L = 0.5$ and Alt = 10668m) through isentropic Mach distributions (M_{is}) for the ANACO compact nacelle in isolated and installed configurations. Installation position: $dx/C^{inst}_{wing} = 0.05$ and $dz/C^{inst}_{wing} = 0.1$. 148
6.2 Set of installation positions assessed. 149
6.3 Effect of the axial and vertical installation position on the nacelle drag, airframe drag, net propulsive force and net vehicle force for the ANACO compact nacelle installed in the airframe at the cruise condition ($M = 0.85$, $MFCR = 0.7$, $C_L = 0.5$ and Alt = 10668m). Metrics reported relative to their lowest value and as a percentage of the standard net thrust (F_N). 150
6.4 Contours of elemental pressure force in the drag direction for the ANACO compact nacelle installed in the airframe at the cruise condition ($M = 0.85$, $MFCR = 0.7$, $C_L = 0.5$ and Alt = 10668m). Pressure side of the wing and unwrapped nacelle surface. Impact of the vertical and horizontal installation position. 153
6.5 Effect of the axial and vertical installation position on the nacelle drag, airframe drag, net propulsive force and net vehicle force for the ANACO conventional nacelle installed in the airframe at the cruise condition ($M = 0.85$, $MFCR = 0.7$, $C_L = 0.5$ and Alt = 10668m). Metrics reported relative to their lowest value and as a percentage of the standard net thrust (F_N). 154

6.6 Effect of the axial and vertical installation position on the net vehicle force benefit of the ANACO compact configuration relative to the ANACO conventional configuration at the cruise condition (M = 0.85, $MFCR = 0.7$, $C_L = 0.5$ and Alt = 10668m). 156
6.7 Distributions of isentropic Mach number (M_{is}) in the inboard side of the nacelle to assess the impact of the axial installation position on the ANACO compact and ANACO conventional configurations at the cruise condition (M = 0.85, $MFCR$ = 0.7, C_L = 0.5 and Alt = 10668m). 156
6.8 Contours of x-component of the wall shear stress (x-WSS) and surface streak-lines for the windmilling diversion operating condition (M = 0.65, $MFCR = 0.33$, $C_L = 0.44$ and Alt = 6096m). ANACO compact and ANACO conventional nacelle designs. Installed configuration at the reference position $dx/C_{wing}^{inst} = 0.0$ and $dz/C_{wing}^{inst} = 0.1$. 158
6.9 Distributions of x-component of the wall shear stress (x-WSS) on the ANACO compact nacelle in isolated configuration at the windmilling diversion condition ($M = 0.65$, $MFCR = 0.33$, $\alpha_{eng} = 4.5°$ and Alt = 6096m). 159
6.10 Sensitivity of installation to MFCR for the ANACO compact and ANACO conventional nacelle designs for windmilling diversion-type of conditions (M = 0.65, C_L = 0.44 and Alt = 6096m). Installed configuration at the reference position $dx/C_{wing}^{inst} = 0.0$ and dz/C_{wing}^{inst} = 0.1. 161
6.11 Contours of elemental pressure force in the drag direction for the ANACO compact and ANACO conventional nacelle designs for windmilling diversion-type of conditions (M = 0.65, C_L = 0.44 and Alt = 6096m) in installed configuration. Contours shown for different MFCR showing separated and attached flow topologies. Reference installation position: $dx/C_{wing}^{inst} = 0$ and $dz/C_{wing}^{inst} = 0.1$. 162

7.1 Polar of the CRM aircraft with the ANACO compact nacelle at cruise-type of conditions ($M = 0.85$, $MFCR = 0.7$ and Alt = 10668m) using the different CFD fidelities: RANS, RANS with wall functions and Euler. 164
7.2 Contours of isentropic Mach number on the ANACO compact nacelle surfaces and pressure coefficient in the wing and pylon at the cruise condition (M = 0.85, $MFCR$ = 0.7, C_L = 0.5 and Alt = 10668m) using the different CFD fidelities: RANS, RANS with wall functions and Euler. 165
7.3 Comparison of isentropic Mach number distributions on the different aero-lines of the ANACO compact nacelle installed in the CRM airframe at the cruise condition (M = 0.85, $MFCR$ = 0.7, C_L = 0.5 and Alt = 10668m) using the different CFD fidelities: RANS, RANS with wall functions and Euler. 167

7.4 Comparison of pressure coefficient distributions on different wingspan sections (η) at the cruise condition ($M = 0.85$, $MFCR = 0.7$, $C_L = 0.5$ and Alt = 10668m) using the different CFD fidelities: RANS, RANS with wall functions and Euler. . . . 168
7.5 Comparison based on the performance metrics of the optimal design space for 2D axi-symmetric nacelles in isolated configuration obtained with the different CFD fidelities: RANS, RANS with wall functions and Euler. . . . 170
7.6 Comparison based on the design variables of the optimal design space for 2D axi-symmetric nacelles in isolated configuration obtained with the different CFD fidelities: RANS, RANS with wall functions and Euler. . . . 171
7.7 Comparison based on both the performance metrics and the design variables of the optimal design space for 2D axi-symmetric nacelles in isolated configuration obtained with the different CFD fidelities: RANS, RANS with wall functions and Euler. . . . 172

8.1 Optimal region of the design space for 2D axi-symmetric nacelles in isolated configuration using the CFD-based optimisation approach. . . . 176
8.2 Sensitivity of the optimal design space to changes in the design variables. Perturbations applied to the down selected design from the CFD-based optimisation ($RANS_{ds}$) of up to 40% of the investigated bounds. . . . 178
8.3 Multi-fidelity neural network architecture applied for the drag of a 2D axi-symmetric nacelle in isolated configuration. . . . 179
8.4 Hyperparameter sensitivity analysis based on the low-fidelity (Euler) ANN for the different operating conditions. Ratio of samples to degrees of freedom of $N_{LF}/N_{DOF} = 100$. Selected region of interest for hyperparameters marked with dashed black rectangle. . . . 181
8.5 Hyperparameter sensitivity analysis based on the low-fidelity (Euler) ANN for the different operating conditions. Ratio of samples to degrees of freedom of $N_{LF}/N_{DOF} = 12.5$. Selected region of interest for hyperparameters marked with dashed black rectangle. . . . 182
8.6 Impact of the number of low- and high-fidelity samples on the computational cost and RMSE of the MFNN surrogate model. . . . 183
8.7 Region of the optimal design space for 2D axi-symmetric nacelles in isolated configuration obtained with the surrogate-based optimisation approach for each combination of low- and high-fidelity samples of the MFNN technique. . . . 185
8.8 Cross-validation based on the optimal region of the design space (Prateo front) of the selected MFNN model ($N_{LF}/N_{DOF} = 50$ and $N_{HF}/N_{DOF} = 12.5$) by comparing the model prediction with the RANS CFD results. . . . 187
8.9 Pareto fronts and down selected designs from the optimisations of 2D axi-symmetric nacelles in isolated configuration using the CFD-in-the-loop and MFNN-based approaches. . . . 188

8.10 Comparison of the isentropic Mach number (M_{is}) distributions for the down selected designs using the CFD-in-the-loop and MFNN-based optimisation approaches for the cruise, ΔMach and end-of-cruise conditions. Aerodynamic obtained from a RANS CFD calculation. . . . 189
8.11 Installed nacelle parameterisation. Design variables considered in the design and optimisation method marked in red. 190
8.12 Design space exploration at the cruise condition ($M = 0.85$, $MFCR = 0.7$, $C_L = 0.5$ and Alt = 10668m) shown in terms of the performance metrics for different $N_{samples}/N_{DOF}$ using the Euler CFD fidelity. Positive values in every metric are benefits relative to the baseline design. 193
8.13 Design space exploration at the cruise condition ($M = 0.85$, $MFCR = 0.7$, $C_L = 0.5$ and Alt = 10668m) shown in terms of the design variables for different $N_{samples}/N_{DOF}$ using the Euler CFD fidelity. . . . 194
8.14 Comparison of the design space exploration at the cruise condition ($M = 0.85$, $MFCR = 0.7$, $C_L = 0.5$ and Alt = 10668m) in terms of performance metrics between the RANS$_T$ data set ($N_{samples}/N_{DOF} = 15$) and the Euler$_{T1}$ data set ($N_{samples}/N_{DOF} = 80$). Positive values in every metric are benefits relative to the baseline design. 196
8.15 Cross correlation at the cruise condition ($M = 0.85$, $MFCR = 0.7$, $C_L = 0.5$ and Alt = 10668m) based on $\Delta NVF/F_N$ between the Euler and RANS CFD fidelities for the RANS$_T$ data set of $N_{samples}/N_{DOF} = 15$. 197
8.16 Comparison of the design space exploration at the cruise condition ($M = 0.85$, $MFCR = 0.7$, $C_L = 0.5$ and Alt = 10668m) in terms of design variables between the RANS$_T$ data set ($N_{samples}/N_{DOF} = 15$) and the Euler$_{T1}$ data set ($N_{samples}/N_{DOF} = 80$). 197
8.17 Cross correlation between the Euler CFD results and the surrogate models prediction evaluated on the independent data set at the cruise condition ($M = 0.85$, $MFCR = 0.7$, $C_L = 0.5$ and Alt = 10668m). Kriging and ANN surrogate models for different $N_{samples}/N_{DOF}$ ratios. 200
8.18 Interrogation of the Kriging and ANN surrogate models for the different $N_{samples}/N_{DOF}$ around the baseline design for the pair $r_{max,90°}$ - $r_{max,135°}$ at the cruise condition ($M = 0.85$, $MFCR = 0.7$, $C_L = 0.5$ and Alt = 10668m). Contour of the model prediction of $\Delta NVF/F_N$ and also the difference of $N_{samples}/N_{DOF} = 20$ and 40 relative to $N_{samples}/N_{DOF} = 80$. 201
8.19 Comparison of performance and geometrical parameters of the optimised designs with each Kriging and ANN model. The designs with highest $\Delta NVF/F_N$ from each Euler DSE are also included. 203
8.20 Comparison of the aerodynamics at the cruise condition ($M = 0.85$, $MFCR = 0.7$, $C_L = 0.5$ and Alt = 10668m) between the baseline and design E1 using M_{is} distributions on the nacelle and wing. RANS CFD prediction. 204

8.21 Interrogation of the Kriging$_{Euler_{T1}}$ model ($N_{samples}/N_{DOF} = 80$) around the baseline design for different pairs of design variables at the cruise condition ($M = 0.85$, $MFCR = 0.7$, $C_L = 0.5$ and Alt = 10668m). . 205
8.22 $\Delta NVF/F_N$ benefits evaluated with the RANS CFD fidelity at the cruise condition ($M = 0.85$, $MFCR = 0.7$, $C_L = 0.5$ and Alt = 10668m) obtained from the optimisations with the RANS-based Kriging model and the different Euler-based Kriging models (red). The designs with highest $\Delta NVF/F_N$ from each Euler DSE are also included (black). 206
8.23 Interrogation of the Kriging$_{RANS_T}$ model ($N_{samples}/N_{DOF} = 15$) around the baseline design for different pairs of design variables at the cruise condition ($M = 0.85$, $MFCR = 0.7$, $C_L = 0.5$ and Alt = 10668m). . 207
8.24 Summary of single-fidelity and multi-fidelity surrogate models. . . . 209
8.25 Comparison of the design space gradients for $\Delta NVF/F_N$ at the cruise condition ($M = 0.85$, $MFCR = 0.7$, $C_L = 0.5$ and Alt = 10668m) obtained through interrogation around the baseline design with the single-fidelity models Kriging$_{RANS_T}$ and Kriging$_{Euler_{T1}}$ and the multi-fidelity models VCM1$_{Kriging}$ and VCM2$_{Kriging}$. Optimal design obtained with each surrogate model marked in the maps. 210
8.26 $\Delta NVF/F_N$ benefits evaluated with the RANS CFD fidelity at the cruise condition ($M = 0.85$, $MFCR = 0.7$, $C_L = 0.5$ and Alt = 10668m) for the optimal designs obtained with the single-fidelity models Kriging$_{RANS_T}$ and Kriging$_{Euler_{T1}}$ and the multi-fidelity models VCM1$_{Kriging}$ and VCM2$_{Kriging}$. 211

B.1 Grid refinement analysis for the Euler model for the 2D isolated nacelle configuration at cruise condition. 247
B.2 Effect of the grid refinement in the Euler CFD prediction across the 2D isolated nacelle design space. 247
B.3 Effect of grid refinement in the Euler CFD prediction across the installed nacelle design space 250
B.4 Grid refinement analysis for the RANS with wall functions model for the 2D isolated nacelle configuration at cruise condition. 252
B.5 Effect of the grid refinement in the RANS with wall fucntions CFD model prediction across the 2D isolated nacelle design space. 252
B.6 Effect of using wall functions to model the boundary layer in the RANS CFD prediction across the installed nacelle design space . . . 253

C.1 Comparison of different time steps for the URANS calculation at end-of-runway. Time signal and discrete Fourier transform. 257
C.2 Comparison of different time steps for the URANS calculation at windmilling diversion. Time signal and discrete Fourier transform. 259
C.3 Statistical convergence of the URANS calculation at end-of-runway based on the cumulative average and standard deviation of the drag coefficient. 260

C.4 Statistical convergence of the URANS calculation at windmilling diversion based on the cumulative average and standard deviation of the drag coefficient. . . . 261
C.5 Time signal of the drag coefficient at windmilling diversion predicted with the DDES CFD model. . . . 262
C.6 Cumulative average and standard deviation for the drag coefficient at windmilling diversion predicted with the DDES CFD model. . . . 262
C.7 Contours of the blending function for the DDES model for the nominal diversion condition at different sections of the model. . . . 263
C.8 Time signal and Fourier transform of a test function composed by the summation of two sinusoidal functions. . . . 264

D.1 MFNN prediction for the one-dimensional and linear correlation benchmark function. . . . 267
D.2 MFNN prediction for the one-dimensional and non-linear correlation benchmark function. . . . 268
D.3 MFNN prediction for the two-dimensional and linear correlation benchmark function. Black dots are low-fidelity training points, red dots are high-fidelity training points. . . . 270
D.4 MFNN prediction for the two-dimensional and non-linear correlation benchmark function. Black dots are low-fidelity training points, red dots are high-fidelity training points. . . . 271

E.1 Schematics of NSGA-II. Based on Deb et al.[232]. . . . 275
E.2 Crossover and mutation operations for the offspring generation. . . . 275
E.3 Blended BLX-α crossover operator. . . . 275
E.4 Pareto fronts for the different optimiser. The blue dot is the down selected design. . . . 278
E.5 Definition of the box plot used to represent the optimal design space for an optimisation using the designs contained in the Pareto data set. Example for f_{max} and NSGA-II. . . . 279
E.6 Optimal design space for every optimisation showed by box plots of the designs in the Pareto front. . . . 280
E.7 Comparative quantification of the convergence rate for each optimiser to meet the convergence criteria. . . . 282

List of Tables

2.1 Comparison of the advantages and disadvantages of the TFN and TPS engine models. . . . 18

4.1 Summary of the key nominal operating conditions considered in this project for isolated nacelle configurations. . . . 81
4.2 Summary of the key nominal operating conditions considered in this project for installed nacelle configurations. . . . 81
4.3 Summary of the operating conditions evaluated for each nacelle configuration with the different computational fluid dynamics models. . . . 82
4.4 Summary of the nacelle aerodynamic optimisations conducted in this project for the different configurations. . . . 110
4.5 Design variables for the installed nacelle design method. . . . 115
4.6 Correlation functions considered for the Gaussian Process Regression single-fidelity surrogate technique. . . . 119
4.7 Activation functions considered for the ANN single-fidelity surrogate technique. . . . 121

5.1 Summary of the instrumentation for the ANACO experimental campaign. . . . 132
5.2 Incidence of flow separation (α_{eng}^{crit}) and reattachment ($\alpha_{eng}^{reattach}$) and range of hysteresis ($\Delta\alpha_{eng}^{hyst}$) for the ANACO compact nacelle at the end-of-runway-type of condition (M = 0.25 and MFCR = 0.32). Comparison between RANS and URANS CFD predictions and experimental data. . . . 142

7.1 Design space bounds considered in the 2D axi-symmetric nacelle optimisations. . . . 169
7.2 Relative cost of the different CFD fidelities for airframe-installed nacelle assessments which involves both the grid generation and the CFD simulation. . . . 173

8.1 Relative cost of the different high-fidelity RANS and low-fidelity Euler CFD methods for 2D axisymmetric isolated nacelle assessments which involves both the grid generation and the CFD simulation. . . . 178

8.2 Drag benefit at every operating condition for the down selected designs from the CFD-in-the-loop and MFNN-based optimisations relative to an initial baseline design. Drag differences evaluated using RANS CFD for every case. 187
8.3 Summary of data sets from independent design space explorations for the proposed method for installed nacelle design. Both Euler and RANS CFD fidelities considered. LHS technique used for the sampling. 191
8.4 RMSE evaluated in an independent data set for the single-fidelity surrogate models generated for the different $N_{samples}/N_{DOF}$ Euler-based data sets at the cruise condition ($M = 0.85$, $MFCR = 0.7$, $C_L = 0.5$ and Alt = 10668m). Comparison of the Kriging and ANN modelling techniques. 199
8.5 Synthesis of the different single- and multi-fidelity models developed for the nacelle aerodynamic design and optimisation problem. The RMSE of the model evaluated in an independent data set and the overall cost associated to build the model are provided. The NVF benefits obtained from a surrogate-based optimisation using each model and evaluated with the RANS and Euler CFD models are included. . 212

B.1 Grid sensitivity study for the RANS model for the isolated 2D axisymmetric nacelle configuration at cruise condition. 243
B.2 Grid sensitivity study for the RANS model for the isolated 3D nacelle configuration at cruise and windmilling diversion conditions. 244
B.3 Grid sensitivity study for the RANS model for the nacelle installed in the airframe at cruise condition. 244
B.4 Grid sensitivity study for the RANS model for the nacelle installed in the airframe at windmilling diversion condition. 245
B.5 Grid sensitivity study for the RANS model for the nacelle installed in the test rig configuration at cruise condition. 245
B.6 Grid sensitivity study for the Euler model for the isolated 2D axisymmetric nacelle configuration at cruise condition. 246
B.7 Grid sensitivity study for the Euler model for the nacelle installed in the airframe at cruise condition. 248
B.8 Grid sizes and associated relative computational costs for the Euler model for the nacelle installed in the airframe at cruise condition. . . 248
B.9 Grid sensitivity study for the RANS with wall functions model for the isolated 2D axisymmetric nacelle configuration at cruise condition. 251

D.1 Network architecture and hyperparameters for the MFNN model used to verify the one-dimensional and linear correlation benchmark function. 266
D.2 Network architecture and hyperparameters for the MFNN model used to verify the one-dimensional and non-linear correlation benchmark function. 268
D.3 Network architecture and hyperparameters for the MFNN model used to verify the two-dimensional and linear correlation benchmark function. 269

D.4 Network architecture and hyperparameters for the MFNN model used to verify the two-dimensional and non-linear correlation benchmark function. 272

E.1 Statistical comparison between IBEA and OMOPSO relative to NSGA-II for the designs with minimum drag at each operating condition. . . 279
E.2 Statistical comparison between IBEA and OMOPSO relative to NSGA-II for the variability of the drag performances of the down selected designs. 281
E.3 Statistical comparison between IBEA and OMOPSO relative to NSGA-II for the variability of the design variables of the down selected designs. 281

Nomenclature

Abbreviations

ANACO Advance Nacelle Aerodynamics Optimisation

ANN Artificial Neural Networks

ARA Aircraft Research Association

BPR Bypass Ratio

CFD Computational Fluid Dynamics

CFL Courant-Friedrichs-Lewy

CNPR Core Nozzle Pressure Ratio

CRM Common Research Model

CST Class-Shape Transformation functions

CU Cranfield University

CV Control Volume

DDES Delayed Detached-Eddy Simulation

DES Detached-Eddy Simulation

DNS Direct Numerical Simulation

DPW Drag Prediction Workshop

DSE Design Space Exploration

FFD Free Form Deformation

FNPR Fan Nozzle Pressure Ratio

GA Genetic Algorithm

GBM Gradient Based Methods

GCI Grid Convergence Index

GFM Gradient Free Methods

GPF Gross Propulsive Force

HF High-Fidelity

HV Hypervolume

IBEA Indicator Based Evolutionary Algorithm

iCST intuitive Class-Shape Transformation

LES Large Eddy Simulation

LF Low-Fidelity

LHS Latin Hypercube Sampling

MF Multi-Fidelity

MFCR Mass Flow Capture Ratio

MFNN Multi-Fidelity Neural Networks

MOO Multi-Objective Optimisation

NPF Net Propulsive Force

NPR Nozzle Pressure Ratio

NSGA-II Non-dominated Sorting Genetic Algorithms - II

NVF Net Vehicle Force

OMOPSO Reyes-Coello Multi-Objective Particle Swarm Optimiser

PSO Particle Swarm Optimiser

RANS Reynolds Averaged Navier-Stokes

RBF Radial Basis Functions

RMSE Root Mean Square Error

SF Single-Fidelity

SFC Specific Fuel Consumption

SFNN Single-Fidelity Neural Networks

SGS Sub-Grid Scale

SLSQP Sequential Least Squares Programming

SQP Sequential Quadratic Programming

SST Shear Stress Transport

TDA Thrust and Drag Accounting

TFN Through-Flow Nacelle

TPS Turbine-Powered Simulator

UHBPR Ultra High Bypass Ratio

URANS Unsteady Reynolds Averaged Navier-Stokes

VCM Variable Complexity Model

Z30 Test rig at the Aircraft Research Association

ZDES Zonal Detached-Eddy Simulation

Greek Symbols

α	Incidence angle	[°]
$\alpha_{aircraft}$	Aircraft angle of attack	[°]
α_{eng}	Nacelle angle of attack	[°]
$\delta\alpha$	Incidence hysteresis range	[°]
δt	Time step	[s]
δx	Grid size	[m]
η	Wing span section	[-]
γ	Rate of specific heats	[-]
ω	Specific turbulence dissipation rate	[1/s]

ω	Turbulence kinetic energy	[J/kg]
ϕ	Wall force on the drag domain	[N]
Ψ	Azimuthal coordinate	[°]
ρ	Density	[kg/m^3]
σ	Standard deviation	[-]
τ	Shear stress	[Pa]
θ	Wall force in the thrust domain	[N]
θ_{pitch}	Installation pith angle	[°]
θ_{toe}	Installation toe angle	[°]

Roman Symbols

β_{nac}	Nacelle boat-tail angle	[°]
δ_{offset}	Intake offset	[m]
$\dot{m}$	Mass flow	[kg/s]
$\hat{n}$	Normal vector	[-]
$\hat{u}$	Unitary vector	[-]
μ	Fluid dynamic viscosity	[kg/m s]
θ_{scarf}	Nacelle scarf angle	[°]
A_{th}	Intake throat area	[m^2]
C_D	Drag coefficient	[-]
C_L	Lift coefficient	[-]
C_P	Pressure coefficient	[-]
C_V	Velocity coefficient	[-]
C_{wing}	Wing chord	[m]
$D_{a/f}$	Airframe drag	[N]
D_{fan}	Fan diameter	[m]

D_{Form}	Form drag component	[N]
$D_{Friction}$	Friction drag component	[N]
$D_{Induced}$	Induced drag component	[N]
d_{max}	Nacelle maximum diameter	[m]
D_{nac}	Nacelle drag	[N]
$D_{Profile}$	Profile drag component	[N]
$D_{Spillage}$	Spillage drag	[N]
D_{tot}	Total aircraft drag	[N]
D_{Wave}	Wave drag component	[N]
F_G	Gauge stream force	[N]
f_{if}	Non-dimensional nacelle initial forebody radius	[-]
f_{max}	Non-dimensional axial location of the nacelle maximum radius	[-]
F_N	Standard nominal net thrust	[N]
L	Lift force	[N]
L/D	Lift-to-drag ratio	[-]
L_{intk}	Intake length	[m]
L_{nac}	Nacelle length	[m]
R	Universal gas constant for ideal gases	[J/kg K]
r_{hi}	Nacelle highlight radius	[m]
r_{if}	Nacelle initial forebody radius	[m]
r_{max}	Nacelle maximum radius	[m]
R_{rake}	Rake radius of the Z30 test rig	[m]
r_{te}	Nacelle trailing edge radius	[m]
S	Side force	[N]
T	Thrust force	[N]

T_{ref}	Reference computational overhead	[-]
y^+	Non-dimensional wall distance	[-]
M	Mach number	[-]
M_{DR}	Drag rise Mach number	[-]
M_{is}	Isentropic Mach number	[-]
M_{peak}	Peak Mach number	[-]
N	Number of samples	[-]
P	Total pressure	[Pa]
p	Static pressure	[Pa]
q	Dynamic pressure	[Pa]
Re	Reynolds number	[-]
T	Total temperature	[K]
t	Static temperature	[K]
U	Velocity	[m/s]

Subscripts

$()^*$	Modified definition of forces
$()^{a/c}$	Relative to the aircraft
$()^{a/f}$	Relative to the airframe
$()^{cirt}$	Relative to the critical condition of flow separation
$()^{cycle}$	Relative to the cycle
$()^{eng}$	Relative to the engine
$()^{FF}$	Relative to a farfield drag extraction approach
$()^{ideal}$	Relative to the ideal conditions
$()^{NC}$	Non corrected definition
$()^{NF}$	Relative to a nearfield drag extraction approach

$()^{reattach}$ Relative to the flow reattachment condition

$()_\infty$ Relative to the freestream

$()_D, ()_S, ()_L$ Relative to drag, side or lift coordinates in the aerodynamic reference frames

$()_x, ()_y, ()_z$ Relative to x, y or z coordinates in the engine or airframe reference frames

$()_{\delta M}$ Relative to the increased Mach number condition

$()_{Cruise}$ Relative to the cruise condition

$()_{Diversion}$ Relative to the windmilling diversion condition

$()_{ds}$ Relative to a down selected design

$()_{EoC}$ Relative to the end-of-cruise condition

$()_{HF}$ Relative to the high-fidelity model

$()_J$ Relative to the Jone's plane

$()_{LF}$ Relative to the low-fidelity model

$()_{nac,aft}$ Relative to the afterbody nacelle surface

$()_{nac,fore}$ Relative to the forebody nacelle surface

$()_{nac}$ Relative to the nacelle surface

$()_{nominal}$ Relative to the experimental nominal condition

$()_{paral.Sting}$ Relative to the parallel sting surface of the Z30

$()_{post}$ Relative to the post-exit streamtube

$()_{pre}$ Relative to the pre-entry streamtube

$()_{prof.Sting}$ Relative to the profile sting surface of the Z30

$()_{twt}$ Relative to the transonic wind tunnel

$()_{wf}$ Relative to the CFD model with wall functions

$()_{wing}$ Relative to the wing of the aircraft

CHAPTER 1

Introduction

1.1 Background

The civil aviation market has extraordinarily grown in the last decades. Before the Covid-19 outbreak, the air traffic was expected to increase at an averaged rate of 3.7% by 2036[1]. However, the pandemic drastically affected the air transportation industry[2]. Relative to the traffic levels of the pre-pandemic year, the world total passengers declined by -60%, -50% and -30% for 2020, 2021 and 2022 respectively[3]. Nevertheless, a full recovery of the market to the levels of 2019 is expected for 2024[4]. In this respect, fuel consumption is one of the key concerns in the commercial aviation industry. The interest of reducing fuel consumption is twofold. On the one hand, the environmental emissions is a pressing issue to address. The European Commission FlightPath 2050 vision[5] requires, relative to year-2000 aircraft technology, a reduction of 75% and 90% in CO2 and NOx emissions respectively. In addition, airlines can generate greater revenue benefits by operating more efficient aircraft. For modern long-range and wide-body transports, the fuel costs account for approximately 30% of the overall operating costs[6].

From a propulsion system point of view, the reduction in fuel consumption to deliver a certain amount of thrust is achieved by the improvement of the specific fuel consumption (SFC) and the propulsive efficiency of the aero-engine[7]. In order to keep the same thrust level the engine mass flow increases and this typically requires a larger fan size and a higher bypass ratio (BPR) which is the current trend for turbofan-type of engines (Figure 1.1). However, there is not a linear trend between fuel consumption and fan size. The reason is that larger fan diameters may increase the overall contribution to the aircraft drag and weight[8] which can offset the new

engine cycle benefits (Figure 1.2). Additionally, ground clearance constraints force the installation to become more close-coupled with the airframe which increases the aerodynamic interference effects[9]. For a commercial wide-body twin-engine aircraft the overall effect of the aero-engines installation can reach up to 15% of the total aircraft drag[10]. The key contributors to the installed propulsion system drag are the nacelle profile drag and interference drag[8]. Consequently, it may be possible to gain overall aircraft performance benefits by the design of more compact nacelles. For example, a reduction of 1% in nacelle drag at cruise is estimated to provide a reduction in fuel consumption of 0.08%.

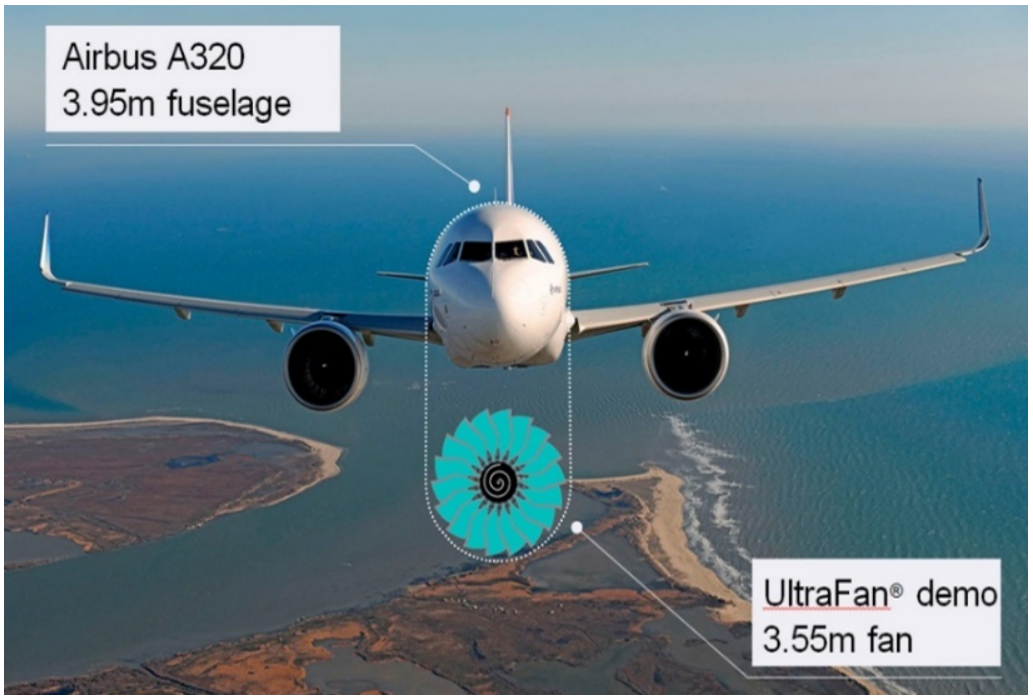

FIGURE 1.1: Trend of aero-engine fan size[11].

Traditionally, design methods for aero-engine nacelles have focused on drag minimisation in an isolated configuration[13–16]. However, aerodynamic characteristics of the nacelle in installed configuration can be substantially different from the isolated case due to the integration effects with the airframe[8,9]. Therefore, modern design technologies need to consider the design space of the aero-engine coupled with the airframe[17]. Additionally, one of the challenges of compact nacelle design is the high sensitivity to important off-design conditions[18]. Therefore, the different flow conditions that arise throughout the aircraft mission have to be considered to achieve aerodynamic robust designs. In addition to mid-cruise operation, the sensitivities to off-design windmilling conditions have to be considered[18,19]. This leads to multi-objective multi-point optimisation approaches.

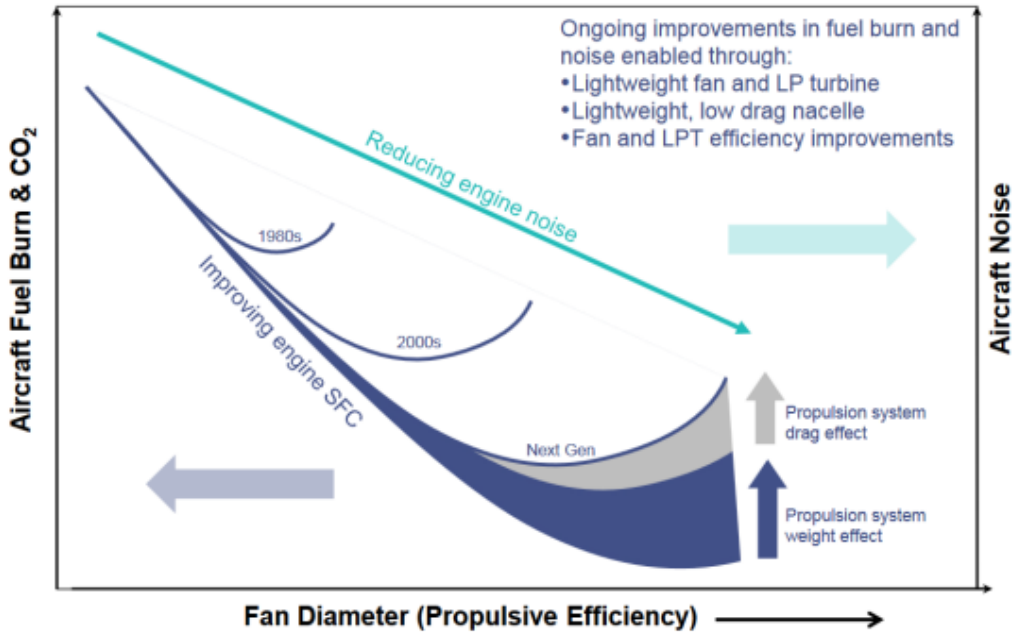

FIGURE 1.2: Fuel and noise efficiency against fan size of the aero-engine[12].

Overall, the aerodynamic design and optimisation of compact nacelles is a complex problem governed by a high number of design variables, transonic non-linear flow physics and time consuming computational methods. Additionally, the larger interference effects of UHBPR aero-engines with the airframe leads to design and optimisation processes that consider the coupled design space of the engine-airframe system which further increases the computational overhead. Although inviscid computational methods have traditionally been used for aerodynamic integration assessments, the closer-coupled installation of UHBPR engines may lead to viscous flow physics like shock-boundary layer interaction and flow separation. Therefore, higher fidelity methods which are acceptable from an industrial time scale may be needed for the nacelle design in installed configuration.

1.2 Research aim and objectives

1.2.1 Overall aim

The main aim is to develop a viable computational approach using multi-fidelity modelling methods for nacelle aerodynamic design and optimisation in installed configurations. In this work, the term fidelity refers to the level of accuracy in modelling the real physics of the problem in-hand and while a RANS CFD model

is considered as high-fidelity both Euler and RANS with wall functions models are used as low-fidelity.

1.2.2 Objectives

The research aim is achieved through the following objectives:

- To assess the fundamentals of nacelle aerodynamics and the benefits of compact nacelles relative to conventional designs through a set of multi-point multi-objective optimisations.
- To evaluate the aerodynamic integration effects between the aero-engine and the airframe and to quantify the impact on the nacelle aerodynamics and the overall system performance. Understand the sensitivities of different installation positions and nacelle sizes.
- To develop a method for aerodynamic nacelle design in installed configuration that combines different levels of Computational Fluid Dynamics (CFD) fidelities. This involve the use of a surrogate modelling technique.
- To assess higher fidelity computational methods for the evaluation of nacelle aerodynamics under off-design conditions including unsteady aerodynamic analyses. This will provide an understanding of the validity of steady CFD methods for multi-point multi-objective nacelle optimisations.
- To validate the CFD methods for nacelle design and optimisation in isolated configuration using experimental data.
- Where appropriate, to integrate new design and analysis capabilities into the Cranfield tool-sets for nacelle design.

CHAPTER 2

Literature review

This chapter provides the reader with an understanding of previous work related to the aerodynamic optimisation of aero-engine nacelles. Section 2.1 gives an overview of the aerodynamics, drag performance and design considerations of aero-engine nacelles. Section 2.2 provides an understanding of the aerodynamic integration effects between the aero-engine and the airframe. Section 2.3 covers the challenges of the aerodynamic shape optimisation problem in a broader sense, with a review of different optimisation algorithms, surrogate modelling techniques and multi-fidelity approaches developed for this purpose. It also discusses previous work conducted for aero-engine nacelle aerodynamic optimisation both in isolated and installed configuration. Finally, Section 2.4 addresses key work conducted for aerodynamic applications using unsteady high fidelity CFD models which is related in this thesis to off-design nacelle assessments.

2.1 Aerodynamics and performance of nacelles

The nacelle of an aero-engine is composed of the intake and the fan-cowl (Figure 2.1). The intake design is a complex problem as it has to meet a wide range of requirements for the aero-engine. The intake has to deliver a specific mass flow to the fan at a certain Mach number and with acceptable flow distortion and intake total pressure loss. Similarly, the fan-cowl not only is designed to minimise the drag contribution of the propulsion system to the aircraft but also has to integrate with the intake a allow acceptable aerodynamics at off-design conditions like cross-wind or take-off. Consequently, intakes and fan-cowls must be designed with common knowledge to meet both sets of requirements[19]. For example, while the highlight

sizing from the intake affects the fan-cowl design, the forebody of the fan-cowl also affects the aerodynamic performance of the intake at cross-wind. This research is focused on the design and optimisation of the fan-cowl which hereafter will be referred as nacelle.

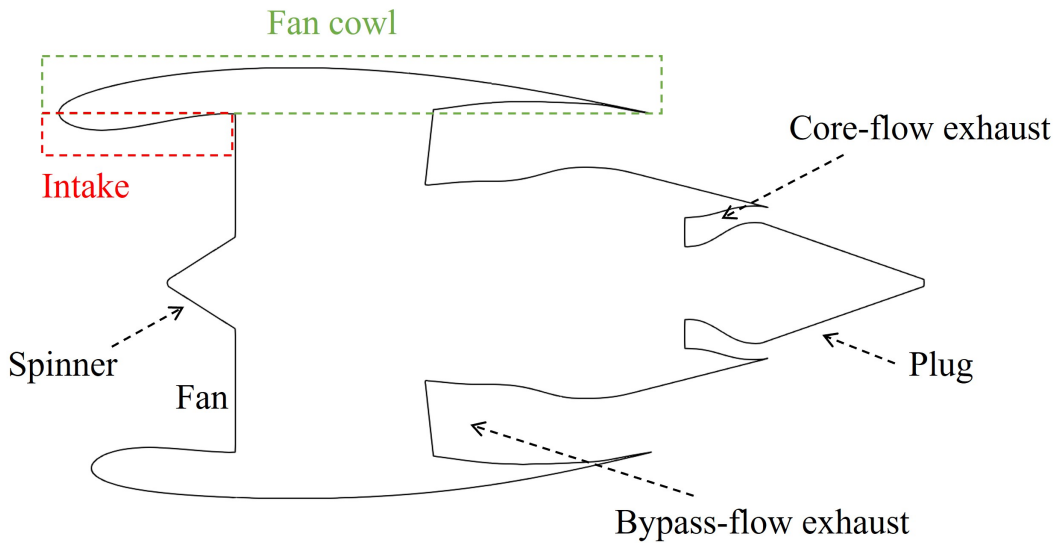

FIGURE 2.1: Definition of the nacelle geometry within the power plant system.

2.1.1 Nacelle aerodynamics and drag

The nacelle aerodynamic design problem is essentially based on the need to minimise drag. It is subjected to many considerations due to the multiple operating conditions that are present in the flight envelope that impact the contribution of the different drag components of the nacelle. The overall drag is broadly divided into friction drag ($D_{Friction}$), the form drag (D_{Form}), the wave drag (D_{Wave}) and the induced drag ($D_{Induced}$) (Equation 2.1)[20].

$$D_{nac} = \underbrace{D_{Friction} + D_{Form}}_{D_{Profile}} + D_{Induced} + D_{Wave} \tag{2.1}$$

$D_{Friction}$ and D_{Form} arise from viscous phenomena and the combination of both results on the profile drag ($D_{Profile}$)[21]. Therefore, the profile drag, also known as parasitic drag, is always present on a object that is moving in a viscous flow. $D_{Friction}$ is the skin friction over the surface of the nacelle moving in a viscous flow. It is affected not only by the surface and gas properties but also the laminar or

turbulent nature of the boundary layer. This term dominates D_{nac} for conditions with mostly attached flows. $D_{Friction}$ is directly related to the overall nacelle area. For UHBPR aero-engine configurations at cruise, this term is the dominant and can reach to around 60% of the overall D_{nac}[22]. On the other hand, D_{Form} comes from the change in the pressure distribution over the nacelle due to the growth of the boundary layer. This is the leading drag term for highly separated flows. The Reynolds number and flow transition from laminar to turbulent boundary layer are key aspects for $D_{Profile}$. While a laminar boundary layer reduces the skin friction coefficient relative to a turbulent boundary layer, the laminar flow is more prone to flow separation which increases D_{Form}[23].

Conversely, $D_{Induced}$ and D_{Wave} are considered as purely pressure drag terms. $D_{Induced}$ is the lift-induced drag component and comes from the pressure distributions over the fan-cowl. D_{Wave} is strongly related to the changes in the aerodynamics associated to transonic and supersonic flight velocities[21]. At these conditions, the flow around the forebody of the nacelle accelerates to supersonic conditions which terminate in a shock wave and a contribution to the drag. As the free stream Mach number increases (M_∞), the peak Mach number (M_{peak}) and the shock strength increase which is translated in a greater D_{Wave}. For transonic aerodynamic applications, the sensitivity of changes in the flight Mach number on the drag is considered by the drag rise Mach number (M_{DR})[24]. This is the Mach number at which the nacelle drag experiences a rapid increase with M_∞. This parameter is typically defined using the gradient of the drag with the flight Mach number (Equation 2.2) and reported values are 0.1[25] or 0.05[26]. Roskam[25] also proposed a method based on an increase in the drag coefficient of 0.002 relative to the incompressible C_D. From a nacelle design standpoint, a common practice is to maintain a margin between the cruise Mach number (M_{cruise}) and M_{DR} of 0.02[27,28]. This wave drag contribution can be reduced by long and thin nacelles that are designed for a curvature driven acceleration on the forebody followed by an isentropic deceleration of the flow[29]. These geometries are typically characterised by high curvature gradients in the leading edge of the forebody which challenges the aerodynamic performance of the nacelle at off-design conditions governed by low engine mass flows[21]. For these engine conditions a key contributor to the nacelle drag is the spillage ($D_{Spillage}$). To describe spillage is necessary to introduce the concept of the aero-engine pre-entry streamtube. It comes from the thrust and drag accounting method used for nacelle drag[20] and defines the control volume from the farfield to the engine fan-face (Figure 2.2). Based on this pre-entry streamtube, the mass flow capture ratio (MFCR) is the ratio between the cross sectional area of the pre-entry streamtube at the farfield

and at the nacelle highlight location (Equation 2.3). This definition of the MFCR is independent of the location of the flow stagnation point in the nacelle which is affected by the operating condition and the mass flow through the engine. These are considered in the MFCR in the A_∞ term. Spillage can be understood as the increase in drag associated to a change in MFCR from MFCR = 1 which is used as reference for $D_{Spillage} = 0$. A reduction in the MFCR below 1 moves the stagnation point of the incoming flow from the highlight to the intake. This results in an higher suction in the nacelle forebody as the flow accelerates over the cowl lip. Therefore, the magnitude of the forebody force ($\phi_{nac,fore}$) acting in a forward direction between the highlight and the nacelle maximum radius is increased (Figure 2.2). In a potential flow formulation $\phi_{nac,fore}$ would be balanced with the rearwards force acting in the pre-entry streamtube (ϕ_{pre}) (Figure 2.2). In the same manner $\phi_{post} = \phi_{nac,aft}$. The reason is that the nacelle can be considered as an infinite body and in potential flow the nacelle drag is zero as it results from the integration of the forces from the upstream infinity to downstream infinity planes[30]. However in a real viscous flow this does not apply and ϕ_{pre}-$\phi_{nac,fore}$ results in a positive drag which is the spillage[31]. For aggressive conditions with very low MFCR, supersonic conditions with strong shock waves may be reached in the forebody due to the large flow suction in the nacelle highlight. Depending on the strength of the shock, shock-induced flow separation may happen. This shows that spillage flow conditions also increase other drag components like $D_{Profile}$ and D_{Wave}. Typical engine operation points with high impact of spillage are the off-design windmilling conditions. In the event of an engine failure the fan rotates freely and the mass flow can be reduced to values of around MFCR = 0.3[32]. Apart from internal loses[33], the drag increases by a factor of approximately 3 relative to the cruise condition[34]. A lower curvature in the forebody of the nacelle through an increase in the r_{if} can improve the aerodynamic performance at these windmilling conditions[21]. However, this would result in poor performance at a high Mach number condition due to the increase in flow suction close to the nacelle crest which would lead to the early formation of a shock wave. Additionally, the profile drag for these thicker nacelles would also increase due to the higher wetted and frontal area. This highlights how the design of the fan cowl geometry is often a compromise to satisfy different requirements.

$$\left.\frac{\partial C_D}{\partial M_\infty}\right|_{M_{DR}} = 0.1 \tag{2.2}$$

$$MFCR = \frac{A_\infty}{A_{hi}} \tag{2.3}$$

2.1.2 Drag extraction methods

Different force extraction methods are available depending on the complexity and amount of information available. They can be divided into two main branches: momentum-based and energy-based methods. Momentum-based approaches have traditionally been used for many drag extraction problems. The general definition of the drag for a certain body and flight velocity (U_∞) comes from the application of the integral momentum balance in steady state (Equation 2.4)[35,36]. The body is assumed inside a closed volume (Ω) surrounded by a set of surfaces (S). The momentum term is composed of the fluid density (ρ), the velocity vector (u) and the surface normal vector ($\hat{n}$). The pressure term is calculated through the normal area contribution of the pressure (p) relative to the farfield static pressure (p_∞). The friction force is computed using the shear stress tensor (τ). If the overall control volume surface is decomposed into the body surfaces (S_{Body}) and the streamtube bounding surfaces (S_{Bounds}) and a tangential flow is considered in the body walls ($u \cdot n = 0$), two analogous expressions for the aerodynamic force (F) exerted on the body can be obtained (Equation 2.5). Assuming the coordinate system aligned with the freestream velocity, the drag force results as the x-component of F. From Equation 2.5 the drag can be computed using a nearfield or a farfield approach: (a) from the body perspective through the integral of the pressure and shear stresses on the solid surface (nearfield method) and (b) from the fluid flow perspective through the momentum flux balance on the outer boundaries of the domain (farfield method). This is an outcome of the third law of Newton as the force on the body due to the fluid flow is opposite to the force imposed by the body on the fluid flow.

$$\int_S \left[\rho U_\infty u\hat{n} + (p - p_\infty)\,\hat{n} - \tau\right] \cdot dS = 0 \tag{2.4}$$

$$F = \underbrace{\int_{S_{Body}} \left[(p - p_\infty)\,\hat{n} - \tau\right] dS}_{Nearfield} = \underbrace{-\int_{S_{Bounds}} \left[\rho U_\infty u\hat{n} + (p - p_\infty)\,\hat{n} - \tau\right] dS}_{Farfield} \tag{2.5}$$

The nearfield methodology calculates independently the pressure and friction drag terms. However the pressure term may include contributions from different physical phenomena like boundary layer displacement, shock waves or trailing edge vortices. A nearfield drag extraction method does not allow a breakdown of these pressure terms[37]. The grid resolution, turbulence model and laminar to turbulent boundary

layer transition are key aspects for nearfield methods. They can affect the pressure and shear stress integration and can cause numerical dissipation and spurious drag terms[36]. Nearfield methods for CFD-based drag extraction are common for nacelle drag applications[20,21,38,39]. They are based on the AGARD[20] industrial practices that provides a thrust and drag bookkeeping approach to evaluate the overall performance of the nacelle (details in Section 4.4.1).The accounting system considers a pre-entry and post-exit streamtubes to bound the flow that goes through the aero-engine (Figure 2.2). While the pre-entry streamtube extends from the upstream farfield to the fan face of the engine, the post-exit streamtube spans from the bypass nozzle exit to the downstream farfield. A breakdown of the forces of the method defines the nacelle drag as the summation of the force on the cowl (ϕ_{nac}) and on the outside of the pre-entry (ϕ_{pre}) and post-exit (ϕ_{post}) streamtubes (Figure 2.2, Equation 2.6). The application of the nearfield method to compute the nacelle drag requires the identification of the flow stagnation point in the leading edge. This is a difficult task for 3D streamtubes and adds an additional source of error which depends on the grid refinement level. This can be overcome by the modified nearfield method[40] which computes the combined $\phi_{pre} + \phi_{nac}$ term. The surface forces from the nacelle trailing edge to the fan face are integrated and then corrected by the subtraction of the gauge stream forces between the upstream infinity plane and the fan face and the wall forces in the spinner (Section 4.4.1).

$$D_{nac} = \phi_{pre} + \phi_{nac} + \phi_{post} \tag{2.6}$$

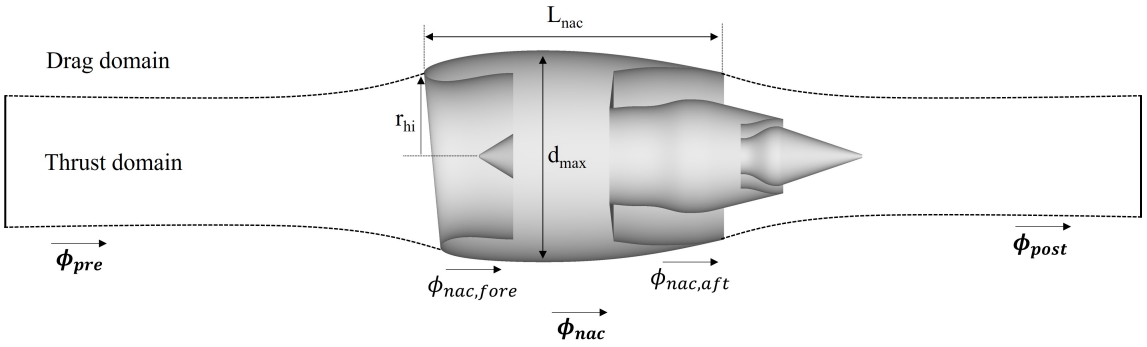

FIGURE 2.2: Definition of the aero-engine thrust and drag domains and nacelle main geometrical parameters.

A farfield approach evaluates the forces acting on a body through the integral of the momentum in the boundaries of the control volume. Different from the nearfield methodology, a farfield method allows a breakdown of the drag into its physical components: viscous drag, wave drag and induced drag[38]. However, the finer grid

resolution needed downstream of the body increases the computational overhead compared to nearfield methods. Some farfield approaches benefit from the reversibility nature of each drag component to extract them[41]. While the viscous and the wave drag come from irreversible processes, the induced drag is an exchange of energy and therefore reversible. This is a complex approach that combines the entropy and enthalpy thermodynamic variables with the equation of state of the flow. This formulation requires an integration over a large area to properly capture all the pressure and momentum flux contribution to the drag[35]. The wake integral method is another typology of farfield approach that calculates the drag based on the momentum loss measured in the wake plane[42]. This wake plane is place sufficiently downstream to ensure no further change in the total pressure. This method is commonly used for wind tunnel applications as total pressure readings can be easily obtained in the wake plane[43,44]. In the context of nacelle design, the wake farfield method has been used for the validation of the CFD methods by comparing against experimental data[45].

As an alternative to conventional momentum-based approaches different energy-based methods have emerged[46,47]. They provide a higher level of information relative to momentum-based formulations at the expense of an increase in the complexity. Energy-based methods rely on the integral energy balance in a closed control volume that encloses the body of interest. The different sources of energy and irreversibilities that affect aerodynamic performance of the body can be identified with these methods. Two formulations can be found: (a) power balance methods[48] and (b) Exergy analysis methods[49]. The greatest advantage of energy-based approaches is that a thrust-drag split is not needed which makes them very useful for the performance assessment of novel aircraft configurations with embedded propulsion system in the airframe. However, for the nacelle design problem such methods are not needed and simpler approaches based on momentum-based methods are more appropriate.

2.1.3 Nacelle design philosophies

For UHBPR aero-engines configurations the skin friction becomes the dominant nacelle drag component due to the large nacelle wetted surface[8] which can account from 60% to 70% of the total drag[22]. Different nacelle design philosophies can be followed depending on the ratio of the two main nacelle design drivers: the maximum diameter (d_{max}) and the overall length (L_{nac}) (Figure 2.2). The maximum diameter is typically fixed or limited by multi-disciplinary constraints like engine

size, subsystems fitting and clearance requirements. This leaves L_{nac} as the defining parameter for the nacelle compactness.

A design approach for this kind of engine configurations is based on compact nacelle designs. These are given by low L_{nac}/d_{max} values. The reduction in L_{nac} decreases the overall nacelle wetted area and therefore the skin friction drag component. However, the high surface curvature gradients associated to very low L_{nac}/d_{max} configurations magnify the rapid acceleration and de-acceleration that the flow undergoes[8] which increases the wave drag component. Consequently, there is a limit in the reduction of L_{nac}/d_{max} when the total nacelle drag is considered (Figure 2.3) which can change depending on the fan diameter[8]. Although L_{nac}/d_{max} defines the overall compactness of the fan-cowl, L_{nac}/r_{hi} is the typical non-dimensional ratio used for the nacelle design problem, where r_{hi} is the highlight radius (Figure 2.2). The benefit of L_{nac}/r_{hi} is that this parameter links the fan-cowl with the intake as r_{hi} is normally determined from the intake contraction ratio $CR = A_{hi}/A_{th}$[50], where A_{hi} and A_{th} are the highlight and intake throat area respectively. For long-range applications of flight Mach number approximately 0.85, while conventional nacelles configurations have L_{nac}/r_{hi} above 3.6[14,27], compact architectures reduce this parameter to $L_{nac}/r_{hi} < 3.1$[51,52]. This design technology has proven benefits in cruise drag reduction of 1.6% of the standard net thrust for a compact nacelle $L_{nac}/r_{hi} = 3.1$ relative to a conventional baseline $L_{nac}/r_{hi} = 3.6$ in isolated configuration[19]. However, the high surface curvature gradients of compact nacelles increase the sensitivity of these designs to off-design operating conditions. Therefore, multi-point approaches and trade-offs have to be considered within the nacelle design and optimisation process to minimise the overall drag and achieve robust designs at off-design conditions[18,19]. This aerodynamic robustness for off-design conditions comes with a substantial penalty in the cruise benefit. For example, while a reduction in the cruise drag of 15% could be achieved by shortening the nacelle from $L_{nac}/r_{hi} = 4.3$ to 3.1, this benefit decreased to 10% when off-design conditions were considered in the optimisation process[18]. Overall, in the installed configuration of the aero-engine in the airframe, these compact designs can provide benefits of up to 1% fuel burn reduction at cruise[53,54]. Section 2.3.4 will provide further details of the aerodynamic shape optimisation problem applied for compact nacelles both in isolated and installed configurations.

A different design technology is based on laminar flow nacelles. This is based on the fact that for the same Reynolds number a laminar boundary layer reduces the friction drag by a factor of 10 relative to the turbulent case[55]. During the 1990s and early

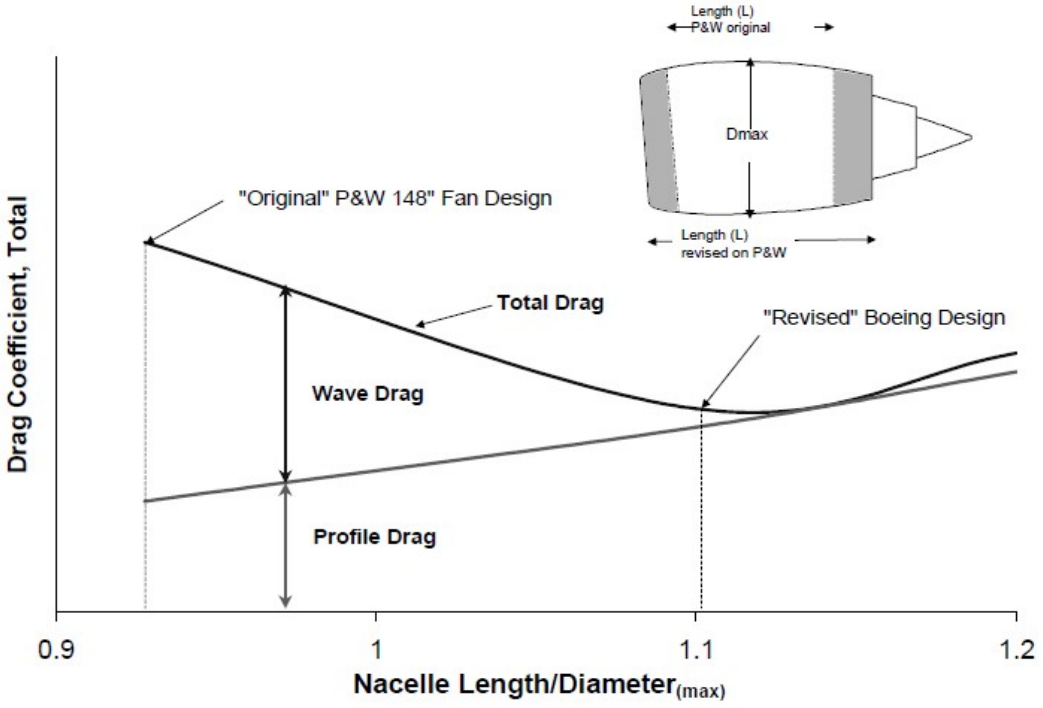

FIGURE 2.3: Impact of the nacelle length over the maximum diameter ratio (L_{nac}/d_{max}) on the total nacelle drag at cruise. From Daggett et al.[8].

2000s the European Commission funded several collaborative projects that investigated laminar flow nacelles: laminar research action (LARA)[56], european laminar flow investigation II (ELFIN II)[57], hybrid laminar flow demonstration on aircraft (HYLDA)[58] or application of hybrid laminar flow technology on transport aircraft (ALLTA)[59]. Additionally, more recent studies have been focused also on natural laminar flow nacelle design and optimisation based on experimental and computational assessments[60–62]. From all of these studies it has been proven the capability to design nacelles in isolated configuration that can delay the laminar to turbulent boundary layer transition to 50-60% of the nacelle length at transonic Mach numbers of around 0.8 and Reynolds numbers of 20 million. This implies reductions in total aircraft drag that can go up to 3.5%[63]. The typical nacelle designs for laminar flows arise from a combination of an increase in the maximum radius and a backward movement of its axial position which generates a favourable pressure gradient along a longer range of the nacelle[55]. However, when the installation effects between the aero-engine and the airframe are considered these benefits are eroded. Riedel et al.[64] assessed the installed performance on the DLR airframe of an axisymmetric nacelle that was designed in isolation to attain laminar flow up to 60% of the overall length. A Mach number of 0.65 and a Reynolds number based on the wing chord of around 10 million were considered. The conclusion was that while the outboard of the nacelle was able to delay the transition to 60% of L_{nac}, the boundary layer

became turbulent at around 15% of L_{nac} in the inboard side. This was caused due to an increase in the flow suction between the airframe and the nacelle that increased the peak Mach number to around 1.5 near the fan-cowl.

2.2 Propulsion system integration

Traditionally, aero-engine nacelles are designed in an isolated configuration by minimising the drag at different operating conditions[13,14,50,51]. However, when the propulsion system is installed in the airframe the resulting interference effects modify the aerodynamics of the fan-cowl relative to the isolated case. For UHBPR aero-engines this is even more significant[8] and the interference drag of the installation can be substantial. Therefore, in the frame of UHBPR it is important to assess the overall system performance as the gains in individual components may be offset by the penalties associated to the integration (Figure 2.4).

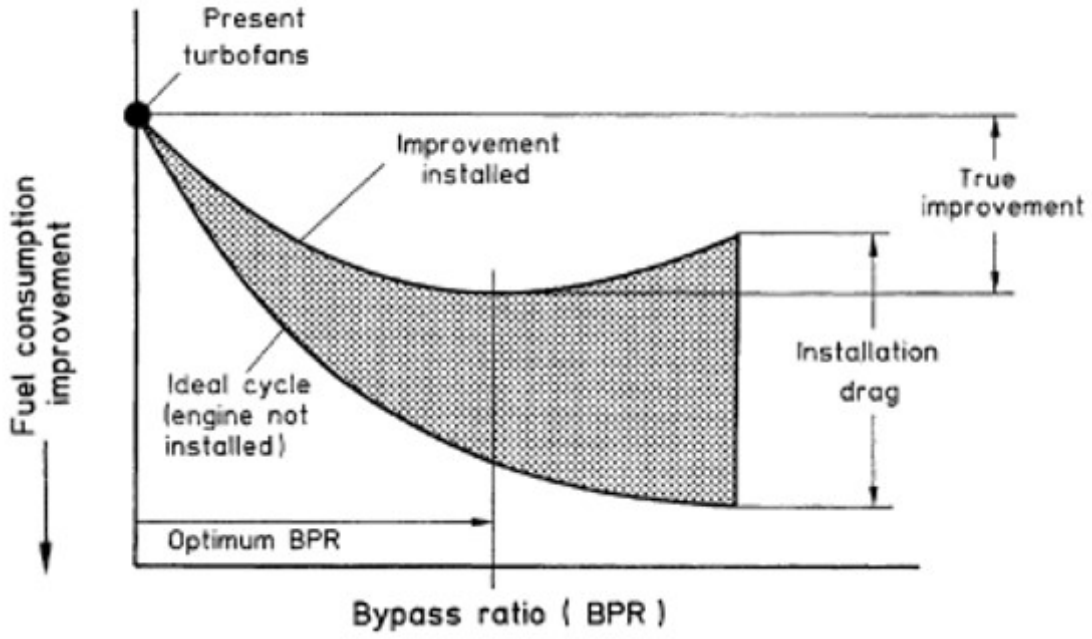

FIGURE 2.4: Impact of installation on the reduction of fuel consumption with bypass ratio. Based on Rudnik et al.[65].

This section intends to provide an overview of the aerodynamic aspects and methods used to assess the installation of the engine in the airframe. A special focus is on the impact of the aero-engine nacelle in the overall aircraft performance. The aircraft model used for these studies is typically composed of 3 main components:

the airframe, the propulsion system and the pylon (Figure 2.5). The airframe is divided into the fuselage, the wing and the empennage (or horizontal stabilizer).

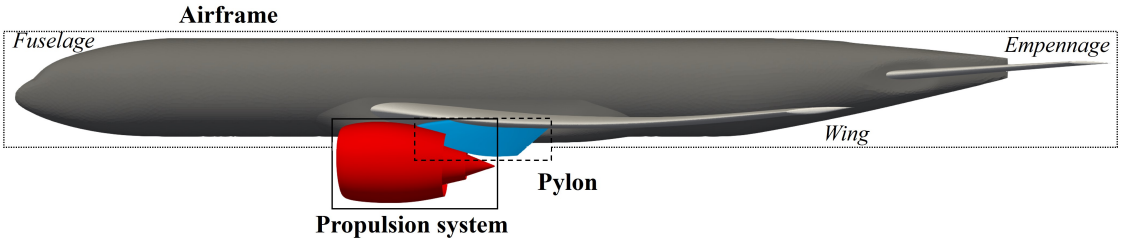

FIGURE 2.5: Components of the aircraft model.

The study of the propulsion integration starts by defining the installation position of the engine in the airframe. While some studies have focused on a fuselage-mounted configuration[66], many others have addressed above-wing engine installations[67,68] and also both forward-[69] and rear-podded[70] under-wing engine positions. The installation position of the propulsion system in the airframe is a multi-disciplinary aspect[71]. For example, while placing the engine beneath the wing is beneficial from a ground maintenance point of view it reduces the ground clearance[72]. Ground clearance can be increased by installed the engine over the wing but on the contrary this reduces the operability of the engine at high incidences and increase the noise to the cabin[72]. A fuselage-mounted configuration also increases ground clearance, reduces structural loads and enables a shorter and lighter landing gear but this normally requires a T-tail architecture which is more prone to deep stall[72]. Hereafter, this review is focused on the forward-podded under-wing installation as it is the configuration for UHBPR engines that this research investigates.

2.2.1 Key aerodynamic installation effects

The aerodynamic aspects of the powerplant integration in the airframe have been under investigation since the early 1950s. Harris et al[73] studied the integration of a turbofan propulsion system representative of high bypass ratio with an advance civil airframe at a high speed flight regime. A large range of aerodynamic interference features were identified (Figure 2.6):

- The wing generates both and upwash and sidewash effect on the leading edge of the nacelle that increases the flow incidence. This changes the flow stagnation point and therefore the spillage drag component of the nacelle.

- The pressure field in the upper side of the nacelle is altered due to the intersection with the leading edge of the pylon.
- The pressure field in the inboard side of the nacelle afterbody is changed due to the interference flow with the wing, pylon and fuselage. This shifts the shock position and strength and generates additional shock waves and potential flow separation.
- The nacelle itself causes a lift redistribution and reduction at constant incidence due to an increase in the flow suction over the pressure side of the wing. This requires to re-trim the aircraft.
- Conditions of over-expanded fan jet flow can appear on the core cowl afterbody with strong shocks that increase the drag and alter the lift distribution from the wing.

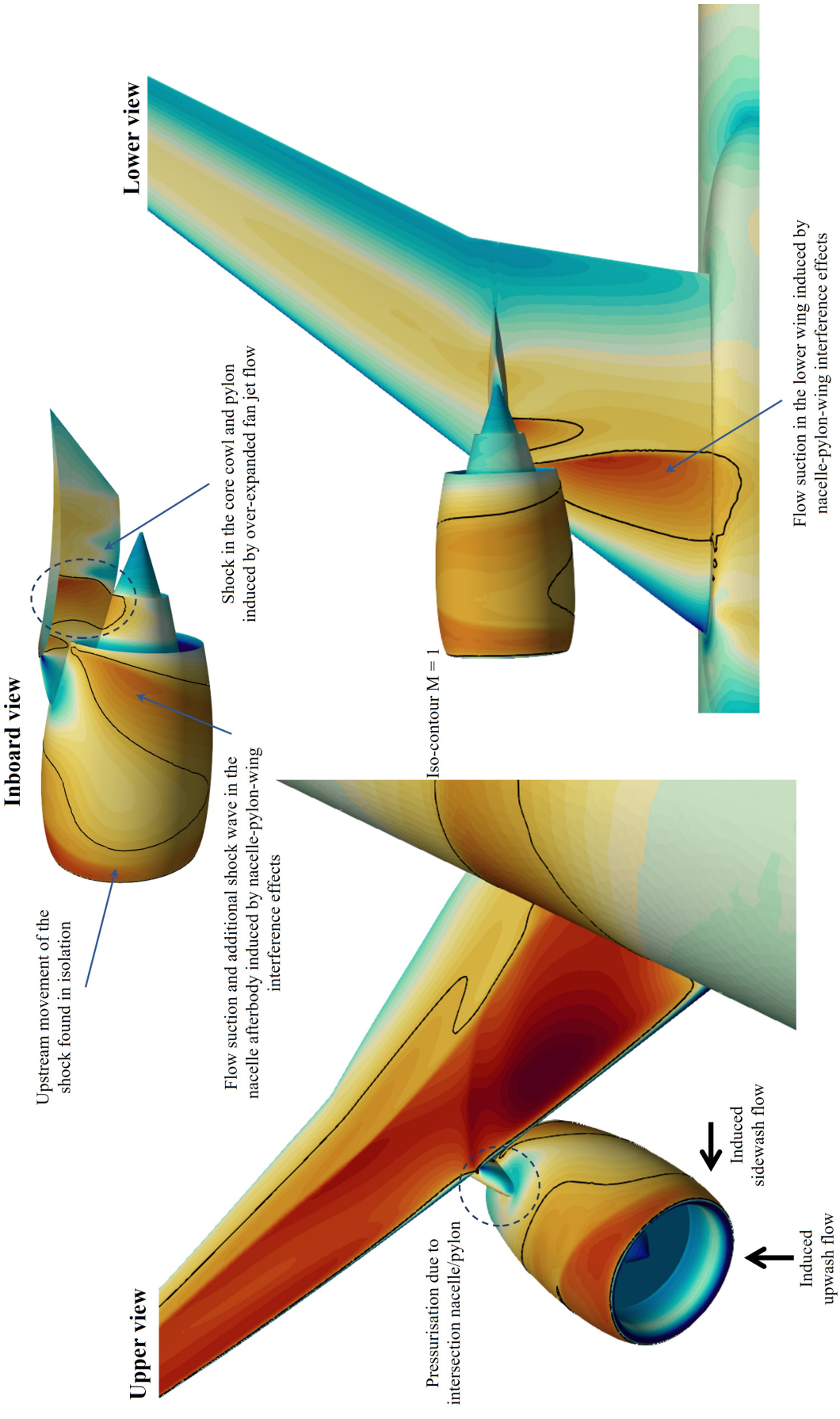

FIGURE 2.6: Summary of aerodynamic installation effects.

2.2.2 Methods for engine integration studies

Initially, wind tunnel techniques were mostly used to study the aerodynamic integration of the aero-engine in the airframe due to the lack of adequate computational tools[74–76]. Based on this, there are two main approaches of different complexity and level of physical representation (Figure 2.7a). The more simplistic one is based on Through-Flow Nacelles (TFNs). A TFN models the external geometry of the engine. It is an unpowered representation of the propulsion system which has an exit area that is sized to accommodate a certain mass flow for the cruise condition. TFNs have been extensively used for experimental studies of the installation effects due to the simplicity to build the model (Table 2.1). However, the TFN technique is not able to address the effect of the jet on the aerodynamics of the airframe or to have an independent control on the MFCR (Table 2.1). In this respect, Turbine-Powered Simulators (TPSs) models are the alternative to represent a similar flow efflux as for the real air flow ejection of the engine nozzles in an experimental set-up. This method also simulates the thrust characteristics of the powerplant which is essential from a thrust and drag bookkeeping standpoint (Table 2.1). Zhang et al[77] compared the pressure distribution on the pressure side of the wing and the pylon for a TFN and TPS configuration at a cruise Mach number of 0.785 (Figure 2.7b). The effect of the jet amplifies the suction in the forebody of the lower wing but increase the pressurisation close to the trailing edge. It also generates a suction peak in the inboard side of the pylon. As a result, the TPS shows relative to the TFN a slight increase in drag of 0.5% and a loss in the cruise C_L of approximately 0.03. Overall, TPS models are a more accurate representation of the engine installation[74].

TABLE 2.1: Comparison of the advantages and disadvantages of the TFN and TPS engine models.

	Advantages	Disadvantages
Through-Flow Nacelle (TFN)	Easy to build the model, cheap and easy to manufacture for experimental measurements.	No engine cycle is used, lack of control in the engine MFCR, impact of the jet in the aerodynamics of the airframe is not assessed.
Turbine-Powered Simulator (TPS)	Considers a realistic engine cycle, able to model/measure the thrust component of the engine.	Expensive and difficult to manufacture for test campaigns.

Different airframe models have been used to assess the installation effects both experimentally and computationally. From the 1990s, important European projects

(DUPRIN-I, DUPRIN-II, ENIFAIR, AIRDATA) that investigated the engine integration considered the DLR-F6 airframe with TFN configurations (Figure 2.8a). The DLR-F6 is representative of a twin-engine, wide-body transonic civil aircraft with a cruise Mach number of 0.75 and a trim lift coefficient of 0.5[79]. It was used in experimental campaigns at DLR and ONERA wind tunnels. The DLR-F6 with TFN was studied in the second AIAA Drag Prediction Workshop (DPW)[80] and pockets of flow separation were found at the wing root and wing/pylon junction. A new high-performance airframe was developed in a collaboration between the DPW Committee and the NASA's Subsonic Fixed Wing Aerodynamics Technical Working Group[81]. It is called NASA Common Research Model (CRM) and is representative of a contemporary wide-body, twin-engine transonic aircraft for long haul applications with a cruise Mach number of 0.85 and a trim lift coefficient of 0.5. The CRM

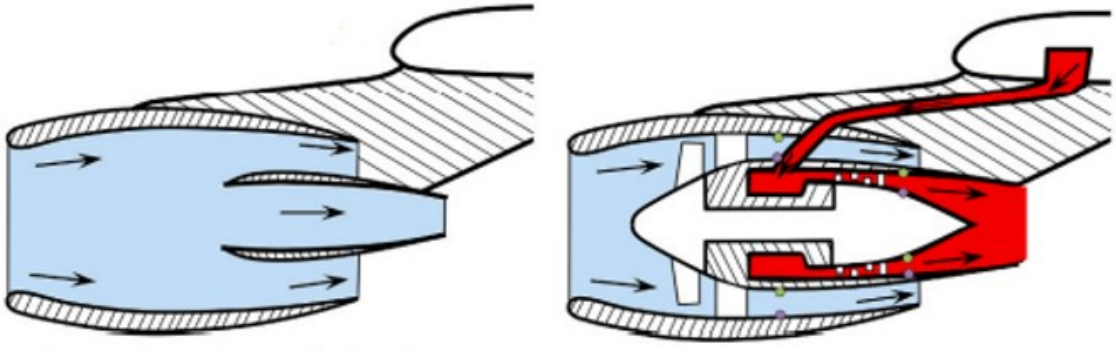

(A) Through-Flow Nacelle (left) and Turbine-Powered Simulator (right) models. Based on Sabater[78].

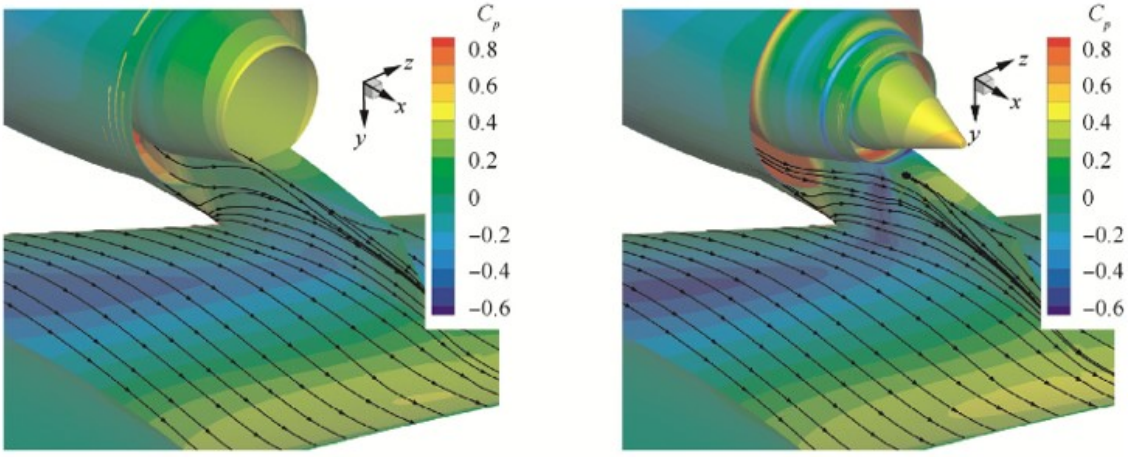

(B) Aerodynamics of a Through-Flow Nacelle (left) and a Turbine-Powered Simulator (right) model. Based on Zhang et al[77]. Under-wing installation inverted for visualisation purposes.

FIGURE 2.7: Propulsion system modelling through Through-Flow Nacelles and Turbine-Powered Simulators.

with TFN was experimentally tested at the NASA Langley National Transonic Facility and the NASA Ames 11ft wind tunnel[82] (Figure 2.8b). It has been chosen as the reference airframe for propulsion system integration studies since the fourth AIAA DPW[83]. With regards to experimental tests for TPS nacelle configurations, the ALVAST airframe has been used[76]. It is representative of a modern airframe similar to the Airbus A320 aircraft with a cruise Mach number of 0.75 and lift coefficient of 0.5. The ALVAST airframe was tested under the DUPRIN and ENIFAIR European projects but the geometry is not publicly available for open research purposes (Figure 2.8c).

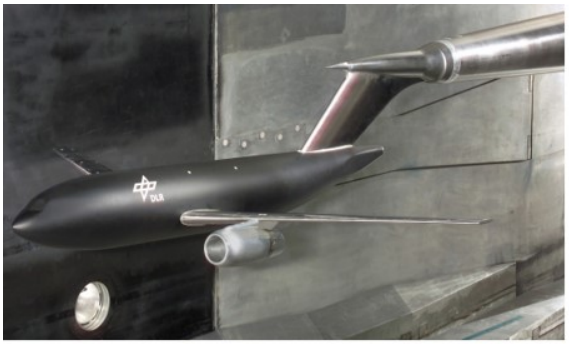

(A) DLR-F6 airframe[79].

(B) NASA CRM airframe[84].

(C) ALVAST airframe[85].

FIGURE 2.8: Different aircraft models used for propulsion system integration studies installed in the wind tunnel.

2.2.2.1 Computational methods of different fidelity

Different computational methods have been applied to study the integration of the propulsion system into the airframe. This involves complex geometries and requires high computational capabilities for a detailed resolution of the physics. The lack of computational resources in the last decades and the current interest to shorten the design time scales motivates the use of low fidelity Computational Fluid Dynamics

(CFD) models to assess the integration aerodynamics. This section delivers a review of the different fidelity of CFD methods used for this design problem and accuracy relative to experimental data.

Starting from the simplest models, panel methods were developed to simulate linear, inviscid and irrotational flows by solving the Laplace equation[86]. They have been successfully applied to predict the aerodynamics of arbitrary configurations at subsonic and supersonic conditions. An example extensively used is the PAN AIR code developed by Johnson et al.[87]. However, it is not able to model highly non-linear flows associated to transonic flow regimes which makes it unsuitable for the current research topic. Non-linear potential CFD solvers, while still neglecting the viscosity and vorticity of the flow, can model non-linearities associated to shock waves of transonic conditions. An example is the Boeing TranAir code[88] which was coupled with a viscous boundary layer model to assess the performance of a business jet nacelle in an above-wing mounted configuration for a cruise Mach number of 0.75 and a lift coefficient of 0.4[89]. General trends were captured but substantial differences relative to high fidelity flow predictions were found like a shift of 30% of the wing chord in the shock location on the wing suction side. These methods can provide representative results for preliminary designs stages at transonic conditions as long as the shocks are weak and do not induce flow separation[90]. In general, more accurate CFD models are required for the analysis of the propulsion integration problem.

An increase in the CFD fidelity comes from the use of the Euler equations to model the flow. Euler equations correspond to the Navier-Stokes equations with zero viscosity and zero thermal conductivity imposed in the formulation[91]. Relative to potential methods, an improvement is the inclusion of the flow vorticity because an inviscid transonic flows can not be properly modelled as irrotational as demonstrated by the Crocco's theorem[92]. However, important flow features like boundary layer growth, transition from laminar to turbulent and flow separation are still not captured. In the context of the propulsion system integration, Rossow et al.[93] compared experimental results with Euler CFD calculations for a TFN installed in the DLR-F6 airframe at the cruise condition ($M_\infty = 0.75$ and $C_L = 0.5$). In spite of a slight shifting of the shock waves location, a generally good agreement in the flow field prediction in the pylon/wing junction and nacelle was observed. A similar conclusion was drawn by Rudnik et al.[65] for the same airframe with TFN and at the same cruise condition. Compared to experiments, the Euler simulations captured the main flow features on the whole system. However, the Euler CFD results under-predicted the suction peak by $\Delta C_p = 0.2$ in both the suction and pressure side of the wing (Figure 2.9). Additionally, in the afterbody of the wing a difference

on the flow pressurisation was observed due to the inability of the Euler solver to model the boundary layer growth. As an extension of this work, the Euler CFD model was combined with a 3D boundary layer correction code to account for the displacement thickness of the boundary layer[65]. At the expense of an increase in the computational overhead by approximately a factor of 3, the prediction of shock waves location was improved and the under-prediction of the peak suction in the pressure wing side was reduced to $\Delta C_p = 0.1$. A better agreement on the pressure distribution at the wing afterbody was also identified (Figure 2.9).

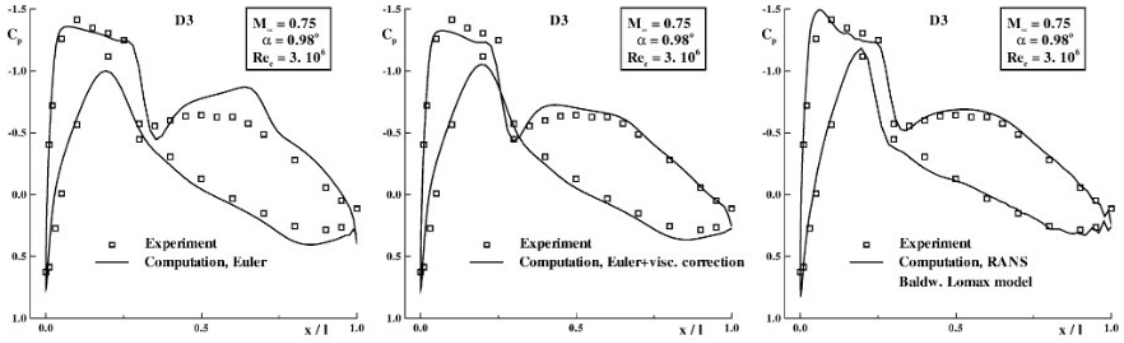

FIGURE 2.9: Distribution of pressure coefficient for a wing section of the DLR-F6 at a location inboard of the nacelle and at the cruise condition ($M_\infty = 0.75$ and $C_L = 0.5$). Comparison of different CFD models: Euler solver on the left, Euler solver coupled with 3D boundary layer correction code on the middle, RANS solver on the right. Taken from Rudnik et al[65].

Although Euler solvers might be acceptable for the aerodynamic prediction of the installation of the propulsion system, the complete Navier-Stokes equations should be solved when viscous flow features like flow separation of shock-boundary layer interaction are key aspects of the aerodynamics. Reynolds-Averaged Navier-Stokes (RANS) solvers increase the computational overhead by a factor of approximately 10 relative to Euler CFD models[65]. However, a RANS solution allows a better prediction of important flow features like shock-boundary layer interaction which is significative for the close-coupled installation of UHBPR aero-engines. Additionally to the Euler and experimental data comparison of pressure distributions on the DLR-F6 airframe shown before by Rudnik et al.[65], a RANS calculation was also incorporated to the comparison. An excellent agreement with experimental data was obtained with great prediction of the shocks location, suction pressure peaks and afterbody pressurisation (Figure 2.9). Apart from a comparison of the local aerodynamics of the interaction between the airframe and the aero-engine, the prediction accuracy of the overall installation effects has to be quantified. Brodersen et al.[94] compared the results from a RANS analysis with experimental data for the DLR-F6

airframe and a TFN. At the cruise point, the total drag of the installation was predicted within 6-8% of the clean airframe drag. Similarly, RANS computations with the $\kappa - \omega$ SST turbulence model[95] have been compared with experimental results for the more modern CRM airframe with TFN using the wind tunnel measurements reported in the DPW[83,96]. Magrini et al.[97] showed a good agreement in the pressure distribution at a wing section inboard of the aero-engine with changes in the peak C_p lower than 0.1 (Figure 2.10). Goulos et al.[98] evaluated the installation drag ($C_D^{Inst.}$) for a range of C_L from approximately 0.2 to 0.6 at $M_\infty = 0.85$. The RANS CFD model was able to reproduce the experimental trend with a maximum difference of 8 drag counts for the investigated C_L range and 2 drag counts ($\approx 0.8\%$ of the total aircraft drag) for the cruise point $C_L = 0.5$ (Figure 2.10).

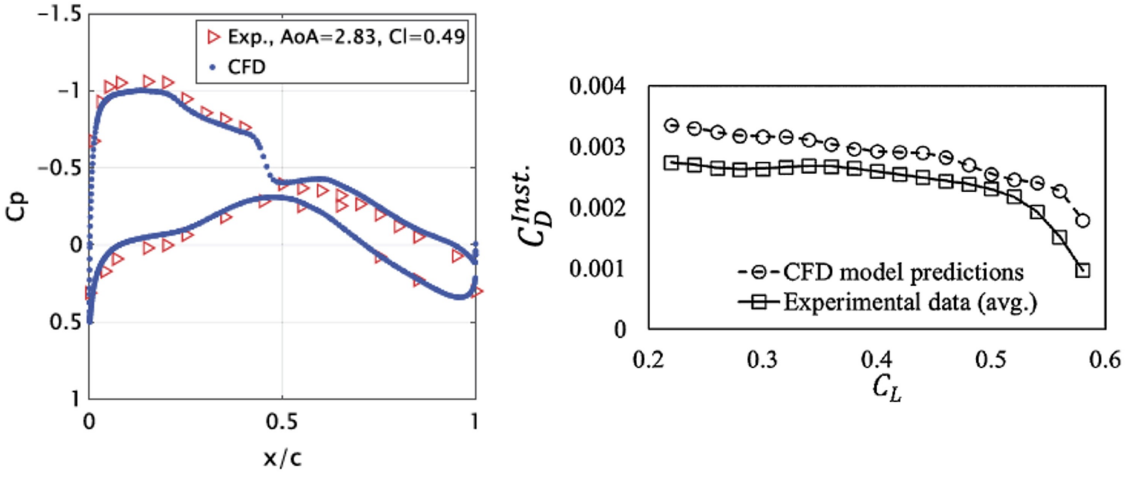

FIGURE 2.10: Comparison between RANS and experiments of (left)[97] the distribution of the pressure coefficient for a wing section of the NASA CRM at a location inboard of the nacelle and at the cruise condition ($M_\infty = 0.85$ and $C_L = 0.5$), and (right)[98] the installation drag with changes in the lift coefficient for $M_\infty = 0.85$.

2.2.3 Performance of the overall engine-airframe system

This section delivers an overview in terms of the methods used to account for the overall performance of the aircraft. Additionally, the current state of the art on the impact of the size of the engine, the installation position and the pylon on the overall aircraft performance is reviewed.

2.2.3.1 Accounting method

The overall performance of the engine-airframe system results from the performance of each component assessed in a fully installed configuration. The performance

of the system is not affected by the split between the thrust and the drag forces. However, without a correct split it is not possible to understand the effect of the aerodynamics of the installation on the performance of each component and trace it back to improvements in the design. Therefore a thrust and drag bookkeeping method to account for every force in the right domain is essential[20,99].

Ideally, in-flight thrust measurements would be the most accurate method for the accounting. There has been some research on this field like the work conducted by Bauer et al.[100] under the APOSEM (Advanced Prediction of Severity effects on Engine Maintenance) project to develop an on-wing engine thrust measurement system. However, this is not currently considered as a practical solution due to the complexity of the systems required[20]. Therefore, the in-flight thrust is normally estimated based on the operating point of the engine and the drag of the aircraft is assumed to be equal to the estimated thrust as dictated by the trimmed flight condition[20,99]. The gross thrust is estimated from the ideal thrust based on the total pressure in the inlet of the bypass and core exhausts corrected by a velocity coefficient of the exhaust (C_V) that is estimated experimentally with static ground tests[101]. Therefore, the validity of this method is subjected to the calibration of C_V which might vary from static to in-flight conditions.

Most of the thrust and drag accounting methods are based on AGARD[20] and SAE[99] standards which describe in detail the determination of in-flight thrust and further forces decomposition. As explained in Section 2.1.2, there are two categories of thrust and drag extraction methods: nearfield methods and farfield methods. A detailed description of different nearfield and farfield methods for this application was provided by Magrini et al.[102]. Destarac et al.[37] applied both methodologies to RANS calculations on a transonic twin-engine wide-body airframe at the cruise point defined by $M_\infty = 0.85$ and $C_L = 0.5$. A difference in the airframe drag of approximately 10 drag counts ($\approx 4\%$ of the total drag) was obtained. This is a significant number as can account for around 4% of the cruise fuel consumption for these kind of aircraft. Nearfield methods are more common for aero-engine installation studies. Yufei et al.[77] applied a thrust and drag bookkeeping method based on a nearfield formulation to evaluate the performance of an engine-airframe installation at cruise. However, in this method the C_V of the exhaust was linearly extrapolated from the static conditions to the cruise point (M_∞). This does not properly capture the impact of the aerodynamic of the installation on the exhausts behaviour. Conversely, Goulos et al.[98] developed a novel thrust and drag accounting methodology in which the velocity coefficient used to correct the ideal thrust is evaluated directly from the CFD solution of the installed aero-engine at a certain

operating condition. Additionally, an integral metric called Net Vehicle Force (NVF) was proposed to quantify the overall performance of the engine-airframe system.

2.2.3.2 Impact of the engine size and installation position

For conventional podded under-wing engines on a transonic wide-body twin-engine aircraft the effect of the installation is estimated to be approximately 10-15% of the total aircraft drag[103]. This penalty is sensitive to the engine size and the installation position[93,103,104] and therefore a coupled study of these effects is required. As future engine developments are heading toward larger fan diameters to increase the BPR and improve SFC, structural considerations like wing-flutter or ground clearance may force the aero-engine to be installed in a more close-coupled position with the airframe. Therefore, the aerodynamic challenge is to install larger engines with a minimal increase in drag[71].

Rudnik et al.[65] evaluated the installation aerodynamics of three different TPS configurations of aero-engines of BPR 6, 9 and 16. The twin-engine narrow-body ALVAST airframe was used at cruise given by $M_\infty = 0.75$ and $C_L = 0.5$. An Euler CFD solver was combined with a 3D viscous boundary layer correction model. The highest BPR aero-engine was found to cause not only the largest upstream movement of the shock in the wing suction side relative to the free flying airframe but also a region of detrimental suction on the wing pressure side. This causes a large loss in the spanwise lift that is proportional to the engine size. While this lift loss can be alleviated by installing the aero-engine in a more axially forward position relative to the wing, the vertical offset between the engine and the wing does not have a significant influence.

The impact of the installation position on the performance of the overall system can be higher than the impact of the engine size. For example, Ingraldi et al.[105] evaluated the aerodynamic interference effects of a UHBPR and a conventional aero-engine with BPR $\approx$ 18 and 6 respectively on a low-wing transonic transport aircraft. The low-BPR engine installed in a more close-coupled position exhibited higher interference drag than the UHBPR engine installed in a less challenging position.

Goulos et al.[98] used a UHBPR aero-engine representative of BPR $\approx$ 15+ and analysed in detail the impact of the installation position on the overall NVF. As introduced in the previous section, NVF quantifies the overall performance of the engine-airframe system. The NASA CRM at $M_\infty = 0.85$ and $C_L = 0.5$ was considered. The analysis was based on numerical computations with a RANS CFD solver and the $\kappa-\omega$ SST turbulence model. The installation method of the nacelle is based

on the axial (dx) and vertical (dz) offset between the nacelle trailing edge in the top line and the local wing leading edge (Figure 2.11). The distribution of change in NVF relative to the standard net thrust of the aero-engine ($F_N \approx 60kN$) is governed by both the axial and vertical installation coordinates (Figure 2.12). The largest penalty is for the most closed-coupled position given by $dx/C = dz/C = 0.05$. Relative to a typical baseline installation position ($dx/C = 0$ and $dz/C = 0.075$) this penalty reaches -1.8% which equates to approximately 1.8% increase in cruise fuel burn[106]. Goulos et al.[98] related the impact of the installation position on the overall NVF performance to the aerodynamics on the inboard and outboard side of the nacelle, pylon and exhaust through normalised pressure distributions (Figure 2.13). For this purpose, the aerodynamics of the baseline position ($dx/C = 0$ and $dz/C = 0.075$) was compared with an axially close-coupled ($dx/C = 0.05$ and $dz/C = 0.075$) and a vertically close-coupled ($dx/C = 0$ and $dz/C = 0.05$) position. The aerodynamic behaviour on the outboard side is quite similar when the engine is moved from the baseline position. On the contrary, there is a notable impact of the installation position in the inboard aerodynamics. This is due to the "aerodynamic channel" that is created between the nacelle, the pylon, the wing and the fuselage, which leads to a reduction in the effective area and a consequent acceleration of the flow in the nacelle afterbody, exhaust core cowl and inboard pylon. Additionally, the sweep angle of the wing further increases the aerodynamic interference effects as the inboard side of the engine is more overlapped with the wing compared to the outboard side.

Stankowski et al.[10,107] investigated in detail the impact of the size of the aero-engine on the aerodynamic and performance of the overall installation. A forward installation position given by $dx/c = -0.05$ and $dz/c = 0.15$ was considered. Two powerplants of different BPR were assessed. A baseline engine (E1) with a $BPR \approx 10$ was used to scaled up to a 23% larger engine (E2) with a $BPR \approx 17$ while keeping the same thrust requirement. Both engines were installed in the NASA CRM at a representative cruise condition of $M_\infty = 0.82$ and $\alpha_{aircraft} = 2.5°$ using conventional TFNs. Numerical computations with a RANS CFD solver and the $\kappa-\omega$ SST turbulence model were used. Notable changes in the flowfield arise between the installation of the different size aero-engines (Figure 2.14). For example, for E2 the suction peak in the upper side of the wing is reduced and the shock is moved upstream (Figure 2.14b). As a result, there is a penalty in loss of lift for the larger E2 configuration as was already pointed by Rudnik et al.[65]. Additionally, the effect of the jet for the larger E2 engine is smaller due to the lower exhaust pressure ratios needed to maintain the thrust requirement (Figure 2.14b). The change in the

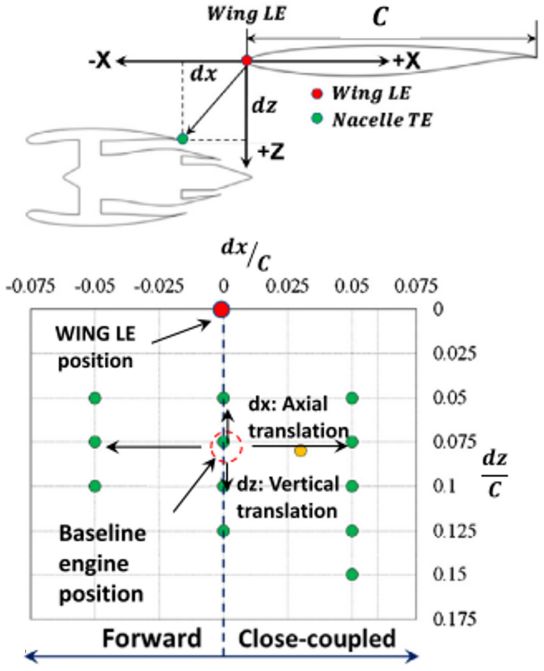

FIGURE 2.11: Method for aero-engine installation. Based on Goulos et al.[98].

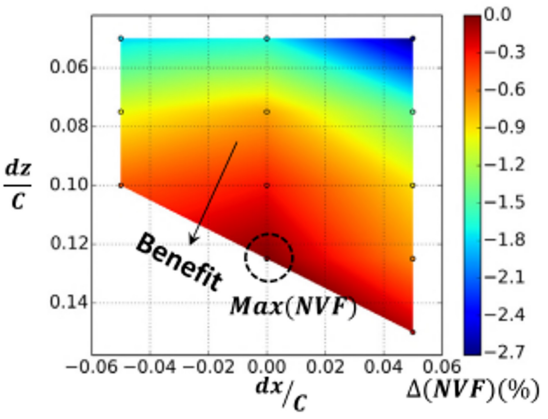

FIGURE 2.12: Distribution of NVF in the investigated installation map. Based on Goulos et al.[98].

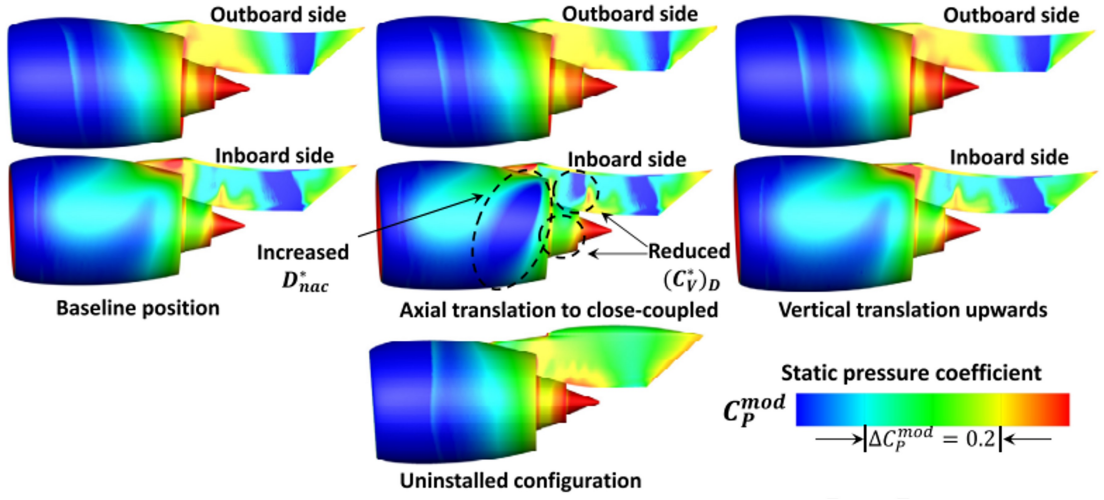

FIGURE 2.13: Normalised static pressure distributions for the baseline position, axially and vertically close-coupled positions and uninstalled configuration.

flowfield is associated to changes in the aerodynamic forces of the installation. At a constant vertical force that includes the aerodynamic lift and the vertical component of the thrust, relative to the smaller E1 configuration the 23% larger E2 engine increases the installation drag by 9 drag counts which corresponds to approximately 3.5% of the standard net thrust. For an assessment over a 10000 km cruise flight, the larger engine E2 exhibits a reduction in the fuel consumption of around 5.8%

relative to the baseline E1 engine. This benefit is estimated only based on the engine cycles. When the aero-engines are installed in the airframe and the aerodynamic interference effects and additional weight are considered, the fuel burn reduction of the E2 engine is 4.8%. However, in this study the pylon is not considered which is known to have an impact on the aerodynamics of the installation. This will be addressed in the next section (Section 2.2.3.3).

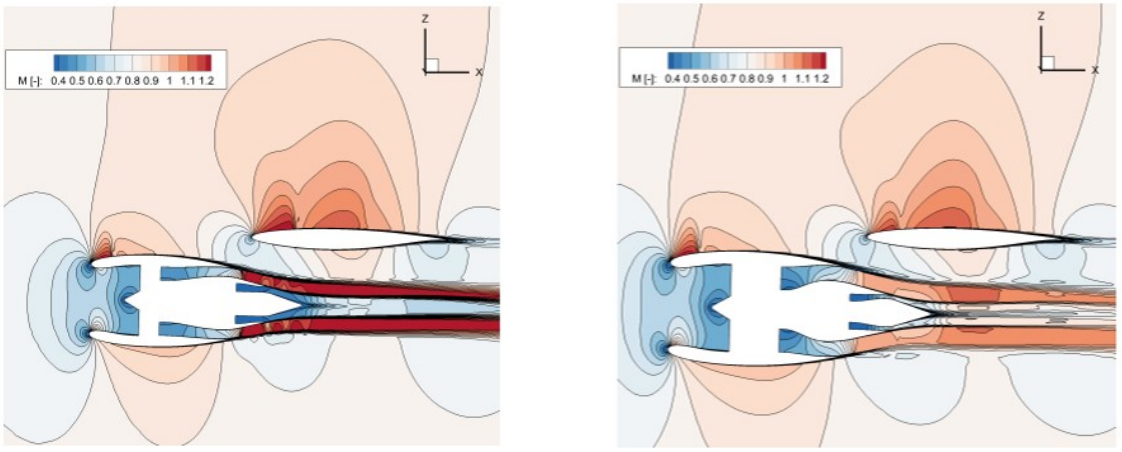

(A) Baseline (E1) engine ($BPR \approx 10$). (B) 23% larger (E2) engine ($BPR \approx 17$).

FIGURE 2.14: Contours of Mach number for the engine-airframe configurations based on the E1 and E2 engines. NASA CRM at $M_\infty = 0.82$, $\alpha_{a/c} = 2.5°$ and $Re = 45\text{x}10^6$. Forward installation position given by $dx/c = -0.05$ and $dz/c = 0.15$. Based on Stańkowski[10].

This increase in the installed drag can potentially be mitigated for UHBPR aero-engines by the design of more compact nacelles. Tejero et al.[54] evaluated the relative performance of a compact ($L_{nac}/r_{hi} = 3.1$) and a conventional ($L_{nac}/r_{hi} = 3.8$) nacelle at cruise condition for a typical installation position of current in-service architectures installed in the NASA CRM. A benefit in NVF of approximately 0.95% of the standard net thrust could be achieved for the compact nacelle relative to the conventional baseline which equates to a similar value of cruise fuel burn reduction.

2.2.3.3 Impact of the pylon

There is a substantial impact of the pylon on the propulsion system integration. Different investigations that include experimental test campaigns in the NASA Langley Research Center have demonstrated the importance of a careful contouring of the pylon geometry to avoid aerodynamic effects like loss of lift or flow separation[65,105,108]. In the context of lower installation drag, Carlson et al.[109] tested in the wind tunnel different pylon designs for a representative high-wing transport aircraft. For a

Mach number of 0.8 and a lift coefficient of 0.45, a reduction of 10 drag counts was obtained relative to conventional pylon designs. Moreover, similar flow velocities to the clean wing configuration were achieved in the inboard pylon-wing junction which reduces the lift loss penalty. However, this study was performed without a nacelle in place. Devine et al.[110] extended this investigation to consider an axisymmetric conventional nacelle installed in the DLR-F6 airframe. A computational approach based on RANS computations with the Spalart-Allmarast[111] turbulence model was used. Relative to a conventional design, an improved pylon design reduced the installation drag by 6 drag counts. This is a substantial improvement considering an average increase in drag due to the installation of approximately 40 drag counts. This reduction comes from a downstream movement of the shock in the inboard side of the wing suction surface. Also, there is a higher pressure recovery in the afterbody of the wing pressure side and increases the lift relative to the conventional pylon configuration. This highlights that although a detailed design of the pylon can improve the integration performance of the propulsion system, it is a bespoke design for a certain nacelle configuration and a certain installation position.

The impact of the pylon on the aerodynamic installation performance of a current in-service aero-engine representative of a BPR ≈ 11 was evaluated by Stankowski[10]. The NASA CRM airframe and pylon were used with the engine installed at the CRM TFN installation position[82]. The operating conditions of the study were $M_\infty = 0.82$ and $\alpha_{aircraft} = 2.5°$, considered as representative of the cruise point. A computational method based on RANS CFD calculations with the $\kappa - \omega$ SST turbulence model was employed. A notable impact of the pylon on the total drag was found with an increase relative to the no-pylon configuration of 5.2 drag counts. This equates approximately to 2.5% of the total aircraft drag. This is in line with previous values reported in the literature for a flight Mach number of 0.80[112]. This overall effect of the pylon on the total drag comes from the direct viscous and pressure drag integration on the pylon (≈ 3.5 drag counts) and the interference between the pylon/wing and pylon/nacelle.

A similar analysis was performed by Otter[113] for an UHBPR-type of aero-engine with a BPR ≈ 18 with a detailed analysis of the aerodynamic changes due to the pylon (Figure 2.15). The engine was installed in the NASA CRM at a typical installation position ($dx/C = 0$ and $dz/C = 0.09$) and evaluated using a computational model based on RANS and $\kappa-\omega$ SST turbulence model at the cruise condition ($M_\infty = 0.85$ and $C_L = 0.5$). The pylon used was designed using the method developed by Otter[113] to avoid regions of flow separation on the pylon itself and on the suction side of the wing. In terms of the aerodynamics of the nacelle, a drag reduction for

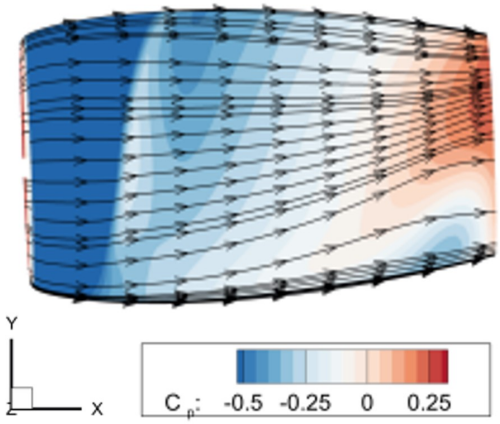

(A) Nacelle aerodynamics without pylon.

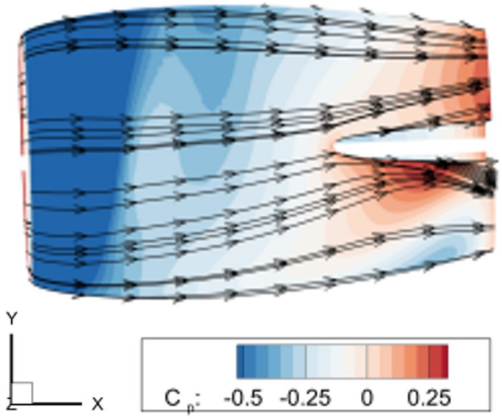

(B) Nacelle aerodynamics with pylon.

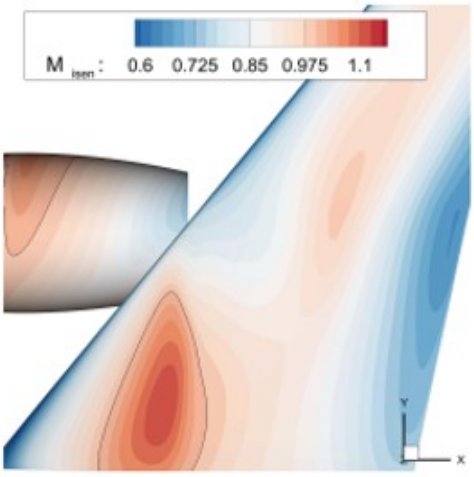

(C) Aerodynamics of the suction side of the wing without pylon.

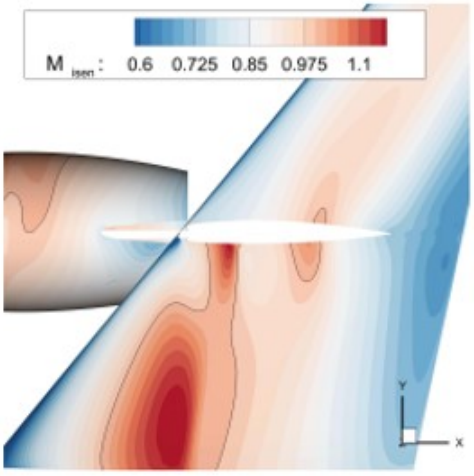

(D) Aerodynamics of the suction side of the wing with pylon.

FIGURE 2.15: Impact of the pylon on the installation aerodynamics of the nacelle and the suction side of the wing. Engine of BPR ≈ 18 installed in the NASA CRM at a typical installation position ($dx/C = 0$ and $dz/C = 0.09$) at cruise condition ($M_\infty = 0.85$ and $C_L = 0.5$). Based on Otter[113].

the configuration with pylon of approximately 3% compared to the case without pylon was found. This can be explained by (a) a reduction in the nacelle wetted area due to the pylon/nacelle intersection and (b) an increase in the static pressure in the nacelle afterbody due to the stagnation of the flow in the leading edge of the pylon/wing junction (Figure 2.15a, Figure 2.15b). On the other side, there is a reduction of 1.5% in the airframe drag for the configuration with pylon. This is caused by the reduction in the static pressure in the forebody of the suction side of the wing when the pylon is considered (Figure 2.15c, Figure 2.15d). As a result, the forebody generates a force in the thrust direction and reduces the drag. However, the overall performance of the case with pylon is worse than the case without pylon

with a reduction in NVF of 2.4%. This comes from a detrimental effect of the pylon to the engine performance which decreases the gross propulsive force. Consequently, the benefits in the drag domain are counterbalanced by the penalties in the thrust domain. This highlights that the system has to be analysed as a whole.

2.3 Aerodynamic shape design and optimisation

This section delivers an overview of the state of the art of aerodynamic shape design and optimisation. Initially the key challenges associated to this complex problem are outlined. Subsequently, the available optimisation approaches which are divided into Gradient-Based Methods and Gradient-Free Methods are described with details of the different optimisation algorithms for each class. Afterwards a variety of surrogate modelling techniques used to overcome the high computational overhead of this problem are presented for a range of aerodynamic applications. Finally, the focus of aerodynamic shape optimisation is taken to aero-engine nacelles both in isolated and installed configurations.

2.3.1 Key challenges

Aerodynamic shape design and optimisation is a complex problem that typically deals with non-linear transonic flow physics and follows a simulation-driven approach[114]. For some applications the high computational overhead of the optimisation process is unaffordable within an industrial time scale. One reason is the use of high fidelity computational methods to achieve realistic designs. Moreover, the optimisation sometimes is subjected to different aerodynamic requirements that necessitates from the assessment of multiple operating conditions. Additionally, aerodynamic shape optimisations are normally dominated by a high number of design variables in order to allow sufficient flexibility to represent a large set of geometries[115]. This increases substantially the number of designs assessed throughout the optimisation process to converge to the optimal design space[114]. The term design space is used in this project as the region defined by the combination of the different geometric design variables within their prescribed bounds. Different strategies have been developed to overcome these challenges such as surrogate models, hybrid methods that combine different level of fidelities, adjoint methods or dimensionality reduction approaches.

2.3.2 Optimisation approaches

The optimal design space for realistic aerodynamic shape optimisation problems is highly constrained and complex[116]. Therefore, depending on the problem, a global optimal solution may not be found and trade-offs between the different optimisation objective functions are often required. Depending on the nature of the problem, different optimisation methods can be more suitable and they are generally divided into: (a) Gradient-Based Methods (GBM) and (b) Gradient-Free Methods (GFM)[114] (Figure 2.16).

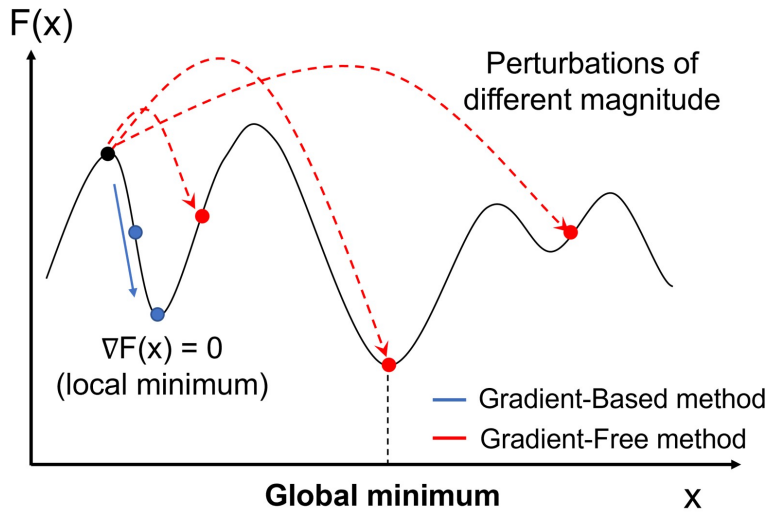

FIGURE 2.16: Overview of the approach followed by Gradient-Free Methods and Gradient-Based Methods within an optimisation. Figure generated by the author for illustration purposes.

GBM rely on the gradient information of an objective function relative to the design variables. They follow a two-step approach in which firstly the gradient is computed to identify the searching direction and secondly a certain step is applied to move in the defined searching line. GBM are very efficient to exploit the search close to the optimal design space to obtain detailed aerodynamic designs rather than for exploration of large design spaces at the initial stages of the optimisation process as they are more prone to get trapped in local optimum[117,118]. GBM require a pre-understanding of the design space to appropriately define a starting point as well as a continuous design space to compute the gradient information[114]. Many GBM use finite-difference approximation for the gradient estimation which are inefficient for highly dimensional problems as the cost is proportional to the number of design variables[119]. Conversely, adjoint methods are very efficient to compute the design space sensitivities (gradients) when the optimisation problem deals with several hundreds

of design variables[120] which makes this method appropriate for perturbations of the geometry like the Free-Form Deformation method[121,122]. Within GBM, different algorithms to minimise or maximise are used such as Sequential Quadratic Programming (SQP) or Sequential Least Squares Programming (SLSQP). GBM have successfully been applied not only for aerodynamic applications like aerofoils[123] or wings[124–126] but also for coupled aero-structural optimisation problems[127].

Aerodynamic shape optimisation problems are normally non-convex and therefore the use of an optimisation method that increases the likelihood of finding the global optima becomes important. In this respect, GFM may be a appropriate method when the computational overhead associated to the dimensionality of the problem is acceptable[128]. In contrast with GBM, GFM do not require a pre-understanding of the continuous and mathematically predictable design space. The research conducted in this thesis is based on GFM.

Within GFM, Genetic Algorithms (GA) and Particle Swarm Optimizers (PSO) have extensively been used for non-linear aerodynamic optimisations[129–132]. Both methods are classified as evolutionary algorithms (EA) as they use mechanisms inspired by nature that emulate the behaviour of living organisms[133]. While GA is based on the Darwinian theory of survival of the fittest the PSO method comes from the swarming motion of collective animal behaviour[114]. GA and PSO are similar in the sense that both methods follow a population-based searching approach which requires the sharing of information among the population members through a set of deterministic and probabilistic rules. However, there are differences that make each algorithm more adequate for a specific optimisation problem. Comparative assessments of GA and PSO algorithms have been reported in the literature[134–137]. The emphasis of these studies was on the relative performance between the optimal individual obtained with each algorithm and on the convergence rate. These studies agree on the computational efficiency superiority of PSO methods over GA. This computational effort saving is problem dependant and is reduced as the optimisation problem is more constrained[137]. As examples of application within the aerodynamic design area, Lyu et al.[138] applied a GA and a PSO algorithms to the non-linear aerodynamic optimisation of the NASA common research model wing at cruise condition. The method used a RANS CFD model and 8 design variables to parameterise the geometry. Both the PSO and the GA algorithms found a very similar optimal design with a difference of around 0.8 aircraft drag counts (lower than 0.5% of the overall aircraft drag). However, the convergence rate of the PSO algorithm relative to the GA one increased by a factor of approximately two. Additionally, Mukesh et al.[139] compared a GA and a PSO method to maximise the lift coefficient of the

NACA 2411 aerofoil at cruise condition. The optimisation problem considered 12 geometric design variables and used inviscid computational flow solutions. While the GA reported an increase in C_L from 0.842 to 0.968, the PSO-based optimisation achieved a $C_L = 1.035$. However, in the open literature there are no studies that statistically compare different algorithms for transonic aerodynamic applications. This is a key gap to fill in order to build confidence that the used algorithm is robust in the convergence to the optimal design space. This aspect is investigated in the current research and reported in Appendix E. Section 2.3.4 will develop on the aerodynamic shape optimisation problem applied to nacelles.

2.3.3 Surrogate models and multi-fidelity techniques for aerodynamic applications

Methods for quick aerodynamic shape optimisations have become fundamental to accelerate the overall design process and evaluate the feasibility of novel design concepts. A low-order model is attractive as once generated it can be quickly interrogated within a design or optimisation process. This kind of global surrogate models (also called *off-line* models) cover the entire searching space[140]. Another approach is to use *on-line* trained surrogate models which are updated within the optimisation loop to increase the predicting performance of the model close to the optimal design space[140]. Sections 2.3.3.1 and 2.3.3.2 cover the state of the art in terms of single-fidelity and multi-fidelity surrogate modelling techniques applied to the aerodynamic shape optimisation problem in a generic sense. Section 2.3.4 will focus on the nacelle application.

2.3.3.1 Single-fidelity surrogate models

In the context of aerodynamic shape design, a variety of well-established surrogate models and new emerging methods are being considered. The Gaussian Process Regression or Kriging interpolation was originally developed in the 1950s by Krige[141] to reduce the bias in the estimation of the average grade of mining panels. Since then, the method has been improved and applied for a multitude of areas until its more recent application to the design and analysis of computer experiments as a low-order model. A Kriging model provides the best linear unbiased prediction at unsampled locations and provides an estimate of the prediction uncertainty[142]. Wang et al.[143] applied a Kriging model for the aerodynamic shape optimisation of the impeller of a centrifugal compressor operating at transonic conditions. The surrogate model

was constructed with compressible RANS data. An optimal design was found with a smaller wake area and a reduced intensity of secondary flows relative to the baseline. This was reported as an increase in the isentropic efficiency of 2.5%. Similarly, Raul et al.[144] used a Kriging regression surrogate model built from unsteady RANS data for the aerodynamic optimisation of a NACA0012 aerofoil. The optimisation was conducted for the stall condition with $M = 0.1$ and $Re = 135,000$. Although this was a subsonic application, the aerofoil aerodynamics are dominated by non-linear effects due to the high flow incidence. An increase in the dynamic stall angle of 3° was achieved for a design with larger thickness and leading edge radius and a greater aft camber compared to the baseline.

A variety of studies in the literature have compared different metamodelling techniques using both benchmark cases[145] and aerodynamic data[146]. The quality of the Kriging interpolation model seems to deteriorate as the dimensionality of the problem increases[145]. Additionally, the training time substantially increases with the number of design variables and training points[147]. Conversely, Radial Basis Functions (RBF) surrogate models are promising in terms of accuracy and training time for highly dimensional problems[145]. For benchmark optimisation problems using evolutionary algorithm, a RBF-based approach was shown to clearly outperform other methods based on Kriging for a problem dimensionality over 30[148]. The RBF is an interpolation technique that was developed in 1971 by Hardy[149] to accurately model valleys and hills for cartography purposes. This surrogate model is built by a linear combination of a basis function per training point which is only dependant on the Euclidean distance between the point to predict and the training point[150]. As examples of application to aerodynamic shape optimisations, Morris et al.[151] used radial basis functions to conduct aerofoil Multi Objective Optimisation (MOO) under viscous and transonic conditions. Reductions in C_D of 45% and 57% were obtained for the NACA0012 and RAE2822 aerofoils respectively. Additionally, radial basis functions were used by Benaouali et al.[152] for the optimisation of the ONERA M6 wing shape at $M = 0.84$ and $Re = 11.7\text{x}10^6$. Relative to the baseline, the optimal design showed a reduction in C_D of approximately 15.4% for the same lift coefficient and weight.

Different machine learning techniques have also been used in the context of aerodynamic shape design and optimisation[153]. In particular, Artificial Neural Networks (ANN) have been proven to have good modelling performance for non-linear aerodynamic problems[154–156] due to the non-linear nature of the ANN back-propagation training method[157]. Compared to polynomial-based techniques, the ANN models exhibit increasingly better performance as the training data set is larger[114]. In this

respect, Zuccolo et al.[158] applied a Kriging and an ANN model for the prediction of the aerodynamic characteristics of exhausts afterbodies for a range of Mach numbers from 0.6 to 1.4. Both models were trained using RANS CFD data. It was concluded that ANN achieved better modelling performance than Kriging. Uncertainties in afterbody drag with 2σ confidence intervals of ± 0.01 and ± 0.013 were obtained for ANN and Kriging models respectively. Bouhlel et al.[159] used ANN to perform aerodynamic shape optimisations of two different aerofoils to minimise C_D in transonic condition at $M = 0.73$. The aerofoils were parameterised using 14 design variables. The models were constructed using RANS data. The method yielded similar optimal designs as those from a CFD-in-the-loop optimisation approach with a difference of 0.12% in C_D relative to the CFD-based optimised design. A reduction in computational cost of more than 95% was obtained with the ANN methodology. Artificial neural networks have also been considered for multi-objective and multi-point optimisations. Kotinis et al.[160] presented a method for aerofoil optimisation that maximized the lift-to-drag ratio at the cruise point ($M = 0.8$ and $Re = 35.6\text{x}10^6$) and minimized the trailing edge noise during the approach to landing condition ($M = 0.215$ and $Re = 28.1\text{x}10^6$). A PSO combined with an ANN surrogate model built out of RANS CFD data were used to conduct the optimisations. Improvements relative to the RAE2822 baseline aerofoil were obtained from down selected designs in the Pareto front but quantitative values were not reported.

2.3.3.2 Multi-fidelity surrogate models

Further computational cost reductions and better modelling performance can be achieved by the combination of different CFD fidelities[161]. The low-fidelity model is used to approximate the gradients of the design space whereas the high-fidelity one corrects these predictions. In this way both fidelities can be combined to create the surrogate model with a reduced number of the high-fidelity samples needed[161]. The low-fidelity model can be selected based on: (a) a simplified physics, (b) a coarsened spatial discretisation or (c) a relaxed convergence criteria[161].

Co-Kriging is a Gaussian Process Regression model based on two sources of data of different fidelity[162]. Although it was initially proposed and applied for the geostatistics community[163], this multi-fidelity surrogate model has been widely used in aerodynamic applications from the simple estimation of aerodynamic coefficients and drag polar of the RAE2822 aerofoil[162] to the prediction of the aerodynamic model of a full Unmanned Combat Aerial Vehicle (UCAV)[164]. In the context of

geometry optimisation, Likeng et al.[165] used a co-Kriging model for the drag reduction of a wing-body configuration at transonic conditions ($M = 0.785$, $\alpha = 2.4°$ and $Re = 25\text{x}10^6$) parameterised with 36 design variables. While the low-fidelity data were generated using a potential flow method with a correction model for the boundary layer, a RANS CFD model was used to produce the high-fidelity data set. Relative to a reference geometry, the co-Kriging method produced a design with a reduction in the drag coefficient of 16.5%. A key aspect with multi-fidelity methods is the ratio between the high- and low-fidelity samples (N_{HF}/N_{LF}). Hueso-Rebassa et al.[166] statistically assessed the impact of this parameter for the co-Kriging technique applied for non-axisymmetric exhausts of UHBPR aero-engines. RANS and Euler CFD data were considered as high- and low-fidelity respectively. Using the Root Mean Squared Error (RMSE) as a measure of modelling accuracy, there were not further improvement in the co-Kriging predicting performance for approximately $N_{HF}/N_{LF} > 0.4$. Additionally, a deterioration in the model accuracy was found for $N_{HF}/N_{LF} > 0.8$ because the model overfitted due to an oversampling in the high-fidelity data points.

Another data fusion technique available is called Variable Complexity Modelling (VCM). This method is based on the idea that the low-fidelity data is used to predict the trends in the design space while the high-fidelity information predicts the absolute values[167]. Therefore, the prediction of this multi-fidelity method is the summation between the low-fidelity evaluations and a correction term. There are two possible approaches to combine the different fidelity data to construct the correction term: (a) the scaling method[168], which uses the ratio between the high- and low-fidelity data, and (b) the incremental method[169], which computes the difference between both data sets. A low-order model is used to approximate the scaling or incremental function such as the Kriging interpolation, ANN or a simple polynomial fitting. This helps to filter the possible numerical noise in the data set that might cause convergence to local optima within an optimisation process[170,171]. Depending on the problem, either the scaling or the incremental approach may be more suitable. For example, for applications with very strong non-linear correlation between the low- and high-fidelity models the scaling method might work better. However, for those problems with zero or low values of the low-fidelity data the scaling approach might cause error amplification and the incremental method may be more appropriate[167]. Different variants of VCM have been used for aerodynamic applications[172–174]. As an example, Thokala et al.[175] applied VCM to the lift-to-drag ratio maximisation of an aerofoil at a high incidence condition given by $M = 0.25$, $\alpha = 9°$ and $Re = 2.9\text{x}10^6$. The symmetric NACA0012 aerofoil was used as baseline and 10

design variables were modified to find an optimised design. RANS CFD data was used for both the low- and high-fidelity models with a coarser grid resolution for the low-fidelity one. Three optimisations were performed: (1) using only high-fidelity data, (2) using a scaling VCM model and (3) using an incremental VCM model. A better design was found by the incremental model with a lift-to-drag ratio of 58.2 and 55.7 for the incremental and scaling VCM models respectively. Furthermore, although the optimisation based only on high-fidelity data achieved a design with the same lift-to-drag ratio of 58.2, the incremental VCM model was able to reduce the computational cost by 30%.

A recently developed multi-fidelity technique is based on two ANN[176]. One is used to model the low-fidelity data and another to model the linear and non-linear correlation between the low- and the high-fidelity data sets. This Multi-Fidelity Neural Network (MFNN) technique was applied by Zhang et al.[177] to aerodynamic shape optimisation problems and compared with a Single-Fidelity Neural Network (SFNN) approach based on high-fidelity data. RANS with boundary layer resolution and wall functions were used as high- and low-fidelity CFD models. Initially, an optimisation of the RAE2822 aerofoil in transonic flow to maximise the lift-to-drag ratio and using 12 degrees of freedom was conducted. For the same number of high-fidelity samples, 1% increase in lift-to-drag ratio relative to the baseline was obtained with MFNN-based optimisation compared to the SFNN-based optimisation. Moreover, a drag minimization of the DLR-F4 wing-body configuration in transonic flow was conducted using 30 degrees of freedom. For the same number of high-fidelity samples, the drag was reduced by 14% with the MFNN-based optimisation method whereas there was only a 3.4% reduction for the SFNN-based optimisation method.

An interesting contribution was the work from He et al.[178] which compared the different multi-fidelity techniques previously presented for an aerodynamic problem. Euler and RANS CFD models were used to generate the low- and high-fidelity data sets to build different surrogate models to predict the C_L and C_D of the NACA0012 aerofoil at different Mach numbers and angles of attack. Co-Kriging, MFNN and VCM based on Kriging were used. The best performing model was achieved by MFNN with a reduction in the Root Mean Squared Error (RMSE) of one order of magnitude for both C_L and C_D relative to the other models.

2.3.4 Nacelle aerodynamic design and optimisation

Until now this section has provided and understanding of the challenges and current methods and techniques of the aerodynamic shaped design and optimisation problem in a broad sense. In this subsection the focus is on the design of nacelles for UHBPR aero-engines. The information is divided into the design work performed for isolated and installed nacelle configurations.

2.3.4.1 Isolated configuration

Although the installation of the propulsion system plays a key role in the aerodynamics of the nacelle (detailed in Section 2.2), the design of aero-engine nacelles using computational methods have traditionally been based in isolated configuration. The main reason is the limitation in the computational time. For an installed CFD calculation, the CPU hours increase by approximately a factor of 20 relative to an isolated 3D case[179]. Moreover, the analysis of the decoupled system is still very useful to understand fundamental aerodynamic features at the different operating conditions and how they are related to the nacelle design space.

The nacelle design space is represented by a set of geometrical parameters as suggested by the ESDU approach for nacelle design[21] (Figure 2.17a). The nacelle length (L_{nac}) is the key parameter that should be minimised as much as possible to reduce the skin friction drag. The highlight radius (r_{hi}) directly determines the highlight area of the nacelle and therefore the MFCR associated to a given mass flow and freestream conditions. For a 3D non-axisymmetric nacelle the r_{hi} can vary azimuthally. In this case, the r_{hi} in the side aero-line is assumed to calculate the highlight area and MFCR. The maximum radius (r_{max}) defines the aero-engine frontal area which affects the form drag of the nacelle. The length of the forebody of the nacelle ($f_{max} \cdot L_{nac}$) expands from the highlight to the crest and it is strongly related to r_{max} to achieve a favourable curvature distribution and therefore pressure distribution. For this purpose, the intial forebody radius (r_{if}) is of importance to control the peak flow acceleration in the leading edge. The nacelle boat-tail angle (β_{nac}) in combination with L_{nac} and f_{max} control the geometry curvature in the afterbody of the nacelle to achieve a smooth adverse pressure gradient. The nacelle trailing edge radius (r_{te}) is constrained by the exhaust engine technology to achieve the cycle design point. In addition, due to the difference in flow in the upper and lower part of the nacelle and to accommodate the incoming flow in the intake, non-axisymmetric designs incorporate scarf angle (θ_{scarf}) and offset (Δ_{offset})[181] (Figure

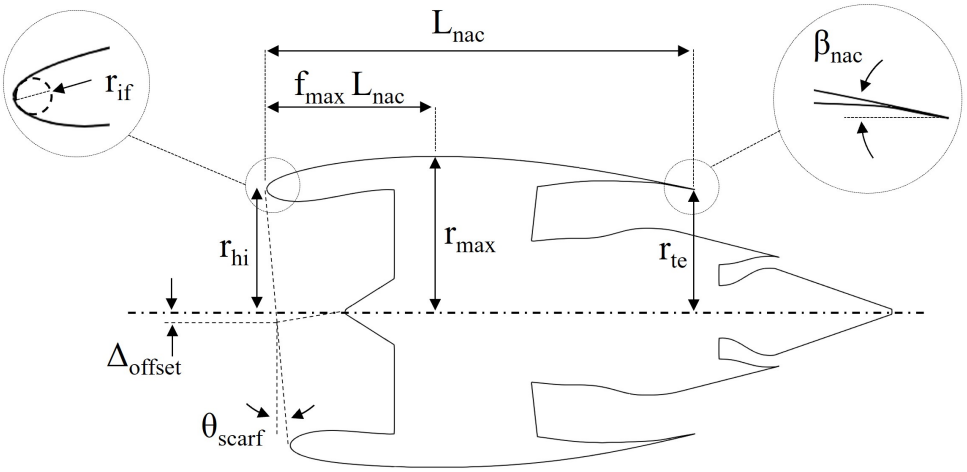

(A) Key parameters that define a nacelle design.

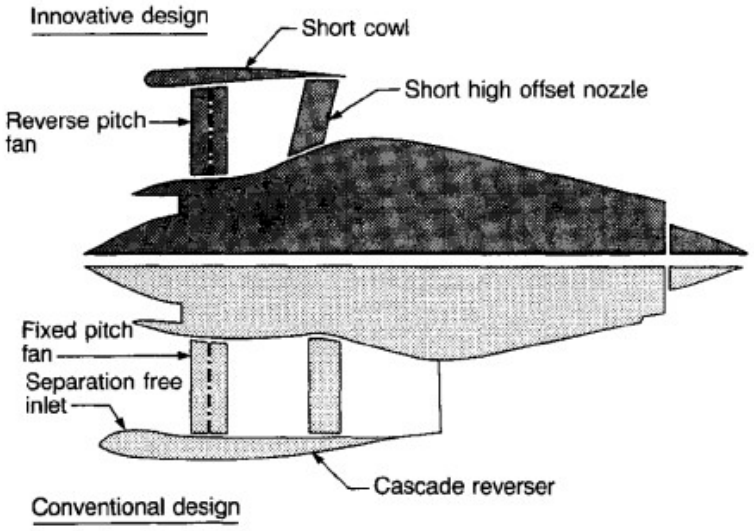

(B) Comparison of aero-engines technology with conventional and compact nacelles. Based on Zimbrick et al.[180].

FIGURE 2.17: Definition of the geometry of a nacelle and the trend towards compact aero-engine nacelle technologies.

2.17a). The scarf is defined as the angle between the fan face and the highlight plane. The offset represent the delta between the center lines of the engine and the highlight plane. These two parameters are used to align the nacelle lip with the incoming flow and improve the performance of the nacelle to the incidence induced by the aircraft angle of attack, the aero-engine installation pitch angle and the up-wash induced by the wing[182]. All of these parameters are strongly related to constitute a non-linear design space which becomes even more complex for compact aero-engine nacelle architectures (Figure 2.17b). These configurations are envisaged for shorter nacelles with a lower thickness relative to the fan diameter. Both drag and weight

savings are expected. Another advance in the technology to allow this thickness reduction is the removal of the thrust reverser system through a variable pitch fan with additional savings in weight (Figure 2.17b). A slim nacelle can be geometrically expressed as a reduction in the nacelle r_{max} for a given r_{hi} and r_{te}. Additionally, compact nacelles are expected to reduce L_{nac} to decrease the wetted area. In this respect, the design space of current and compact nacelles can be better understood by the ratios L_{nac}/r_{hi}, r_{max}/r_{hi} and r_{te}/r_{hi} (Figure 2.18). Compact configurations for UHBPR aero-engines are for $L_{nac}/r_{hi} < 3.1$, $r_{max}/r_{hi} < 1.2$ and $r_{te}/r_{hi} < 0.9$ (Figure 2.18). In general, r_{hi} is fixed in these ratios and L_{nac}, r_{max} and r_{te} are varied to define the compactness of a nacelle.

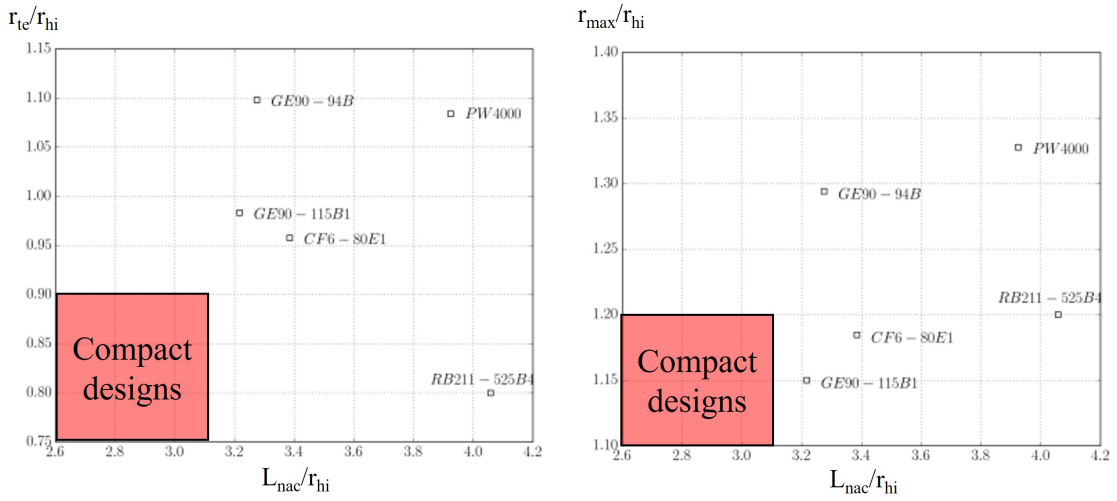

(A) r_{te} and L_{nac}.

(B) r_{max} and L_{nac}.

FIGURE 2.18: Design space for current and novel compact nacelle configurations based on L_{nac}/r_{hi}, r_{max}/r_{hi} and r_{te}/r_{hi} for long-range applications of Mach number around 0.85. Based on Robinson[183].

Robinson[183] studied the optimal design space of 2D axisymmetric nacelles for different configurations of compact and conventional architectures. L_{nac}/r_{hi} of 3.1 and 3.8 and r_{te}/r_{hi} of 1, 0.95 and 0.911 resulted in six different nacelle configurations. While $L_{nac}/r_{hi} = 3.8$ and $r_{te}/r_{hi} = 1$ is the most conventional configuration, $L_{nac}/r_{hi} = 3.1$ and $r_{te}/r_{hi} = 0.911$ is in the limit of the region of compact designs. Three objective functions were considered: cruise drag, drag rise Mach number and spillage drag (Section 2.1.1). Four design variables were optimised: r_{max}, f_{max}, r_{if} and β_{nac} (Figure 2.17a). A GFM using the Non-dominated Sorting Genetic Algorithm II (NSGA-II) was combined with a fully computational CFD-in-the-loop optimisation approach. A RANS solver with the $\kappa - \omega$ SST turbulence model[95] was used. The optimal design spaces based on the performance metrics were compared using the

Pareto plots (Figure 2.19). Regardless of r_{te}/r_{hi}, the shorter nacelle configurations reduced the minimum achievable cruise drag by approximately 15%. However, as r_{te}/r_{hi} is reduced, this minimum cruise drag comes at the expense of a reduction in the drag rise Mach number. Although this is also applicable for the longer nacelle ($L_{nac}/r_{hi} = 3.8$), it is more influential for the short designs. The opposite behaviour between M_{DR} and spillage drag is common for every configuration. The designs with the highest M_{DR} are those with the most adverse spillage. This can be explained by the different impact of r_{max} in the aerodynamic performance for high Mach numbers and spillage flow conditions. A reduction in r_{max} increases the M_{DR} as the theory for supercritical aerofoils explains. However, if r_{max} is reduced and the rest of the geometrical parameters are kept constant, the curvature in the nacelle forebody increases. As a result, there is a more severe flow acceleration around the lip of the nacelle for spillage conditions governed by low MFCR.

On the other hand, the sensitivity to increase in spillage drag with a reduction in r_{te}/r_{hi} is higher for the shorter nacelle ($L_{nac}/r_{hi} = 3.1$) (Figure 2.19). This can be explained from the distribution of the design variables of the Pareto data sets (Figure 2.20). r_{max} is consistently lower for the shorter nacelle compared to the longer design and is also further reduced when r_{te}/r_{hi} is decreased. This is consistent from the point of view of reducing the nacelle thickness for short designs as previously introduced. The behaviour of f_{max} is very related to r_{max} as the combination of both parameters define the curvature in the forebody of the nacelle. A monotonic curvature is desired to allow a smooth deceleration of the flow after the high flow suction in the highlight. This is beneficial both for a cruse drag reduction and an improvement in the off-design performance. Therefore, as r_{te}/r_{hi} decreases and induces a reduction in r_{max}, the crest of the nacelle moves forward and f_{max} is reduced. This correlation between r_{max} and f_{max} to achieve monotonic curvature gradients and also avoid inflected designs is more sensitive to changes in r_{te}/r_{hi} for short nacelles (Figure 2.20). There is a lower impact of the nacelle sizes on r_{if} (nondimensionalised as f_{if} in Figure 2.20) and β_{nac}. In particular, while β_{nac} tends to increase for reduction in r_{te}/r_{hi} for the long nacelle, the opposite trend is seen for the short nacelle. This second order impact of β_{nac} on the design space of isolated nacelles was also appreciated in other optimisation works[16].

Tejero et al.[16] went one step further and considered a more aggressive part of the design space for very short nacelles. Twelve combinations given by $L_{nac}/r_{hi} = 3.0, 2.8, 2.6, 2.4$ and $r_{te}/r_{hi} = 1.0, 0.95, 0.89$ were analysed. As Robinson[183], the optimal design space for these 2D axisymmetric nacelle configurations was explored using a GFM with the NSGA-II algorithm and a CFD-in-the-loop approach based on

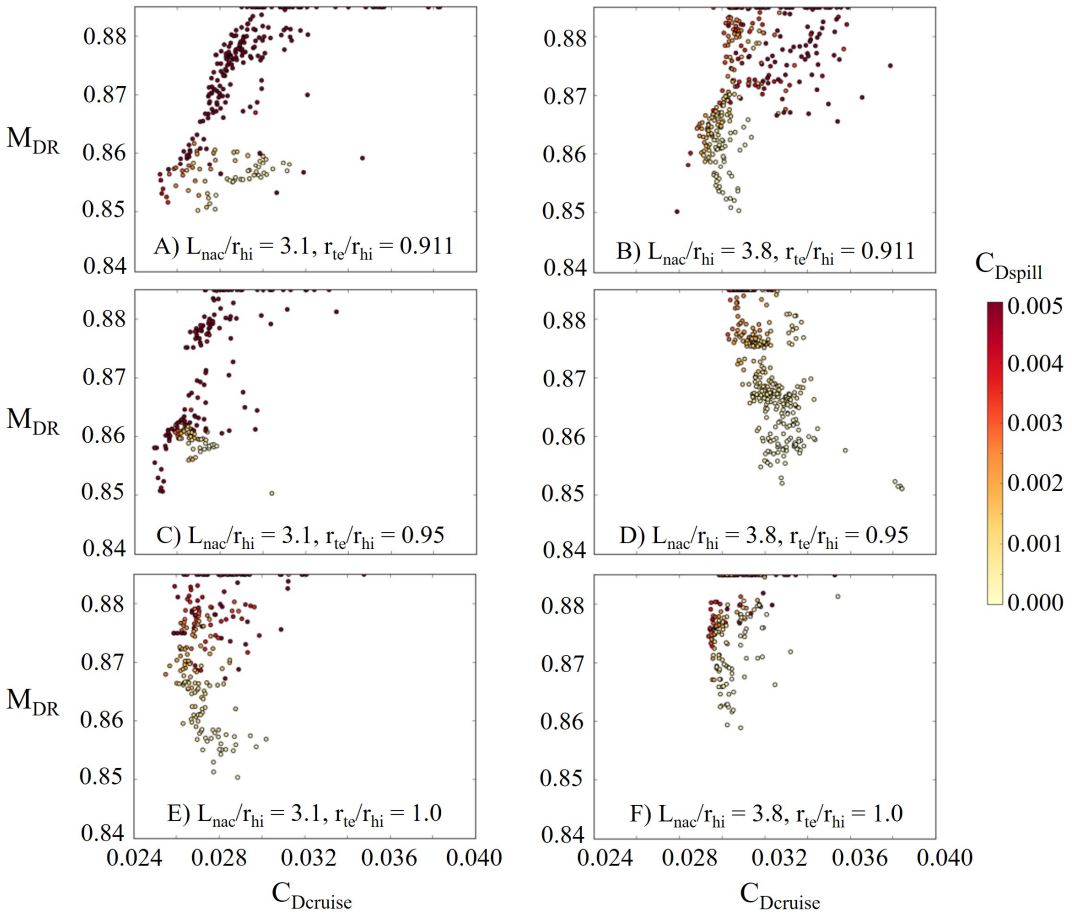

FIGURE 2.19: Pareto data sets resulting from 2D axisymmetric nacelle optimisations for different nacelle lengths and trailing edge radius. Results shown based on the performance metrics: cruise drag, drag-rise Mach number and spillage drag. Based on Robinson[183].

a RANS solver and the $\kappa-\omega$ SST turbulence model. Three objective functions were considered: cruise drag, spillage and the increase of +0.02 in the cruise Mach number. Four design variables were optimised: r_{max}, f_{max}, r_{if} and β_{nac} (Figure 2.17a), with the second derivative in the trailing edge(y''_{te}) being internally calculated given the previous four design variables. The distributions of the design variables in the optimal space shown by parallel coordinate plots highlights a narrowing of the design space for lower L_{nac} and r_{te} nacelle configurations (Figure 2.21). Additionally, as Robinson[183] indicated, β_{nac} and r_{if} are less influential in the optimal design space with a higher variability compared to r_{max} and f_{max} (Figure 2.21). However, it does not show a trend for reducing r_{max} and f_{max} when both L_{nac} and r_{te} are decreased as clear as Robinson[183] presented in Figure 2.20. The difference is that Robinson was comparing a compact and a conventional designs, while Tejero quantifies the differences only for compact configurations. In terms of performance metrics, there

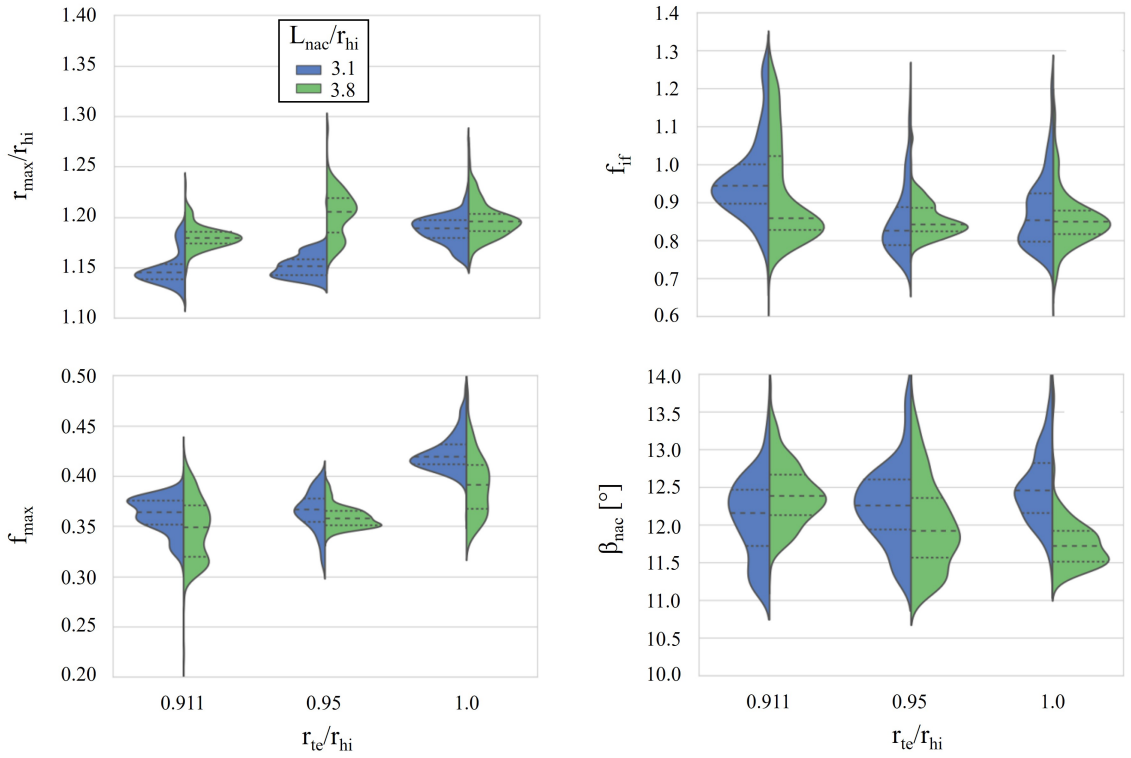

FIGURE 2.20: Pareto data sets resulting from 2D axisymmetric nacelle optimisations for different nacelle lengths and trailing edge radius. Results shown based on distributions of the geometrical parameters. The dashed line represents the median while the dotted line indicates the quartiles. Based on Robinson [183].

is a big cruise drag penalty of going towards a very aggressive configuration (Figure 2.21). This is due to the large flow acceleration and strong shock waves that arise from very high curvature gradients in the fan cowl. In particular, the optimisation for the most compact configuration ($L_{nac}/r_{hi} = 2.4$ and $r_{te}/r_{hi} = 0.89$) was not able to find any design with a peak isentropic Mach number lower than 1.3 as this aerodynamic constraint was imposed throughout the optimisation. The design space was analysed in more detail for the cruise drag as key metric by selecting from each MOO the design with lowest $C_{D-cruise}$ (Figure 2.22). A variation of 37% in $C_{D-cruise}$ was observed across the space of L_{nac}/r_{hi} and r_{te}/r_{hi}. For any fixed nacelle length, the drag can be reduced by moving the trailing edge outward towards $r_{te}/r_{hi} = 1$. However, for a fixed r_{te}/r_{hi} there is an optimum nacelle length L_{nac}/r_{hi}. For example, while for a compact $r_{te}/r_{hi} = 0.89$ the minimum cruise drag is found for $L_{nac}/r_{hi} = 2.8$, it is reduced to $L_{nac}/r_{hi} = 2.6$ when the trailing edge is increased towards $r_{te}/r_{hi} = 1$. The reason lies in the trade-off that exists between fan cowl curvature and wetted area. Shorter nacelles present a lower wetted area but also a higher surface curvature which caused wave drag penalties. Therefore, going towards a more compact nacelle in terms of r_{te} the penalties associated with

curvature are bigger than those associated with wetted area and a longer nacelle is required.

The previous analysis by Robinson[183] and Tejero[16] showed a more constrained design space and higher sensitivities to changes in the cruise operating condition for compact designs. In this respect, Schreiner et al.[18] performed MOO considering off-design windmilling conditions using a RANS CFD-in-the-loop approach for different L_{nac}/r_{hi} from 4.3 to 2.5. It was demonstrated that the inclusion of off-design conditions in the optimisation led to a different part of the design space. Using a traditional MOO approach that considers only the cruise segment a 20% in the cruise drag reduction can be obtained for a shortening of the nacelle from $L_{nac}/r_{hi} = 4.3$ to 2.5. To quantify the impact of the off-design conditions, Schreiner defined the Robustness Factor (RF) as the ratio $C_{D-windmilling}/C_{D-cruise}$ used to select a design. For example, for $RF = 3$, the previous 20% reduction in cruise drag is now changed to an increased in drag of 39% (Figure 2.23). This highlights the increased sensitivity to the consideration of off-design conditions in the MOO for compact nacelle configurations.

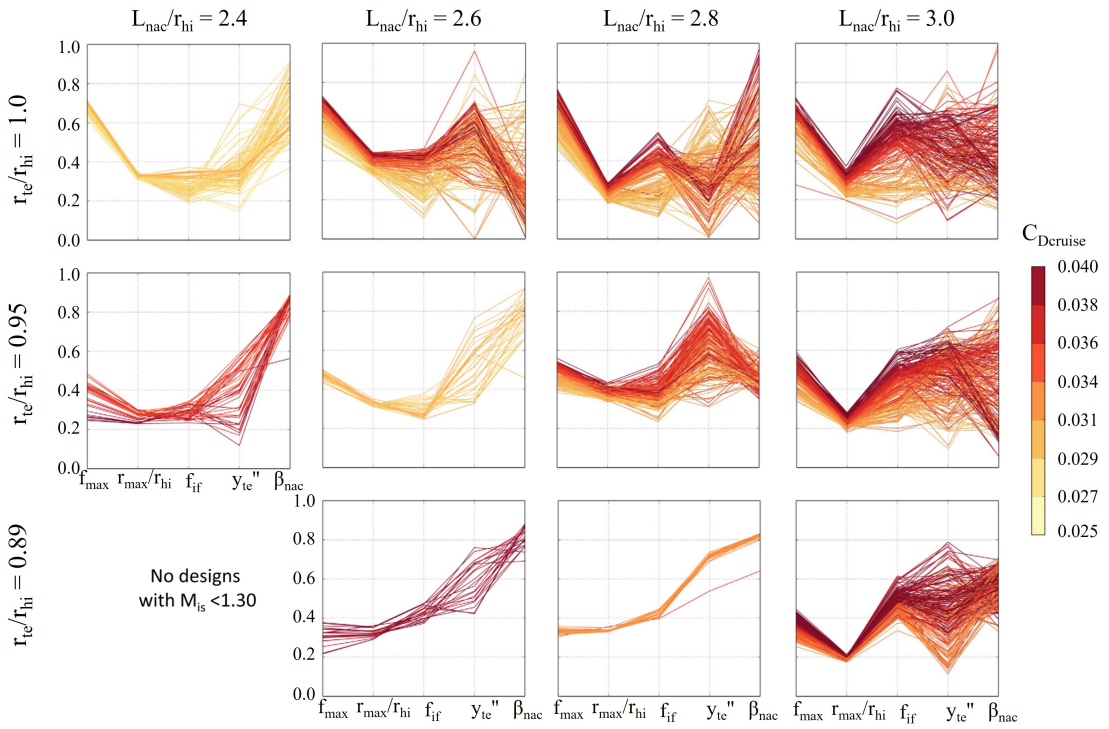

FIGURE 2.21: Optimal design space shown in terms of geometric parameters for 2D axisymmetric nacelles of different lengths and trailing edge radius. Parallel coordinate plot coloured by cruise drag. Based on Tejero et al.[16].

As introduced before in Section 2.3.3, the aerodynamic shape design and optimisation problem sometimes becomes computationally prohibitive from industrial time

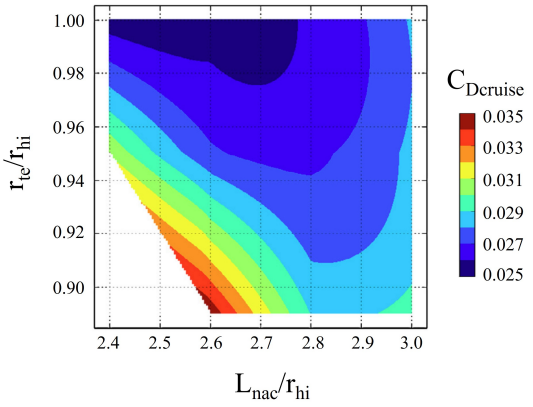

FIGURE 2.22: Distribution of cruise drag in the space L_{nac}/r_{hi} and r_{te}/r_{hi} for the selected designs with minimum cruise drag from each multi-objective optimisation. Based on Tejero et al.[16].

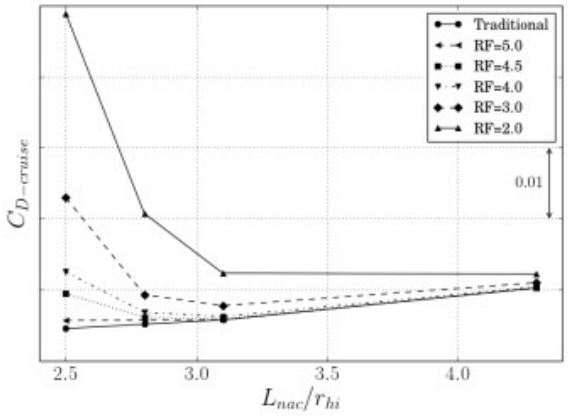

FIGURE 2.23: Impact of off-design conditions in MOO of different nacelle lengths. Based on Schreiner et al.[18].

scales. In the context of nacelle aerodynamic design, previous studies have investigated the use of surrogate models to reduce the computational overhead compared to CFD-based approaches[27,51,184–186]. Heidebrecht et al.[184] developed a metamodel based on Kriging interpolation for rapid assessment of drag for 2D axisymmetric nacelle geometries as a function of the Mach number and MFCR (Figure 2.24). It was constructed by exploiting self-similarities in the input data generated from RANS DSE. For the cruise condition this method predicts drag with a standard error of 3.6%. Additionally, the predictions of drag are consistent and smooth enough to allow an estimation of the first derivative of the drag relative to the Mach number. In this way the drag rise Mach number is possible to be predicted with a standard error of 0.014. Although this methodology is very useful to predict drag metrics at preliminary design stages, one limitation is that it does not provide any detail of the aerodynamics.

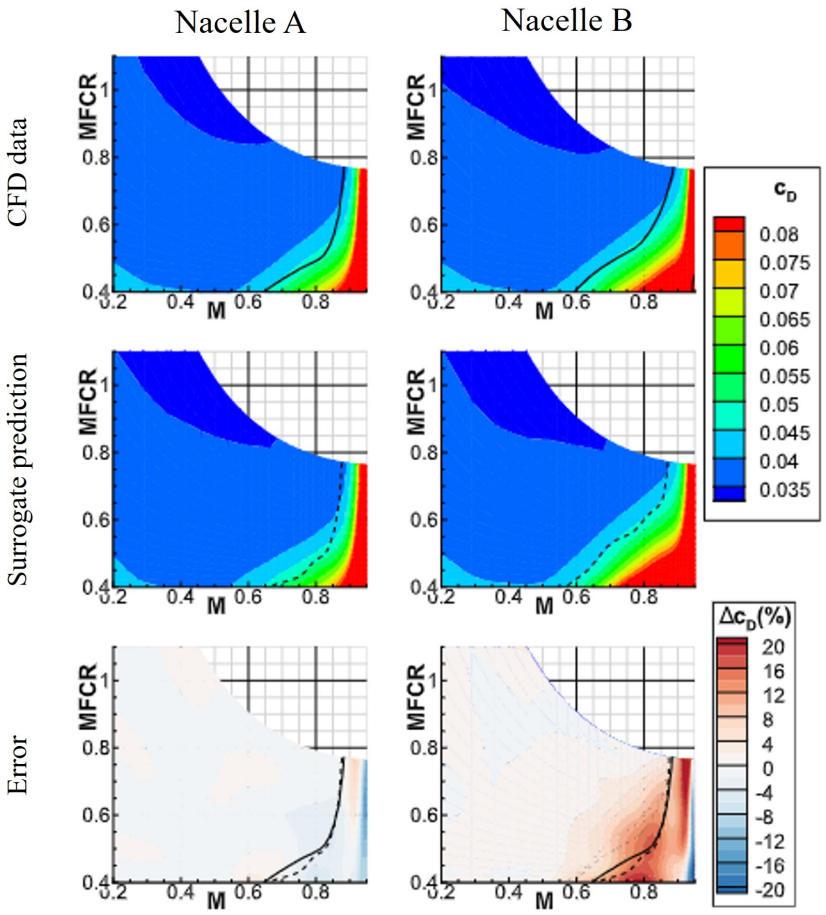

FIGURE 2.24: Comparison of CFD and surrogate model prediction for nacelle drag in the as function of Mach number and MFCR. Two different nacelles geometries are shown. Solid and dashed lines represent the M_{DR}. A positive error of the surrogate prediction relative to the CFD data indicates an over-prediction of the surrogate model. Based on Heidebrecht et al.[184].

Within the nacelle optimisation process, after completing the initial estimates at preliminary design stages the fidelity of the method has to be increased to enable a more detailed assessment of the aerodynamics. In this respect, Tejero et al.[185] combined a genetic algorithm with a Kriging interpolation model for a transonic MOO of a 2D axisymmetric compact nacelle ($L_{nac}/r_{hi} = 3.0$). The surrogate model was trained using RANS CFD data. An adaptive method (AM) was developed using an infilling strategy that updated the model at every generation of the optimisation to improve the prediction performance. This was compared with a traditional method (TM) in which the surrogate model was trained using only the data set of a design space exploration at the beginning of the optimisation with no infilling strategy. The AM provided a similar Pareto front to that from a CFD-in-the-loop approach with a reduction in the computational cost of 25% (Figure 2.25). This AM methodology was extended to MOO optimisations of 3D non-axisymmetric compact

nacelles[51]. The computational cost saving relative to the CFD-in-the-loop approach increased to 65% for a similar set of non-dominated designs in the Pareto. As an example of application, a similar method developed by Fang et al.[186] was used for the transonic optimisation of a 3D non-axisymmetric nacelle of $L_{nac}/r_{hi} = 3.32$. Geometry constraints were introduced to maintain the overall nacelle volume between limits in order to accommodate internal components of the aero-engine. Relative to an axisymmetric baseline geometry, the cruise drag was reduced by approximately 4.0%. This aerodynamic improvement was achieved by a reduction of the shock wave strength in the forebody of top of the nacelle and an increase in the pressurisation in the afterbody of the nacelle (Figure 2.26).

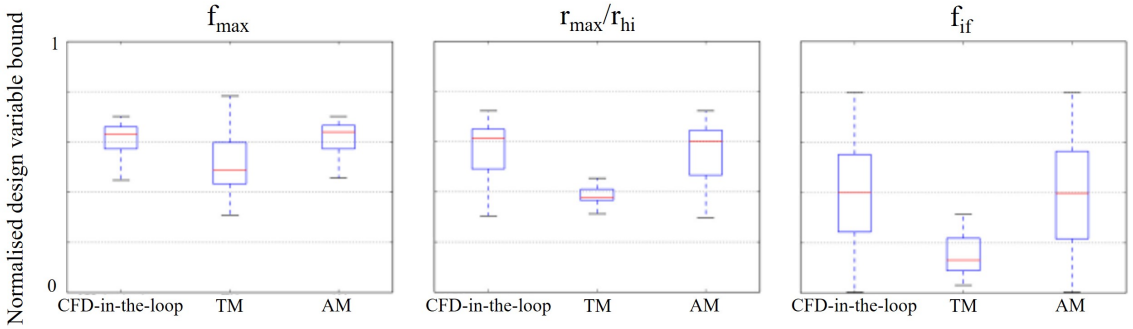

FIGURE 2.25: Box plots showing the optimal design space for the design variables f_{max}, r_{max}/r_{hi} and f_{if} with the three MOO optimisation strategies compared: CFD-in-the-loop and both TM and AM surrogate-based approaches. Based on Tejero et al.[185].

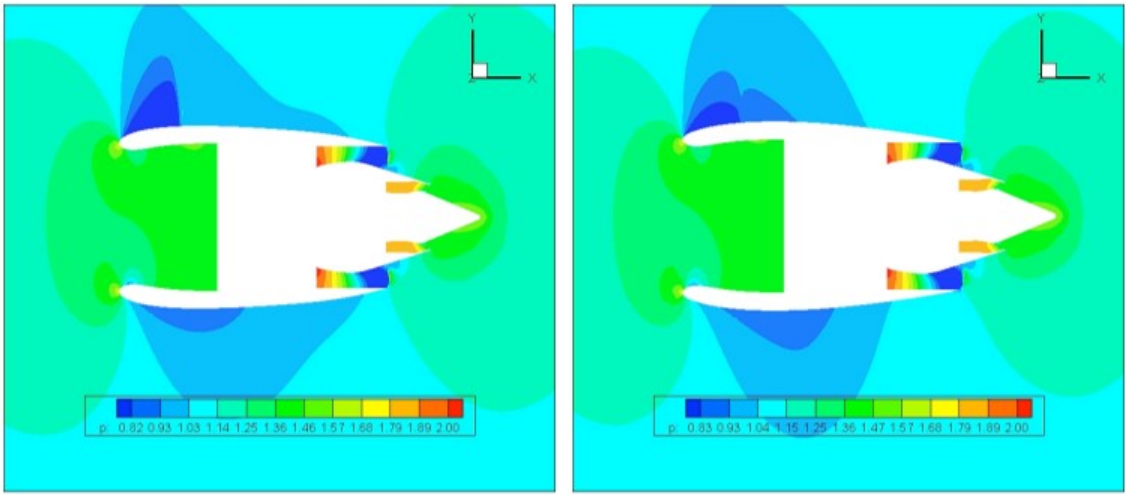

(A) Initial design. (B) Optimised design.

FIGURE 2.26: Pressure distribution for the initial design and the optimised non-axisymmetric nacelle design. $M_\infty = 0.8$, $MFCR = 0.75$ and $\alpha = 4°$. Based on Fang et al.[186].

Coupled intake-cowl design

The reduction of the size of the nacelle in proportion to the engine for compact configurations has implications on the design of exhausts and intakes. Although the exhaust are normally design independently[187,188], there are some examples in the literature of coupled design and optimisation of intake and fan-cowl[13,14,19,52,189]. This is a complex problem with contradicting guidelines in the design from each component. For example, while the cowl is intended to produce as less drag as possible and thin lips are preferred, the intake is required to provide airflow to the engine with a minimal pressure loss at different off-design conditions for which thick lips are more suitable to avoid flow separation. Consequently, the design strategy for short intakes and nacelles is based on trade-offs between nacelle drag reduction and penalties in fan efficiency due to flow distortion in the intake.

There have been previous optimisation works in this area. For example, Albert et al.[13] performed a MOO for 2D intakes and nacelle shapes using a RANS CFD model and a GA. The objectives were to minimise the peak Mach number (M_{peak}) in the external cowl at cruise ($M = 0.73$) and in the intake at off-design static run condition ($M = 0.05$) as they account for cruise drag and intake pressure loss respectively. Compare to a baseline, a reduction in M_{peak} for the nacelle at cruise and intake at static run of 14% and 29% respectively were achieved with the presented method. However, as this work is a 2D application it did not consider cross-wind which is a key scenario for intakes performance. Additionally, although not reported, the intake configuration seems quite conventional with a intake length over fan diameter ratio L_{intk}/D_{fan} estimated to be around 0.45.

Peters et al.[189] performed a more detailed design work. An integrated intake and nacelle design framework was developed which coupled a spline-based approach to define the geometries with a body-force model for the fan rotor and stator cascades. Not only the cruise condition for a medium range application ($M = 0.8$) was considered but also different off-design conditions like cross-wind, wing maximum lift C_{Lmax} and take-off rotation condition. A baseline design for $L_{intk}/D_{fan} = 0.5$ and two candidates designs for $L_{intk}/D_{fan} = 0.25$ and 0.19 were considered and evaluated using an unsteady RANS CFD solver with the Spalart-Allmaras[111] turbulence model (Figure 2.27, Figure 2.28). Relative to the baseline design, a short intake with $L_{intk}/D_{fan} = 0.25$ was able to maintain a similar fan efficiency with separation-free flow at off-design conditions (Figure 2.28) while reducing the nacelle drag by 16% at cruise condition (Figure 2.27). For the candidate design 2 with $L_{intk}/D_{fan} = 0.19$ the further reduction in nacelle drag at cruise was outweighed by a high penalty in

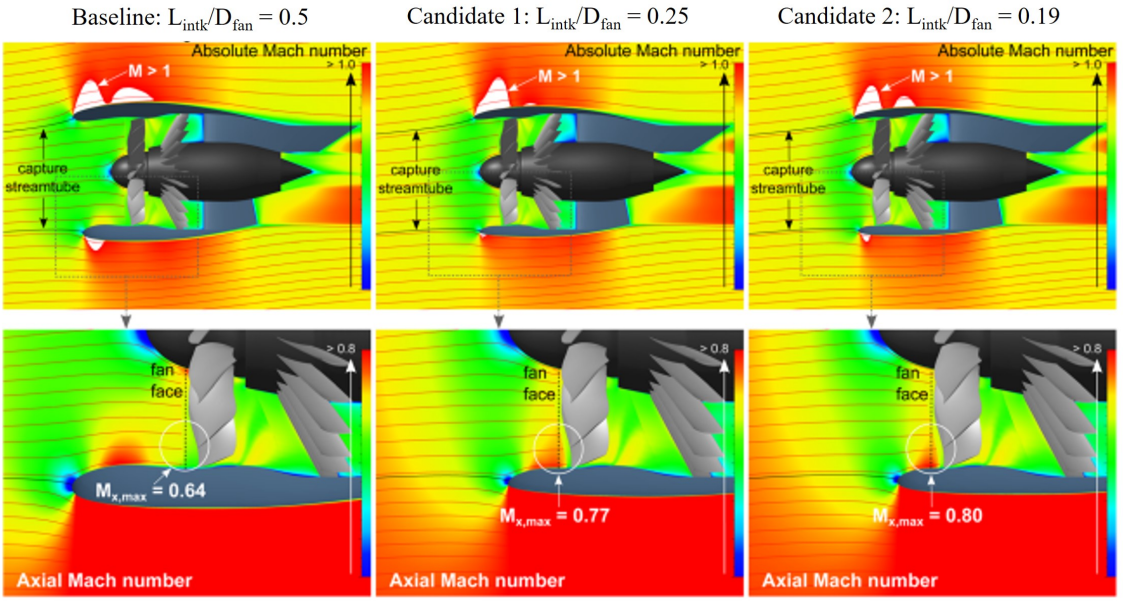

FIGURE 2.27: Mach number distribution (top) and axial Mach number distribution (bottom) at cruise condition ($M = 0.8$ and $\alpha = 5°$) for the baseline (left), candidate 1 for $L_{intk}/D_{fan} = 0.25$ (middle) and candidate 2 for $L_{intk}/D_{fan} = 0.19$ (right). Based on Peters et al.[189].

the fan efficiency at off-design condition caused by the interaction between the fan rotor and a region of high Mach number and low flow straightening at the fan face (Figure 2.28). Therefore, it was recommended a range of L_{intk}/D_{fan} between 0.25 and 0.4 to achieve overall benefits for compact nacelle designs without jeopardizing the fan operability.

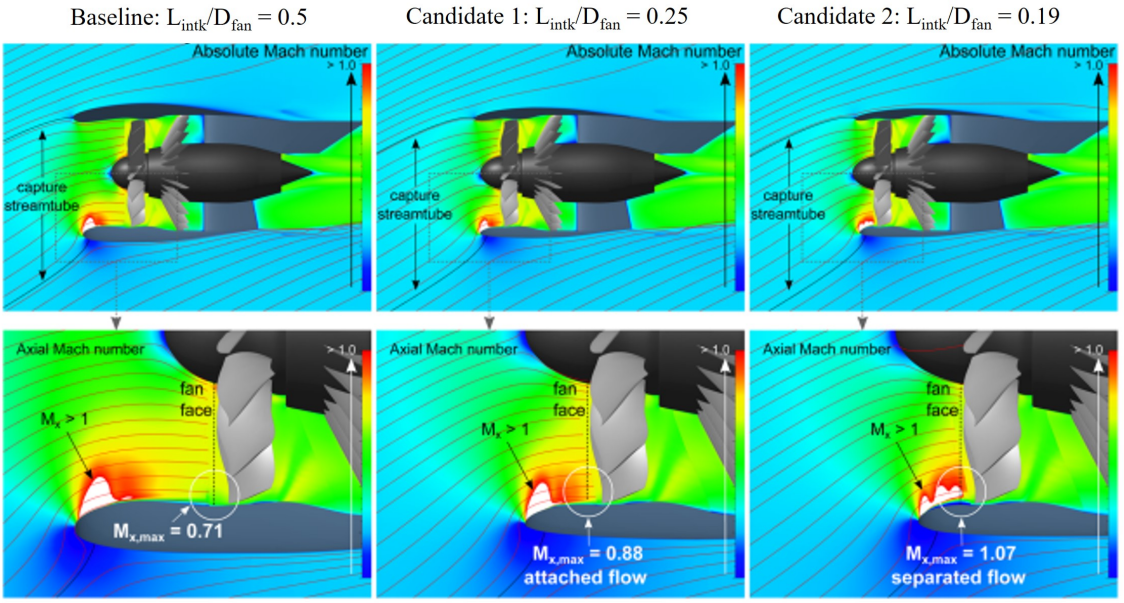

FIGURE 2.28: Mach number distribution (top) and axial Mach number distribution (bottom) at maximum wing lift coefficient condition ($M = 0.25$ and $\alpha = 29°$) for the baseline (left), candidate 1 for $L_{intk}/D_{fan} = 0.25$ (middle) and candidate 2 for $L_{intk}/D_{fan} = 0.19$ (right). Based on Peters et al.[189].

2.3.4.2 Installed configuration

As explained in Section 2.2.3, the aerodynamic performance of the nacelle installed in the airframe can deviate substantially from the isolated case due to the aero-engine integration effects specially in the inboard side. Therefore modern design technologies need to consider the design space of the aero-engine coupled with the airframe.

Some of the previous work on optimisation of the combined engine-airframe system have kept fixed the nacelle shape and changed the wing and pylon geometries or the aero-engine installation position and angles. For example, Li et al.[190] optimised the position of the nacelle/pylon on a the transonic DLR-F6 airframe at cruise condition ($M = 0.75$ and $C_L = 0.5$) with the aim to reduce the drag of the total aircraft. A Free-Form Deformation method controlled by 12 variables was used to modify the vertical and horizontal positioning of the nacelle relative to the wing. A smooth deformation of the pylon was needed to adjust the nacelle to each installation position. A RANS CFD model was used to evaluate 24 different installation positions to construct a Kriging surrogate model. A surrogate-based optimisation using a PSO optimiser delivered a configuration with a reduction of 1% in total cruise drag relative to the baseline geometry. The optimal geometry was found for a nacelle

position axially forward and vertically closer to the wing. The drag reduction of this configuration came from a reduction in the strength of the shock wave located in the junction between the pylon and the wing.

An additional optimisation of the combined engine-airframe system was performed by Koc et al.[191] for $M = 0.74$ and $C_L = 0.14$ using the DLR-F6. Although this operating point was reported as representative of climb condition the lift coefficient is remarkably low for this kind of flight phase. The configuration obtained from the optimisation exhibited a penalty in the cruise condition ($M = 0.74$ and $C_L = 0.54$) of +0.8% in total aircraft drag relative to a baseline. Consequently, Saitoh et al.[192] extended the previous work to consider also the cruise condition within a multi-point optimisation approach. In the optimisation the shapes of the inboard side of the pylon and wing were changed and also the nacelle vertical position and pitch installation angle which resulted in overall 82 design variables. The nacelle shape was kept constant. The transonic DLR-F6 airframe was used. The flow analysis was performed through an Euler CFD solver and the optimisation was based on a GBM method with the SQP algorithm and an adjoint approach for the computation of the gradients. Relative to a baseline design, a reduction in the total aircraft drag of -15% and -5% was obtained for the climb and cruise condition respectively. The benefit at cruise comes from a reduction of the shock strength and extent over the wing due to the shape optimisation of the wing inboard side and a downward movement of the nacelle relative to the wing (Figure 2.29a). At the low lift condition, the very strong shock present in the baseline inboard side between the pylon, lower wing and nacelle afterbody was notably weakened (Figure 2.29b). In this work the optimal configuration was found for a reduction in the pitch angle of the installation and an increase in the vertical separation of the nacelle with the wing. This is in opposition with the findings of Li et al.[190] which reported benefits for a closer vertical location of the nacelle and wing. However, it is not possible to determine if this different outcome is due to the consideration of the low lift condition in the optimisation performed by Saitoh et al.[192].

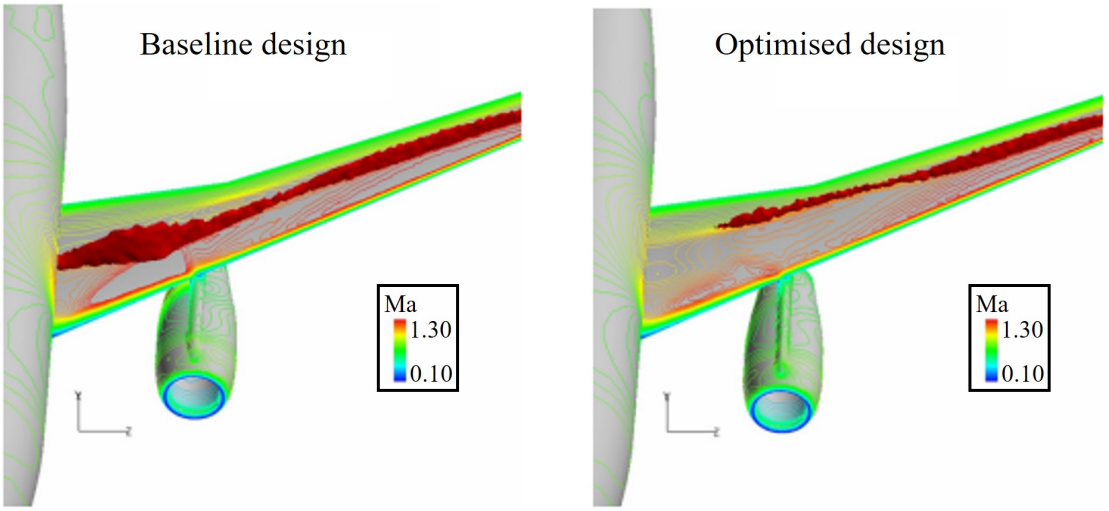

(A) Cruise condition: $M = 0.74$ and $C_L = 0.54$. Shock visualisation through iso-surface of $M = 1$.

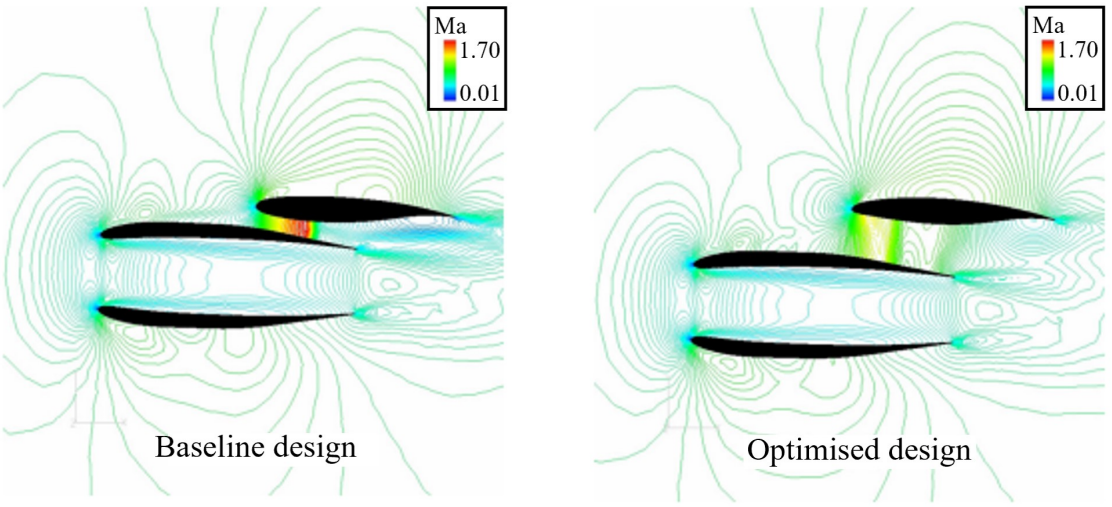

(B) Low lift condition: $M = 0.74$ and $C_L = 0.14$. Plane section at 34% of the wing span.

FIGURE 2.29: Mach contours for baseline and optimised designs at cruise and low lift conditions. Based on Saitoh et al.[192].

The state of art of design and optimisation of the combined engine-airframe system in which the nacelle geometry is optimised is very scarce. Two examples have been found in the open literature: (1) an over-the-wing nacelle mounted configuration for a mid-range application of $M = 0.7$[68] and (2) a under-the-wing configuration for a UHBPR aero-engine of BPR $\approx$ 15 installed in a single-aisle transport of cruise $M = 0.785$[193].

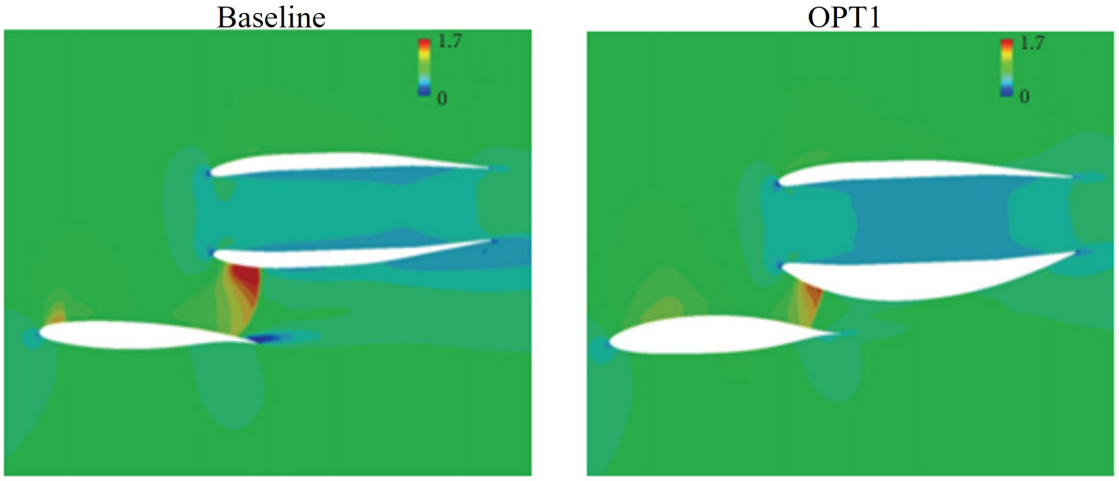

(A) Comparison of wing, nacelle and installation positions from optimisation 1. Plane section at 32% of the wing span located in the inboard side.

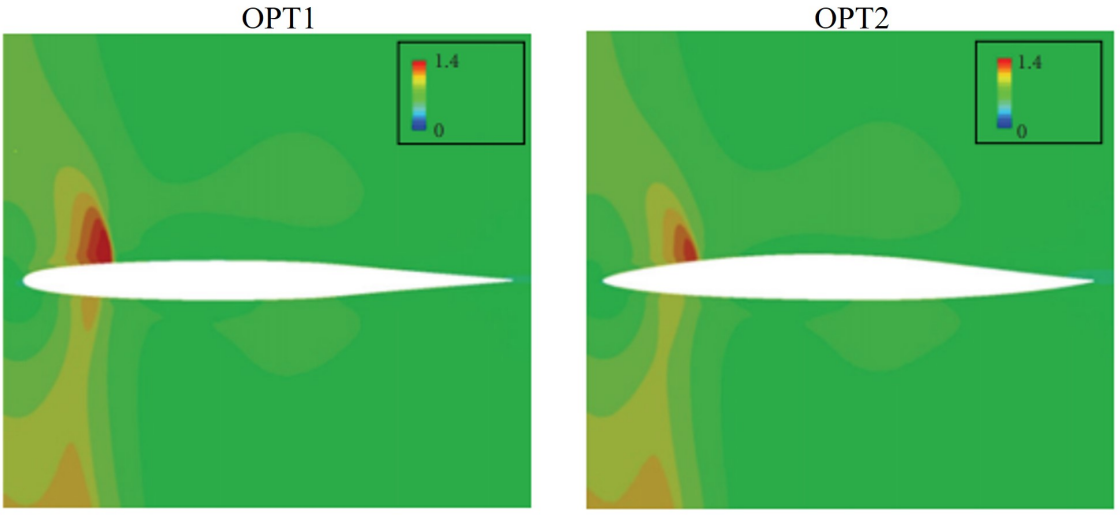

(B) Comparison of pylon designs from optimisation 2.

FIGURE 2.30: Mach contours for baseline and optimised designs at cruise condition. and low lift conditions. Based on Saitoh et al.[192].

Sasaki et al.[68] optimised the wing-nacelle-pylon system for an over-the-wing installation. The objective was to maximise the lift-to-drag ratio (L/D) of the whole aircraft for the cruise condition defined by $M = 0.7$ and $C_L = 0.57$. A compressible Euler CFD solver was used for the flow analysis. The optimisation was based on a GFM method with a GA coupled with an adaptive Kriging model built from Euler CFD data. Throughout the optimisation, the wing aerofoil, lower half of the nacelle, pylon profile and installation position were changed. The wing planform and upper side of the TFN nacelle were kept as the DLR-F6 designs. The optimisation was performed in two steps. Initially the wing aerofoil (30 design variables), the lower

nacelle (12 design variables) and the installation position (2 design variables) were optimised together. The pylon shape was fixed to the symmetric NASA SC(2)-0008 aerofoil. Relative to the baseline value of $L/D = 25$, the optimum design (OPT1) increased to $L/D = 34.5$. More benign aerodynamics between the nacelle and the wing resulted from a reduction in the shock strength between the wing and the nacelle (Figure 2.30a). This was primarily achieved by increasing the thickness of the lower half of the nacelle and the aft wing which reduces the curvature gradients and flow acceleration. This also highlights that in spite of a reduction in the gap between the wing and the nacelle for OPT1 relative to the baseline design, an appropriate reshape of the wing and nacelle can reduce the aerodynamic interference effects (Figure 2.30a). In the second optimisation step, using the OPT1 design, the pylon profile was optimised using 15 design variables. The final optimum design (OPT2) further increased the aerodynamic efficiency to $L/D = 35.4$ due to a reduction of 5 drag counts relative to the OPT1 design. The optimised non-symmetric pylon shape weakened the shock in the inboard side due to an increase in the thickness and a reduction in the curvature (Figure 2.30b).

On the other hand, Smith et al.[193] performed a coupled optimisation of the wing and UHBPR aero-engine nacelle (BPR ≈ 15). The airframe used was representative of a single-aisle transport configuration with a cruise point of $M = 0.785$ and $C_L = 0.52$. The optimisation was based on compressible Euler calculations coupled with a GBM method and an adjoint approach to compute the gradients. Corrections with a viscous solver were applied to the optimised design. The optimisation objective was to maximise the aerodynamic efficiency L/D. Throughout the optimisation, the wing aerofoils at seven span sections were changed. The nacelle shape, pitch and toe installation angles as well as the pylon camber were also optimised. The optimisation problem was controlled by a total of 159 design variables. The optimal design achieved an inviscid $L/D = 39.7$ but it was not possible to compare with the baseline value as it was not reported. However, the optimised design exhibited an improved aerodynamic compared to the baseline based on inviscid computations (Figure 2.31). A similar pressure distribution in the upper and lower lips of the nacelle with the elimination of the shock in the lower lip was achieved primarily due to a better alignment of the nacelle with the local flow (Figure 2.31a). Additionally, the reshaping of the nacelle, wing and pylon managed to mitigate the shock wave in the nacelle-pylon-wing junction (Figure 2.31a). On the suction side of the wing the double shock topology was replaced with a weak single sock in a more downstream position which is representative of a more desirable supercritical pressure distribution (Figure 2.31b). The optimal design was evaluated to correct

for the viscous effects and the aerodynamic was compared with Pressure Sensitivity Paint (PSP) measurements in the wind tunnel (Figure 2.32). A good agreement was found between the inviscid (Figure 2.31b) and viscous CFD solutions and the experimental measurements (Figure 2.32), which confirms that the relevant interference aerodynamic phenomena are captured with lower fidelity inviscid CFD methods.

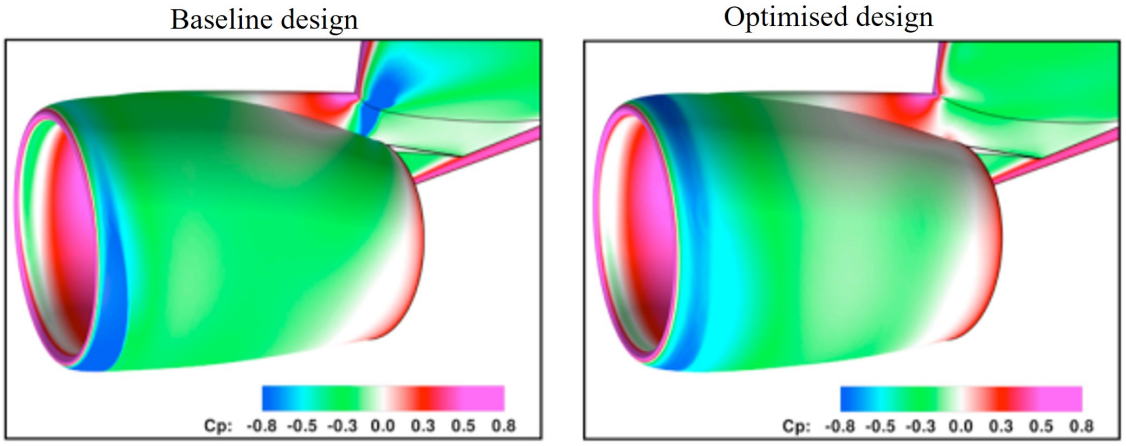

(A) Inboard view of the wing-pylon-nacelle configuration.

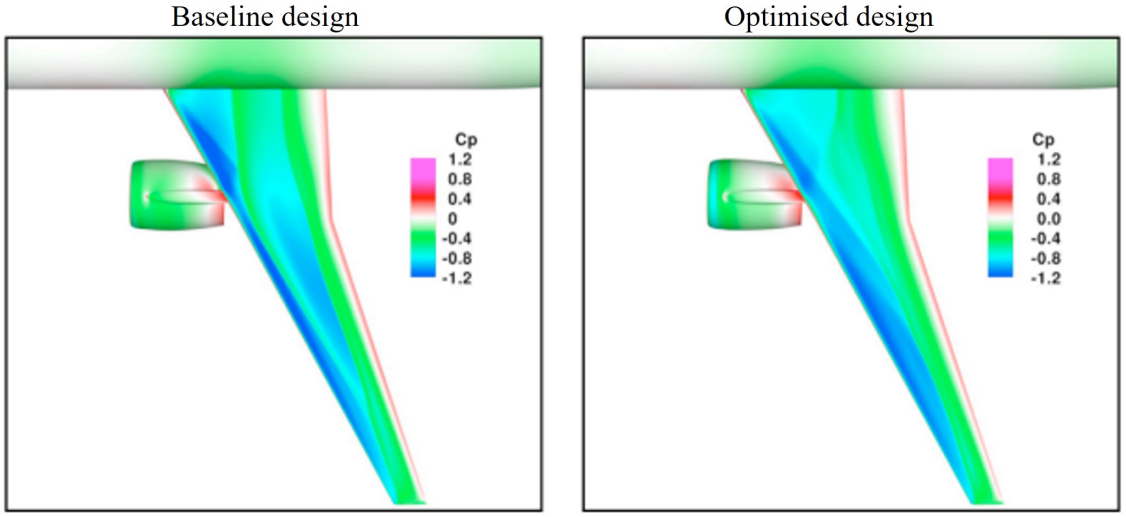

(B) Upper view of body-wing-nacelle-pylon configuration.

FIGURE 2.31: Contours of pressure coefficient for baseline and optimised designs at cruise condition ($M = 0.785$ and $C_L = 0.52$). Inviscid CFD solutions. Based on Smith et al.[193].

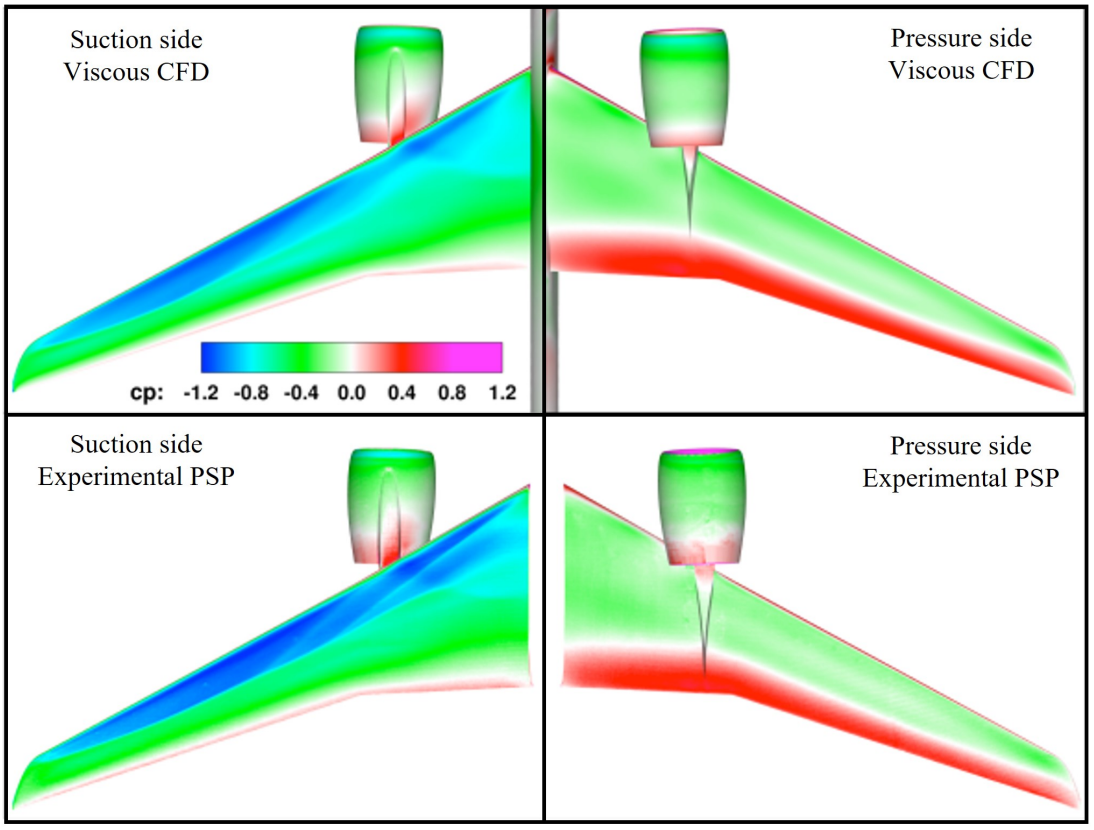

FIGURE 2.32: Comparison of distributions of pressure coefficient for the wing-body-nacelle-pylon optimised design between viscous CFD calculations and experimental PSP measurements at the cruise point ($M = 0.785$ and $C_L = 0.52$). Based on Smith et al.[193].

2.4 Computational methods for off-design conditions

As explained in Section 2.3, aerodynamic shape design and optimisation is a complex problem that involves trade-offs between multiple operating conditions to achieve robust designs. While for cruise-type operating conditions with benign aerodynamics RANS models might be enough to predict the flow physics, challenging flow features like shock-induced or diffusion-induced flow separation, shock and boundary layer interaction or wake interaction may arise at off-design conditions. The choice of the computational method used to predict such aerodynamic phenomena requires a careful thinking. This section provides details of the resolution level of the different computational methods and the viability from the point of view of industrial design time scales. Examples of comparison of different computational methods for representative aerodynamic applications are provided with an special focus on the limitations of RANS-based approaches.

2.4.1 Computational methods

Most of the real aerodynamic applications are governed by high Reynolds numbers and fully turbulent flows. A wide range of turbulent scales can be distinguished through the turbulent energy cascade (Figure 2.33). The large turbulent structures (κ_L) are associated to perturbations generated by the geometry length scales like flow separation. These are the most energetic structures. The large scale turbulent structures are rearranged into smaller structures in the Kolmogorov microscale (κ_ϵ) where the turbulent kinetic energy is dissipated by viscosity in the form of heat[194].

There are different computational techniques available to solve the Navier-Stokes equations depending on the range of turbulent scales that are resolved and modelled (Figure 2.33). While Direct Numerical Simulation (DNS) solves all the turbulent length scales, RANS was developed to model the full turbulent energy spectrum. Different turbulence models have been developed for RANS methods based on the Boussinesq´s hypothesis. It assumes that the stress tensor resulting from applying the Reynolds decomposition to the Navier-Stokes equations is proportional to the product of the deformation rate of the mean flow (mean velocity gradient) and the turbulent eddy viscosity. In the middle, Large Eddy Simulation (LES) offers a compromise to solve the big scales in the flow and model those close to the dissipation range. This is based on the fact that large scales are very case dependant while the Kolmogorov microscale is more universal in nature[195]. This is achieved by applying a Sub-Grid Scale (SGS) model in the form of a low-pass filter to the Navier-Stokes equations.

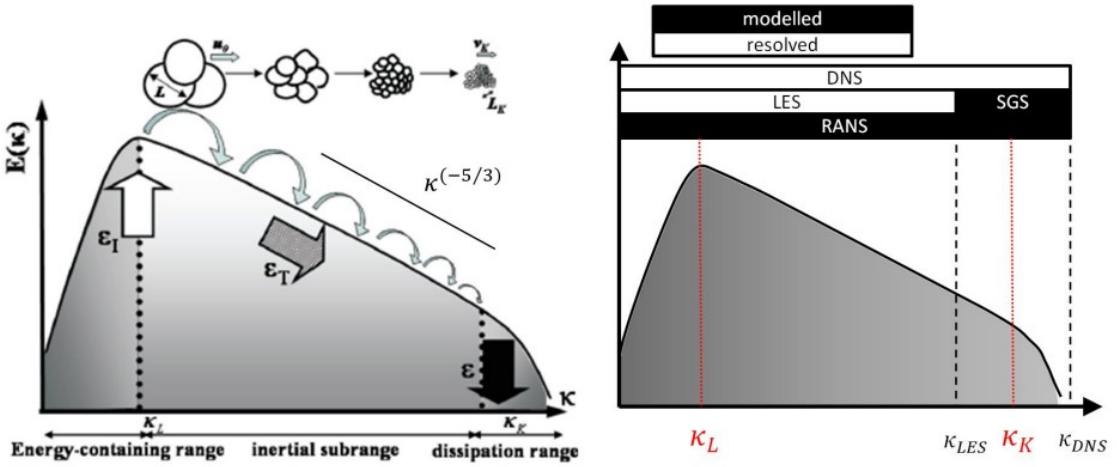

FIGURE 2.33: Turbulent energy cascade and resolution levels with different CFD strategies. Based on Sagaut et al.[196].

2.4.1.1 Hybrid RANS/LES method

It is known that RANS methods struggle to simulate cases with complex separated unsteady flows regardless of the turbulence model used[197]. On the other hand, DNS or LES approaches are too expensive alternatives from a computational cost standpoint. While DNS is directly out of the scope, Spalart et al.[198] estimated a grid size for a LES simulation of minimum 10^{11} cells for normal aerodynamic applications of Reynolds number of about 10^7. Additionally, a very fine time step is required for the resolved turbulent time scales. Relative to a RANS calculation, Gourdain et al.[199] reported an increase in the computational time of a LES calculation by a factor of 5000. With the current computational resources, LES is out of reach from an industrial design process point of view. This is the reason of the development of hybrid LES-RANS schemes. An example is the Detached Eddy Simulation (DES) method[198]. This method applies an unsteady RANS (URANS) approach to model the unsteady fluctuations in the regions where the flow is attached which normally is in the boundary layer. A LES method is used for the turbulent structures in the region of separated flows or mixing layers with a LES-type of grid[200]. The key challenge of a DES method is related to the switch from the RANS to the LES model. This is controlled through the boundary layer grid sizes. However, ambiguity can appear when a grid size in the direction parallel to the wall is similar to the thickness of the boundary layer (Figure 2.34a). This can trigger a switch to LES within the boundary layer. As a result, the velocity fluctuations in the LES region of the boundary layer are not developed enough to compensate for the loss of RANS eddy viscosity in that same region. This is called Modelled-Stress Depletion (MSD) and can lead to an under-prediction of the skin friction coefficient and an unphysical premature flow separation called Grid-Induced Separation (GIS)[201,202] (Figure 2.34b).

Several methods were developed to overcome MSD[203]. Zonal DES (ZDES) was proposed as an alternative in which the user can prescribe the location of the switch between the RANS and the LES models regardless of the grid resolution[204]. This allows to perform grid refinements in the LES region of interest without corrupting the boundary layer properties. However, this method requires an a priori knowledge of the flow field. Spalart et al.[205] presented an updated version of DES called Delayed DES (DDES) that used a shielding function to ensure the use of the RANS method within the attached boundary layer regardless of the grid sizes. This shielding function was able to automatically assess if a cell was within the boundary layer and therefore no prior knowledge of the flow field was required.

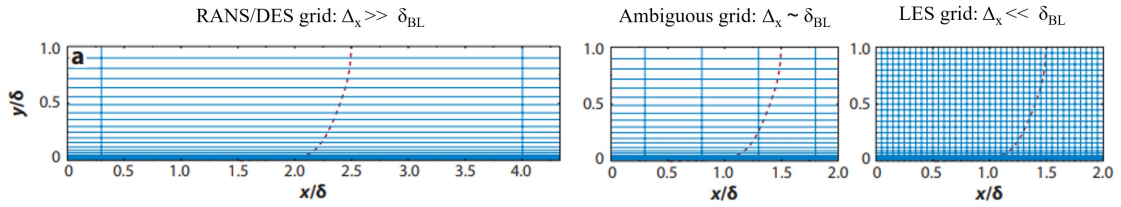

(A) Types of grids in boundary layer. Based on Spalart[201].

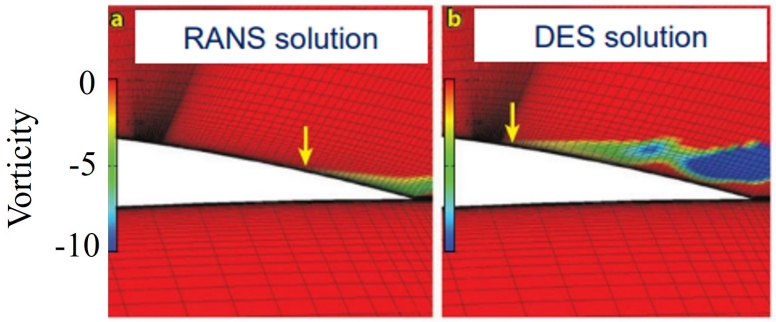

(B) Example of grid induced separation on an aerofoil. Based on Menter et al.[202]

FIGURE 2.34: Challenges of the DES computational method.

2.4.2 Aerodynamic applications

The focus of this section is on the comparison of RANS and unsteady higher fidelity computational models for aerodynamic applications in the presence of flow separation. There is no previous work in the open literature about unsteady computational methods for nacelle aerodynamic assessments or design, which is the topic of this project. However, there are some investigations comparing computational methods for representative external aerodynamics applications. For example, Shur et al.[206] compared URNAS with different turbulence models and DES for the turbulent flow of the symmetric NACA0012 aerofoil at $\alpha = 90°$ flow incidence ($Re = 10^4$). It was found an influential dependence of RANS-based methods with the turbulence model. $\kappa - \omega$ SST was able to model smaller eddy structures compared to the one-equation Spalart-Allmarast model. However, such impact of the turbulent model was not found for the DES model, which uses a RANS approach in the generally attached boundary layer. This is clearly showing the impact of using turbulence models for separated flows as they are calibrated trying to model a standard behaviour of the turbulent structures and many of them are very problem-dependant. Additionally, URANS methods largely suppress the three-dimensionality of the turbulent flow with no improvement as the grid becomes finer as opposed to DES method. In a

DES method the grid size is related to the SGS and therefore the length scale of the revolved eddies.

Wang et al.[207] compared experimental measurements with DES and RANS CFD results for a co-flow jet (CFJ) aerofoil. CFJ aerofoils use flow control to delay stall at very high incidences. A high energy jet (V_{j1}) is tangentially injected in the suction surface close to the leading edge which is sucked near the trailing edge (V_{j2}) (Figure 2.35). A span of one chord length was considered. The Reynolds and free stream Mach numbers were about 3.8x10^5 and 0.11 respectively. While both experiments and DES found the critical incidence of flow separation at 37°, the RANS CFD model predicted flow separation at 30° (Figure 2.36). This is a interesting comparison from the point of view of nacelle design since the critical incidence at the windmilling end-of-runway condition is considered in the optimisation process.

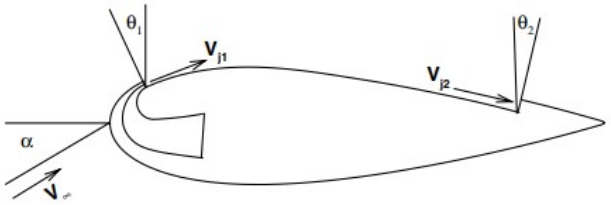

FIGURE 2.35: Co-flow jet aerofoil technology. Based on Wang et al.[207].

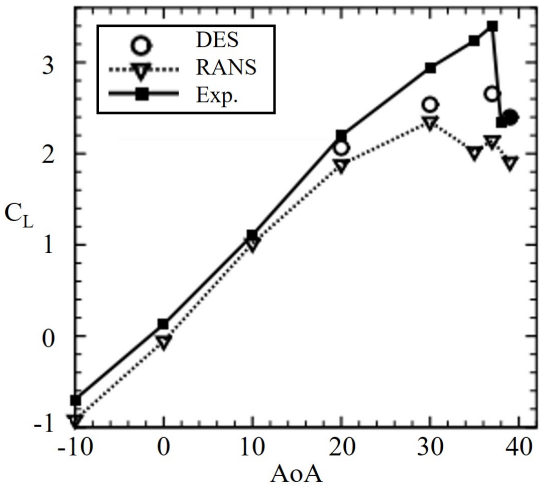

FIGURE 2.36: C_L against incidence for the CFJ0025-065-196 aerofoil between experiments and DES and RANS CFD calculations. Based on Wang et al.[207].

CHAPTER 3

Scope of the project

This research project about nacelle aerodynamic design involves a range of techniques and methods which go from direct design space explorations to optimisation approaches. Although the work is basically computational, experimental data is also used for validation purposes. Different levels of CFD fidelities are considered. Additionally, a variety of both single-fidelity and multi-fidelity surrogate modelling techniques are assessed.

3.1 Research gaps and novel contributions

The literature review presented in Chapter 2 helped to identify the gaps in the knowledge that motivate this project. This section states these gaps and the novel contributions from this research to address them.

- **Do multi-fidelity methods offer benefits for nacelle design and optimisation?**

Due to computational cost constraints, previous works about nacelle aerodynamic design in installed configurations use inviscid computational methods to drive the design process. For UHBPR aero-engine configurations, closer-coupled installation positions relative to current in-service architectures are expected and viscous phenomena like shock-boundary layer interaction or flow separation might become more influential. To assess this, different single- and multi-fidelity modelling techniques that combine Euler and RANS CFD data have been systematically evaluated based

on the trades between aerodynamic performance benefits and computational effort. A multi-fidelity neural network (MFNN) modelling technique was implemented. While for the isolated nacelle optimisation problem, the MFNN method provided a reduction in computation cost of around 90% compared to traditional RANS CFD-in-the-loop optimisations, the high sensitivity of neural network models to scarce data sets and the prohibitive computational overhead of airframe-installed RANS CFD calculation makes MFNN a non-feasible modelling technique for installed nacelle design. As an alternative multi-fidelity technique to MFNN, variable complexity models (VCM) that combine the high- and low-fidelity data sets using Kriging models were tested. This was based on the fact that for the scarce RANS data sets the Kriging technique has better modelling performance than neural networks. However, for the same overall computational cost, the multi-fidelity technique did not show any benefit compared to a traditional single-fidelity Euler-based Kriging model. Therefore, it was found for the first time that multi-fidelity methods are not useful for nacelle design in installed configuration due to the high cost of RANS calculations and the best method consists on highly populated design spaces based on Euler calculations.

- **What are the design space and performance benefits for installed nacelle design?**

As shown in Chapter 2, there is very little previous work that modifies the nacelle geometry within a design and optimisation process for an engine-airframe system. Additionally, it is a time consuming problem within the context of industrial time scales. In this respect, this thesis has developed an approach to design and optimise the nacelle installed in the airframe which is primarily driven by surrogate modelling techniques. The method is based on the traditional Euler-based approach with a posteriori evaluation of the optimal design using the higher fidelity RANS model. This method provides Euler-based design maps for the installed nacelle design variables that show the potential performance improvements across the design space and enables trade studies. A heavily populated design space has been found to be the most important parameter to identify the best design and develop the design maps. This method has shown potential benefits in the optimised designs that can go up to 0.6% reduction in the fuel burn at the cruise condition.

- **What are the limitations of RANS models for nacelle design at off-design conditions?**

The aerodynamic performance of compact nacelle configurations are sensitive to off-design operating conditions and flow separation may happen. Although RANS methods struggle to accurately simulate separated flows, unsteady methods are not computationally feasible for aerodynamic shape design and optimisation purposes. The limits of RANS models for key off-design conditions of compact nacelles have been assessed by comparing with an eddy-resolving DDES computational method and experimental data. For shock-induced flow separation physics that occur at windmilling diversion condition, the RANS model under predicts the separation extent by a factor of around 2 with respect to DDES solutions. The key parameter on the aerodynamics at this operating condition is the aero-engine mass flow capture ratio (MFCR). A higher sensitivity of the flow separation extent to MFCR has been found for the DDES model compared to the RANS model. A proper estimation of MFCR for windmilling diversion is crucial for RANS-based nacelle design and optimisation approaches. To account for this sensitivity within RANS-based approaches, a margin of around -0.02 in the nominal windmilling diversion MFCR condition is proposed. For diffusion-induced flow separation behaviours that occurs at windmilling end-of-runway condition, RANS is optimistic compared to experimental measurements in the prediction of the critical incidence at which separation starts. For a RANS-based design and optimisation approach the end-of-runway condition is recommended to be increased by around 1.5° to consider this sensitivity.

3.2 Results overview

This section provides an overview of the technical content of this research project which is split into three main parts (Figure 3.1). The first one is presented in Chapter 5 and addresses the validation of the RANS CFD methods used for nacelle design and optimisation in isolated configuration using experimental measurements (Figure 3.1). Unsteady RANS and DDES CFD methods are also used to computationally assess the aerodynamics of a compact nacelle at off-desing conditions.

The second part of the project is presented in Chapter 6 and covers the analysis of the integration aerodynamics of the engine-airframe system (Figure 3.1). Different installation positions and nacelle sizes are considered. The analysis is performed for both cruise and windmilling diversion conditions.

The third part covers Chapter 7 and Chapter 8 (Figure 3.1). In Chapter 7 different CFD fidelities based on Euler and RANS models are analysed from two points of view: (1) convergence to the optimal design space in a 2D axisymmetric and isolated configuration and (2) prediction of the nacelle and wing aerodynamics for installed aero-engine configuration. Chapter 8 covers the nacelle aerodynamic optimisation of both 2D isolated and installed non-axisymmetric configurations using CFD data and surrogate models built from different CFD fidelities.

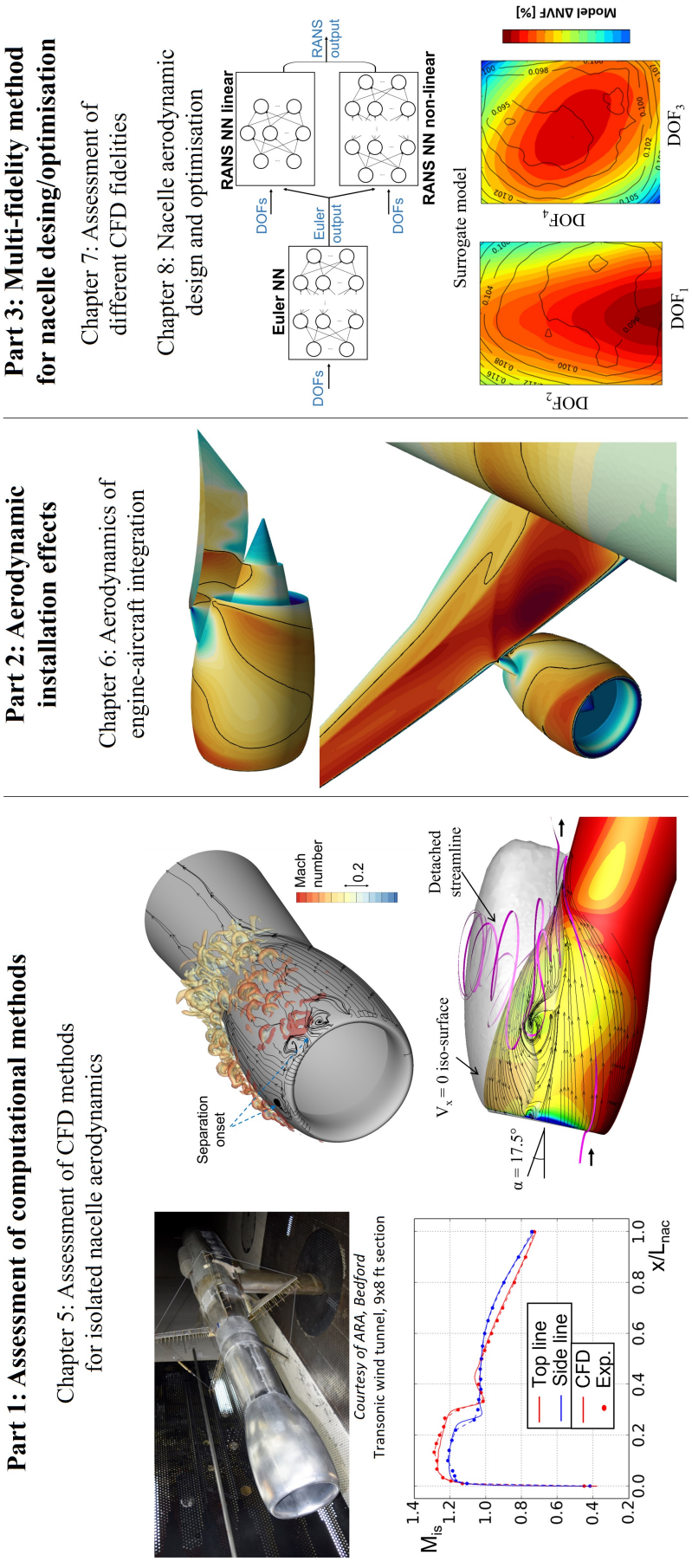

FIGURE 3.1: Results overview.

CHAPTER 4

Methodology

This chapter comprises all the methods used in this project for the design and optimisation of aero-engine nacelles both in isolated and airframe-installed configuration using different computational methods and surrogate modelling techniques. Section 4.1 details the geometry definition of the aero-engine, the airframe and the installation method. The nacelle model for the wind tunnel configuration is also presented. Section 4.2 provides the specifications of all the operating conditions used in this project. The Computational Fluid Dynamics (CFD) methods used to evaluate the aerodynamic performance of the different nacelle configurations are explained in Section 4.3. Section 4.4 explains the different drag extraction and the thrust and drag bookkeeping method used to evaluate the metrics of interest. In Section 4.5 the approaches for nacelle design and optimisation are provided, with details about the design variables, sampling techniques, optimisation algorithms and combination of operating conditions. Finally, Section 4.6 outlines the different single-fidelity and multi-fidelity surrogate modelling techniques used for the design and optimisation of nacelles.

4.1 Geometry definition of the different models

This section provides a explanation of the geometry definition of the different model configurations assessed in this project (Figure 4.1). In the isolated configuration only the propulsion system is considered (Section 4.1.1). For the installed configuration the aero-engine is mounted under the wing of the airframe using a pylon (Section 4.1.2). An additional configuration in which the nacelle is installed in a wind tunnel

rig is considered for the validation of the computational methods using experimental data (Section 4.1.3).

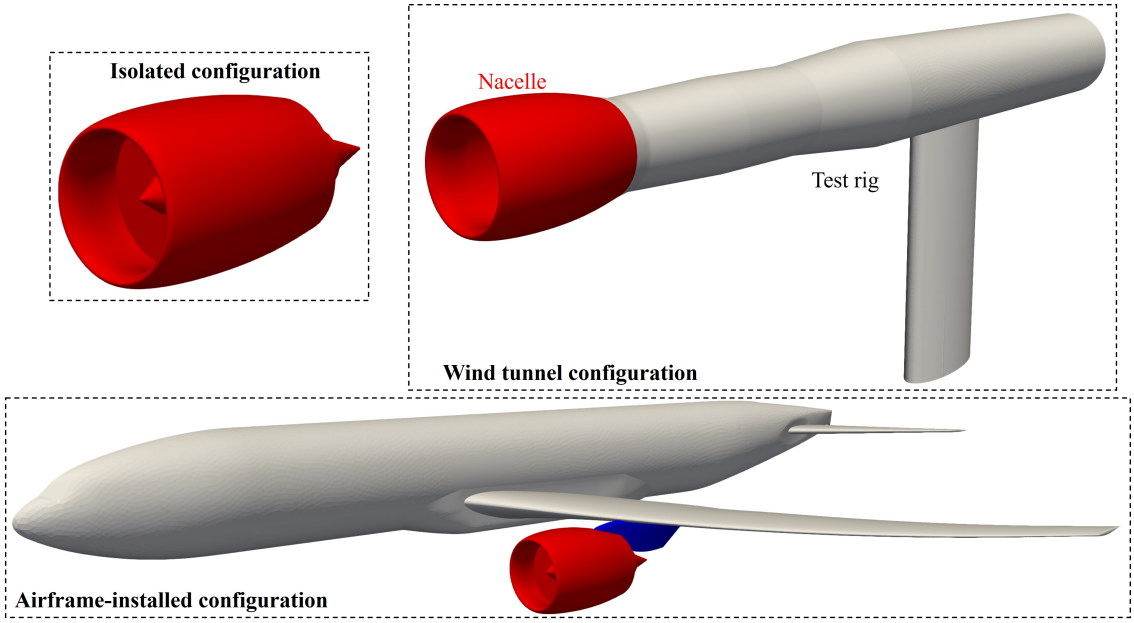

FIGURE 4.1: Nacelle configurations assessed in this project.

4.1.1 Isolated engine

The propulsion system comprises different elements: the spinner, intake, nacelle, bypass-flow and core-flow exhausts and plug (Figure 4.2). These geometries are parameterised through the Class Shape Transformation (CST) method developed by Kulfman[208]. CSTs are polynomial functions that model aerodynamic shapes based on different geometric constraints. This approach has been extensively used for aerodynamic problems to parameterise airfoil and wing shapes[209–211]. A CST curve is built through the product of a class function ($C(\varphi)$) and a shape function ($S(\varphi)$) plus an offset between the end points to define the trailing edge of the geometry ($\Delta\xi_{te}$) (Equation 4.1). φ and ξ are the non-dimensional abscissa and ordinate and c is the curve length. The class function is selected based on the underlying geometry to represent by adjusting the different control parameters N_1 and N_2 which results in polynomials of different order (Equation 4.2). The shape function applies the geometrical constraints to the class function in order to fit the targeted geometry (Equation 4.3). The Bernstein Polynomials ($BP(\varphi)$) are typically used as shape functions where $K_{i,n}$ are the polynomials coefficients (Equation 4.4). bp_i are weighting factors to the Bernstein Polynomials used to manipulate the shape function (Equation 4.3). However there is not an obvious correlation between the

polynomials coefficients and the resulting curves. To address this problem, Christie et al.[212] extended this method to the intuitive CST (iCST) approach. This allows a more straightforward relation between the design parameters and the Bernstein polynomial coefficients which makes the geometry parameterisation problem more intuitive and automatic and allows parametric analyses and derivation of design guidelines. Each design variable can be applied as a constraint k to the CST curve (Equation 4.1) and results in a linear equation that relates the constraint with a Bernstein Polynomial coefficient (Equation 4.5). Derivatives of the ordinate ξ up to the n^{th} order can also be imposed as constraints (Equation 4.6). Each constraint add a new equation to the system. Overall, a linear set of equations can be expressed in a matrix form (Equation 4.7) where $\mathbf{A}$ is the matrix of coefficients, $\mathbf{B}$ is the constant term and $\mathbf{X}$ is the column vector of the Bernstein Polynomial coefficients.

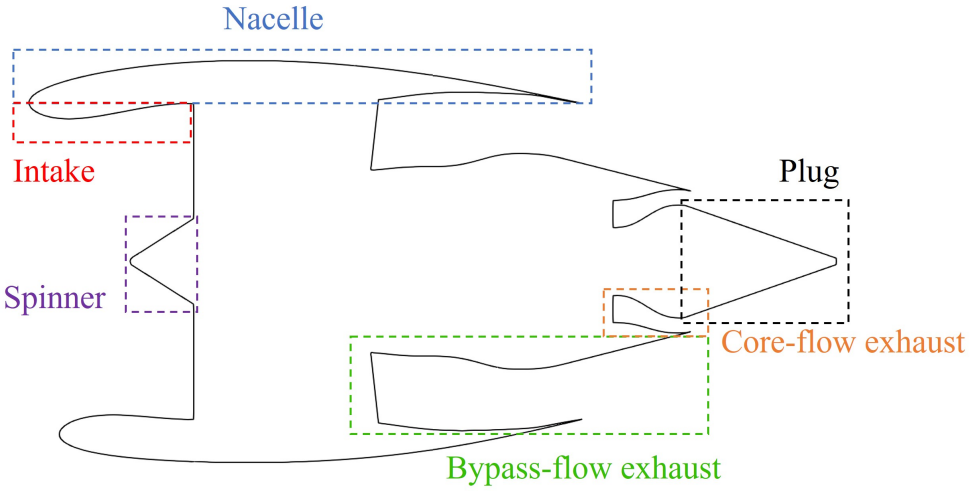

FIGURE 4.2: Definition of the main components of an aero-engine.

$$\xi(\varphi) = S(\varphi)\, C(\varphi) + \varphi \Delta\xi_{te}; \quad \xi = \frac{y}{c}; \quad \varphi = \frac{x}{c} \tag{4.1}$$

$$C(\varphi)_{N_2}^{N_1} = \varphi^{N_1} (1-\varphi)^{N_2} \quad for \quad 0 \leq \varphi \leq 1 \tag{4.2}$$

$$S(\varphi) = \sum_{i=0}^{n} \left[bp_i K_{i,n} \left(\varphi^i (1-\varphi)^{n-1} \right) \right] \tag{4.3}$$

$$BP(\varphi) = \textstyle\sum_{i=0}^{n} \left[K_{i,n} \left(\varphi^i (1-\varphi)^{n-1} \right) \right]; \quad K_{i,n} = \frac{n!}{i!(n-1)!} \tag{4.4}$$

$$\xi^{(k)}(\varphi) = \left[\sum_{i=0}^{n}\left[bp_i K_{i,n}\left(\varphi^i\left(1-\varphi^i\right)^{n-1}\right)\right] C(\varphi) + \varphi\Delta\xi_{te}\right]^{(k)} \tag{4.5}$$

$$\frac{d}{d\varphi} BP_{i,n}(\varphi) = n\left[BP_{k-1,n-1}(\varphi) - BP_{k,n-1}(\varphi)\right] \tag{4.6}$$

$$\mathbf{A}\cdot\mathbf{X} = \mathbf{B} \tag{4.7}$$

This section focuses on the parameterisation of the nacelle geometry as it is the topic of the research. The method was developed and implemented by Christie et al.[213] and has been adopted in this thesis for the nacelle design work. The other components of the propulsion system (Figure 4.2) are kept fixed throughout the design and optimisation process of the nacelle. A detailed description of the intake and exhaust parameterisations was provided by Christie et al.[213] and Goulos et al.[187] respectively.

A 3D non-axisymmetric nacelle geometry is constructed from 2D aero-lines in the plane $x-r$ that variates azimuthally in the plane $\Psi-r$ (Figure 4.3). A 2D aero-line is described through 7 geometrical parameters (Figure 4.3a). For clarification, the term "parameter" is used interchangeable in this thesis to refer to geometrical variables, operating conditions variables or number of samples in a design space exploration among others. The overall size of the nacelle is controlled by the highlight radius (r_{hi}), the trailing edge radius (r_{te}) and the nacelle length (L_{nac}). The maximum radius of the nacelle (r_{max}) and its axial position (f_{max}), the initial forebody radius (r_{if}) and the boat-tail angle (β_{nac}) define the curvature distributions of the aero-line. These parameters can be converted into constraints to build the iCST curves that represent the geometry. For the parameterisation of a nacelle a rounded leading edge and sharp trailing edge profile are selected by using a class function given by $N_1 = 1.0$ and $N_2 = 0.5$ (Equation 4.2). To build the 3D geometry of the nacelle, the constraints applied in the 2D aero-lines are variated azimuthally using additional iCST curves in a cylindrical coordinate system. Each of the 7 design variables are controlled with an independent azimuthal iCST with a linear class function. Different azimuthal control points can be defined. For isolated nacelle design, left-right symmetry is considered and 5 azimuthal positions are considered at $\Psi = 0°$ (top line), 45° (top-control line), 90° (side line), 135° (bottom-control line) and 180° (bottom line) (Figure 4.3b). With this approach the full nacelle geometry is analytically defined. In addition to this, the 3D non-axisymmetric

nacelle incorporates scarf angle (θ_{scarf}) and offset (Δ_{offset}) (Figure 4.3a). The scarf is defined as the angle between the fan face and the highlight plane. The offset represent the delta between the center lines of the engine and and intake at the highlight plane. These two parameters are used to align the nacelle lip and intake with the incoming flow angle and improve the performance to incidence.

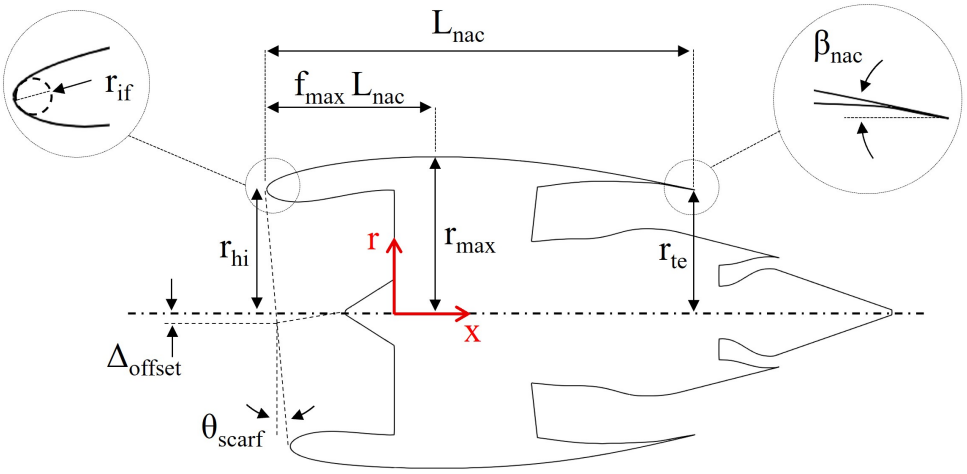

(A) Parameterisation of a 2D aero-line of the nacelle.

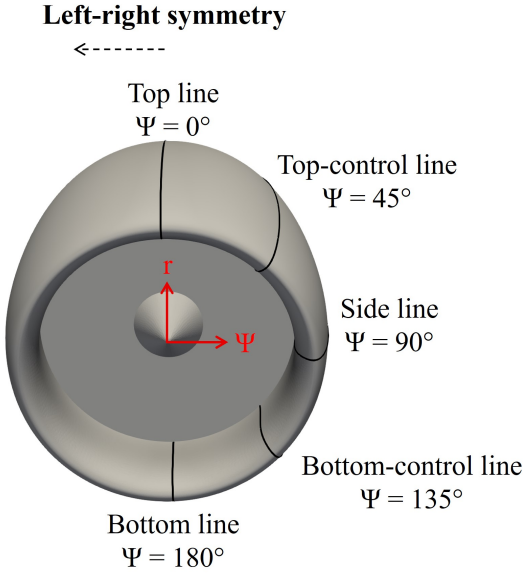

(B) Azimuthal aero-lines of a non-axisymmetric nacelle with left-right symmetry in isolated configuration.

FIGURE 4.3: Geometry definition of a non-axisymmetric nacelle in isolated configuration with left-right symmetry.

4.1.2 Airframe and engine installation

The NASA Common Research Model (CRM) airframe is used to assess the nacelle in installed configuration. The CRM is an open source airframe that was developed for the 4th AIAA Drag Prediction Workshop[83] (DPW) between the DPW Committee and the NASA's Subsonic Fixed Wing Aerodynamics Technical Working Group[81]. It is representative of a contemporary wide-body, twin-engine transonic aircraft for long haul applications. There are different configurations of the airframe available depending on the type and conditions of the study such as the high-speed[81,83] (or cruise), the high-lift[214] and the wind tunnel[82] configurations. In this project the high-speed CRM is used with a cruise Mach number of 0.85, a flight altitude of 10668m and a trim lift coefficient of 0.5[82]. The full scale CRM is used with a wing span of approximately 58m and a cruise Reynolds number of around 55 million based on the wing chord.

The framework that generates the geometry model of the complete engine-airframe configuration was developed previously by colleagues in Cranfield University[98,113,215] and has been adopted for this work. The aero-engine is installed in a podded under-wing position. The spanwise location of the installation is fixed at 33.4% of the semi-span length from the fuselage mean axis (Figure 4.4). This is consistent with the guidelines provided by the AIAA DPW for the CRM airframe with TFN[82] and also with other studies of the propulsion system integration using this airframe[54,98,113,215]. The installation position of the engine in the airframe is defined by the vertical (dz) and axial (dx) offset between the nacelle top-line trailing edge and the local wing leading edge coordinates (Figure 4.4). These parameters are normally expressed relative to the local wing chord at the spanwise installation position ($C^{inst}_{wing} \approx 7.9m$). While negative values of dx/C^{inst}_{wing} define a forward installation position, $dx/C^{inst}_{wing} > 0$ refers to close-coupled locations (Figure 4.4).

The aero-engine is installed in the airframe considering the toe (θ_{toe}) and pitch (θ_{pitch}) angles. To define these angles it is needed to introduce the different coordinate systems used for the studies of installed aero-engines (Figure 4.5). A reference system local to the engine is given by the trihedral $\left\{\hat{u}^{eng}_x, \hat{u}^{eng}_y, \hat{u}^{eng}_z\right\}$ with the origin in the middle of the fan face plane. $\hat{u}^{eng}_x$ is aligned with the engine axis and points downstream. $\hat{u}^{eng}_y$ is perpendicular to the symmetry plane of an aero-engine with inboard-outboard symmetry and it is oriented towards the outboard side. $\hat{u}^{eng}_z$ is normal to the previous ones and positive in the upward direction. Similarly, a coordinate system local to the airframe is used $\left\{\hat{u}^{a/f}_x, \hat{u}^{a/f}_y, \hat{u}^{a/f}_z\right\}$ with the origin on the CRM nose. $\hat{u}^{a/f}_x$ is parallel to the center line of the fuselage and points

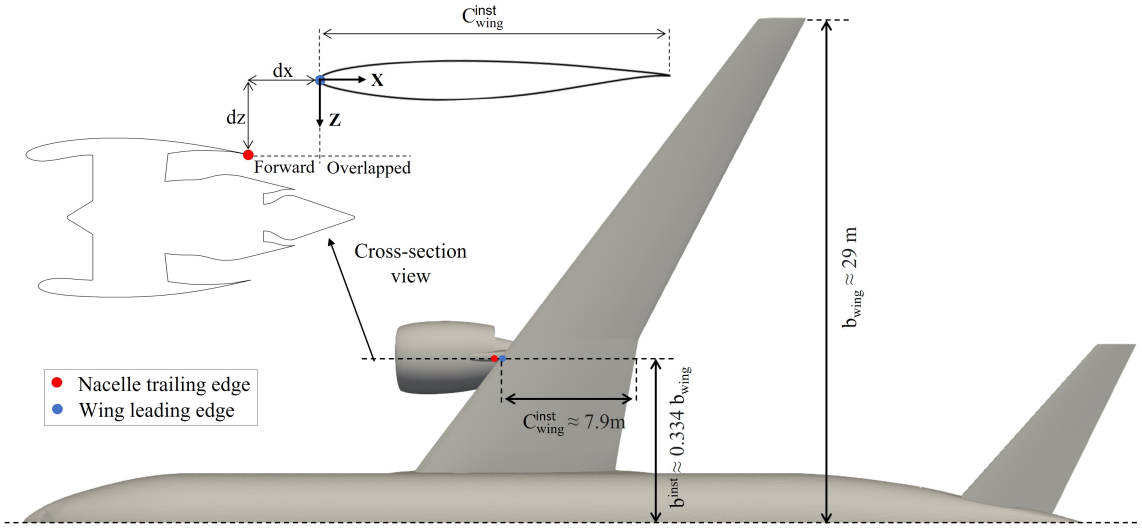

FIGURE 4.4: Definition of the installation position of the aero-engine in the NASA CRM airframe.

downstream. $\hat{u}_y^{a/f}$ is perpendicular to the airframe symmetry plane and positive in the outboard direction. Finally, $\hat{u}_z^{a/f}$ is normal to $\hat{u}_x^{a/f}$ and $\hat{u}_y^{a/f}$ and points upwards. The third reference system is given by the aerodynamic forces $\{\hat{u}_D, \hat{u}_S, \hat{u}_L\}$ where D, S and L represent the Drag, Side and Lift forces respectively. This is a global system which is useful to decompose every force component in the aerodynamic axes as per the thrust and drag accounting method (Section 4.4). From the definition of the drag, $\hat{u}_D$ goes in the direction of the velocity vector U_∞. It is used to define the aircraft angle of attack ($\alpha_{aircraft}$). $\hat{u}_S$ is normal to the aircraft symmetry plane and points towards the outboard side. Finally, $\hat{u}_L$ is perpendicular to both $\hat{u}_D$ and $\hat{u}_S$ and positive in the upward direction.

The relative angles between the two local reference systems in different planes describe the toe and pitch angles. While the angle between $\hat{u}_x^{a/f}$ and $\hat{u}_x^{eng}$ in the plane $\hat{u}_L - \hat{u}_D$ defines θ_{pitch} (Figure 4.5a), the same relative angle in the plane $\hat{u}_S - \hat{u}_D$ determines θ_{toe} (Figure 4.5b). From the guidelines provided by the AIAA DPW for the CRM airframe with TFN[82], $\theta_{pitch} = 1.75°$ and $\theta_{toe} = 2.25°$ are used in this project.

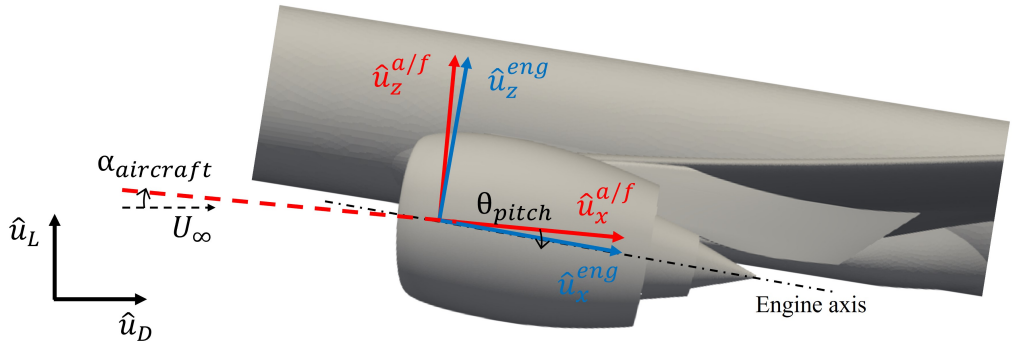

(A) Pitch angle (θ_{pitch}).

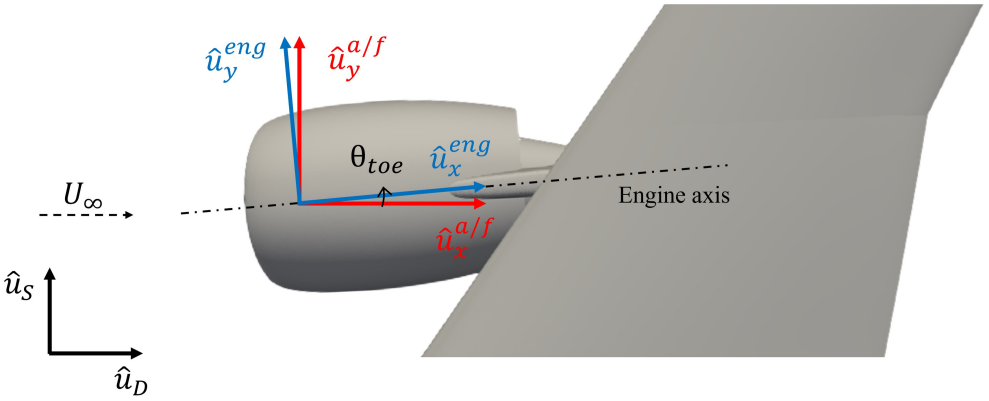

(B) Toe angle (θ_{toe}).

FIGURE 4.5: Definition of the installation angles of the aero-engine in the NASA CRM airframe.

4.1.2.1 Pylon

The methodology to generate the geometry of the pylons used in this project was developed by Otter[113]. The pylon is constructed by a set of different aerofoils defined in the $\hat{u}_x$ - $\hat{u}_y$ plane and stacked in the vertical $\hat{u}_z$ direction (Figure 4.6a). The different aerofoil sections are parameterised using iCSTs (Equations 4.1 to 4.4). Seven geometrical parameters are controlled to define a certain aerofoil section: the location of the leading edge (x_{le}), the location of the trailing edge (x_{te}), the maximum thickness (y_{max}) and its axial location (x_{max}), the radius of curvature in the leading edge (r_{if}), the boat-tail angle (β_{pylon}) and the offset in the y direction in the trailing edge of the aerofoil ($y_{te,offset}$) which for the designs used in this project is set to zero. Each of these parameter is controlled in the vertical direction using an additional iCST (Figure 4.6b). As a result, a full parametric definition of the pylon geometry is obtained. The pylons designed with this methodology share some design rules

(Figure 4.6b). As the vertical coordinate $\hat{u}_z$ increases towards the junction with the wing, the sectional thickness y_{max} is larger and its axial position x_{max} is moved downstream. The trailing edge x_{te} is also displaced downstream at the same time as the pylon boat-tail angle β_{pylon} reduces. Additionally, the radius of curvature in the leading edge r_{if} increases from the junction with the nacelle to the junction with the wing.

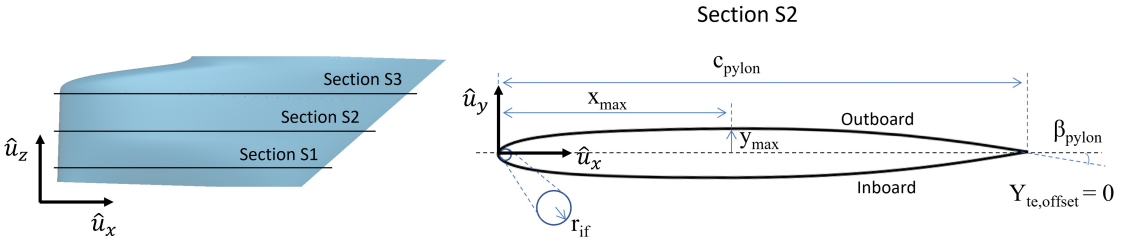

(A) Geometrical definition of a single pylon aerofoil in the $\hat{u}_x$ - $\hat{u}_y$ plane and stacking of aerofoil in the $\hat{u}_z$ direction.

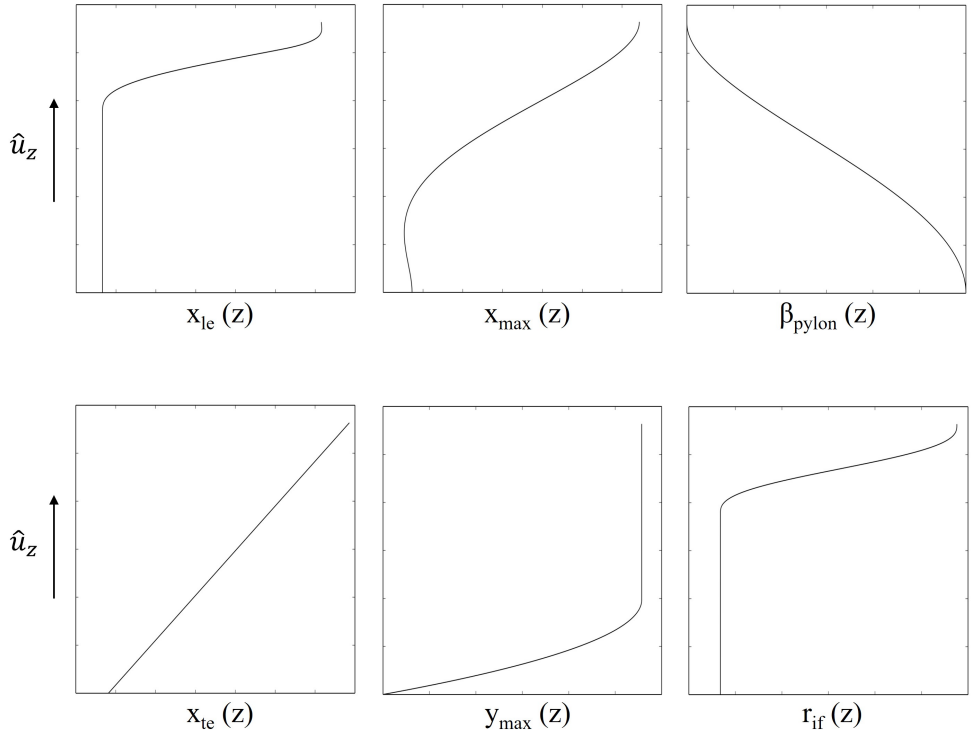

(B) Variation of the pylon section parameters with the vertical $\hat{u}_z$ coordinate.

FIGURE 4.6: Pylon design method and parameterisation.

The parametric shape of the pylon is trimmed to adjust for the intersection with the wing in the upper side and with the engine in the lower side (Figure 4.7). The leading edge of the pylon is located downstream of the Outlet Guide Vane (OGV) plane to avoid intersection with the inlet of the bypass exhausts. However, this

causes flow blockage in this bypass exhaust. The pylon is also trimmed with a heatshield which is in contact with the hot stream flow of the core exhaust (Figure 4.7). The heatshied is defined with an iCST which initially follows the boat-tail angle of the core-cowl but it is straightened until it is parallel to $\hat{u}_x$ in the trailing edge. The pylons used in this project were aerodynamically designed to avoid flow separation in the rear part of the junction with the wing. This is one of the most challenging regions due to the low flow velocity and the adverse pressure gradient that the flow undergoes. This makes the pylon design dependant on the installation position and the nacelle and exhaust configurations used.

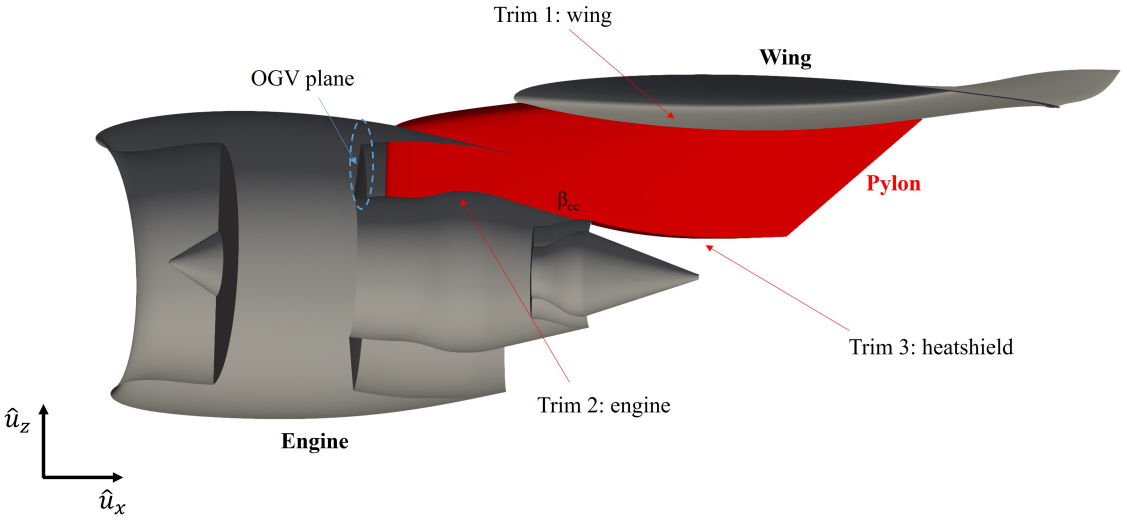

FIGURE 4.7: Final pylon geometry (red) after a sectional trimming with the wing, the engine and the heatshield.

4.1.3 Wind tunnel configuration

Experimental data was measured for different nacelle geometries within the Horizon 2020 ANACO project which was used for validation studies of the numerical methods. The nacelle geometries (Section 4.1.1) are approximately 1/15th scale of the full actual size. The Aircraft Research Association (ARA) Z30 rig was recommissioned for the test programme and tested in the ARA 8x9ft (2.44x2.74m) transonic wind tunnel. The rig consists of (Figure 4.8):

- A support strut that pivots to provide control in the flow incidence.
- A rake with five arms that contains probes for static and total pressure.

- A profile sting that connects the nacelle with the rig. This profile sting is instrumented with static pressure measurements along the top, side and bottom azimuthal aero-lines.
- A parallel sting between the profile sting and the rake which is also instrumented with static pressure tappings.

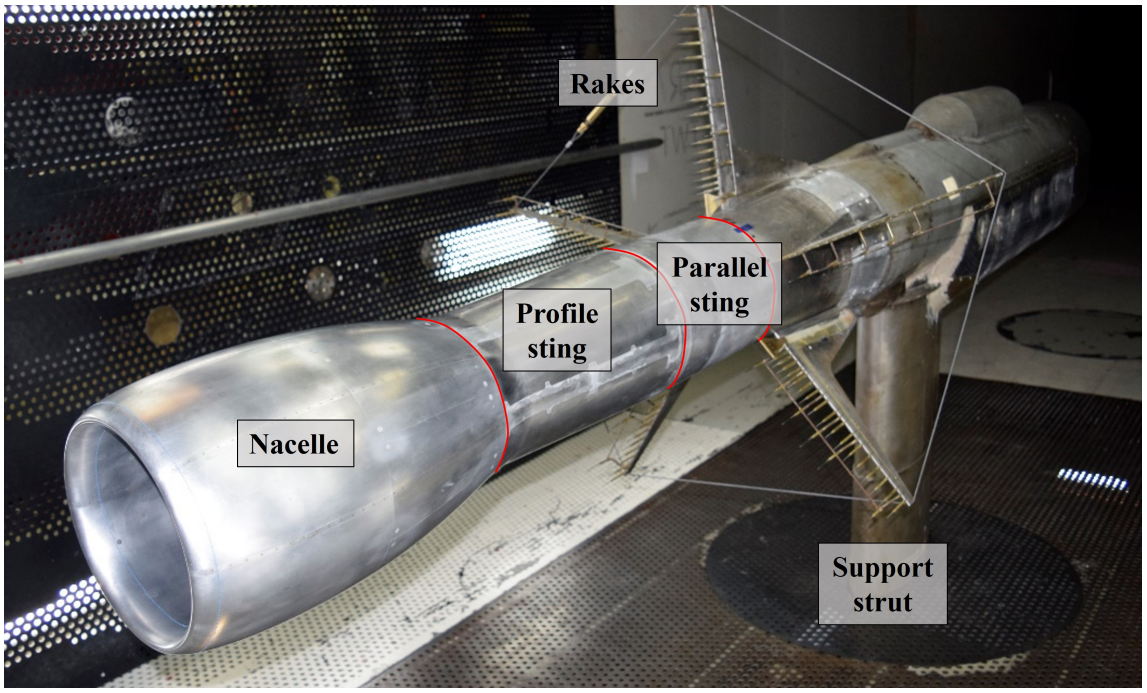

FIGURE 4.8: Nacelle installed in the Z30 rig in the ARA Transonic Wind Tunnel. Courtesy of ARA.

4.2 Operating conditions

Throughout this project there are many references to key operating conditions for the nacelle aerodynamic design problem both in the cruise segment and at off-design scenarios[18,51,216]. For the full scale isolated nacelle configurations, these conditions are defined in terms of flight Mach number, MFCR, altitude and engine incidence (α_{eng}), with the Reynolds number defined as Re and using the fan diameter as reference length (Table 4.1). For the scaled wind tunnel configurations, the pressure and temperatures come from the wind tunnel conditions instead of the ISA atmosphere model for a given altitude. The same Mach number, MFCR and incidence are used and the Reynolds number is defined as Re_{twt} (Table 4.1). For installed nacelle assessments the incidence is replaced by the trim lift coefficient of the aircraft (Table 4.2).

For the isolated case, the nominal cruise condition is defined by M = 0.85, MFCR = 0.7, Altitude = 10668m (35000ft) and α_{eng} = 4.5° (Table 4.1). In this cruise segment two additional operating conditions are considered to assess the sensitivity to the Mach number and the MFCR. Relative to the cruise nominal values, the cruise ΔM condition increases the Mach number from 0.85 to 0.87 and the end-of-cruise condition reduces the MFCR from 0.7 to 0.65 (Table 4.1).

Additionally, three off-design conditions are considered:

- On the one hand, the cruise engine-out is the transient condition in which an engine fails and the mass flow is suddenly reduced from MFCR = 0.7 to MFCR = 0.35 while keeping M = 0.85, Altitude = 10668m and α_{eng} = 4.5° as per the cruise point (Table 4.1).
- In the event of an engine failure, the route is diverted to land in an alternative airport. This operating condition is called windmilling diversion and is defined by M = 0.65, MFCR = 0.33, Altitude = 6096m and α_{eng} = 4.5° (Table 4.1).
- Finally, the end-of-runway point is representative of a failure engine condition at high-incidence that can happen at take-off. At zero altitude, the incidence is increased to 20° and the Mach number and MFCR are reduced to 0.25 and 0.32 respectively (Table 4.1).

The aerodynamic of the aero-engine installed in the airframe was assessed for the nominal cruise and the windmilling diversion conditions (Table 4.2). This windmilling diversion scenario is chosen due to its interest for the Extended-range Twin-engine Operational Performance Standards (ETOPS) requirements. The aircraft lift coefficient at the cruise point is fixed to 0.5 as per the 4^{th} AIAA DPW[83]. For the windmilling diversion case, $C_{L_{Diversion}}$ = 0.44 was estimated by matching the overall aircraft lift at cruise and diversion to the aircraft weight (W). Considering the dynamic pressure (q) at both cruise and diversion the $C_{L_{Diversion}}$ can be obtained (Equation 4.8).

$$C_{L_{Diversion}} = C_{L_{Cruise}} \frac{q_{Cruise}}{q_{Diversion}} \tag{4.8}$$

The exhausts conditions are defined by the Fan Nozzle Pressure Ratio (FNPR) and Core Nozzle Pressure Ratio (CNPR). FNPR and CNPR represent the ratio between the total pressure at the inlet of the bypass and core exhausts and the farfield static

pressure. Representative values of an engine cycle given by 2.2 and 1.5 for the FNPR and CNPR are used for the cruise segment conditions[98]. For the off-design conditions, the value of the total pressure in the farfield is prescribed at the inlet of both exhausts through a FNPR = CNPR = 1.33.

TABLE 4.1: Summary of the key nominal operating conditions considered in this project for isolated nacelle configurations.

		M	MFCR	α_{eng} [°]	Alt [m]	Re	Re_{twt}
Cruise segment	Cruise	0.85	0.7	4.5	10668	25x10^6	3x10^6
	Cruise ΔM	0.87	0.7	4.5	10668	25x10^6	3x10^6
	End-of-cruise	0.85	0.65	4.5	10668	25x10^6	3x10^6
Off-design	Cruise engine-out	0.85	0.35	4.5	10668	25x10^6	3x10^6
	Windmilling diversion	0.65	0.33	4.5	6096	30x10^6	3x10^6
	End-of-runway	0.25	0.32	20	0	10x10^6	1x10^6

TABLE 4.2: Summary of the key nominal operating conditions considered in this project for installed nacelle configurations.

	M	MFCR	C_L	Alt [m]	Re
Cruise	0.85	0.7	0.5	10668	25x10^6
Windmilling diversion	0.65	0.33	0.44	6096	30x10^6

4.3 Computational fluid dynamics methods

This section explains the different computational fluid dynamics (CFD) methods used in this project for the range of nacelle configurations that were investigated (Figure 4.9). A different set of operating conditions were evaluated for each nacelle configuration and CFD model (Table 4.3). A finite volume method was used for the spatial discretisation of the Navier-Stokes equations (Appendix A.2). The discretised equations were solved with ANSYS Fluent[217].

The nominal CFD method used for nacelle design is based on the Favre-Averaged Navier-Stokes equations (Appendix A.2.1) which model the viscous, compressible and turbulent flow. For simplicity, hereafter this model will be referred as RANS. Although RANS is established as the CFD method to evaluate the performance of a nacelle design, other CFD models of lower fidelity are used to understand and explore the design space at a reduced computational overhead. Two kind of low-fidelity models are considered in this work. One is based on a simplified physics of

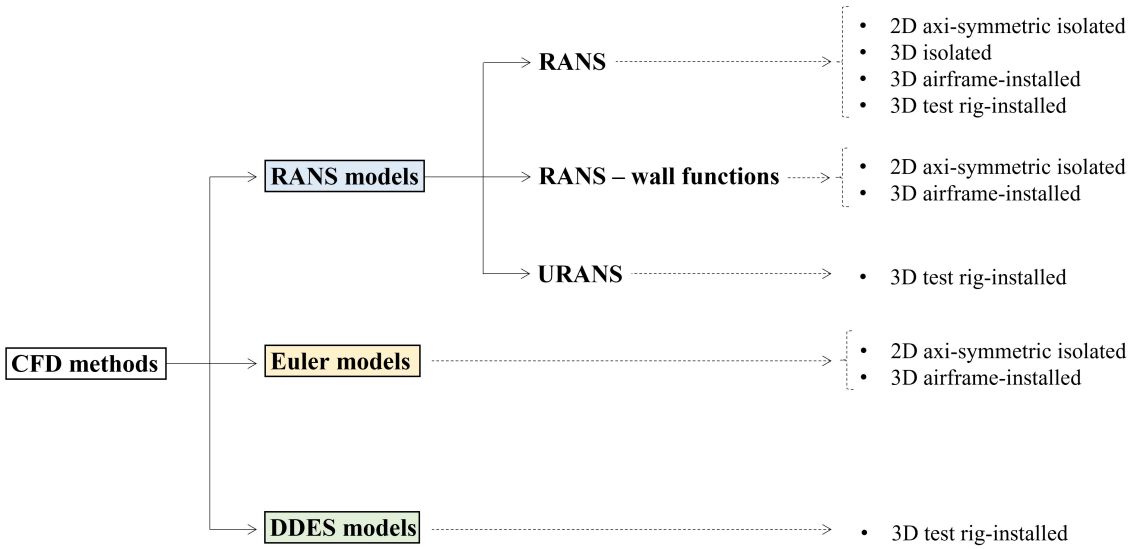

FIGURE 4.9: Schematic of the different computational fluid dynamics models used for each nacelle configuration.

TABLE 4.3: Summary of the operating conditions evaluated for each nacelle configuration with the different computational fluid dynamics models.

	2D axi-symmetric isol.	3D isol.	3D airframe-inst.	3D test rig-inst.
RANS	Cruise segment	Cruise Diversion	Cruise Diversion	Cruise segment Diversion/End-of-runway
$RANS_{wf}$	Cruise segment		Cruise	
URANS				Diversion/End-of-runway
Euler	Cruise segment		Cruise	
DDES				Diversion

the problem which considers the fluid as inviscid. The Euler equations are solved for this low-fidelity model (Appendix A.2.3). The other comes from a coarsened spatial discretisation of the control volume which uses wall functions to model the complete boundary layer on the surfaces of the geometry (Appendix A.2.1.2). Additionally, two unsteady CFD methods are applied for the aerodynamics prediction at off-design condition of the nacelle installed in the wind tunnel rig: (a) unsteady RANS (URANS) (Section 4.3.1.3) and Delayed Detached Eddy Simulation (DDES) (Section 4.3.3). While the RANS and Euler CFD methods are based on collaborative efforts with colleagues at Cranfield University, the DDES, URANS and RANS with wall functions numerical models are specifically developed as part of this research.

4.3.1 RANS models

The RANS modelling approach is used to obtain a viscous and compressible solution of the flow. The Favre-Averaged Navier-Stokes equations are solved using the $\kappa - \omega$ SST[95] turbulence model (Appendix A.2.1.1) for closure of the transport equations. The solver considers an implicit formulation and a density-based approach. A second order upwind scheme is used for the spatial discretisation with a Green-Gauss node-based gradient interpolation method. The Sutherland's law[218] and the molecular kinematic theory are used to calculate the dynamic viscosity and the thermal conductivity of the fluid respectively (Appendix A.1).

4.3.1.1 RANS

4.3.1.1.1 2D axi-symmetric isolated configuration

The 2D nacelle geometry is placed in a semi-circular domain. From a domain independence study[16], a radius of 80 times the nacelle maximum radius ($r_{Domain} = 80 r_{max}$) is used (Figure 4.10). This domain is discretised using a structured mesh with a C-grid strategy using the ANSYS ICEM software[219]. The boundary layer is discretised using a set of inflation layers with a growth ratio of 1.2 and a first cell height estimated to achieve a y^+ smaller than one. A grid independence study is conducted based on the Grid Convergence Index[220] (GCI) parameter for the nacelle cruise drag. The GCI estimates how close the calculated drag is from the asymptotic value. A GCI of about 0.3% for cruise D_{nac} is obtained for a mesh with approximately 70k elements (Appendix B.2.1).

In terms of boundary conditions, the free stream conditions are imposed in the farfield through the static pressure (p_∞), static temperature (t_∞) and flight Mach number (M_∞) (Figure 4.10). To match the requirements from the engine cycle, the static pressure (p_2), total temperature ($T2$) and mass flow ($\dot{m}_2$) are prescribed in the fan-face. Both in the core and bypass exhausts, total pressure and temperature are imposed. The total pressures P_{13} and P_7 come from the cycle FNPR and CNPR (Section 4.2). Finally, the surfaces of the geometry are modelled as adiabatic and viscous non-slip walls (Figure 4.10).

The convergence strategy starts from a full multi-grid initialisation method that calculates an initial potential solution of the flow. After that, the numerical schemes for the continuity, momentum, energy and turbulent variables are set to first order

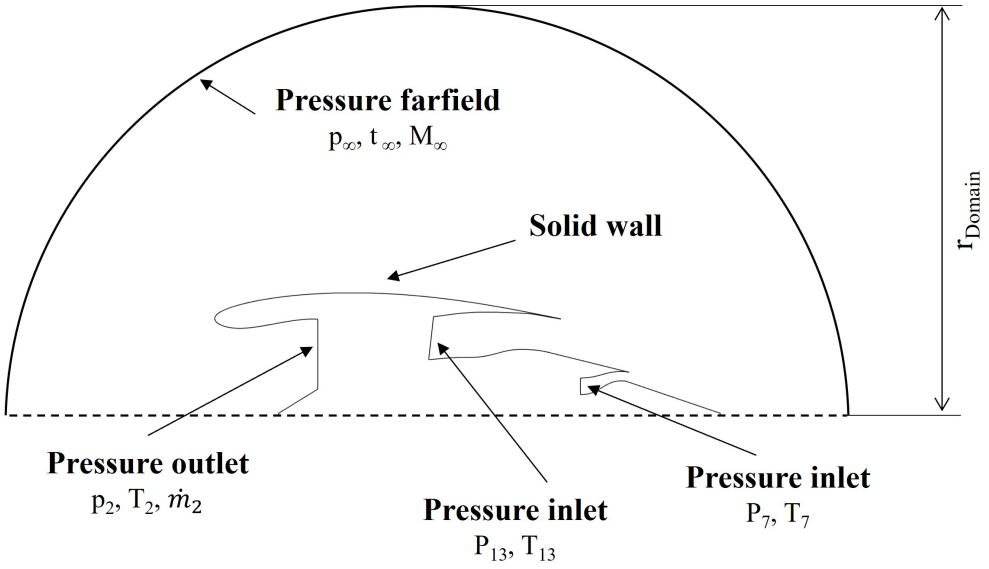

FIGURE 4.10: Schematics of the fluid domain and boundary conditions of the RANS CFD model for the 2D axi-symmetric nacelle in isolated configuration.

and the solution is converged by a conservative increase in the Courant Friedrich Levy (CFL) number. Finally, the numerical scheme is switched to second order and the CFL is again sequentially increased until convergence. The convergence criteria is defined by a reduction in the normalised equation residuals of five order of magnitude and an oscillation in the fan-cowl force over the final 500 iterations lower than 0.05%[18].

This CFD model was validated by Robinson et al.[39] with experimental data available for 2D axi-symmetric nacelles for a range of Mach numbers from 0.8 to 0.89 and MFCR from 0.45 to 0.7. At cruise type condition ($M_\infty = 0.85$ and MFCR = 0.7) the predicted nacelle drag was within 3.5% of the measurements. Additionally, the difference in the drag rise Mach number between the CFD and the experiments was within 0.005.

4.3.1.1.2 3D isolated configuration

The isolated aero-engine is located in a hemispheric domain with a radius of 80 times the nacelle maximum radius ($r_{Domain} = 80 r_{max}$). An hybrid meshing strategy is employed using ANSYS Meshing[221]. Structured prism layers are used near the viscous walls to cover the boundary layer (Figure 4.11) with a growth ratio of 1.2 and the first cell size in the surface normal direction adjusted for $y^+ < 1$ (Figure 4.12). The rest of the domain is discretised in an unstructured fashion using tetrahedral

elements. Aside from the inflation and face refinements for the surface mesh and the boundary layer respectively, the volumetric mesh is refined in the regions where key flow features are expected through density boxes (Figure 4.11). A toroidal density box is located close to the nacelle highlight to properly capture the high flow suction and possible shock wave. Different levels of cylindrical density box refinements are set up around the propulsion system, core and bypass exhausts and jet flow. Grid independence studies for this mesh were based both at cruise and windmilling diversion condition. A mesh with approximately 72 million elements was selected with a GCI based on the nacelle drag of 1.95% and 1.01% for cruise and diversion respectively (Appendix B.2.2).

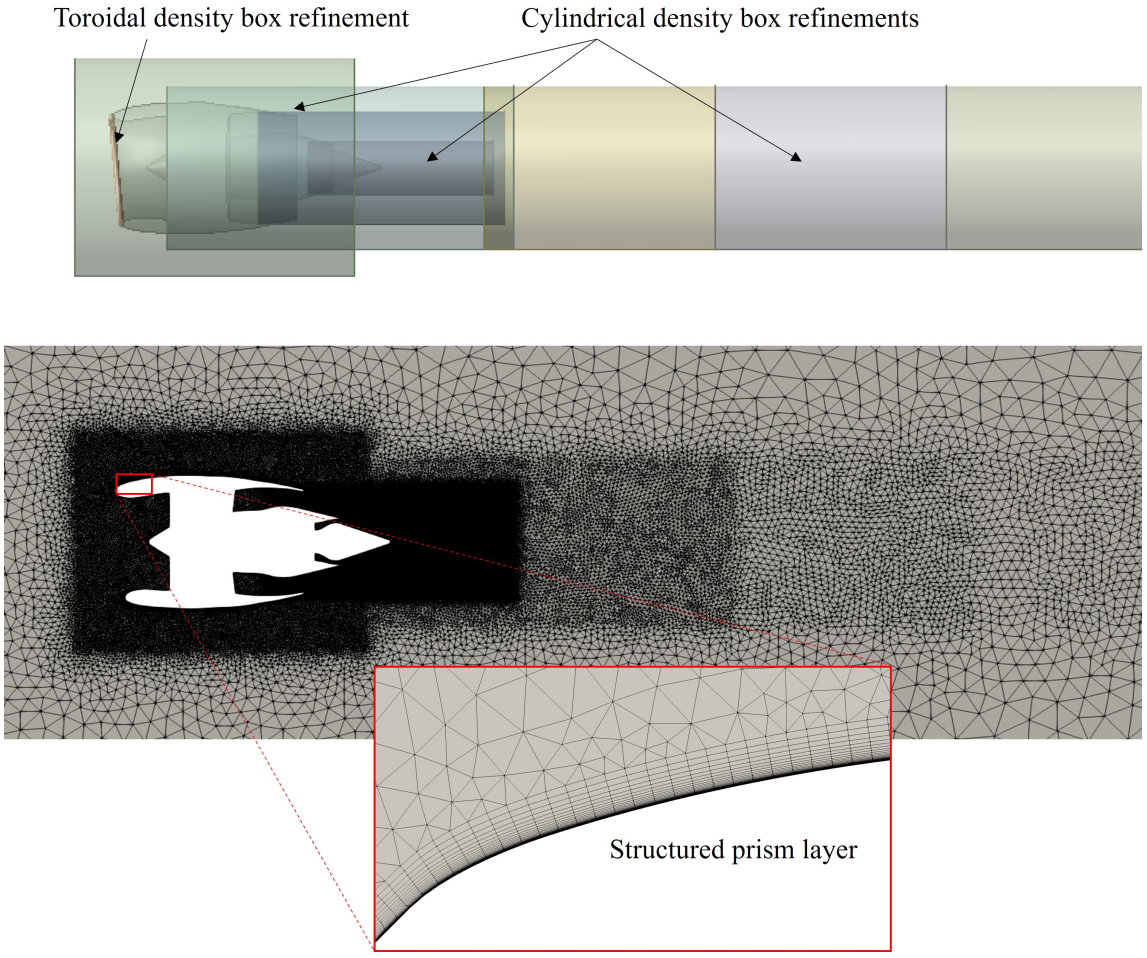

FIGURE 4.11: RANS mesh for the 3D isolated model and volumetric mesh refinements.

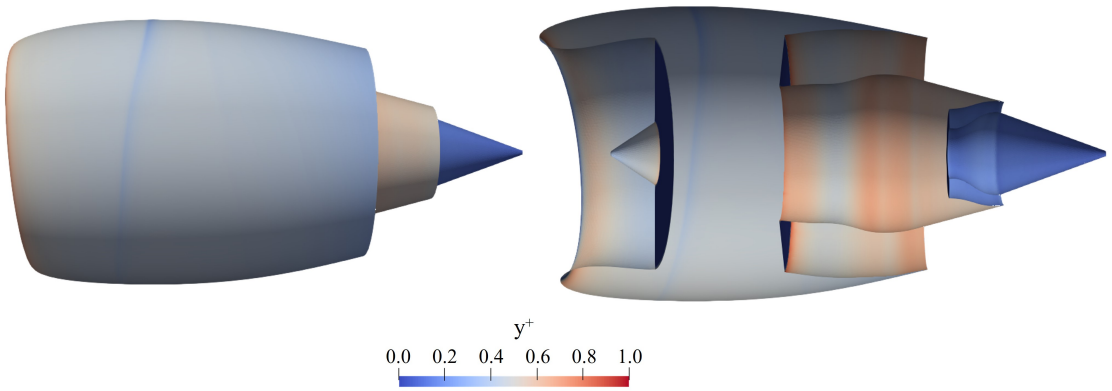

FIGURE 4.12: Contours of y^+ on every wall surface for the RANS CFD model of the 3D isolated configuration.

The boundary conditions applied in the surface walls, fan-face and core and bypass exhausts inlets are the same as in the 2D axi-symmetric isolated model presented in Section 4.3.1.1.1. The farfield boundary condition includes now the aero-engine incidence. Additionally, a symmetry boundary condition is imposed in the $\hat{u}_z - \hat{u}_x$ symmetry plane (Figure 4.13).

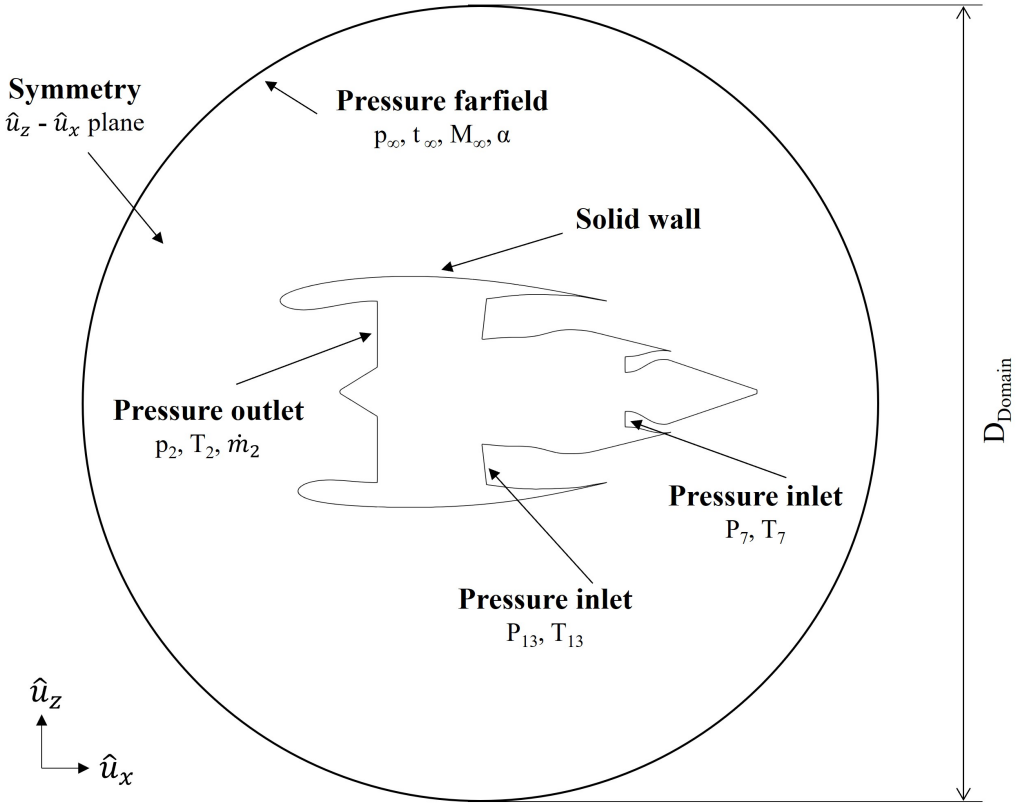

FIGURE 4.13: Schematics of the fluid domain and boundary conditions of the RANS CFD model for the 3D nacelle in isolated configuration.

The convergence strategy starts with a full multi-grid initialisation that provides an initial solution using a potential flow model. Subsequently, the numerical schemes for every variable are defined as first order and no target mass flow is specified in the boundary condition in the fan-face. The simulation is evaluated until convergence by increasing the CFL up to 64. At that point, the boundary condition in the fan-face is adjusted to specify the required mass flow for the engine. In the last step, the numerical schemes are set to second order and the CFD is increased in a conservative manner until 200. Convergence is achieved after a reduction of at least five order of magnitude in the normalised equation residuals and an oscillation in the fan-cowl force of less than 0.05% in the last 500 iterations[18].

4.3.1.1.3 3D airframe-installed configuration

Half of the aircraft is considered in this CFD model due to the symmetry of the configuration. The geometry is enclosed in a hemispherical domain with a radius of 100 times the CRM local wing chord at the spanwise installation position ($r_{domain} = 100C_{ref}$) (Figure 4.14). The domain discretisation follows a hybrid meshing strategy. Both the domain size and the meshing sizes for this configuration are in accordance with the guidelines established at the 4^{th} AIAA drag prediction workshop[83]. Structured prism layers are employed in the proximity of the wall surfaces with a growth ratio of 1.2 and a first cell size adjusted for $y^+ < 1$ (Figure 4.15). The remainder of the domain is discretised in an unstructured manner using tetrahedral elements. Local refinement of the surface grid are applied in the leading and trailing edges of wing, empenage, nacelle, exhausts and pylon and also on the intersection between wing-fuselage, empenage-fuselage and wing-pylon (Figure 4.16). Volumetric refinements are applied through density boxes. In the proximity of the propulsion system the same refinement topology as in the 3D isolated case is applied (Figure 4.17). In addition to these, two prismatic density boxes are placed around the wing in the spanwise direction. Two cylindrical density boxes refine the volume mesh close to the wing leading and trailing edges. Finally, one cylindrical density box covers the pylon (Figure 4.17). When different density boxes overlap in a region of the domain, the smallest grid size is kept. A grid independence study provided GCI values of 0.48% and 1.57% for the nacelle and airframe drag at cruise for a mesh with approximately 115 million elements (Appendix B.2.3). For the windmilling diversion scenario, a grid independence analysis reported a GCI on nacelle drag of around 1.73% for the selected cruise mesh (Appendix B.2.3).

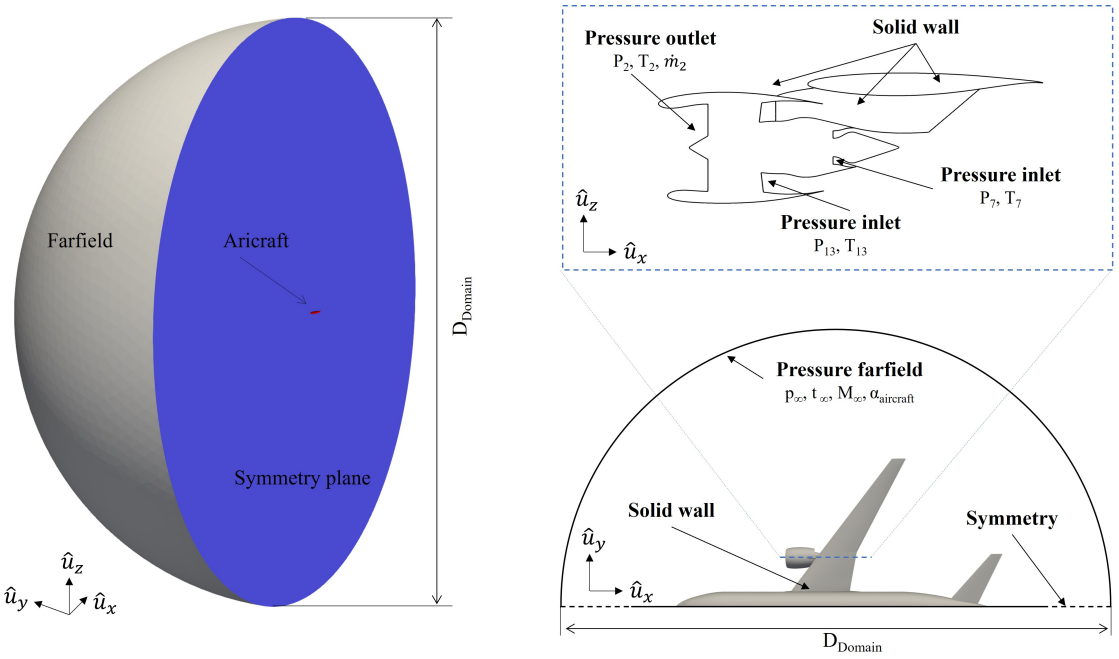

FIGURE 4.14: Schematics of the fluid domain and boundary conditions of the RANS CFD model for the nacelle in the configuration installed with the airframe.

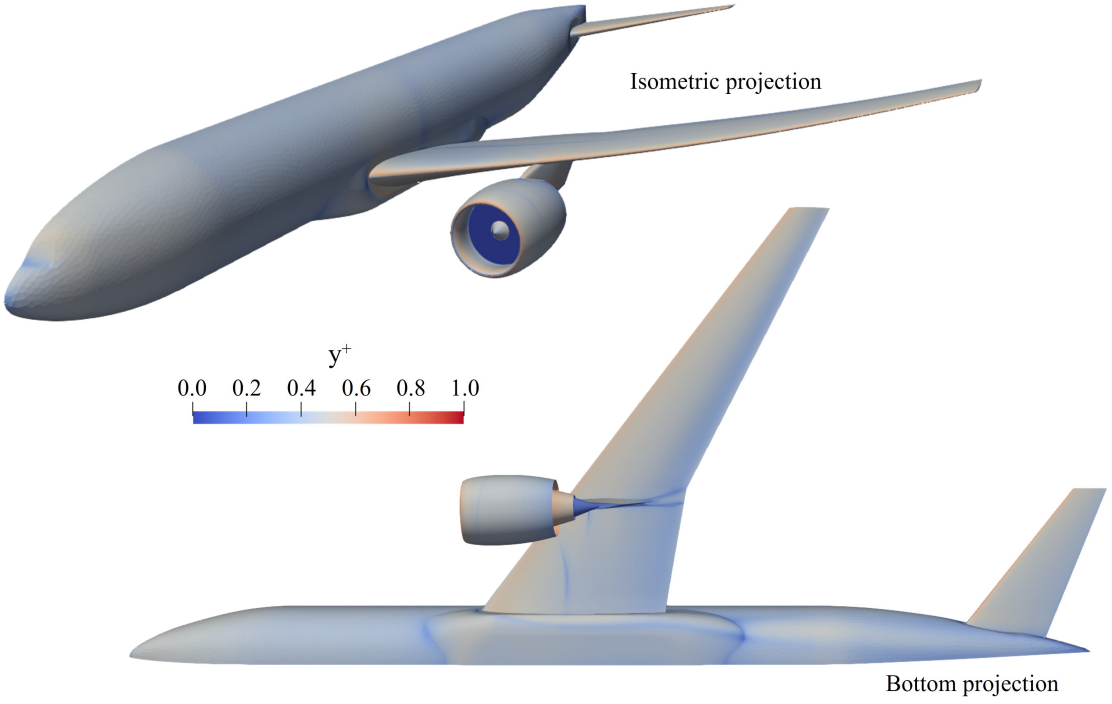

FIGURE 4.15: Contours of y^+ on every wall surface for the RANS CFD model of the 3D airframe-installed configuration.

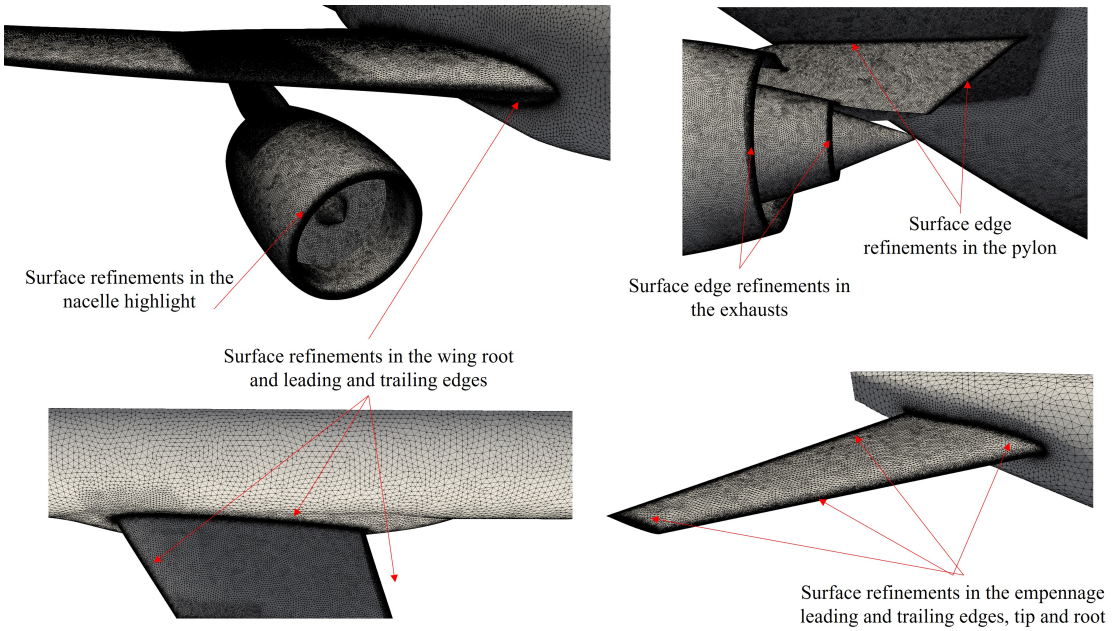

FIGURE 4.16: Surface mesh refinements for the RANS model of the 3D airframe-installed configuration.

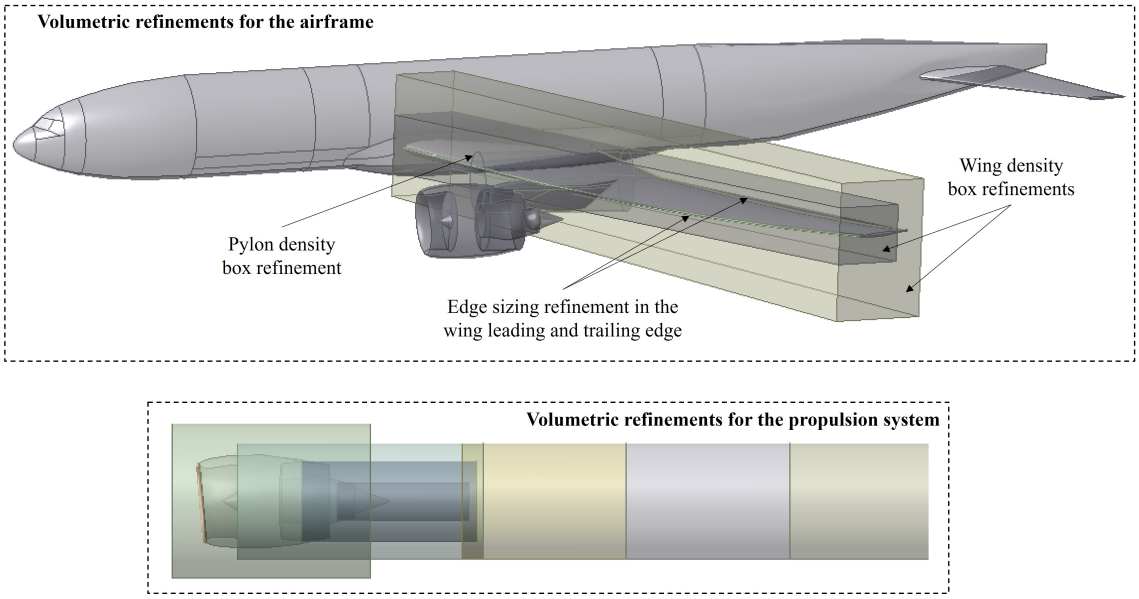

FIGURE 4.17: Volumetric mesh refinements for the RANS model of the 3D airframe-installed configuration.

The same boundary conditions as for the 3D isolated configuration are applied in the walls, fan-face and exhausts of the propulsion system. The farfield boundary condition is also similarly defined but considering now the aircraft angle of attack ($\alpha_{aircraft}$). A symmetry boundary condition is prescribed in the $\hat{u}_z - \hat{u}_x$ symmetry plane of the model. Finally, adiabatic and viscous walls conditions are imposed in the airframe and pylon walls (Figure 4.14).

The same convergence strategy as in the 3D isolated case is used (Section 4.3.1.1.2). The numerical convergence was assessed by a reduction of at least five orders of magnitude in the continuity, velocity and energy residuals and four order of magnitude in the turbulent kinetic energy and specific turbulent dissipation rate. Additionally, the aero-engine mass flow and the airframe lift and drag forces were monitored and a variation lower than 0.01% in the last 100 iterations was obtained[54].

The numerical approach was validated by Goulos et al.[98] in terms of airframe drag using experimental data for the NASA CRM using TFN[82]. The installation drag is over-predicted by approximately two drag counts at cruise condition which is about 0.8% of the total aircraft drag.

4.3.1.1.4 3D test rig-installed configuration

The CFD model developed for the wind tunnel configuration does not consider the rakes mounted in the rig. The nacelle geometry is installed in the test rig as explained in Section 4.1.3 and enclosed in a spherical domain of radius 80 times the nacelle maximum radius (Figure 4.18). A range of different domain sizes were considered ($80r_{max}$, $60r_{max}$, $80r_{max}$, $100r_{max}$) for the domain independence study. A change from to $80r_{max}$ to $100r_{max}$ resulted in an increment on nacelle drag of 0.10% and $r_{Domain} = 80r_{max}$ was selected for this work. A hybrid meshing approach is employed with structured prism layers near the walls to cover the boundary layer and tetrahedral elements in the remainder of the domain (Figure 4.19a). The first cell height was adjusted to satisfy a $y^+ < 1$ in the viscous walls. Volumetric grid refinements were applied through density boxes around the complete nacelle geometry and nacelle highlight to capture the local wall curvatures and the flow gradients associated to transonic conditions and shock waves (Figure 4.19b). A grid independence study provided a GCI based on the nacelle drag of 1.49% for a mesh of approximately 16 million elements (Appendix B.2.4).

A boundary condition in the farfield of the domain was imposed to mimic the test conditions. As for the previous RANS models, the static pressure (p_∞) and temperature (t_∞), the operating Mach number (M_∞) and the flow incidence (α) were prescribed (Figure 4.18). Similarly, a target mass flow, static pressure and total temperature were imposed in the fan-face (ff) to match the operating MFCR. Finally, the surfaces were modelled as adiabatic and viscous walls (Figure 4.10).

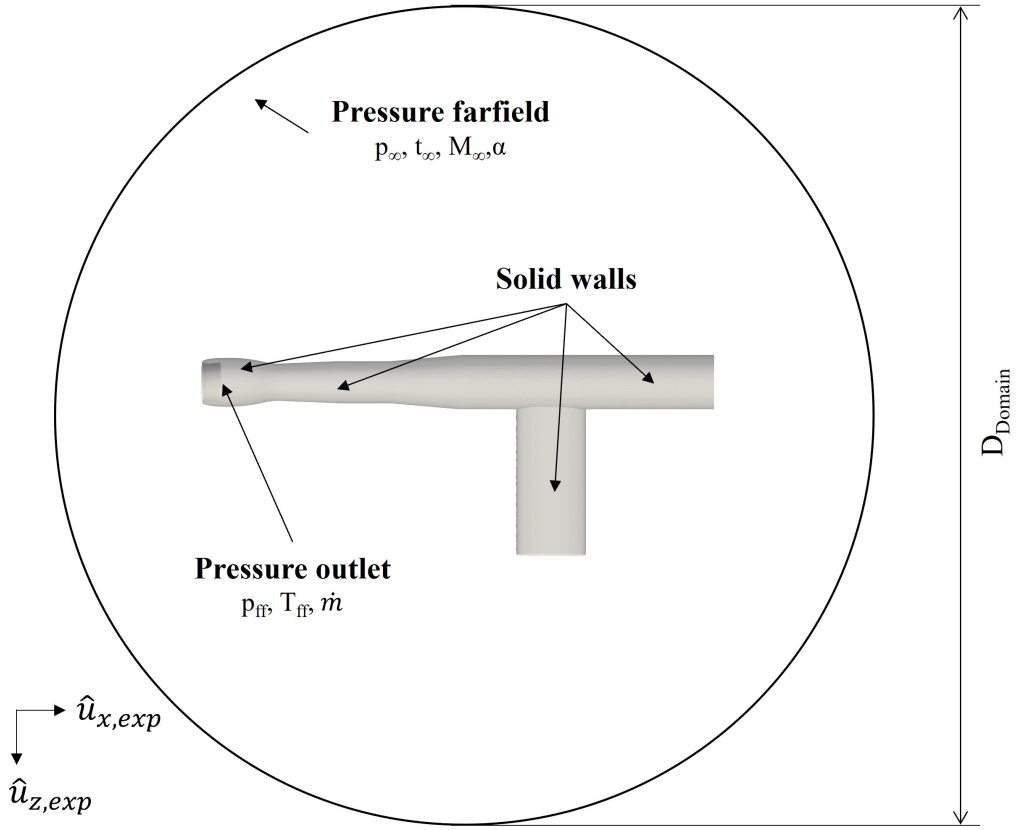

FIGURE 4.18: Schematics of the fluid domain and boundary conditions of the RANS CFD model for the nacelle in the configuration installed with the test rig.

The same convergence strategy as for the 2D axi-symmetric case of the isolated nacelle was applied for this CFD model (Section 4.3.1.1.1). This CFD method is validated using experimental data and is presented in Chapter 5 of the present project.

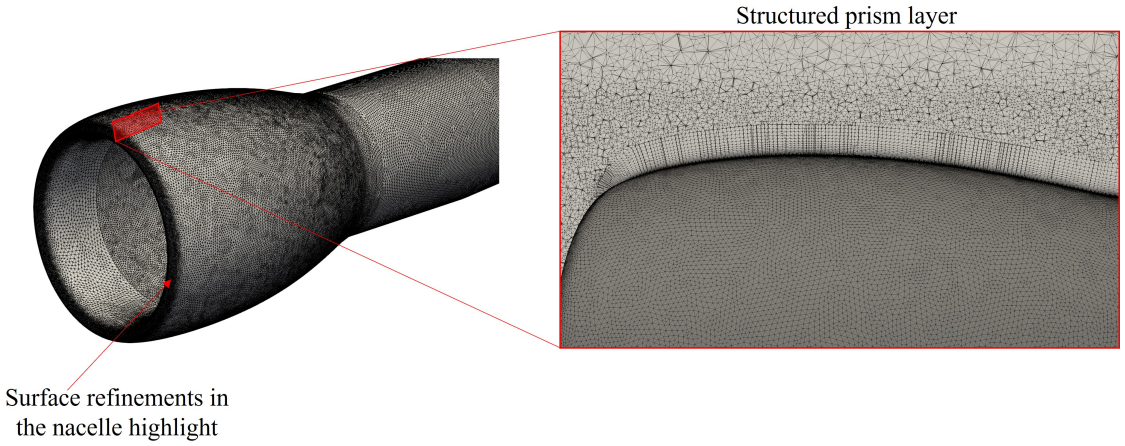

(A) Surface mesh and structured prism layers.

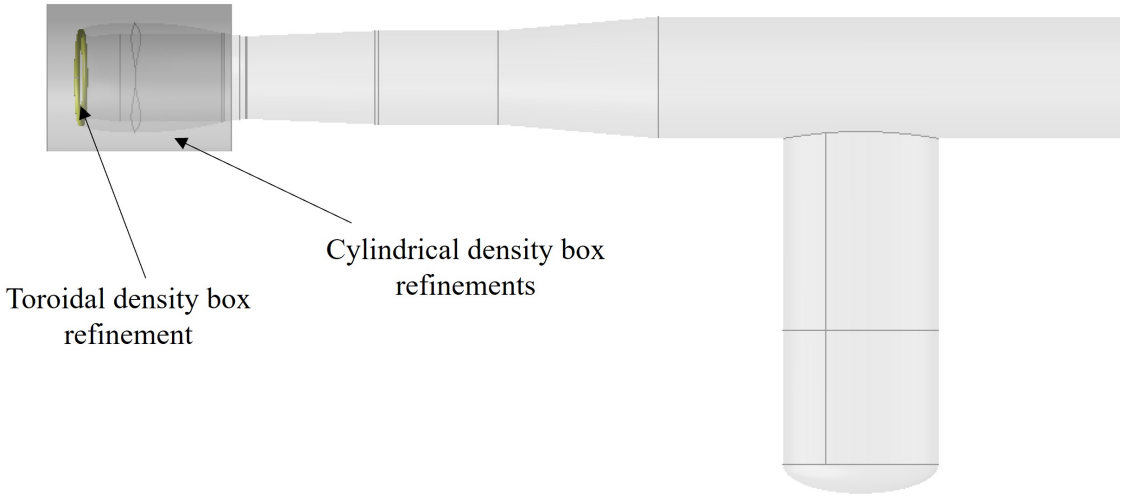

(B) Volumetric mesh refinements.

FIGURE 4.19: Details of the grid of the RANS CFD model for the nacelle in the configuration installed with the test rig.

4.3.1.2 RANS wall functions

ANSYS Fluent[222] is the software used for the numerical simulations. This code automatically handles the wall treatment of the boundary layer based on the y^+ value when the $\kappa-\omega$ SST turbulence model is used (Appendix A.2.1.2). In order to use wall functions for the boundary layer modelling, $y^+ > 11.225$ and 10-20 inflation layers are recommended[222].

In this work a RANS CFD model with wall functions treatment is developed for: (a) the 2D axi-symmetric nacelle design in isolated configuration and (b) the 3D

aero-engine configuration installed in the airframe (Figure 4.9). The domain size and boundary conditions remain as in the RANS models with $y^+ < 1$ previously detailed in Section 4.3.1.1. The inflation grids are coarsened in both cases for a targeted y^+ of around 50 (no lower than 30 and no higher than 150) and 15 layers with a growth ratio of 1.2. The convergence strategies follow the same steps but less number of iterations are needed.

These CFD models are used as a low-fidelity method in the design and optimisation process of nacelles. As such, the surface and volumetric mesh sizings are coarsened by a factor of two relative to the higher fidelity RANS method (Section 4.3.1.1). The purpose of a low-fidelity model is not to get the correct absolute results but to approximate the gradients of the design space while reducing the computational overhead of the design process. Consequently, an approach based on the GCI error is not efficient to verify the grids of these low-fidelity models. An alternative approach has been used that estimates the uncertainty on the prediction of key integral parameters with these grids relative to the prediction obtained with a grid independent mesh (Appendix B.4).

- For the model that considers a 2D axi-symmetric nacelle in isolation, a 2σ uncertainty of around 3% in the nacelle drag is obtained (Appendix B.4.1). The grid cell count is approximately 25000 elements and reduces the computational cost by a factor of 2 relative to the high-fidelity RANS model.
- For the CFD model of the aero-engine installed in the airframe, a maximum 2σ uncertainty in the key performance parameters of the installation of 0.06% is obtained (Appendix B.4.2) which is of the order of the uncertainty carried in the estimation of the Net Vehicle Force (Section 4.4.1.1). The grid cell count is around 20 million elements and reduces the computational cost by a factor of 15 relative to the high-fidelity RANS model.

4.3.1.3 Unsteady RANS

Unsteady RANS (URANS) calculations are applied to the nacelle configuration installed in the test rig (Figure 4.1) at two different off-design conditions. One is the windmilling diversion operating point (Table 4.1). It is representative of a flow physics governed by shock-induced flow separation. This happens because the MFCR is substantially low and a strong shock is located close to the highlight of the nacelle. The other off-design condition is windmilling end-of-runway

(Table 4.1). This operating conditions is representative for diffusion-induced flow separation which occurs at high flow incidences and low velocities (stall conditions).

The domain size, mesh and boundary conditions are exactly the same as the steady RANS model detailed in Section 4.3.1.1.4. For this particular RANS model the temporal terms are considered. A second order and implicit temporal discretisation is used. A total of 40 iterations per time step sufficed to reduce the normalised equation residuals by 3 order of magnitude. Force monitors were also checked to ensure iterative convergence. The time step (Δt) used depends on the problem and a refinement study is required. In this work, a Δt of $1.19 \cdot 10^{-3}$ and $2.33 \cdot 10^{-4}$ seconds are used for end-of-runway and windmilling diversion respectively. The details of the time step study are reported in Appendix C.1.1. Additionally, an assessment of the statistical convergence of the URANS calculations show an acceptable number of 140 and 250 convective times to ensure convergence for windmilling end-of-runway and diversion respectively (Appendix C.1.2). A convective time (τ) is defined as the ratio between the nacelle length (L_{nac}) and the free-stream velocity (U_∞) (Equation 4.9).

$$\tau = \frac{L_{nac}}{U_\infty} \tag{4.9}$$

4.3.2 Euler models

The Euler equations in fluid dynamics do not consider the viscous effects of the flow. Therefore, it is important to understand what components of the total drag are considered with this inviscid approach. As explained in Section 2.1.1 for a nacelle, the overall nacelle drag (D_{nac}) can be defined as the summation of different terms: friction drag ($D_{Friction}$), form drag (D_{Form}), induced drag ($D_{Induced}$) and wave drag (D_{Wave}) (Equation 4.10). The combination of $D_{Friction}$ and D_{Form} is called profile drag ($D_{Profile}$) and is related to viscous phenomena (Section 2.1.1). Therefore, in a Euler-based design approach this term is not considered. Conversely, the wave drag and the induced drag are solved with the Euler equations.

$$D_{nac} = \underbrace{D_{Friction} + D_{Form}}_{D_{Profile}} + D_{Induced} + D_{Wave} \tag{4.10}$$

Although for UHBPR configurations $D_{Friction}$ accounts for around 60% of the total nacelle drag at cruise, this component is directly proportional to the nacelle wetted

area. Additionally, in conditions of generally attached flow, like the cruise point, D_{Form} does not change substantially. Therefore, from a nacelle design point of view in which the shape is modified but the overall surface is kept broadly constant and the flow is attached, the changes in drag are expected to be dominated by the pressure terms $D_{Induced}$ and D_{Wave}. As a consequence, an Euler-based computational model is considered to be appropriate to capture the gradients in the design space. This is assessed in Section 8.2.1.2 for the installed nacelle design problem.

In this project, the Euler CFD method is used as a low-fidelity model to obtain the steady state, compressible and inviscid solution of the flow. The formulation of these Euler equations is presented in Appendix A.2.3. The solver considers an implicit formulation and a pressure-based approach[222]. As in the RANS method, a second order upwind scheme is used for the spatial discretisation with a Green-Gauss node-based gradient interpolation method.

In this work, an Euler CFD model is applied for two configurations: (a) the 2D axi-symmetric nacelle in isolated configuration and (b) the 3D aero-engine installed with the airframe (Figure 4.9). For both cases, the same boundary conditions are defined as per the RANS CFD models (Section 4.3.1.1.1 and 4.3.1.1.3) except for the solid walls. Inviscid slip walls are imposed. The convergence strategies follow the same steps but less number of iterations are used.

In terms of the meshing strategy for the two nacelle configurations assessed, the same principals but coarser sizings as per the RANS grids are applied. The same domain sizes, type of discretisation elements and refinement features (density boxes and edge sizings) are used. The meshing parameters are coarsened by a factor of 2 compared to the RANS sizings. The inflation layer can be removed from the grid as the Euler CFD method does not model the boundary layer. However, several prism layers are kept in the grid to improve the smoothness of the mesh near the wall and avoid sharp edge or corners. These grids have been verified using the method established for low-fidelity meshes presented in Appendix B.3 and already explained for the RANS model with wall functions in the previous section. It is essentially based on ensuring a similar prediction of the design space gradients relative to a fine mesh.

- For the Euler CFD model of the 2D axi-symmetric nacelle configuration in isolation, a 2σ uncertainty in the drag prediction of 4.3% relative to a grid independent mesh is obtained (Appendix B.3.1). This provides an overall cell count of 45000 elements and a reduction in the computational cost relative to the high-fidelity RANS model by a factor of 3.

- For the Euler CFD model of the aero-engine installed in the airframe, a maximum 2σ uncertainty in the key performance parameter of the installation of 0.22% is obtained relative to a grid independent mesh (Appendix B.3.2). A mesh with approximately 25 million elements is used which reduces the computational cost by a factor of 36 relative to the high-fidelity RANS model.

4.3.3 DDES models

For some applications with large flow separation regions RANS models are not accurate enough. In these cases, Large Eddy Simulation (LES) methods offer a more realistic flow field prediction as large turbulence scales are solved (Appendix A.2.2). Large eddies are responsible for most of the mass, momentum and energy transport and depend on the geometry and boundary conditions of the problem[222]. As opposed to this, the small scales of the turbulence respond to a more universal behaviour and therefore are easier to model[223]. LES works as a low-pass filter of the Navier-Stokes equations using the mesh discretisation[222]. However, for wall-bounded flows the computational cost of LES increases substantially because even large turbulence scales become smaller and the required grid refinement becomes prohibitive[222]. An alternative are Detached Eddy Simulation (DES) methods[198]. DES is a hybrid RANS/LES method that combines LES in highly unsteady regions far from the walls with URANS methods to model the boundary layer. In this work, an improved version of DES called Delayed Detached Eddy Simulation (DDES)[205] is used. It avoids the transition from URANS to LES within the boundary layer through the use of blending functions which avoids problems like grid-induced flow separation[201,202].

In this project, DDES calculations are applied for the nacelle installed in the test rig configuration (Figure 4.9). The windmilling diversion condition governed by low engine MFCRs and representative of shock-induced flow separation is considered. The RANS solver of the DDES method is set up as detailed in Section 4.3.1 for pure RANS models with the $\kappa - \omega$ SST turbulence model. A second order implicit temporal discretisation is used for the transient terms of the equations. A number of 40 iterations per time step were sufficient to ensure iterative convergence. The normalised equation residuals were reduced by 3 order of magnitude which is a conservative value compared to the minimum reduction of one order or magnitude recommend by Menter[223]. Monitors were also considered to assess the convergence with changes lower than 0.1% and 0.01% for the wall forces on the fan-cowl and mass flow in the fan face respectively. The time step selection is directly dictated

by the Courant Friedrich Lewy (CFL) number which relates the time (Δt) and spatial discretisation (Δx) for the expected turbulence to be resolved (Equation 4.11). Therefore considering $CFL = 1$[223] and the local velocity as U in the CFL formulation (Equation 4.11), a time step of $1.7 \cdot 10^{-5}$ seconds is determined for the windmilling diversion condition.

$$CFL = \frac{U\Delta t}{\Delta x} \tag{4.11}$$

The same fluid domain size and set-up of boundary conditions as for the RANS and URANS models are used (Section 4.3.1.1.4 and 4.3.1.3). Using the RANS mesh as starting point, the DDES grid is generated by incorporating a volumetric refinement for the LES region. The mesh in the boundary layer is kept as per the RANS grid with a $y^+ < 1$ and a growth ratio of 1.2[200]. The LES volumetric refinement consists on a toroidal density box that extends from $5r_{if}$ ahead of the nacelle top-line leading edge to $0.3L_{nac}$ downstream of the nacelle trailing edge (Figure 4.20a). The radial dimension spans from the intake throat ($r_{th,intk}$) to $1.3r_{max}$ of the top-line (Figure 4.20a). No refinement is applied in the intake as the focus is on the fan-cowl aerodynamics. These sizes of the toroidal density box are conservatively estimated from flow separation predictions with RANS models.

The minimum grid size that is define in the LES volumetric refinement is estimated from common practices[224] which assume to resolve 80% of the turbulent kinetic energy (κ) (Figure 4.21). From this assumption, the grid size Δx can be estimated as the ratio with the integral length scale (l_0) of $l_0/\Delta x = 4.8$[224] (Figure 4.21). It is known that the turbulent kinetic energy peaks at the integral length scale (Figure 4.21). From RANS calculations, the integral length scale can be approximated using the correlation $l_0 = \kappa^{0.5}/(C_\mu \omega)$. κ is the turbulent kinetic energy, ω is the turbulent specific dissipation rate and $C_\mu = 0.09$ is a constant of the correlation model. This procedure provides a LES grid size of $2 \cdot 10^{-3}$ meters for the windmilling diversion condition. This increases the overall cell count from 14.2 million elements for the RANS mesh to 61 million for the DDES mesh.

The DDES solution is initialised from a converged RANS solution which is interpolated into the DDES grid. The statistical convergence of the calculations is assessed in Appendix C.2.1 for a sample case at the nominal diversion condition. Cumulative average and standard deviation of the drag coefficient shows that a minimum of 15 convective times (Equation 4.9) after removing the initial transient are needed for convergence. Moreover, checks for the DDES blending functions show the proper

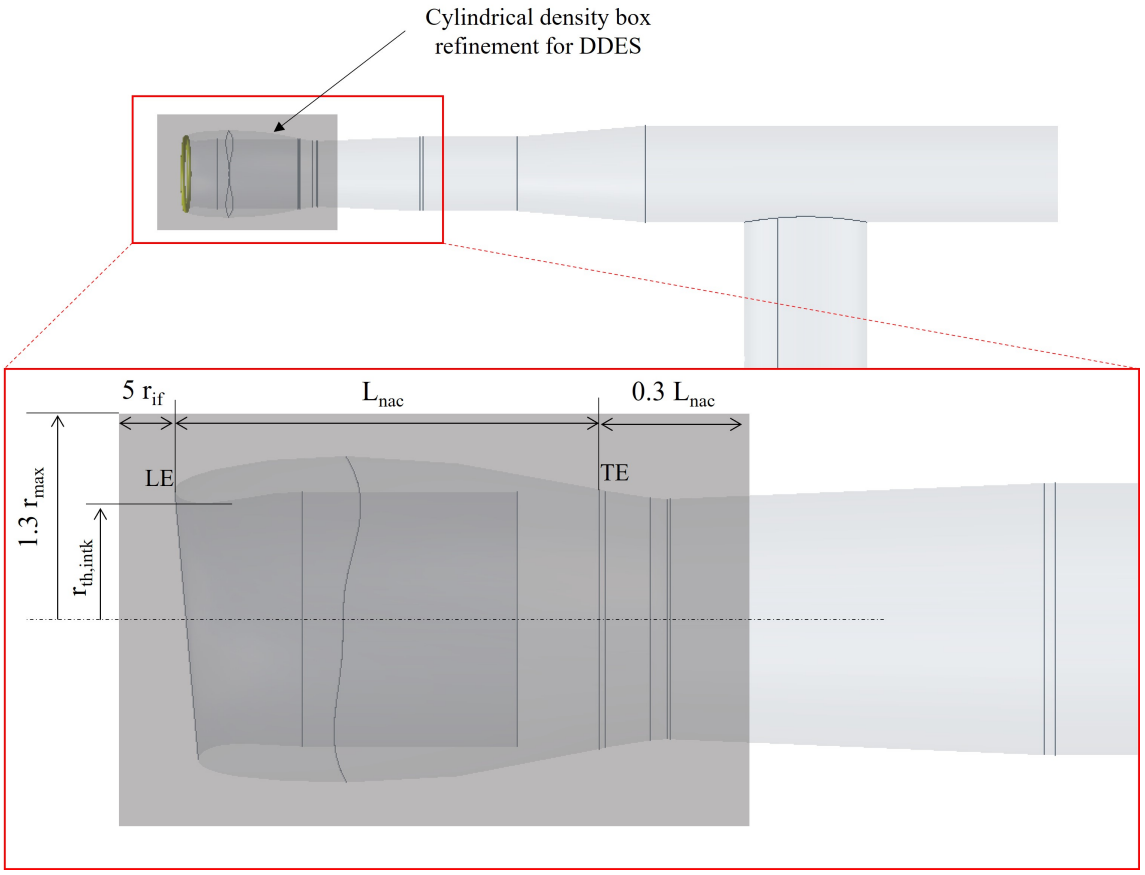

(A) Volumetric mesh refinement for DDES grids.

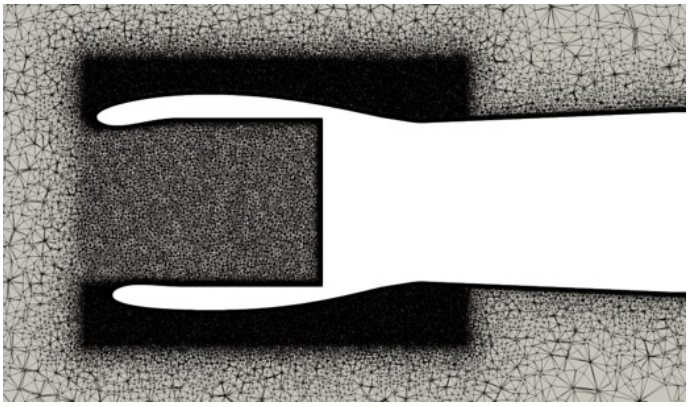

(B) Side view of the DDES grids.

FIGURE 4.20: Details of the grid of the DDES CFD model for the nacelle in the configuration installed with the test rig.

transition from the RANS to the LES mode, where the boundary layer is modelled using the RANS mode (Appendix C.2.2).

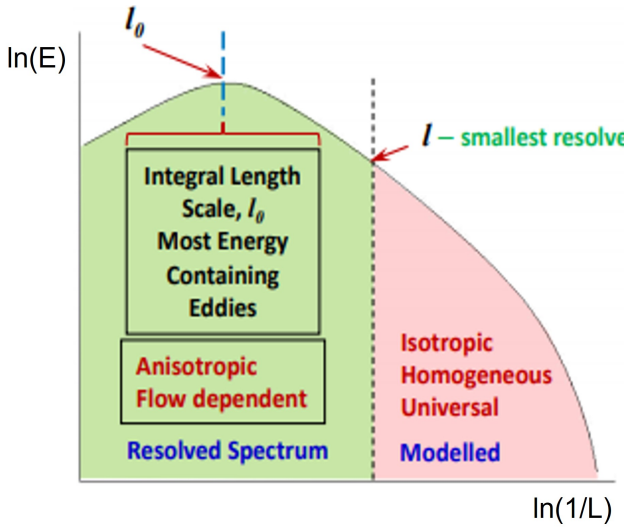

	l / l_0	l_0 / Δ
$k(l) = 0.1k$ (10%)	6.10	0.33
$k(l) = 0.5k$ (50%)	1.6	1.25
$k(l) = 0.8k$ (80%)	0.42	4.8
$k(l) = 0.9k$ (90%)	0.16	12.5

FIGURE 4.21: Turbulent energy cascade and tabulated grid sizes. Based on Gerasimov[224].

4.4 Thrust and drag accounting method

The overall aerodynamic performance of either the isolated engine or the coupled engine-airframe system is not affected by the split between the thrust and drag forces. However, with a correct split of each force term it is possible to relate the aerodynamic performance to geometrical design rules. Therefore, the use of a thrust and drag bookkeeping method is essential. In this section, the nearfield method used for the performance evaluation of isolated engines and engine-airframe installations is presented (Section 4.4.1). Additionally, the farfield method employed to evaluate the nacelle installed in the test rig for the wind tunnel configuration is detailed (Section 4.4.2).

4.4.1 Nearfield method

The Thrust and Drag Accounting (TDA) method based on a nearfield approach for the force extraction that is used to evaluate the aero-engine performance in isolated configuration is based on industrial standard practices from AGARD[20]. To assess the overall performance of the engine-airframe system, Goulos et al.[98] expanded the TDA method to consider the aero-engine integration effects (Figure 4.22) and this approach has been adopted in this thesis. The methodology allows a resolution of the forces in the aerodynamic axes $\{\hat{u}_D, \hat{u}_S, \hat{u}_L\}$. All the forces are considered positive in the downstream direction. The exerted forces on the engine walls and streamtube

boundaries (ϕ, θ) are calculated by integrating the gauge static pressure ($p-p_\infty$) and shear stress terms (τ) on the normal ($\overrightarrow{dS}$) and tangential ($\overrightarrow{dA}$) surfaces (Equation 4.12). The streamtube-external forces define the drag domain and are represented by ϕ while the streamtube-internal forces correspond to the thrust domain and are expressed by θ. By definition, the internal and external forces in the streamtube boundaries are of the same magnitude and opposite direction: $\phi = -\theta$. The gauge stream forces across the boundaries (F_G) are computed by integrating the pressure and momentum terms over the area of interest where ρ and $\overrightarrow{U}$ denote the fluid density and velocity vector (Equation 4.13). The mass flow ($\dot{m}$) can also be obtained by numerical integration in the fan-face (2) and inlet of bypass (13) and core (7) exhausts (Equation 4.14).

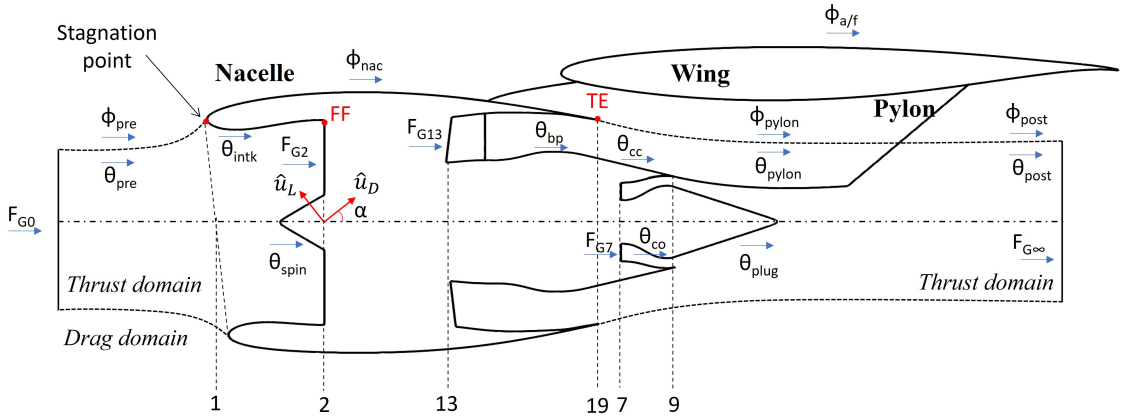

FIGURE 4.22: Schematic of the thrust and drag accounting method for an installed aero-engine with a separated-jet exhaust.

$$\phi, \theta = \iint_S (p - p_\infty)\hat{n}\overrightarrow{dS} + \iint_A \tau \overrightarrow{dA} \tag{4.12}$$

$$F_G = \iint_S (\rho |\overrightarrow{U}| \overrightarrow{U} + (p - p_\infty))\hat{n}\overrightarrow{dS} \tag{4.13}$$

$$\dot{m} = \iint_S \rho \overrightarrow{U}\, \hat{n}\overrightarrow{dS} \tag{4.14}$$

The key metric to assess the overall drag of the propulsion system is the nacelle drag (D_{nac}) which includes the pre-entry (ϕ_{pre}) and post-exit (ϕ_{post}) stream-tube forces and the wall forces on the cowl (ϕ_{nac}) and the region of the pylon in the drag domain (ϕ_{pylon}) (Equation 4.15). However, calculating ϕ_{post} is complex for this kind of problems. Therefore, the modified definition of the metric represented

by the superscript $()^*$ is used by neglecting ϕ_{post}. It is called modified nacelle drag (D^*_{nac}) (Equation 4.16). ϕ_{pre} can be calculated from the control volume in the intake (Equation 4.17). This approach requires to find the stagnation point in the leading edge of the nacelle that splits ϕ_{pre}, ϕ_{nac} and θ_{intk}. This is difficult to automatise and include a source of error in the calculation related to the grid refinement level. To overcome this challenge the modified nearfield method was developed by Christie et al.[40] which computes the combined $\phi_{pre}+\phi_{nac}$ (Equation 4.18). This method directly integrates the wall forces from the fan-face to the nacelle trailing edge (F_{FF-TE}) which avoid the need to find the stagnation point.

$$D_{nac} = (\phi_{pre} + \phi_{nac} + \phi_{post} + \phi_{pylon})_D \tag{4.15}$$

$$D^*_{nac} = (\phi_{pre} + \phi_{nac} + \phi_{pylon})_D \tag{4.16}$$

$$(\phi_{pre})_D = -(\theta_{pre})_D = (-F_{G0} + F_{G2} + \theta_{intk} + \theta_{spin})_D \tag{4.17}$$

$$(\phi_{pre} + \phi_{nac})_D = \left(-F_{G0} + F_{G2} + \underbrace{\theta_{intk} + \phi_{nac}}_{F_{FF-TE}} + \theta_{spin} \right)_D \tag{4.18}$$

The thrust component of the propulsion system comes from the exhaust and is quantified through the Gross Propulsive Force (GPF). As for the nacelle drag, the modified definition of this metric (GPF^*) is used (Equation 4.19). It is computed through the gauge stream forces in the inlet of the bypass (F_{G13}) and core (F_{G7}) exhausts and the wall forces in the bypass duct (θ_{bp}), the core duct (θ_{co}), the core-cowl (θ_{cc}), the plug (θ_{plug}) and the region of the pylon in the thrust domain (θ_{pylon}). The superscript $()^{nc}$ means "non-corrected" as this definition of the GPF^* considers the mass flows in the bypass ($\dot{m}_{13}^{CFD}$) and core ($\dot{m}_{7}^{CFD}$) nozzle obtained from the CFD calculation. However, these mass flows might be different from the cycle values due to flow suppression induced by the interaction with the airframe or pylon. This is corrected through the modified velocity coefficient of the exhaust (C_v^*) which is independent of the mass flows (Equation 4.20). It is defined as the GPF^* divided by the ideal propulsive force ($\dot{m}_{13}V_{13}^{ideal} + \dot{m}_7 V_7^{ideal}$). In this case the ideal propulsive force considers the mass flows from the CFD calculation to be consistent with the $(GPF^*)_D^{nc}$ (Equation 4.20). The ideal propulsive force is calculated by the exhaust

mass flows times the ideal velocity of the jet (V^{ideal}). V^{ideal} is defined for an isentropic and fully expanded exhaust[225] where γ is the ratio of specific heats of the fluid ($\gamma = \frac{C_p}{C_v}$), R is the universal constant for ideal gases, T_0 is the total temperature at the inlet of the nozzle and NPR is the nozzle pressure ratio ($NPR = P_0/p_\infty$) defined by the total pressure at the nozzle inlet (P_0) divided by the farfield static pressure (p_∞) (Equation 4.21). Although $(C_v^*)_D$ refers to the modified velocity coefficient in the drag axis, the analogous terms can be calculated for the side $(C_v^*)_S$ and lift $(C_v^*)_L$ axis. The overall velocity coefficient $\|C_v^*\|$ can be computed by the norm of the vector (Equation 4.22). The correction for the $(GPF^*)^{nc}$ in each axis is applied through the modified velocity coefficient on the corresponding axis times the ideal propulsive force based on cycle mass flows ($\dot{m}_{13}^{cycle} V_{13}^{ideal} + \dot{m}_7^{cycle} V_7^{ideal}$) (Equation 4.23). This ensures a mass flow balance between the intake and the exhaust. Otter[113] statistically assessed the impact of this mass flow imbalance by resizing the nozzle areas to achieve the cycle mass flows. A small impact on the thrust accounted by the thrust and drag bookkeeping method was found.

$$(GPF^*)_D^{nc} = (F_{G13} + F_{G7} - (\theta_{bp} + \theta_{co} + \theta_{cc} + \theta_{plug} + \theta_{pylon}))_D \tag{4.19}$$

$$(C_v^*)_D = \frac{(GPF^*)_D^{nc}}{\dot{m}_{13}^{CFD} V_{13}^{ideal} + \dot{m}_7^{CFD} V_7^{ideal}} \tag{4.20}$$

$$V^{ideal} = \sqrt{\frac{2\gamma R T_0}{\gamma - 1}\left(1 - \left(\frac{1}{NPR}\right)^{\frac{\gamma-1}{\gamma}}\right)} \tag{4.21}$$

$$\|C_v^*\| = \sqrt{(C_v^*)_D^2 + (C_v^*)_S^2 + (C_v^*)_L^2} \tag{4.22}$$

$$(GPF^*)_D = (C_v^*)_D \left(\dot{m}_{13}^{cycle} V_{13}^{ideal} + \dot{m}_7^{cycle} V_7^{ideal}\right) \tag{4.23}$$

The aerodynamic balance between the thrust and drag components of the propulsion system is quantified by the Net Propulsive Force (NPF). The thrust component in the drag axis ($(T)_D$) is considered for this purpose (Equation 4.24). $(T)_D$ requires the calculation of the post-exit term of the thrust domain (θ_{post}) as it considers the nominal definition of GPF. However, the NPF can be calculated using the modified definition of the metrics as $\theta_{post} = -\phi_{post}$ and they cancel out each other in GPF^* and D_{nac}^* (Equation 4.25).

$$(T)_D = (GPF - F_{G0})_D \tag{4.24}$$

$$NPF = (T)_D - D_{nac} = (GPF^* - F_{G0})_D - D^*_{nac} \tag{4.25}$$

NPF can be used as key metric to quantify the aero-engine performance in isolation. When the integration of the engine-airframe system is considered the TDA method needs to account for the airframe forces ($\phi_{a/f}$) (Figure 4.22). $\phi_{a/f}$ considers the contribution from the wings, the fuselage and the empenage. A metric is defined to assess the overall aerodynamic performance of the combined airframe and powerplant system called Net Vehicle Force (NVF). It is calculated as the difference between the NPF and the airframe drag ($D_{a/f} = \left(\phi_{a/f}\right)_D$) (Equation 4.26).

$$NVF = NPF - \left(\phi_{a/f}\right)_D \tag{4.26}$$

NVF is a key parameter in the context of this project about aero-engine nacelle design in installed configuration as it can be related to fuel burn savings. A decrease in NVF of 1% of the standard net thrust of the engine (F_N) equates approximately to 1% reduction in fuel consumption at the cruise condition[106]. Therefore, a method to correct for trimmed flight is required to ensure the analysis at the cruise operation point. From the definition of the cruise condition of the CRM (Section 4.1.2), an overall lift coefficient of the aircraft of $C_L^{a/c} = 0.5$ is targeted[82] (Equation 4.27), where q_∞ is the free-stream dynamic pressure and A_{ref} is the wing area of the CRM used as reference. The total lift force of the aircraft ($L_{a/c}$) results from the summation of the modified gross propulsive force and modified nacelle force in the lift axis ($(GPF^*)_L$,L^*_{nac}) and the lift component of the airframe forces ($L_{a/f}$) (Equation 4.28). As for NPF, the θ_{post} and ϕ_{post} terms of the $(GPF^*)_L$ and L^*_{nac} are cancelled out and the definition of $L_{a/c}$ in modified metrics is fully consistent.

$$C_L^{a/c} = \frac{L_{A/C}}{q_\infty A_{ref}} = 0.5 \tag{4.27}$$

$$L_{a/c} = (GPF^*)_L + L_{a/f} + L^*_{nac} \tag{4.28}$$

4.4.1.1 Uncertainty estimate in NVF

The uncertainty associated to a model comes from three different types of errors: discretisation error, iterative convergence error and physical approximation error. In a computational model for numerical simulations, the discretisation error depends on the grid. The iterative convergence error is related to the convergence criteria and the software used for the simulation. The physical approximation error derives from the model selected to simulate the real physical problem and requires further knowledge of the exact solution or another source of data like experiments.

Just the discretisation error is used to get an estimate of the uncertainty in the NVF prediction. The iterative convergence error is discarded as it is typically one order of magnitude smaller than the discretisation error for sensible convergencence criteria[226]. Moreover, no experimental data on aero-engine installation assessments is available to estimate the physical approximation error for this project.

The discretisation error of the CFD mesh is calculated in a grid independence study and reported using the GCI (Appendix B). The GCI considers a security factor of 1.25 in the estimation of the error (Equation B.7). For the RANS CFD model, a GCI in NPF and $D_{a/f}$ of 0.34% and 1.57% were obtained (Table B.3). Therefore, using errors in quadrature (Equation 4.29), the NVF in the RANS computational calculation has a discretisation error of around 1.60%. A more useful way to express this uncertainty in the calculation of the NVF of a design is relative to the standard net thrust of the aero-engine (F_N=60000N) as it can be compared with the uncertainty of the surrogate models that are used in the design process. For the investigated design space in this project, the uncertainty in NVF/F_N reaches around 0.06% which is below the uncertainties of the surrogate models (Sections 8.2.2.2 and 8.2.2.3).

$$GCI_{NVF} = \sqrt{GCI_{NPF}^2 + GCI_{D_{a/f}}^2} \tag{4.29}$$

4.4.2 Farfield method for wind tunnel configuration

As presented in the previous section, the nacelle drag for an isolated nacelle using a nearfield method (NF) results from the summation of ϕ_{pre}, ϕ_{nac} and ϕ_{post} projected in the drag direction $()_D$. For the configuration in which the nacelle is installed in the test rig (Section 4.1.3), the post-exit streamtube is modelled through the profile and parallel stings. The force in each of these surfaces has a friction and

pressure component (Equation 4.31). For the nacelle drag in this configuration using the modified nearfield approach, the term ϕ_{post} is calculated as the integral of the normal pressure forces to the profile and parallel stings (Equation 4.32) (Figure 4.23).

$$\begin{cases} \phi_{prof.Sting} = \phi_{prof.Sting}|_{press} + \phi_{prof.Sting}|_{visc} \\ \phi_{paral.Sting} = \phi_{paral.Sting}|_{press} + \phi_{paral.Sting}|_{visc} \end{cases} \tag{4.30}$$

$$\phi_{post} = \phi_{post}|_{press} + \phi_{post}|_{visc} \begin{cases} \phi_{post}|_{press} = \phi_{prof.Sting}|_{press} + \phi_{paral.Sting}|_{press} \\ \phi_{post}|_{visc} = \phi_{prof.Sting}|_{visc} + \phi_{paral.Sting}|_{visc} \end{cases} \tag{4.31}$$

$$D_{nac}^{NF} = \left(\phi_{pre} + \phi_{nac} + \phi_{prof.Sting}|_{press} + \phi_{paral.Sting}|_{press}\right)_D \tag{4.32}$$

However, from a validation point of view, the drag has to be calculated in the same manner as in the experiments which follows a farfield approach (FF). A farfield accounting approach based on a wake method has been developed in collaboration with colleagues in Cranfield University and adopted for this research. For this method, a control volume (CV) is used. It goes from the farfield upstream of the nacelle where freestream conditions apply (station 0) to the rake plane (station 3) (Figure 4.23). Gauge forces (Equation 4.13) apply in these inlet and outlet surfaces: F_{G0} and F_{G3}. The control volume is closed in the outer side by the bounding streamlines. The force there ϕ_{bs} is calculated by the integration of the shear and normal pressure terms (Equation 4.12). The terms ϕ_{pre} and ϕ_{nac} in the lower side of the control volume are calculated using the modified near-field approach (Section 4.4.1) that avoids the need to identify the stagnation point.

Finally, the wall forces in the profile sting ($\phi_{prof.Sting}$) and parallel sting ($\phi_{paral.Sting}$) close the control volume and are calculated by the integration of the shear and normal pressure terms (Equation 4.30). These wall forces constitute the post-exit streamtube term (Equation 4.31). From the momentum conservation law applied to a control volume in steady state, all the forces on the fluid within the control volume are equal to the balance of momentum flow rate out and in of the control volume. Consequently, the summation of all the gauge and wall forces within the control volume is equal to zero (Equation 4.33). This provides a definition to the

nacelle drag both from a nearfield (NF) and a farfield (FF) approaches (Equation 4.34).

$$-F_{G0} + \phi_{bs} + F_{G3} + \phi_{pre} + \phi_{nac} + \phi_{prof.Sting} + \phi_{paral.Sting} = 0 \tag{4.33}$$

$$\begin{aligned} D_{nac} &= \underbrace{\left(\phi_{pre} + \phi_{nac} + \phi_{prof.Sting}|_{press} + \phi_{paral.Sting}|_{press}\right)_D}_{D_{nac}^{NF}} \\ &= \underbrace{\left(F_{G0} - F_{G3} - \phi_{bs} - \phi_{prof.Sting}|_{visc} - \phi_{paral.Sting}|_{visc}\right)_D}_{D_{nac}^{FF}} \end{aligned} \tag{4.34}$$

In the experiments, the total pressure measurements at the rake plane are used to calculate the momentum deficit from the freestream conditions. The flow variables are insentropicaly expanded to the Jone's plane (Figure 4.23). This is a plane downstream of the rake where static variables are recovered to freestream conditions. This recovers the force associated with the static pressure field as a momentum force. For this isentropic expansion, the static pressure and temperature in the Jone's plane are assumed to be the same as in the freestream: $t_J = t_\infty$ and $p_J = p_\infty$. Additionally, the total pressure and temperature in the Jone's plane are set as per the values in the rake plane: $T_{0,J} = T_{0,3}$ and $P_{0,J} = P_{0,3}$. The mass flow in Jone's and in the rake plane is considered the same due to continuity: $\dot{m}_J = \dot{m}_3$. From this expansion, two additional terms appear that close the control volume from the rake plane to the Jone's plane: ϕ_{Jbs} and ϕ_{Jis} (Figure 4.23). However, in the experimental approach, the bounding streamtube terms ϕ_{bs}, ϕ_{Jbs} and ϕ_{Jis} can not be measured. Therefore, the nacelle drag using the farfield approach is calculated as in Equation 4.35.

$$D_{nac}^{EXP} = \left(F_{G0} - F_{GJ} - \phi_{prof.Sting}|_{visc} - \phi_{paral.Sting}|_{visc}\right)_D \tag{4.35}$$

The viscous terms in the profile and parallel sting ($\phi_{prof.Sting}|_{visc}$ and $\phi_{paral.Sting}|_{visc}$) are calculated for the experimental drag using the Green's method[227]. This is a software that estimates the skin friction force from the surface pressure data measured using pressure tappings. Therefore, these skin friction terms are extracted and applied as a correction term to the momentum loss in Equation 4.35. An alternative definition of the experimental drag arises if this correction term is not considered. It is called uncorrected drag ($D_{nac}^{EXP,Unc}$) (Equation 4.36) and is used to estimate the sectional drag contributions on the nacelle.

$$D_{nac}^{EXP,Unc} = (F_{G0} - F_{GJ})_D \tag{4.36}$$

In the CFD model, the drag is calculated in a manner that replicates the experimental method as closely as possible. The flow primitives are extracted at the rake plane and interpolated from the high-resolution unstructured mesh on to radial grid which matches the experimental resolution. This is then expanded to Jone's as detailed above. The skin friction and surface normal terms of the wall forces are directly calculated in the CFD model.

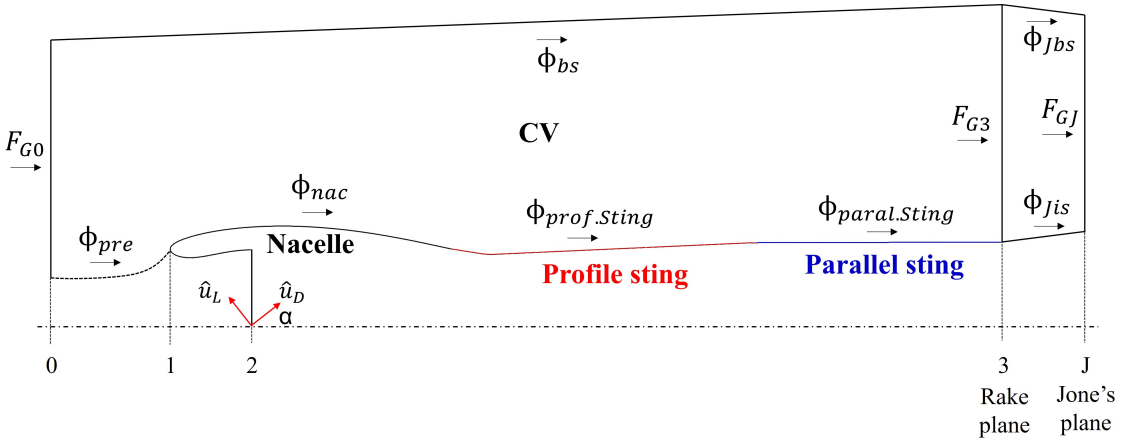

FIGURE 4.23: Schematic of the farfield method for the drag extraction of the nacelle installed in the test rig.

4.5 Nacelle design and optimisation methods

This section gives an overview of the different methods for nacelle design used in this project. The explanation covers from the simplest approach based on a design space exploration up to the different optimisation methods based on CFD or surrogate models. Moreover, further details related to the nacelle optimisation methods for both the isolated and airframe-installed configurations are provided. The sampling technique and optimisation algorithms used are also described.

4.5.1 Design space exploration

A Design Space Exploration (DSE) is essential at preliminary design stages as it characterises the design space of the problem. It provides an understanding of the relationship between design variables and performance metrics and shows the

location of the optimal design space. Some design methods are just based on DSEs. Relative to a certain baseline design, a DSE can provide designs with improved performance. This depends on the population level of the DSE which is controlled through the ratio of the number of samples to design variables ($N_{samples}/N_{DOF}$). The sampling technique plays a key role to ensure a reasonable coverage of the design space while using the lowest number of sample as possible due to computational cost constraints. In this project the Latin Hypercube Sampling technique is used which is detailed in Section 4.5.1.1. Furthermore, from the point of view of an optimisation process, the DSE constitutes a key part as it is used to initialise the search across the design space.

A full body of work on the design space exploration for isolated nacelles is already available in the open literature[16,18,50,228,229]. One of the challenges of this research project deals with installed nacelle design. Therefore, the exploration of the design space is mostly focused on the installed nacelle configuration. Although the relationship between the different metrics of the thrust and drag bookkeeping method across the design space is assessed, the NVF is used as the key metric for the propulsion system integration (Section 4.4.1). One-dimensional distributions of the different design variables based ranges of NVF benefit show the impact of each variable and the trends towards the optimal design space. Additionally, surrogate models are interrogated to understand the coupled behaviour between different design variables on the NVF.

4.5.1.1 Sampling technique

The Latin Hypercube Sampling (LHS) technique[230,231] is a statistical sampling method for multi-dimensional spaces. It is used in this project to populate the design space and generate the CFD databases. LHS is widely used in aerodynamic design problems due to its ability to avoid clustering and uniformly distribute samples in the design space. This provides computational cost benefits relative to standard full factorial sampling methods. LHS also allows an easy implementation of sub-sampling techniques from a large data set which avoids further CFD calculations to obtain reduced data sets. This is useful to assess the impact of the sampling ratio $N_{samples}/N_{DOF}$ on the performance of surrogate models and relate it to computational cost savings in the design method. The sub-sampling method follows two main steps:

- Firstly, the design space is populated with the reduced $N_{samples}/N_{DOF}$ ratio of samples using a standard LHS ($LHS_{reduced}$).
- Each sample of the $LHS_{reduced}$ is translated to the closest sample location of the original LHS ($LHS_{original}$). Euclidean distance is used. In the case that two samples from $LHS_{reduced}$ have the same target sample from $LHS_{original}$, the second closest sample is used.

4.5.2 Optimisation approaches

The aerodynamic shape optimisation of a nacelle is governed by non-linear flow physics which makes the problem non-convex. Therefore, as explained in Section 2.3.2, Gradient-Free Methods (GFM) for optimisation are a reasonable choice to increase the likelihood of finding the global optima[128]. In this work two GFM approaches are considered which use an evolutionary algorithm to lead the optimisation. They are divided into CFD-based (or CFD-in-the-loop) and surrogate-based optimisations (Figure 4.24). In the CFD-based optimisation method each design in every generation is evaluated with CFD (Figure 4.24a). In the surrogate-based optimisation approach, only the initial DSE is evaluated with CFD. This CFD data set is used to build the surrogate model. Subsequently, the evolutionary algorithm is applied to the surrogate model to find the Pareto front without any additional CFD computational cost (Figure 4.24b). Significant acceleration in the optimisation process can be achieve relative to the CFD-based method at the expense of a reduced accuracy in the Pareto front. A Pareto front is a N-dimensional representation of the non-dominated designs in the space of the N objective functions. The concept of non-domination between two designs A and B stands while no design is better than the other for every objective function. A summary of the optimisation activities of this project are presented in Table 4.4 which shows the different configurations, optimisation approaches, CFD fidelity, surrogate modelling technique and aim.

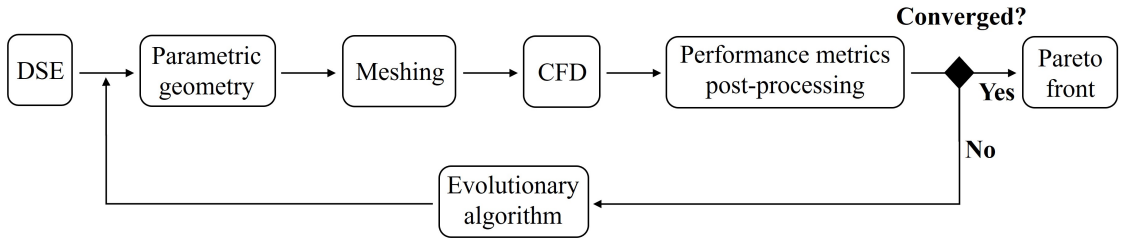

(A) CFD-based optimisation approach used for the isolated configuration.

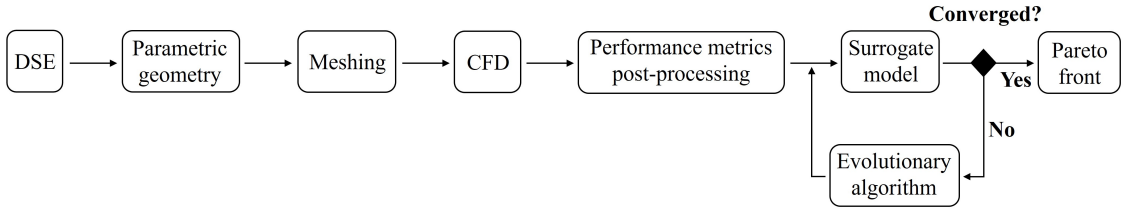

(B) Surrogate-based optimisation approach used for both the isolated and installed configurations.

FIGURE 4.24: Schematic of the different optimisation approaches.

TABLE 4.4: Summary of the nacelle aerodynamic optimisations conducted in this project for the different configurations.

Configuration	Approach	CFD Fidelity	Surrogate	Aim
2D axi-symmetric isol. (Section 4.5.2.2)	CFD-based	RANS	-	Assess the impact of every CFD fidelity on the convergence to the optimal design space.
		$RANS_{wf}$	-	
		Euler	-	
	Surrogate-based	Euler + RANS	MFNN	Assess the benefits compared to a CFD-based approach and provide guidelines on the number of samples.
3D airframe-inst. (Section 4.5.2.3)	Surrogate-based	Euler	ANN	Obtain an optimal design.
		Euler	Kriging	
		RANS	Kriging	
		Euler + RANS	VCM	

4.5.2.1 Optimisation algorithm

The optimisation algorithm is an essential element of the process as it drives the exploration and exploitation of the design space. The convergence to the correct optimal design space with the lowest variability possible and at a high convergence rate are the key aspects of an optimiser. To ensure a good performance of the optimisation algorithm, two Genetic Algorithms (NSGA-II[232] and IBEA[233]) and a Particle Swarm Optimiser (OMOPSO[234]) were statistically compared for CFD-based optimisations of 2D axi-symmetry nacelles. OMOPSO resulted as the most

suitable algorithm for this optimisation problem. The detailed analysis can be found in Appendix E.

OMOPSO is based on the ability of semi-autonomous particles that explore the design space to communicate with each other and to update their status. In this method the particles are able to sense their surroundings in the design space. This particular searching approach is modelled by the individual position $\overrightarrow{X_i^t}$ (Equation 4.37) and velocity $\overrightarrow{V_i^t}$ (Equation 4.38) vectors which are updated in each generation. The position vector shows the particle position in the design space. The velocity vector indicates the direction and intensity of the movement of that particle in the landscape. Three components constitute the velocity vector. The first term $w\overrightarrow{V_i^t}$ is the inertial one which essentially maintain the current direction of the movement of the particle. The second term of the velocity vector $c_1 r_1 \left(\overrightarrow{P_i^t} - \overrightarrow{X_i^t}\right)$ is the individual or cognitive component which considers the personal best position of the particle $(\overrightarrow{P_i^t})$. The last term $c_2 r_2 \left(\overrightarrow{G^t} - \overrightarrow{X_i^t}\right)$ is the social term that takes into account the global best position achieved within the whole population $(\overrightarrow{G^t})$. w, c_1 and c_2 are weighting factors to tune the balance between the exploration and exploitation in the searching process. While high values of w and $c_2 = 0$ maximise the exploration, low values of w and $c_1 = 0$ maximise exploitation. A high exploration ability is interesting for the initial generations of the optimisation. Exploitation is preferred when the optimisation is close to reach convergence. OMOPSO applies bounded random values to the weighting coefficients of the particle velocity vector. In particular, w is randomly set from 0.1 to 0.5 and c_1 and c_2 vary from 1.5 to 2. r_1 and r_2 are also random values bounded from 0 to 1 that are applied to the learning terms. For a multi-objective optimisation the leader selection becomes challenging. For this purpose, OMOPSO applies the Pareto dominance criteria and a crowding distance factor[232] to the set of possible leaders. The algorithm divides the swarm in three equal groups applying three different mutation approaches to the velocity vector update of each group: no-mutation, uniform mutation, non-uniform mutation. A mutation probability factor of 0.1 is used in the present work[235].

$$\overrightarrow{X_i^{t+1}} = \overrightarrow{X_i^t} + \overrightarrow{V_i^{t+1}} \tag{4.37}$$

$$\overrightarrow{V_i^{t+1}} = w\overrightarrow{V_i^t} + c_1 r_1 \left(\overrightarrow{P_i^t} - \overrightarrow{X_i^t}\right) + c_2 r_2 \left(\overrightarrow{G^t} - \overrightarrow{X_i^t}\right) \tag{4.38}$$

4.5.2.2 Isolated nacelle optimisation method

The nacelle optimisation method for the isolated configuration was developed by Tejero et al.[16] and has been adopted in this research. It has been applied to the 2D axisymmetric nacelle optimisation problem. The reason is the low computational overhead of CFD models for this configuration which allows comparative assessments of CFD-in-the-loop optimisations with surrogate-based optimisations for different ratios of samples to degree of freedom. For this problem the nacelle is parameterised using a single aero-line (Section 4.1.1). The highlight radius (r_{hi}), the trailing edge radius (r_{te}) and the nacelle length (L_{nac}) are the key parameters that define the compactness of the nacelle design. They are fixed in the optimisation problem for a compact configuration given by $L_{nac}/r_{hi} = 3.1$ and $r_{te}/r_{hi} = 0.95$. This leaves four parameters to be floated throughout the optimisation process: the maximum radius of the nacelle (r_{max}) and its axial position (f_{max}), the initial forebody radius (r_{if}) and the nacelle boa-tail angle (β_{nac}) (Figure 4.25). No hard-points are considered in this optimisation problem. The full aero-engine is constructed by combining the nacelle geometry with a representative spinner, intake[213] and separate jet exhaust[187] for UHBPR applications.

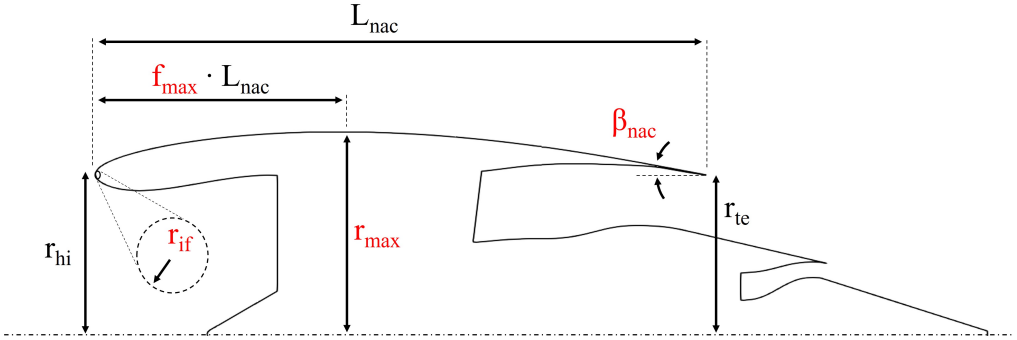

FIGURE 4.25: Design variables used in the optimisation for the 2D axi-symmetric nacelle in isolated configuration.

Compact nacelles have large surface curvature gradients which increase the aerodynamic sensitivity to off-design conditions. Consequently, multi-point optimisation approaches are needed to ensure robust designs[16,18]. In addition to the cruise condition ($C_{D-cruise}$) given by $M = 0.85$ and $MFCR = 0.7$ (Equation 4.39) the sensitivities to an increase in the flight Mach number ($C_{D-\Delta M}$) from 0.85 to 0.87 (Equation 4.40) and a decrease in the aero-engine MFCR from 0.7 to 0.65 (C_{D-EoC}) (Equation 4.41) are also considered. The minimisation of the nacelle drag at these conditions defines the three objective functions of the optimisation approach. Additionally, the sensitivity of compact nacelles to off-design conditions is also considered through an

aerodynamic constraint that is imposed in the optimisation process: every design evaluated with a peak M_{is} above 1.3 at cruise is discarded[16].

$$C_{D-cruise} = \frac{D_{nac}|_{M=0.85,MFCR=0.7}}{\frac{1}{2}\rho_\infty V_\infty^2 A_{hi}} \tag{4.39}$$

$$C_{D-\Delta M} = \frac{D_{nac}|_{M=0.87,MFCR=0.7}}{\frac{1}{2}\rho_\infty V_\infty^2 A_{hi}} \tag{4.40}$$

$$C_{D-EoC} = \frac{D_{nac}|_{M=0.85,MFCR=0.65}}{\frac{1}{2}\rho_\infty V_\infty^2 A_{hi}} \tag{4.41}$$

The optimisation starts with a DSE that uses the LHS technique to populate the design space with a sample ratio of $N_{samples}/N_{DOF} = 100$. This generates 400 non-inflected designs evenly spaced in the design space. The size of this initial generation can have a substantial impact on the scatter in the Pareto front and the convergence rate of the optimisation. Previous work by Robinson et al.[27] established a sample ratio of $N_{samples}/N_{DOF} = 100$ to be an acceptable value for this optimisation problem. Subsequently, 39 additional generations with a sample ratio of $N_{samples}/N_{DOF} = 12.5$ per generations are established to ensure convergence to the Pareto front. However, the convergence criteria of the optimisation is defined based on the Hypervolume (HV) index. This metric quantifies the N-dimensional space that is covered by a non-dominated solution set (Pareto front) after a generation relative to an arbitrary point used as a global reference[236], where N is the number of objective functions (Figure 4.26). The optimisation is considered to be converged when the HV change in the last three generations is smaller than 1%.

From the Pareto front a design can be down selected based on a weighted criterion of the different objective functions. From all the designs with ratios for $C_{D-\Delta M}/C_{D-cruise}$ and $C_{D-EoC}/C_{D-cruise}$ lower than prescribed factors K_1 and K_2, the design with lowest cruise drag is selected (Equation 4.42).

$$min\ C_{D-cruise}\ subjected\ to: \begin{cases} C_{D-\Delta M} < K_1 C_{D-cruise} \\ C_{D-EoC} < K_2 C_{D-cruise} \end{cases} \tag{4.42}$$

Both CFD-based and surrogate-based optimisations methods (Figure 4.24) are applied to this optimisation problem. Different CFD fidelities are used for the CFD-based one: RANS (Section 4.3.1.1.1), RANS with wall function modelling (Section

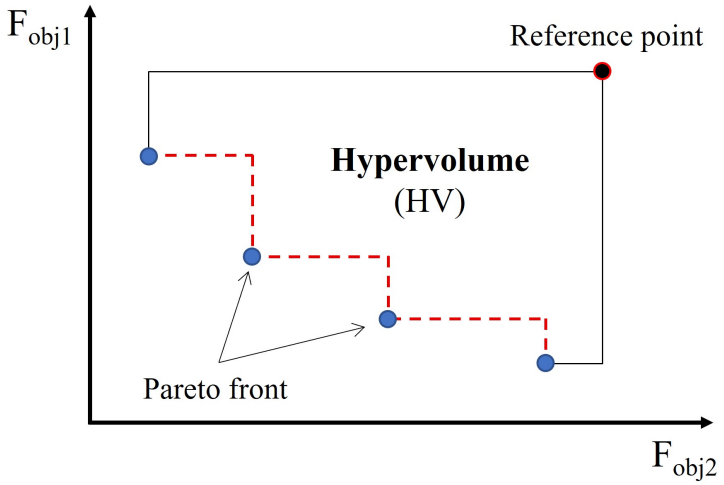

FIGURE 4.26: Schematics of hypervolume for a two-dimensional application. Based on Deb et al.[236].

4.3.1.2) and Euler (Section 4.3.2). For the surrogate-based approach, the Multi-Fidelity Neural Network technique explained later in Section 4.6.2.2 is used.

4.5.2.3 Airframe-installed nacelle optimisation method

The geometry of a nacelle installed in the airframe is parameterised using 8 aero-lines as both the inboard and outboard sides have to be considered due to the lack of aerodynamic symmetry (Figure 4.27a). As this work is focused on a compact nacelle architecture given by $L_{nac}/r_{hi} = 3.1$ and $r_{te}/r_{hi} = 0.95$, there are 4 design variables left per aero-line than can be changed in the design process: r_{if}, r_{max}, f_{max} and β_{nac}. This results in an overall number of 32 degrees of freedom. This constitutes a high-dimensional design problem that is not feasible to approach given the high computational overhead of the airframe-installed CFD calculations. In the proposed methodology the design variables are selected following the next reasoning (Table 4.5):

- The aerodynamic integration effects over the aero-engine affect primarily the inboard side, where the flow topology is completely different to the isolated case (Figure 4.28). A shock wave appears in the rear part due to the interaction with the pylon, wing and fuselage that the isolated model does not predict. Consequently, for the installed optimisation method the 3 inboard aero-lines are considered: $\Psi = 45°$ (top-control inboard), $\Psi = 90°$ (side inboard) and $\Psi = 135°$ (bottom-control inboard) (Figure 4.27a).

- The aerodynamics in the outboard aero-lines and bottom aero-line is similar to the isolated case. Although there are differences in the shock location and peak Mach number of around $0.1L_{nac}$ and $\Delta M = 0.05$ respectively, the flow topology is the same (Figure 4.28). Therefore, they are fixed to a baseline design which comes from an isolated optimisation with left-right symmetry. This isolated optimisation followed the CFD-based approach developed and presented by Tejero et al.[16].

- There is a notable difference in the top aero-line between the installed and the isolated cases due to the intersection nacelle/pylon. However, the aerodynamics in this aero-line in installed configuration is quite constrained with a strong shock around the 20% of the nacelle length (Figure 4.28). Therefore, small benefit is obtained by including the top line in the design process in comparison with the increase in the computational overhead.

- In this installed design method, it is intended to consider the aerodynamic performance of the installed nacelle at windmillng diversion (Table 4.2). Windmilling diversion condition is characterized by a very low MFCR and the initial forebody radius at the nacelle leading edge (r_{if}) becomes the key parameter to control flow separation over the nacelle forebody. As the nacelle design used as baseline is optimised in isolation considering the diversion conditions, r_{if} is kept constant as per this reference design in every aero-line. This is expected to enable acceptable aerodynamics at windmilling diversion conditions.

- Fixed intake offset and scarf angle ($\theta_{scarf} = 5°$) are considered to improve the aerodynamic performance of the nacelle at incidence[182].

- Overall, the design method proposed considers 9 design variables. Although the reduction in the dimensionality from the full geometry parameterisation is considerable, it is still a challenging design space.

TABLE 4.5: Design variables for the installed nacelle design method.

Aero-line	Parameters	Considered?	Reasoning
$\Psi = 0°$	r_{if},r_{max},f_{max},β_{nac}	No	Aerodynamics very constraint due to the intersection with the pylon.
$\Psi = 180°,\ 225°,\ 270°,\ 315°$	r_{if},r_{max},f_{max},β_{nac}	No	Similar aerodynamics to the isolated configuration.
$\Psi = 45°,\ 90°,\ 135°$	r_{if}	No	Fixed to the baseline to maintain acceptable performance at diversion.
$\Psi = 45°,\ 90°,\ 135°$	r_{max},f_{max},β_{nac}	Yes	Higher impact of installation on the aerodynamics.

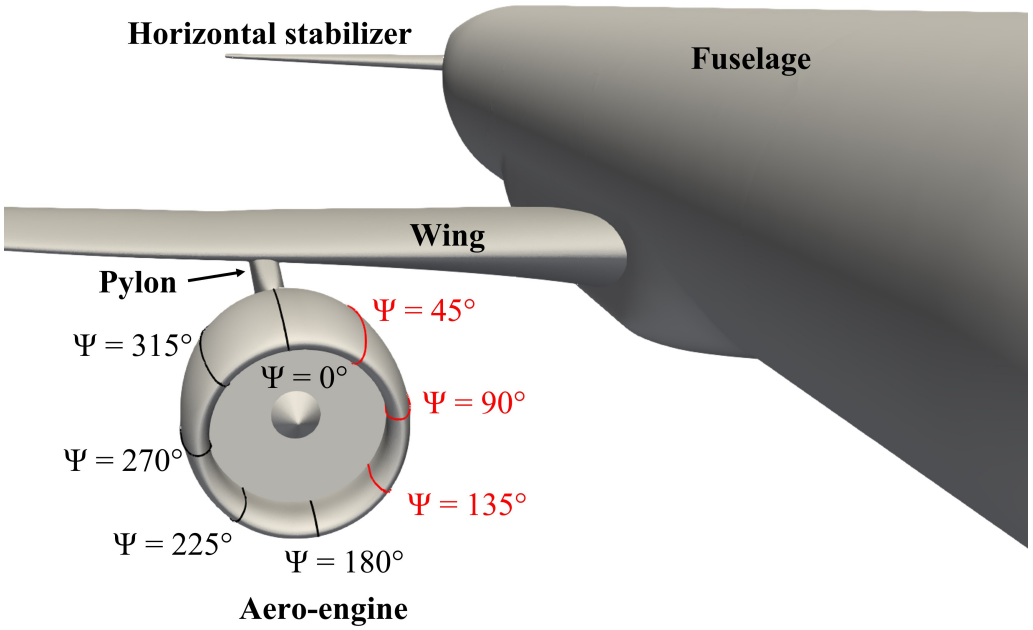

(A) Azimuthal aero-lines selected.

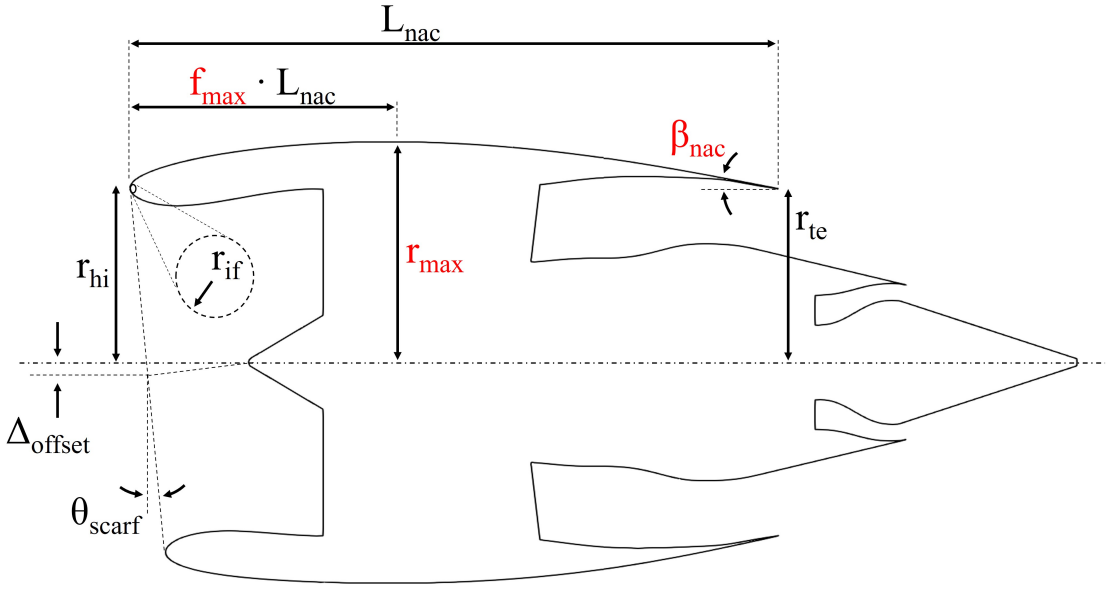

(B) Geometric parameters per aero-line selected.

FIGURE 4.27: Installed nacelle parameterisation. Design variables selected for nacelle design and optimisation marked in red.

The full aero-engine configuration is generated by combining the nacelle design with a representative intake[213] and separate jet exhaust[187] which have been designed to alleviate adverse flow features across the investigated design space. Additionally, no

hard-points are considered for any of the 9 selected design variables in this design and optimisation problem. Although the methodology is applicable for any installation position, the design work of this project is for an expected installation position for future civil aero-engines: $dx/C_{wing}^{inst} = 0$ and $dz/C_{wing}^{inst} = 0.1$ (Section 4.1.2, Figure 4.4).

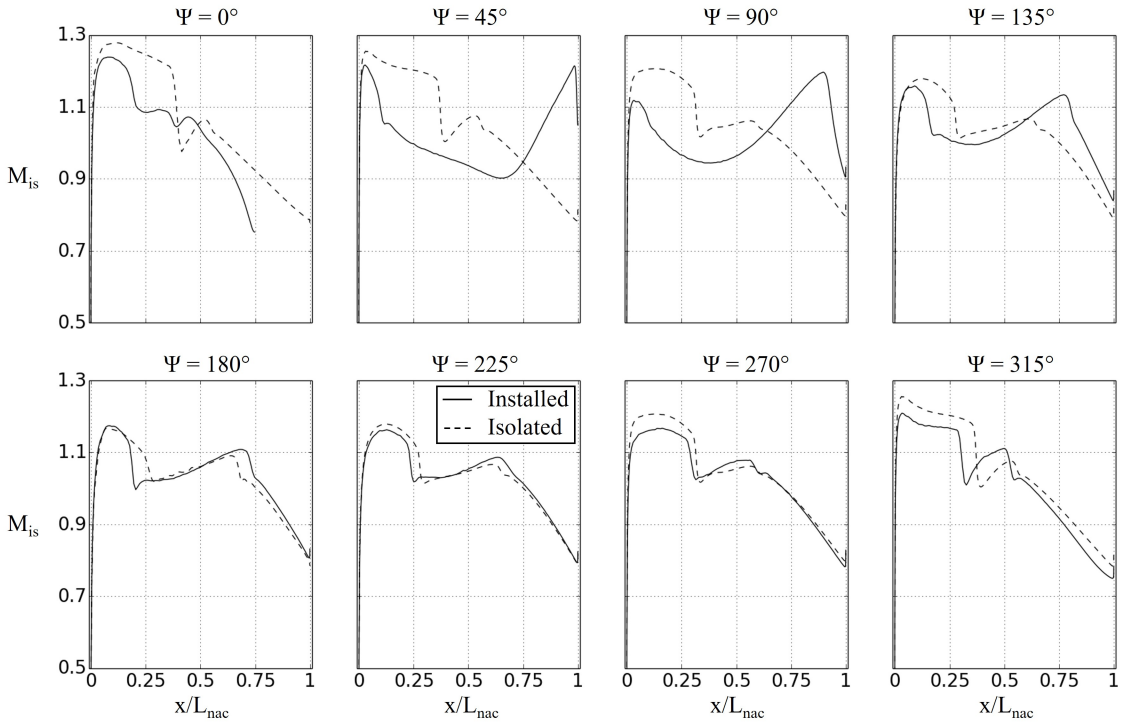

FIGURE 4.28: Comparison of isentropic Mach number (M_{is}) distributions between isolated and installed configuration for the different aero-lines.

The optimisation method is based on a surrogate-based approach (Figure 4.24b). CFD data sets of different fidelities and $N_{samples}/N_{DOF}$ ratios are used not only to train the surrogate model that leads the optimisation process but also to understand the design space for installed nacelles as mentioned in Section 4.5.1. The optimisation follows a single-objective approach that is focused on maximising the NVF at the cruise condition (Table 4.2). The OMOPSO algorithm is used due to its low variability in the convergence to the optimal part of the design space for transonic and non-linear aerodynamic problems (Section 4.5.2.1). The computational cost of this surrogate-based optimisation is very low due to the almost instantaneous interrogation time of the surrogate models. In order to ensure convergence of the optimisation, the first generation uses a sample ratio of $N_{gen=0}/N_{DOF} = 100$ to explore the design space and 100 more generations with a sample ratio per generation of $N_{gen,i}/N_{DOF} = 25$ are configured. The one-dimensional HV index is used to assess

the convergence with a change smaller than 1% in the last 3 generations. The optimal design with the highest NVF benefit relative to the baseline is evaluated using the high-fidelity RANS CFD model both at the cruise and at windmilling diversion conditions. A maximum threshold in the flow separation at diversion of $0.1L_{nac}$ is permitted. This is an estimate used in previous works for isolated nacelle design to avoid gross flow separation.

4.6 Surrogate modelling techniques

A surrogate model or Response Surface Model (RSM) is an approximation of more complex and higher order models that provide a quick prediction as accurate as possible. Once a surrogate models is constructed using a training data set, it can be used to interpolate and obtain the performance of a design which was not considered in the training samples. Surrogate models can be broadly divided into single-fidelity (SF) and multi-fidelity (MF) models depending on the sources of data used in the training process. In this project both types are considered. As SF methods, Gaussian Process Regression and Artificial Neural Networks (ANN) are used (Section 4.6.1). Additionally, two MF methods are used which are Variable Complexity Models (VCM) and Multi-Fidelity Neural Networks (MFNN) (Section 4.6.2).

4.6.1 Single-fidelity approaches

SF surrogate models just consider one fidelity of data and therefore are normally easier to build. Although these methods might be sometimes limited in accuracy to predict absolute values (depending on the fidelity used), they may acceptably capture the gradients in the design space. In most of the cases this is enough from an optimisation standpoint.

4.6.1.1 Gaussian Process Regression

The Gaussian Process Regression (GPR) technique used in this project was implemented by Hueso-Rebassa[215]. This GPR method, commonly known as Kriging, approximates the target function $y(x)$ through the linear combination of a regression ($\mu(x)$) and a correlation ($z(x)$) function[163] (Equation 4.43). $\hat{y}(x)$ represents the approximation of the target function. The regression function comes from a

set of p polynomials of order $0 \leq p \leq 2$ linearly combined[237] (Equation 4.44). $\beta = (\beta_0, ..., \beta_k, ..., \beta_p)$ are the polynomials coefficients. The correlation function has the form of a stochastic process of Gaussian distributions with zero mean and standard deviation σ[237] (Equation 4.45). Different one-dimensional correlations which are a function of the relative position of a certain point x with respect to the remainder data set N are combined using γ_i weighting coefficients. The correlation matrices are represented by R_j which have dimension of NxN. R_j depends on the distance between two data sets points w and x denoted by $w_{ij} - x_{ij}$ and a correlation parameter between the input samples (θ). $r\left(\theta, (w_{ij} - x_j)\right)$ is a vector of size $Nx1$ that considers the distances of the target point x with respect to the remainder input points. The self-correlation in the correlation matrix is represented by ones in the diagonal. This forces the model to pass through the input training samples which may cause overfitting[158]. To overcome this challenge, a controlled uncertainty parameter called nugget (ϵ) is introduced to the diagonal of the correlation matrix. This allows the kriging model to float around the training samples. There are different correlation functions that can be used. In this project four are considered: linear, cubic, absolute exponential and squared exponential (Table 4.6).

$$\hat{y}(x) = \mu(x) + z(x) \tag{4.43}$$

$$\mu(x) = \sum_{k=0}^{p} \beta_k f_k(x) \tag{4.44}$$

$$z(x) = \sum_{i=1}^{N} \gamma_i \prod_{j=1}^{dim} f(R_j\left(\theta, (w_{ij} - x_{ij})\right), r(\theta, (w_{ij} - x_j)) \tag{4.45}$$

TABLE 4.6: Correlation functions considered for the Gaussian Process Regression single-fidelity surrogate technique.

	$R_j\left(\theta, w_j, x_j\right)$
Absolute exponential	$e^{-\theta\lvert w_j - x_j\rvert}$
Squared exponential	$e^{-\theta(w_j - x_j)^2}$
Cubic	$1 - 3\varepsilon^2 + 2\varepsilon^3,\ \varepsilon = min(1, \theta\lvert w_j - x_j\rvert)$
Linear	$max(0, 1 - \theta\lvert w_j - x_j\rvert)$

The training of a Kriging model consists on adjusting the different hyperparameters previously introduced: β_k, γ_i and θ. This is addressed through the minimisation of a

logarithmic likelihood function[237,238]. The nugget parameter and the regression and correlation functions are specified by the user. The best combination is normally problem dependant. In this project a full factorial combination is used to find the best performing model.

4.6.1.2 Artificial Neural Networks

Artificial Neural Network (ANN) is a machine learning technique that is suitable for complex aerodynamic problems due to the ability to handle non-linear and discontinuous data and a high number of design variables[154–156]. In this project, the implementation of the method was conducted as a collaborative effort with colleagues at Cranfield University. The elemental processing unit in a ANN is called neuron. These neurons are organised in different layers to create an ANN (Figure 4.29a). The first and last layers are the input and output layers, respectively. In between of these a variable number of hidden layers are present which depend on the complexity of the problem to model[157] (Figure 4.29a).

There are two types of ANN depending on the way the information is managed. While in a feed-forward network the signal goes from the input to the output layer, a recurrent network allows for a back-flow of the information. Although recurrent networks can lead to models with better performances, the current learning algorithms for this type of ANN are less powerful and efficient. In this work feed-forward ANN are used. In the ANN model, a certain neuron k is connected to every j neuron in the previous layer[239]. This can be mathematically modelled with weighting coefficients w_{kj} between every pair of neurons in different layers[239] (Figure 4.29b). Moreover, a constant bias b_k is added to the neuron which helps to improve the modelling capability of the ANN[239] (Equation 4.46). An activation function φ is applied to the full weighted input of the neuron k to limit the amplitude of the output and enhance the training process[239] (Figure 4.29b) (Equation 4.47). The choice of the activation function has a notable impact on the performance of the ANN as it determines the type of predictions that the model can make[240]. This choice is highly problem dependant and an initial assessment has to be done for each case. Some of the most used activation functions are the Rectified Linear unit (ReLu), the sigmoid function and the hyperbolic tangent function (Table 4.7). The process of learning for an ANN is based on finding the combination of weights and biases that minimises a cost function. Different cost functions like mean squared error (MSE), root mean squared error (RMSE) or mean absolute error (MAE) can be used depending on the application. RMSE is used in the present work both in its

relative and absolute format (Equation 4.48). A gradient descent algorithm is used to minimise the cost function. The Adaptive Moment (ADAM) optimizer is used in the present work due to the ability to handle large data sets and parameters, the computational efficiency and the fast convergence[241].

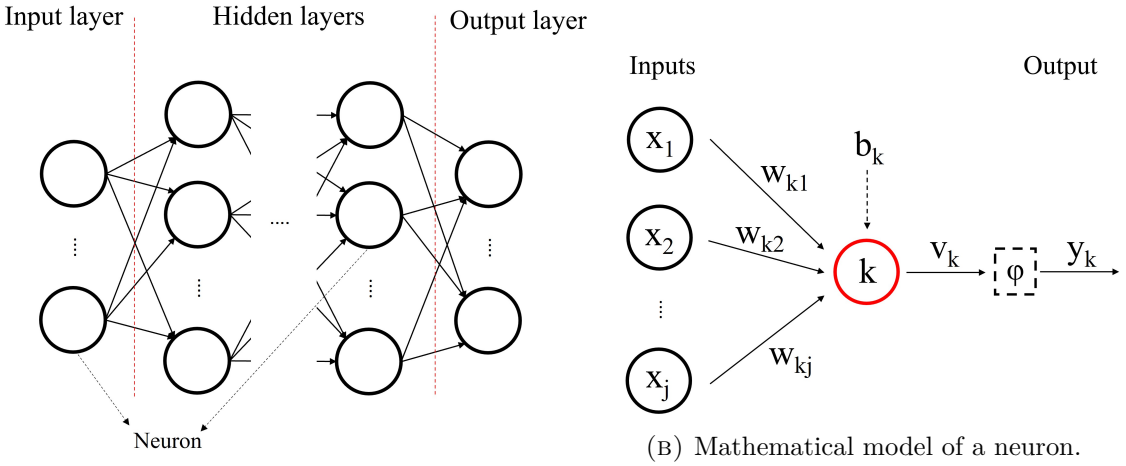

(A) Architecture of an artificial neural network.

(B) Mathematical model of a neuron.

FIGURE 4.29: Artificial neural network model.

$$v_k = \sum_j w_{kj} x_j + b_k \tag{4.46}$$

$$y_k = \varphi(v_k) \tag{4.47}$$

$$RMSE_{rel} = \sqrt{\frac{1}{n}\sum_{i=1}^{n}\left(\frac{y - \hat{y}_{ANN}}{y}\right)^2}, \quad RMSE_{abs} = \sqrt{\frac{1}{n}\sum_{i=1}^{n}\left(y - \hat{y}_{ANN}\right)^2} \tag{4.48}$$

TABLE 4.7: Activation functions considered for the ANN single-fidelity surrogate technique.

$\varphi(v_k)$	
ReLu	$max(0, v_k)$
Sigmoid	$(1 + e^{-v_k})^{-1}$
Hyperbolic tangent	$tanh(v_k)$

Special care is needed to avoid overfitting with ANN models. This can happen for different reasons: the data set is not large enough, the architecture of the ANN is oversized in terms of hidden layers and neurons or the training process was composed of too many back-propagation iterations[242]. Overfitted models are not able to generalise to different data sets than the training one. One approach to overcome this challenge from a modelling point of view is to include L2 norm regularization factors[157]. These constitute extra hyperparameters to train.

4.6.2 Multi-fidelity approaches

Multi-fidelity (MF) techniques for surrogate modelling are based on the idea that the low-fidelity (LF) data is used to estimate the trends in the design space while the high-fidelity (HF) information corrects these predictions and approximates better to the absolute values. This provides not only an improvement in the modelling accuracy but also a reduction in the overall cost as fewer high-fidelity samples might be needed.

4.6.2.1 Variable Complexity Models

The implementation of the Variable Complexity Model (VCM) approach that is used in this project was carried out by Hueso-Rebassa[215]. In a VCM method the prediction of the surrogate model comes from the combination of the low-fidelity prediction and a correction term[167]. In the correction term both the low- and high-fidelity are included. There are two types of VCM methods depending on the way that the correction term is constructed. In the incremental VCM[168] (VCM_{inc}) approach the multi-fidelity prediction is obtained by the summation of the low-fidelity prediction ($RSM_{LF}(x)$) and the incremental correction term ($\beta(x)$) (Equation 4.49). $\beta(x)$ constitutes a RSM that is built by the difference between the high- and low-fidelity data sets (Equation 4.50). In a similar manner, the ratio between the high- and low-fidelity data can be used to construct the scaling correction term ($\sigma(x)$) (Equation 4.52). This approach is called scaling VCM[169] (VCM_{sc}) and the multi-fidelity prediction is obtained through the product of the low-fidelity prediction times the correction (Equation 4.51). Depending on the problem, either the scaling or the incremental approach may be more suitable. For applications with very strong non-linear correlation between the low- and high-fidelity models the scaling method might work better. However, for those problems with zero or low values of

the low-fidelity data the scaling approach might cause error amplification and the incremental method may be more appropriate[167]. Due to this reason, the incremental approach is used in this project.

$$VCM_{inc}(x) = RSM_{LF}(x) + \beta(x) \tag{4.49}$$

$$\beta(x) = RSM_{corr}(HF - LF) \tag{4.50}$$

$$VCM_{sc}(x) = RSM_{LF}(x)\sigma(x) \tag{4.51}$$

$$\sigma(x) = RSM_{corr}(\frac{HF}{LF}) \tag{4.52}$$

The surrogate models for the low-fidelity (RSM_{LF}) and correction term (RSM_{corr}) are trained with the number of low- and high-fidelity samples respectively. Different single-fidelity techniques can be used for each model which are trained independently. In this project Kriging interpolation is used for both. The training process is as detailed in Section 4.6.1.1. The combination of RSM_{LF} and RSM_{corr} that provides the best prediction performance for the resulting VCM_{inc} is selected.

4.6.2.2 Multi-Fidelity Neural Networks

The Multi-Fidelity Neural Networks (MFNN) technique is an expansion of the single-fidelity ANN method presented in Section 4.6.1.2. In a MFNN two different ANN are combined[176] (Figure 4.30). Firstly, an ANN is trained using the low-fidelity data ($LF - ANN$) to approximate the design space gradients. Secondly, an additional ANN composed of two sub-networks is fitted to capture the linear ($HF - ANN_{linear}$) and non-linear ($HF - ANN_{non-linear}$) correlation between the low- and high-fidelity models (Figure 4.30). This ANN is trained using the high-fidelity data set and the predicted output from the low-fidelity ANN for this data set. Only one hidden layer and a linear activation function is used for the high-fidelity linear sub-network. The final output of the MFNN constitutes the prediction of the multi-fidelity model.

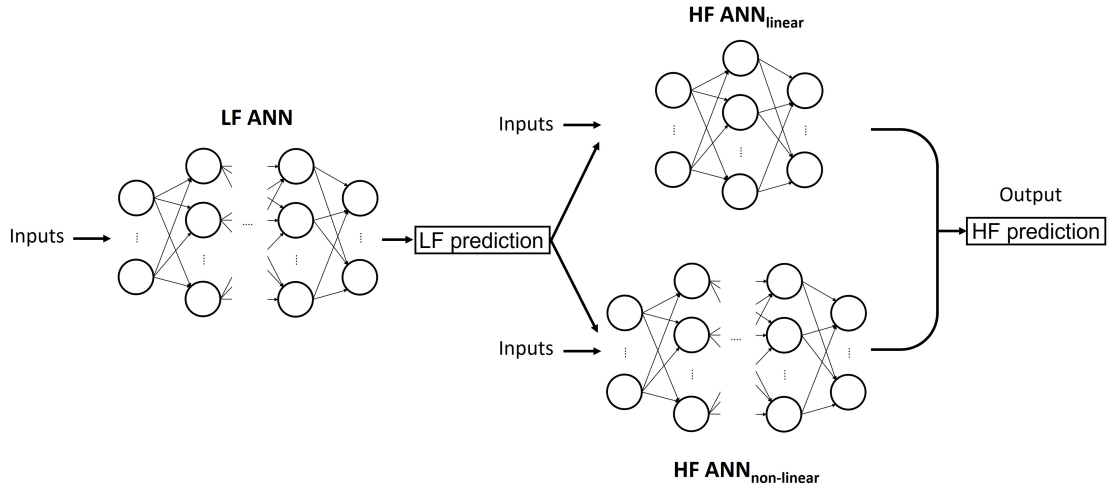

FIGURE 4.30: Multi-fidelity neural network architecture.

4.6.3 Verification of surrogate models

There are two type of verifications needed for each surrogate modelling technique. One is at programming level to test the implementation of the code. This is normally based on different benchmark functions. For the surrogate modelling methods used in this project, the MF techniques are extensions of the SF ones. The coding of both MF techniques used here were carefully verified. The VCM method was thoroughly verified by Hueso-Rebassa[215] using not only one-dimensional and multi-dimensional test functions but also aerodynamic data for non-axisymmetric exhausts systems. The MFNN technique was developed and implemented for nacelle aerodynamic design as part of this work. The implementation was assessed using 2 one-dimensional and 2 multi-dimensional test functions with both linear and non-linear correlation between the high- and low-fidelities. The verification was successful for every case with a 2σ uncertainty of the prediction relative to the analytical function lower than 10% for every case. 10% is the maximum threshold accepted for low-order model uncertainties in preliminary design stages[184,243]. More details of the MFNN verification can be found in Appendix D.

Additionally, every surrogate model generated with aerodynamic data regardless of the fidelity or technique is verified at the level of the predicting performances. For this purpose, an independent validation data set is available. This allows to cross-correlate the CFD results with the model prediction for each design within the validation data set. The RMSE (Equation 4.48) is used as a global parameter to quantify the deviations in the prediction of the surrogate model. This verification

process helps to identify overfitted models which are not able to generalise to different data sets than the training one.

CHAPTER 5

Assessment of CFD methods for isolated nacelle aerodynamics

The Horizon 2020 Advance Nacelle Aerodynamic Optimisation (ANACO) project was a collaboration between Cranfield University (CU) and the Aircraft Research Association (ARA). The research of this thesis was conducted as part of the ANACO project. Under ANACO, an extensive experimental and computational investigation of nacelle drag and aerodynamics was conducted. For a long-range application ($M = 0.85$), both a compact and a conventional isolated nacelle designs were tested.

Within ANACO parts of the verification and validation of the CFD methods used in this research were conducted in collaboration with colleagues at CU and ARA. Some of the key aspects from these studies are pertinent to this research and are briefly presented here for completeness. The work done by others is clearly acknowledged and referenced. Specific research undertaken by the author as part of this thesis are also clearly identified.

- The CFD-based design work[51,182,185,244] and down selection[245] of the ANACO compact and ANACO conventional nacelles was done by Tejero et al. at CU. Section 5.1 gives an overview of the down selection criteria for these designs.
- Section 5.2 provides a description of the experiments that covers the range of operating conditions tested and the different measurement techniques used and the instrumentation required. The experimental measurements were conducted by ARA.
- Section 5.3 provides an overview of the assessment of the steady computational methods for the cruise-type of conditions and the sensitivities to key flow

parameters. This was done primarily by Tejero[246] with some contributions from the author of this thesis on grid independence studies and data processing and analysis.

- Finally, Section 5.4 shows the assessment of steady and unsteady CFD methods for two off-design operating conditions: windmilling end-of-runway and windmilling diversion. This work was specifically conducted as part of this research project.

5.1 Nacelle design down selection

In previous work within the ANACO project, two nacelle designs were down selected from an isolated multi-point optimisation process by Tejero[245]. These nacelles are important parts for this research and therefore a description of the down selection is included. The nacelles are representative of a conventional configuration with a nacelle length of $L_{nac}/r_{hi} = 3.6$ and a compact architecture that is expected for future civil aero-engines with $L_{nac}/r_{hi} = 3.1$. Hereinafter, they will be referred as ANACO conventional and ANACO compact respectively. Both nacelle configurations have the same trailing edge radius of $r_{te}/r_{hi} = 0.95$ which was limited by the maximum mass flow capacity of the test rig (Section 4.1.3). Throughout the optimisation process different flight conditions that may be encountered in the flight envelope were considered. The main objective was to ensure aerodynamic robustness of the down selected configurations. In addition to the cruise segment, the windmilling off-design conditions for cruise engine-out, diversion and end-of-runway were used (Table 4.1). The final down selection was based on the minimum achievable cruise drag that met the following additional off-design requirements:

- Fully attached flow at windmilling end-of-runway condition ($M = 0.25$, $MFCR = 0.32$, $\alpha_{eng} = 20°$, Re= 10x10^6) (Table 4.1).
- Flow separation lower than $0.1L_{nac}$ evaluated across the 5 different azimuthal aero-lines of the nacelle (Figure 4.3b) at windmilling cruise engine-out ($M = 0.85$, $MFCR = 0.35$, $\alpha_{eng} = 4.5°$, Re= 25x10^6) and windmilling diversion ($M = 0.65$, $MFCR = 0.33$, $\alpha_{eng} = 4.5°$, Re= 30x10^6) (Table 4.1).
- Drag rise Mach number above the cruise Mach number of $M = 0.85$ (Table 4.1).

5.2 Experimental description

The Aircraft Research Association (ARA) Z30 rig was recommissioned for this test campaign. The ANACO compact and ANACO conventional nacelles were integrated onto the Z30 rig and tested in the ARA 8x9ft (2.44x2.74m) transonic wind tunnel (Figure 5.1).

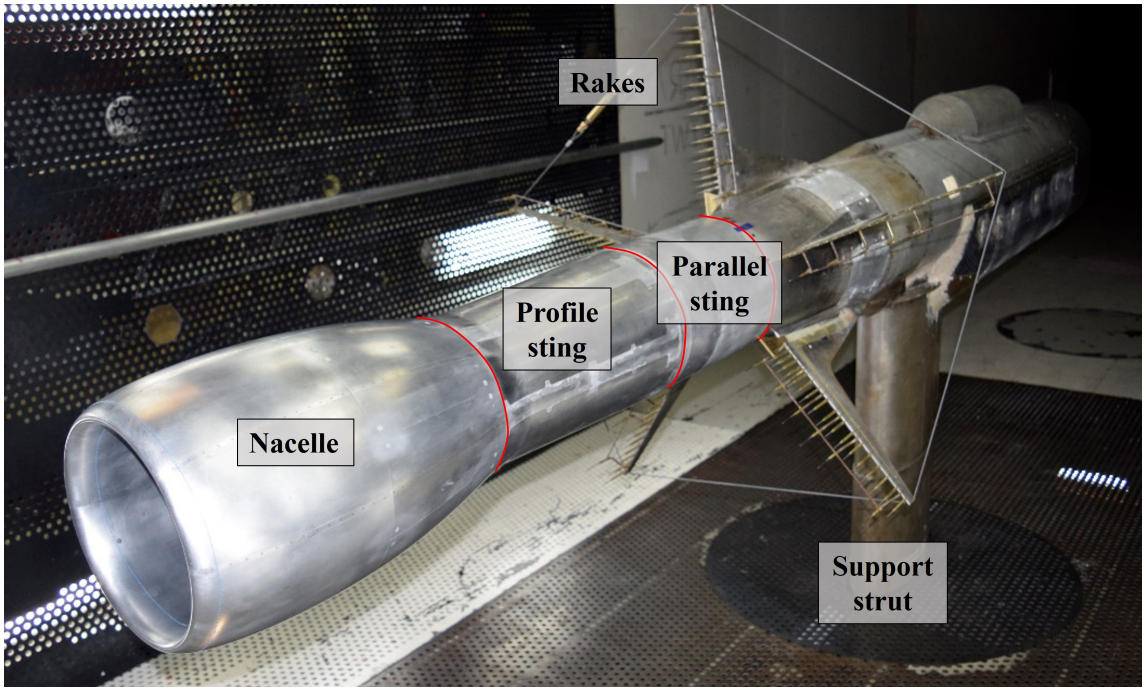

FIGURE 5.1: Nacelle installed in the Z30 rig in the ARA Transonic Wind Tunnel. Image courtesy of ARA.

5.2.1 Wind tunnel test matrix

A range of different operating conditions were measured which covered on-design and off-design points (Figure 5.2). The cruise segment was investigated by assessing the sensitivity to the main operating parameters: Mach number (M), MFCR and angle of attack (α_{eng}). It is important to highlight that the sensitivities to MFCR and α_{eng} were measured at a slightly lower Mach number from the cruise point ($M_{cruise} = 0.85$). The difference comes from the adjustments for the Mach number corrections that were applied after the experiments. This slightly lower Mach number is referred hereinafter as the nominal Mach number ($M_{nominal} = 0.84$) (Figure 5.2). The three off-design scenarios considered in the optimisation process (Section 5.1) were assessed: windmilling diversion, cruise engine-out and end-of-runway. For the end-of-runway condition, the experimental measurements covered a wide range

of incidences at fixed Mach number and MFCR. The focus was on capturing the hysteresis effect on flow separation as a function of the incidence α_{eng}. The hysteresis loop started from an attached flow condition and the incidence was sequentially increased until reaching flow separation followed by a continuous reduction in the incidence until the flow reattached. Due to budgetary constraints more conditions were assessed for the compact nacelle compared with the conventional configuration (Figure 5.2).

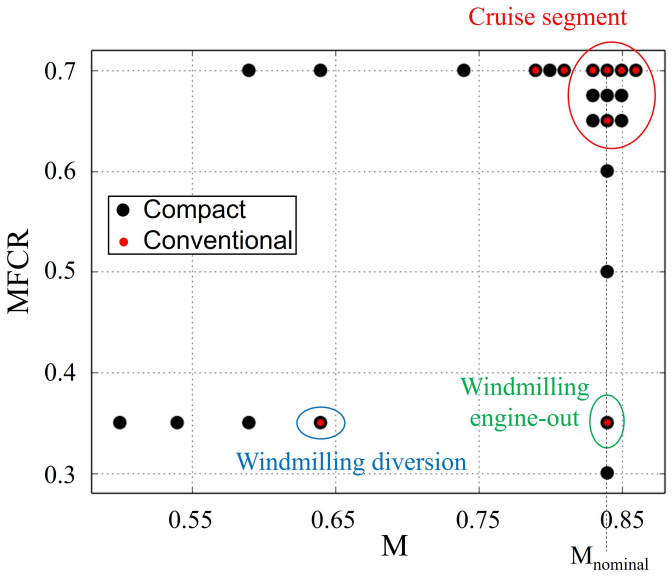

FIGURE 5.2: Coverage of experimental test points on the M - MFCR plane for the ANACO experimental campaign. While the black dots represent the operating points tested for the compact nacelle, the red dots denote the conditions measured for the conventional design. Fewer conditions were tested for the conventional nacelle due to budgetary constraints in the project.

5.2.2 Measurements and instrumentation

A range of measuring techniques were employed to obtain different type of data (Figure 5.3) depending on the nacelle design (Table 5.1). For this purpose, the nacelles were instrumented accordingly (Figure 5.4). Transition from laminar to turbulent boundary layer was forced using a strip on the nacelle surface at around 5% of the local nacelle length (Figure 5.4). This was confirmed through a sublimation test.

- **Pressure (or M_{is}) distributions**. Static pressure distributions were measured for both compact and conventional nacelles at every operating condition. For this purpose, the nacelles were instrumented with static pressure

taps along the 5 aero-lines used for the geometry parameterisation (Figure 5.4). On the top and top-control aero-lines ($\Psi = 0°, 45°$) a total of 26 taps were used (Table 5.1). The side aero-line ($\Psi = 90°$) was instrumented with 23 taps. Finally, 18 taps were distributed along the bottom-control and bottom aero-lines ($\Psi = 135°, 180°$). Additionally, a total of 10 and 4 static pressure taps were located on the top, side and bottom aero-lines of the profile sting and cylindrical sting respectively (Table 5.1).

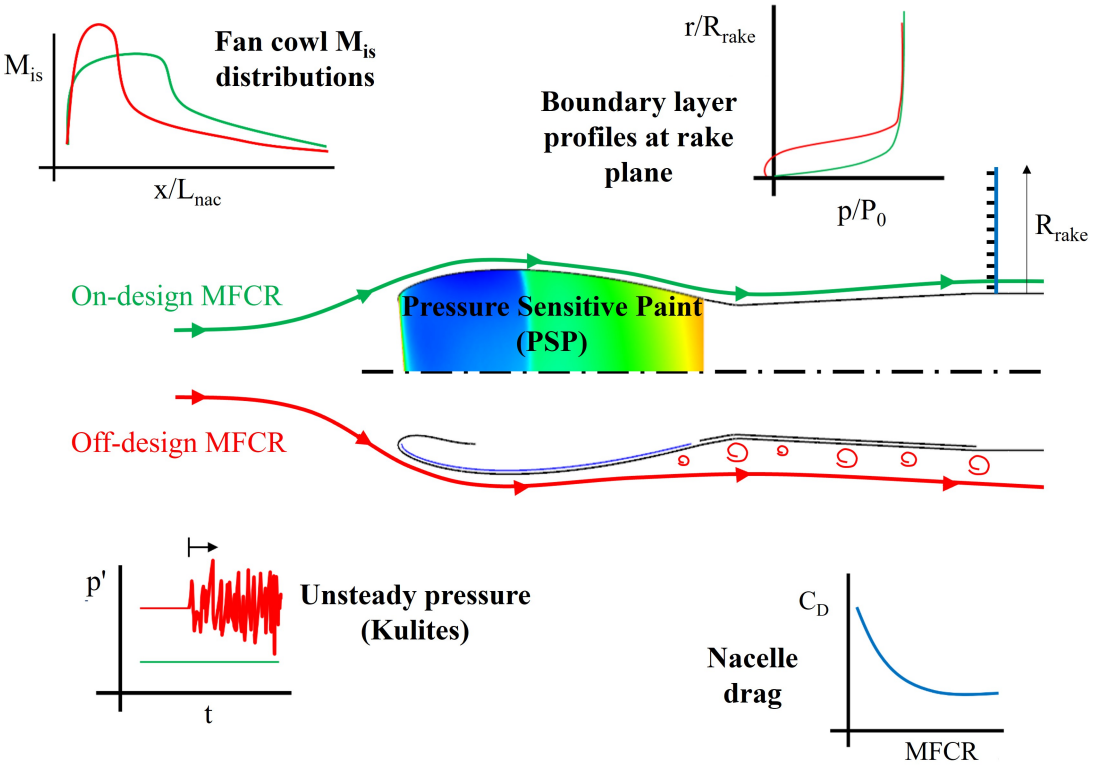

FIGURE 5.3: Schematic of the different types of data measured on the ANACO experimental campaign. Based on Schreiner[247].

- **Boundary layer profiles**. Distributions of total pressure were measured on the rakes of the Z30 rig for both nacelle configurations at every operating condition. Each of the five rakes were instrumented with 29 total pressure Pitot tubes with higher resolution near the wall (Table 5.1,Figure 5.3, Figure 5.4).

- **Nacelle drag**. Nacelle drag was obtained for both nacelle configurations using a wake method (Section 4.4.2). The instrumentation used to apply this farfield drag extraction method uses the total pressure measurements on the rakes previously explained: 5 rakes with 29 total pressure probes per rake arm.

However, the rakes were rotated twice to provide 15 azimuthal positions with a resolution of 24° (Figure 5.5). Additionally, the pressure taps on the profile sting and parallel stings were used to calculate the viscous sting corrections with the ARA Green's method as explained in Section 4.4.2. An uncertainty on the experimental drag measurements of 1.2% was provided by ARA[248].

TABLE 5.1: Summary of the instrumentation for the ANACO experimental campaign.

Measurement	Location	Quantity	Nacelles
Total pressure	Rakes	29 probes/rake	Comp. / Conv.
Static pressure	Rakes	6 probes/rake	Comp. / Conv.
	Nacelle	$\Psi = 0°$ (x26) $\Psi = 45°$ (x26) $\Psi = 90°$ (x23) $\Psi = 135°$ (x18) $\Psi = 180°$ (x18)	Comp. / Conv.
	Profile sting	$\Psi = 0°$ (x10) $\Psi = 90°$ (x10) $\Psi = 180°$ (x10)	Comp. / Conv.
	Cylindrical sting	$\Psi = 0°$ (x4) $\Psi = 90°$ (x4) $\Psi = 180°$ (x4)	Comp. / Conv.
Unsteady static pressure	Nacelle	$\Psi = 0°$ (x3) $\Psi = 45°$ (x1)	Comp.
Pressure Sensitive Paint	Nacelle	$\sim$ half nacelle with two cameras	Comp.

- **Unsteady static pressure**. The compact nacelle was instrumented with four Kulites which measured unsteady static pressure (Figure 5.4). In the top aero-line ($\Psi = 0°$) three Kulites where distributed at $x/L_{nac,top} = 0.32$, 0.38 and 0.42, where $L_{nac,top}$ is the nacelle length in the top aero-line (Figure 5.6). An additional Kulite was placed in the top-control aero-line ($\Psi = 45°$) at $x/L_{nac,top} = 0.42$. The data was recorded for around 4.6 seconds with a sampling frequency of about 40kHz.
- **Contours of static pressure**. The Pressure-Sensitive Paint (PSP) technique was used to measure surface static pressure (Figure 5.4). Using two cameras,

around half of the nacelle was visible which included the top, top-control and side aero-lines. This technique was used for the following operating conditions: cruise, increased Mach number at cruise, decreased MFCR at cruise and the off-design conditions windmilling diversion and cruise engine-out.

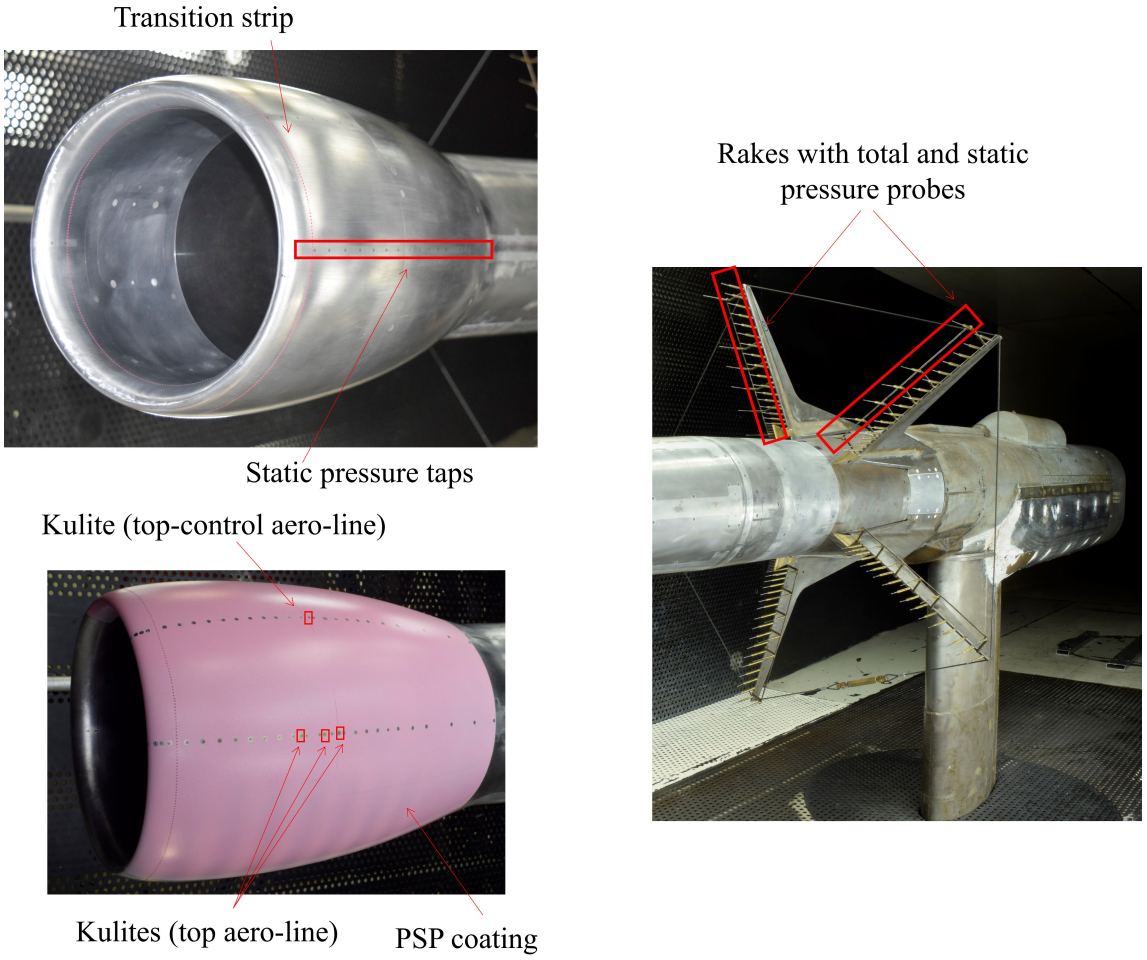

FIGURE 5.4: Instrumentation on the ANACO compact nacelle installed in the Z30 test rig for the ANACO experimental campaign. Images courtesy of ARA.

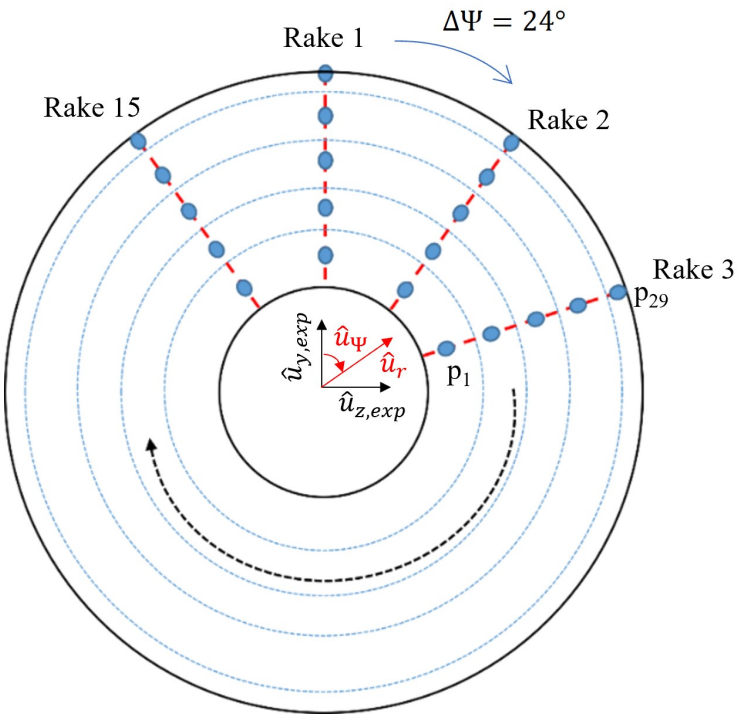

FIGURE 5.5: Radial ($\hat{u}_r$) and azimuthal ($\hat{u}_\Psi$) experimental discretisation of the rakes for the farfield drag calculation.

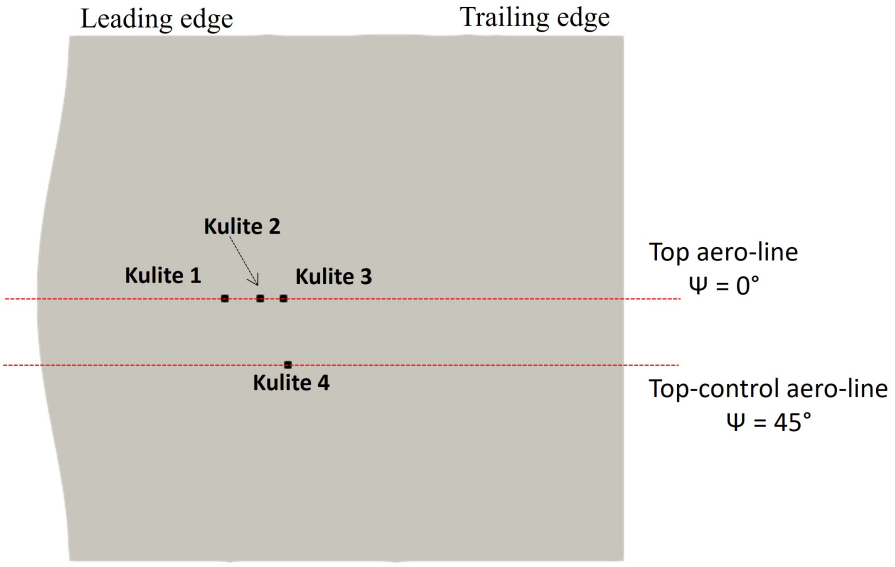

FIGURE 5.6: Location of the 4 Kulites on the ANACO compact nacelle for the ANACO experimental campaign. Nacelle surface represented in an unwrapped manner.

5.3 Nacelle aerodynamics in the cruise segment

The steady numerical methods for nacelle designs based on a RANS CFD model (Section 4.3.1.1.4) were validated using experimental data from this test campaign primarily by Tejero[246]. A brief overview of the results is presented in this section as it constitutes a building block for the unsteady CFD assessment in the next section. The assessment of these steady CFD methods covers both the compact and conventional nacelles that were down selected as presented in Section 5.1. For the validation, nacelle drag assessed using the farfield method explained in Section 4.4.2 is compared between RANS CFD and experiments. The comparison covered the sensitivity of drag to changes in the main aerodynamic parameters: Mach number, aero-engine MFCR and flow incidence. As an example, the results for the Mach number sensitivity at the cruise incidence and MFCR are discussed in this section (Figure 5.7). Across the range of Mach number investigated, the drag coefficient obtained from the CFD is on average within 2% of the experimental drag for both the compact and the conventional configurations. In particular, for the cruise point (M_{cruise}), there is an under prediction of the CFD drag relative to the experiments of about 0.2% and 0.8% for the compact and conventional configurations respectively (Figure 5.7). This is within the estimated experimental uncertainty of 1.2% for changes in the nacelle drag at these conditions[248]. The drag benefit of the compact nacelle relative to the conventional one estimated with the CFD and measured in the experiments if of 8.8% and 9.8% respectively. Overall, this shows that the CFD method used in the nacelle design approach is able to predict the majority of the drag benefits expected for compact nacelles of UHBPR civil aero-engine.

A key element in the drag calculation using the farfield approach is the total pressure measurements on the rakes. A systematic comparison of the CFD predictions and actual measurements for both nacelles at different azimuthal locations (Figure 5.5) was assessed for changes in Mach number, aero-engine MFCR and flow incidence[246]. As an illustrative example, this section shows the comparison for both nacelles at the $\Psi = 0°$ rake (Figure 5.5) (aligned with the nacelle top aero-line) for changes in the Mach number at the cruise $\text{MFCR}_{cruise} = 0.7$ and incidence $\alpha_{eng} = 4.5°$ (Figure 5.8). For the compact nacelle, there is a good agreement at every operating condition between CFD and experiments both in terms of the size and shape of the boundary layer (Figure 5.8b). For the conventional configuration, although the CFD has a slightly greater deficit compared to experiments there is an acceptable agreement (Figure 5.8b).

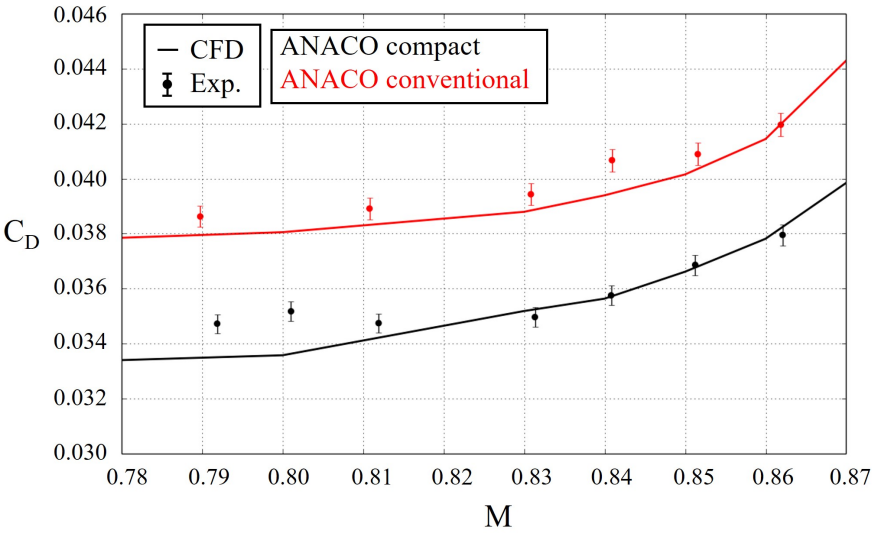

FIGURE 5.7: Comparison of the nacelle drag coefficient as a function of the Mach number at the fixed cruise $\text{MFCR}_{cruise} = 0.7$ and incidence $\alpha_{eng} = 4.5°$ between RANS CFD and experiments for the ANACO compact and ANACO conventional nacelles. Based on Tejero et al.[246].

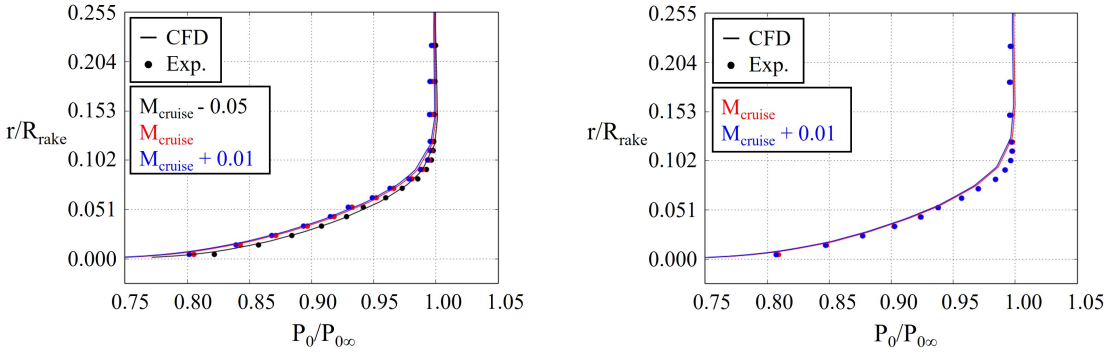

(A) ANACO compact nacelle.

(B) ANACO conventional nacelle.

FIGURE 5.8: Comparison of boundary layer profiles for rake arm aligned with the nacelle top aero-line between RANS CFD and experiments. Sensitivity to changes in the Mach number at the fixed cruise $\text{MFCR}_{cruise} = 0.7$ and incidence $\alpha_{eng} = 4.5°$. Based on Tejero et al.[246].

The aerodynamics of the nacelles across the different operating conditions of the flight envelope can vary substantially. For the validation work, a comparison of the isentropic Mach number (M_{is}) distributions at the different aero-lines of the compact and conventional nacelles was assessed for changes in the Mach number, MFCR and incidence[246]. For example, the sensitivity to changes in Mach number for the cruise incidence $\alpha_{eng} = 4.5°$ and $\text{MFCR}_{cruise} = 0.7$ (Figure 5.9a, Figure 5.9b) and also the sensitivity to changes in the MFCR at the nominal Mach number $M_{nominal} = 0.84$ and cruise incidence $\alpha_{eng} = 4.5°$ (Figure 5.9c, Figure 5.9d) are compared for both

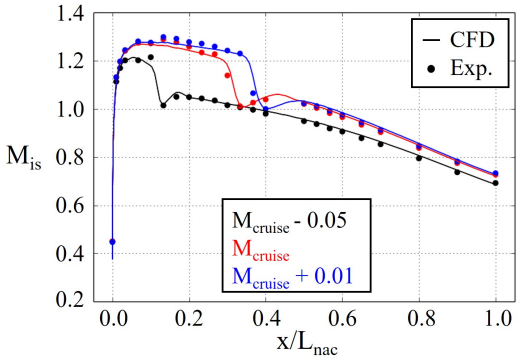

(A) ANACO compact nacelle, sensitivity to changes in Mach number at the cruise $\text{MFCR}_{cruise} = 0.7$ and incidence $\alpha_{eng} = 4.5°$.

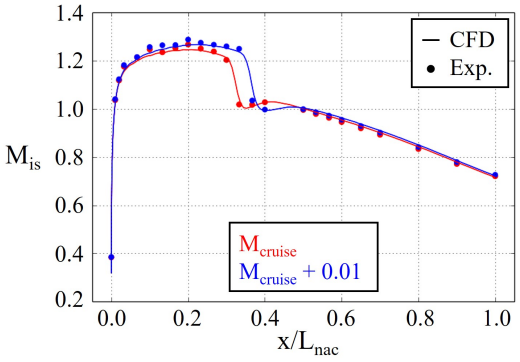

(B) ANACO conventional nacelle, sensitivity to changes in Mach number at the cruise $\text{MFCR}_{cruise} = 0.7$ and incidence $\alpha_{eng} = 4.5°$.

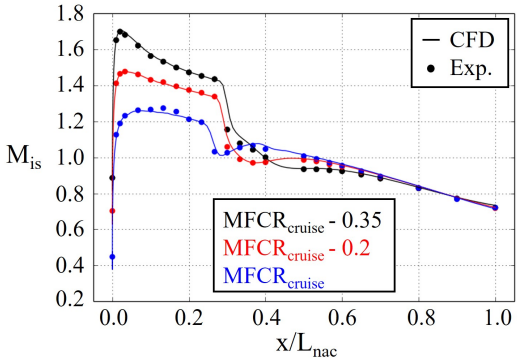

(C) ANACO compact nacelle, sensitivity to changes in MFCR at the nominal Mach number $M_{nominal} = 0.84$ and cruise incidence $\alpha_{eng} = 4.5°$.

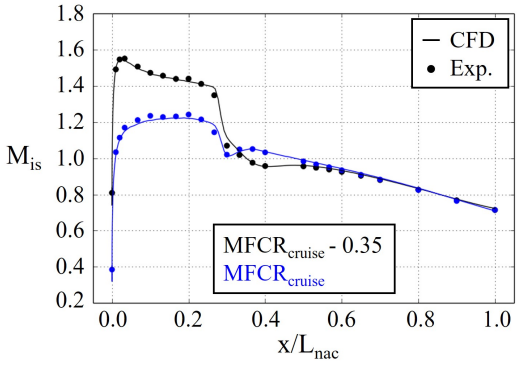

(D) ANACO conventional nacelle, sensitivity to changes in MFCR at the nominal Mach number $M_{nominal} = 0.84$ and cruise incidence $\alpha_{eng} = 4.5°$.

FIGURE 5.9: Comparison of M_{is} distributions along the top aero-line of the nacelle between RANS CFD and experiments. Based on Tejero et al.[246].

nacelles using the top aero-line. For every case, there is a very good agreement between CFD and experiments in terms of key flow features such us peak M_{is}, pre-shock M_{is}, shock location or flow diffusion in the afterbody of the nacelle. In the comparison for the changes in MFCR, the reduction from $\text{MFCR}_{cruise} = 0.7$ to 0.35 corresponds to the windmilling cruise engine-out operation. This is a challenging condition with a strong shock wave close the nacelle crest. Even for this condition the match between the RANS CFD prediction and the experiments for the pressure distribution is excellent (Figure 5.9c, Figure 5.9d).

5.4 Off-design nacelle aerodynamics

Two additional off-design conditions that were considered in the optimisation of the ANACO nacelles are windmilling diversion and end-of-runway. The assessment of the CFD methods for these conditions was undertaken as part of this research. As was explained in the down selection method in Section 5.1, for this off-design conditions the interest is primarily on the flow separation. The separation at the end-of-runway condition is governed by flow diffusion that normally is initiated in the afterbody of the nacelle due to the adverse pressure gradient. The nacelle reaches a fully separated flow condition (Figure 5.10). At the windmilling diversion condition the flow can separate due to shock-boundary layer interaction which triggers a variety of turbulent structures which are inherently unsteady (Figure 5.11). RANS-based CFD methods tends to have difficulties to predict meaningful results for complex and very unsteady separated flows. Therefore, in addition to steady RANS, two unsteady CFD methods are evaluated for the windmilling end-of-runway (Section 5.4.1) and windmilling diversion (Section 5.4.2) conditions: URANS and DDES. The main objective of this section is to compare the unsteady computational predictions with the RANS results and deliver recommendations for RANS-based nacelle optimisations. Due to the high computational effort of unsteady CFD calculations, this study is focused on just one nacelle. The ANACO compact nacelle is considered due to the high sensitivity of compact nacelle configurations to off-design flow conditions. This work within the ANACO project was fully conducted within this thesis.

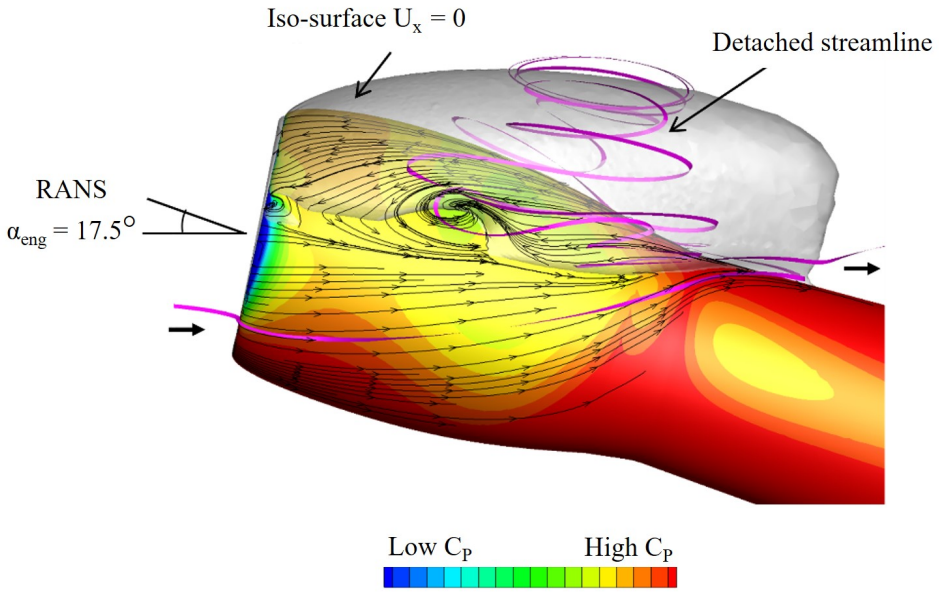

FIGURE 5.10: RANS prediction of the ANACO compact nacelle aerodynamics for the windmilling end-of-runway-type of condition at $\alpha_{eng}^{crit} = 17.5°$, M = 0.25 and MFCR = 0.32. Fully separated flow represented through contours of pressure coefficient, a detached streamline and iso-surface of axial velocity (V_x) equal to 0 that shows the approximate boundary of separated flow.

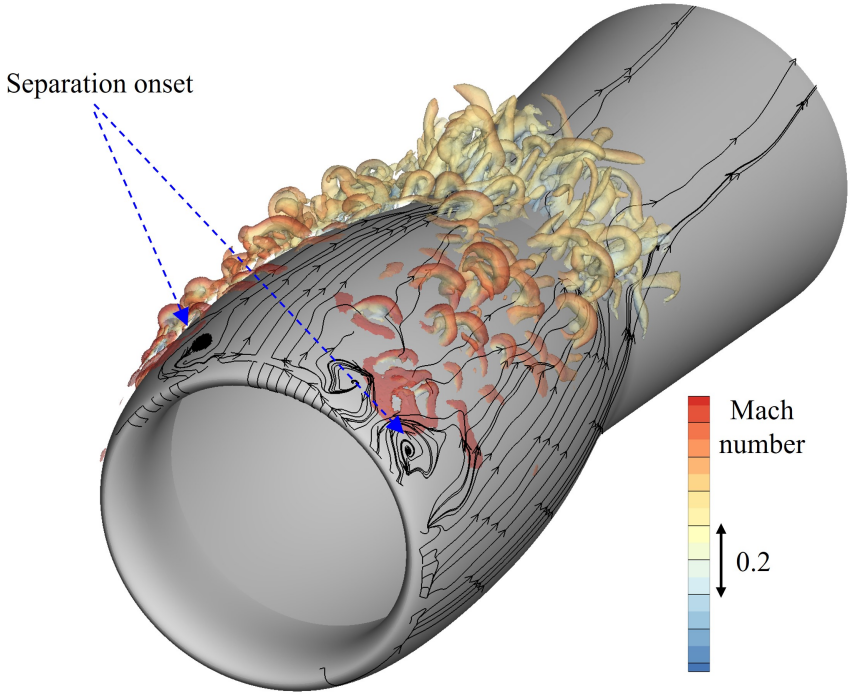

FIGURE 5.11: DDES prediction of the ANACO compact nacelle aerodynamics for the windmilling diversion condition (M = 0.65, MFCR = 0.33 and $\alpha_{eng} = 4.5°$). Surface streamlines are used to identify the onset of the flow separation and iso-surfaces of Q-criterion represent the turbulent structures that appear in the flow.

5.4.1 Windmilling end-of-runway condition

For the end-of-runway-type of conditions the key aspect from a nacelle design point of view is the critical incidence of flow separation (α_{eng}^{crit}). The nacelle design problem targets fully attached flow at this condition and therefore a proper identification of α_{eng}^{crit} is required. In the experimental campaign, no drag data was measured for the end-of-runway-type of conditions and therefore the $\alpha_{eng}^{Exp.\ crit}$ is assessed by the M_{is} distributions on the nacelle aero-lines through a sweep in the incidence α_{eng}. The peak M_{is} is used to identify this separation incidence (Figure 5.12). The starting incidence is 12° with a peak M_{is} of around 0.55. The incidence is increased in steps of $\Delta\alpha_{eng} = 1°$ until the flow separates at $\alpha_{eng}^{Exp.\ crit} = 16.0°$ (Figure 5.12). From $\alpha_{eng} = 15°$ to 16° the peak M_{is} decreases from around 0.63 to approximately 0.35 and the M_{is} distribution over the fan-cowl becomes substantially flat which is a clear signature of separated flow (Figure 5.13).

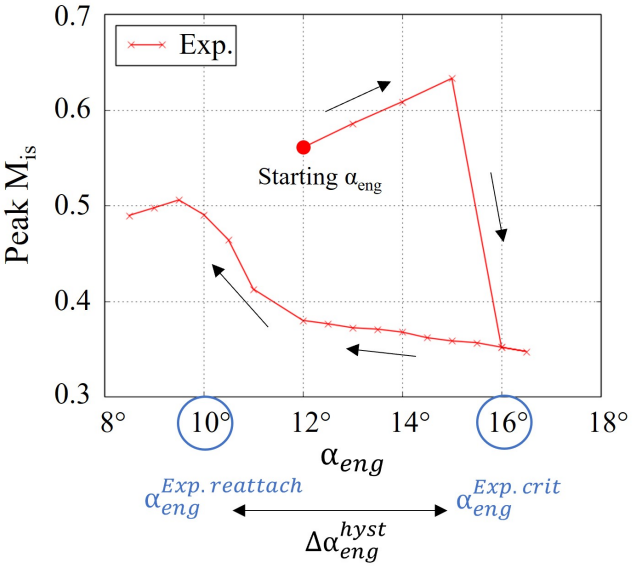

FIGURE 5.12: Experimental measurements of the peak M_{is} in the top aero-line ($\Psi = 0°$) as a function of the nacelle incidence α_{eng} for the ANACO compact nacelle at the end-of-runway-type of condition (M = 0.25 and MFCR = 0.32). Effect of increasing and decreasing the incidence.

For the computational methods, a similar approach is followed using the same α_{eng} and $\Delta\alpha_{eng}$ as per the experiments. Both RANS and URANS CFD models are considered. A comparison of the flow field through M_{is} distributions in the top aero-line between the experiments and the steady RANS model shows an excellent agreement for the pre-$\alpha_{eng}^{Exp.\ crit}$ incidences (Figure 5.13). In terms of the critical incidences for both computational models, $\alpha_{eng}^{RANS\ crit} = 17.5°$ and $\alpha_{eng}^{URANS\ crit} = 17.0°$ are identified for the RANS and URANS models respectively (Table 5.2).

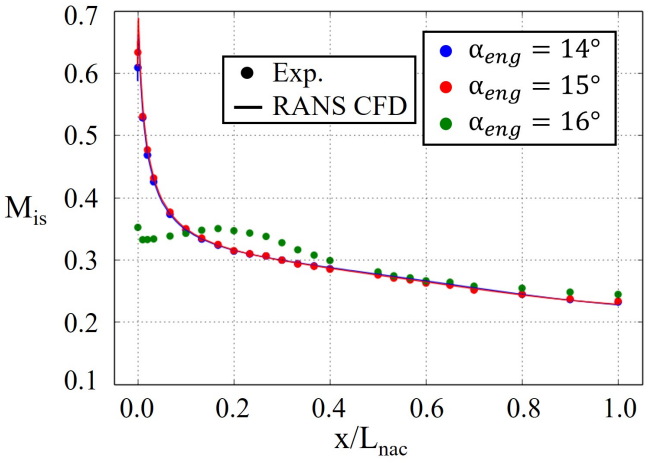

FIGURE 5.13: M_{is} distributions in the top aero-line ($\Psi = 0°$) of the ANACO compact nacelle at the end-of-runway-type of condition (M = 0.25 and MFCR = 0.32). Experimental measurements and RANS CFD predictions. The incidence is increased until flow separation at $\alpha_{eng}^{Exp.\ crit}$ (ramp-up).

Going one step further, the CFD results show a clear effect of hysteresis of nacelle drag coefficient for changes in the incidence (Figure 5.14). For both CFD methods the flow reattaches at $\alpha_{eng}^{reattach} = 13.5°$. This provides a hysteresis range $\Delta\alpha_{eng}^{hyst}$ of 4° and 3.5° for RANS and URANS respectively (Table 5.2). Consequently, there is no substantial benefit of URANS methods compared to steady RANS computations for the assessment of the key incidences at end-of-runway conditions. The experimental reattachment point was found at $\alpha_{eng}^{Exp.\ reattach} = 10°$ from the pressure distributions in the aero-lines (Table 5.2). This shows a large difference of 3.5° compared to the RANS-based numerical methods (Figure 5.14). The reason behind might be that the flow before the reattachment is fully separated and the RANS methods are not accurate for these cases. In contrast, the better agreement between experiments and the RANS-based methods for the critical incidence can be explained as the flow starts from an attached state. Therefore, for the assessment of the windmilling end-of-runway condition within a RANS-based optimisation point of view, the following recommendations are derived:

- Relative to RANS calculations, URANS do not provide substantial improvements in the accuracy for predicting the onset of flow separation and the reattachment.
- RANS-based methods predict the onset of separation at an angle of attack that is approximately 1.5° larger than the measurements. Therefore, it is recommended to use a margin of +1.5° in this operating condition for RANS-based optimisations. In terms of the reattachment point, although it is interesting

from a CFD validation point of view, it is of the secondary importance for the design and optimisation of compact aero-engine nacelles.

TABLE 5.2: Incidence of flow separation (α_{eng}^{crit}) and reattachment ($\alpha_{eng}^{reattach}$) and range of hysteresis ($\Delta\alpha_{eng}^{hyst}$) for the ANACO compact nacelle at the end-of-runway-type of condition (M = 0.25 and MFCR = 0.32). Comparison between RANS and URANS CFD predictions and experimental data.

	α_{eng}^{crit}	$\alpha_{eng}^{reattach}$	$\Delta\alpha_{eng}^{hyst}$
RANS	17.5°	13.5°	4.0°
URANS	17.0°	13.5°	3.5°
Experiments	16.0°	10.0°	6.0°

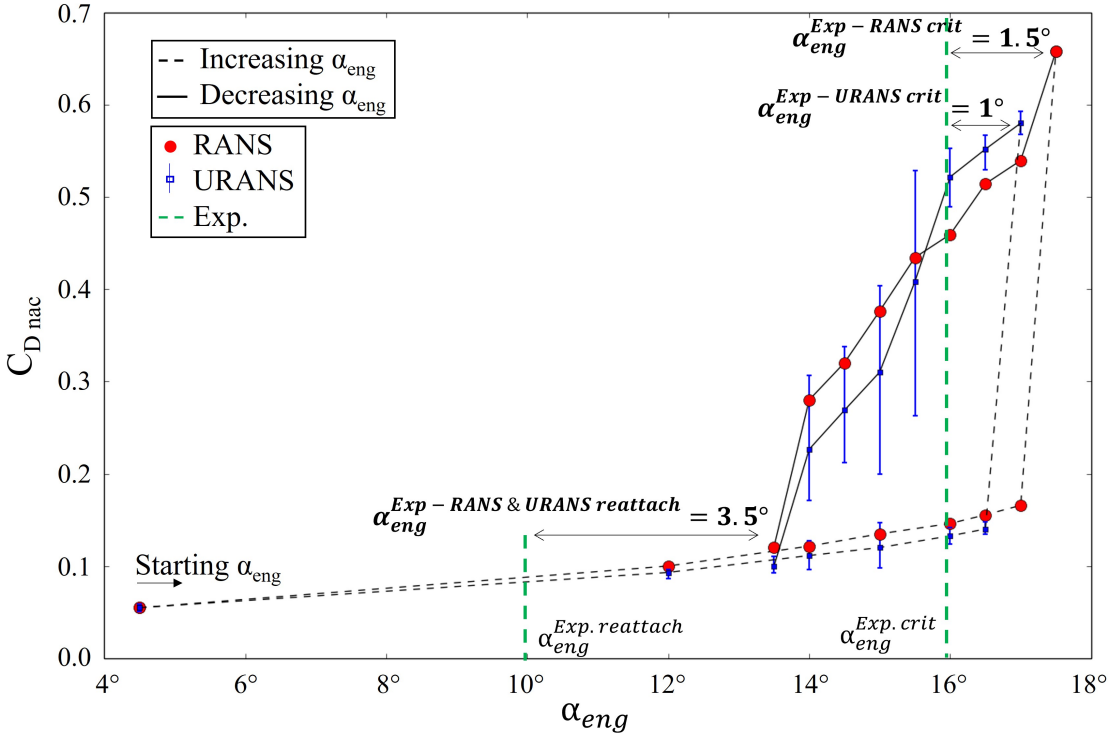

FIGURE 5.14: Nacelle drag coefficient ($C_{D\,nac}$) as a function of the nacelle incidence (α_{eng}) for the ANACO compact nacelle at the end-of-runway-type of condition (M = 0.25 and MFCR = 0.32). Effect of increasing and decreasing the incidence.

5.4.2 Windmilling diversion condition

Windmilling diversion is a challenging condition from a computational modelling point of view due to the combination of a low engine MFCR = 0.33 and a notable

Mach number M = 0.65. The high flow suction in the leading edge typically generates a strong shock wave that may trigger flow separation. The analysis in this section is focused on the ANACO compact nacelle. It is important to note that there is a difference in the operating condition between the experimental measurements and the actual windmilling diversion condition. The differences are due to the achieved operating condition during the experiments which, when adjusted for the Mach number corrections, were slightly different from the intended conditions. While the nominal condition is defined by a M = 0.65, MFCR = 0.33 and α_{eng} = 4.5° (Table 4.1), the experimental condition measured was M = 0.64, MFCR = 0.35 and α_{eng} = 4.5°. For this measured condition, the comparison of the M_{is} in the top aero-line between the experiments and the RANS CFD prediction shows a good agreement with similar values of peak M_{is}, pre-shock M_{is} and shock location (Figure 5.15).

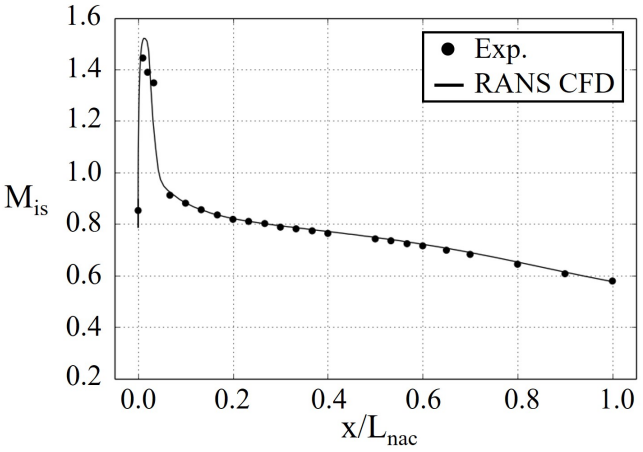

FIGURE 5.15: Comparison between experiments and RANS CFD prediction of the M_{is} distribution on the top aero-line of the ANACO compact nacelle for the windmilling diversion condition measured in the test campaign (M = 0.64, MFCR = 0.35 and α_{eng} = 4.5°).

However, as the nacelle aerodynamics at this kind of flight conditions normally exhibits flow separation, an eddy-resolving DDES CFD method is used to analyse this operating point. The DDES calculations were performed in advance of the experiments at the nominal windmilling diversion condition (M = 0.65, MFCR = 0.33 and α_{eng} = 4.5°). Although this makes the computational operating condition slightly more aggressive both in Mach and MFCR compared to the experimental measured condition (M = 0.64, MFCR = 0.35 and α_{eng} = 4.5°), these slight changes are not expected to significantly affect the key findings. To provide an further insight of the flow physics, the M_{is} distributions on the top and top-control aero-lines of the nacelle are compared between the different methods and type of data (Figure 5.16).

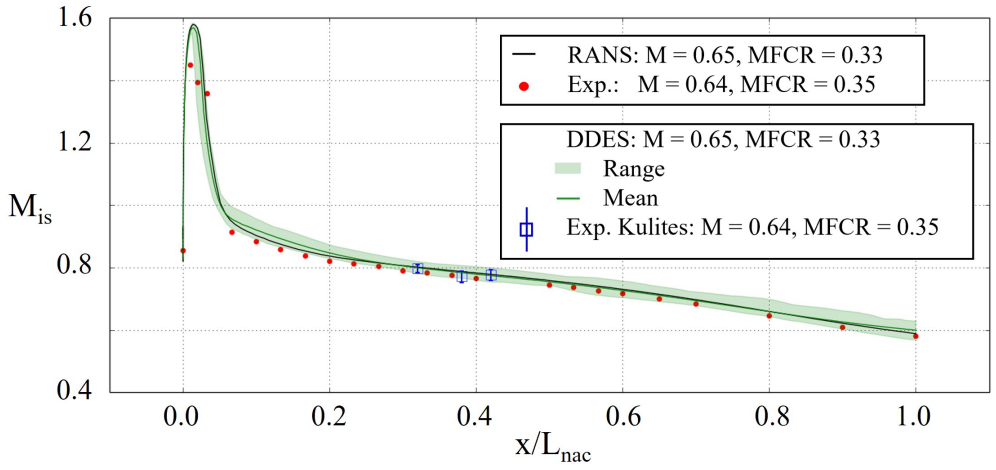

(A) Top aero-line ($\Psi = 0°$).

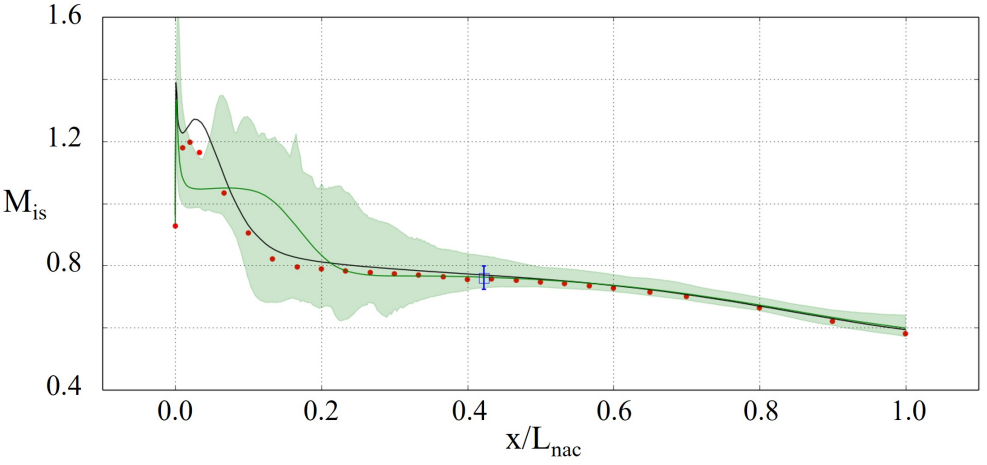

(B) Top-control aero-line ($\Psi = 45°$).

FIGURE 5.16: Comparison of isentropic Mach number (M_{is}) distributions on the top and top-control aero-lines between steady/unsteady experiments and computational methods. Windmilling diversion condition: M = 0.64, MFCR = 0.35 and $\alpha_{eng} = 4.5°$ in experiments and M = 0.65, MFCR = 0.33 and $\alpha_{eng} = 4.5°$ in CFD.

The steady data composed of RANS CFD and experimental pressure measurements show a good agreement albeit differences in the peak Mach number of around 0.1. This is mainly due to the slight change in the operating conditions and confirms that not a big impact in the conclusions is expected. The unsteady DDES distributions are represented with the mean value and the range of variability. Similarly, the mean value and variability range are used to show the experimental unsteadiness in M_{is} measured with the Kulites. In spite of the small differences in Mach number and MFCR between experiments and CFD, the variability of the Kulites is predicted by

the DDES CFD model in both aero-lines (Figure 5.16). For the top-control aero-line (Figure 5.16b) there is slightly greater variability in the DDES-predicted M_{is} compared to the top aero-line (Figure 5.16a), especially in the forebody. The reason may be related to the larger region of flow separation in the top-control line which travels downstream (Figure 5.17).

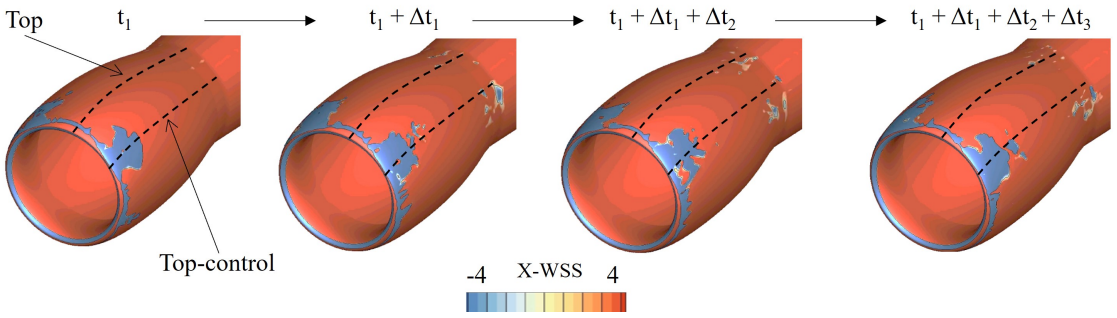

FIGURE 5.17: Snapshots of axial component of wall shear stress on the surface of the ANACO compact nacelle predicted using the DDES CFD model for the windmilling diversion condition (M = 0.65, MFCR = 0.33 and $\alpha_{eng} = 4.5°$).

The DDES CFD model is used as the highest CFD fidelity to deliver guidelines for windmilling diversion from a RANS-based optimisation point of view. The key parameter for this off-design condition is the aero-engine MFCR as it controls the flow suction in the nacelle leading edge and consequently the shock strength and the possible flow separation. In this respect, the sensitivity to the MFCR for windmilling diversion-type of conditions (M=0.65 and $\alpha_{eng} = 4.5°$) has been assessed using RANS and DDES models (Figure 5.18). For the isolated nacelle optimisation method and down selection criteria used in this project (Section 5.1) the diversion condition is accounted in terms of the extent of flow separation relative to the nacelle length. However, at this condition the nacelle drag can be an important parameter as well. Therefore, the nacelle drag coefficient evaluated with a nearfield method is also considered in the analysis of the sensitivity to MFCR (Figure 5.18a).

In addition to DDES and RANS calculations at the nominal windmilling diversion condition (MFCR=0.33), a URANS calculations is included for completeness. However, as it was already pointed out in the previous section for the analysis at windmilling end-of-runway, URANS does not show any benefit with respect to the steady RANS method when they are compared to the higher fidelity DDES results (Figure 5.18). At the nominal condition of MFCR=0.33, the DDES model predicts a high level of unsteadiness. Consequently, relative to RANS, the DDES model provides an increase in the nacelle drag coefficient of up to around 15% (Figure 5.18a) and a larger flow separation extent by a factor of approximately 2 (Figure 5.18b). For a small increase from MFCR=0.33 to 0.35 the DDES CFD method reaches a

steady flow condition with very similar values of flow separation and nacelle drag as the RANS model (Figure 5.18a and Figure 5.18b). This highlights the high sensitivity of this parameter to the performances at windmilling diversion condition and the importance of a proper identification of this operating parameter. In conclusion, to account for this difference in the sensitivity of the DDES and RANS models to MFCR, a margin of around -0.02 in the nominal windmilling diversion MFCR is recommended from a RANS-based optimisation approach standpoint.

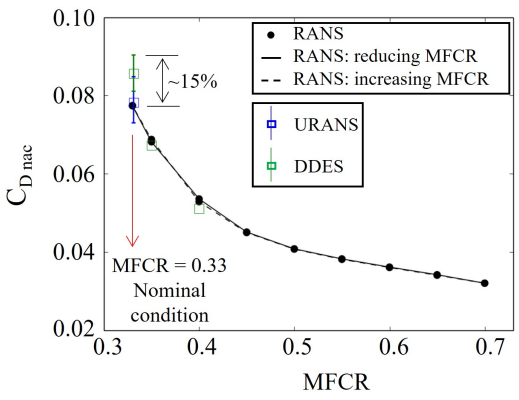

(A) Nacelle drag coefficient as function of MFCR.

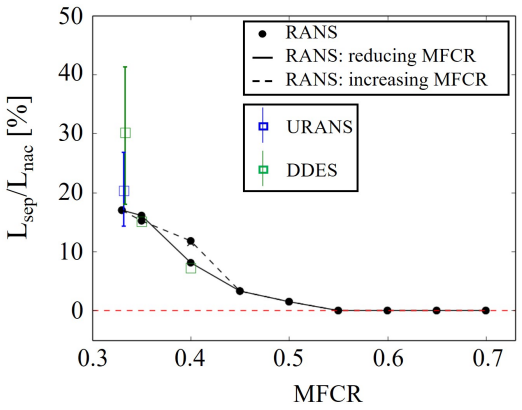

(B) Axial extent of flow separation as function of MFCR.

FIGURE 5.18: Sensitivity of nacelle drag coefficient and axial flow separation to changes in MFCR at windmilling diviersion-type of conditions (M = 0.65 and $\alpha_{eng} = 4.5°$). Comparison of RANS, URANS and DDES CFD predictions.

CHAPTER 6

Aerodynamics of engine-aircraft integration

This chapter assesses the integration effects of the down selected ANACO compact and ANACO conventional nacelle designs installed in the NASA CRM airframe. While in Section 6.1 the analysis is focused on the cruise condition, Section 6.2 evaluates the aerodynamic integration effects at the windmilling diversion scenario.

6.1 Analysis at cruise condition

As reported in Section 4.2, the cruise condition for the installed nacelle configuration is given by M=0.85, MFCR=0.7, C_L = 0.5, Altitude = 10668m and Re = 25x10^6 (Table 4.2). At this operating condition, Section 6.1.1 uses the ANACO compact nacelle to understand the aerodynamic changes in the nacelle from the isolated case to the airframe-installed configuration. For the same nacelle, the effect of different installation positions is detailed in Section 6.1.2. Finally, the impact of the nacelle compactness is assessed for different installation positions by comparing the ANACO compact with the ANACO conventional design (Section 6.1.3).

6.1.1 Impact on the nacelle aerodynamics

The aerodynamics of a nacelle installed in the airframe deviates from the isolated case due to the interference with the airframe. The changes are more notable as the installation position is more close-coupled. Isentropic Mach number distributions (M_{is}) are used to evaluate the changes in the cruise aerodynamics for the ANACO compact configuration when installed at a close-coupled position dx/C_{wing}^{inst} = 0.05 and dz/C_{wing}^{inst} = 0.1 (Figure 6.1). The main changes are in the inboard side of

the nacelle where there is a greater interaction in the flow between the fuselage, wing, pylon and nacelle. In the afterbody of this inboard side of the nacelle, there is an increase in the flow suction which reduces the static pressure and therefore is detrimental from a nacelle drag standpoint (Figure 6.1). This flow suction terminates in a shock wave that affects the nacelle but also the pylon and the pressure side of the wing. As a result, the upstream pressure field is altered. There is an increase in the flow pressurisation that weakens and moves forward the shock wave in the forebody (Figure 6.1). The nacelle forebody becomes less forward-loaded which increases the contribution to the nacelle drag. On the other hand, slight changes on the shock position and pre-shock Mach number happen on the outboard side of the installed nacelle relative to the isolated case (Figure 6.1). Overall, for the outboard side the flow topology is the same and the effect of the installation on the M_{is} distribution is minor.

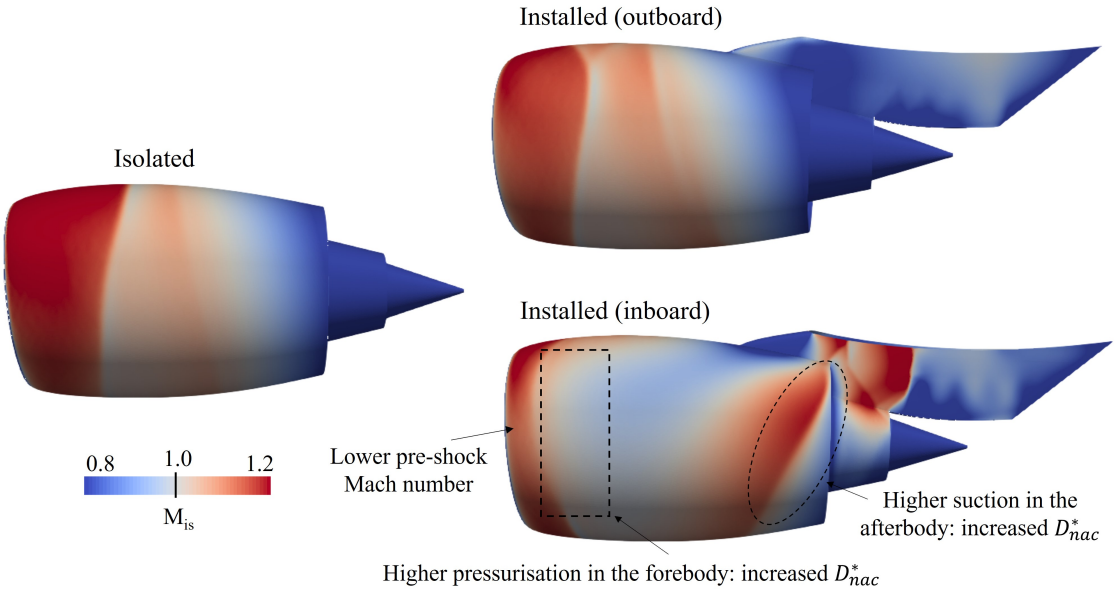

FIGURE 6.1: Aerodynamic comparison at cruise condition ($M = 0.85$, $MFCR = 0.7$, $C_L = 0.5$ and Alt = 10668m) through isentropic Mach distributions (M_{is}) for the ANACO compact nacelle in isolated and installed configurations. Installation position: $dx/C^{inst}_{wing} = 0.05$ and $dz/C^{inst}_{wing} = 0.1$.

6.1.2 Impact of the aero-engine installation position

Once the impact of the installation on the nacelle flow field is understood (Section 6.1.1), the analysis is extended in this section to evaluate the effect of the installation position. A set of 12 podded under-wing positions are assessed (Figure 6.2). These are defined through the axial and vertical offset between the nacelle trailing edge in

the top line and the wing leading edge at the spanwise installation position (Section 4.1.2). The axial offset dx/C_{wing}^{inst} ranges from -0.05 to 0.05 to cover both forward and overlapped positions. The vertical offset dz/C_{wing}^{inst} ranges from 0.05 to 0.15 depending on dx/C_{wing}^{inst} (Figure 6.2).

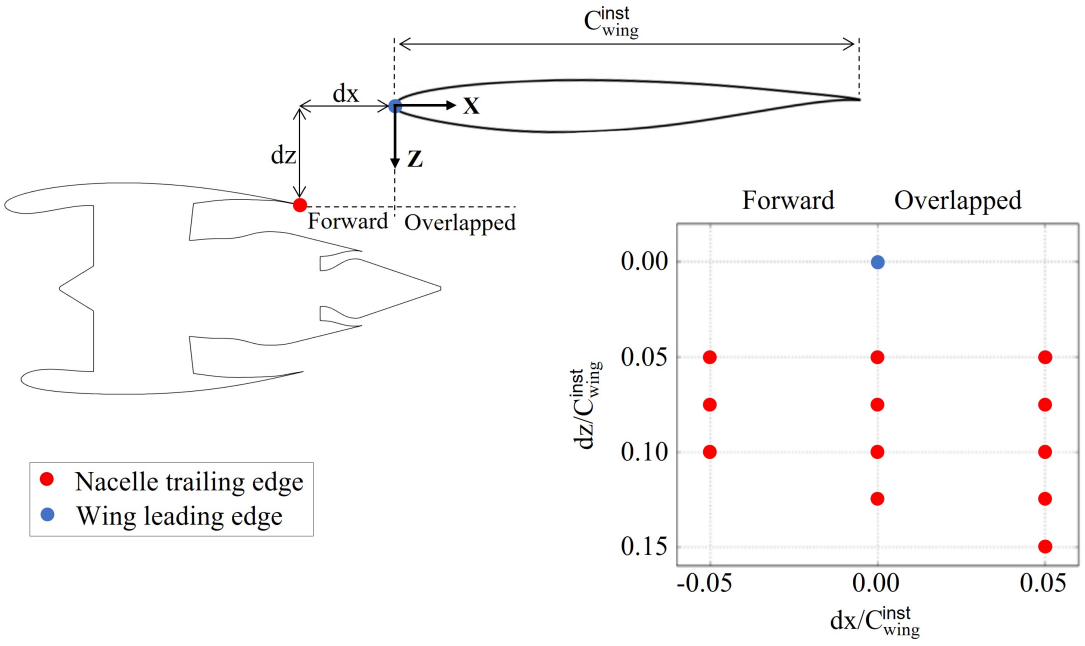

FIGURE 6.2: Set of installation positions assessed.

The ANACO compact nacelle installed in the airframe is used to analyse the impact of the installation position on the overall system performance and aerodynamics. The change of each metric across the installation map is reported relative to the lowest metric value and as a percentage of the standard net thrust ($F_N = 60kN$) (Figure 6.3). This helps to understand the individual range of sensitivity of each metric. Using the NVF as the key metric to evaluate the performance of the overall system, there is a change of $\Delta NVF/F_N = 5.3\%$ across the installation map (Figure 6.3d). This highlights the high sensitivity of the compact nacelle to the installation. The effect of the installation position on the overall NVF is a balance of the sensitivities of its constituent metrics: NPF, $D_{a/f}$ and D_{nac}^* (Section 4.4.1). NPF and D_{nac}^* are primarily affected by the axial installation position with the region of highest benefit located at the most forward position ($dx/C_{wing}^{inst} = -0.05$) (Figure 6.3c, Figure 6.3a). Conversely, $D_{a/f}$ depends on both the axial and vertical coordinates (Figure 6.3b). The highest benefit is found at the largest vertical offset from the wing leading edge and the most overlapped position ($dx/C_{wing}^{inst} = 0.05$, $dz/C_{wing}^{inst} = 0.15$) (Figure 6.3b). The optimal regions in the axial coordinate for NPF and $D_{a/f}$ are opposite. From the balance between this two metrics, the region of highest NVF

is located at the largest vertical and the most forward position ($dx/C^{inst}_{wing} = -0.05$, $dz/C^{inst}_{wing} = 0.1$) (Figure 6.3d).

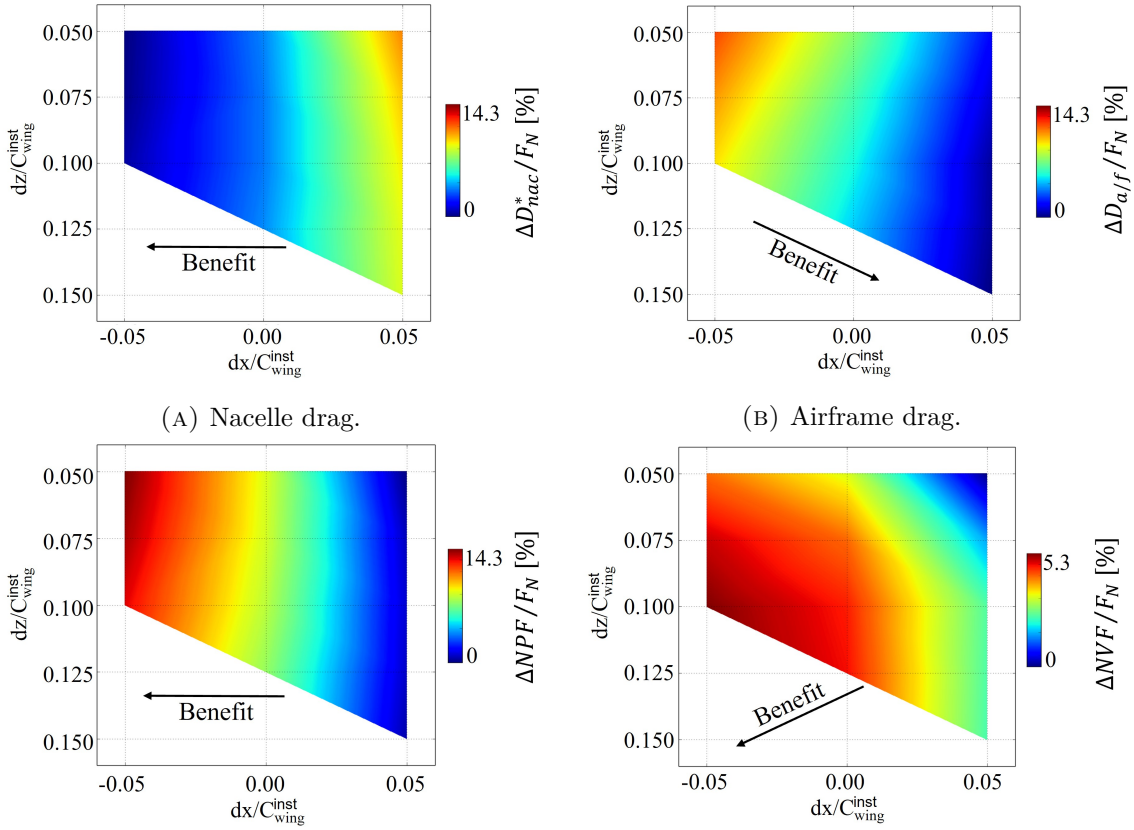

(A) Nacelle drag.

(B) Airframe drag.

(C) Net propulsive force.

(D) Net vehicle force.

FIGURE 6.3: Effect of the axial and vertical installation position on the nacelle drag, airframe drag, net propulsive force and net vehicle force for the ANACO compact nacelle installed in the airframe at the cruise condition ($M = 0.85$, $MFCR = 0.7$, $C_L = 0.5$ and Alt = 10668m). Metrics reported relative to their lowest value and as a percentage of the standard net thrust (F_N).

To relate the performance metrics across the installation map to the flow field, the aerodynamics of the combined engine-airframe system is assessed through distributions of elemental pressure force in the drag direction ($\frac{1}{q_\infty}\frac{dF_p}{dS}\Big|_D$), where q_∞ represents the dynamic pressure in the farfield and F_p the normal pressure component of the force on the surface (Figure 6.4). The skin friction component of the drag is not considered. The reasoning behind is that for fully attached flows the skin friction is essentially related to the wetted area of the configuration. Therefore, as the nacelle design evaluated is the same, this friction term is considered to be similar for every installation position and the changes in the drag are expected to be governed by the different pressure fields (to support this point, Section 8.2.1.2 addresses later the impact of the viscous effects on the nacelle aerodynamic design

problem). The analysis is focused on the pressure side of the wing and the full nacelle surface represented in an unwrapped manner. The typical installation position given by $dx/C_{wing}^{inst} = 0.0$ and $dz/C_{wing}^{inst} = 0.1$ is used as reference to understand the surface pressure drag distributions. In the nacelle, the largest contribution to the drag is on the rear section of the inboard side (Figure 6.4). This comes from the increase in the flow suction that occurs due to the interference flow with the airframe as highlighted in Section 6.1.1 (Figure 6.1). However, this flow suction produces a drag benefit in the pressure side of the wing. The reason is that it is located on the forebody of the wing where the normal force generated goes in the thrust direction. The same reasoning explains the drag benefit in the forebody of the nacelle where the flow suction comes from the flow acceleration around the leading edge (Figure 6.4).

Relative to the reference location, the influence of the installation position is assessed by changing the vertical and axial offset independently.

- For the vertical position, $dx/C_{wing}^{inst} = 0$ is fixed and $dz/C_{wing}^{inst} = 0.075$ and 0.125 are compared. The impact of the vertical coordinate on the nacelle drag is small. D_{nac}^{*} changes by just $0.003F_N$ between $dz/C_{wing}^{inst} = 0.075$ and $dz/C_{wing}^{inst} = 0.125$ (Figure 6.3a). This is related to a slight change in the intensity of the flow suction in the rear inboard region of the nacelle (Figure 6.4). There is a larger impact on the airframe drag. In the inboard forebody region of the wing, the intensity of the flow suction is greater for $dz/C_{wing}^{inst} = 0.125$ which reduces $D_{a/f}$ by $0.016F_N$ relative to $dz/C_{wing}^{inst} = 0.075$ (Figure 6.3b and 6.4). However, there is a substantial impact on GPF^{*} with a penalty of around $0.014F_N$ from $dz/C_{wing}^{inst} = 0.075$ to $dz/C_{wing}^{inst} = 0.125$ which is accounted in the NPF. Overall, this results in an increase in $\Delta NVF/F_N$ of around 0.5% when the vertical position is changed from $dz/C_{wing}^{inst} = 0.075$ to $dz/C_{wing}^{inst} = 0.125$ (Figure 6.3d)

- To assess the impact of the axial installation position, $dz/C_{wing}^{inst} = 0.1$ is maintain and $dx/C_{wing}^{inst} = -0.05$ and 0.05 are compared. In this case, the sensitivity of the changes in the airframe and nacelle aerodynamics are of the same order of magnitude. For the overlapped position $dx/C_{wing}^{inst} = 0.05$, the flow suction in the inboard side of both the nacelle afterbody and the wing forebody is increased in area and magnitude relative to the forward position $dx/C_{wing}^{inst} = -0.05$ (Figure 6.4). This increases D_{nac}^{*} by $0.090F_N$ (Figure 6.3a) and reduces $D_{a/f}$ by $0.092F_N$ (Figure 6.3b) for the overlapped case. However,

as in the previous case, there is a large penalty on GPF^* of $0.031F_N$ for the axially overlapped position $dx/C_{wing}^{inst} = 0.05$ relative to $dx/C_{wing}^{inst} = -0.05$. Overall, the forward installation position $dx/C_{wing}^{inst} = -0.05$ reaches a $\Delta NVF/F_N$ of approximately 2.9% which emphasises the stronger sensitivity to the axial installation position compared to the vertical one (Figure 6.3d).

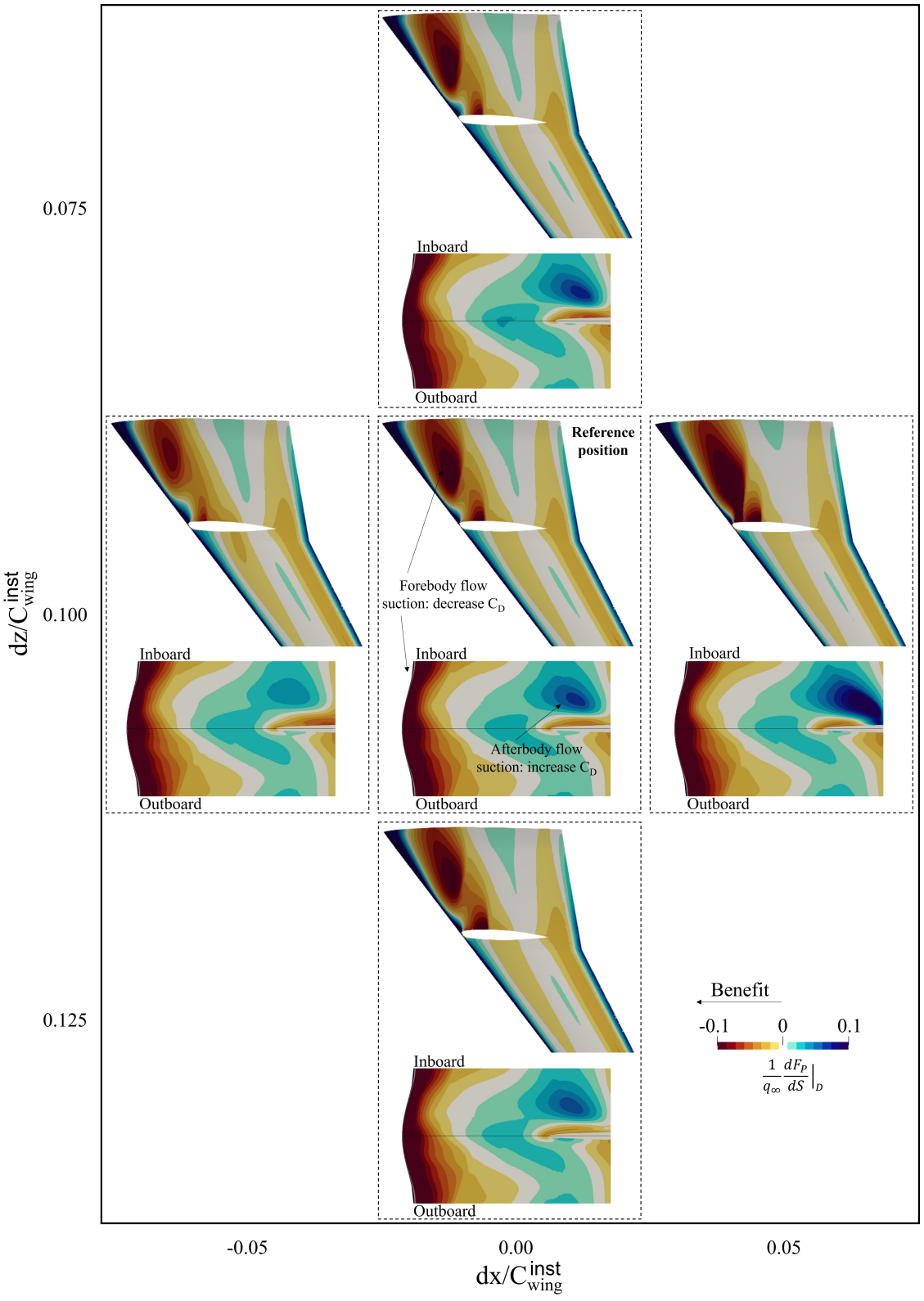

FIGURE 6.4: Contours of elemental pressure force in the drag direction for the ANACO compact nacelle installed in the airframe at the cruise condition ($M = 0.85$, $MFCR = 0.7$, $C_L = 0.5$ and Alt = 10668m). Pressure side of the wing and unwrapped nacelle surface. Impact of the vertical and horizontal installation position.

6.1.3 Impact of the aero-engine nacelle compactness

The impact of the nacelle compactness on the aerodynamics of the propulsion system integration is assessed by comparing the ANACO compact configuration ($L_{nac}/r_{hi} = 3.1$) previously analysed with the installation of the ANACO conventional configuration ($L_{nac}/r_{hi} = 3.6$). In terms of the distributions of the performance metrics across the installation map, the trends and region of benefit are the same for both nacelles (Figure 6.3 and 6.5). However, there are differences in the magnitudes. In particular, while the variation in the NVF in the installation design space for the compact design is $0.053F_N$ (Figure 6.3d), it is $0.039F_N$ for the conventional nacelle (Figure 6.5d). These variations highlight the greater sensitivity of the compact configuration to the installation.

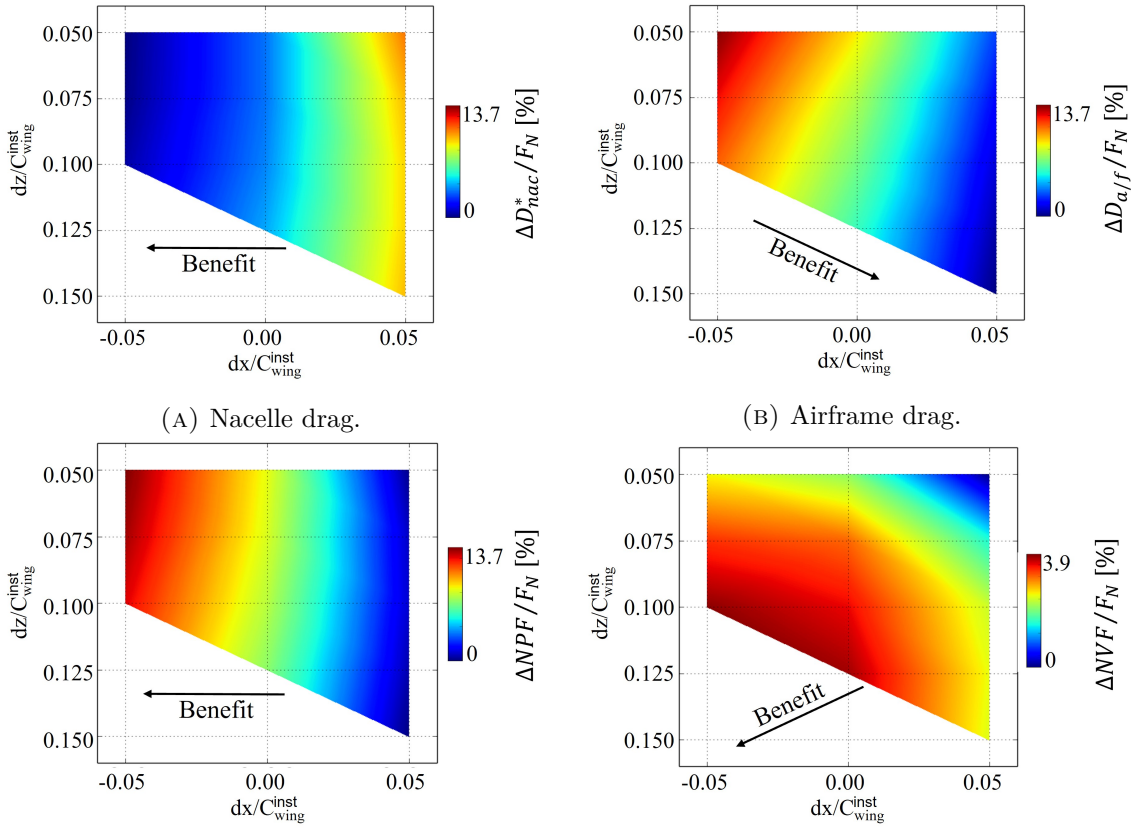

(A) Nacelle drag.

(B) Airframe drag.

(C) Net propulsive force.

(D) Net vehicle force.

FIGURE 6.5: Effect of the axial and vertical installation position on the nacelle drag, airframe drag, net propulsive force and net vehicle force for the ANACO conventional nacelle installed in the airframe at the cruise condition ($M = 0.85$, $MFCR = 0.7$, $C_L = 0.5$ and Alt = 10668m). Metrics reported relative to their lowest value and as a percentage of the standard net thrust (F_N).

The key metric for this analysis is the NVF benefit of the compact configuration with respect to the conventional one which is defined relative to the standard net thrust as $\Delta NVF_{comp-conv} = (NVF_{comp} - NVF_{conv})/F_N$. The distribution across the installation map of this metric is broadly governed by the axial installation position (Figure 6.6). For the most forward installation position given by $dx/C_{wing}^{inst} = -0.05$ and a vertical offset of $dz/C_{wing}^{inst} = 0.05$ there is a maximum $\Delta NVF_{comp-conv}$ benefit of 1%. However, at around $dx/C_{wing}^{inst} \sim 0.025$ there is change in the polarity of $\Delta NVF_{comp-conv}$ (Figure 6.6). Consequently, for overlapped positions at $dx/C_{wing}^{inst} = 0.05$ the compact configuration has a NVF penalty relative to the conventional one up to -0.8%. This means that for so close-coupled installations, the drag benefits obtained from a lower wetted area for compact nacelle designs is offset by the penalty in the more adverse flow interaction with the airframe. The sensitivity of the adverse flow suction in the afterbody of the inboard side of the compact nacelle to a change from the axially aligned position $dx/C_{wing}^{inst} = 0.0$ to the overlapped position $dx/C_{wing}^{inst} = 0.05$ is substantially greater compared to the conventional configuration (Figure 6.7). This is a challenging result as compact nacelles for UHBPR aero-engines may be installed in a more close-coupled installation position due to multi-disciplinary constraints like ground clearance or pylon structural loads. Additionally, for a typical installation position given by $dx/C_{wing}^{inst} = 0$ and $dz/C_{wing}^{inst} = 0.1$ the benefit of the compact configuration is around $\Delta NVF_{comp-conv} \approx 0.44\%$ (Figure 6.6). This equates to a reduction in the aircraft fuel burn at cruise of the same order[106]. However this is below the benefit obtained in isolated configuration of around 0.7% (Figure 6.6). As explained in Section 6.1.1, the aerodynamics on the nacelle changes when it is installed in the airframe and the isolated benefit may be eroded. Overall, this highlights the need to consider the integration effects throughout the compact nacelle design phase when the aero-engine is installed in closer positions to the airframe.

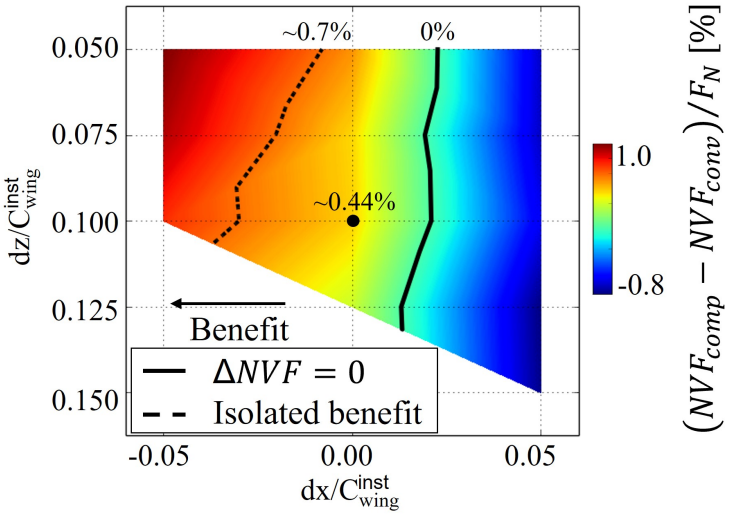

FIGURE 6.6: Effect of the axial and vertical installation position on the net vehicle force benefit of the ANACO compact configuration relative to the ANACO conventional configuration at the cruise condition ($M = 0.85$, $MFCR = 0.7$, $C_L = 0.5$ and Alt = 10668m).

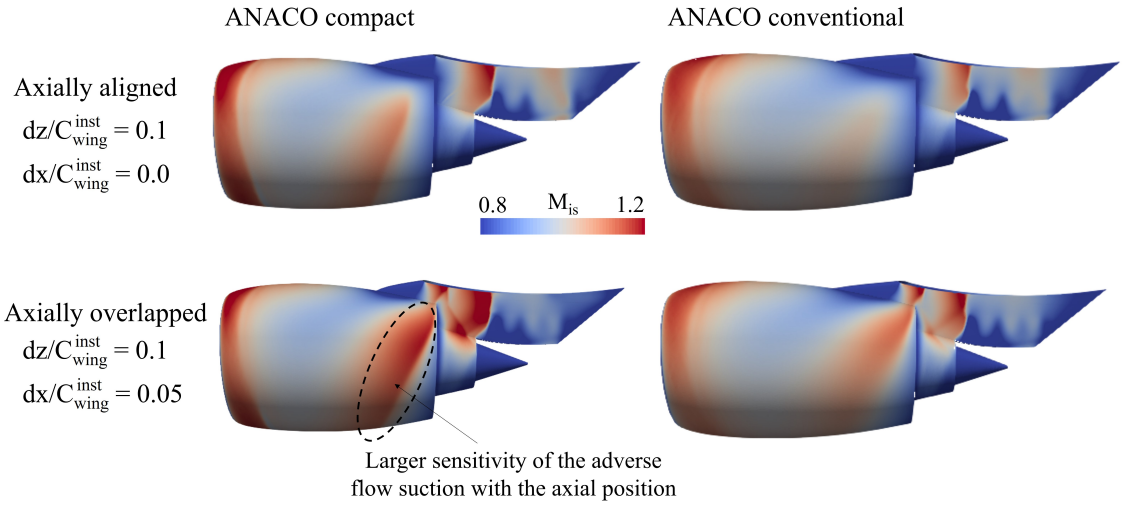

FIGURE 6.7: Distributions of isentropic Mach number (M_{is}) in the inboard side of the nacelle to assess the impact of the axial installation position on the ANACO compact and ANACO conventional configurations at the cruise condition ($M = 0.85$, $MFCR = 0.7$, $C_L = 0.5$ and Alt = 10668m).

6.2 Analysis at windmilling diversion

One of the key consideration in the design and optimisation of compact nacelles is to ensure acceptable aerodynamic performances at off-design conditions. In the isolated optimisation of ANACO compact and ANACO conventional nacelles different windmilling conditions were considered (Section 5.1). In this section, both nacelle

designs are evaluated at the windmilling diversion condition in the airframe-installed configuration given by $M = 0.65$, $MFCR = 0.33$, $C_L = 0.44$ and Altitude = 6096m (Table 4.2). The CFD method presented in Section 4.3.1.1.3 is used.

The windmilling diversion scenario is the off-design condition selected for this analysis due to its interest from the ETOPS requirements point of view. The reference installation position is considered: $dx/C_{wing}^{inst} = 0$ and $dz/C_{wing}^{inst} = 0.1$. From this assessment a penalty in $\Delta NVF_{comp-conv}/F_N$ of around -2.6% is obtained for the compact configuration relative to the conventional design at the windmilling diversion condition. This shows the higher sensitivity of compact nacelle designs to this type off-design condition when the overall system is considered. From an aerodynamic standpoint, windmilling diversion is normally governed by shock-induced flow separation close to the highlight of the nacelle. The high curvature gradients on the geometry of the compact nacelle trigger a larger extent of flow separation relative to the conventional configuration. Using contours of x-component of wall shear stress (x-WSS) to estimate the region of flow separation on the surface, the maximum axial extent of the separation for the compact and conventional configurations reach $\sim 0.23L_{nac}$ and $\sim 0.02L_{nac}$ respectively (Figure 6.8a, Figure 6.8b). The separation in the inboard region of the compact nacelle ($\sim 0.23L_{nac}$) is larger compared to the outboard part ($\sim 0.15L_{nac}$) due to the cross-flow induced by the interaction with the airframe and pylon and also because of the toe installation angle (Figure 6.8a). However, there are no notable differences in the overall extent of flow separation between the isolated ($\sim 0.21L_{nac}$) and installed ($\sim 0.23L_{nac}$) configurations apart from the separated region being symmetric for the isolated case (Figure 6.8a, Figure 6.8c). This highlights the low impact of the aero-engine installation on the flow separation length for windmilling diversion for both the compact and the conventional configurations. It is the spillage flow in the leading edge of the nacelle caused by the low engine mass flow what governs the flow separation at this off-design condition.

An important aspect is related to the maximum axial flow separation that was considered in the down selection criteria for these designs. As explained in Section 5.1, a flow separation lower than $0.1L_{nac}$ was considered across the 5 different nacelle aero-lines. The x-component of the wall shear stress evaluated for the isolated ANACO compact nacelle at the 5 different aero-lines shows a maximum axial length of flow separation of around $0.08L_{nac}$ in the top-control aero-line (Figure 6.9b). However, the full azimuthal distribution of the x-component of the wall shear stress shows a maximum separation length of approximately $0.21L_{nac}$ (Figure 6.9a) which does not meet the threshold imposed in the down selection criteria. Therefore, in the

design and optimisation approach developed in this project the $0.1L_{nac}$ threshold is assessed in the full azimuthal coordinate of the nacelle.

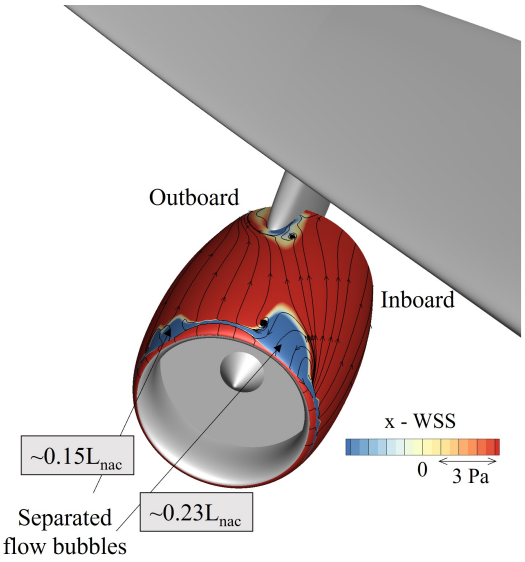

(A) Compact, installed configuration.

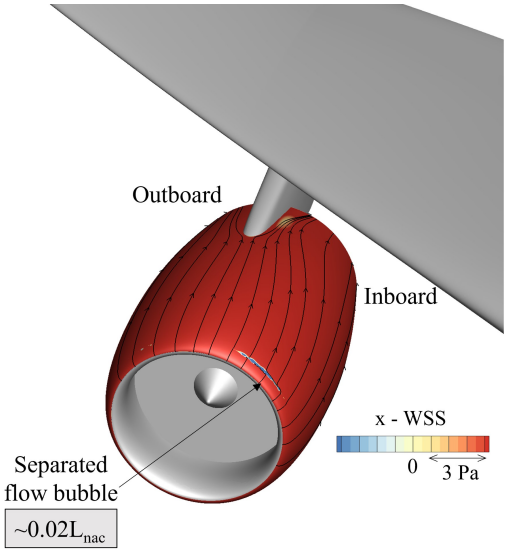

(B) Conventional, installed configuration.

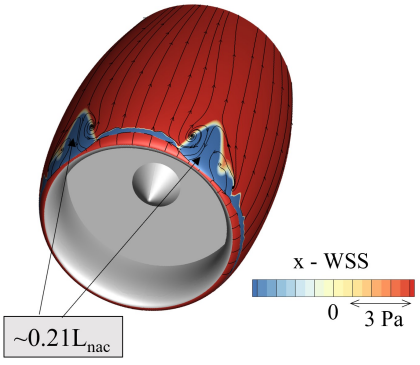

(C) Compact, isolated configuration.

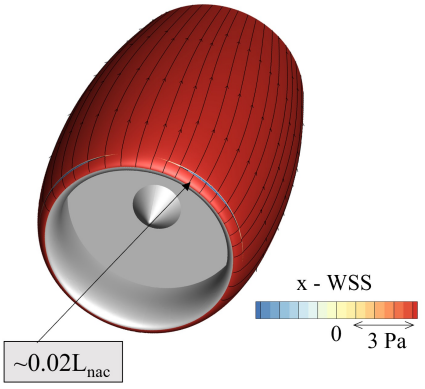

(D) Conventional, isolated configuration.

FIGURE 6.8: Contours of x-component of the wall shear stress (x-WSS) and surface streak-lines for the windmilling diversion operating condition ($M = 0.65$, $MFCR = 0.33$, $C_L = 0.44$ and Alt = 6096m). ANACO compact and ANACO conventional nacelle designs. Installed configuration at the reference position $dx/C^{inst}_{wing} = 0.0$ and $dz/C^{inst}_{wing} = 0.1$.

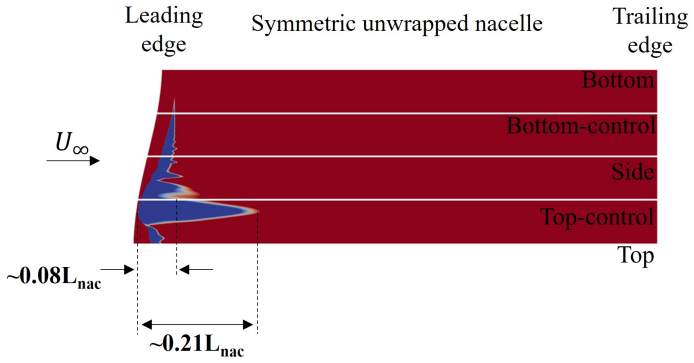

(A) x-WSS distribution in the azimuthal sector $0° - 180°$ due to symmetry of the isolated configuration. Representation in an unwrapped manner of the surface.

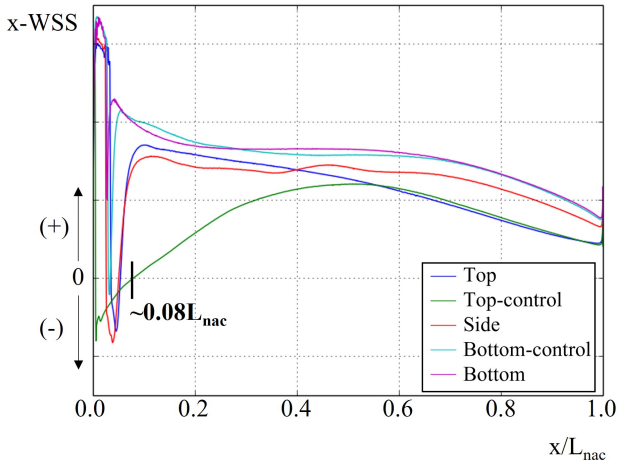

(B) x-WSS distribution along the 5 aero-lines.

FIGURE 6.9: Distributions of x-component of the wall shear stress (x-WSS) on the ANACO compact nacelle in isolated configuration at the windmilling diversion condition ($M = 0.65$, $MFCR = 0.33$, $\alpha_{eng} = 4.5°$ and Alt = 6096m).

6.2.1 Impact of the mass flow capture ratio

For the windmilling diversion-type of conditions, the key flow parameter is the MFCR of the aero-engine. The MFCR affects the location of the stagnation point in the intake and consequently the flow suction around the nacelle leading edge. In this section, a sensitivity analysis of the MFCR for both the ANACO compact and ANACO conventional nacelle designs in the airframe-installed configuration is evaluated. The ranges of the MFCR values investigated depends on the nacelle design. For the conventional nacelle, relative to the nominal windmilling diversion operating point named as A2 (Figure 6.10), the MFCR was varied by about +/-0.05 to encompass both: (a) fully attached flow and (b) the case with separation larger than the threshold of $0.1L_{nac}$ marked as A1 (Figure 6.10). For the compact configuration, the

flow was already fully separated ($0.23L_{nac}$) at the nominal MFCR condition named as B2 (Figure 6.10). Therefore, the MFCR was increased by about 0.17 (case B3) to achieve attached flow condition (Figure 6.10).

For low values of MFCR, the installed performance of the compact nacelle based on NVF is more sensitive to changes in MFCR. For example, a decrease in MFCR of 0.05 reduces the NVF of the installation with respect to the NVF of the clean CRM airframe and relative to the aircraft drag at the nominal diversion condition by $\Delta NVF_{installation} = 1\%$ and 3% for the conventional and compact nacelle designs respectively (Equation 6.1, Figure 6.10a). The NVF of the clean CRM is defined as $NVF_{CleanCRM_{Div}} = -D_{a/f_{Div}}$ to express every term in the NVF currency. For the same variation in MFCR, the change in D^*_{nac} for the conventional and compact nacelle is about 0.5% and 2% of the diversion aircraft drag respectively (Figure 6.10b). For both the conventional and compact nacelle designs, the change in the airframe drag component with MFCR is minor. This is sensible since MFCR is a parameter that at windmilling diversion essentially affects the forebody of the nacelle with very little impact on the installation (Section 6.2). Overall the $D_{a/f}$ increases slightly by about 0.3% across the range of MFCR studied (Figure 6.10c). This shows that the different sensitivities in $\Delta NVF_{installation}$ are governed by the nacelle drag. Moreover, the large sensitivity of the compact nacelle to the changes in MFCR strongly highlights the importance of a proper estimation of the MFCR for this off-design operating conditions for compact nacelle configurations.

$$\Delta NVF_{installation} = \frac{NVF - NVF_{CleanCRM_{Div}}}{D_{aircraft_{Div}}} \tag{6.1}$$

Distributions of elemental pressure force in the drag direction is compared for both nacelles in conditions of generally attached flow (A2 and B3) and grossly separated flow of greater than $0.1L_{nac}$ (A1 and B2). The comparison indicates a clear higher impact of the forebody on the drag force (Figure 6.11). There is a minor effect of the installation in the inboard part of the rear nacelle that reduces the elemental drag due to the flow suction induced by the interference with the pylon and wing but this is unaffected by the aero-engine MFCR setting. The gradients of this elemental drag force around the crest and the afterbody of the nacelle are one order of magnitude smaller than near the leading edge (Figure 6.11). This topology in the distribution applies regardless of the nacelle compactness and flow separation. For the cases with separated flow, the signature can be seen close to the leading edge. This reduces the flow suction in that region and increases the drag substantially. For example, for the compact configuration, D^*_{nac} increases by around 4% of the aircraft drag at

diversion from the fully attached flow case (B3) to the grossly separated case at the nominal diversion scenario (B2) (Figure 6.11).

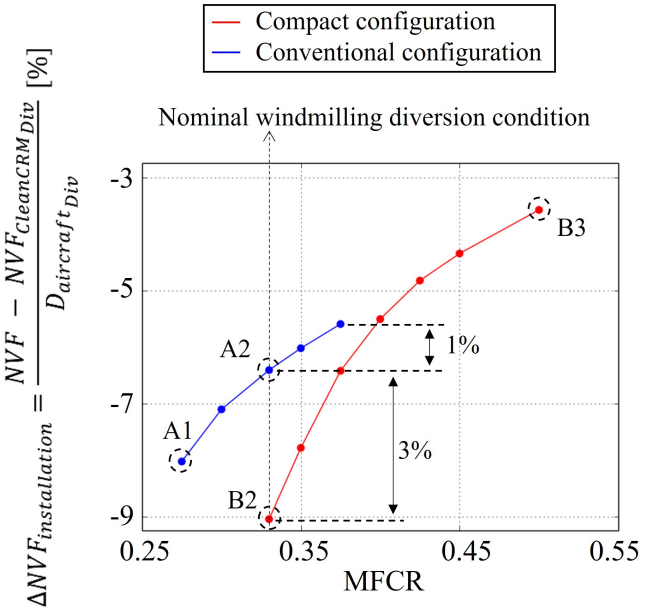

(A) Net vehicle force of the installation relative to the clean airframe ($NVF_{installation}$).

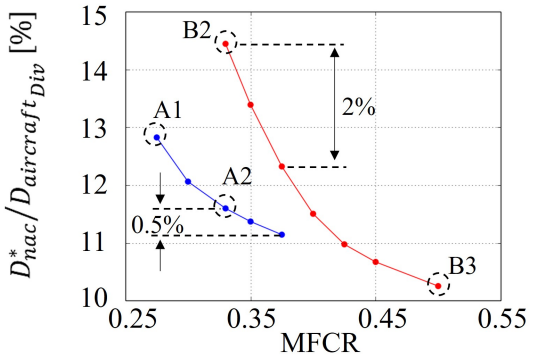

(B) Modified nacelle drag (D^*_{nac}).

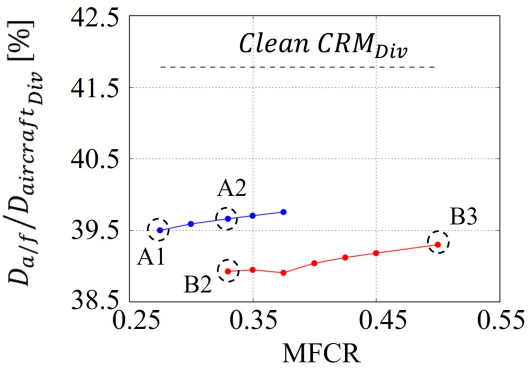

(C) Airframe drag ($D_{a/f}$).

FIGURE 6.10: Sensitivity of installation to MFCR for the ANACO compact and ANACO conventional nacelle designs for windmilling diversion-type of conditions ($M = 0.65$, $C_L = 0.44$ and Alt = 6096m). Installed configuration at the reference position $dx/C^{inst}_{wing} = 0.0$ and $dz/C^{inst}_{wing} = 0.1$.

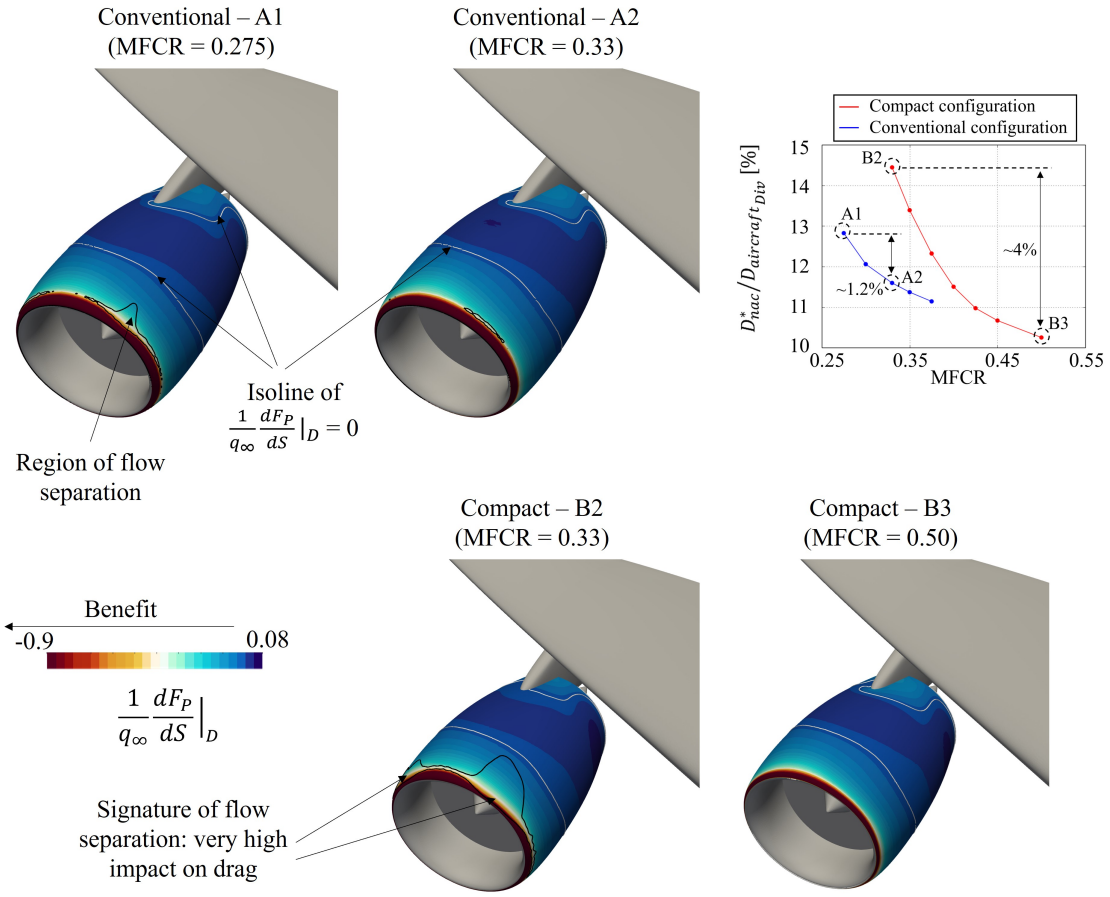

FIGURE 6.11: Contours of elemental pressure force in the drag direction for the ANACO compact and ANACO conventional nacelle designs for windmilling diversion-type of conditions ($M = 0.65$, $C_L = 0.44$ and Alt = 6096m) in installed configuration. Contours shown for different MFCR showing separated and attached flow topologies. Reference installation position: $dx/C^{inst}_{wing} = 0$ and $dz/C^{inst}_{wing} = 0.1$.

CHAPTER 7

Assessment of different CFD fidelities

To develop a multi-fidelity method, an analysis of different fidelities is required. The RANS CFD method is used as the established high-fidelity model to evaluate the performance of a nacelle design. In this project, RANS CFD is considered as high fidelity just in the context of the multi-fidelity studies. In a wider sense, high fidelity CFD models are eddy-resolving methods like DES, LES or DNS. Two different kind of low-fidelity models are assessed for the multi-fidelity approach. One based on the Euler flow equations that simplifies the physics of the problem by neglecting the viscosity of the fluid (Section 4.3.2). The other one comes from a coarsened spatial discretisation of the RANS model which uses wall functions to model the complete boundary layer (RANS_{wf}) (Section 4.3.1.2). Two aspects are considered in the analysis: (a) a comparison of the flow field predictions for the airframe-installed configuration (Section 7.1) and (b) the impact of the CFD fidelity on the convergence to an optimal design space (Section 7.2). As this is not computationally feasible for the installed configuration, the CFD-in-the-loop optimisation approach for 2D axi-symmetric isolated nacelles detailed in Section 4.5.2.2 is used. Although the optimal design space is expected to be different between the installed and isolated configurations, the flow physics are similarly transonic and non-linear in both cases.

7.1 Aerodynamic prediction of the installation

For this analysis, the aero-engine with the ANACO compact nacelle design selected in Section 5.1 is used. A typical installation position given by $dx/C_{wing}^{inst} = 0$ and $dz/C_{wing}^{inst} = 0.1$ is considered. The assessment is focused on the cruise condition given by $M = 0.85$, $MFCR = 0.7$, Altitude = 10668m and $C_L = 0.5$ (Table 4.2).

The CFD methods are detailed in Section 4.3. Relative to the RANS CFD model, the lower fidelity RANS$_{wf}$ and Euler methods reduce the overall computation cost by a factor of 15 and 36 respectively. These cost reductions involve the savings both in the mesh generation and in the numerical calculation.

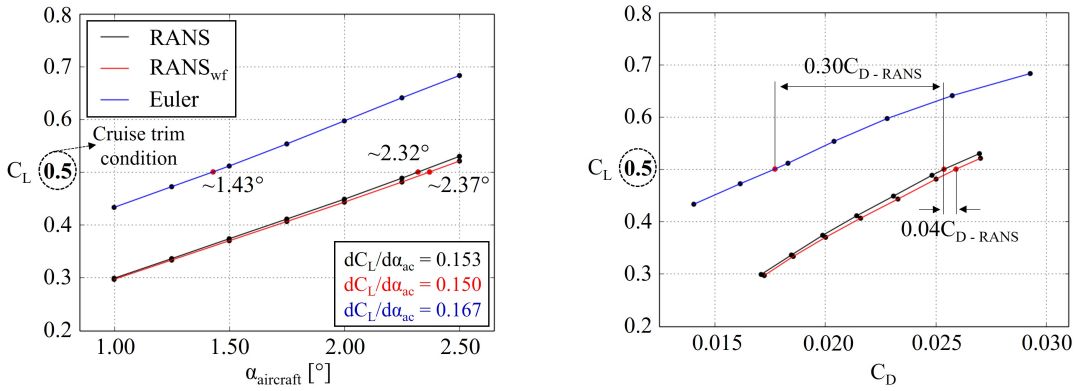

(A) Polar $C_L - \alpha$.

(B) Polar $C_L - C_D$.

FIGURE 7.1: Polar of the CRM aircraft with the ANACO compact nacelle at cruise-type of conditions ($M = 0.85$, $MFCR = 0.7$ and Alt = 10668m) using the different CFD fidelities: RANS, RANS with wall functions and Euler.

The $C_L - \alpha$ and $C_L - C_D$ polars of the aircraft were generated with each CFD fidelity to assess the impact of incidence on the lift and drag coefficients. This helps to understand the differences between fidelities in the cruise trim condition given by $C_L = 0.5$ (Figure 7.1). The polar curves for both RANS models are very similar with very close aircraft trim angle of attack ($\alpha_{aircraft}$) of $\sim 2.32°$ and $\sim 2.37°$ for the high-fidelity RANS and RANS$_{wf}$ models respectively (Figure 7.1a). An increase in the cruise drag of approximately 4% is obtained for the RANS$_{wf}$ model (Figure 7.1b). Larger differences are observed between the Euler and the high-fidelity RANS model. For each incidence angle, an over prediction in C_L of around 0.14 is obtained with the Euler model (Figure 7.1a). This is related to the differences in the pressure distribution on the suction side of the wing. The boundary layer of the RANS model changes the effective wing shape and results in an overall reduction of the flow suction compared to the Euler model. In the pressure side of the wing the less adverse pressure gradient keeps the RANS boundary layer thinner. This reduces the impact on the aerodynamics and similar pressure distributions are obtained with the RANS and Euler models. Overall, the trim $\alpha_{aircraft}$ in the Euler CFD model reduces from $\sim 2.32°$ to $\sim 1.43°$ (Figure 7.1a). This lower incidence combined with the inviscid flow behaviour of the Euler model results in an under prediction of the cruise drag relative to the high-fidelity RANS model by about 30% (Figure 7.1b).

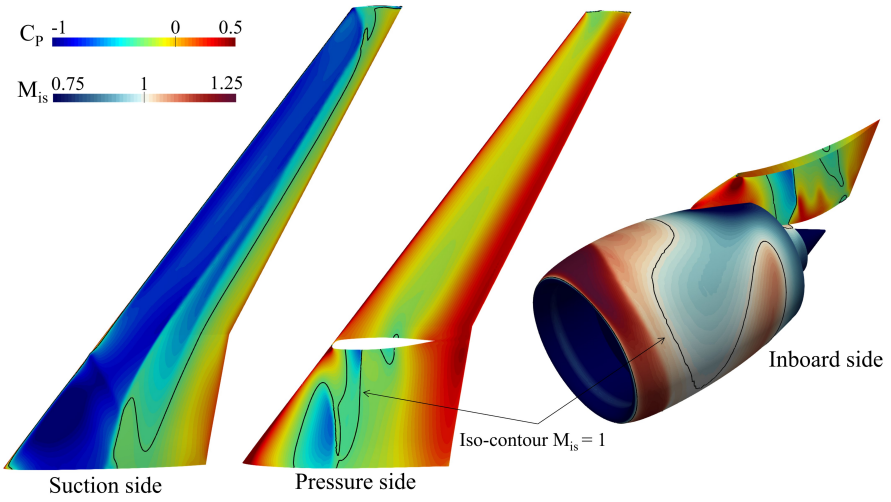

(A) RANS model.

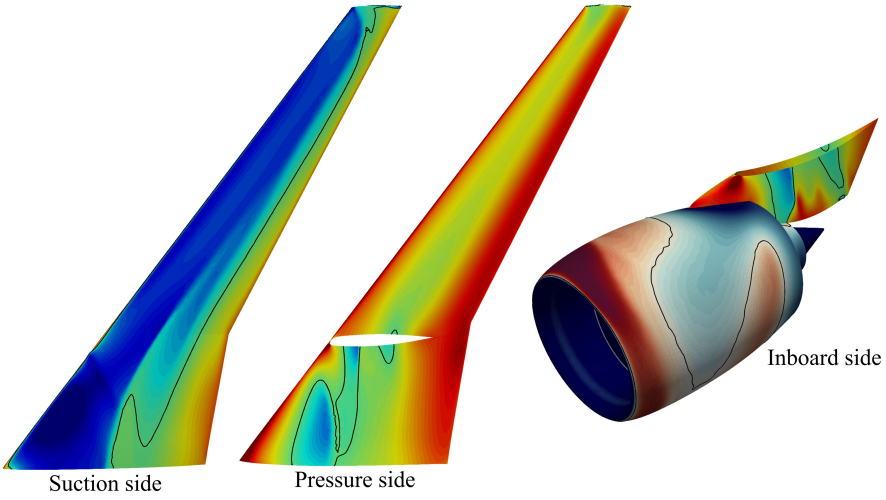

(B) RANS with wall functions model.

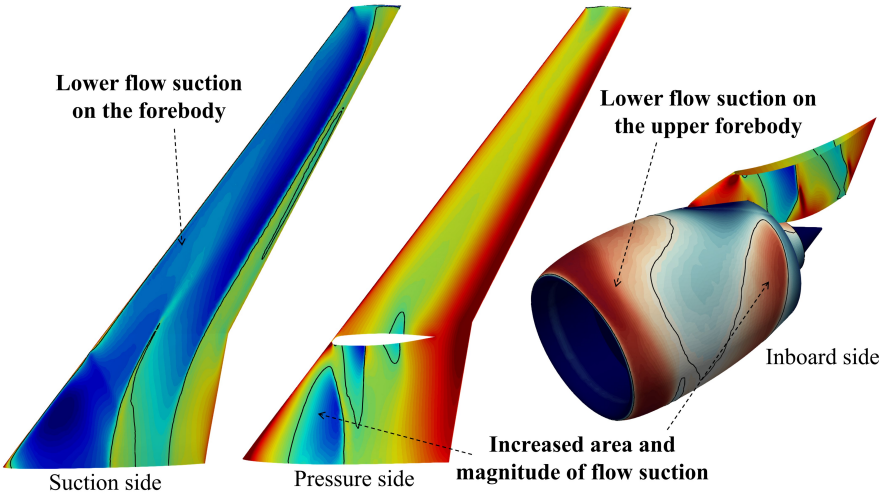

(C) Euler model.

FIGURE 7.2: Contours of isentropic Mach number on the ANACO compact nacelle surfaces and pressure coefficient in the wing and pylon at the cruise condition ($M = 0.85$, $MFCR = 0.7$, $C_L = 0.5$ and Alt = 10668m) using the different CFD fidelities: RANS, RANS with wall functions and Euler.

The aerodynamics at the trim condition are compared through contours distributions of isentropic Mach number (M_{is}) on the nacelle and pressure coefficient (C_P) on the wing surfaces and pylon (Figure 7.2). Additionally, profiles of M_{is} on the nacelle aero-lines (Figure 7.3) and C_P on different spanwise sections of the wing (Figure 7.4) are presented to allow a more quantitative comparison. As could be expected from the previous polar analysis, both RANS methods predicts very similar flow field distributions in magnitude and gradients (Figures 7.2a and 7.2b). The M_{is} distributions on the nacelle are almost coincident. The same peak Mach number, pre-shock Mach number, shock location and flow diffusion are captured (Figure 7.3). The same applies for the pressure and suction sides of the different wing sections analysed with a slight difference in the shock resolution for the outer section at the mid wingspan ($\eta = 0.5$) (Figure 7.4).

More notable differences are obtained between the RANS and Euler methods (Figures 7.2a and 7.2c). In the forebody of the nacelle, the Euler model predicts a lower flow suction in the upper side ($\Psi = 0°$, 45° and 315°) with a maximum reduction in the peak Mach number of around 0.1 (Figure 7.3). The opposite occurs in the lower side ($\Psi = 135°$, 180° and 225°) with an increase in the Euler peak Mach number of the same magnitude. This is essentially due to the lower trim $\alpha_{aircraft}$ of the Euler model (Figure 7.1a). It is confirmed in the side aero-lines ($\Psi = 90°$ and 270°) where there is no impact of the incidence and the same peak Mach number is reached. A similar behaviour is seen on the forebody of the different wing sections through the C_P distributions. While the suction sides experience an increase in the pressurisation up to around $\Delta C_P \approx 0.2$, the pressure side slightly increases the flow suction around $\Delta C_P < -0.1$ (Figure 7.4).

Another aspect that differs the aerodynamics predicted by the RANS and Euler models is the boundary layer. The boundary layer in RANS changes the effective shape of the wing/nacelle section. This effect, together with the different peak Mach numbers, cause a mismatch in the shock location and strength. On the nacelle, although it is not straightforward to quantify and varies with the aero-line, there is a maximum difference on the shock location and pre-shock Mach number of around $0.05L_{nac}$ and $\Delta M_{is} \approx 0.05$ respectively (Figure 7.3). The key difference between the RANS and Euler models arises in the rear part of the inboard side of the nacelle ($\Psi = 45°$ and 90°). Euler over predicts the flow suction resulting from the aero-engine integration with the airframe (Figure 7.3). Similar conclusions are drawn from the comparison of the aerodynamics on the wing where the impact of the boundary layer and the different flow incidence cause a shifting on the shocks up to approximately $0.07C_{wing}$ (Figure 7.4). Differences on the shock strength are similarly

appreciated which depends on the wing section. Finally, changes in the flow diffusion in the afterbody increase towards the trailing edge which highlights the impact of the boundary layer growth (Figure 7.4).

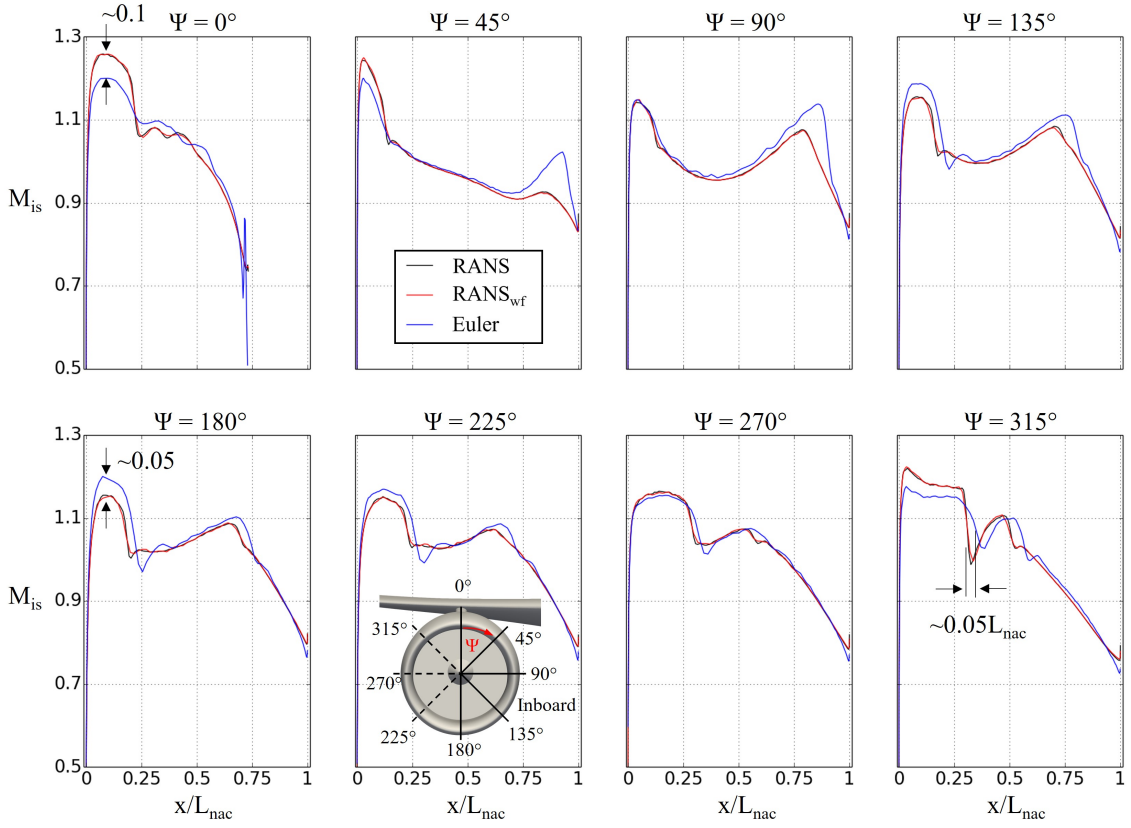

FIGURE 7.3: Comparison of isentropic Mach number distributions on the different aero-lines of the ANACO compact nacelle installed in the CRM airframe at the cruise condition ($M = 0.85$, $MFCR = 0.7$, $C_L = 0.5$ and Alt = 10668m) using the different CFD fidelities: RANS, RANS with wall functions and Euler.

Overall, while the low-fidelity RANS$_{wf}$ model predicts very similar aerodynamics to the high-fidelity RANS model, the low-fidelity Euler model exhibits larger differences. However, to decide the most suitable low-fidelity model to be used within a multi-fidelity optimisation method standpoint, it is still needed to understand: (a) the impact of each CFD fidelity on the convergence to an optimal design space and (b) the trade-off with the computational overhead. In Section 7.2 the different fidelities are applied to a CFD-based optimisation problem of a 2D axi-symmetric nacelle configuration in isolation. Finally, Section 7.3 provides the low-fidelity model selection.

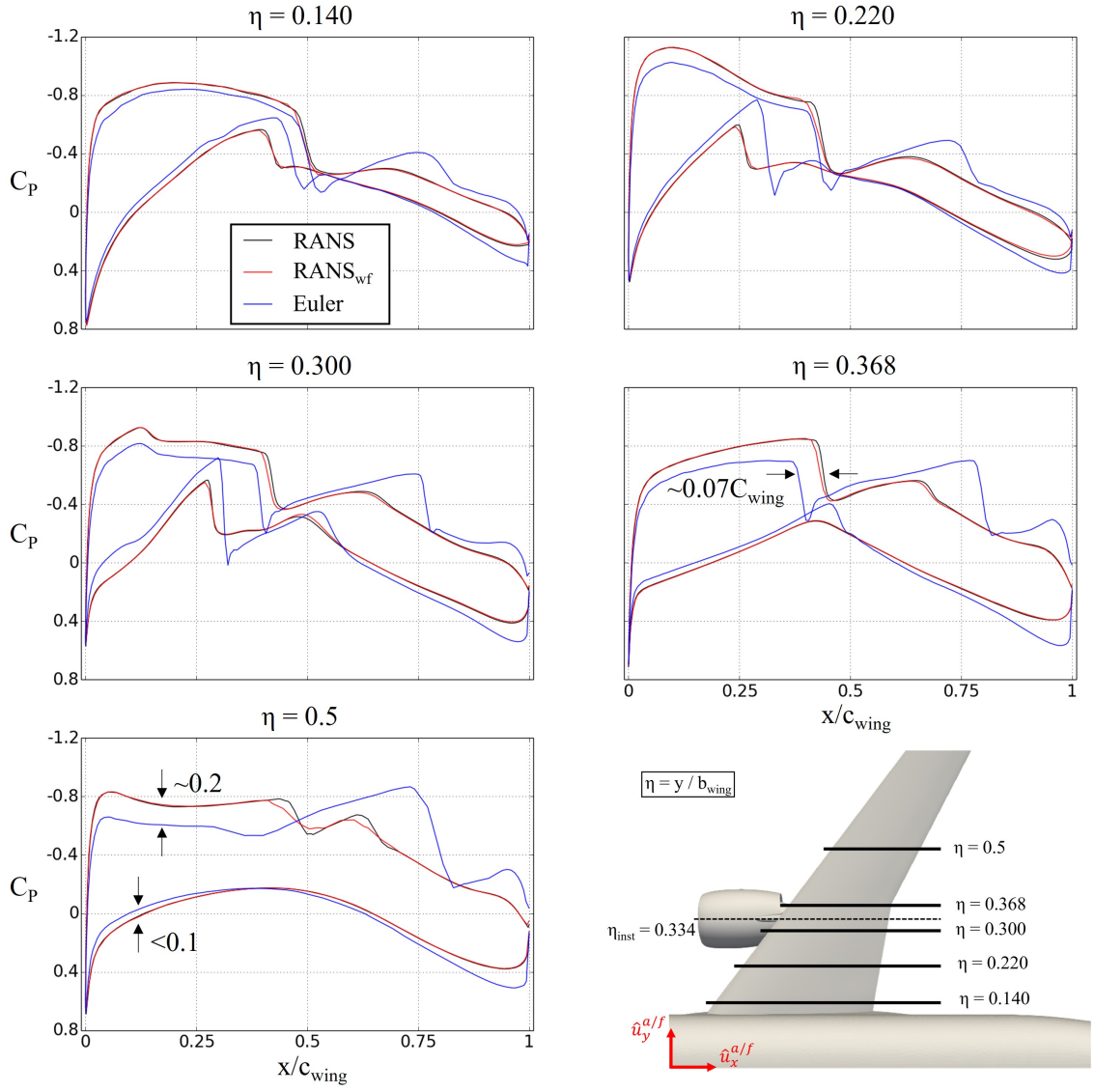

FIGURE 7.4: Comparison of pressure coefficient distributions on different wingspan sections (η) at the cruise condition ($M = 0.85$, $MFCR = 0.7$, $C_L = 0.5$ and Alt = 10668m) using the different CFD fidelities: RANS, RANS with wall functions and Euler.

7.2 Optimal design space of the 2D axi-symmetric configuration

The CFD-in-the-loop optimisation approach explained in Section 4.5.2.2 is used for the three different fidelities investigated. The CFD methods for the 2D axi-symmetric nacelle configuration were detailed in Section 4.3.1.1.1 for RANS, Section 4.3.1.2 for RANS$_{wf}$ and Section 4.3.2 for Euler.

A compact nacelle configuration given by $L_{nac}/r_{hi} = 3.1$ and $r_{te}/r_{hi} = 0.95$ is used. The design space bounds for each degree of freedom (DOF) floated in the optimisation are considered based on previous experiences[183] (Table 7.1). Several operating conditions are used in the optimisation for aerodynamic robustness of the designs. In addition to the cruise condition ($C_{D-cruise}$), the sensitivities to an increase in the flight Mach number from 0.85 to 0.87 ($C_{D-\Delta M}$) and a decrease in the aero-engine MFCR from 0.7 to 0.65 (C_{D-EoC}) are also considered (Table 4.1). Representative values of engine cycle for an UHBPR configuration given by FNPR $\backsim$ 2.2 and CNPR $\backsim$ 1.5 are used (Section 4.2).

TABLE 7.1: Design space bounds considered in the 2D axi-symmetric nacelle optimisations.

	f_{max}	r_{max}/r_{hi}	f_{if}	β_{nac}
DOF_{min}	0.3	1.1	0.7	10°
DOF_{max}	0.5	1.3	1.4	15°

The optimal design space is represented as the non-dominated set of designs contained in the Pareto front. A comparison based on the performance metrics shows large discrepancies in the magnitude of C_D between the Euler and the RANS models. The reason is basically that the drag predicted with the Euler CFD model just include the pressure terms. For example, at the cruise condition the drag from the Euler CFD model reduces by up to 70% relative to the RANS model (Figure 7.5). This is consistent with what was found in the literature review (Section 2.1.3): for UHBPR aero-engine configurations the skin friction component is the leading term of the nacelle drag for mostly attached flows and can account from 60% to 70% of the total drag. However, the changes in the performance metrics between designs is the key aspect from an optimisation point of view rather than the absolute values. In this work, each Pareto front is represented as a two-dimensional projection on the plane defined by $C_{D-cruise} - C_{D-\Delta M}$ in which every design is coloured by C_{D-EoC}. The individual Pareto fronts of each CFD fidelity show a similar shape with the same relationship between each objective function. As $C_{D-\Delta M}$ decreases there is a penalty in C_{D-EoC} which highlights the compromise between these two performance metrics. For $C_{D-cruise}$, the Pareto is divided into two branches: while for the upper branch a reduction in $C_{D-cruise}$ implies a penalty in C_{D-EoC}, a reduction of $C_{D-cruise}$ in the lower branch penalises $C_{D-\Delta M}$ (Figure 7.5). Compared to the Pareto front obtained with the high-fidelity RANS model, Euler converges to a less populated Pareto in which the front is not so well defined (Figure 7.5). On the contrary, RANS_{wf} reaches a similar Pareto front to RANS (Figure 7.5).

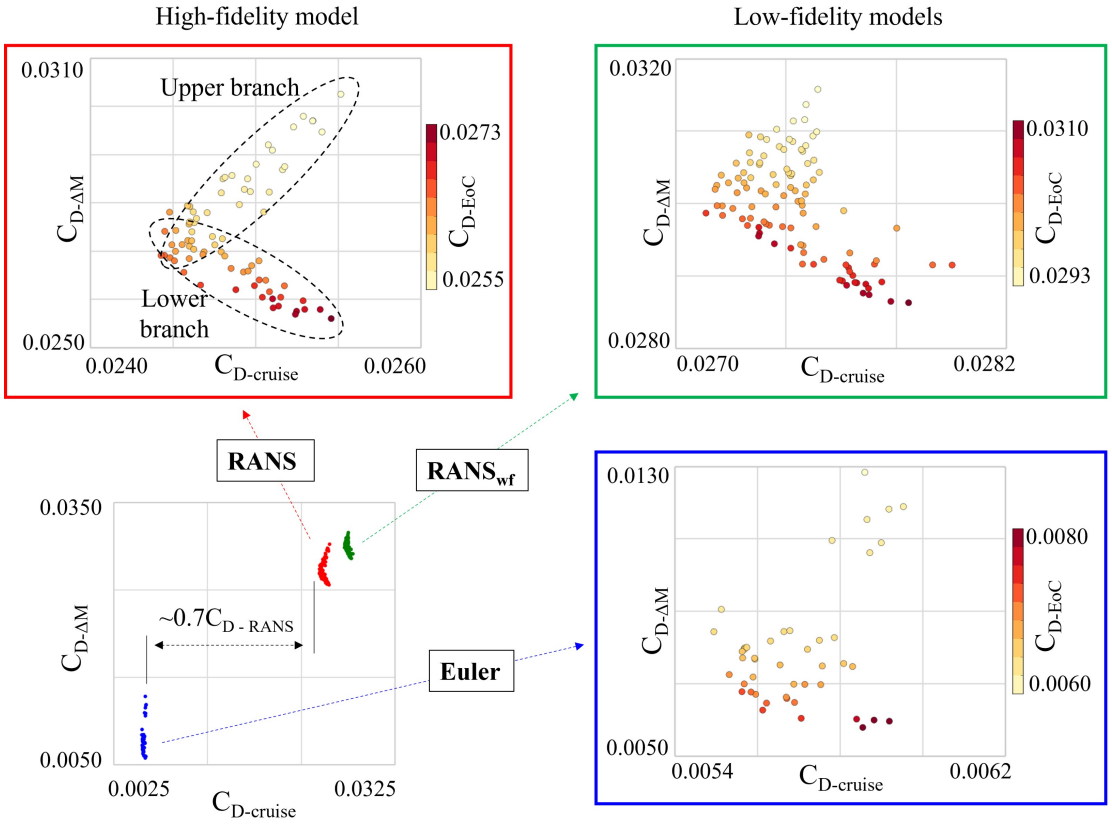

FIGURE 7.5: Comparison based on the performance metrics of the optimal design space for 2D axi-symmetric nacelles in isolated configuration obtained with the different CFD fidelities: RANS, RANS with wall functions and Euler.

Another approach to assess the optimal design space is through the distribution of the design variables of the non-dominated designs (Figure 7.6). In line with the previous results based on drag performances (Figure 7.5), both RANS models converge very closely to the same optimal part of the design space for f_{max}, r_{max}/r_{hi} and f_{if}. There is a slight difference on β_{nac} of less than 0.5° in the median value. The reason is that β_{nac} is less influential in the nacelle drag and therefore this parameter can have a higher variability in the optimal design space. This is in accordance with the conclusions of previous RANS CFD work in this area by Tejero et al.[16]. Overall, RANS and RANS$_{wf}$ are highly correlated. Conversely, the optimal design space reached by Euler is slightly different compared to the high-fidelity RANS model. While for f_{if} the agreement is quite good, there is an increase in the median for f_{max} and r_{max}/r_{hi} of around $0.05L_{nac}$ and $0.025r_{hi}$ respectively (Figure 7.6). As explained before, there is a substantially larger discrepancy for β_{nac} of around 4° in the median value.

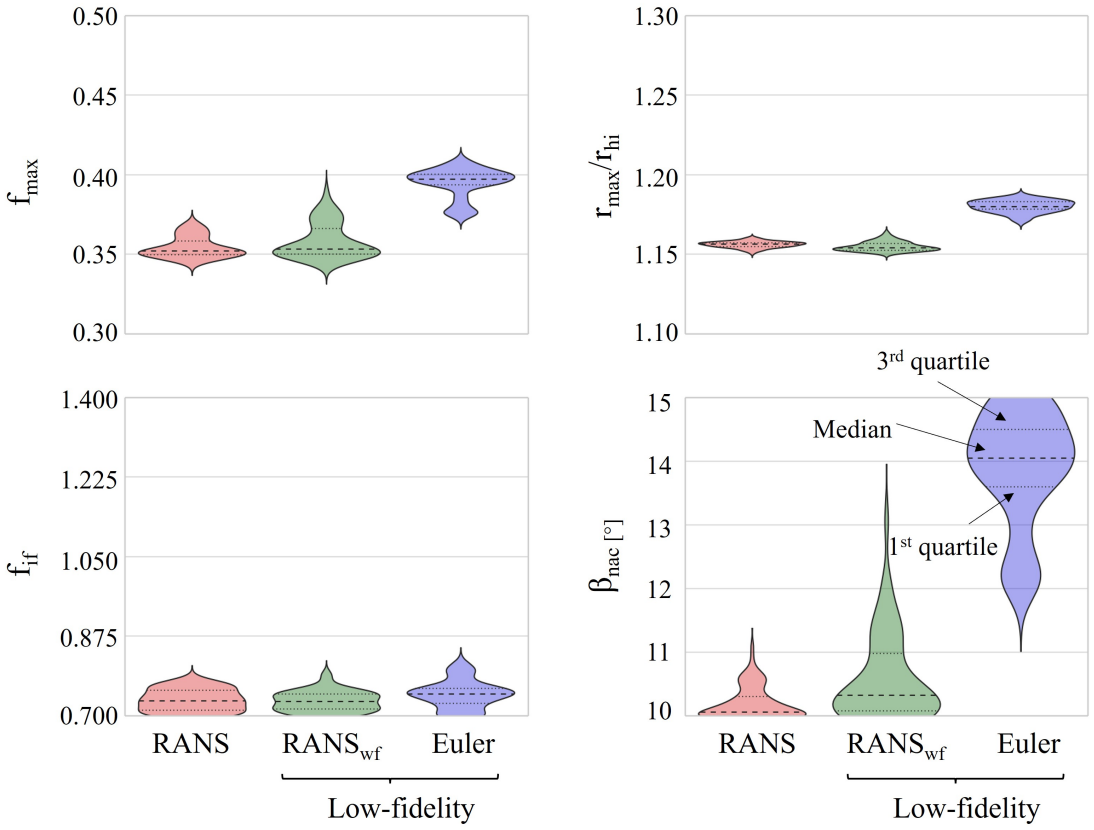

FIGURE 7.6: Comparison based on the design variables of the optimal design space for 2D axi-symmetric nacelles in isolated configuration obtained with the different CFD fidelities: RANS, RANS with wall functions and Euler.

Finally, a qualitative assessment of the optimal design space based on the combination of design variables and drag metrics is enabled through parallel coordinate plots (Figure 7.7). These plots show the distribution of the design variables in the optimal design space and how they are related to the performance metrics. Each line constitutes a non-dominated design which is coloured by the normalised nacelle drag for every condition. Additionally, each line shows the location of the corresponding design variables on the investigated design space from DOF_{min} to DOF_{max}. The interest is not on the absolute drag values but in the trends of drag with the design variables. RANS and RANS$_{wf}$ exhibit the same behaviour for each operating condition. Low drag values at cruise and end-of-cruise (EoC) are associated to the design variables closer to the lower bound (DOF_{min}) (Figure 7.7). The opposite trend is appreciated for the drag at the increased Mach number condition (ΔM). In terms of results obtained with the Euler model, the relation between drag and design variables is less apparent. This might be due to the reduced populated Pareto and less defined front in comparison with the RANS models.

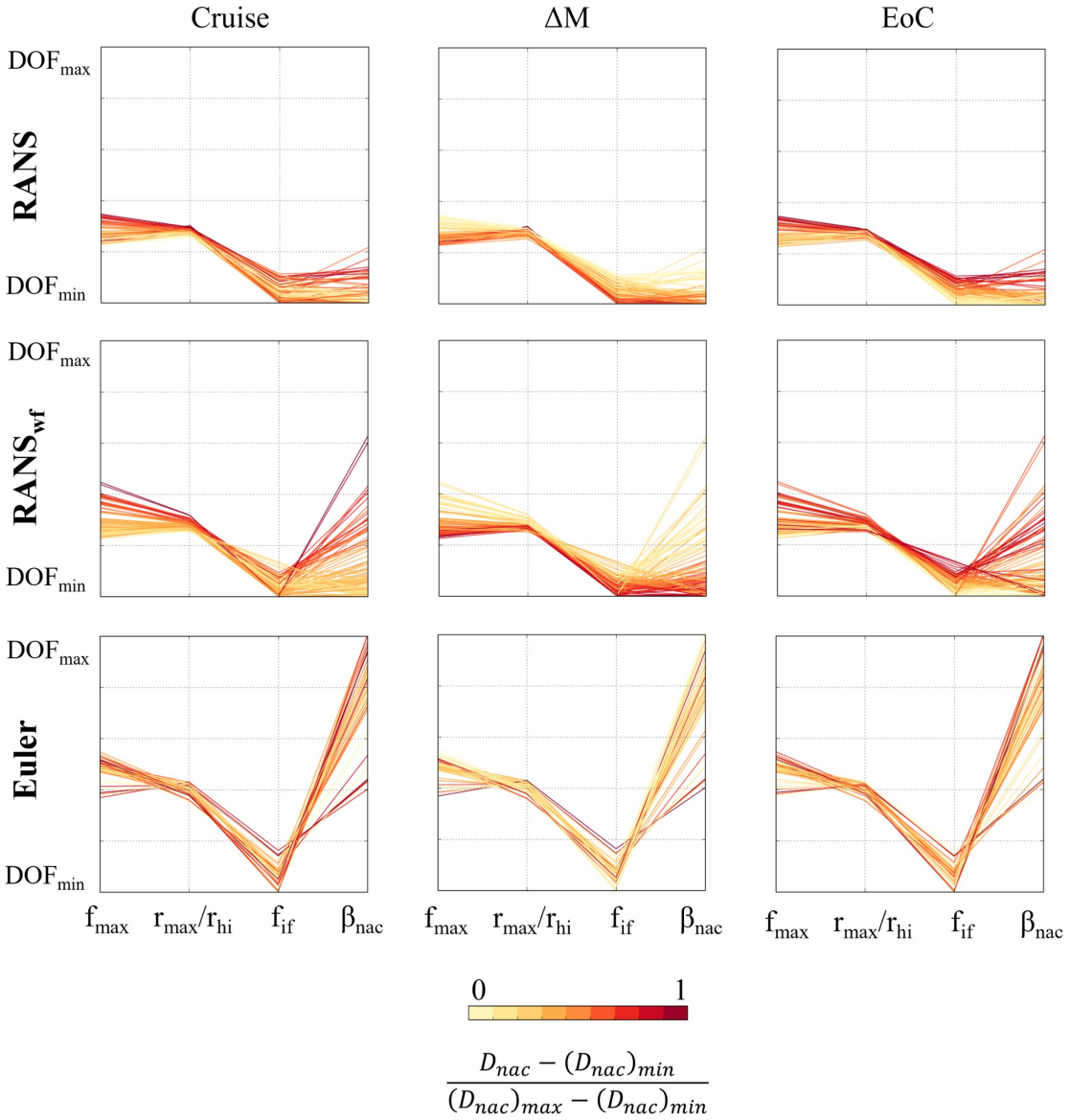

FIGURE 7.7: Comparison based on both the performance metrics and the design variables of the optimal design space for 2D axi-symmetric nacelles in isolated configuration obtained with the different CFD fidelities: RANS, RANS with wall functions and Euler.

7.3 Selection of the low-fidelity model

The two key aspects to select a low-fidelity model are the correlation level and the computational cost savings with respect to the high-fidelity model. These cost savings are assessed for the airframe-installed nacelle configuration. Relative to the high-fidelity RANS model, the RANS$_{wf}$ model reduces the overall computational cost of the CFD by a factor of 15 (Table 7.2). This involves both the time savings

in the grid generation and in the CFD simulation. However, a very similar aerodynamic prediction and convergence to the optimal design space is achieved with both RANS and RANS$_{wf}$. There is very little benefit of combining two different levels of fidelities within a multi-fidelity technique when both models are so correlated. On the other hand, the Euler low-fidelity model further reduces the overall computational overhead of a CFD case relative to RANS by a factor of 36 (Table 7.2) at the expense of a lower correlation level. Again, this cost saving accounts for both the grid generation and the simulation time. However, the deviations in the aerodynamics between the Euler and RANS models are acceptable and the optimisation does not converge to a totally different part of the design space. Therefore, the Euler model is selected as low-fidelity which will be combined and corrected with the high-fidelity RANS information within the multi-fidelity approach.

TABLE 7.2: Relative cost of the different CFD fidelities for airframe-installed nacelle assessments which involves both the grid generation and the CFD simulation.

	High-fidelity	Low-fidelity	
CFD model	RANS	RANS$_{wf}$	Euler
Cost	t	$t/15$	$t/36$

CHAPTER 8

Nacelle aerodynamic design and optimisation

This chapter addresses the aerodynamic design and optimisation of compact nacelles for UHBPR aero-engine configurations. Section 8.1 is focused on 2D axi-symmetric nacelles in isolated configuration. Due to the low computational overhead associated to these CFD calculations, this work is used as a building block to develop and establish the multi-fidelity neural network (MFNN) method (Section 4.6.2.2) for nacelle optimisations. The nacelle design and optimisation work for the airframe-installed configuration is presented in Section 8.2. It comprises the exploration of the design space and optimisation using different surrogate modelling techniques based on of both single-fidelity and multi-fidelity.

8.1 2D axi-symmetric isolated configuration

This section follows the methodology for the multi-point optimisation of 2D axi-symmetric nacelles in isolation presented in Section 4.5.2.2. A compact nacelle configuration given by $L_{nac}/r_{hi} = 3.1$ and $r_{te}/r_{hi} = 0.95$ is used. Four design variables are considered: r_{max}, f_{max}, r_{if} and β_{nac} (Figure 4.25). The nacelles are optimised to minimise drag at three operating conditions: the cruise point ($C_{D-cruise}$, Equation 4.39) and the sensitivities to both an increase in the Mach number ($C_{D-\Delta M}$, Equation 4.40) and a reduction in the engine MFCR (C_{D-EoC}, Equation 4.41). While a CFD-based approach is used in Section 8.1.1, a surrogate MFNN-based optimisation method is followed in Section 8.1.2.

8.1.1 CFD-in-the-loop optimisation

A CFD-in-the-loop optimisation approach (Figure 4.24a) is used with the RANS method detailed in Section 4.3.1.1.1. This is considered as the highest standard optimisation method in this project. The purpose of this RANS CFD-based optimisation for isolated nacelles is to find the region of the optimal design space and a design which can be compared with the results obtained from the MFNN-based optimisations in the next section. The optimal region of the design space is defined by all the non-dominated designs contained in the Pareto front (Figure 8.1a). In terms of f_{max} and r_{max}, this region is located between 20% and 30% of the normalised design space that is investigated (Figure 8.1b). r_{if} and β_{nac} show a slightly larger variability and are located below the 20% of the normalised bounds. In particular, β_{nac} is essentially located in the lower bound of the investigated design space (Figure 8.1b). The lower bound for β_{nac} considered in this work is constrained to avoid geometry intersection between the nacelle trailing edge and the bypass duct of the exhaust.

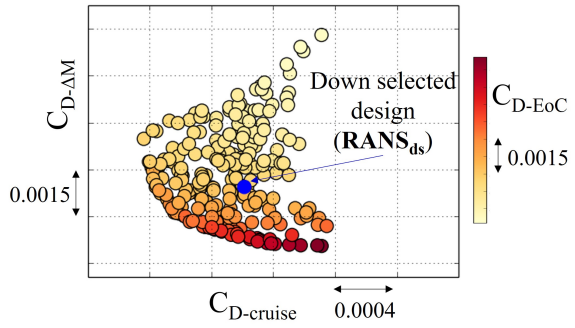

(A) Optimal region of the design space represented on the drag performance metrics (Pareto front). Down selected design marked in blue.

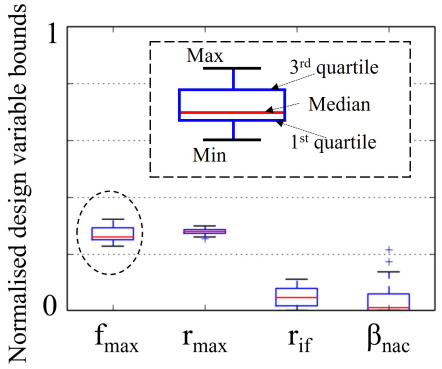

(B) Optimal region of the design space represented on the design variables.

FIGURE 8.1: Optimal region of the design space for 2D axi-symmetric nacelles in isolated configuration using the CFD-based optimisation approach.

From the set of designs that constitute the Pareto front and define the optimal region of the design space, one nacelle geometry is down selected which is called $RANS_{ds}$ (Figure 8.1a). The down selection criterion targets a minimum cruise drag while ensuring aerodynamic robustness to changes in the Mach number and MFCR by maintaining low drag ratios between the conditions in the cruise segment. More explicitly, $RANS_{ds}$ is the design with the minimum cruise drag from the sets of designs that fulfil $C_{D-\Delta M}/C_{D-cruise} < 1.1$ and $C_{D-EoC}/C_{D-cruise} < 1.1$.

This design is perturbed with changes on each design variable to understand the sensitivities on the optimal design space. The perturbations are applied for each design variable independently. The magnitude of the changes are of 40% of the design space investigated for each variable (Figure 8.2). Every design is evaluated using the RANS CFD model. The impacts of each perturbation on the nacelle drag at cruise, increased Mach number and end-of-cruise conditions are quantified relative to the down selected $RANS_{ds}$ design. The results show that f_{max} and r_{max} are the dominant parameters with changes on the nacelle drag of up to 80% (Figure 8.2a) and 90% (Figure 8.2b) respectively. Conversely, there is a much lower impact of r_{if} and β_{nac} on the optimal design space with maximum changes of 15% in nacelle drag (Figure 8.2c, Figure 8.2d). This results are in line with the conclusions of previous RANS CFD work in this area by Tejero et al.[16].

8.1.2 Multi-fidelity surrogate-based optimisations

The surrogate modelling technique used in this section for isolated nacelle optimisations is the multi-fidelity neural networks (MFNN) which was explained in Section 4.6.2.2 and verified with benchmark functions in Appendix D. The implementation of this technique and application for this aerodynamic shape optimisation problem constitute a novelty of this research. As concluded in Chapter 7, the RANS and Euler CFD models are used as high- and low-fidelity respectively. Given the low cost of RANS calculations for 2D axisymmetric isolated nacelle configurations, the reduction in the overall overhead associated to the lower fidelity Euler model is modest. A reduction in the cost by a factor of 1.54 is obtained which considers both the saving in the grid generation and in the numerical simulation (Table 8.1). The lower computational cost of RANS CFD calculations for 2D axi-symmetric nacelles in isolation compared to other configurations enables the establishment of the method. Additionally, the impact of the ratio of number of samples to degree of freedom for each CFD fidelity is systematically assessed. Although the objective of the multi-fidelity optimisation method is to be applied to airframe-installed configurations, this development work for the 2D isolated case is considered as a valid approach since the flow physics are similarly compressible, transonic and non-linear.

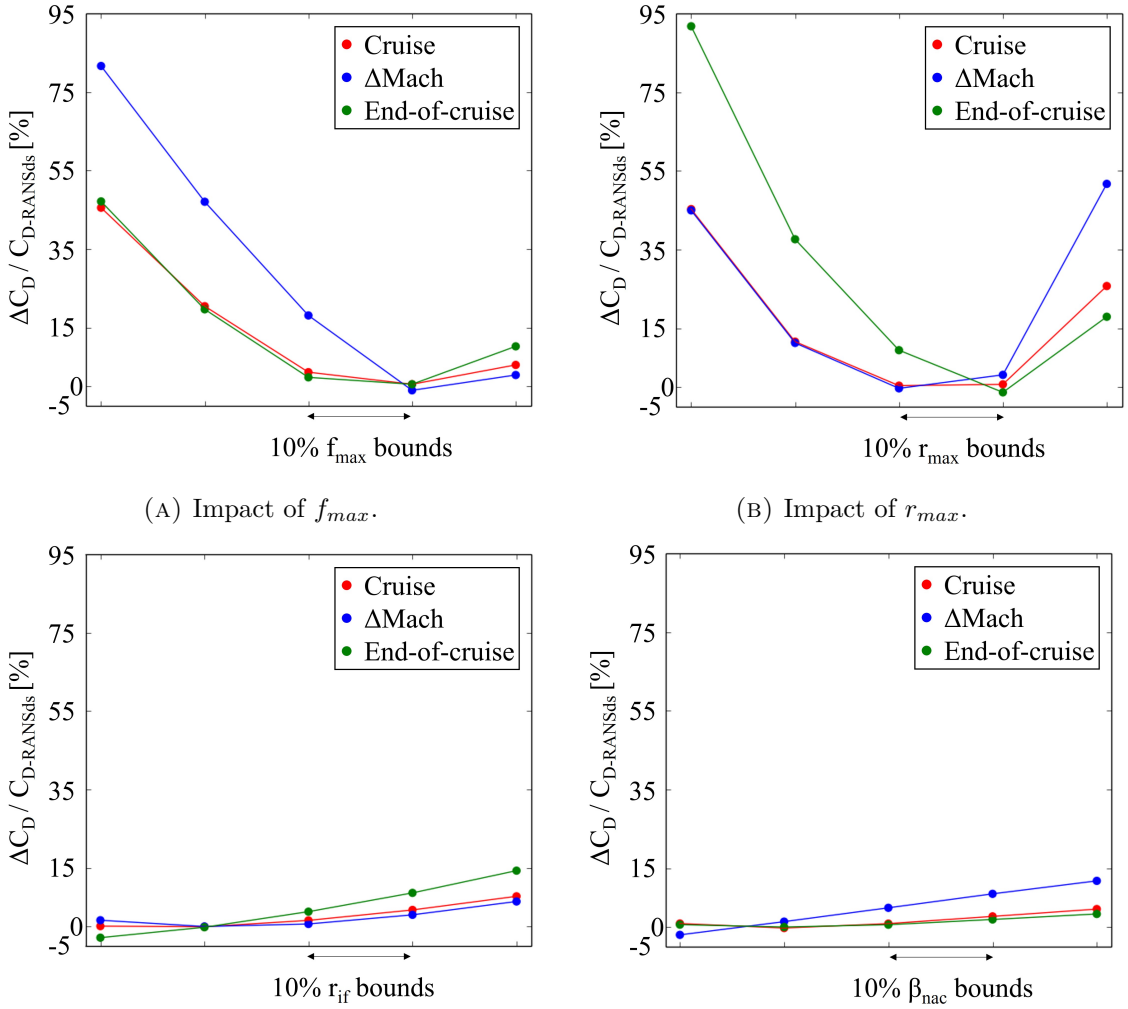

(A) Impact of f_{max}.

(B) Impact of r_{max}.

(C) Impact of r_{if}.

(D) Impact of β_{nac}.

FIGURE 8.2: Sensitivity of the optimal design space to changes in the design variables. Perturbations applied to the down selected design from the CFD-based optimisation ($RANS_{ds}$) of up to 40% of the investigated bounds.

TABLE 8.1: Relative cost of the different high-fidelity RANS and low-fidelity Euler CFD methods for 2D axisymmetric isolated nacelle assessments which involves both the grid generation and the CFD simulation.

	High-fidelity	Low-fidelity
CFD model	RANS	Euler
Cost	t	$t/1.54$

8.1.2.1 Tuning of the hyperparameters of the models

The hyperparameters of a surrogate model refer to the set of degrees of freedom available to tune the model. One characteristic of the surrogate modelling technique based on artificial neural networks (ANN) is that the optimal combination of

hyperparameters is highly dependant on the problem. The tuning process requires a large number of combination of the different parameters with enough variability in each one to ensure that the optimal combination is captured. Consequently, the model construction may become computationally expensive. This is even more critical for the MFNN technique as it involves different interconnected ANN (Section 4.6.2.2). Therefore, there are more hyperparameters to combine and the cost to find the optimal model grows exponentially.

In this section, the objective is to assess the sensitivity of some hyperparameters on the model performance allowing a wide variability on each parameter. This helps to identify the region of interest for each parameter and narrow down the bounds used in the optimisation of the surrogate models. This study is focused on the Euler ANN which includes 4 hyperparameters: the activation function, the number of hidden layers, the number of neuron per layer and the L2 regularization factors (Figure 8.3). Due to the increased computational cost associated to the large number of hyperparameters of the full MFNN architecture, the conclusion obtained from just the Euler ANN are extended for the corresponding hyperparameters of the linear and non-linear RANS ANN (Figure 8.3).

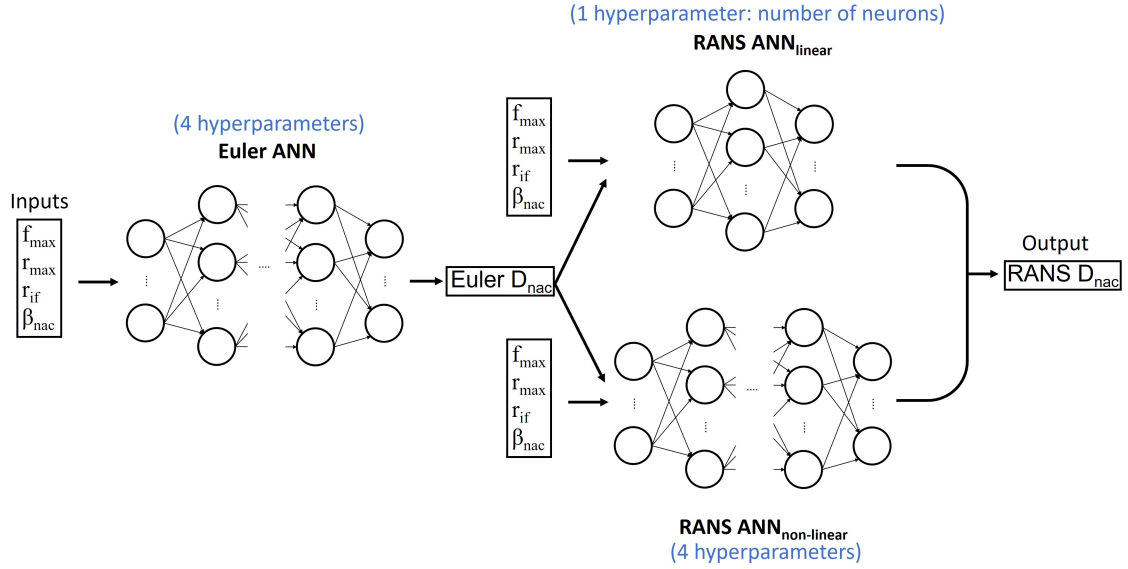

FIGURE 8.3: Multi-fidelity neural network architecture applied for the drag of a 2D axi-symmetric nacelle in isolated configuration.

In this sensitivity analysis, three of the most common activation functions are used: ReLu, sigmoid and hyperbolic tangent (Table 4.7). A range of networks architectures are built for each activation function. The number of hidden layers and neurons per layer varied from 2 to 8 and 10 to 320 respectively. Moreover, for each of the resulting combinations, different L2 regularization factors are considered which range

from 10^{-3} to 10^{-6}. In this study, two sizes of the training data set are considered with ratios of number of low-fidelity (Euler) samples to degrees of freedom of $N_{LF}/N_{DOF} = 100$ and 12.5. This shows the impact of the population size used to train the model on the guidelines extracted for the hyperparameters. The data sets are sampled using the LHS technique introduced in Section 4.5.1.1 and evaluated with the Euler CFD model detailed in Section 4.3.2. The RMSE (Equation 4.48) evaluated in a common validation data set of size $N_{LF}/N_{DOF} = 50$ is used to assess the prediction performance of the models created with each combination of parameters. The assessment addresses the drag prediction for the three operating conditions considered in the optimisation method: cruise, the sensitivity to an increased Mach number (ΔMach) and the sensitivity to a reduced MFCR (End-of-cruise).

For this aerodynamic design problem, the ReLu activation function outperforms the hyperbolic tangent and sigmoid functions regardless of the operating condition and sample ratio N_{LF}/N_{DOF} (Figure 8.4, Figure 8.5). Using the cruise condition for $N_{LF}/N_{DOF} = 100$ as example, while the sigmoid and hyperbolic tangent functions in general produce models with RMSE above 30%, ReLu is able to generate models with RMSE lower than 5% (Figure 8.4). The same happens for $N_{LF}/N_{DOF} = 12.5$ although the minimum RMSE values for ReLu are increased to around 12% due to a reduced size of the training data set (Figure 8.5). In terms of the neural network architecture complexity, there is always a trade-off between good modelling performances and overfitting[242,249]. More neurons and hidden layers tend to improve the model accuracy but may cause the model to overfit. Low L2 regularization factors help to avoid overfitting. Based on this and on the motivation to narrow down the bounds to reduce the computational cost, a decision is made for the hyperparameters training space to be exploited in subsequent models. Overall, the best modelling performance are found for a number of neurons per hidden layers between 160 and 320 (Figure 8.4, Figure 8.5). The number of hidden layers is kept between 2 to 4. This avoids the risk to overfitting by making the model more complex and reduces the training cost. Regularization factors from 10^{-6} to 10^{-5} are selected (Figure 8.4, Figure 8.5). The same conclusions are drawn for the three operating conditions considered in this work: cruise, ΔMach and end-of-cruise. This highlights the low dependence of any specific hyperparameter of the neural network on the different flow physics to model. Overall, the same guidelines are obtained for both $N_{LF}/N_{DOF} = 100$ and 12.5 (Figure 8.4, Figure 8.5). Therefore the selected bounds for the hyperparameters are used in the study of the impact of the number of sample in the next section.

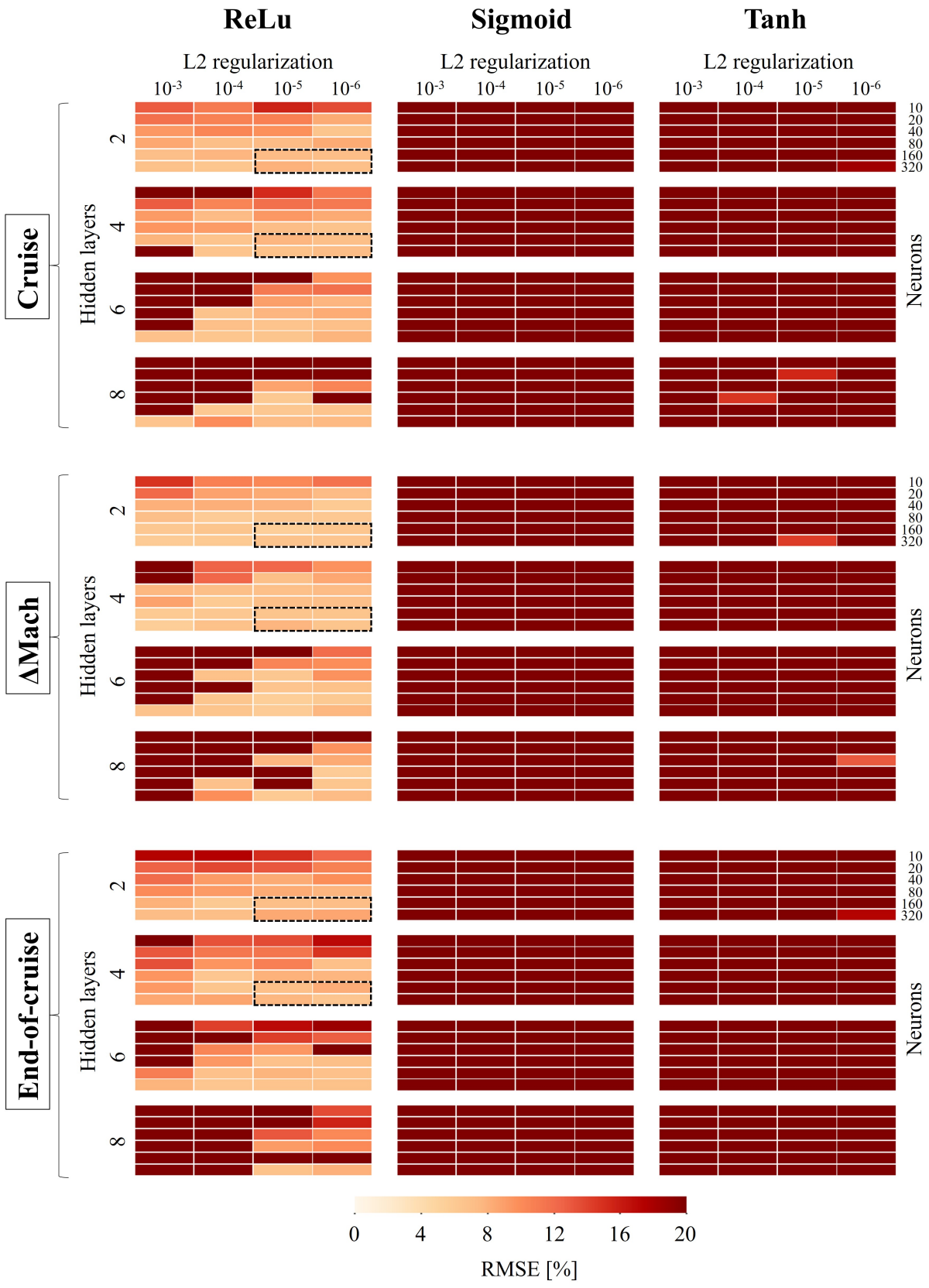

FIGURE 8.4: Hyperparameter sensitivity analysis based on the low-fidelity (Euler) ANN for the different operating conditions. Ratio of samples to degrees of freedom of $N_{LF}/N_{DOF} = 100$. Selected region of interest for hyperparameters marked with dashed black rectangle.

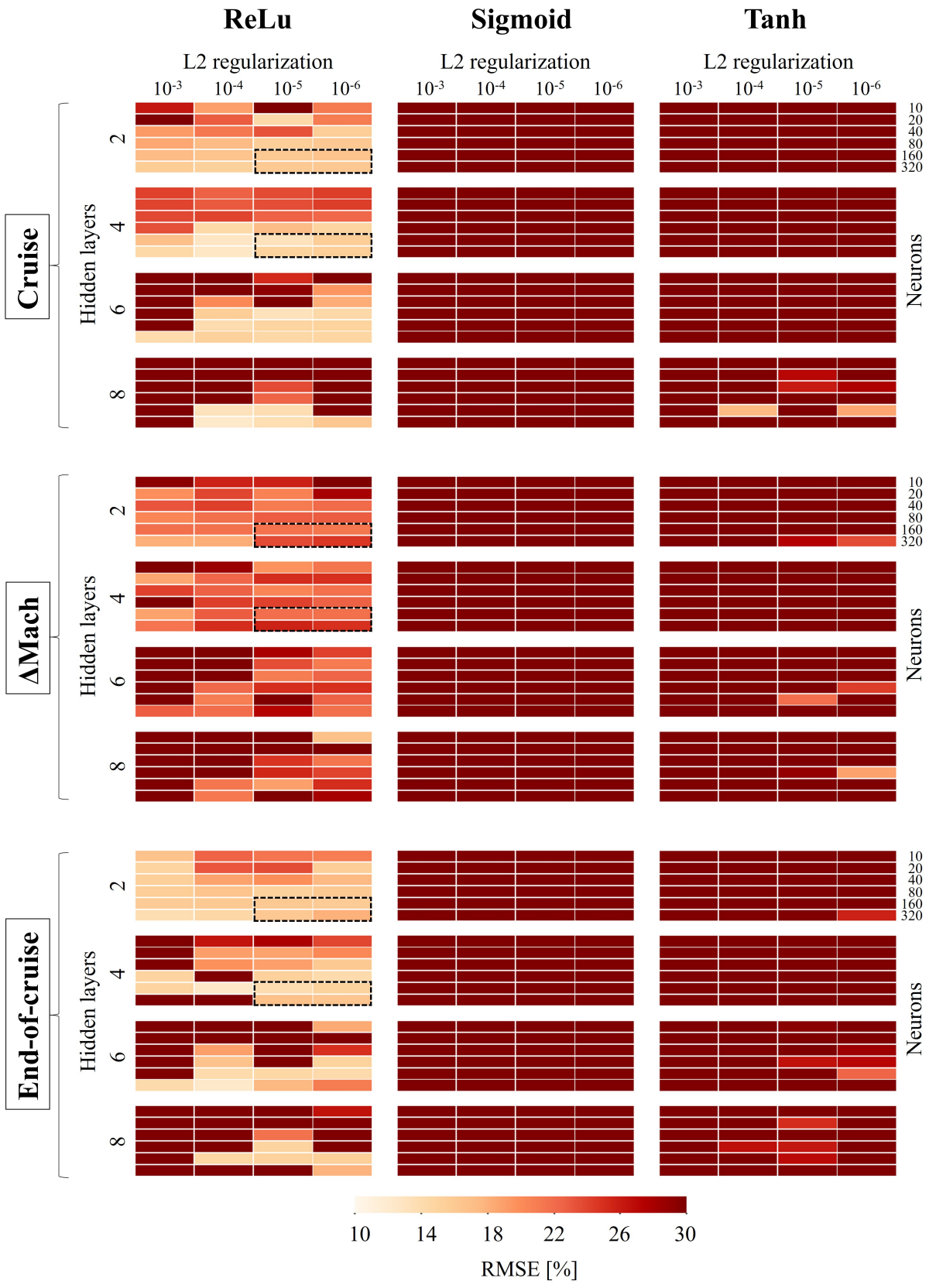

FIGURE 8.5: Hyperparameter sensitivity analysis based on the low-fidelity (Euler) ANN for the different operating conditions. Ratio of samples to degrees of freedom of $N_{LF}/N_{DOF} = 12.5$. Selected region of interest for hyperparameters marked with dashed black rectangle.

8.1.2.2 Impact of the number of samples

In the field of multi-fidelity modelling, the ratios of the number of low- and high-fidelity samples to degree of freedom (N_{LF}/N_{DOF} and N_{HF}/N_{DOF}) play a key role. These parameters have a substantial impact on the performance of the surrogate model and the overall computational cost required to build the model[250,251] and trade-offs are normally needed. In this work, the impact of N_{LF}/N_{DOF} and N_{HF}/N_{DOF} are assessed for MFNN models that predict drag of 2D axi-symmetric nacelles in isolation at cruise, ΔMach and end-of-cruise conditions. N_{HF}/N_{DOF} is ranged from 6.25 to 100 and N_{LF}/N_{DOF} from 0 to 100 (Figure 8.6). $N_{LF}/N_{DOF} = 0$ is used to consider the single-fidelity neural network (SFNN) cases based on RANS. This helps to understand the benefits of introducing low-fidelity (Euler) data in the modelling performance and computational cost. A different training data set is generated using the LHS technique and evaluated using the corresponding RANS or Euler CFD model for each N_{HF}/N_{DOF} and N_{LF}/N_{DOF} ratios. This results in 5 RANS and Euler training data sets.

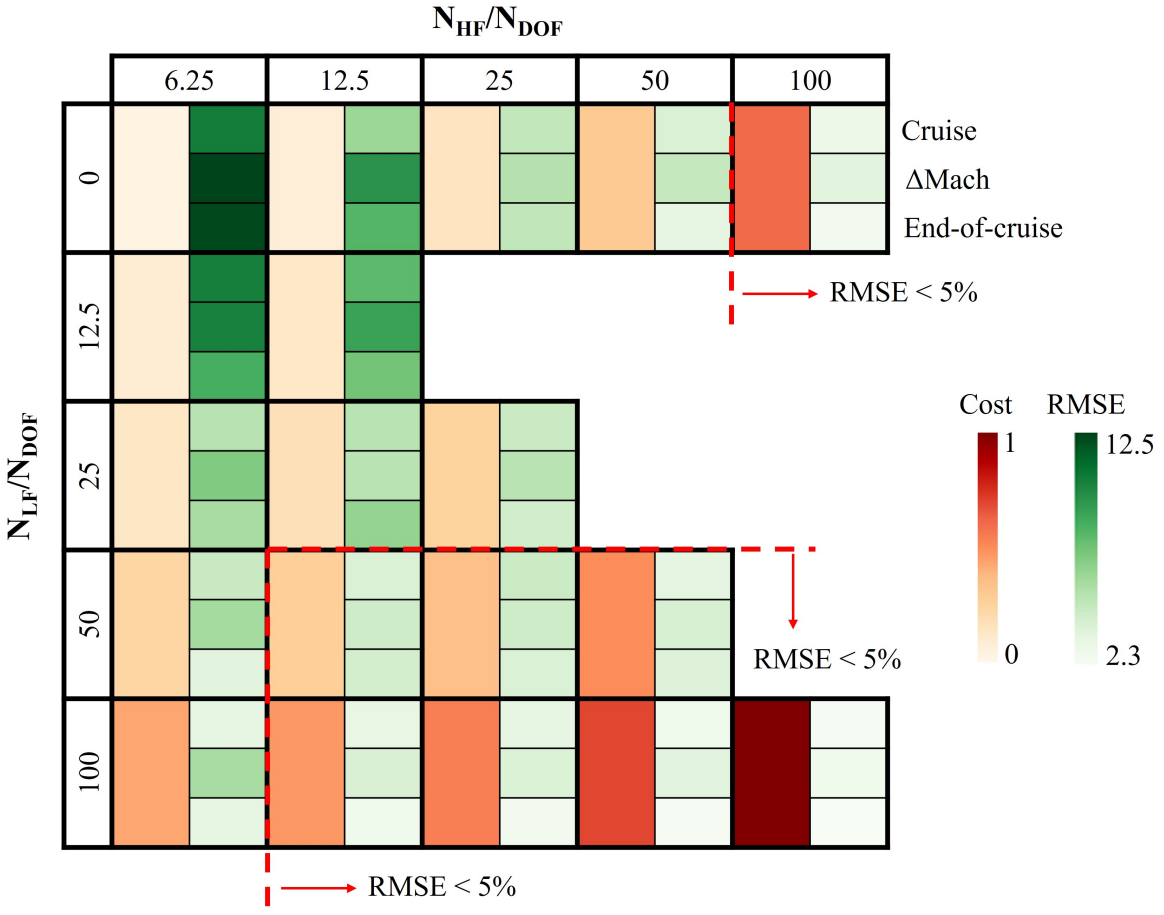

FIGURE 8.6: Impact of the number of low- and high-fidelity samples on the computational cost and RMSE of the MFNN surrogate model.

For each combination of the different N_{LF}/N_{DOF} and N_{HF}/N_{DOF} ratios, a MFNN surrogate model is generated. The guidelines and bounds obtained in Section 8.1.2.1 for the different hyperparameters are used to optimise each surrogate model. This model optimisation process to find the best modelling performance is based on the minimisation of the RMSE (Equation 4.48) evaluated on an independent validation data set (Section 4.6.3). For this purpose, a low- and a high-fidelity data sets of $N_{LF}/N_{DOF} = N_{HF}/N_{DOF} = 50$ are generated.

There is always an opposite trend between the model prediction performance and the associated computational overhead. As the number of samples to train the model becomes larger, the RMSE of the model on the validation data set decreases but the computational cost increases (Figure 8.6). As could be expected, there is a higher gradient in the change of the computational cost with N_{HF}/N_{DOF} than with N_{LF}/N_{DOF}. However, there is no such difference in the gradient of the RMSE of the models. This highlights the benefit of including the low-fidelity data to build the MFNN model with respect to the SFNN-RANS model. This means that similar modelling performance can be obtained between the MFNN and SFNN-RANS techniques with a reduction of the computational overhead for the MFNN case (Figure 8.6). A common error threshold for preliminary design stages is 5-10%[243]. As low-order models are typically used for preliminary design, a maximum RMSE of 5% is considered as acceptable in this work to be more restrictive. For the SFNN-RANS modelling technique, RMSE<5% is met for $N_{HF}/N_{DOF} = 100$ (Figure 8.6). In the case of the MFNN method, a RMSE<5% is obtained with the lowest computational cost for the combination given by $N_{LF}/N_{DOF} = 50$ and $N_{HF}/N_{DOF} = 12.5$. Between both models of similar prediction ability ($\sim 5\%$), the MFNN one reduces the cost by a factor of 2.2 relative to the SFNN-RANS model.

The impact of the sample ratios is also assessed based on the convergence to the optimal region of the design space. A surrogate-based optimisation (Figure 4.24b) is evaluated with each model previously generated from the different combinations of N_{LF}/N_{DOF} and N_{HF}/N_{DOF}. The optimal region of the design space obtained for each optimisation is compared with the results from the RANS CFD-in-the-loop optimisation showed in Section 8.1.1. This RANS CFD-based optimisation is considered as the highest standard for 2D axi-symmetric nacelles in isolation within this project. The optimisation set-ups of the CFD-based and surrogate-based optimisations are the same in order to be comparable.

The comparison of the optimal region of the design space is focused on the design variables (f_{max}, r_{max}, r_{if} and β_{nac}) of the non-dominated designs (Pareto front)

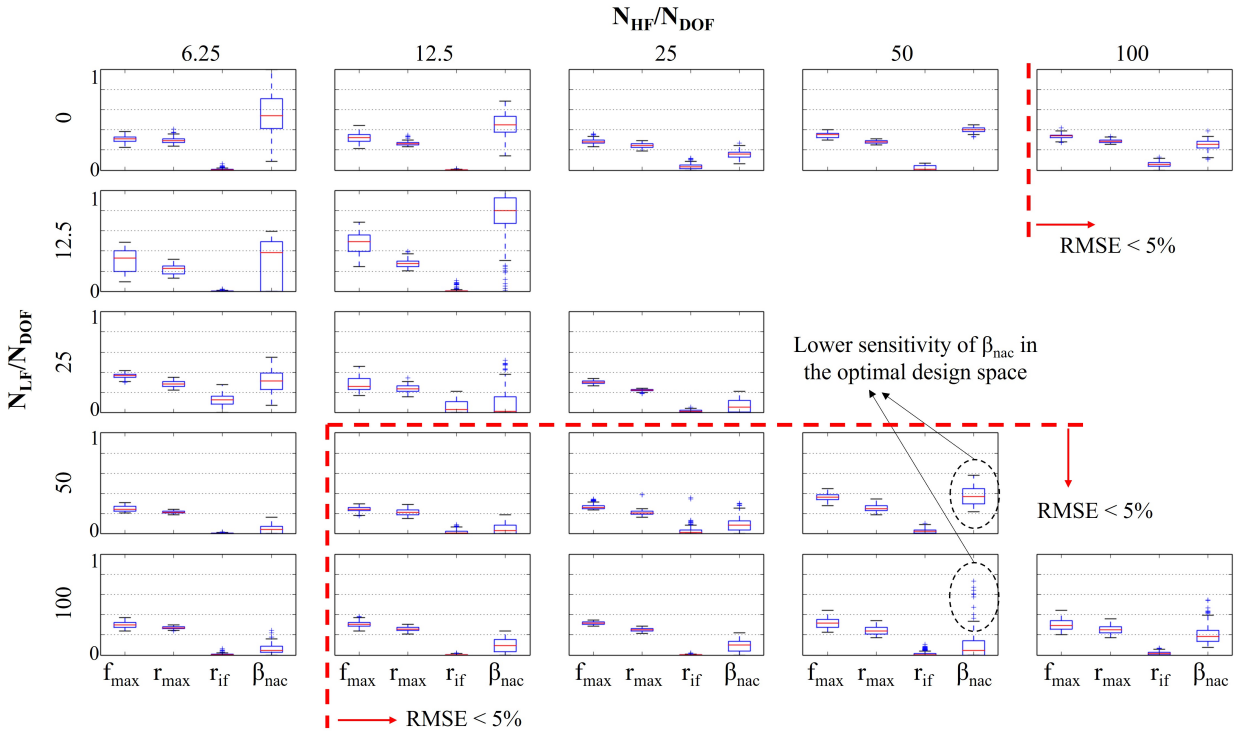

FIGURE 8.7: Region of the optimal design space for 2D axi-symmetric nacelles in isolated configuration obtained with the surrogate-based optimisation approach for each combination of low- and high-fidelity samples of the MFNN technique.

(Figure 8.7). For both $N_{LF}/N_{DOF} \leq 12.5$ and $N_{HF}/N_{DOF} \leq 12.5$, the optimisations lead to a substantially different part of the design space compared to the CFD-based reference (Figure 8.1b compared to Figure 8.7). Although the optimal design space is similar for r_{max}, both f_{max} and β_{nac} show a higher variability across the investigated design space for some cases. For example, the median of the distribution for f_{max} can deviate from the CFD-based results up to 10% of the investigated design space and up to 80% for β_{nac}. Although the sensitivity of the nacelle drag on β_{nac} is substantially lower compared to r_{max} and f_{max} (Figure 8.2), a deviation of 80% in the geometry for β_{nac} is not considered acceptable. These differences for $N_{LF}/N_{DOF} \leq 12.5$ and $N_{HF}/N_{DOF} \leq 12.5$ can be explained by the limited predicting performance of the surrogate models (overall RMSE>8%) caused by a sparse training data set (Figure 8.6). An increase in N_{HF}/N_{DOF} to over 25 (using the SFNN-RANS models) corrects some deviations in the optimal design space at the expense of a considerable increase in the computational cost required to build the models. The variability on the distributions of f_{max} and β_{nac} is substantially reduced (Figure 8.7). As in the CFD-based optimisation, the median of f_{max} is around 30% of the investigated design space. There are still differences for β_{nac} with a deviation on the median of around 40%. Again this can be explained by the lower

correlation between β_{nac} and the nacelle drag.

On the other hand, $N_{LF}/N_{DOF} = 50$ is enough for an acceptable approximation of the optimal region of the design space regardless of the high-fidelity sample size N_{HF}/N_{DOF} (Figure 8.7). Consistent results are obtained for the dominant nacelle parameters f_{max} and r_{max} which are very close to the CFD-based results (Figure 8.1b). The median value of β_{nac} is consistently below 20% of the investigated design space except for the case given by $N_{LF}/N_{DOF} = N_{HF}/N_{DOF} = 50$ (Figure 8.7). However, the trends of β_{nac} with the sample ratios are maintained and a certain variability on the distribution is accepted due to the lower correlation of this geometrical parameter with nacelle drag. Finally, r_{if} is generally located between 0-10% of the investigated designs space (Figure 8.7) which is in accordance with the results from the CFD-in-the-loop optimisation (Figure 8.1b). For some cases, r_{if} is trapped in the lower bound of the investigated design space. However, as β_{nac}, the variability in r_{if} has a low impact on the nacelle drag (Figure 8.2) and therefore a certain variability on r_{if} is accepted which is not higher than 10% in any case.

Overall, based on the previous analyses, $N_{LF}/N_{DOF} = 50$ and $N_{HF}/N_{DOF} = 12.5$ is selected as the combination with the lowest computational cost that provides both acceptable surrogate model accuracy (RMSE $< 5\%$, Figure 8.6) and a similar convergence to the optimal design space as the equivalent CFD-in-the-loop optimisation (Figure 8.7). This surrogate-based optimisation approach provides a reduction in the overall computational cost of 92% relative to the RANS CFD-in-the-loop method.

8.1.2.3 Down selected design and benefits

To assess the prediction performance of the selected MFNN model ($N_{LF}/N_{DOF} = 50$ and $N_{HF}/N_{DOF} = 12.5$) in the optimal region of the design space, a cross-validation study shows the agreement between the surrogate model predictions and the corresponding RANS CFD results for the designs contained in the Pareto front (Figure 8.8). For each model at every flight condition, most of the designs are within the $\pm 5\%$ bounds. The model RMSE for the cruise, ΔMach and end-of-cruise conditions is reduced from approximately 5% in the full validation data set (Figure 8.6) to 1.40%, 2.5% and 1.6% respectively in the optimal region of the design space. This highlights the reliability of the MFNN model in the down selection of the optimal design.

A nacelle design from the chosen MFNN-based optimisation in the previous section ($N_{LF}/N_{DOF} = 50$ and $N_{HF}/N_{DOF} = 12.5$) is down selected. The purpose is to

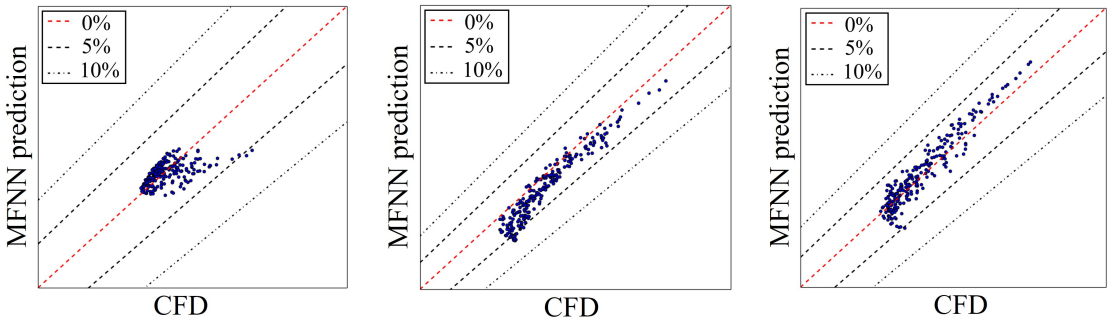

(A) Cruise. (B) Increased Mach number. (C) End-of-cruise.

FIGURE 8.8: Cross-validation based on the optimal region of the design space (Prateo front) of the selected MFNN model ($N_{LF}/N_{DOF} = 50$ and $N_{HF}/N_{DOF} = 12.5$) by comparing the model prediction with the RANS CFD results.

compare the drag benefits, geometry and the aerodynamics of this design with the corresponding down selected design from the CFD-in-the-loop optimisation (Section 8.1.1). As explained at the beginning of Section 8.1, the design with minimum cruise drag that meets the sensitivity ratios of $C_{D-\Delta M}/C_{D-cruise}$ and $C_{D-EoC}/C_{D-cruise}$ lower than 1.1 is down selected[252] (Equation 4.42). The down selection criteria is applied to the non-dominated designs contained in the Pareto front (Figure 8.9). The Pareto fronts that result from the CFD-in-the-loop optimisation (Figure 8.9a) and the MFNN-based optimisation method (Figure 8.9b) show a similar relationship between metrics. While the drag data on the CFD-based Pareto come from RANS CFD calculations, the drag on the surrogate-based Pareto is predicted with the MFNN model. For both down selected designs evaluated using RANS CFD calculations, similar drag reductions at each operating condition relative to an initial baseline design $\Delta C_D = (C_{D-selected} - C_{D-baseline})/C_{D-baseline}$ are obtained with a difference of 1% (Table 8.2).

TABLE 8.2: Drag benefit at every operating condition for the down selected designs from the CFD-in-the-loop and MFNN-based optimisations relative to an initial baseline design. Drag differences evaluated using RANS CFD for every case.

	$\Delta C_{D-cruise}$	$\Delta C_{D-\Delta M}$	ΔC_{D-EoC}
CFD-in-the-loop	-6%	-21%	-1%
MFNN-based	-7%	-22%	0%

In terms of design variables, there is a good agreement between the geometries of the two down selected designs. Relative to the CFD-in-the-loop optimal geometry,

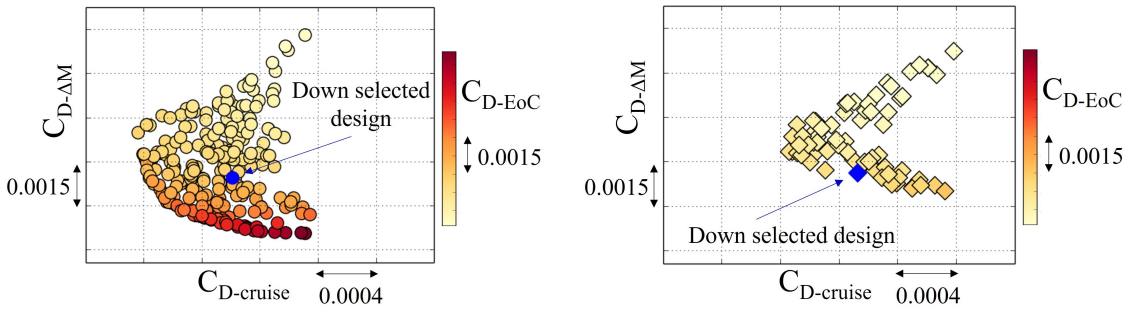

(A) CFD-in-the-loop approach. Drag data from RANS CFD.

(B) MFNN-based approach. Drag data from MFNN prediction.

FIGURE 8.9: Pareto fronts and down selected designs from the optimisations of 2D axi-symmetric nacelles in isolated configuration using the CFD-in-the-loop and MFNN-based approaches.

the MFNN-based down selected design shows a reduction in f_{max}, r_{max} and r_{if} of $0.008L_{nac}$, $0.012r_{hi}$ and $0.003r_{hi}$ respectively. Similar flow physics are obtained for both nacelle designs using a RANS CFD evaluation (Figure 8.10). A slight over-prediction of approximately 0.1 in the peak isentropic Mach number is apparent for the MFNN-based design which is caused by the $0.003r_{hi}$ reduction in r_{if}. At the cruise condition, the same flow topology is exhibited by both geometries. The flow reacceleration close to the nacelle crest is captured in the aerodynamics of both designs with a reduction in the axial extent of approximately $0.05L_{nac}$ (Figure 8.10). The same flow topology is also captured for the ΔMach operating condition with a forward movement of the shock of $0.05L_{nac}$ approximately for the MFNN-based selected design (Figure 8.10). For the end-of-cruise operating condition, similar shock location and pre-shock Mach number are obtained with both designs. There is a slight underprediction in the flow reacceleration after the shock of $0.05M_{is}$ approximately for the surrogate-based design (Figure 8.10). Overall, similar geometry with similar flow physics and drag performance benefits are obtained with both optimisation approaches with a significant reduction of 92% in the computational cost for the proposed MFNN optimisation method.

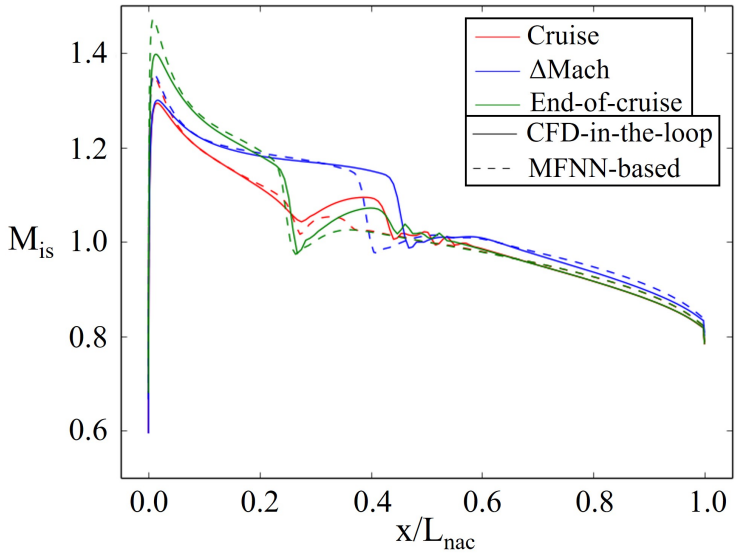

FIGURE 8.10: Comparison of the isentropic Mach number (M_{is}) distributions for the down selected designs using the CFD-in-the-loop and MFNN-based optimisation approaches for the cruise, ΔMach and end-of-cruise conditions. Aerodynamic obtained from a RANS CFD calculation.

8.2 Installed non-axisymmetric configuration

This section addresses the design and optimisation of non-axisymmetric aero-engine nacelles in the airframe-installed configuration using the method presented in Sections 4.5.1 and 4.5.2.3. RANS and Euler CFD fidelities are used in this design work as high- and low-fidelity respectively. Initially, the design space is investigated for the cruise condition with the focus on both the geometry design variables and the performance metrics of the nacelles (Section 8.2.1). This provides a better understanding of the design problem and delivers design guidelines. Subsequently, Section 8.2.2 shows the results of the different surrogate-based optimisations using single- and multi-fidelity techniques.

In this work an UHBPR-type of aero-engine is considered with a compact configuration given by $L_{nac}/r_{hi} = 3.1$ and $r_{te}/r_{hi} = 0.95$. A typical installation position is used: $dx/C^{inst}_{wing} = 0$ and $dz/C^{inst}_{wing} = 0.1$ (Section 4.1.2, Figure 4.4). For this configuration, a baseline nacelle geometry is used to assess performance improvements of the optimised designs. This baseline nacelle is down selected from the isolated multi-point and multi-objective optimisation undertaken under the ANACO project by Tejero et al.[245]. A modified version of the ANACO down selection method that was presented in Section 5.1 is used to select the baseline. The threshold of $0.1L_{nac}$

in the flow separation extent is evaluated in the full azimuth of the nacelle rather than just in the parameterisation aero-lines as was considered in ANACO. Relative to this baseline design, 9 design variables are changed within the design and optimisation process (Section 4.5.2.3). These design parameters are r_{max}, f_{max} and β_{nac} (Figure 8.11b) in the 3 inboard aero-lines $\Psi = 45°$, $90°$ and $135°$ (Figure 8.11a). Intake offset and scarf angle ($\theta_{scarf} = 5°$) are kept fixed for every design.

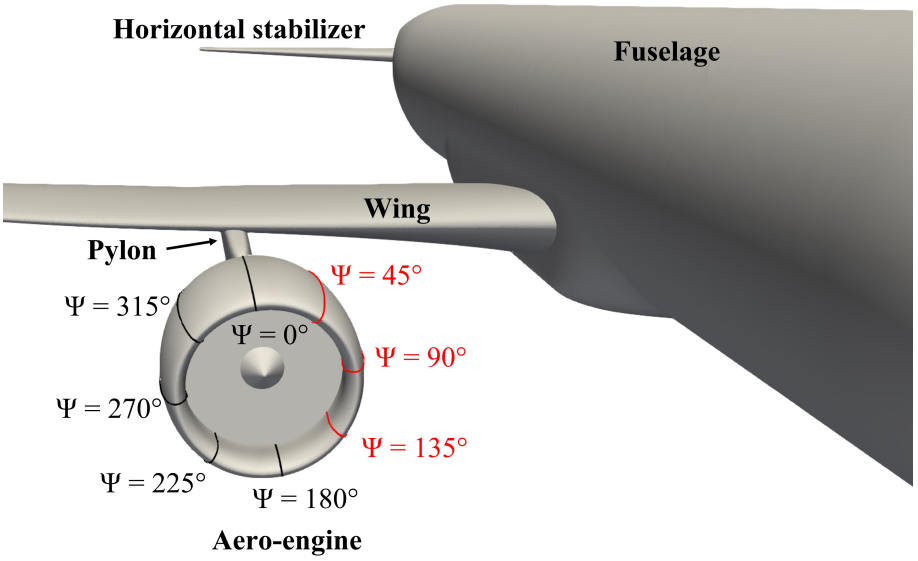

(A) Azimuthal aero-lines.

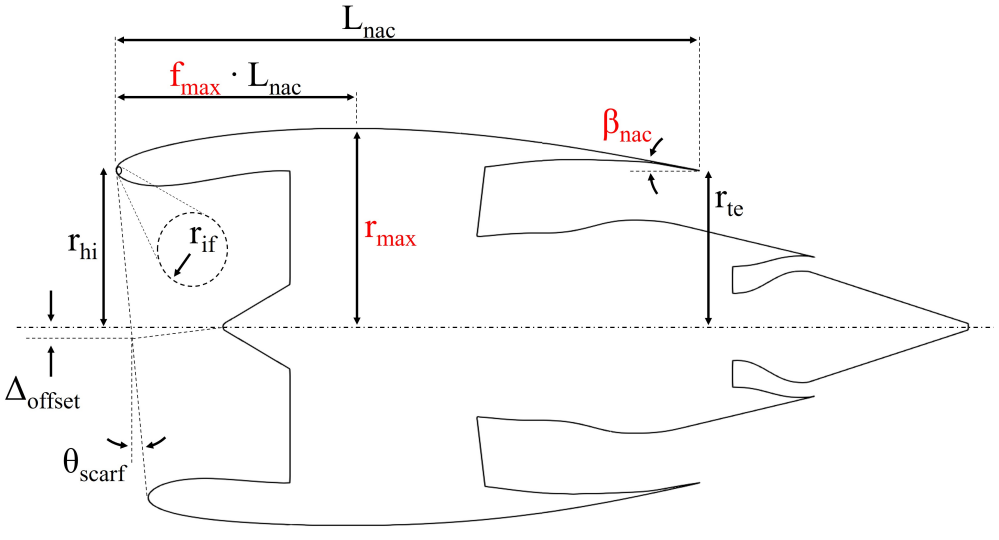

(B) Geometric parameters per aero-line.

FIGURE 8.11: Installed nacelle parameterisation. Design variables considered in the design and optimisation method marked in red.

8.2.1 Exploration of the design space

The understanding of the design space is a key aspect for every aerodynamic shape optimisation problem. It provides information about the relationship between different design variables and performance metrics and also guidelines towards the optimal design space. In this section, the design space for airframe-installed nacelles at cruise condition is investigated. RANS and Euler computational models are used to understand the correlation between both CFD fidelities. The high computational overhead of RANS CFD calculations limits the number of samples for the design space exploration (DSE). As a result, there is a question about whether the sparse RANS data set can identify the proper gradients in the design space. To address this, the impact of different $N_{samples}/N_{DOF}$ on the identified designs space is assessed using the low-fidelity Euler method. This use of Euler data to assess the sampling density for RANS data sets is based on the fact that the pressure terms are dominant and the design space does not change substantially between Euler and RANS, which is shown in Section 8.2.1.2. Overall, a range of CFD data sets (Table 8.3) are generated using the LHS technique for a uniform distribution of samples in the design space (Section 4.5.1.1). Three Euler-based data sets called Euler_{T1}, Euler_{T2} and Euler_{T3} are used with $N_{samples}/N_{DOF}$ of 80, 40 and 20 respectively. In terms of the high-fidelity data, one RANS-based data set called RANS_T is available with $N_{samples}/N_{DOF} = 15$. RANS_T is sub-sampled from the largest Euler data set Euler_{T1} using the sub-LHS technique explained in Section 4.5.1.1. This allows a direct comparison between the RANS and Euler fidelities. T_{ref} is considered as the reference computational overhead for sensible industrial time scales with the computational resources that are available. The cost of every data set is reported relative to T_{ref} (Table 8.3).

TABLE 8.3: Summary of data sets from independent design space explorations for the proposed method for installed nacelle design. Both Euler and RANS CFD fidelities considered. LHS technique used for the sampling.

	RANS	Euler		
Data set name	RANS_T	Euler_{T1}	Euler_{T2}	Euler_{T3}
N_{DOF}	9	9	9	9
$N_{samples}/N_{DOF}$	15	80	40	20
Relative cost	$\sim 6.75T_{ref}$	$\sim T_{ref}$	$\sim 0.5T_{ref}$	$\sim 0.25T_{ref}$

8.2.1.1 Impact of the number of samples

The design space is initially analysed based on the performance metrics of the nacelles. The key parameters of the thrust and drag bookkeeping method used for the assessment of the propulsion system installed on the airframe are considered (Section 4.4.1). The design space is visualised by pairing different variables in a two-dimensional plot in which every design is coloured by the change in NVF relative to the baseline design (ΔNVF) and normalised with the standard net thrust of the engine model used (F_N) (Figure 8.12). A positive value in every metric denotes a benefit relative to the baseline design. In the most generic way, the designs are presented in the $\Delta GPF^*/F_N$ - $\Delta D_{tot}/F_N$ map (Figure 8.12a). This shows the direct relationship between the changes in the thrust ΔGPF^* and total drag $\Delta D_{tot} = \Delta D_{a/f} + \Delta D^*_{nac}$ of the complete aircraft. The balance between these two metrics is the NVF which is used to color every design. This shows that in general a design with a benefit in total drag has an associated penalty in gross thrust and vice versa. This penalty in $\Delta GPF^*/F_N$ comes primarily from changes in the pressure distributions on the core cowl and plug surfaces of the exhaust as a concomitant effect of the change in the interference flow between the nacelle and the airframe. Overall, the most optimal region of the design space with the highest NVF benefits is found for $\Delta D_{tot}/F_N$ benefits and ΔGPF^* penalties (Figure 8.12a). Going one step forward, $\Delta D_{tot}/F_N$ can be split into its constituent metrics $\Delta D_{a/f}/F_N$ and $\Delta D^*_{nac}/F_N$ (Figure 8.12b). Again, there is a general opposite trend in the identified design space between benefits in $\Delta D_{a/f}/F_N$ and $\Delta D^*_{nac}/F_N$. This was already mentioned in Section 6.1.2 where the aerodynamics of the engine-airframe installation was explained. For example, one part of the reason is that the reduction in the flow suction in the afterbody of the inboard side of the nacelle decreases the nacelle drag. However, the flow suction in the forebody of the pressure side of the wing is also reduced and this increases the airframe drag (Figure 6.4). Nevertheless, in overall the optimal part of the design space for benefits in $\Delta NVF/F_N$ is located towards benefits in $\Delta D^*_{nac}/F_N$ at the expense of some penalties in $\Delta D_{a/f}/F_N$ (Figure 8.12b). These trends are maintained for every DSE with different $N_{samples}/N_{DOF}$ ratios (Figure 8.12). The only change is on the magnitude of the maximum $\Delta NVF/F_N$ achieved. As the sample ratio reduces from $N_{samples}/N_{DOF} = 80$ to 40 and 20, the $\Delta NVF/F_N$ benefit predicted using the Euler CFD fidelity are 0.75%, 0.67% and 0.61% respectively (Figure 8.12).

Additionally, the regions of the design space based on geometric design variables that provide benefits in NVF are identified by presenting the data sets in the form

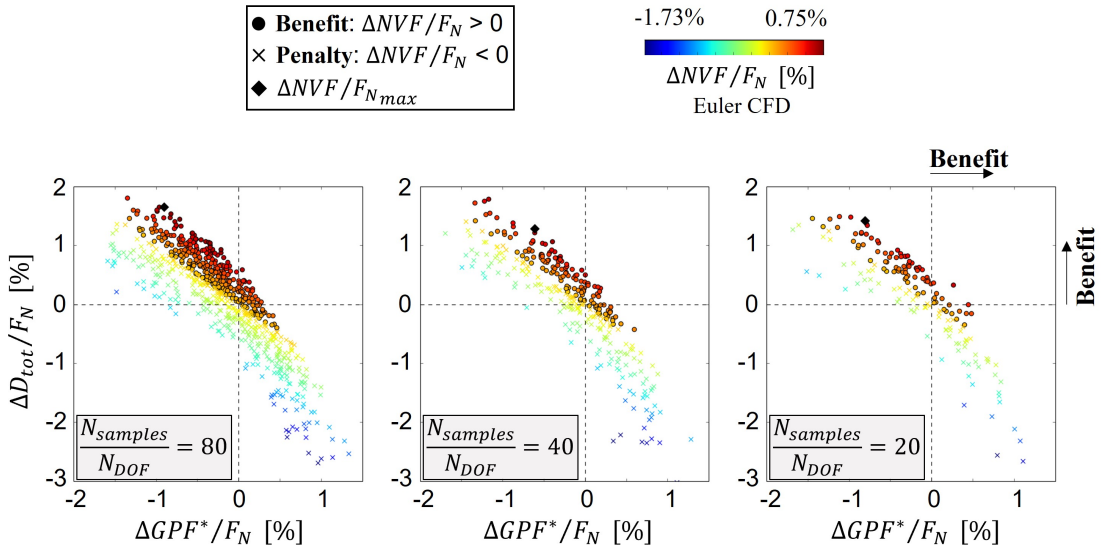

(A) Samples in the $\Delta GPF^*/F_N$ - $\Delta D_{tot}/F_N$ plane coloured by $\Delta NVF/F_N$.

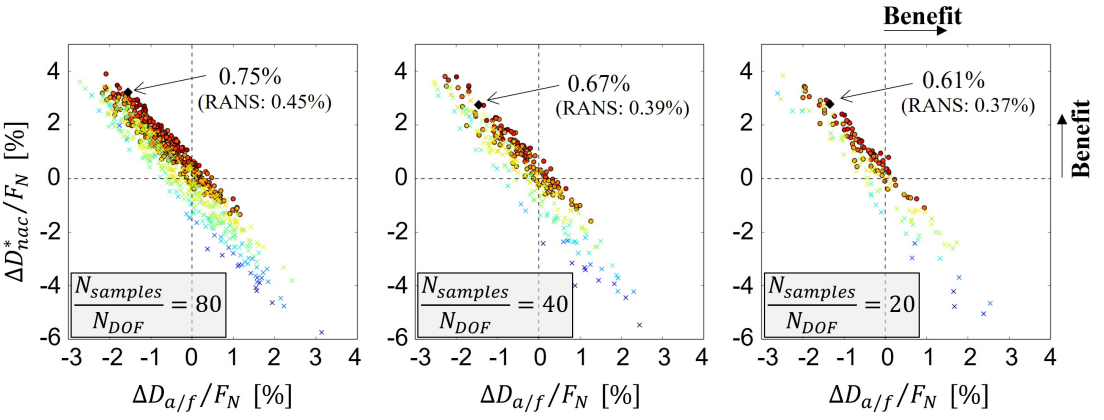

(B) Samples in the $\Delta D_{a/f}/F_N$ - $\Delta D^*_{nac}/F_N$ plane coloured by $\Delta NVF/F_N$.

FIGURE 8.12: Design space exploration at the cruise condition ($M = 0.85$, $MFCR = 0.7$, $C_L = 0.5$ and Alt = 10668m) shown in terms of the performance metrics for different $N_{samples}/N_{DOF}$ using the Euler CFD fidelity. Positive values in every metric are benefits relative to the baseline design.

of histograms (Figure 8.13). For this purpose, the results are divided in bands of different levels of $\Delta NVF/F_N$ benefit. In this way, the histograms show the density distribution of designs in each band of NVF benefit. Although it can be extended for every design variables, only the three design parameters in the top-control aero-line ($\beta_{nac,45°}$, $f_{max,45°}$ and $r_{max,45°}$) are compared to assess the impact of $N_{samples}/N_{DOF}$ on the DSE (Figure 8.13). In terms of $\beta_{nac,45°}$, every band of $\Delta NVF/F_N$ is spread similarly across the investigated design space for all the $N_{samples}/N_{DOF}$ data sets and not a clear trend to maximise $\Delta NVF/F_N$ is identified. Moreover, similar trends towards the optimal design space are found for $f_{max,45°}$ and $r_{max,45°}$ with every $N_{samples}/N_{DOF}$ (Figure 8.13). In particular, $\Delta NVF/F_N$ increases as both $f_{max,45°}$

and $r_{max,45^\circ}$ move from high to low values within the investigated design space.

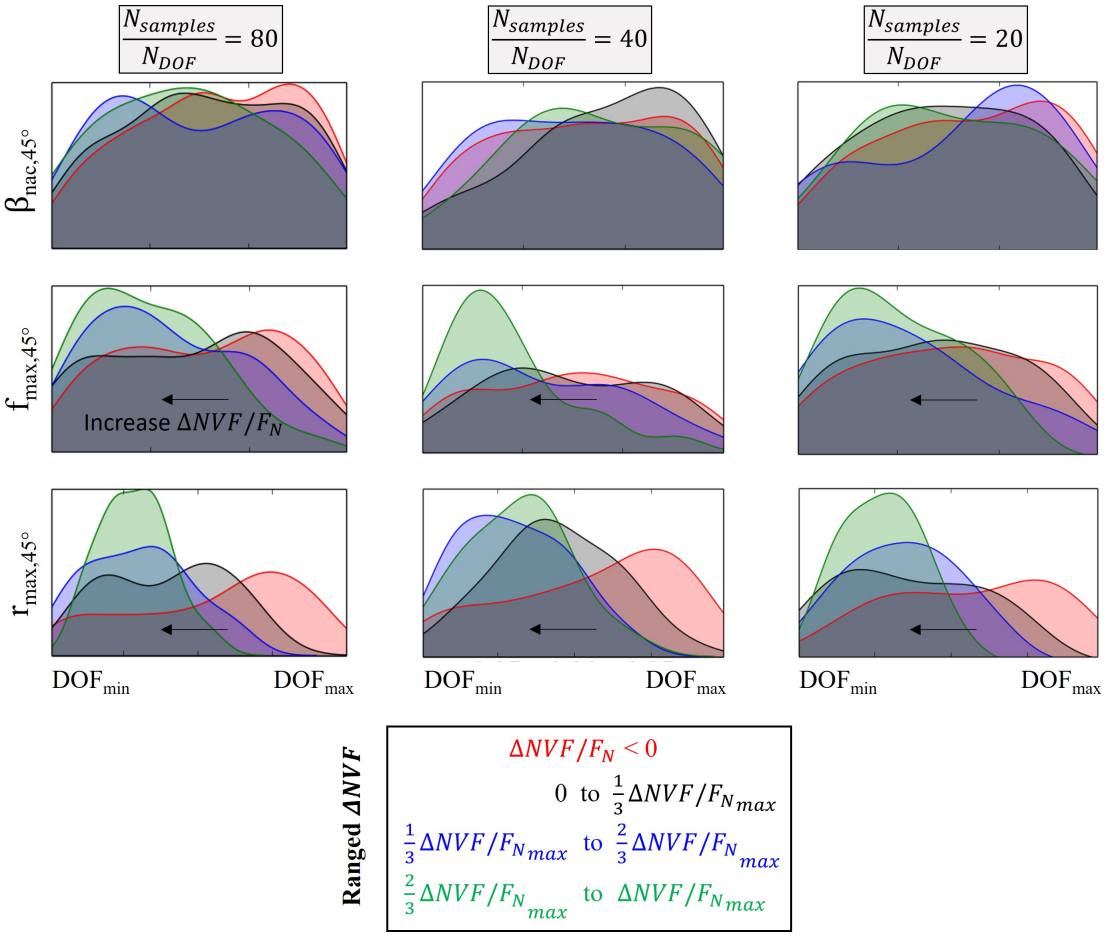

FIGURE 8.13: Design space exploration at the cruise condition ($M = 0.85$, $MFCR = 0.7$, $C_L = 0.5$ and Alt = 10668m) shown in terms of the design variables for different $N_{samples}/N_{DOF}$ using the Euler CFD fidelity.

From this section it is concluded that sparse data sets for DSE with $N_{samples}/N_{DOF}$ around 20 are able to capture the gradients in the design space both in terms of performance metrics and design parameters. Therefore, the RANS-based data set (RANS_T) with $N_{samples}/N_{DOF} = 15$ is assumed to provide representative information of the design space. This is accepted on the basis that both Euler and RANS predicts similar gradients of the design space, which is shown in the next section.

8.2.1.2 Impact of the CFD fidelity

The DSE with the RANS_T and Euler_{T1} data sets (Table 8.3) are compared in this section to understand the level of correlation between these two CFD fidelities for the nacelle optimisation problem in the airframe-installed configuration. Looking at the design space based on the aerodynamic performance metrics, the same trends

are observed between the high-fidelity RANS and the low-fidelity Euler CFD models (Figure 8.14). As explained in the previous section, the optimal region of the design space for benefits of $\Delta NVF/F_N$ is in the area of $\Delta D^*_{nac}/F_N$ benefit and penalties of $D_{a/f}/F_N$ and $\Delta GPF^*/F_N$. Although there is a high similarity in the gradients, there are differences in the absolute values of the changes of the metrics. For example, the designs with highest NVF benefit found with the Euler and RANS DSE and evaluated using the RANS CFD fidelity have a very similar $\Delta NVF/F_N$ of 0.45% and 0.47% respectively (Figure 8.14b). However, this best design from the Euler data set evaluated using the Euler CFD fidelity reports an increased $\Delta NVF/F_N$ of 0.75% (Figure 8.14b). The reason is that the Euler CFD model does not account for viscous terms in the forces. This viscous terms have a greater impact on the airframe drag $D_{a/f}$ component which is substantially under predicted with the Euler model compared to the RANS model. The changes in the other components are minor compared to $D_{a/f}$. As a result, the overall NVF computed with the Euler CFD method increases relative to the RANS prediction. However, to understand the implication of this difference in the magnitude of NVF on the convergence to the optimal design space, the RANS_T data set is cross correlated between the Euler and the RANS CFD fidelities (Figure 8.15). This is possible because, as explained before, the RANS_T data set was sub-sampled from the Euler_{T1} data set. The samples adjusts to a linear regression model with $R^2 = 0.920$ and slope 1.011 (Figure 8.15). Therefore, although the results of the cross correlation show a general over prediction of $\Delta NVF/F_N$ of the Euler model compared to the RANS CFD model as explained before, it can be assumed that the Euler CFD model lead to a similar optimal design space based on NVF for this design problem. This shows that the pressure terms of the forces dominate the changes in the aerodynamics over the viscous terms.

Similar conclusion are extracted from the comparison of the design space based on the design variables. As before, the results are sorted in ranges of $\Delta NVF/F_N$ and the distributions are represented across the investigated design space (Figure 8.16). A similar region for the optimal design space is identified using both fidelities. While there is not a clear relationship of β_{nac} at every aero-line with $\Delta NVF/F_N$, f_{max} and r_{max} are the dominant variables from a NVF optimisation point of view (Figure 8.16). In particular, there is a clear trend for $r_{max,45^\circ}$ and f_{max} of every aero-line to low values between 20% and 30% of the investigated design space (Figure 8.16). On the contrary, $r_{max,90^\circ}$ and $r_{max,135^\circ}$ for high NVF are between 50% and 75% of the investigated design space (Figure 8.16).

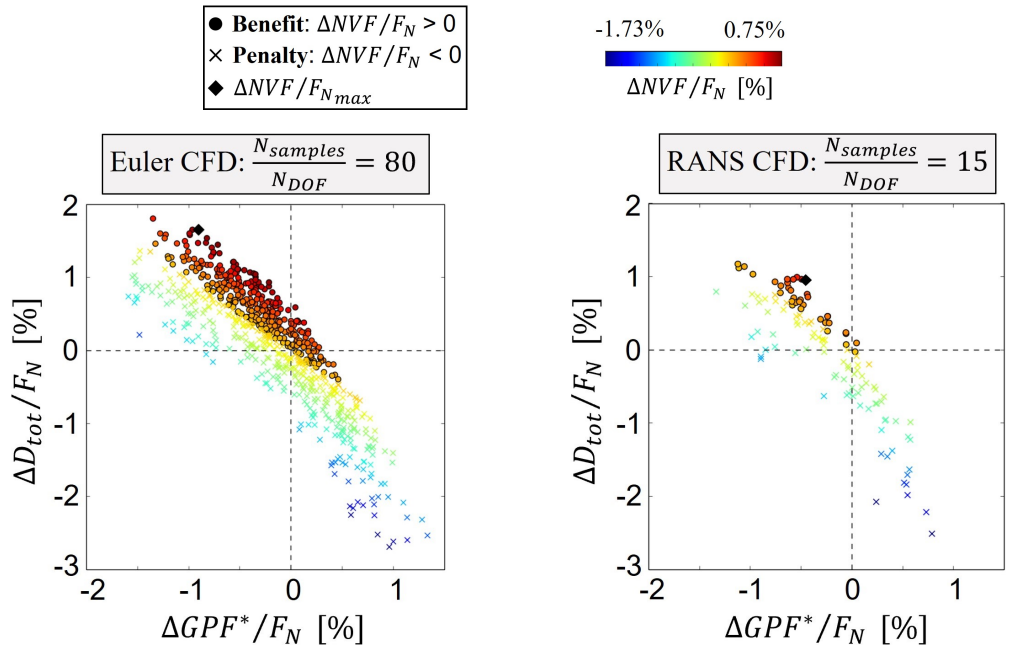

(A) Samples in the $\Delta GPF^*/F_N$ - $\Delta D_{tot}/F_N$ plane coloured by $\Delta NVF/F_N$.

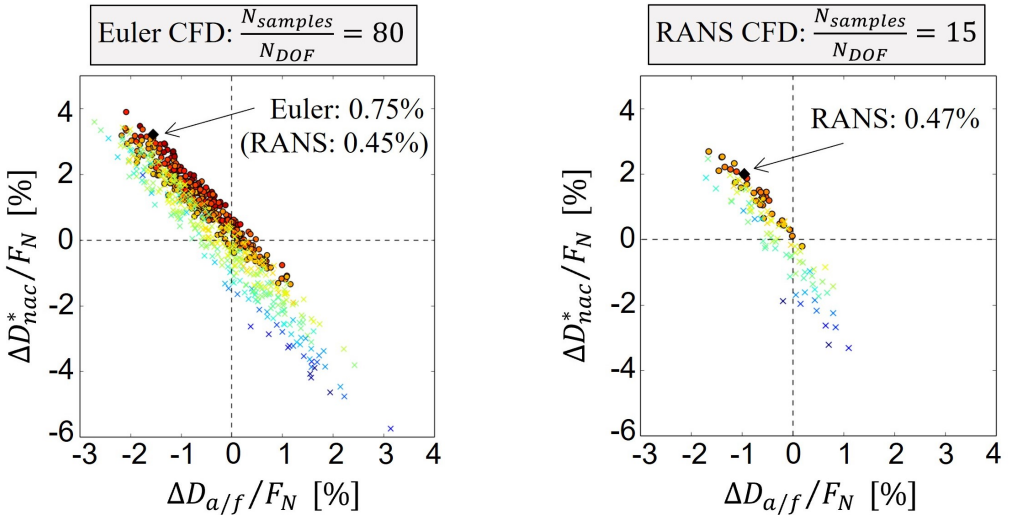

(B) Samples in the $\Delta D_{a/f}/F_N$ - $\Delta D^*_{nac}/F_N$ plane coloured by $\Delta NVF/F_N$.

FIGURE 8.14: Comparison of the design space exploration at the cruise condition ($M = 0.85$, $MFCR = 0.7$, $C_L = 0.5$ and Alt = 10668m) in terms of performance metrics between the RANS$_T$ data set ($N_{samples}/N_{DOF} = 15$) and the Euler$_{T1}$ data set ($N_{samples}/N_{DOF} = 80$). Positive values in every metric are benefits relative to the baseline design.

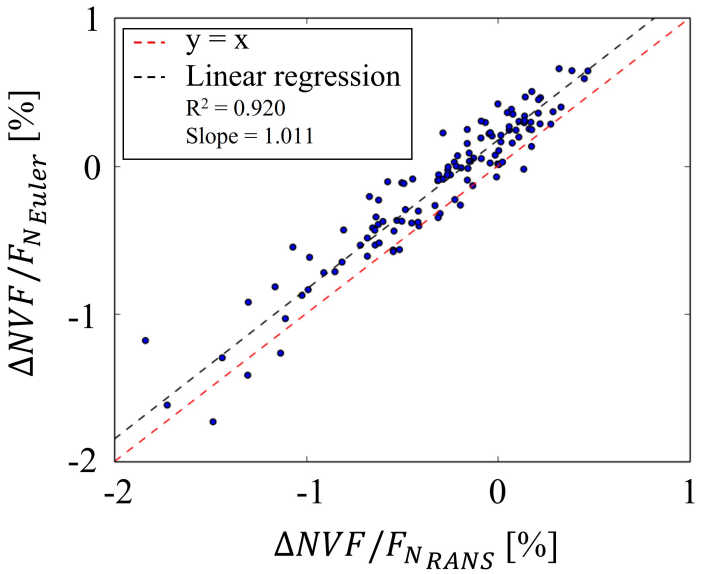

FIGURE 8.15: Cross correlation at the cruise condition ($M = 0.85$, $MFCR = 0.7$, $C_L = 0.5$ and Alt = 10668m) based on $\Delta NVF/F_N$ between the Euler and RANS CFD fidelities for the RANS$_T$ data set of $N_{samples}/N_{DOF} = 15$.

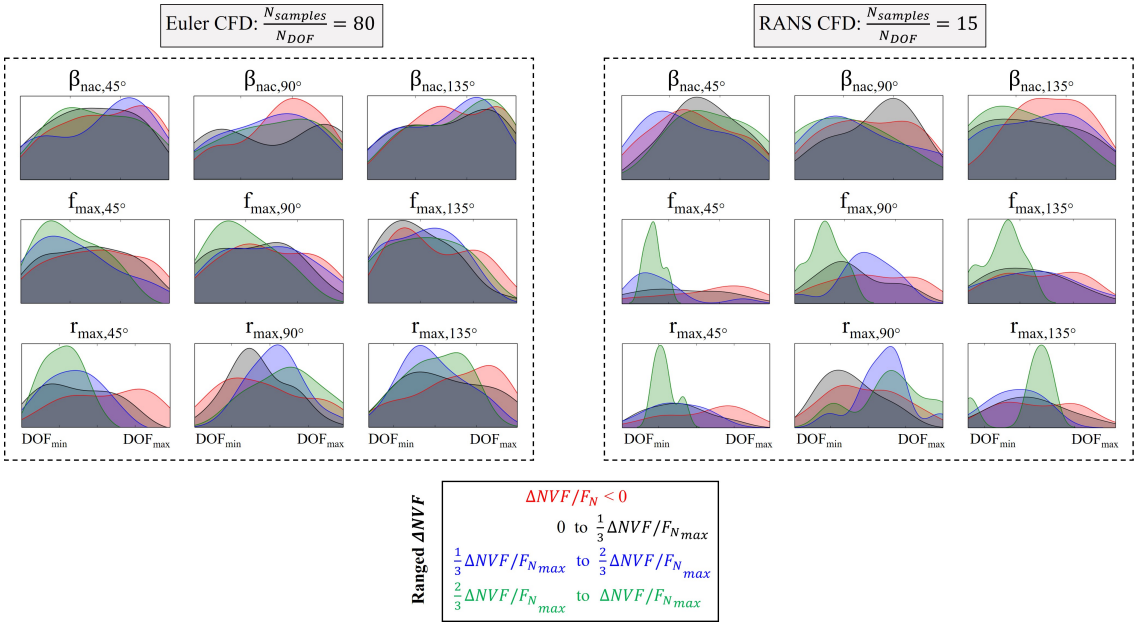

FIGURE 8.16: Comparison of the design space exploration at the cruise condition ($M = 0.85$, $MFCR = 0.7$, $C_L = 0.5$ and Alt = 10668m) in terms of design variables between the RANS$_T$ data set ($N_{samples}/N_{DOF} = 15$) and the Euler$_{T1}$ data set ($N_{samples}/N_{DOF} = 80$).

8.2.2 Surrogate modelling and optimisation

A variety of surrogate models are generated using the range of data sets available for non-axisymmetric nacelles in airframe-installed configuration (Table 8.3). Different techniques of both single-fidelity (Section 8.2.2.1 and 8.2.2.2) and multi-fidelity (Section 8.2.2.3) surrogate models are assessed. The objective of the study is to analyse the trade-offs between overall computational cost and the ability to model the design space gradients and the NVF benefit of the optimal designs. In this section, a surrogate-based method for nacelle aerodynamic optimisation in installed configuration within the expected reference limit T_{ref} is delivered.

8.2.2.1 Single-fidelity Euler-based models

As single-fidelity surrogates, the Gaussian Process Regression or Kriging (Section 4.6.1.1) and the Artificial Neural Network (ANN) (Section 4.6.1.2) techniques are considered. Using the Euler data sets, the impact of $N_{samples}/N_{DOF}$ on the modelling performance is assessed. Overall, depending on the Euler data set and technique, 6 different surrogate models are built: $\text{Kriging}_{Euler_{T1}}$, $\text{Kriging}_{Euler_{T2}}$, $\text{Kriging}_{Euler_{T3}}$, $\text{ANN}_{Euler_{T1}}$, $\text{ANN}_{Euler_{T2}}$, $\text{ANN}_{Euler_{T3}}$. For each model, the different hyperparameters are optimised in a similar manner as reported in Section 8.1.2.1 for the 2D axi-symmetric nacelle case. Surrogate models are generated for a full factorial combination of the different hyperparameters of the ANN and Kriging models. Every model is evaluated in an independent Euler-based data set of $N_{samples}/N_{DOF} = 20$. The model with lowest RMSE (Equation 4.48) is selected. Using the $\Delta NVF/F_N$ as the metric of interest to evaluate the RMSE, the ANN technique is more sensitive to changes in $N_{samples}/N_{DOF}$ compared to the Kriging interpolation method (Table 8.4). For the Kriging method, reducing the number of samples from $N_{samples}/N_{DOF} = 80$ to 20 slightly increases $RMSE_{\Delta NVF/F_N}$ from around 0.12% to 0.14% (Table 8.4). However, for the ANN technique, $RMSE_{\Delta NVF/F_N}$ increases from 0.12% to 0.42% (Table 8.4). For highly populated data sets used to train the model ($N_{samples}/N_{DOF} = 80$), both Kriging and ANN have similar modelling performance (Table 8.4). However, the RMSE is an absolute parameter that provides an overall quantification of the model prediction performance. A more detailed analysis of the data shows the cross correlation between the prediction of the model and the Euler CFD results for each design in the validation data set (Figure 8.17). Again, this analysis shows a low impact of $N_{samples}/N_{DOF}$ on the prediction performance of the Kriging interpolation technique for the ratios of samples considered. Conversely, there is an overprediction

in $\Delta NVF/F_N$ of the ANN model relative to the CFD results when $N_{samples}/N_{DOF}$ is reduced from 80 to 40 and 20 (Figure 8.17). This deviation is not a constant offset for every design. Rather, it increases from designs with $\Delta NVF/F_N > 0$ (benefit) towards designs with $\Delta NVF/F_N < 0$ (penalty). This suggests differences in the prediction of the design space gradients and potentially the optimal region of the design space.

To further understand this, every model is interrogated for $\Delta NVF/F_N$ around the baseline design for different pairs of the design variables considered. This provides contour plots coloured by $\Delta NVF/F_N$ that show the design space. For example, the pair of design variables $r_{max,90^\circ}$ - $r_{max,135^\circ}$ is considered for this analysis (Figure 8.18) although similar conclusions are obtained for different pairs. Similar gradients and $\Delta NVF/F_N$ magnitudes in the design space are obtained with every Kriging model regardless of $N_{samples}/N_{DOF}$. As mentioned in the previous section, the optimal designs are located in the middle of the investigated region for both $r_{max,90^\circ}$ and $r_{max,135^\circ}$. On the other hand, there are more notable differences in the gradients for the ANN models as $N_{samples}/N_{DOF}$ is reduced (Figure 8.18). For $N_{samples}/N_{DOF} = 20$, the model predicts benefits of $\Delta NVF/F_N$ in the design space given by high $r_{max,90^\circ}$ and low $r_{max,135^\circ}$ which is corrected as $N_{samples}/N_{DOF}$ increases (Figure 8.18). This affects the location of the optimal region and the model may lead to sub-optimal designs within an optimisation process.

TABLE 8.4: RMSE evaluated in an independent data set for the single-fidelity surrogate models generated for the different $N_{samples}/N_{DOF}$ Euler-based data sets at the cruise condition ($M = 0.85$, $MFCR = 0.7$, $C_L = 0.5$ and Alt = 10668m). Comparison of the Kriging and ANN modelling techniques.

Technique	Model name	$N_{samples}/N_{DOF}$	$RMSE_{\Delta NVF/F_N}$
Kriging	$\text{Kriging}_{Euler_{T1}}$	80	0.117%
Kriging	$\text{Kriging}_{Euler_{T2}}$	40	0.141%
Kriging	$\text{Kriging}_{Euler_{T3}}$	20	0.139%
ANN	$\text{ANN}_{Euler_{T1}}$	80	0.124%
ANN	$\text{ANN}_{Euler_{T2}}$	40	0.289%
ANN	$\text{ANN}_{Euler_{T3}}$	20	0.421%

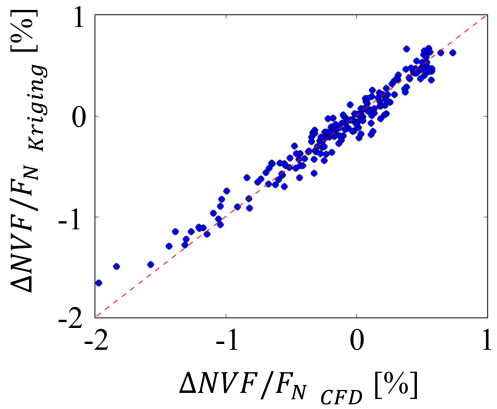

(A) Kriging model for $N_{samples}/N_{DOF} = 80$ ($\text{Kriging}_{Euler_{T1}}$).

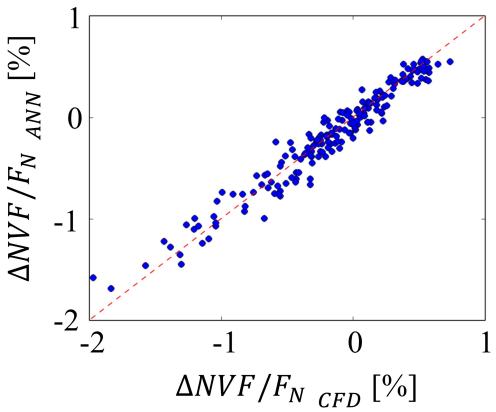

(B) ANN model for $N_{samples}/N_{DOF} = 80$ ($\text{ANN}_{Euler_{T1}}$).

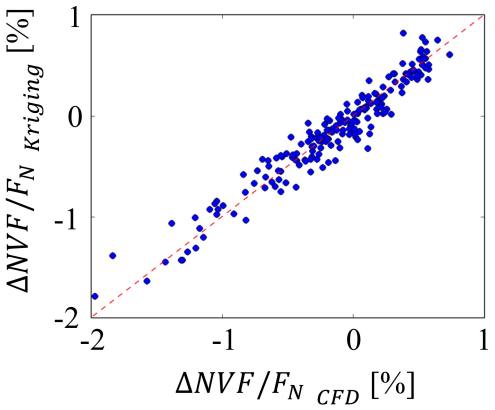

(C) Kriging model for $N_{samples}/N_{DOF} = 40$ ($\text{Kriging}_{Euler_{T2}}$).

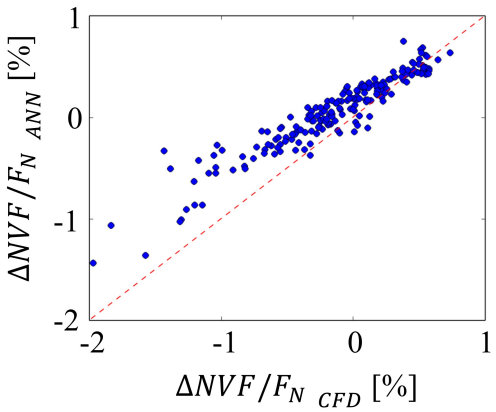

(D) ANN model for $N_{samples}/N_{DOF} = 40$ ($\text{ANN}_{Euler_{T2}}$).

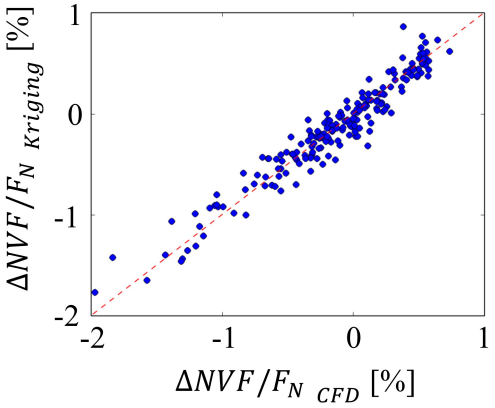

(E) Kriging model for $N_{samples}/N_{DOF} = 20$ ($\text{Kriging}_{Euler_{T3}}$).

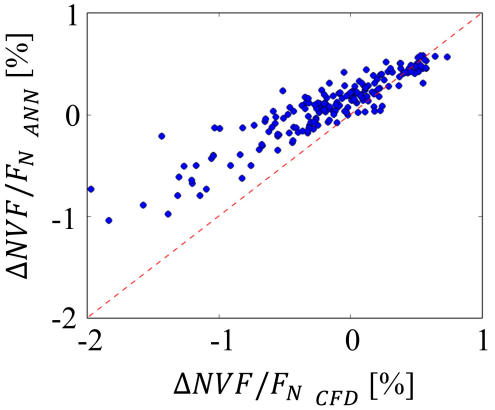

(F) ANN model for $N_{samples}/N_{DOF} = 20$ ($\text{ANN}_{Euler_{T3}}$).

FIGURE 8.17: Cross correlation between the Euler CFD results and the surrogate models prediction evaluated on the independent data set at the cruise condition ($M = 0.85$, $MFCR = 0.7$, $C_L = 0.5$ and Alt = 10668m). Kriging and ANN surrogate models for different $N_{samples}/N_{DOF}$ ratios.

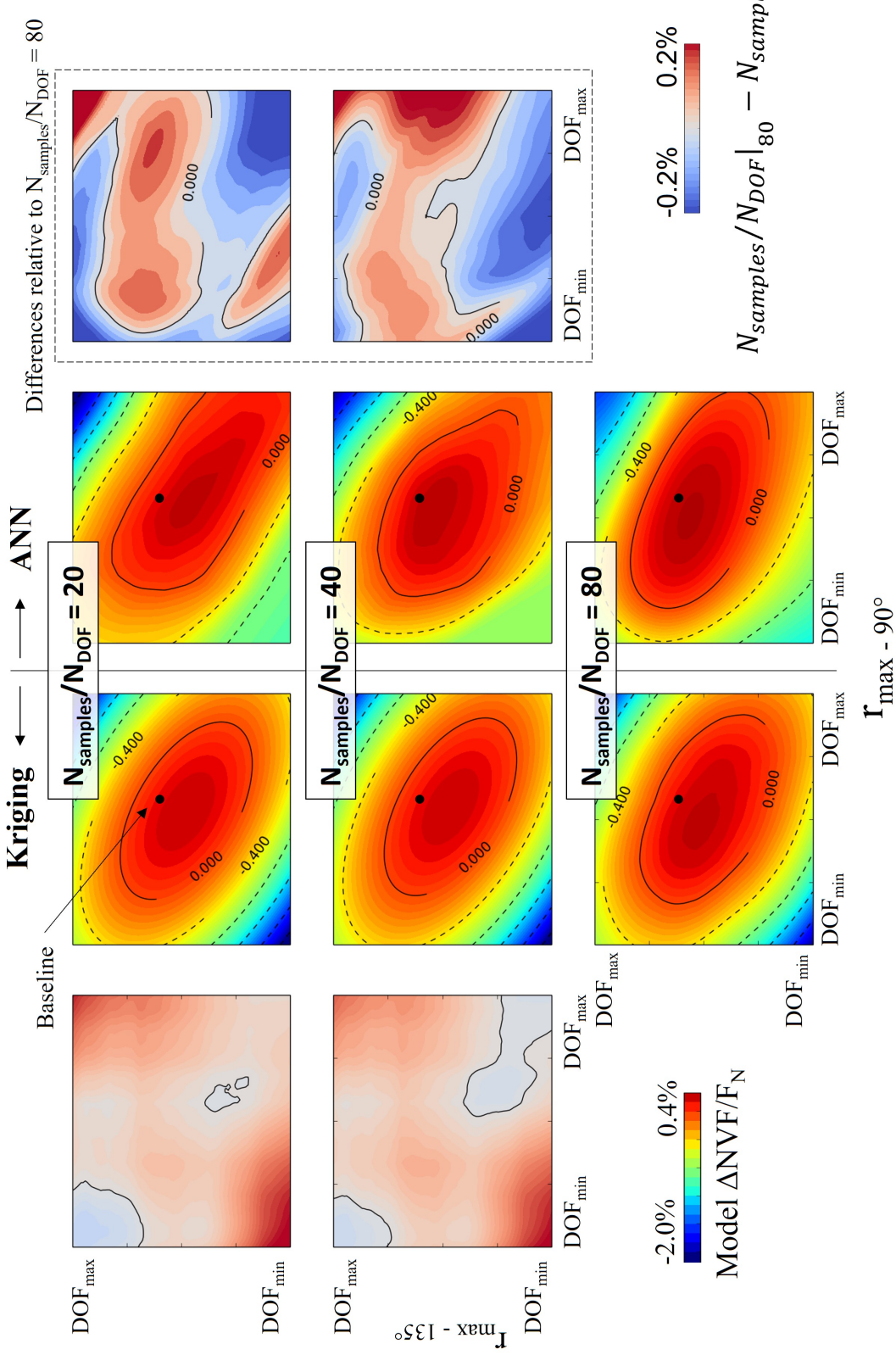

FIGURE 8.18: Interrogation of the Kriging and ANN surrogate models for the different $N_{samples}/N_{DOF}$ around the baseline design for the pair $r_{max,90°}$ - $r_{max,135°}$ at the cruise condition ($M = 0.85$, $MFCR = 0.7$, $C_L = 0.5$ and Alt $= 10668$m). Contour of the model prediction of $\Delta NVF/F_N$ and also the difference of $N_{samples}/N_{DOF} = 20$ and 40 relative to $N_{samples}/N_{DOF} = 80$.

The impact of each surrogate modelling technique and the ratio $N_{samples}/N_{DOF}$ on the $\Delta NVF/F_N$ performance is also assessed within an optimisation standpoint. In this respect, the different surrogate models are used to lead a surrogate-based optimisation process (Figure 4.24b) as described in Section 4.5.2.3. A single-objective approach focused on the maximisation of the cruise $\Delta NVF/F_N$ is followed with OMOPSO as the optimisation algorithm. An initial generation of sample size $N_{gen=0}/N_{DOF} = 100$ with 100 additional generations of size $N_{gen=i}/N_{DOF}$ are considered. The convergence criteria for the optimisation is met when the one-dimensional HV index changes by less than 1% in three subsequent generations. The optimal designs are evaluated using the Euler CFD fidelity at cruise in order to be comparable. Additionally, every optimal design is compared with the best design with highest $\Delta NVF/F_N$ from each Euler DSE training data set. For $N_{samples}/N_{DOF} = 40$ and 20 the optimal designs with both surrogate models report a $\Delta NVF/F_N$ benefit lower than the best design from the corresponding DSE (Figure 8.19a). For example for $N_{samples}/N_{DOF} = 40$ while the highest benefit from the DSE is 0.67% the optimised designs with the surrogate models provide a benefit of around 0.5%. As a result, there is no interest on using this surrogate modelling techniques based on Euler data for nacelle optimisation for ratios of $N_{samples}/N_{DOF} < 40$. Conversely, for $N_{samples}/N_{DOF} = 80$ the Kriging surrogate model slightly improves the $\Delta NVF/F_N$ compared to the best design from the DSE from 0.75% to 0.79% (Figure 8.19a). However, the optimised design with the ANN model reports a benefit of 0.63%.

In terms of the design variables, there is a clear dominance of r_{max} and f_{max} over β_{nac} as was already commented in Section 8.2.1. In particular, every model regardless of the ratio $N_{samples}/N_{DOF}$ converges to a very close optimal region in r_{max} (Figure 8.19b). There is more variability in f_{max} with some models getting trapped in the minimum bound of the design space. However, the three f_{max} parameters at the different aero-lines ($f_{max,45°}$, $f_{max,90°}$ and $f_{max,135°}$) follow the guidelines from the design space exploration presented in Section 8.2.1 and are generally below 30% of the investigated design space bounds of this parameter. Finally, there is a large variability in β_{nac} between the different optimal designs without clear indications of the optimal region of the design space as was highlighted in Section 8.2.1. This comparative analysis of Kriging and ANN surrogate modelling techniques from the point of view of surrogate-based optimisations shows again a better performance of the Kriging modelling technique compared to ANN for this aerodynamic design problem.

Overall, an optimised design called E1 is obtained using Kriging interpolation and $N_{samples}/N_{DOF} = 80$ (model $\text{Kriging}_{Euler_{T1}}$) with a $\Delta NVF/F_N$ benefit in cruise

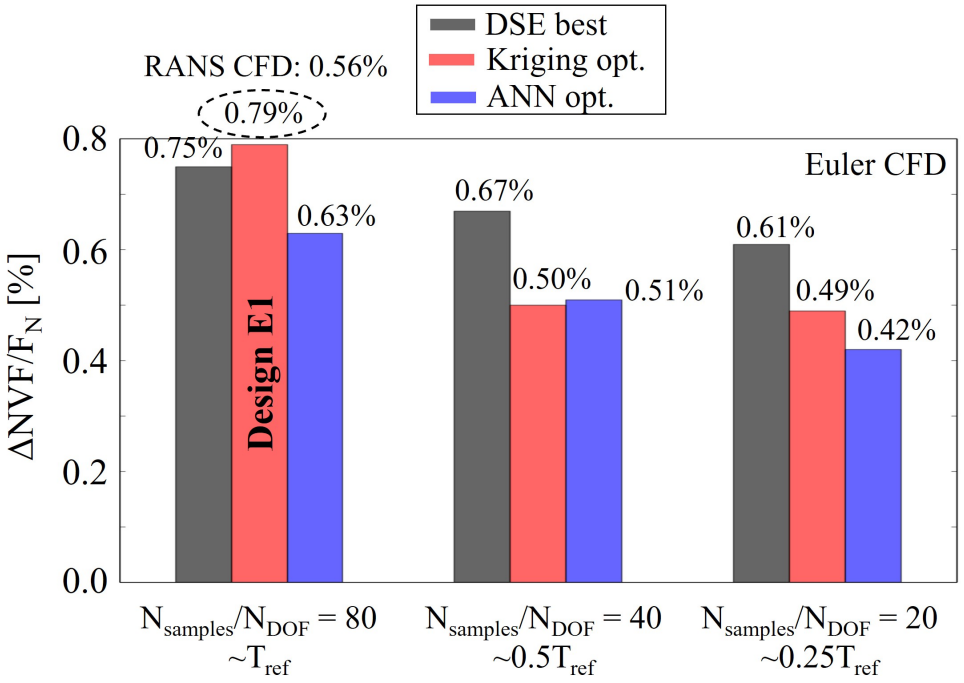

(A) $\Delta NVF/F_N$ benefits evaluated with Euler CFD fidelity at the cruise condition ($M = 0.85$, $MFCR = 0.7$, $C_L = 0.5$ and Alt = 10668m).

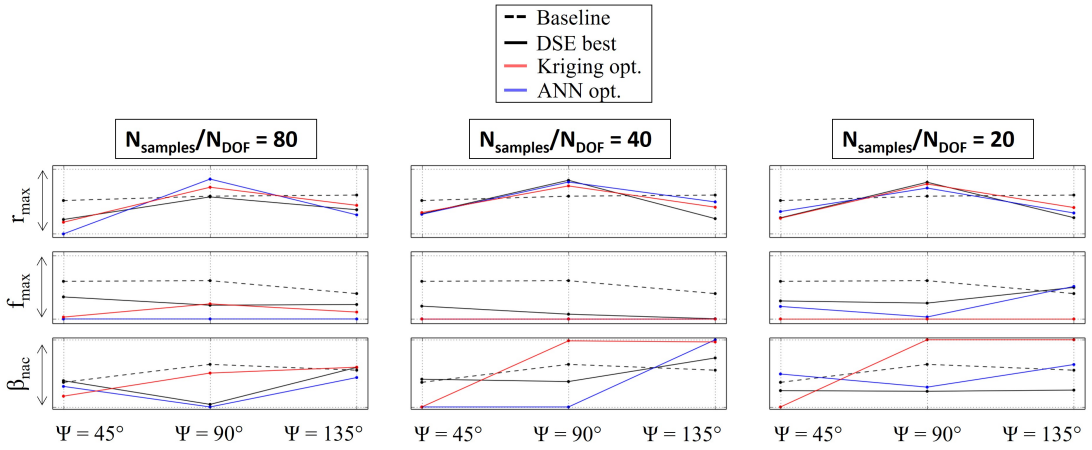

(B) Geometrical parameters.

FIGURE 8.19: Comparison of performance and geometrical parameters of the optimised designs with each Kriging and ANN model. The designs with highest $\Delta NVF/F_N$ from each Euler DSE are also included.

evaluated with Euler CFD of 0.79%. An a posteriori evaluation of this design at cruise using RANS CFD delivers a $\Delta NVF/F_N$ benefit of 0.56% (Figure 8.19a). This equates to a fuel burn reduction at cruise of around 0.56% [106] relative to the baseline design.

This $\Delta NVF/F_N$ benefit of the design E1 comes primarily from a reduction of the nacelle drag (as explained in Figure 8.14b). There are two contributors to this nacelle

drag reduction (Figure 8.20): (a) an increase in the flow suction in the forebody of the nacelle (forward loaded) and (b) an increase in the static pressure in the inboard side of the nacelle afterbody. Additionally, from a RANS calculation at windmilling diversion condition, the flow separation extent on the nacelle is $0.096L_{nac}$. This meets the requirement imposed in Section 4.5.2.3 of $L_{sep,div} < 0.1L_{nac}$ to avoid gross flow separations.

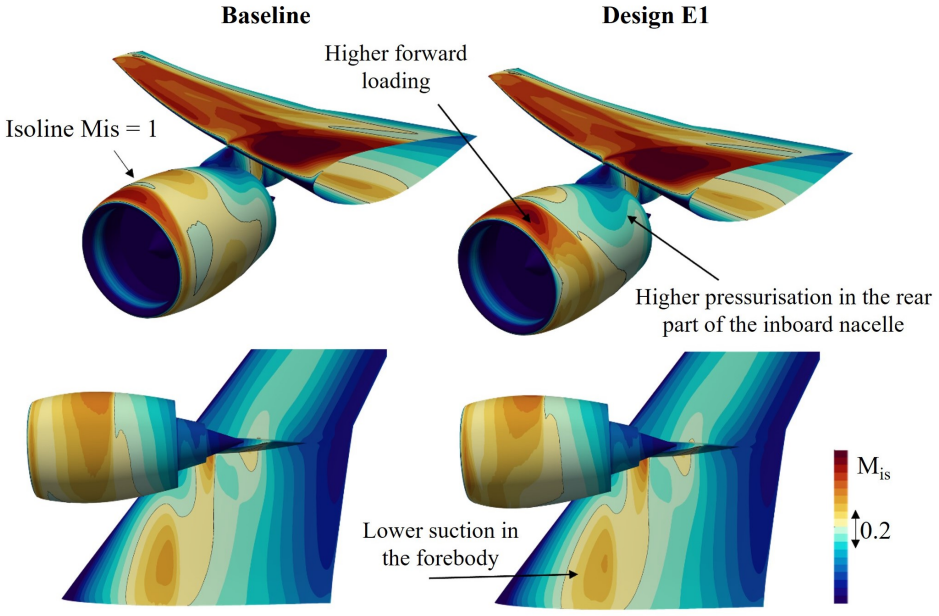

FIGURE 8.20: Comparison of the aerodynamics at the cruise condition ($M = 0.85$, $MFCR = 0.7$, $C_L = 0.5$ and Alt = 10668m) between the baseline and design E1 using M_{is} distributions on the nacelle and wing. RANS CFD prediction.

The selected Kriging interpolation model $\text{Kriging}_{Euler_{T1}}$ is used to interrogate the design space around the baseline design. This is an important and novel contribution of this project as it shows that maps of the design space can be generated for this design problem which enables an understanding of the design space and trade studies between design variables. For example, adjoint methods which are broadly used for aerodynamic shape optimisations of very high dimensional problems would not provide this maps but just the optimal design.

Interrogating the $\text{Kriging}_{Euler_{T1}}$ model around the baseline design, projections onto different pairs of design variables show the gradients and optimal region for $\Delta NVF/F_N$ (Figure 8.21). The baseline and optimal design E1 are marked in the maps. Although there is some uncertainty associated with the model which affects the design space interrogation, the optimal design E1 is located in the regions of high $\Delta NVF/F_N$ as could be expected (Figure 8.21). The maps show the sensitivity of $\Delta NVF/F_N$ to changes in the different geometrical parameters for the investigated design space.

The largest gradients are found across r_{max} in the different aero-lines. For example, relative to the baseline, an increase in $r_{max,45°}$, $r_{max,90°}$ and $r_{max,135°}$ of $0.05r_{hi}$ to accommodate any engine subsystem is estimated to erode the $\Delta NVF/F_N$ by 0.5%, 0.4% and 0.5% respectively (Figure 8.21). In the same manner, increasing $f_{max,45°}$, $f_{max,90°}$ and $f_{max,135°}$ by $0.05L_{nac}$ erodes the $\Delta NVF/F_N$ by approximately 0.15%, 0.20% and 0.25%. There is a negligible impact of changes in β_{nac} on the $\Delta NVF/F_N$ as was already explained in Section 8.2.1 (Figure 8.21). This is independent of the design used to interrogate around and is more a feature of the design space of this problem.

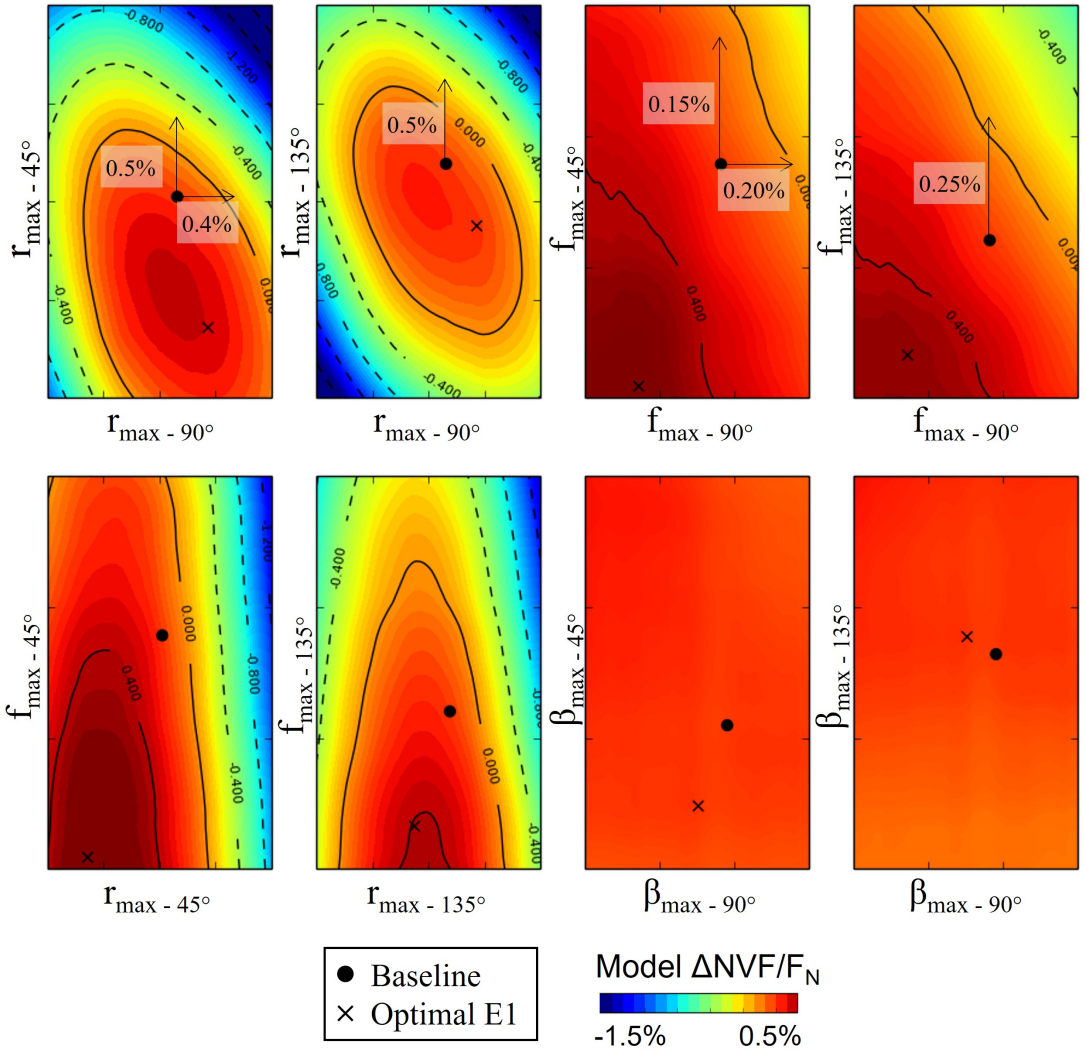

FIGURE 8.21: Interrogation of the Kriging$_{Euler_{T1}}$ model ($N_{samples}/N_{DOF} = 80$) around the baseline design for different pairs of design variables at the cruise condition ($M = 0.85$, $MFCR = 0.7$, $C_L = 0.5$ and Alt = 10668m).

8.2.2.2 Single-fidelity RANS-based models

From the previous section, a surrogate-based optimisation method based on Euler CFD provides an optimal design with a reduction in the cruise fuel burn of 0.56% assessed in RANS (Design E1) within the expected reference limit T_{ref}. However, there may be a possibility to combine Euler data sets with high-fidelity RANS samples from the RANS_T data set (Table 8.3) to further increase the benefit of the optimal design. The purpose of this section is to analyse the highest achievable benefit that can be obtained using the full RANS data set RANS_T and understand where the optimum design lies in the design space compared to the optimal design E1 and the baseline.

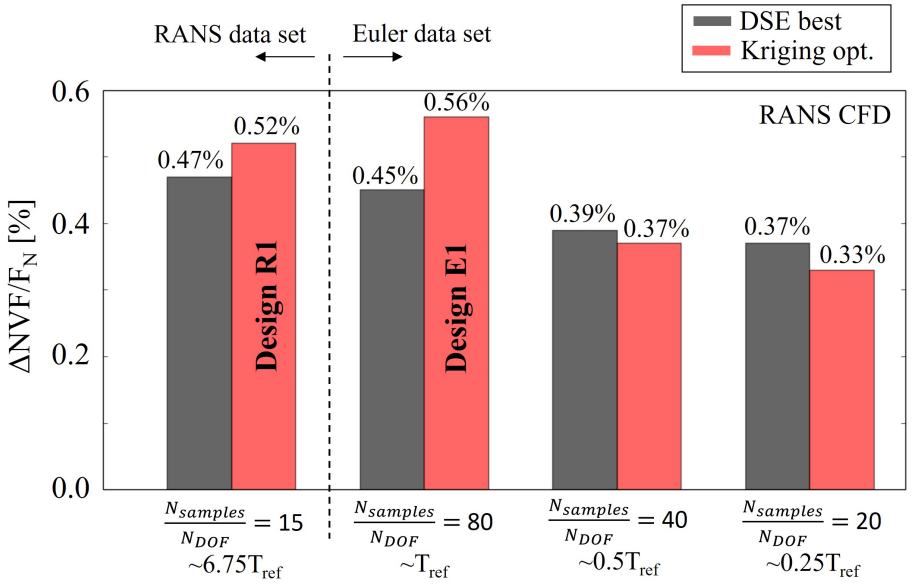

FIGURE 8.22: $\Delta NVF/F_N$ benefits evaluated with the RANS CFD fidelity at the cruise condition ($M = 0.85$, $MFCR = 0.7$, $C_L = 0.5$ and Alt = 10668m) obtained from the optimisations with the RANS-based Kriging model and the different Euler-based Kriging models (red). The designs with highest $\Delta NVF/F_N$ from each Euler DSE are also included (black).

The analysis on the previous section showed acceptable modelling performance of the Kriging interpolation model for ratios $N_{samples}/N_{DOF} \sim 20$. Consequently, a Kriging model based on the full RANS data set RANS_T of ratio $N_{samples}/N_{DOF} = 15$ (Table 8.3) is constructed. The model is optimised through a full factorial combination of the different hyperparameters. An independent RANS-based data set of $N_{samples}/N_{DOF} = 2$ is used to evaluate the RMSE and select the optimal model. The RMSE of this selected model (called Kriging_{RANS_T}) is 0.122% which is in line

with the values reported in Table 8.4 for Kriging models. A surrogate-based optimisation led by this Kriging$_{RANS_T}$ model converges to an optimal design R1 with a $\Delta NVF/F_N$ of 0.52% evaluated using RANS CFD fidelity (Figure 8.22). Although it is slightly higher than the best design from the RANS$_T$ data set used to train the model (0.47%), it is still below the 0.56% benefit obtained for design E1 in the previous section. However, it is important to note that this difference between designs E1 and R1 is within the RMSE of the model. In any case, design E1 is obtained with a reduction in the cost of a factor of 6.75 (Table 8.3) compared to design R1. Therefore, single-fidelity surrogate models based on RANS CFD data are not worth for installed nacelle design and optimisation.

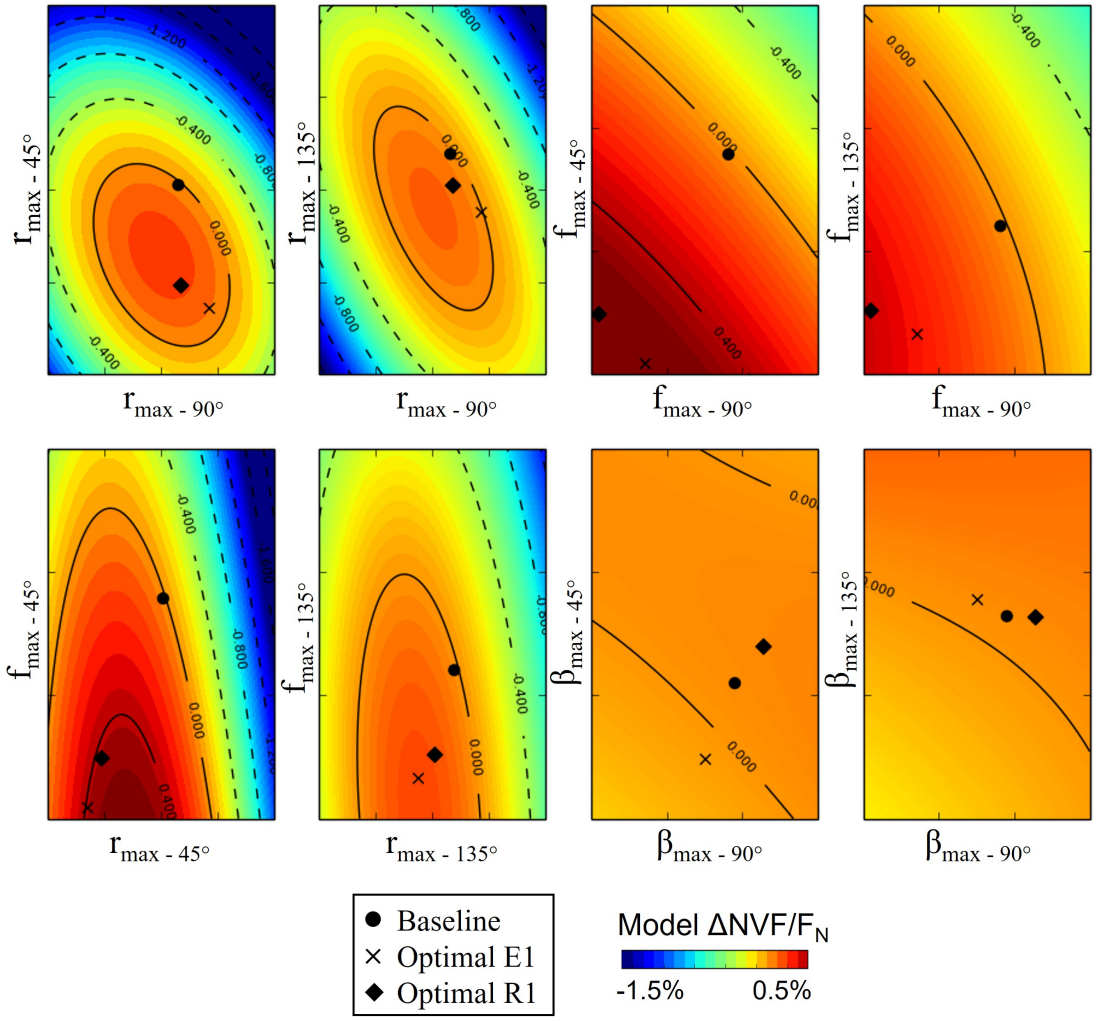

FIGURE 8.23: Interrogation of the Kriging$_{RANS_T}$ model ($N_{samples}/N_{DOF} = 15$) around the baseline design for different pairs of design variables at the cruise condition ($M = 0.85$, $MFCR = 0.7$, $C_L = 0.5$ and Alt = 10668m).

As before, the design space is interrogated for $\Delta NVF/F_N$ through 2D projections of different pairs of design variables using the Kriging$_{RANS_T}$ model (Figure 8.23).

Compared to the Euler-based Kriging$_{Euler_{T1}}$ model (Figure 8.21), although there are differences in the magnitudes the gradients and optimal region are not substantially different. Additionally, the largest sensitivities are for changes in r_{max} and the the impact of β_{nac} is negligible.

8.2.2.3 Multi-fidelity models

Multi-fidelity surrogate models could be generated by combining the Euler data set for $N_{samples}/N_{DOF} = 40$ and 20 with RANS data points sub-sampled from the RANS$_T$ data set for an overall computational time of T_{ref}. As a result, the limited modelling performance of ANN for these ratios $N_{samples}/N_{DOF}$ of 40 and 20 (Section 8.2.2.1) makes multi-fidelity neural network (MFNN) a non-viable method for the installed nacelle application. Consequently, the incremental variable complexity modelling technique (VCM_{inc}) is evaluated which combines a base Kriging model for the low-fidelity Euler prediction and another correction Kriging model for the high-fidelity RANS data (Section 4.6.2.1). In this way, the Kriging model used with the low-fidelity data to estimate the design space gradients has acceptable modelling performance for these ratios of $N_{samples}/N_{DOF} = 40$ and 20. The limitation is on the correction Kriging model, which considers scarce RANS data points sub-sampled from RANS$_T$ to meet the cost constraint. Two VCM models are generated (Figure 8.24):

- VCM1$_{Kriging}$: this model combines the Euler$_{T2}$ data set of $N_{samples}/N_{DOF} = 40$ for the base Kriging model with a ratio of $N_{samples}/N_{DOF} = 1.1$ RANS data sub-sampled from the RANS$_T$ data set for the correction Kriging model. As before, the models are optimised through the minimisation of the RMSE in an independent data set for a full factorial combinations of the different hyperparameters. A RMSE = 0.168% is obtained for the VCM1$_{Kriging}$ model.
- VCM2$_{Kriging}$: similarly, the Euler$_{T3}$ data set of $N_{samples}/N_{DOF} = 20$ is used for the base Kriging model and is combined with a ratio of $N_{samples}/N_{DOF} = 1.7$ RANS data sub-sampled from the RANS$_T$ data set for the correction Kriging model. A RMSE = 0.159% is obtained.

The design space predicted with the multi-fidelity models VCM1$_{Kriging}$ and VCM2$_{Kriging}$ is compared with the previous predictions of the RANS-based (Kriging$_{RANS_T}$) and Euler-based (Kriging$_{Euler_{T1}}$) single-fidelity Kriging models. The dominant design variables r_{max} and f_{max} are used. In general, compared to the single-fidelity Kriging$_{Euler_{T1}}$

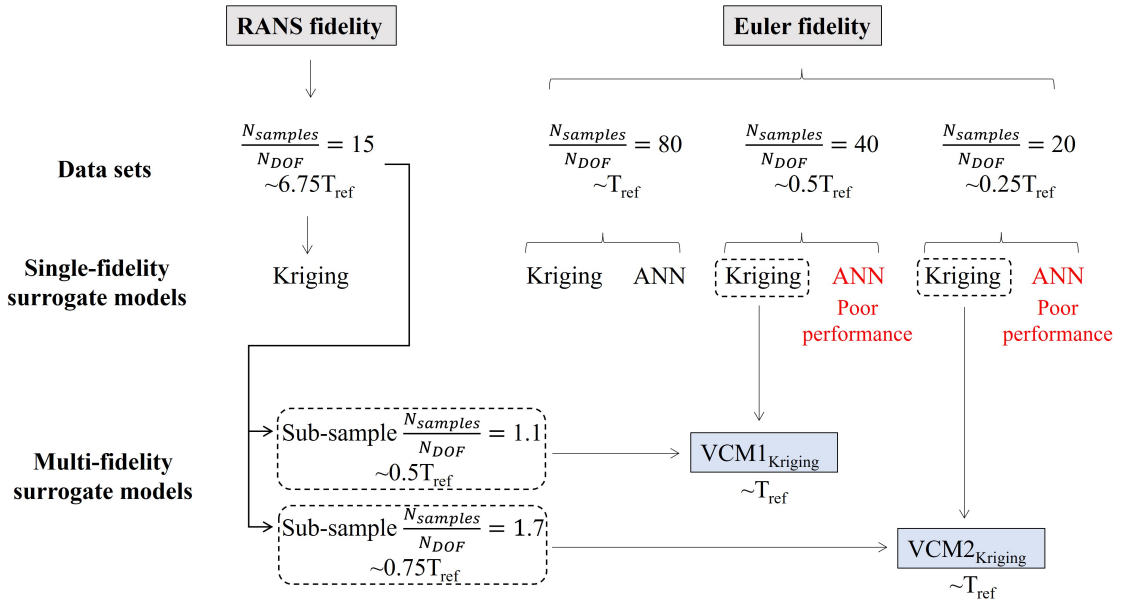

FIGURE 8.24: Summary of single-fidelity and multi-fidelity surrogate models.

model, the multi-fidelity models predicts more similar gradients of the design space to the high-fidelity Kriging$_{RANS_T}$ model (Figure 8.25). Besides, both multi-fidelity models correct for the over prediction in the magnitude of $\Delta NVF/F_N$ of the Kriging$_{Euler_{T1}}$ model (as shown in Figure 8.15 Euler CFD fidelity over predict $\Delta NVF/F_N$ compared to RANS CFD). In particular, there is a higher similarity for VCM2$_{Kriging}$ as it considers more high-fidelity RANS samples.

In the same manner as in the previous sections for single-fidelity models, both multi-fidelity models VCM1$_{Kriging}$ and VCM2$_{Kriging}$ are used to lead a surrogate-based optimisation. The optimal designs MF1 and MF2 are obtained with a $\Delta NVF/F_N$ evaluated with RANS CFD fidelity of 0.24% and 0.32% respectively (Figure 8.26). These benefits are substantially lower compared to the 0.52% and 0.56% obtained for the single-fidelity RANS-based and Euler-based Kriging models (Figure 8.26). A comparison of the r_{max} and f_{max} design variables for the optimal designs does not show substantial changes apart from $f_{max,135^\circ}$ for desing MF2. However, the combination of slight changes in several design variables can incur into a large change in $\Delta NVF/F_N$ for such challenging design spaces. Overall, the reason might be related to the higher uncertainty carried in the multi-fidelity models which seems to substantially impact the convergence to the optimal design space within an optimisation process. While the RMSE for the single-fidelity models is around 0.12%, it increases to around 0.17% for the multi-fidelity models.

In summary, for the nacelle aerodynamics optimisation problem in installed configuration constrained to sensible industrial time scales, there is no benefit of using a

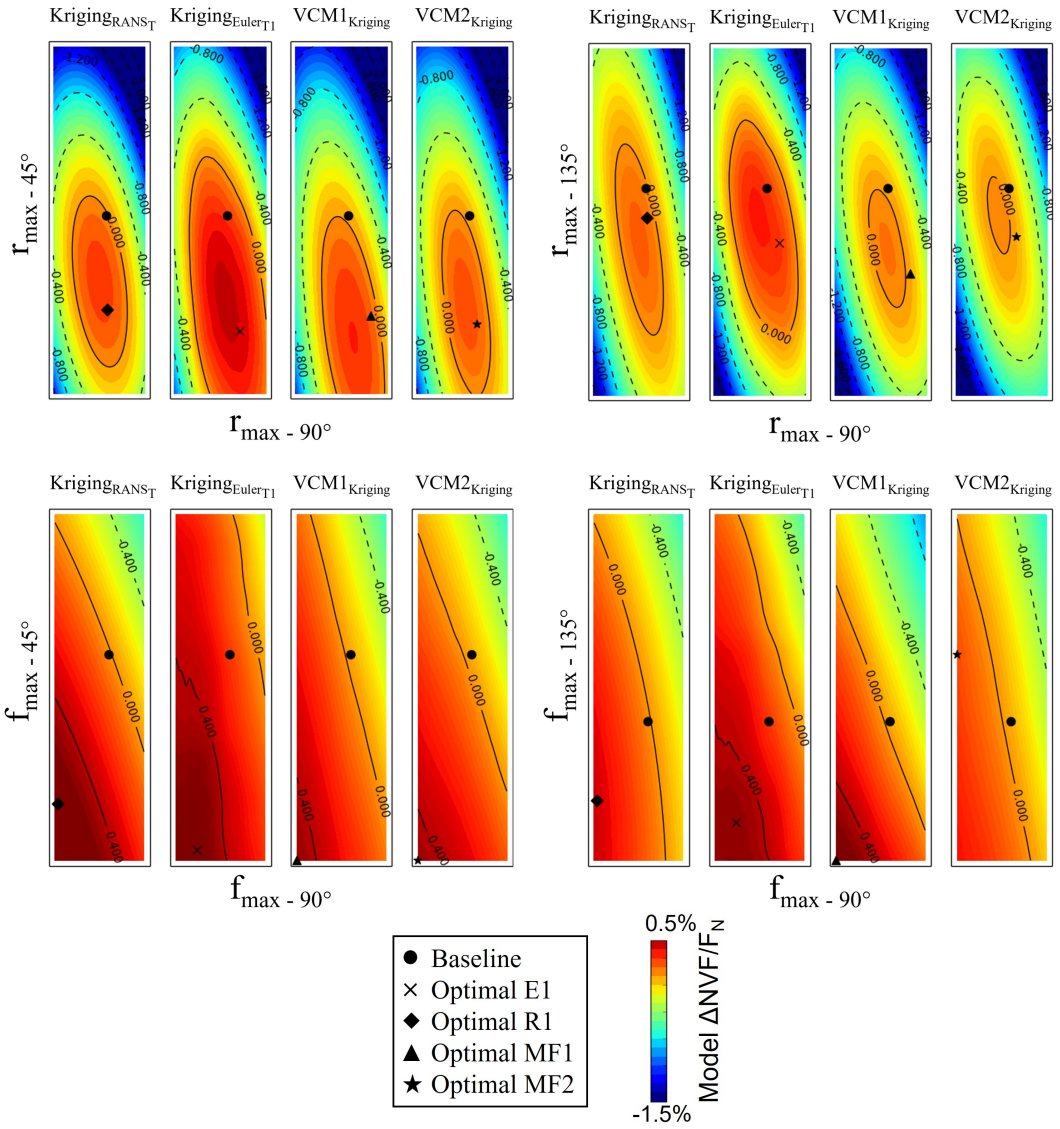

FIGURE 8.25: Comparison of the design space gradients for $\Delta NVF/F_N$ at the cruise condition ($M = 0.85$, $MFCR = 0.7$, $C_L = 0.5$ and Alt = 10668m) obtained through interrogation around the baseline design with the single-fidelity models Kriging$_{RANS_T}$ and Kriging$_{Euler_{T1}}$ and the multi-fidelity models VCM1$_{Kriging}$ and VCM2$_{Kriging}$. Optimal design obtained with each surrogate model marked in the maps.

multi-fidelity methodology. As the nacelle wetted surface is kept broadly constant in the optimisation process, the changes in nacelle drag are governed by the pressure terms. Therefore, there is a high similarity of the design space between the Euler and RANS fidelities. As a consequence, exploitation of the design space with a higher population of low-fidelity Euler CFD calculations is more efficient than correction of the gradients with high-fidelity data. In conclusion, the proposed method for nacelle optimisation is based on a single-fidelity Euler-based Kriging interpolation model constructed from a data set of $N_{sample}/N_{DOF} = 80$. This provides a design E1

within the reference limit T_{ref} that alleviates the flow interaction between the nacelle and the airframe (Figure 8.20) with an associated reduction in the fuel consumption of the aircraft at cruise of around 0.56% (Figure 8.26).

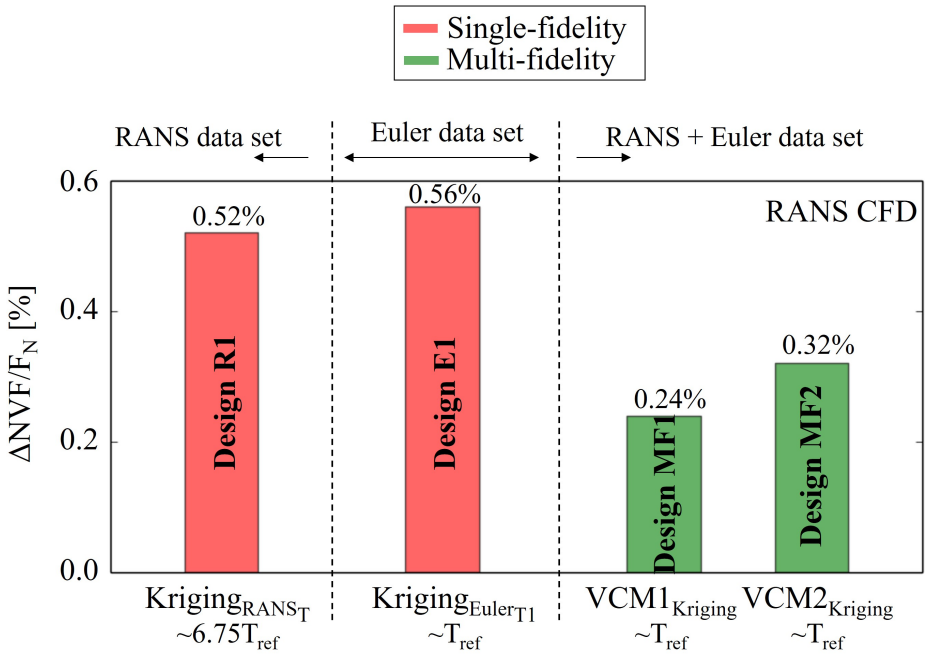

FIGURE 8.26: $\Delta NVF/F_N$ benefits evaluated with the RANS CFD fidelity at the cruise condition ($M = 0.85$, $MFCR = 0.7$, $C_L = 0.5$ and Alt = 10668m) for the optimal designs obtained with the single-fidelity models Kriging_{RANS_T} and $\text{Kriging}_{Euler_{T1}}$ and the multi-fidelity models $\text{VCM1}_{Kriging}$ and $\text{VCM2}_{Kriging}$.

8.3 Synthesis and discussion

A range of modelling techniques and CFD fidelities have been used in this project for the nacelle aerodynamic design and optimisation problem in installed configuration. This section aims to provide a synthesis of the whole work and deliver the key messages and recommendations.

- From a single-fidelity modelling point of view, it has been confirmed based on the RMSE the poorer predicting performance of ANN compared to Kriging as the number of samples used to train the model is reduced (Table 8.5). This is eventually translated into a lower NVF benefit of the optimal design obtained with ANN compared to Kriging.
- The poor modelling performance of ANN for scarce data sets ($N_{samples}/N_{DOF} =$ 40 and 20) together with the constraint in the overall cost to meet industrial

time scales makes the multi-fidelity neural network (MFNN) technique a non-viable method for installed nacelle design and optimisation.

- Variable complexity models (VCM) that consider the high-fidelity RANS data through Kriging interpolation and adjust to the cost constraint T_{ref} provide a lower NVF benefit (0.32%) compared to a traditional Euler-based Kriging model (0.56%) for the same cost T_{ref} (Table 8.5).

- Overall, it has been shown for the first time that the multi-fidelity methods investigated do not provide benefits relative to traditional methods for the installed nacelle design and optimisation problem. The recommended design approach is based on Euler CFD calculations with highly populated design spaces to build the surrogate model.

TABLE 8.5: Synthesis of the different single- and multi-fidelity models developed for the nacelle aerodynamic design and optimisation problem. The RMSE of the model evaluated in an independent data set and the overall cost associated to build the model are provided. The NVF benefits obtained from a surrogate-based optimisation using each model and evaluated with the RANS and Euler CFD models are included.

	Model	$\frac{N_{s,Euler}}{N_{DOF}}$	$\frac{N_{s,RANS}}{N_{DOF}}$	RMSE	Cost	$\frac{\Delta NVF_{Euler}}{F_N}$	$\frac{\Delta NVF_{RANS}}{F_N}$
SF (Euler)	$\text{ANN}_{Euler_{T1}}$	80	0	0.124%	T_{ref}	0.63%	-
	$\text{ANN}_{Euler_{T2}}$	40	0	0.289%	$T_{ref}/2$	0.51%	-
	$\text{ANN}_{Euler_{T3}}$	20	0	0.421%	$T_{ref}/4$	0.42%	-
	$\text{Kriging}_{Euler_{T1}}$	80	0	0.117%	T_{ref}	0.79%	0.56%
	$\text{Kriging}_{Euler_{T2}}$	40	0	0.141%	$T_{ref}/2$	0.50%	0.37%
	$\text{Kriging}_{Euler_{T3}}$	20	0	0.139%	$T_{ref}/4$	0.49%	0.33%
MF (Euler + RANS)	$\text{VCM1}_{Kriging}$	40	1.1	0.168%	T_{ref}	-	0.24%
	$\text{VCM2}_{Kriging}$	20	1.7	0.159%	T_{ref}	-	0.32%

CHAPTER 9

Conclusions and future work

9.1 Conclusions

This research project has addressed the aerodynamic shape optimisation problem of aero-engine nacelles considering the integration effects with the airframe. To enable this, a series of activities emerged as building blocks which delivered important conclusions to this field.

- A multi-fidelity surrogate method based on neural networks (MFNN) was first used for 2D axi-symmetric nacelle optimisations in an isolated configuration. It was shown that MFNN can successfully be adopted for these applications. Compared to a RANS CFD-in-the-loop optimisation approach, the MFNN converged to a very similar optimal design with a reduction in the overall computational cost in the order of 90%.
- For the first time, a systematic assessment of different modelling techniques for nacelle design and optimisation in installed configuration was conducted. This was based on the trades between the aerodynamic performance benefits and the computational cost. It was found that multi-fidelity surrogate modelling techniques do not offer benefits compared to the traditional single-fidelity Euler-based approach. The reason comes from the combination of the high computational cost of the RANS simulations for these cases and the need to adjust to industrial time scales in the design process which limits the size of the RANS data set that is used to construct the multi-fidelity model. For the installed nacelle design and optimisation problem, a highly populated design space, even with lower fidelity data, was found as the most important parameter to develop design space maps and identify the best design.

- A computational method for the design and optimisation of fully parametric nacelle shapes in an airframe-installed configuration at the cruise condition was developed. The approach uses a traditional Euler-based approach with a Kriging interpolation model and adjusts to an overall computational overhead that is in line with industrial time scales. The method generates design maps of the installed nacelle design variables that show the potential performance improvements across the design space and enables trade studies. This approach provides an optimised nacelle that alleviates the flow interference with the airframe and delivers a reduction in fuel burn at cruise of around 0.6% relative to a baseline nacelle. Additionally, this design meets the constraint in flow separation extent under windmilling diversion of $0.1L_{nac}$ evaluated with a RANS model that was imposed in the derivation of the baseline design.

- This work assessed the aerodynamics of the propulsion system integration in the airframe for a compact and a conventional nacelle configurations. For a typical installation position a reduction in the cruise fuel burn of around 0.44% was obtained for the compact design relative to the conventional one. However, the installation of the compact design at close-coupled positions, which are expected for UHBPR configurations, was shown to be more challenging with greater aerodynamic interference effects. Additionally, for the first time, the aerodynamics of the propulsion system integration was evaluated at the off-design windmilling diversion condition. A low impact of the aero-engine installation on the aerodynamics of both the compact and conventional nacelles was found which is governed by the spillage flow in the nacelle leading edge caused by the low engine mass flow of this kind of operating conditions.

- This research partially contributed to a wider programme on the validation of the CFD method for isolated nacelle optimisation using experimental data. This work specifically contributed to the off-design conditions evaluations and also to establish the mesh independence requirements. Within the cruise segment, the RANS CFD model shows good agreement with the measurements to predict nacelle drag and the sensitivities to important flow parameters such as Mach number and engine mass flow capture ratio. At the nominal cruise condition, the CFD drag coefficient is within 1% of the wind tunnel measurement which is within the experimental uncertainty. At the off-design windmilling diversion and end-of-runway conditions, there is a good agreement between experiments and RANS predictions for key flow features on the nacelle such as shock location, pre-shock Mach number, peak Mach number and flow diffusion in the afterbody.

- Unsteady CFD methods were assessed and compared with experimental data for the key off-design conditions considered in the nacelle optimisation problem. URANS CFD methods for high incidences at windmilling end-of-runway-type of conditions do not show any benefit with respect to steady RANS method in terms of the critical incidence of flow separation and reattachment. From the point of view of a RANS-based method for nacelle optimisation, a margin of $+1.5°$ is recommended for the end-of-runway condition. For windmilling diversion-type of conditions, and eddy-resolving DDES CFD method shows a higher sensitivity of flow separation and nacelle drag to MFCR changes at low values of MFCR compared to RANS methods. To account for this sensitivity within a RANS-based optimisation approach, a margin of around -0.02 in the nominal windmilling diversion MFCR condition is proposed.

9.2 Future work

From this project, a series of recommendations for future research activities emerged.

- For the design and optimisation method developed in this project which is governed by a high computational overhead, a key aspect is the proper selection of the design variables. It allows to obtain the highest benefit possible with a certain amount of computational resources. For example, in this design problem, β_{nac} in the three inboard aero-lines were considered as they were expected to play a great role in the interference aerodynamics between the engine, pylon and airframe. However, these parameters were found to have little impact on the NVF benefit of the full aircraft compared to r_{max} and f_{max}. Therefore, it would be useful to apply dimensionality reduction techniques like active subspaces or principal component analysis to identify the dominant geometrical parameters of the nacelle in installed configuration. The generation of RANS data sets large enough to extract the key design variables might not be computationally feasible. However, as very similar relationships between these design variables and NVF have been found between the RANS and the Euler CFD methods, the dimensionality reduction techniques are proposed to be deployed in Euler data sets.

- The design and optimisation method developed in this research has shown the potential improvement that can be achieved by designing nacelles in an airframe-installed configuration. A reduction in the cruise fuel consumption of

the aircraft of 0.6% is substantial. This suggests that further benefits may be obtained with more flexibility in the design space. Additionally, this research has identified that the optimal region of the design space for installed nacelles is governed by penalties in the airframe drag. Therefore, a coupled optimisation of the full nacelle geometry with the pressure side of the wing is proposed as future work. However, the design method developed in this project is not able to handle such a high dimensional problem and other techniques are needed. An adjoint-based optimisation approach is proposed. This method will provide the best design from the optimisation but will not be able to deliver design guidelines or maps of the design space gradients. The reason is that adjoint uses a geometry perturbation approach like the free form deformation method while the method developed here considers an analytical parameterisation of the nacelle geometry.

- The investigation of the design space in this research has shown that the optimal region of these design space is located in the areas of penalties in the gross propulsive force. Therefore, it is recommended to perform a coupled design of the nacelle and the exhaust system to investigate the possibility to recover the thrust lost due to the installation. This looks promising as recent technologies of non-axisymmetric exhaust systems have shown benefits in the reduction of cruise fuel burn in the order of 1%.

- The pylon geometries considered in this work come from initial design capabilities available in the research group. They are designed with the basis of allowing propulsion system integration studies while avoiding flow separation at cruise in the surrounding of the pylon. However it is acknowledged that a more representative design would not be symmetric and would intersect with the fan cowl geometry further upstream. This might affect the design space and the dominant design variable. Therefore, a more representative pylon should be included for similar studies in the future.

References

References

[1]International Air Transport Association (IATA). Aircraft Technology Roadmap to 2050. Technical report, 2019. https://www.iata.org/contentassets/8d19e716636a47c184e7221c77563c93/Technology-roadmap-2050.pdf Accessed: 24/10/2022.

[2]Advisory Council for Aviation Research and Innovation (ACARE). Time for change - The need to rethink Europe's FlightPath 2050. Technical report, 2020.

[3]International Civil Aviation Organization (ICAO). Effects of novel coronavirus (covid-19) on civil aviation: economic impact analysis. Technical report, 2022. https://www.icao.int/sustainability/Documents/Covid-19/ICAO_coronavirus_Econ_Impact.pdf Accessed: 29/11/2022.

[4]Airports Council International. The impact of COVID-19 on airports and the path to recovery. https://aci.aero/2022/06/28/the-impact-of-covid-19-on-airportsand-the-path-to-recovery/, Accessed: 29/11/2022.

[5]European Commission. *Flightpath 2050 : Europe's vision for aviation : maintaining global leadership and serving society's needs*. Publications Office of the European Union, 2011.

[6]International Air Transport Association (IATA). Industry statistics fact sheet. Technical report, IATA, 2019. https://www.iata.org/en/iata-repository/pressroom/fact-sheets/industry-statistics/Accessed: 29/11/2022.

[7]M. Daly, editor. *Jane's Aero-Engines*, page 64. IHS Global, 28th edition, 2009.

[8]D. L. Daggett, S. T. Brown, and R. T. Kawai. Ultra Efficient Engine Diameter Study. Technical Report CR-2003-212309, NASA, 2003. https://ntrs.nasa.gov/api/citations/20030061085/downloads/20030061085.pdf, Accessed: 27/08/2021.

[9]A. Haines. Aerodynamic Interference – A General Overview, Special Course on Subsonic/-Transonic Aerodynamic Interference for Aircraft. Technical Report No. 712, Advisory Group for Aerospace Research and Development (AGARD), 1983.

[10]T. P. Stańkowski. *Aerodynamics of Propulsion System Integration for Modern Aero-Engines*. PhD Thesis, Cranfield University, 2016.

[11]Clean Sky 2 JU. The UHBR engine flight testing programme gathers momentum. Technical report, European Commission, 2018. https://clean-aviation.eu/sites/default/files/2021-10/CLEAN_SKY_Article_UHBR.pdf, Accessed: 15/07/2022.

[12]J. Whurr. Future civil aeroengine architectures & technologies. In *10th European Conference on Turbomachinery, Guest lecture*, Lappeenranta, Finland, 2013.

[13]M. Albert and D. Bestle. Aerodynamic Design Optimization of Nacelle and Intake. In *Proceedings of ASME Turbo Expo 2013: Turbine Technical Conference and Exposition, GT2013-94857*, San Antonio, Texas, USA, June 2013. American Society of Mechanical Engineers.

[14]H. Toubin, I. Salah El Din, and M. Meheut. Multipoint Aerodynamic High Fidelity Shape Optimization of an Isolated Engine Nacelle. In *52nd Aerospace Sciences Meeting, AIAA 2014-0903*, National Harbor, Maryland, USA, January 2014. American Institute of Aeronautics and Astronautics.

[15]W. Song and A. J. Keane. Surrogate-Based Aerodynamic Shape Optimization of a Civil Aircraft Engine Nacelle. *AIAA Journal*, 45(10):2565–2574, October 2007.

[16]F. Tejero, M. Robinson, D. G. MacManus, and C. Sheaf. Multi-objective optimisation of short nacelles for high bypass ratio engines. *Aerospace Science and Technology*, 91:410–421, 2019.

[17]F. Tejero, D. MacManus, J. Hueso-Rebassa, F. Sanchez-Moreno, I. Goulos, and C. Sheaf. Aerodynamic optimisation of civil aero-engine nacelles by dimensionality reduction and multi-fidelity techniques. *International Journal of Numerical Methods for Heat & Fluid Flow*, ahead-of-print, 2022.

[18]B. D. J. Schreiner, F. Tejero, D. G. MacManus, and C. Sheaf. Robust Aerodynamic Design of Nacelles for Future Civil Aero-Engines. In *Proceedings of ASME Turbo Expo 2020: Power for Land, Sea, and Air, GT2020-14470*, Virtual, September 2020.

[19]F. Tejero, D. MacManus, J. García-Matesanz, A. Swarthout, and C. Sheaf. Towards the design and optimisation of future compact aero-engines: intake/fancowl trade-off investigation. *International Journal of Numerical Methods for Heat & Fluid Flow*, ahead-of-print, 2022.

[20]MIDAP Study group. Guide to in-Flight Thrust Measurement of Turbo- jets and Fan Engines. Technical Report No. AG-237, AGARD, Neuilly sur Seine, France, 1979.

[21]ESDU. Drag of axisymmetric cowls at zero incidence for subsonic mach numbers. Technical Report ESDU 81024, ESDU International, London, UK, November 1981. `http://www.esdu.com/cgi-bin/ps.pl?sess=unlicensed_1130621151056wkc&t=doc&p=di_81024a`.

[22]O. Vermeersch and X. Bouteiller. Numerical study of laminar nacelles: natural and hybrid laminar flow designs. *International Journal of Engineering Systems Modelling and Simulation 48*, 6(3-4):191–204, 2014.

[23]F. M. White. *Viscous Fluid Flow*. McGraw-Hill Education, Singapore, third edition, 2006.

[24]J. T. Kutney and S. P. Piszkin. Reduction of drag rise on the Convair 990 airplane. *Journal of Aircraft*, 1(1):8–12, 1964.

[25]J. Roskam and C.T.E. Lan. *Airplane Aerodynamics and Performance*, page 141. DAR corporation, Lawrence, Kansas, USA, 1997.

[26]R. S. Shevell and F. P. Bayan. Development of a method for predicting the drag divergence mach number and the drag due to compressibility for conventional and supercritical wings. Technical Report SUDAAR 522, Department of Aeronautics and Astronautics, Stanford University, 1981.

[27]M. Robinson, D. G. MacManus, A. Heidebrecht, and N. Grech. An optimisation method for nacelle design. In *AIAA SciTech Forum, AIAA 2017-0708*, Grapevine, Texas, USA, January 2017. American Institute of Aeronautics and Astronautics.

[28]J. A. Borradaile. Towards the optimum ducted UHBR engine. In *24th AIAA/SAE/ASME/ASEE Joint Propulsion Conference, AIAA-88-2954*, Boston, Massachusetts, USA, July 1988. American Institute of Aeronautics and Astronautics.

[29]Faust, G. K. and Mungur, P. Nacelle design. Technical Report N90-12551, NASA, 1987.

[30]Street, P. G. Thrust/drag analysis for a front fan nacelle having two separate co-axial exhaust streams. Technical Report ARC/CP-1311, Aeronautical Research Council, 1975. `https://reports.aerade.cranfield.ac.uk/handle/1826.2/1324` Accessed: 15/10/2022.

[31]ESDU. Mass flow and momentum functions for one-dimensional flow of gas in ducts. Technical Report ESDU 81004, ESDU International, London, UK, March 1981.

[32]E. Obert. *Aerodynamic design of transport aircraft.* IOS Press, 2009.

[33]P. K. Zachos. *Gas Turbine Sub-idle Performance Modelling; Altitude Relight and Windmilling.* PhD Thesis, Cranfield University, 2010.

[34]M. J. Langley. The design of axisymmetric cowls for podded nacelles for high by-pass ratio turbofan engines. Technical Report R&M No. 3846, Aeronautical Research Council, 1979.

[35]C. P. Van Dam. Recent experience with different methods of drag prediction. *Progress in Aerospace Sciences*, 35(8):751–798, 1999.

[36]J. B. Vos and S. Sanchi. DPW4 Results Using Different Grids Including Near-Field/Far-Field Drag Analysis. In *28th AIAA Aplied Aerodynamics Conference, AIAA 2010-4552*, Chicago, Illinois, USA, June 2010. American Institute of Aeronautics and Astronautics.

[37]D. Destarac and J. Van Der Vooren. Drag/thrust analysis of jet-propelled transonic transport aircraft; definition of physical drag components. *Aerospace science and technology*, 8(6):545–556, 2004.

[38]L. G. Trapp and H. G. Argentieri. Evaluation of nacelle drag using computational fluid dynamics. *Journal of Aerospace Technology and Management*, 2:145–154, 2010.

[39]M. Robinson, D. G. MacManus, and C. Sheaf. Aspects of aero-engine nacelle drag. *Proceedings of the Institution of Mechanical Engineers, Part G: Journal of Aerospace Engineering*, 233(5):1667–1682, 2019.

[40]R. Christie, S. Ramirez, and D. G. MacManus. Aero-engine installation modelling and the impact on overall flight performance. In *Advanced Aero Concepts, Design and Operations*, Bristol, UK, July 2014.

[41]Y. Fan and W. Li. Review of far-field drag decomposition methods for aircraft design. *Journal of Aircraft*, 56(1):11–21, 2019.

[42]J. M. Janus and A. Chatterjee. Use of a wake-integral method for computational drag analysis. *AIAA journal*, 34(1):188–190, 1996.

[43]M. B. Giles and R. M. Cummings. Wake integration for three-dimensional flowfield computations: theoretical development. *Journal of Aircraft*, 36(2):357–365, 1999.

[44]A. C. Hansen, J. A. Peterka, and J. E. Cermak. Wind tunnel measurements in the wake of a simple structure in a simulated atmospheric flow. Technical report, NASA, 1975.

[45]J. Joo, G. Tillman, and R. Lin. Nacelle external drag prediction using computational fluid dynamics. In *48th AIAA/ASME/SAE/ASEE Joint Propulsion Conference and Exhibit, AIAA 2012-3998*, Atlanta, Georgia, USA, August 2012. American Institute of Aeronautics and Astronautics.

[46]D. S. Sanders and P. Laskaridis. Full-aircraft energy-based force decomposition applied to boundary-layer ingestion. *AIAA Journal*, 58(10):4357–4373, 2020.

[47]A. Arntz and O. Atinault. Exergy-based performance assessment of a blended wing–body with boundary-layer ingestion. *AIAA journal*, 53(12):3766–3776, 2015.

[48]M. Drela. Power balance in aerodynamic flows. *AIAA Journal*, 47(7):1761–1771, 2009.

[49]M. A. Aguirre. *Exergy analysis of innovative aircraft with aeropropulsive coupling*. PhD Thesis, Institut Supérieur de l'Aéronautique et de l'Espace, SUPAERO, 2022.

[50]A. Cheval. *Multi-Objective Optimisation of Ultrafan Nacelles*. MSc Thesis, Cranfield University, 2019.

[51]F. Tejero, R. Christie, D. MacManus, and C Sheaf. Non-axisymmetric aero-engine nacelle design by surrogate-based methods. *Aerospace Science and Technology*, 117, 10 2021.

[52]V. T. Silva, A. Lundbladh, O. Petit, and C. Xisto. Multipoint Aerodynamic Design of Ultrashort Nacelles for Ultrahigh-Bypass-Ratio Engines. *Journal of Propulsion and Power*, 38(4):1–18, 2022.

[53]A. Magrini, D. Buosi, and E. Benini. Analysis of installation aerodynamics and comparison of optimised configuration of an ultra-high bypass ratio turbofan nacelle. *Aerospace Science and Technology*, 128, 2022.

[54]F. Tejero, I. Goulos, D. MacManus, and C. Sheaf. Effects of aircraft integration on compact nacelle aerodynamics. In *AIAA Scitech 2020 Forum, AIAA 2020-2225*, Orlando, Florida, USA, January 2020. American Institute of Aeronautics and Astronautics.

[55]Y. Zhong and S. Li. A 3D Shape Design and Optimization Method for Natural Laminar Flow Nacelle. In *Proceedings of ASME Turbo Expo: Power for Land, Sea and Air, GT2017-64379*, Charlotte, North Carolina, USA, June 2017. American Society of Mechanical Engineers.

[56]P. P. Shipley, J. L. Lecordix, and J. L. Godard. The design optimisation of a hybrid laminar flow nacelle. Technical report, Rolls Royce, 1993.

[57]Muellender A. J., Lecordix J. L., Lecossaos E.and Godard J. L., and Hepperle M. The Elfin II and LARA HLF nacelles: Design, Manufacture and Test. Technical Report PNR92296, Rolls Royce, 1996.

[58]P. Meyer. Application of HLF Technology to Civil Nacelle. In *Aerodynamic Drag Reduction Technologies*, Berlin, Germany, 2001. Springer Berlin Heidelberg.

[59]G. Schrauf and W. Kühn. Future needs and laminar flow technology. *Air and Space Europe*, 3(3):98–100, 2001.

[60]X. He, J. Bai, L. Xia, S. Chen, and L. Qiao. Natural laminar flow nacelle optimization design based on effd method. *Journal of Aerospace Power*, 29:2311–2320, 2014.

[61]S. Wang, G. Sun, and C. Li. Natural laminar flow optimization of transonic nacelle based on differential evolution algorithm. *Journal of Aerospace Engineering*, 32, 2019.

[62]Y. Yao, D. Ma, M. Yang, L. Zhang, and Y. Guo. Adaptive-surrogate-based robust optimization of transonic natural laminar flow nacelle. *Chinese Journal of Aeronautics*, 34(10):36–52, 2021.

[63]R. Radespiel, K.H. Horstmann, and G. Redeker. Feasibility study on the design of a laminar flow nacelle. *Journal of Aircraft*, 27(11):1–7, 1990.

[64]H. Riedel, K. H. Horstmann, A. Ronzheimer, and M. Sitzmann. Aerodynamic design of a natural laminar flow nacelle and the design validation by flight testing. *Aerospace Science and Technology*, 2(1):1–12, 1998.

[65]R. Rudnik, C. C. Rossow, and H. F. V. Geyr. Numerical simulation of engine/airframe integration for high-bypass engines. *Aerospace Science and Technology*, 6(1):31–42, 2002.

[66]D. J. Kettle and D. A. Kirby. Low-speed wind-tunnel tests on the effects of tailplane and nacelle position on the superstall characteristics of transport aircraft. Technical Report R. and M. No. 3571, Aeronautical Research Council, 1969.

[67]O. D. Wells, M. L. Lopez, H. R. Welge, P. A. Henne, and A. E. Sewell. Wind tunnel and analytical investigation of over-the-wing propulsion/airframe interferences for a short-haul aircraft at Mach numbers from 0.6 to 0.78. Technical Report CR-2905, NASA, 1977.

[68]R. Yoneta, D. Sasaki, and K. Nakahashi. Aerodynamic optimization of an over-the-wing-nacelle-mount configuration. In *48th AIAA Aerospace Sciences Meeting Including the New Horizons Forum and Aerospace Exposition, AIAA 2010-1016*, Orlando, Florida, USA, January 2010. American Institute of Aeronautics and Astronautics.

[69]Convair Aerospace Division of General Dynamics. Experimental investigation of parametric models in support of a nasa advanced transport technology program. Technical Report CR-112133, NASA, 1972.

[70]L. H. Bangert, D. K. Krivec, and R. N. Segall. Effects of nacelle configuration/position on performance of subsonic transport. Technical Report CR-3743, NASA, 1983.

[71]D. L. Berry. The Boeing 777 Engine/Aircraft Integration Aerodynamic Design Process. In *ICAS Congress 1994, ICAS-94-6.4.4*, Anaheim, California, USA, September 1994. International Council of the Aeronautical Sciences.

[72]N. J. Blaesser. *Interference Drag Due to Engine Nacelle Location for a Single-Aisle, Transonic Aircraft*. PhD Thesis, Virginia Tech, 2020.

[73]A. E. Harris and K. C. Paliwal. Civil Turbofan Propulsion System Integration Studies Using Powered Testing Techniques at ARA. In *13th Aerodynamic Testing Conference, AIAA 84-0593*, San Diego, California, USA, March 1984. American Institute of Aeronautics and Astronautics.

[74]G. Krenz. Engine/Airframe Interference, Special Course on Subsonic/Transonic Aerodynamic Interference for Aircraft. Technical Report No. 712, AGARD, 1983.

[75]A. W. Chen and E. N. Tinoco. Pan air applications to aero-propulsion integration. *Journal of Aircraft*, 21(3):161–167, 1984.

[76]W. Burgsmüller and H. Hoheisel. ENIFAIR—EU research into engine integration on future transport aircraft. *Air and Space Europe*, 2(2):81–85, 2000.

[77]Y. Zhang, H. Chen, S. Fu, M. Zhang, and M. Zhang. Drag prediction method of powered-on civil aircraft based on thrust drag bookkeeping. *Chinese Journal of Aeronautics*, 28(4):1023–1033, 2015.

[78]C. C. Sabater. *External Flow Effects in the Engine/Airframe Integration Testing Technique: A New Thrust/Drag Bookkeeping Approach at the German-Dutch Wind Tunnels*. MSc Thesis, Delft University of Technology, 2017.

[79]G. Gatlin, M. Rivers, S. Goodliff, R. Rudnik, and M. Sitzmann. Experimental investigation of the DLR-F6 transport configuration in the national transonic facility. In *26th AIAA Applied Aerodynamics Conference, AIAA 2008-6917*, Honolulu, Hawaii, USA, August 2008. American Institute of Aeronautics and Astronautics.

[80]O. Brodersen, M. Rakowitz, S. Amant, P. Larrieu, D. Destarac, and M. Sutcliffe. Airbus, ONERA, and DLR results from the second AIAA drag prediction workshop. *Journal of Aircraft*, 42(4):932–940, 2005.

[81]J. Vassberg, M. Dehaan, M. Rivers, and R. Wahls. Development of a common research model for applied cfd validation studies. In *26th AIAA applied aerodynamics conference, AIAA 2008-6919*, Honolulu, Hawaii, USA, August 2008. American Institute of Aeronautics and Astronautics.

[82]M. B. Rivers and A. Dittberner. Experimental investigations of the nasa common research model. *Journal of Aircraft*, 51(4):1183–1193, 2014.

[83]J. C. Vassberg, E. N. Tinoco, M. Mani, B. Rider, T. Zickuhr, D. W. Levy, O. P. Brodersen, B. Eisfeld, S. Crippa, R. A. Wahls, et al. Summary of the fourth aiaa computational fluid dynamics drag prediction workshop. *Journal of Aircraft*, 51(4):1070–1089, 2014.

[84]NASA.gov. 6th AIAA CFD Drag Prediction Workshop. `https://aiaa-dpw.larc.nasa.gov/Workshop4/`, Accessed: 22/09/2022.

[85]H. Hoheisel and H. F. V. Geyr. The influence of engine thrust behaviour on the aerodynamics of engine airframe integration. *CEAS Aeronautical Journal*, 3(1):79–92, 2012.

[86]L. L. Erickson. Panel methods: An introduction. Technical Report NASA-TP-2995, NASA, 1990.

[87]F. Johnson and P. Rubbert. Advanced panel-type influence coefficient methods applied to subsonic flows. In *13th Aerospace Sciences Meeting*, Pasadena, California, USA, January 1975. American Institute of Aeronautics and Astronautics.

[88]F. T. Johnson, S. S. Samant, M. B. Bieterman, R. G. Melvin, D. P. Young, J. E. Bussoletti, and C. L. Hilmes. TranAir: A full-potential, solution-adaptive, rectangular grid code for predicting subsonic, transonic, and supersonic flows about arbitrary configurations. Technical Report NASA-CR-4348, NASA, 1992.

[89]Y. Gisin and D. Marshall. Wing-nacelle assembly multidisciplinary performance optimization. In *45th AIAA Aerospace Sciences Meeting and Exhibit, AIAA 2007-1463*, Reno, Nevada, USA, January 2007. American Institute of Aeronautics and Astronautics.

[90]M. Hafez. Finite element/finite volume solutions of full potential, Euler and Navier-Stokes equations for compressible and incompressible flows. *International Journal for Numerical Methods in Fluids*, 20:713–741, 1995.

[91]J. D. Anderson. *Modern compressible flow: with historical perspective*. McGraw-Hill Education, Singapore, third edition, 2004.

[92]L. Crocco. Eine neue Stromfunktion für die Erforschung der Bewegung der Gase mit Rotation. *ZAMM-Journal of Applied Mathematics and Mechanics*, 17(1):1–7, 1937.

[93]C. C. Rossow, J. L. Godard, H. Hoheisel, and V. Schmitt. Investigations of propulsion integration interference effects on a transport aircraft configuration. *Journal of Aircraft*, 31(5):1022–1030, 1994.

[94]O. Brodersen. Drag prediction of engine-airframe interference effects using unstructured navier-stokes calculations. *Journal of Aircraft*, 39(6):927–935, 2002.

[95]F. R. Menter. Two-equation eddy-viscosity turbulence models for engineering applications. *AIAA Journal*, 32(8):1598–1605, 1994.

[96]E. N. Tinoco, O. P. Brodersen, S. Keye, K. R. Laflin, E. Feltrop, J. C. Vassberg, M. Mani, B. Rider, R. A. Wahls, J. H. Morrison, D. Hue, C. J. Roy, D. J. Mavriplis, and M. Murayama. Summary data from the sixth AIAA CFD drag prediction workshop: CRM cases. *Journal of Aircraft*, 55(4):1352–1379, 2018.

[97]A. Magrini, D. Buosi, and E. Benini. Maximisation of installed net resulting force through multi-level optimisation of an ultra-high bypass ratio engine nacelle. *Aerospace Science and Technology*, 119, 2021.

[98]I. Goulos, J. Otter, F. Tejero, J. Hueso Rebassa, D. MacManus, and C. Sheaf. Civil turbofan propulsion aerodynamics: Thrust-drag accounting and impact of engine installation position. *Aerospace Science and Technology*, 111, 2021.

[99]Society of Automotive Engineers (SAE). Advanced ducted propulsor in-flight thrust determination. Technical Report AIR5450, SAE International, August 2008.

[100]M. Bauer, J. Friedrichs, D. Wulff, and C. Werner-Spatz. Development and validation of an on-wing engine thrust measurement system. In *Proceedings of ASME Turbo Expo 2017: Power for Land, Sea and Air, GT2017-63277*, Charlotte, North Carolina, USA, June 2017. American Society of Mechanical Engineers.

[101]ESDU. The Determination of Gross Thrust and Mass flow in Flight. (Air Breath-ing Ducted-Flow Engines with Convergent Nozzles). Technical Report No. 69007, ESDU, 1981.

[102]A. Magrini, E. Benini, H. D. Yao, J. Postma, and C. Sheaf. A review of installation effects of ultra-high bypass ratio engines. *Progress in Aerospace Sciences*, 119, 2020.

[103]H. Hoheisel. Aerodynamic aspects of engine-aircraft integration of transport aircraft. *Aerospace Science and Technology*, 1(7):475–487, 1997.

[104]O. Brodersen. Computation of engine-airframe installation drag. In *MEGAFLOW - Numerical Flow Simulation for Aircraft Design*, Berlin, Germany, 2005. Springer Berlin Heidelberg.

[105]Ingraldi A. M. Interference Effects of Very High Bypass Ratio Nacelle Installations on a Low-Wing Transport. *Journal of Engineering for Gas Turbines and Power*, 114(1), 1992.

[106]I. Goulos. Private communication - 10/06/2022, June 2022.

[107]T. P. Stankowski, D. G. MacManus, M. Robinson, and C. T. Sheaf. Aerodynamic effects of propulsion integration for high bypass ratio engines. *Journal of Aircraft*, 54(6):2270–2284, 2017.

[108]W. P. Henderson. Airframe/propulsion integration at transonic speeds. *Journal of Engineering for Gas Turbines and Power*, 113(1):51–59, 1991.

[109]J. R. Carlson and M. Lamb. Integration effects of pylon geometry on a high-wing transport airplane. Technical Report TR-2877, NASA, 1989.

[110]R. Devine, R. K. Cooper, R. Gault, J. K. Watterson, and E. Bénard. Comparison of conventional and compression pylon designs for an underwing nacelle. *Journal of Aircraft*, 46(1):325–328, 2009.

[111]P. Spalart and S. Allmaras. A one-equation turbulence model for aerodynamic flows. In *30th Aerospace Sciences Meeting and Exhibit, AIAA-92-0439*, Reno, Nevada, USA, January 1992. American Institute of Aeronautics and Astronautics.

[112]E. E. Lee and O. C. Pendergraft Jr. Installation effects of long-duct pylon-mounted nacelles on a twin-jet transport model with swept supercritical wing. Technical Report TR-2457, NASA, 1985.

[113]J. J. Otter. *Aerodynamics and Performance of Civil Aero-Engine Exhaust Systems.* PhD Thesis, Cranfield University, 2018.

[114]S. N. Skinner and H. Zare-Behtash. State-of-the-art in aerodynamic shape optimisation methods. *Applied Soft Computing*, 62:933–962, 2018.

[115]J. Lepine, F. Guibault, J. Y. Trepanier, and F. Pepin. Optimized nonuniform rational B-spline geometrical representation for aerodynamic design of wings. *AIAA Journal*, 39(11):2033–2041, 2001.

[116]N. E. Antoine and I. M. Kroo. Framework for aircraft conceptual design and environmental performance studies. *AIAA Journal*, 43(10):2100–2109, 2005.

[117]D. E. Goldberg. *Genetic algorithms in seraching optimisation and machine learning*. Addison-Wesley Longman Publishing, 1989.

[118]J. Li and M. Zhang. Data-based approach for wing shape design optimization. *Aerospace Science and Technology*, 112, 2021.

[119]G. K. W. Kenway, C. A. Mader, P. He, and J. R. R. A. Martins. Effective adjoint approaches for computational fluid dynamics. *Progress in Aerospace Sciences*, 110, 2019.

[120]O. Pironneau. On optimum design in fluid mechanics. *Journal of Fluid Mechanics*, 64(1):97–110, 1974.

[121]Z. Lyu, G. K. W. Kenway, and J. R. R. A. Martins. Aerodynamic shape optimization investigations of the common research model wing benchmark. *AIAA Journal*, 53(4):968–985, 2015.

[122]D. A. Burdette, G. K. Kenway, and J. R. R. A. Martins. Performance evaluation of a morphing trailing edge using multipoint aerostructural design optimization. In *57th AIAA/ASCE/AHS/ASC Structures, Structural Dynamics, and Materials Conference, AIAA 2016-0159*, San Diego, California, USA, January 2016. American Institute of Aeronautics and Astronautics.

[123]A. Jameson. Automatic design of transonic airfoils to reduce the shock induced pressure drag. In *Proceedings of the 31st Israel Annual Conference on Aviation and Aeronautics*, Tel Aviv-Yafo, Israel, February 1990.

[124]J. J. Reuther, A. Jameson, J. J. Alonso, M. J. Rimllnger, and D. Saunders. Constrained multipoint aerodynamic shape optimization using an adjoint formulation and parallel computers, part 2. *Journal of Aircraft*, 36(1):61–74, 1999.

[125]A. Jameson, L. Martinelli, and N. A. Pierce. Optimum aerodynamic design using the navier-stokes equations. *Theoretical and Computational Fluid Dynamics*, 10(1):213–237, 1998.

[126]J. J. Reuther. *Aerodynamic Shape Optimization Using Control Theory*. PhD Thesis, University of California Davis, 1996.

[127]J. R. R. A. Martins, J. J. Alonso, and J. J. Reuther. A coupled-adjoint sensitivity analysis method for high-fidelity aero-structural design. *Optimization and Engineering*, 6(1):33–62, 2005.

[128]J. H. Kim, B. Ovgor, K. H. Cha, J. H. Kim, S. Lee, and K. Y. Kim. Optimization of the aerodynamic and aeroacoustic performance of an axial-flow fan. *AIAA Journal*, 52(9):2032–2044, 2014.

[129]V. Nejati and K. Matsuuchi. Aerodynamics design and genetic algorithms for optimization of airship bodies. *JSME International Journal Series B Fluids and Thermal Engineering*, 46(4):610–617, 2003.

[130]A. P. Antunes and J. L. F. Azevedo. Studies in aerodynamic optimization based on genetic algorithms. *Journal of Aircraft*, 51(3):1002–1012, 2014.

[131]S. Haghighat, J. R. R. A. Martins, and H. H. T. Liu. Aeroservoelastic design optimization of a flexible wing. *Journal of Aircraft*, 49(2):432–443, 2012.

[132]C. C. Xia, T. T. Jiang, and W. F. Chen. Particle swarm optimization of aerodynamic shapes with nonuniform shape parameter–based radial basis function. *Journal of Aerospace Engineering*, 30(3):04016089, 2017.

[133]A. Slowik and H. Kwasnicka. Evolutionary algorithms and their applications to engineering problems. *Neural Computing and Applications*, 32(16):12363–12379, 2020.

[134]A. C. Godínez, L. E. M. Espinosa, and E. M. Montes. An experimental comparison of multiobjective algorithms: NSGA-II and OMOPSO. In *2010 IEEE Electronics, Robotics and Automotive Mechanics Conference*, Cuernavaca, Mexico, September 2010. Institute of Electrical and Electronics Engineers.

[135]R. C. Eberhart and Y. Shi. Comparison between genetic algorithms and particle swarm optimization. In *International Conference on Evolutionary Programming*, San Diego, California, USA, March 1998.

[136]R. Hassan, B. Cohanim, O. De Weck, and G. Venter. A comparison of particle swarm optimization and the genetic algorithm. In *46th AIAA/ASME/ASCE/AHS/ASC Structures, Structural Dynamics and Materials Conference, AIAA 2005-1897*, Austin, Texas, USA, April 2005. American Institute of Aeronautics and Astronautics.

[137]F. D. Wihartiko, H. Wijayanti, and F. Virgantari. Performance comparison of genetic algorithms and particle swarm optimization for model integer programming bus timetabling problem. *IOP Conference Series: Materials Science and Engineering*, 332, 2018.

[138]Z. Lyu, Z. Xu, and J. R. R. A. Martins. Benchmarking optimization algorithms for wing aerodynamic design optimization. In *Proceedings of the 8th International Conference on Computational Fluid Dynamics*, Chengdu, Sichuan, China, July 2014.

[139]R. Mukesh, K. Lingadurai, and S. Karthick. Aerodynamic optimization using proficient optimization algorithms. In *2012 International Conference on Computing, Communication and Applications*, Dindigul, India, February 2012. Institute of Electrical and Electronics Engineers.

[140]K. C. Giannakoglou. Design of optimal aerodynamic shapes using stochastic optimization methods and computational intelligence. *Progress in Aerospace Sciences*, 38(1):43–76, 2002.

[141]D. G. Krige. A statistical approach to some basic mine valuation problems on the witwatersrand. *Journal of the Southern African Institute of Mining and Metallurgy*, 52(6):119–139, 1951.

[142]S. Y. Chung, S. Venkatramanan, H. E. Elzain, S. Selvam, and M. V. Prasanna. Supplement of missing data in groundwater-level variations of peak type using geostatistical methods. *GIS and Geostatistical Techniques for Groundwater Science*, pages 33–41, 2019.

[143]X. F. Wang, G. Xi, and Z. H. Wang. Aerodynamic optimization design of centrifugal compressor's impeller with kriging model. *Proceedings of the Institution of Mechanical Engineers, Part A: Journal of Power and Energy*, 220(6):589–597, 2006.

[144]V. Raul and L. Leifsson. Surrogate-based aerodynamic shape optimization for delaying airfoil dynamic stall using kriging regression and infill criteria. *Aerospace Science and Technology*, 111, 2021.

[145]A. Díaz-Manríquez, G. Toscano, and C. A. Coello Coello. Comparison of metamodeling techniques in evolutionary algorithms. *Soft Computing*, 21(19):5647–5663, 2017.

[146]G. Giangaspero, D. MacManus, and I. Goulos. Surrogate models for the prediction of the aerodynamic performance of exhaust systems. *Aerospace Science and Technology*, 92:77–90, 2019.

[147]S. Shan and G. G. Wang. Survey of modeling and optimization strategies to solve high-dimensional design problems with computationally-expensive black-box functions. *Structural and Multidisciplinary Optimization*, 41(2):219–241, 2010.

[148]X. Cai, L. Gao, X. Li, and H. Qiu. Surrogate-guided differential evolution algorithm for high dimensional expensive problems. *Swarm and Evolutionary Computation*, 48:288–311, 2019.

[149]R. L. Hardy. Multiquadric equations of topography and other irregular surfaces. *Journal of Geophysical Research*, 76(8):1905–1915, 1971.

[150]M. D. Buhmann. *Radial basis functions: theory and implementations*, volume 12. Cambridge university press, 2003.

[151]A. M. Morris, C. B. Allen, and T. C. S. Rendall. CFD-based optimization of aerofoils using radial basis functions for domain element parameterization and mesh deformation. *International Journal for Numerical Methods in Fluids*, 58(8):827–860, 2008.

[152]A. Benaouali and S. Kachel. A surrogate-based integrated framework for the aerodynamic design optimization of a subsonic wing planform shape. *Proceedings of the Institution of Mechanical Engineers, Part G: Journal of Aerospace Engineering*, 232(5):872–883, 2018.

[153]S. L. Brunton, B. R. Noack, and P. Koumoutsakos. Machine learning for fluid mechanics. *Annual Review of Fluid Mechanics*, 52:477–508, 2020.

[154]K. Lindhorst, M. C. Haupt, and P. Horst. Efficient surrogate modelling of nonlinear aerodynamics in aerostructural coupling schemes. *AIAA Journal*, 52(9):1952–1966, 2014.

[155]N. Thuerey, K. Weißenow, L. Prantl, and X. Hu. Deep learning methods for Reynolds-Averaged Navier-Stokes simulations of airfoil flows. *AIAA Journal*, 58(1):25–36, 2020.

[156]E. R. Lalonde, B. Vischschraper, G. Bitsuamlak, and K. Dai. Comparison of neural network types and architectures for generating a surrogate aerodynamic wind turbine blade model. *Journal of Wind Engineering and Industrial Aerodynamics*, 216, 2021.

[157]S. Shanmuganathan and S. Samarasinghe. *Artificial Neural Netwok Modelling*. Springer, 2016.

[158]G. Zuccolo, R. Christie, D. MacManus, I. Goulos, and P. Martin. Low order models for transonic afterbody aerodynamic characteristics. In *AIAA Scitech 2020 Forum, AIAA 2020-1997*, Orlando, Florida, USA, January 2020. American Institute of Aeronautics and Astronautics.

[159]M. A. Bouhlel, S. He, and J. R. R. A. Martins. Scalable gradient-enhanced artificial neural networks for airfoil shape design in the subsonic and transonic regimes. *Structural and Multidisciplinary Optimization*, 61(4):1363–1376, 2020.

[160]M. Kotinis and A. Kulkarni. Multi-objective shape optimization of transonic airfoil sections using swarm intelligence and surrogate models. *Structural and Multidisciplinary Optimization*, 45(5):747–758, 2012.

[161]L. Leifsson and S. Koziel. *Simulation-driven aerodynamic design using variable-fidelity models*. World Scientific, 2015.

[162]Z. Han, Zimmermann, and S. Görtz. Alternative cokriging method for variable-fidelity surrogate modeling. *AIAA Journal*, 50(5):1205–1210, 2012.

[163]M. Bancheri, F. Serafin, M. Bottazzi, W. Abera, G. Formetta, and R. Rigon. The design, deployment, and testing of kriging models in geoframe with sik-0.9. 8. *Geoscientific Model Development*, 11(6):2189–2207, 2018.

[164]H. Kaya, H. Tiftikçi, U. Kutluay, and E. Sakarya. Generation of surrogate-based aerodynamic model of an UCAV configuration using an adaptive co-Kriging method. *Aerospace Science and Technology*, 95, 2019.

[165]H. Likeng, G. Zhenghong, and Z. Dehu. Research on multi-fidelity aerodynamic optimization methods. *Chinese Journal of Aeronautics*, 26(2):279–286, 2013.

[166]J. Hueso-Rebassa, F. Tejero, J. Otter, I. Goulos, and D. G. MacManus. Multi-Fidelity Assessment of Exhaust Systems for Complete Engine-Airframe Configurations. In *Aerospace Europe Conference 2020, 00337*, Bordeaux, France, February 2020.

[167]C. Tang, K. Gee, and S. Lawrence. Generation of aerodynamic data using a design of experiment and data fusion approach. In *43rd AIAA Aerospace Sciences Meeting and Exhibit, AIAA 2005-1137*, Reno, Nevada, USA, January 2005. American Institute of Aeronautics and Astronautics.

[168]R. T. Haftka. Combining global and local approximations. *AIAA Journal*, 29(9):1523–1525, 1991.

[169]R. Lewis and S. Nash. A multigrid approach to the optimization of systems governed by differential equations. In *8th Symposium on Multidisciplinary Analysis and Optimization, AIAA 2000-4890*, Long Beach, California, USA, September 2000. American Institute of Aeronautics and Astronautics.

[170]D. Knill, A. Giunta, C. Baker, B. Grossman, W. Mason, R. Haftka, and L. Watson. HSCT configuration design using response surface approximations of supersonic Euler aerodynamics. In *36th AIAA Aerospace Sciences Meeting and Exhibit*, Reno, Nevada, USA, January 1998. American Institute of Aeronautics and Astronautics.

[171]C. A. Baker, D. Grossman, R. T. Haftka, W. H. Mason, and L. T. Watson. High-speed civil transport design space exploration using aerodynamic response surface approximations. *Journal of Aircraft*, 39(2):215–220, 2002.

[172]L. Xia and G. Zheng-Hong. Application of variable-fidelity models to aerodynamic optimization. *Applied Mathematics and Mechanics*, 27(8):1089–1095, 2006.

[173]N. V. Nguyen, M. Tyan, and J. W. Lee. A modified variable complexity modeling for efficient multidisciplinary aircraft conceptual design. *Optimization and Engineering*, 16(2):483–505, 2015.

[174]S. Choi, J. J. Alonso, I. M. Kroo, and M. Wintzer. Multifidelity design optimization of low-boom supersonic jets. *Journal of Aircraft*, 45(1):106–118, 2008.

[175]P. Thokala and J. R. R. A. Martins. Variable-complexity optimization applied to airfoil design. *Engineering Optimization*, 39(3):271–286, 2007.

[176]X. Meng and G. E. Karniadakis. A composite neural network that learns from multi-fidelity data: Application to function approximation and inverse PDE problems. *Journal of Computational Physics*, 401, 2020.

[177]X. Zhang, F. Xie, T. Ji, Z. Zhu, and Y. Zheng. Multi-fidelity deep neural network surrogate model for aerodynamic shape optimization. *Computer Methods in Applied Mechanics and Engineering*, 373, 2021.

[178]L. He, W. Qian, T. Zhao, and Q. Wang. Multi-fidelity aerodynamic data fusion with a deep neural network modeling method. *Entropy*, 22(9), 2020.

[179]A. Magrini, D. Buosi, and E. Benini. Comparison of nacelle models for the evaluation of an ultra-high bypass engine aerodynamics. In *AIAA SciTech 2022 Forum, AIAA 2022-0205*, San Diego, California, USA, January 2022. American Institute of Aeronautics and Astronautics.

[180]R. A. Zimbrick and J. L. Colehour. Investigation of very high bypass ratio engines for subsonic transports. *Journal of Propulsion and Power*, 6(4):490–496, 1990.

[181]T. Crum, D. Yates, T. Andeew, and N. Stockman. Low speed test results of subsonic, turbofan scarf inlets. In *29th AIAA/SAE/ASME/ASEE Joint Propulsion Conference and Exhibit, AIAA 93-2301*, Monterey, California, USA, June 1993. American Institute of Aeronautics and Astronautics.

[182]F. Tejero, D. MacManus, and C. Sheaf. Impact of droop and scarf on the aerodynamic performance of compact aero-engine nacelles. In *AIAA Scitech 2020 Forum, AIAA 2020-1522*, Orlando, Florida, USA, January 2020. American Institute of Aeronautics and Astronautics.

[183]M. H. Robinson. *The Aerodynamics of Aero-Engine Nacelles*. PhD Thesis, Cranfield University, 2018.

[184]A. Heidebrecht and D. G. MacManus. Surrogate model of complex non-linear data for preliminary nacelle design. *Aerospace Science and Technology*, 84:399–411, 2019.

[185]F. Tejero, D. G. MacManus, and C. Sheaf. Surrogate-based aerodynamic optimisation of compact nacelle aero-engines. *Aerospace Science and Technology*, 93, 2019.

[186]X. Fang, Y. Zhang, S. Li, and H. Chen. Transonic nacelle aerodynamic optimization based on hybrid genetic algorithm. In *17th AIAA/ISSMO Multidisciplinary Analysis and Optimization Conference, AIAA 2016-3833*, Washington, DC, USA, June 2016. American Institute of Aeronautics and Astronautics.

[187]I. Goulos, T. Stankowski, J. Otter, D. MacManus, N. Grench, and C. Sheaf. Aerodynamic Design of Separate-Jet Exhausts for Future Civil Aero-engines Part I: Parametric Geometry Definition and Computational Fluid Dynamics Approach. *Journal of Engineering for Gas Turbines and Power*, 138(8), 2016.

[188]I. Goulos, J. Otter, T. Stankowski, D. MacManus, N. Grench, and C. Sheaf. Aerodynamic Design of Separate-Jet Exhausts for Future Civil Aero-engines Part II: Dsign Space Exploration, Surrogate Modeling and Optimization. *Journal of Engineering for Gas Turbines and Power*, 138(8), 2016.

[189]A. Peters, Z. S. Spakovszky, W. K. Lord, and B. Rose. Ultrashort nacelles for low fan pressure ratio propulsors. *Journal of Turbomachinery*, 137(2), 2015.

[190]J. Li, Z. Gao, J. Huang, and K. Zhao. Aerodynamic design optimization of nacelle/pylon position on an aircraft. *Chinese Journal of Aeronautics*, 26(4):850–857, 2013.

[191]S. Koc, H. J. Kim, and K. Nakahashi. Aerodynamic design of wing-body-nacelle-pylon configuration. In *17th AIAA Computational Fluid Dynamics Conference, AIAA 2005-4856*, Toronto, Ontario, Canada, June 2005. American Institute of Aeronautics and Astronautics.

[192]T. Saitoh, H. J. Kim, K. Takenaka, and K. Nakahashi. Multi-point design of wing-body-nacelle-pylon configuration. In *24th AIAA Applied Aerodynamics Conference, AIAA 2006-3461*, San Francisco, California, USA, June 2006. American Institute of Aeronautics and Astronautics.

[193]S. Smith, M. Nemec, and S. Krist. Integrated nacelle-wing shape optimization for an ultra-high bypass fanjet installation on a single-aisle transport configuration. In *51st AIAA Aerospace Sciences Meeting including the New Horizons Forum and Aerospace Exposition, AIAA 2013-0543*, Grapevine, Texas, USA, January 2013. American Institute of Aeronautics and Astronautics.

[194]J. H. Ferziger, M. Perić, and R. L. Street. *Computational methods for fluid dynamics*. Springer, 2002.

[195]P. G. Tucker. *Unsteady computational fluid dynamics in aeronautics*. Springer, 2013.

[196]P. Sagaut, M. Terracol, and S. Deck. *Multiscale and multiresolution approaches in turbulence: LES, DES and Hybrid RANS/LES Methods: Applications and Guidelines*. World Scientific, 2013.

[197]M. Breuer, N. Jovičić, and K. Mazaev. Comparison of DES, RANS and LES for the separated flow around a flat plate at high incidence. *International Journal for Numerical Methods in Fluids*, 41(4):357–388, 2003.

[198]P. R. Spalart, W. H. Jou, M. Strelets, and S. R. Allmaras. Comments on the feasibility of LES for wings, and on a hybrid RANS/LES approach. In *Proceedings of first AFOSR international conference on DNS/LES*, Ruston, Louisiana, USA, August 1997.

[199]N. Gourdain, L. Y. M. Gicquel, and E. Collado. RANS and LES for the heat transfer prediction in turbine guide vane. *Journal of Propulsion and Power*, 28(2):423–433, 2012.

[200]P. R. Spalart and C. Streett. Young-person's guide to detached-eddy simulation grids. Technical Report NASA-CR-2001-211032, NASA, 2001.

[201]P. R. Spalart. Detached-eddy simulation. *Annual Review of Fluid Mechanics*, 41(1):181–202, 2009.

[202]F. R. Menter and M. Kuntz. Adaptation of eddy-viscosity turbulence models to unsteady separated flow behind vehicles. In *The Aerodynamics of Heavy Vehicles: Trucks, Buses, and Trains. Lecture Notes in Applied and Computational Mechanics*. Springer Berlin Heidelberg, 2004.

[203]J. Fröhlich and D. Von Terzi. Hybrid LES/RANS methods for the simulation of turbulent flows. *Progress in Aerospace Sciences*, 44(5):349–377, 2008.

[204]S. Deck. Zonal-detached-eddy simulation of the flow around a high-lift configuration. *AIAA Journal*, 43(11):2372–2384, 2005.

[205]P. R. Spalart, S. Deck, M. L. Shur, K. D. Squires, M. K. Strelets, and A. Travin. A new version of detached-eddy simulation, resistant to ambiguous grid densities. *Theoretical and Computational Fluid Dynamics*, 20(3):181–195, 2006.

[206]M. Shur, P. R. Spalart, K. D. Squires, M. Strelets, and A. Travin. Three dimensionality in Reynolds-Averaged Navier-Stokes solutions around two-dimensional geometries. *AIAA Journal*, 43(6):1230–1242, 2005.

[207]B. Wang and G. C. Zha. Detached-eddy simulation of a coflow jet airfoil at high angle of attack. *Journal of Aircraft*, 48(5):1495–1502, 2011.

[208]B. M. Kulfan. Universal parametric geometry representation method. *Journal of Aircraft*, 45(1):142–158, 2008.

[209]B. M. Kulfan. Recent extensions and applications of the cst universal parametric geometry representation method. *The Aeronautical Journal*, 114(1153):157–176, 2010.

[210]E. D. Olson. Three-dimensional piecewise-continuous class-shape transformation of wings. In *16th AIAA/ISSMO Multidisciplinary Analysis and Optimization Conference, AIAA 2015-3238*, Dallas, Texas, USA, June 2015. American Institute of Aeronautics and Astronautics.

[211]K. Lane and D. Marshall. Inverse airfoil design utilizing CST parameterization. In *48th AIAA Aerospace Sciences Meeting Including the New Horizons Forum and Aerospace Exposition, AIAA 2010-1228*, Orlando, Florida, USA, January 2010. American Institute of Aeronautics and Astronautics.

[212]R. Christie, A. Heidebrecht, and D. MacManus. An Automated Approach to Nacelle Parameterization Using Intuitive Class Shape Transformation Curves. *Journal of Engineering for Gas Turbines and Power*, 139(6), 2017.

[213]R. Christie, M. Robinson, F. Tejero, and D. G. MacManus. The use of hybrid intuitive class shape transformation curves in aerodynamic design. *Aerospace Science and Technology*, 1, 2019.

[214]D. S. Lacy and A. J. Sclafani. Development of the high lift common research model (HL-CRM): A representative high lift configuration for transonic transports. In *54th AIAA Aerospace Sciences Meeting, AIAA 2016-0308*, San Diego, California, USA, January 2016. American Institute of Aeronautics and Astronautics.

[215]J. Hueso-Rebassa. *Design, Performance and Aerodynamics of Non-Axisymmetric Exhaust Systems for Civil Aero-Engines*. PhD Thesis, Cranfield University, 2022.

[216]F. Sánchez-Moreno, D. G. MacManus, F. Tejero, J. Matesanz-García, and C. T. Sheaf. Robustness of optimisation algorithms for transonic aerodynamic design. In *9th European Conference for Aeronautics and Space Sciences*, Lille, France, July 2022.

[217]ANSYS INC. ANSYS Fluent User's Guide. Technical report, ANSYS Inc, Canonsburg, Pennsylvania, USA.

[218]W. Sutherland. The Viscosity of Gases and Molecular Forces. *Philsophical Magazine*, 5(36):507–531, 1893.

[219]ANSYS INC. ANSYS ICEM CFD User Manual. Technical report, ANSYS Inc, Canonsburg, Pennsylvania, USA.

[220]I. B. Celik, U. Ghia, P. J. Roache, C. J. Freitas, H. Coleman, and P. E. Raad. Procedure for estimation and reporting of uncertainty due to discretization in CFD applications. *Journal of Fluids Engineering, Transactions of the ASME*, 130(7):0780011–0780014, 2008.

[221]ANSYS INC. ANSYS Meshing User's Guide. Technical report, ANSYS Inc, Canonsburg, Pennsylvania, USA.

[222]ANSYS INC. ANSYS Fluent UDF Manual. Technical report, ANSYS Inc, Canonsburg, Pennsylvania, USA.

[223]Menter, F. R. Best practice: scale-resolving simulations in ANSYS CFD. Technical report, ANSYS Inc, Canonsburg, Pennsylvania, USA, 2012.

[224]A. Gerasimov. Quick guide to setting up LES-type simulations, 2016. ANSYS,`http://www.tfd.chalmers.se/~lada/comp_turb_model/postscript_files/Quick_Guide_to_Setting_Up_LES_version_1.4_for_Lars.pdf`.

[225]J. J. Otter, T. Stańkowski, M. Robinson, and D. G. MacManus. Installation aerodynamics of civil aero-engine exhaust systems. *Aerospace Science and Technology*, 89:345–355, 2019.

[226]J. Matesanz Garcia. *Porpulsion integration design and evaluation for novel aircraft configurations*. PhD Thesis, Cranfield University, 2022.

[227]A. Hill. Private communication - 01/03/2022, 2022.

[228]A. Magrini, D. Buosi, E. Benini, and C. Sheaf. Ultra-high bypass nacelle geometry design space exploration. In *AIAA Scitech 2021 Forum, AIAA 2021-0990*, Virtual, January 2021. American Institute of Aeronautics and Astronautics.

[229]A. Petrusson. Aerodynamic evaluation of nacelles for engines with ultra high bypass ratio. MSc Thesis, 2017.

[230]M. D. McKay, R. J. Beckman, and W. J. Conover. A comparison of three methods for selecting values of input variables in the analysis of output from a computer code. *Technometrics*, 21(2):239–245, 1979.

[231]A. Olsson, G. Sandberg, and O. Dahlblom. On latin hypercube sampling for structural reliability analysis. *Structural Safety*, 25(1):47–68, 2003.

[232]K. Deb, A. Pratap, S. Agarwal, and T. Meyarivan. A fast and elitist multiobjective genetic algorithm: NSGA-II. *IEEE Transactions on Evolutionary Computation*, 6(2):182–197, 2002.

[233]E. Zitzler and S. Künzli. Indicator-based selection in multiobjective search. *Lecture Notes in Computer Science*, 3242:832–842, 2004.

[234]M. R. Sierra and C. A. Coello Coello. Improving PSO-based Multi-Objective optimization using crowding, mutation and ϵ-dominance. *Lecture Notes in Computer Science*, 3410:505–519, 2005.

[235]Hadka, D. Platypus manual, 2018. url = https://platypus.readthedocs.io/_/downloads/en/latest/pdf/.

[236]K. Deb. *Multiobjective Optimization Using Evolutionary Algorithms*. John Wiley and Sons, New York, New York State, USA, 2001.

[237]A. I. J. Forrester and A. J. Keane. Recent advances in surrogate-based optimization. *Progress in Aerospace Sciences*, 45(1-3):50–79, 2009.

[238]A. Sobester, A. Forrester, and A. Keane. *Engineering design via surrogate modelling: a practical guide*. John Wiley and Sons, 2008.

[239]S. Haykin. *Neural networks and learning machines*. Pearson Education, 2008.

[240]M. M. Lau and K. H. Lim. Review of adaptive activation function in deep neural network. In *IEEE-EMBS Conference on Biomedical Engineering and Sciences*, Kuching, Sarawak, Malaysia, December 2018. Institute of Electrical and Electronics Engineers.

[241]D. P. Kingma and J. Ba. Adam: a method for stochastic optimization. In *International Conference on Learning Representation*, San Diego, California, USA, May 2015.

[242]X. Ying. An overview of overfitting and its solutions. 1168(2), 2019.

[243]E. Torenbeek. *Advanced aircraft design: conceptual design, analysis and optimization of subsonic civil airplanes*. John Wiley and Sons, 2013.

[244]F. Tejero, N. Schreiner, and D. MacManus. ANACO, WP1.3 and WP1.4, Milestone M5: Investigation of design space of non-axisymmetric UltraFan type nacelle configurations. Technical report, Propulsion Engineering Centre; School of Aerospace, Transport, and Manufacturing; Cranfield University, 2020.

[245]F. Tejero, N. Schreiner, and D. MacManus. ANACO, WP1.5, Milestone M6: Short and slim nacelle design down select. Technical report, Propulsion Engineering Centre; School of Aerospace, Transport, and Manufacturing; Cranfield University, 2020.

[246]F. Tejero, F. Sanchez-Moreno, N. Schreiner, and D. MacManus. ANACO, WP5.2, Deliverable 10: Comparison of CFD predictions and wind tunnerl experimental data for validation cases. Technical report, Centre for Propulsion Engineering; School of Aerospace, Transport, and Manufacturing; Cranfield University, 2022.

[247]B. D. J. Schreiner. Private communication - 01/05/2022, 2022.

[248]A. Hill. Private communication - 25/10/2022, 2022.

[249]G. Paris, D. Robilliard, and C. Fonlupt. Exploring overfitting in genetic programming. In *International Conference on Artificial Evolution*, Marseilles, France, October 2003.

[250]C. Park, R. T. Haftka, and N. H. Kim. Remarks on multi-fidelity surrogates. *Structural and Multidisciplinary Optimization*, 55(3):1029–1050, 2017.

[251]K. Tian, X. Ma, Z. Li, S. Lin, B. Wang, and A. M. Waas. A multi-fidelity competitive sampling method for surrogate-based stacking sequence optimization of composite shells with multiple cutouts. *International Journal of Solids and Structures*, 193:1–12, 2020.

[252]F. Tejero. Private communication - 01/03/2020, 3 2020.

[253]G. Tanguy. *Experimental and computational aerodynamic studies of convoluted intake ducts*. PhD Thesis, Cranfield University, 2019.

[254]P. P. Walsh and P. Fletcher. *Gas turbine performance*. John Wiley and Sons, 2004.

[255]L. F. Richardson. The approximate arithmetical solution by finite differences of physical problems involving differential equations, with an application to the stresses in a masonry dam. *Philosophical Transactions of the Royal Society of London. Series A, Containing Papers of a Mathematical or Physical Character*, 210:307–357, 1911.

[256]L. F. Richardson and J. A. Gaunt. The deferred approach to the limit. *Philosophical Transactions of the Royal Society of London. Series A, containing papers of a mathematical or physical character*, 226:299–361, 1927.

[257]A. Heidebrecht and D. G. MacManus. Surrogate model of complex non-linear data for preliminary nacelle design. *Aerospace Science and Technology*, 84:399–411, 2019.

[258]A. I. J. Forrester, A. Sóbester, and A. J. Keane. Multi-fidelity optimization via surrogate modelling. *Proceedings of the Royal Society A: Mathematical, Physical and Engineering Sciences*, 463(2088):3251–3269, 2007.

[259]C. Currin, T. Mitchell, M. Morris, and D. Ylvisaker. Bayesian prediction of deterministic functions, with applications to the design and analysis of computer experiments. *Journal of the American Statistical Association*, 86(416):953–963, 1991.

[260]S. Xiong, P. Z. G. Qian, and C. F. J. Wu. Sequential design and analysis of high-accuracy and low-accuracy computer codes. *Technometrics*, 55(1):37–46, 2013.

[261]Y. Zhang, N. H. Kim, C. Park, and R. T. Haftka. Multifidelity surrogate based on single linear regression. *AIAA Journal*, 56(12):4944–4952, 2018.

[262]E. Zitzler, K. Deb, and L. Thiele. Comparison of Multiobjective Evolutionary Algorithms: Empirical Results. *Evolutionary Computation*, 8:173–195, 2000.

[263]L. J. Eshelman and J. D. Schaffer. Real-coded genetic algorithms and interval-schemata. *Foundations of Genetic Algorithms*, 2:187–202, 1993.

APPENDIX A

Governing equations

This appendix summarises the fluid dynamics governing equations pertinent for this thesis and the different computational methods used for the resolution. The equations of the fluid properties and the formulation of both the viscous RANS method with the $\kappa - \omega$ SST turbulence model and also the inviscid Euler method are adopted from Otter[113]. The equations of the wall functions for the RANS CFD model are based on the Fluent manual[217]. Finally, the details provided for the DDES formulation are adopted from Tanguy[253].

A.1 Fluid properties

The fluid properties in this research are modelled by the ideal gas law which is used as the equation of state (Equation A.1). It relates the static pressure (p) and temperature (t) with the density of the fluid (ρ) through the universal specific constant of gases $R = 287\ J/kg \cdot K$.

$$p = \rho R t \tag{A.1}$$

The fluid heat capacity at constant pressure (C_p) is defined by an 8th order polynomial expression as a function of the static temperature (Equation A.2 and Equation A.3)[254]. The heat capacity of the fluid at constant volume is derived by the subtraction of C_p and R (Equation A.4). C_v and C_p are used to calculate the fluid specific internal energy and enthalpy respectively (Equation A.5 and Equation A.6).

$$C_p(t) = a_0 + \sum_{i=1}^{8} a_i \left(\frac{t}{1000}\right)^i \tag{A.2}$$

$$\begin{aligned} a_0 = 0.99231, a_1 = 0.236688, a_2 = -1.852148, \\ a_3 = 6.083152, a_4 = 8.893933, a_5 = 7.097112, \\ a_6 = -3.234725, a_7 = 0.794571, a_8 = -0.081873 \end{aligned} \tag{A.3}$$

$$C_v(t) = C_p(t) - R \tag{A.4}$$

$$e = C_v(t)t \tag{A.5}$$

$$h = C_p(t)t \tag{A.6}$$

The molecular kinematic theory is used to model the thermal conductivity of the fluid (Π) (Equation A.7). M_w is the fluid molecular weight which is 28.96 g/mol for the air.

$$\Pi = \frac{15}{4}\frac{R}{M_w}\mu\left(\frac{4}{15}\frac{C_p}{R} + \frac{1}{3}\right) \tag{A.7}$$

The Sutherland's law[218] is used to calculate the dynamic viscosity of the fluid (μ) as a function of the static temperature (Equation A.8), where μ_{ref}, t_{ref} and S are the constants of the model (Equation A.9).

$$\mu = \mu_{ref}\left(\frac{t}{t_{ref}}\right)^{\frac{3}{2}}\frac{t_{ref} + S}{t + S} \tag{A.8}$$

$$\mu_{ref} = 1.716x10^{-5}\frac{kg}{ms}, t_{ref} = 273.11K, S = 110.56K \tag{A.9}$$

A.2 Navier-Stokes equations

The Navier-Stokes equations are a set of partial differential equations that describe a Newtonian fluid flow. They are based on the conservation of the mass or continuity

(Equation A.10), conservation of momentum (Equation A.11) and conservation of energy (Equation A.12). The evolution of these conservative variables can be determined by the resolution of the equations for given initial conditions and boundary conditions. In the equations, ρ is the fluid density, $\mathbf{U}$ represents the three components velocity vector, p is the static pressure, τ_v is the viscous stress tensor and φ is the conductive heat flux. Additionally, the total energy E can be expressed as $E = e + \frac{U^2}{2}$ by the sum of the internal energy (e) and the kinetic energy.

$$\frac{\partial \rho}{\partial t} + \nabla(\rho \mathbf{U}) = 0 \tag{A.10}$$

$$\frac{\partial \rho \mathbf{U}}{\partial t} + \underbrace{\nabla(\rho \mathbf{U} \times \mathbf{U})}_{convection} = -\overbrace{\nabla p}^{pressure\ gradient} + \underbrace{\nabla \tau_v}_{viscous\ difussion} + \overbrace{\rho \mathbf{g}}^{body\ forces} \tag{A.11}$$

$$\frac{\partial \rho \mathbf{E}}{\partial t} + \underbrace{\nabla(\rho \mathbf{E}\mathbf{U} + p\mathbf{U})}_{convection} = \overbrace{\nabla(\tau_v \mathbf{U})}^{viscous\ work} - \underbrace{\nabla \varphi}_{heat\ conduction} \tag{A.12}$$

A.2.1 Favre-Averaged Navier-Stokes formulation

An approximation to the Navier-Stokes equations for stationary, compressible and turbulent flows is obtained by applying the Favre averaging which decomposes a field variable in its fluctuating and averaged components. As a result the Favre-Averaged Navier-Stokes equations (hereafter called RANS) are derived (Equations A.13 to A.16) for the conservation of mass, momentum and energy. In this thesis the terms for heat addition and body forces in the Navier-Stokes equations are not considered and therefore they are neglected in the RANS equations. Note that a tilde in a field variable ($\tilde{x}$) represent a mass averaged value while a over-bar ($\overline{x}$) denotes the mean value. The RANS equations depend on the density (ρ), velocity vector ($\mathbf{U}$), static pressure (p), specific enthalpy (h), molecular viscosity (μ), eddy viscosity (μ_T), turbulent kinetic energy (κ) and laminar and turbulent Prandtl numbers (Pr_L and Pr_T). The application of the Reynolds decomposition to the viscous diffusion term in the momentum equation gives rise to the instantaneous stress tensor (t_{ij}) and the Reynolds stress tensor ($\overline{\rho}\tau_{ij}$) (Equation A.16). The Reynolds stress tensor includes additional unknowns to the system of equations and therefore an extra set of equations is required to close the system. This is called closure problem of the RANS equations. There are different ways to model the Reynolds stress tensor.

A first order approach relies on the Boussinesq's hypothesis which considers the Reynolds stress tensor to be proportional to the deformation rate of the mean flow field and the turbulent eddy viscosity μ_T which constitute some types of turbulence models.

$$\frac{\partial \overline{\rho}}{\partial t} + \frac{\partial(\overline{\rho}\tilde{U}_i)}{\partial x_i} = 0 \tag{A.13}$$

$$\frac{\partial \overline{\rho}\tilde{U}_i}{\partial t} + \frac{\partial \overline{\rho}\tilde{U}_i\tilde{U}_j}{\partial x_j} = -\frac{\partial \overline{p}}{\partial x_j} + \frac{\partial(\bar{t}_{ij} + \overline{\rho}\tau_{ij})}{\partial x_j} \tag{A.14}$$

$$\begin{aligned}\frac{\partial \overline{\rho}((\tilde{e} + \frac{1}{2}\tilde{U}_i\tilde{U}_j) + k)}{\partial t} + \frac{\partial \overline{\rho}\tilde{U}_j(\tilde{h} + \frac{1}{2}\tilde{U}_i\tilde{U}_i) + k)}{\partial x_j} = \frac{\partial}{\partial x_j}\left[\tilde{U}_i(\tilde{t}_{ij} + \overline{\rho}\tau_{ij})\right] + \\ \frac{\partial}{\partial x_j}\left[(\frac{\mu}{Pr_L} + \frac{\mu_T}{Pr_T})\frac{\partial \tilde{h}}{\partial x_j} + (\mu + \sigma_k\mu_T)\frac{\partial k}{\partial x_j}\right]\end{aligned} \tag{A.15}$$

$$\bar{t}_{ij} = 2\mu\overline{S}_{ij}, \overline{\rho}\tau_{ij} = 2\mu_T - \frac{2}{3}\overline{\rho}k\delta_{ij}, \overline{S}_{ij} = S_{ij} - \frac{1}{3}\frac{\partial \tilde{U}_k}{\partial x_k}\delta_{ij} \tag{A.16}$$

A.2.1.1 $\kappa - \omega$ SST turbulence model

In this project, the two-equations eddy-viscosity $\kappa-\omega$ Shear Stress Transport (SST) turbulence model of Menter[95] is used, where κ is the turbulent kinetic energy and ω is the specific dissipation rate (Equations A.17 to A.22). The transport equations for κ and ω are given by Equations A.17 and A.18 respectively.

$$\frac{\partial \overline{\rho}k}{\partial t} + \frac{\partial \overline{\rho}k\tilde{U}_i}{\partial x_i} = \tau_{ij}\frac{\partial \tilde{U}_i}{\partial x_j} - \beta^*\overline{\rho}k\omega + \frac{\partial}{\partial x_j}\left[(\mu + \sigma_k\mu_T)\frac{\partial k}{\partial x_j}\right] \tag{A.17}$$

$$\begin{aligned}\frac{\partial(\overline{\rho}\omega)}{\partial t} + \frac{\partial(\overline{\rho}\omega\tilde{U}_i)}{\partial x_i} = \frac{\gamma}{\nu_T}\tau_{ij}\frac{\partial \tilde{U}_i}{\partial x_j} - \beta\overline{\rho}\omega^2 + \frac{\partial}{\partial x_j}\left[(\mu + \sigma_\omega\mu_T)\frac{\partial \omega}{\partial x_j}\right] + \\ 2(1 - F_1)\overline{\rho}\sigma_{\omega 2}\frac{1}{\omega}\frac{\partial k}{\partial x_j}\frac{\partial \omega}{\partial x_j}\end{aligned} \tag{A.18}$$

In this model, Ω represents the absolute value of the vorticity and y denotes the dimensional distance to the wall. The model constants ψ are calculated using Equation

A.20 and considering the constant of the first (Equation A.21) and second (Equation A.22) sets for ψ_1 and ψ_2 respectively.

$$\mu_T = \frac{a_1 k}{max(a_1\omega, \Omega tanh(arg_2^2))}, arg_2 = max(2\frac{\sqrt{k}}{0.09\omega y}, \frac{500\nu}{y^2\omega}), a_1 = 0.31 \tag{A.19}$$

$$\begin{aligned} \psi = F_1\psi_1 + (1-F_1)\psi_2, F_1 = tanh(arg_1^4), \\ arg_1 = min\left[max(\frac{\sqrt{k}}{0.09\omega y}, \frac{500y}{y^2\omega}), \frac{4\overline{\rho}\sigma_{\omega_2}k}{CD_{k\omega}y^2}\right], \\ CD_{k\omega} = max(2\overline{\rho}\sigma_{\omega 2}\frac{1}{\omega}\frac{\partial k}{\partial x_j}\frac{\omega}{\partial x_j}, 10^{-20}) \end{aligned} \tag{A.20}$$

$$\begin{aligned} \sigma_{k1} = 0.85, \sigma_{\omega 1} = 0.5, \beta_1 = 0.075, \beta^* = 0.09, \kappa = 0.41, \\ \gamma_1 = \beta_1/\beta^* - \sigma_{\omega 1}\kappa^2/\sqrt{\beta^*} \end{aligned} \tag{A.21}$$

$$\begin{aligned} \sigma_{k2} = 1.0, \sigma_{\omega 2} = 0.856, \beta_2 = 0.0828, \beta^* = 0.09, \kappa = 0.41, \\ \gamma_2 = \beta_2/\beta^* - \sigma_{\omega 2}\kappa^2/\sqrt{\beta^*} \end{aligned} \tag{A.22}$$

A.2.1.2 Wall functions for the $\kappa-\omega$ SST turbulence model

The boundary layer treatment in a RANS model depends on the grid size of the first cell in the normal direction (y). This size is normally nondimensionalised into y^* (Equation A.23), where ρ and μ are the fluid density and dynamic viscosity, κ_P is the turbulent kinetic energy at the near-wall node P, y_P is the near-wall distance from the wall to the node P and C_μ is a constant equal to 0.09. Wall functions are used to model the boundary layer using a logarithmic law for the velocity (U^*) (Equation A.24), where $E = 9.793$ is an empirical constant of the model. For the $\kappa-\omega$ SST turbulence model, the y^* threshold above which the wall function mode is activated is given by $y^* > 11.225$[217].

$$y^* = \frac{\rho C_\mu^{\frac{1}{4}} \kappa_P^{\frac{1}{2}} y_P}{\mu} \tag{A.23}$$

$$U^* = \frac{1}{\kappa} ln\,(Ey^*) \tag{A.24}$$

A.2.2 DDES formulation

Delayed Detached Eddy Simulation (DDES) is a hybrid RANS/LES method. The RANS formulation of the Navier-Stokes equations was presented in Appendix A.2.1. The Large Eddy Simulation (LES) formulation is obtained through a low-pass spatial filtering of the Navier-Stokes equations. This spatial filtering is implicitly determined by the finite volume discretisation method in a way that the flow variables are spatially-averaged for low scales. As a result, Reynolds stresses (τ_{ij}) and turbulent heat flux (q_j) terms are obtained (Equation A.25) that are different from those derived in the RANS formulation (Equation A.16). Apart from this, the LES equations are formally similar to the RANS equations by changing the time-averaging operator ($\bar{x}$) by the spatial filter operator ($\hat{x}$).

$$\tau_{ij} = -\widehat{\rho U_i U_j} + \hat{\rho}\tilde{U}_i\tilde{U}_j, \quad q_j = \widehat{\rho U_j h} - \hat{\rho}\tilde{U}_j\tilde{h} \tag{A.25}$$

The LES resolution becomes computationally prohibitive in regions of the domain near the walls where smaller turbulent structures are present and smaller grid sizings are required. This is even more critical for high Reynolds numbers. As a result, hybrid RANS/LES methods were developed. One example is Detached Eddy Simulation (DES) which combines RANS models in the boundary layer and LES models away from the walls where separated flows or turbulent structures are located. DDES is an improved model of DES that includes a blending function to ensure that RANS is used within the boundary layer at all time.

A.2.3 Euler equations

Under the assumption of inviscid fluids, the Navier-Stokes equations can be simplified by neglecting the viscous stress tensor terms. As a result the Euler equations are derived for the conservation of mass (Equation A.26), momentum (Equation A.27) and energy (Equation A.28) with compressibility effects.

$$\frac{\partial \rho}{\partial t} + \frac{(\rho U_i)}{\partial x_i} = 0 \tag{A.26}$$

$$\frac{\partial (\rho U_i)}{\partial t} + \frac{\partial (\rho U_i U_j + p)}{\partial x_i} = 0 \tag{A.27}$$

$$\frac{\partial \rho(e+\frac{1}{2}|U|^2)}{\partial t} + \frac{\partial(\rho(e+\frac{1}{2}|U|^2)U_i)}{\partial x_i} + \frac{\partial(pU_i)}{\partial x_i} = 0 \tag{A.28}$$

APPENDIX B

Grid sensitivity studies

This appendix covers the grid sensitivity studies of each CFD model used in the project. Initially, a summary of the methodology used to compute the Grid Convergence Index (GCI) is provided. This is applied to the assessment of the grid independence for the RANS CFD models (Section 4.3.1.1). Different nacelle configuration models are considered: isolated nacelle (2D and 3D), installed nacelle in the airframe (3D) and installed nacelle in the wind tunnel rig (3D).

The grids for the low-fidelity models used in this project are verified using a different approach. The objective of a low-fidelity model is to approximate the gradients of the design space while reducing the computational overhead of the design process. As such, the focus is not on getting the correct absolute results but consistent design space gradients compared to a mesh independent model. An inviscid CFD model based on the Euler equations and a viscous RANS model with wall functions for the boundary layer modelling are used as low-fidelity. Both isolated nacelle (2D) and airframe-installed nacelle (3D) configurations are considered.

While the 2D models are developed for structured meshes generated with ANSYS ICEM[219], the 3D models are based on unstructured meshes created with ANSYS Meshing[221].

B.1 Grid Convergence Index (GCI)

The quantification of the discretisation error associated to the CFD grid follows the method proposed by Celik et al.[220]. It is based on a Grid Convergence Method that

computes a Grid Convergence Index (GCI) as a measure of discretisation error relative to the Richardson Extrapolation (RE)[255,256]. In other words, the GCI estimates how close the calculated value is from the asymptotic value. Three meshes with different levels of refinement are considered: coarse, medium and fine. A representative cell size h is calculated for each grid using the overall cell count N and the individual cell area ΔA_i or volume ΔV_i for 2D and 3D meshes respectively (Equation B.1). The grid refinement factor r between coarse-medium and medium-fine meshes can be obtained by the ratio between the different representative cell size (Equation B.2). The apparent order of the method p is iteratively calculated using the metric of interest ϕ obtained for each grid (Equation B.3) which allows to compute the value of the RE for ϕ (Equation B.4). Finally, the relative error (Equation B.5), the extrapolated relative error (Equation B.6) and the GCI error (Equation B.7) can be computed. The GCI represents a measure of the error relative to the RE with a safety factor of 1.25.

$$\begin{aligned} h_{(3D)} &= \left[\frac{1}{N}\sum_{i=1}^{N}\Delta V_i\right]^{\frac{1}{3}} \\ h_{(2D)} &= \left[\frac{1}{N}\sum_{i=1}^{N}\Delta A_i\right]^{\frac{1}{2}} \end{aligned} \tag{B.1}$$

$$\begin{aligned} r_{coarse-medium} &= \frac{h_{coarse}}{h_{medium}} \\ r_{medium-fine} &= \frac{h_{medium}}{h_{fine}} \end{aligned} \tag{B.2}$$

$$\begin{cases} p &= \frac{1}{ln\left(r_{medium-fine}\right)}\left|ln\left|\frac{\epsilon_{coarse-medium}}{\epsilon_{medium-fine}}\right|+q(p)\right| \\ q(p) &= ln\left(\frac{r_{medium-fine}^{p}-s}{r_{coarse-medium}^{p}-s}\right) \\ s &= 1\cdot sgn\left(\frac{\epsilon_{coarse-medium}}{\epsilon_{medium-fine}}\right) \\ \epsilon_{coarse-medium} &= \phi_{medium}-\phi_{coarse} \\ \epsilon_{medium-fine} &= \phi_{fine}-\phi_{medium} \end{cases} \tag{B.3}$$

$$\begin{aligned} \phi_{ext}^{coarse-medium} &= \frac{r_{coarse-medium}^{p}\phi_{medium}-\phi_{coarse}}{r_{coarse-medium}^{p}-1} \\ \phi_{ext}^{medium-fine} &= \frac{r_{medium-fine}^{p}\phi_{fine}-\phi_{medium}}{r_{medium-fine}^{p}-1} \end{aligned} \tag{B.4}$$

$$\begin{aligned} e_a^{medium-fine} &= \left|\frac{\phi_{fine}-\phi_{medium}}{\phi_{fine}}\right| \\ e_a^{coarse-medium} &= \left|\frac{\phi_{medium}-\phi_{coarse}}{\phi_{medium}}\right| \end{aligned} \tag{B.5}$$

$$\begin{aligned} e_{ext}^{fine} &= \left|\frac{\phi_{ext}^{medium-fine}-\phi_{fine}}{\phi_{ext}^{medium-fine}}\right| \\ e_{ext}^{medium} &= \left|\frac{\phi_{ext}^{coarse-medium}-\phi_{fine}}{\phi_{ext}^{coarse-medium}}\right| \end{aligned} \tag{B.6}$$

$$\begin{aligned} GCI^{fine} &= \frac{1.25e_a^{medium-fine}}{r^p_{medium-fine}} \\ GCI^{medium} &= \frac{1.25e_a^{coarse-medium}}{r^p_{coarse-medium}} \end{aligned} \tag{B.7}$$

B.2 RANS models

B.2.1 2D isolated configuration

The grid independence study was performed at the typical long-range cruise condition of $M_\infty = 0.85$ and $MFCR = 0.7$. A 2D axisymmetric compact nacelle configuration given by $L_{nac}/r_{hi} = 3.1$ and $r_{te}/r_{hi} = 0.95$ was considered in isolated configuration. Three meshes were generated and evaluated using the RANS CFD model with $y^+ < 1$. The nacelle drag D_{nac} which accounts for the post-exit terms (ϕ_{post}) was used as the metric of interest to assess the mesh independence. The medium mesh was selected with an overall cell count of 67000 and a GCI of 0.31% for cruise D_{nac} (Table B.1).

TABLE B.1: Grid sensitivity study for the RANS model for the isolated 2D axisymmetric nacelle configuration at cruise condition.

	Coarse	Medium	Fine
Elements	40×10^3	67×10^3	155×10^3
GCI D_{nac}	-	0.308%	0.006%

B.2.2 3D isolated configuration

The 3D isolated nacelle work involves both the cruise and windmilling diversion conditions. A large flow separations may arise at the off-design condition which may require a refined grid standard. Therefore, a grid independence study was performed for the cruise ($M_\infty = 0.85$, $MFCR = 0.7$ and $\alpha_{eng} = 4.5°$) and the windmilling diversion ($M_\infty = 0.65$, $MFCR = 0.33$ and $\alpha_{eng} = 5.1°$) conditions. A compact nacelle configuration given by $L_{nac}/r_{hi} = 3.1$ and $r_{te}/r_{hi} = 0.95$ was employed. Nacelle drag D_{nac} was used as key metric for the analysis. Three levels of mesh refinement were generated and evaluated with the RANS $y^+ < 1$ CFD model. Based on the overall cell count and the GCI obtained, the medium grid was selected

with 72 million elements and a discretisation error relative to the RE of 1.95% and 1.01% for cruise and diversion D_{nac} respectively (Table B.2).

TABLE B.2: Grid sensitivity study for the RANS model for the isolated 3D nacelle configuration at cruise and windmilling diversion conditions.

		Coarse	Medium	Fine
Elements		35×10^6	72×10^6	141×10^6
GCI D_{nac}	Cruise	-	1.953%	1.205%
	Diversion	-	1.010%	0.289%

B.2.3 3D airframe-installed configuration

The grid independence study was performed using the same compact nacelle design used in Appendix B.2.2 for the 3D isolated study. The nacelle was installed in the NASA CRM airframe at an expected installation position given by $dx/C_{wing}^{inst} = 0$ and $dz/C_{wing}^{inst} = 0.1$ (Section 4.1.2). Three meshes with different levels of refinement were generated. The trimmed cruise condition given by $M_\infty = 0.85$, $MFCR = 0.7$, $H = 10669$m and $C_L = 0.5$ was considered. The RANS $y^+ < 1$ CFD model was used. Based on the GCI results and the computational overhead of the different mesh refinement levels, the medium mesh was selected with an overall cell count of 115 million elements and a GCI of 0.48% and 1.57% for the modified nacelle drag D_{nac}^* and the airframe drag $D_{a/f}$ respectively (Table B.3). This study was done in collaboration with *Josep Hueso Rebassa*[215] as this CFD model is shared across both theses. The author of the present thesis performed the grid generation and CFD evaluation of the fine mesh. Hueso-Rebassa[215] generated the coarse and medium grids and assessed the CFD for both.

TABLE B.3: Grid sensitivity study for the RANS model for the nacelle installed in the airframe at cruise condition.

		Coarse	Medium	Fine
Elements		60×10^6	115×10^6	220×10^6
GCI	NPF	-	0.340%	0.118%
	D_{nac}^*	-	0.476%	0.103%
	GPF^*	-	0.018%	0.005%
	$D_{a/f}$	-	1.568%	0.266%

The windmilling diversion operating point is a challenging condition due to the low mass flow through the engine that might cause shock-induced flow separation on the forebody of the nacelle. Therefore the grid refinement study was extended to this off-design condition defined by $M_\infty = 0.65$, $MFCR = 0.33$, $H = 6069$m and $C_L = 0.44$. As the main effect is on the nacelle, the selected mesh for cruise condition was used as reference and a local refinement over the fan-cowl geometry was applied. A coarser and a finer mesh were generated. Based on the modified nacelle drag at diversion condition, the medium mesh was selected with a GCI of 1.73% (Table B.4).

TABLE B.4: Grid sensitivity study for the RANS model for the nacelle installed in the airframe at windmilling diversion condition.

	Coarse	Medium	Fine
Elements	51×10^6	115×10^6	238×10^6
GCI D_{nac} Diversion	-	1.726%	0.274%

B.2.4 3D test rig-installed configuration

The grid independence study was performed for the cruise condition given by $M_\infty = 0.85$, $MFCR = 0.7$ and $\alpha_{eng} = 4.5°$. A compact nacelle configuration given by $L_{nac}/r_{hi} = 3.1$ and $r_{te}/r_{hi} = 0.95$ was considered. The nacelle was installed in the Z30 test rig as explained in Section 4.1.3. Three meshes were generated and evaluated using the RANS CFD model with $y^+ < 1$. The nacelle drag D_{nac} was used as the metric of interest to assess the mesh independence. This nacelle drag was evaluated using the farfield method detailed in Section 4.4.2. The medium mesh was selected with an overall cell count of 16 million elements and a discretisation error relative to the RE of 1.5% for cruise D_{nac} (Table B.5).

TABLE B.5: Grid sensitivity study for the RANS model for the nacelle installed in the test rig configuration at cruise condition.

	Coarse	Medium	Fine
Elements	4.4×10^6	15.9×10^6	46.2×10^6
GCI D_{nac}	-	1.489%	0.183%

B.3 Euler models

B.3.1 2D isolated configuration

The grid independence study was performed for the cruise condition given by $M_\infty = 0.85$ and $MFCR = 0.7$. A 2D axisymmetric compact nacelle configuration given by $L_{nac}/r_{hi} = 3.1$ and $r_{te}/r_{hi} = 0.95$ was considered in isolated configuration. Three meshes were generated and evaluated using the inviscid CFD model governed by the Euler equations. The nacelle drag D_{nac} was used as the metric of interest to assess the mesh independence. The medium mesh was selected with a GCI error of 2.5% for cruise drag which equates to an error relative to the RE of 9 Newtons (Table B.6).

However, the purpose of a low-fidelity model is to accelerate the design process by an approximation of the design space gradients rather than an accurate prediction of integral values. In this respect, a model that is not mesh independent could be used as long as the deviations in the design space gradients are sufficiently constant. This would lead the design process to the same optimal part of the design space. A mesh called "Target" that is not in the asymptotic region but enables a reduction in the computational cost of approximately 75% relative to the selected medium mesh (Figure B.1) was assessed. For this purpose, a DSE based on the LHS technique was generated for the cruise operating condition. Four design variables (x_{max}, r_{max}, r_{if} and β_{nac}) and 400 samples were simulated. The samples were evaluated using the medium mesh (GCI = 2.5%) and the "Target" mesh (Figure B.2). A comparison of the results in the region of interest for low cruise nacelle drag shows a good fitting of the samples to a linear regression with a $R^2 = 0.995$ (Figure B.2). The slope of the linear regression model of 0.99 shows a deviation of 1% from a exact constant offset relative to the $y = x$ line (Figure B.2). Relative to this linear regression model, the samples are fitted with a 2σ uncertainty level of 4.26% which meets the uncertainty threshold of 10% typically used for low order models[185,257].

TABLE B.6: Grid sensitivity study for the Euler model for the isolated 2D axisymmetric nacelle configuration at cruise condition.

	Coarse	Medium	Fine
Elements	213×10^3	306×10^3	381×10^3
GCI D_{nac}	-	2.485%	1.068%

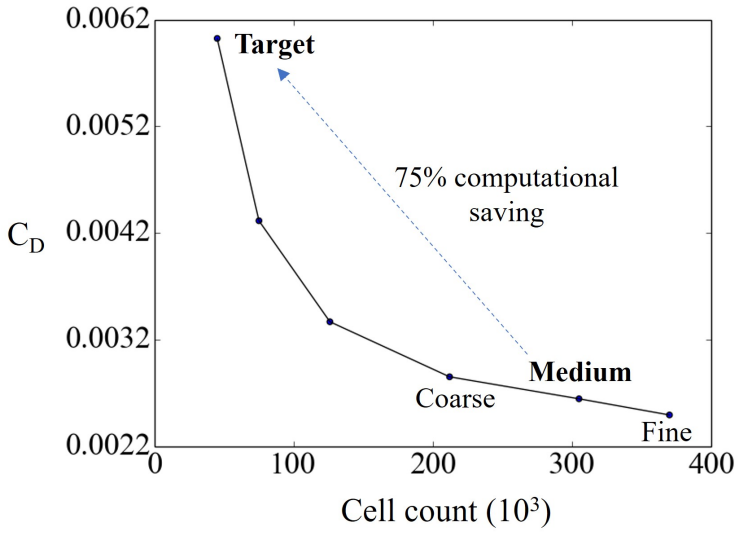

FIGURE B.1: Grid refinement analysis for the Euler model for the 2D isolated nacelle configuration at cruise condition.

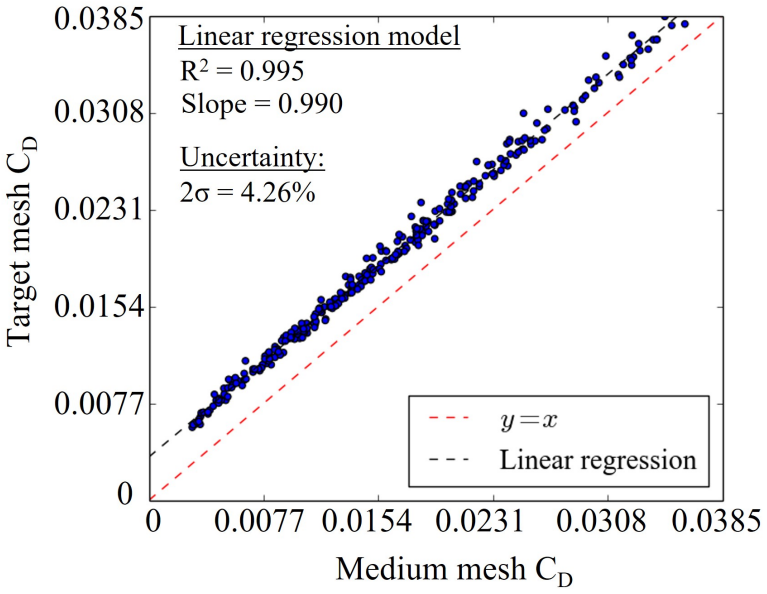

FIGURE B.2: Effect of the grid refinement in the Euler CFD prediction across the 2D isolated nacelle design space.

B.3.2 3D airframe-installed configuration

The same method as in Appendix B.3.1 has been followed. For the installed configuration this approach is even more sensible due to the high computational cost associated to the CFD calculations. A compact nacelle configuration given by $L_{nac}/r_{hi} = 3.1$ and $r_{te}/r_{hi} = 0.91$ installed in the NASA CRM at $dx/C_{wing}^{inst} = 0.03$

and $dz/C_{wing}^{inst} = 0.075$ was considered. Three meshes with different levels of refinement were generated. The trimmed cruise condition given by $M_\infty = 0.85$, $MFCR = 0.7$, $H = 10669$m and $C_L = 0.5$ was considered. The Euler CFD model was used. This study was done in collaboration with Hueso-Rebassa[215] as this CFD model is shared across both theses. The generation of the coarse, medium and fine grids and CFD evaluations to compute the GCI values were performed by Hueso-Rebassa[215].

TABLE B.7: Grid sensitivity study for the Euler model for the nacelle installed in the airframe at cruise condition.

		Coarse	Medium	Fine
Elements		25×10^6	80×10^6	180×10^6
GCI	NPF	-	0.359%	0.200%
	D^*_{nac}	-	0.874%	0.679%
	GPF^*	-	0.041%	0.020%
	$D_{a/f}$	-	7.154%	2.784%

TABLE B.8: Grid sizes and associated relative computational costs for the Euler model for the nacelle installed in the airframe at cruise condition.

		Coarse	Medium	Fine
Elements		25×10^6	80×10^6	180×10^6
Relative cost t	t/t_{Coarse}	1	4	9
	t/t_{RANS}	1/36	1/9	1/4

Although the GCI results for the NPF, D^*_{nac} and GPF^* show a good enough discretisation level with the medium mesh, the GCI value for the airframe drag $D_{a/f}$ is substantially high (Table B.7). However, the computational costs relative to the coarse mesh increase by a factor of 4 and 9 for the medium and fine meshes respectively (Table B.8). Moreover, the cell count for the fine mesh is even higher than the corresponding to the selected mesh for the high-fidelity RANS CFD model (Appendix B.2.3). As the purpose of the Euler CFD model is to establish a low-fidelity method to guide and speed up the design process, the coarse mesh has been selected with a reduction in computational cost relative to the RANS model by a factor of 36. Nevertheless, it is needed to ensure that the deviation in the prediction of the design space gradients is sufficiently constant compared to a denser mesh. For this purpose, a DSE in installed configuration of 46 samples based on the LHS technique was evaluated. The coarse mesh was compared against the medium mesh

due to computational cost constraints. While the author of the present work created the grids and evaluated the CFD for the 46 samples using the medium mesh standard, Hueso-Rebassa[215] was responsible for the grids and CFD calculations of the coarse mesh standard. As this study initially emerged in the context of the thesis of Hueso-Rebassa[215], the DSE was evaluated for a non-axisymmetric design problem governed by 6 design variables. This can be extended to the nacelle design problem as the CFD model verification has to be valid for both applications. As in Appendix B.3.1, the correlation of the design space gradients between both meshes has been evaluated with the help of a linear regression model fitted on the data points. This has been quantified using the coefficient of determination (R^2) and slope of the model and also the uncertainty based on two standard deviations (2σ) between the coarse mesh and the linear regression model data. ΔNPF, ΔD^*_{nac}, ΔGPF^* and $\Delta D_{a/f}$ have been used as metrics of interest. They are expressed as the difference between each design and the reference design and relative to the standard net thrust ($F_N \approx 60kN$).

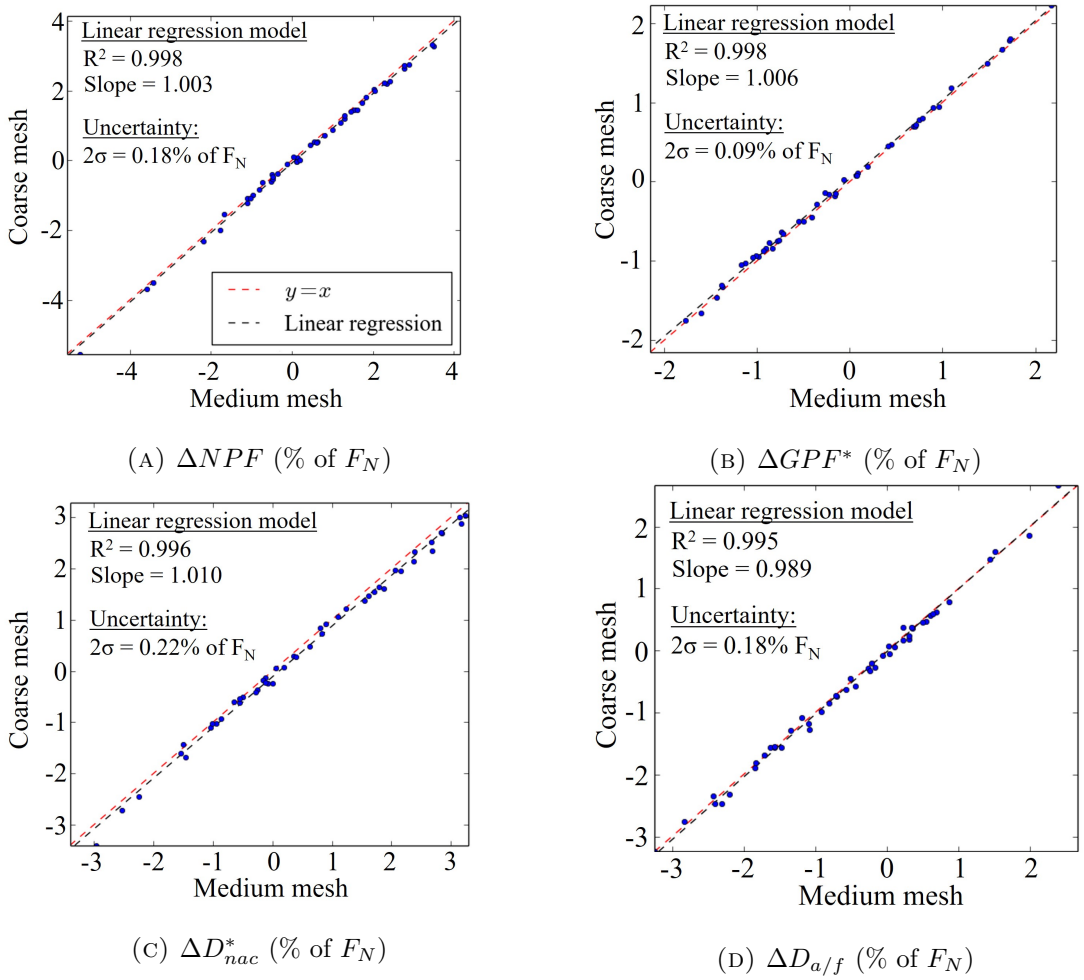

(A) ΔNPF (% of F_N)

(B) ΔGPF^* (% of F_N)

(C) ΔD^*_{nac} (% of F_N)

(D) $\Delta D_{a/f}$ (% of F_N)

FIGURE B.3: Effect of grid refinement in the Euler CFD prediction across the installed nacelle design space

The results show that the data from both meshes follow a linear trend with a R^2 parameter higher than 0.995 for every metric (Figure B.3). Additionally, the slope of the regression models indicate a maximum deviation from $y = x$ of 1.1% (Figure B.3). Finally, the highest uncertainty based on 2σ is reached for ΔD^*_{nac} of 0.22% of F_N (Figure B.3c). This is an acceptable value as it is much smaller compared to the variability range of the metric in the design space. Therefore, it can be concluded that the coarse and medium meshes capture similar gradients of the design space.

B.4 RANS with wall function models

B.4.1 2D isolated configuration

This study followed the same approach as in Appendix B.3.1 for the low-fidelity Euler model. Same cruise condition and nacelle configuration were considered. Three meshes were generated and evaluated using the RANS model with wall functions for the boundary layer. The nacelle drag D_{nac} was used as the metric of interest to assess the mesh independence. The medium mesh was selected as grid independent with a GCI error of 0.53% for cruise drag (Table B.9).

In the same manner as for the low-fidelity Euler model, a "Target" mesh that enables a reduction in the computational cost of approximately 60% relative to the selected medium mesh (Figure B.4) was assessed. A DSE based on the LHS technique was generated for the cruise operating condition and 400 samples were evaluated both with the "Target" and the medium meshes. A comparison of the results in the region of interest for low cruise nacelle drag shows a good fitting of the samples to a linear regression with a $R^2 = 0.998$ (Figure B.5). The slope of the linear regression model of 1.003 shows a deviation of 0.3% from the exact constant offset relative to the $y = x$ line (Figure B.5). Relative to this linear regression model, the samples are fitted with a 2σ uncertainty level of 2.97%.

TABLE B.9: Grid sensitivity study for the RANS with wall functions model for the isolated 2D axisymmetric nacelle configuration at cruise condition.

	Coarse	Medium	Fine
Elements	72×10^3	121×10^3	205×10^3
GCI D_{nac}	-	0.530%	0.123%

B.4.2 3D airframe-installed configuration

A similar approach as in Appendix B.3.2 has been followed. In this case, the gradients of the design space captured by the RANS with wall functions CFD model have been directly compared with the high-fidelity RANS CFD results. Due to computational cost reasons, a LHS composed of 70 samples that had been already calculated with the high-fidelity RANS model was simulated using the proposed grid for the RANS with wall functions model. As for the Euler grid study, NPF, D^*_{nac},

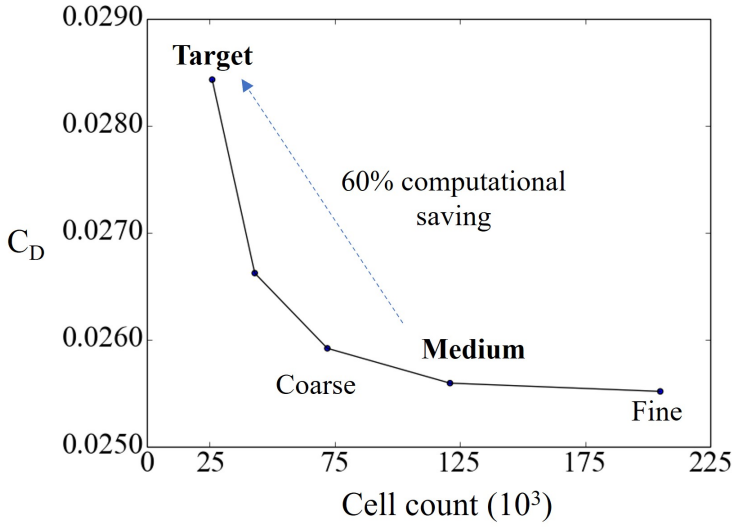

FIGURE B.4: Grid refinement analysis for the RANS with wall functions model for the 2D isolated nacelle configuration at cruise condition.

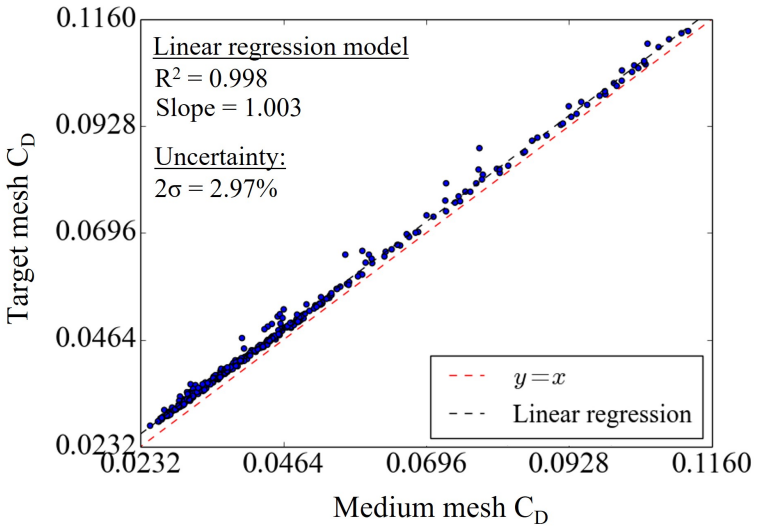

FIGURE B.5: Effect of the grid refinement in the RANS with wall fucntions CFD model prediction across the 2D isolated nacelle design space.

GPF^* and $D_{a/f}$ have been used as metrics of interest. A compact nacelle configuration given by $L_{nac}/r_{hi} = 3.1$ and $r_{te}/r_{hi} = 0.95$ installed at $dx/C^{inst}_{wing} = 0.00$ and $dz/C^{inst}_{wing} = 0.01$ has been considered.

The results showed that the data from both CFD models follow a linear trend with a R^2 parameter higher than 0.994 (Figure B.6). The slope of the linear regression models fitted to the data showed a deviation from the $y = x$ line lower than 3%. Additionally, the estimated uncertainty based on 2σ reaches a maximum value of

0.06% of F_N. This justify the validity of the proposed mesh for the RANS with wall functions CFD model for a reduction in the computational overhead relative to the high-fidelity model by a factor of 15.

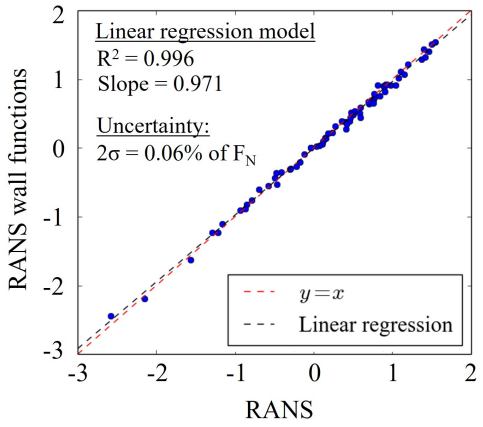

(A) ΔNPF (% of F_N)

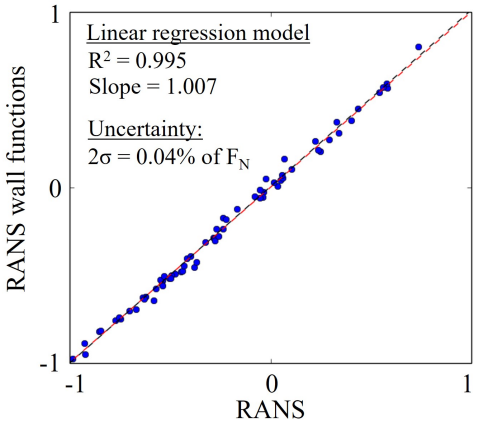

(B) ΔGPF^* (% of F_N)

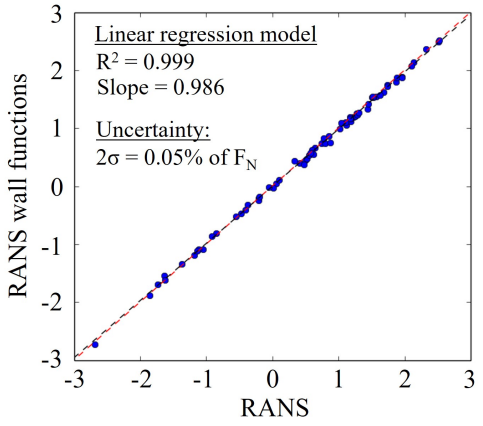

(C) ΔD^*_{nac} (% of F_N)

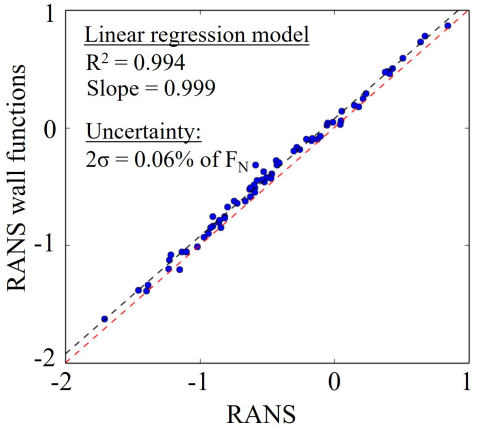

(D) $\Delta D_{a/f}$ (% of F_N)

FIGURE B.6: Effect of using wall functions to model the boundary layer in the RANS CFD prediction across the installed nacelle design space

APPENDIX C

Unsteady CFD methods

This appendix provides further details of the unsteady results of this thesis. Section C.1 shows the results about impact of time step and statistical convergence for the URANS calculations at the two off-design conditions assessed. Section C.2 provides the analyses about statistical convergence and blending functions for the DDES calculations of this thesis. Finally, in Section C.3 the implementation for the Fourier transform is verified using a test function.

C.1 URANS

C.1.1 Time step study

The time steps used in the URANS calculations were verified for both off-design operating conditions analysed. A coarse time step was estimated using the convective time (τ) of the problem defined as the ratio between the nacelle length (L_{nac}) and the free-stream velocity (U_∞) (Equation C.1). This time step was refined by a factor of 2 and 4 to get a medium and fine time step solutions. The comparison is based on the nacelle drag, both in the time and frequency domains. The frequencies (f) are non-dimensionalised through the Strouhal number (St), where the nacelle highlight diameter (D_{hi}) and free-stream velocities (U_∞) are used as characteristics lengths and velocities respectively (Equation C.2). The frequency content is represented in a non-dimensional manner through the Power Spectral Density (PSD).

$$\tau = \frac{L_{nac}}{U_\infty} \tag{C.1}$$

$$St = \frac{f D_{hi}}{U_\infty} \tag{C.2}$$

C.1.1.1 End-of-runway condition

Three time steps were considered: $\Delta t_{coarse} = 2.37 \cdot 10^{-3}$s, $\Delta t_{medium} = 1.19 \cdot 10^{-3}$s, $\Delta t_{fine} = 0.59 \cdot 10^{-3}$s. The URANS CFD model explained in Section 4.3.1.3 was used to run a calculation per time step. The time signals of the drag coefficient show an initial transient before the solution reaches a periodic behaviour (Figure C.1a). It is the period of time that takes to the simulation to evolve from the steady RANS solution used for initialisation to the unsteady regime. The size in time of this initial transient (τ_{trans}) depends on the case and has to be checked for each calculation. For the discrete Fourier transform the initial transient is removed from the signal. For this application, a conservative decision was to remove the first 50 convective times which gave around 180 convective times for the Fourier transform. Similar time signals (Figure C.1a) and dominant frequencies (Figure C.1b) were obtained with the medium and fine time steps. As a trade-off between accuracy and computational cost the medium time step was selected for the URANS calculations.

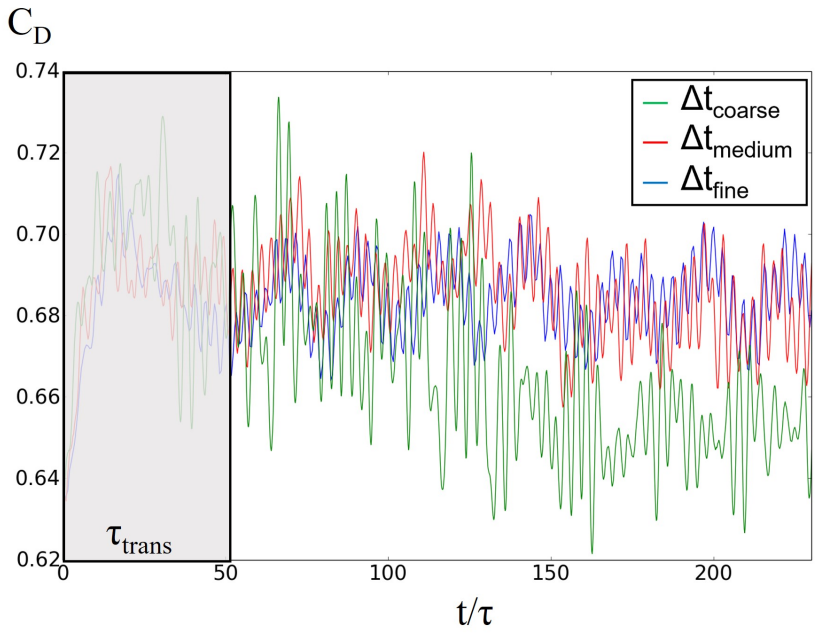

(A) Time domain.

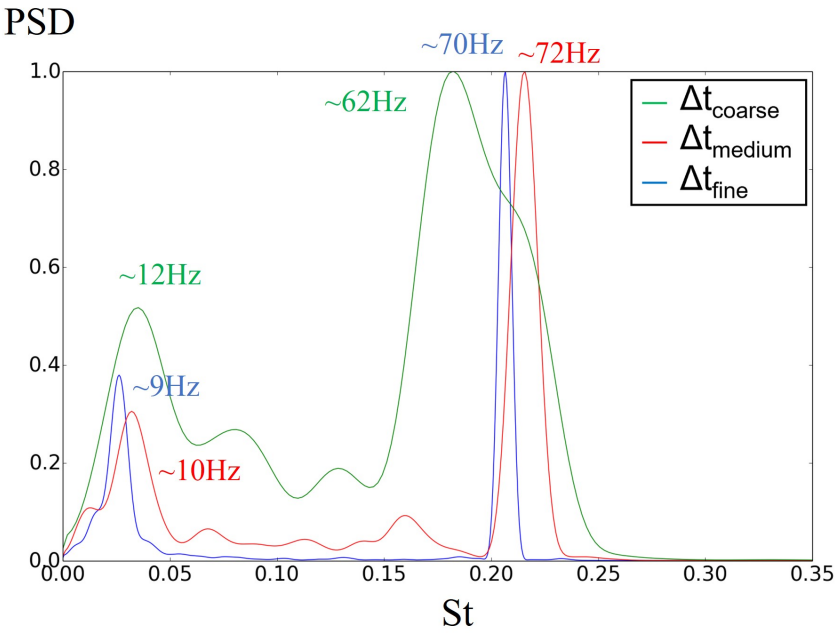

(B) Frequency domain.

FIGURE C.1: Comparison of different time steps for the URANS calculation at end-of-runway. Time signal and discrete Fourier transform.

C.1.1.2 Windmilling diversion condition

The next three time steps were considered: $\Delta t_{coarse} = 9.30 \cdot 10^{-4}$s, $\Delta t_{medium} = 4.65 \cdot 10^{-4}$s, $\Delta t_{fine} = 2.33 \cdot 10^{-4}$s. The URANS CFD model detailed in Section 4.3.1.3 was used for the calculations. The fist 50 convective times were removed to discard the initial transient for the Fourier transform, which was computed over around 500 convective times (Figure C.2a). The frequency spectra of the different signals shows differences between the medium and fine time steps as the fine one captures some frequency content at higher frequencies. Therefore, a conservative decision was to select the fine time step for the URANS calculations at this operating condition.

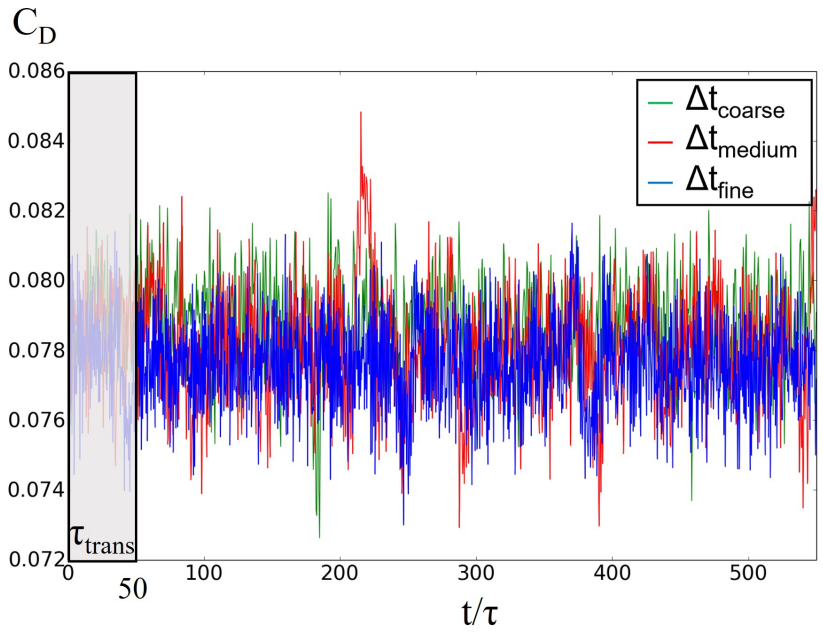

(A) Time domain.

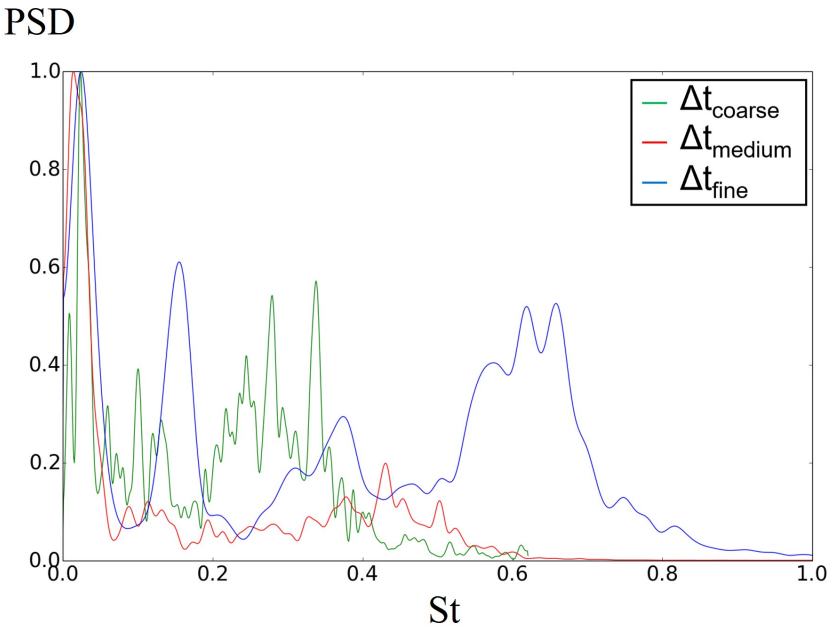

(B) Frequency domain.

FIGURE C.2: Comparison of different time steps for the URANS calculation at windmilling diversion. Time signal and discrete Fourier transform.

C.1.2 Statistical convergence

The convergence of the unsteady solution was checked through an statistical converge study using statistical descriptors for the drag coefficient signal. This ensures that the simulation was run for long enough to obtain meaningful statistical results. This study is focused on the selected time steps for the end-of-runway and windmilling diversion conditions (Section C.1.1). The cumulative average and standard deviation are computed over an increasing period of time until convergence. The initial transient (τ_{trans}) is removed for the time signal for this calculation.

C.1.2.1 End-of-runway condition

For the end-of-runway case, the statistical descriptors show a converged trend with low change for high number of convective times. Relative to the last time step, at around 140τ there is a change in the cumulative average and standard deviation of the C_D lower than 0.5% and 2% respectively (Figure C.3). It is assumed that 140 convective times after the initial transient is enough to reach statistical convergence.

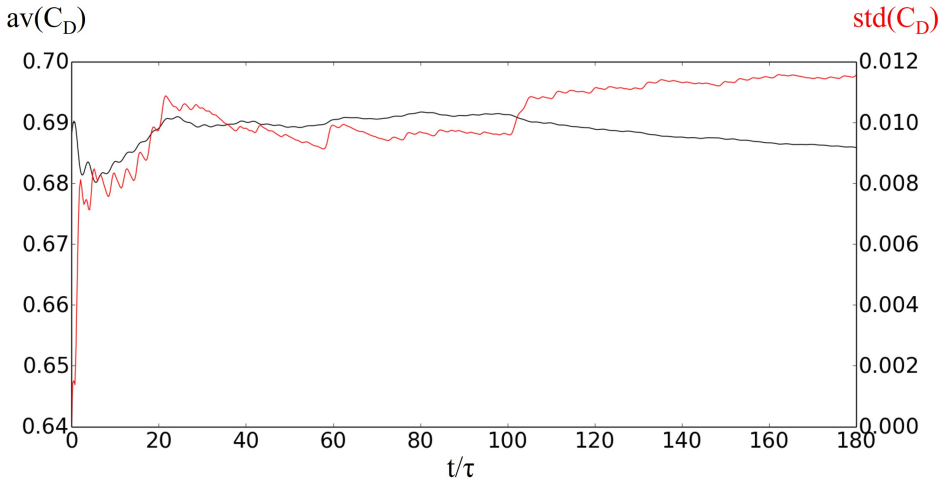

FIGURE C.3: Statistical convergence of the URANS calculation at end-of-runway based on the cumulative average and standard deviation of the drag coefficient.

C.1.2.2 Windmilling diversion condition

The statistical descriptors show a converged solution for 500 convective times. However, around 250τ after the initial transient can be a compromise decision to accept

convergence. For this case the change in the cumulative average and standard deviation of C_D relative to 500τ is lower than 0.1% and 1.5% respectively (Figure C.4)

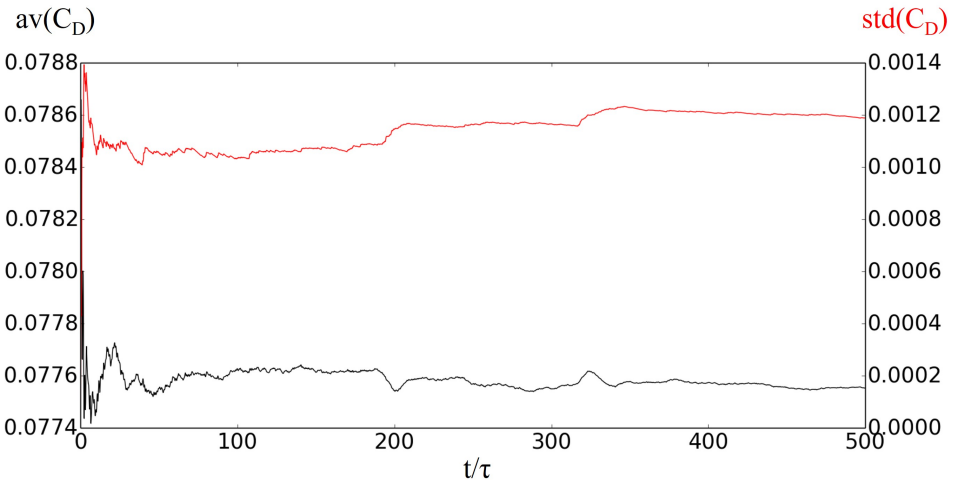

FIGURE C.4: Statistical convergence of the URANS calculation at windmilling diversion based on the cumulative average and standard deviation of the drag coefficient.

C.2 DDES

C.2.1 Statistical convergence

The same approach as in the URANS method (Section C.1.2) is followed to assess the statistical convergence of the DDES calculations at the nominal windmilling diversion condition (Table 4.1). The first 7 convective times (τ) of the time signal are considered as the initial transient period from the steady RANS solution used for initialisation to the fully transient regime (Figure C.5). After removing this τ_{trans}, around 30 convective times are left to apply the statistical descriptors. The cumulative average and standard deviation on the drag coefficient are used. It is concluded that a minimum of 15 convective times are needed to accept convergence. At this 15τ, the change relative to 30τ in the cumulative average and standard deviation is lower than 0.1% and 2% respectively (Figure C.6).

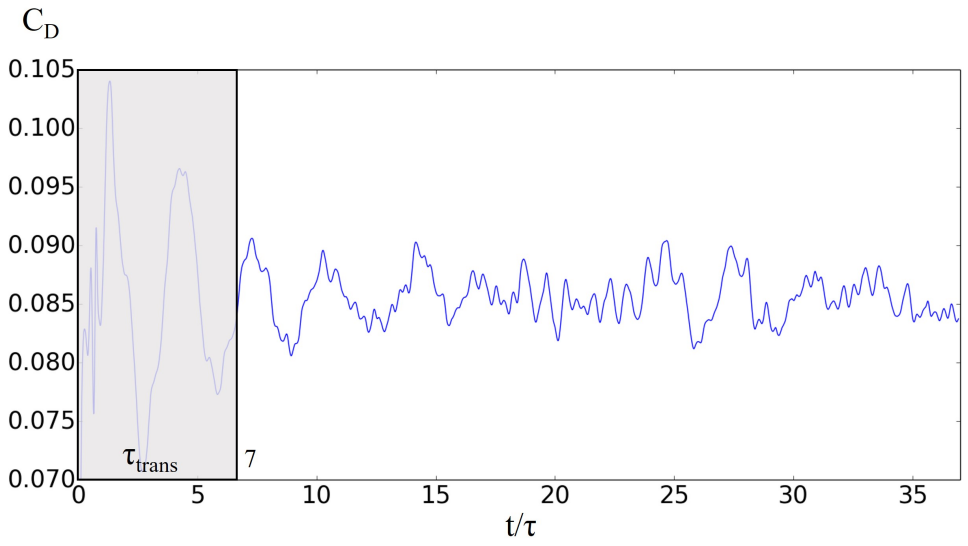

FIGURE C.5: Time signal of the drag coefficient at windmilling diversion predicted with the DDES CFD model.

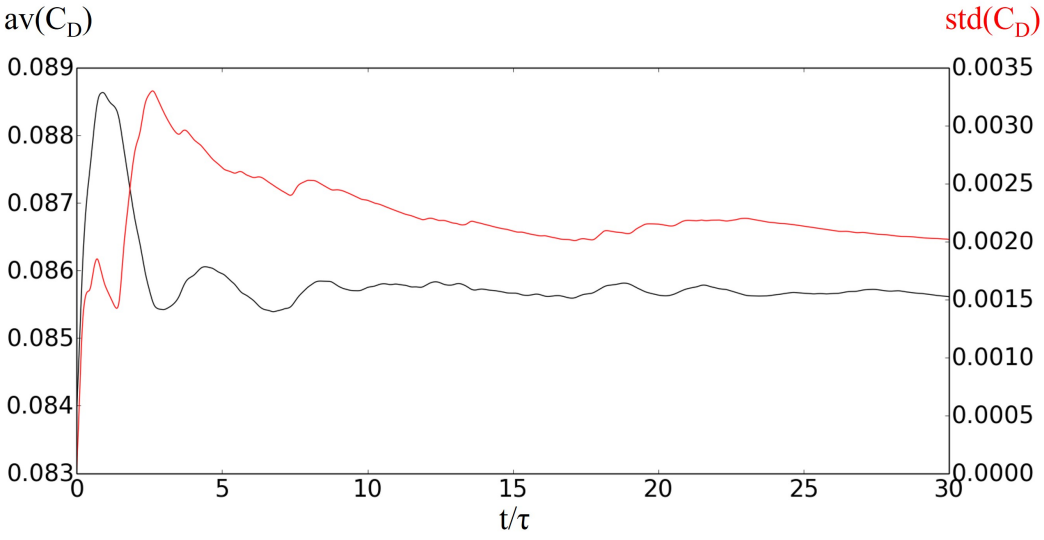

FIGURE C.6: Cumulative average and standard deviation for the drag coefficient at windmilling diversion predicted with the DDES CFD model.

C.2.2 Blending functions

DDES uses blending functions to ensure the modelling of the boundary layer using the RANS mode. In this section, contours of the blending functions are checked for the DDES CFD model at the nominal windmilling diversion condition (Table 4.1). Two nacelle cross-section planes are shown: one at the fan-face and another one $0.2L_{nac}$ ahead of the fan-face. Additionally, another slice at the top-line azimuthal position is analysed. In the contours, black zones are modelled using RANS while

white zones are LES regions. The boundary layer is in the RANS domain of the DDES calculation (Figure C.7).

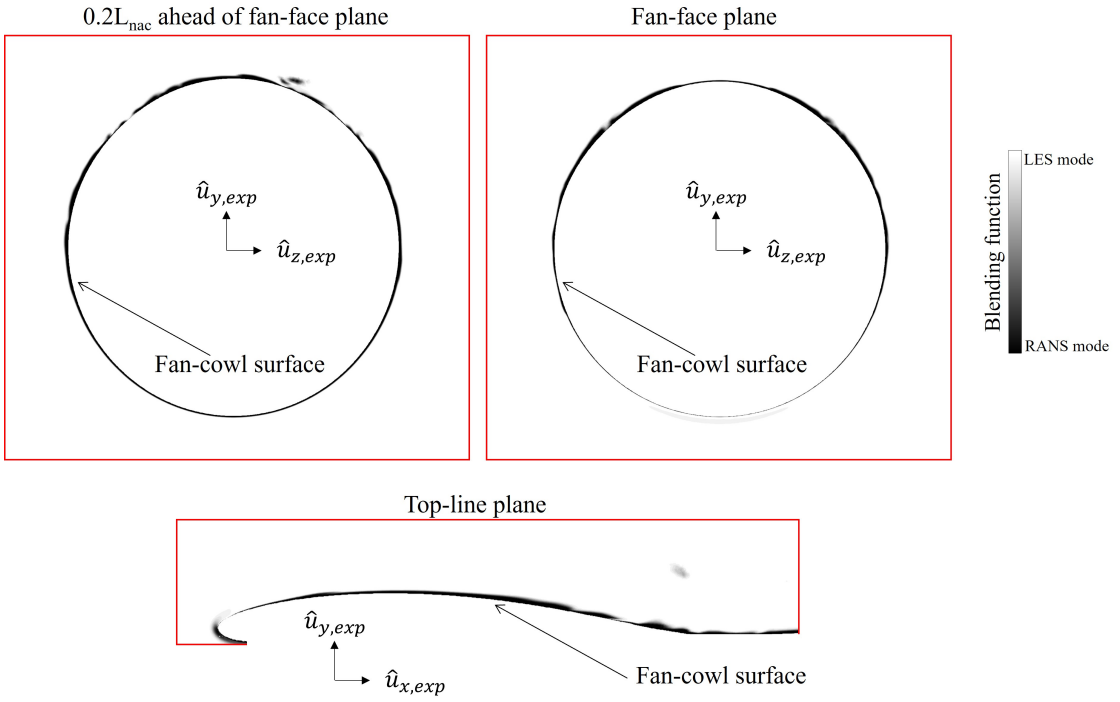

FIGURE C.7: Contours of the blending function for the DDES model for the nominal diversion condition at different sections of the model.

C.3 Fourier analysis

For the unsteady analysis of this thesis, the discrete Fourier transform is used to calculate the frequency characteristics of the flow. A manufactured solution was considered to test the implementation of the Fourier transform. The test function ($y(t)$) consists of the summation of two sinusoidal functions of different amplitude and frequencies (Equation C.3). In particular, while the first sinusoidal function has amplitude 1 and frequency 3Hz, the second one has amplitude of 0.5 and 80Hz frequency (Figure C.8a). The discrete Fourier transform properly captures the frequencies (f) and amplitudes ($\hat{y}$) of the test signal (Figure C.8b). No aliasing is present as the sample frequency is greater than twice the maximum frequency to observe according to the Nyquist theorem. Negligible level of leakage can be seen in the frequency peaks due to the finite nature of the signal.

$$y(t) = sin(3 \cdot 2\pi t) + 0.5sin(80 \cdot 2\pi t) \tag{C.3}$$

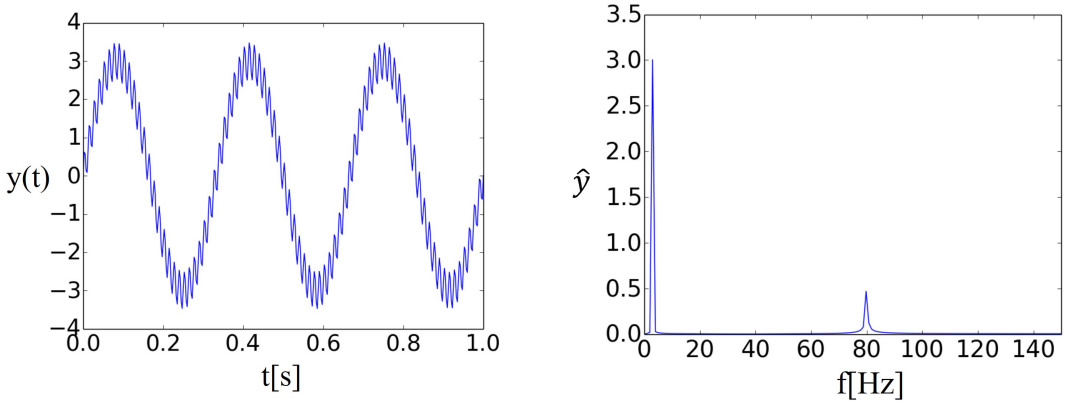

(A) Time domain.

(B) Frequency domain.

FIGURE C.8: Time signal and Fourier transform of a test function composed by the summation of two sinusoidal functions.

APPENDIX D

Verification of the MFNN method

This appendix covers the verification of the Multi-Fidelity Neural Network (MFNN) method implemented in this work. Different benchmark cases widely used in the literature for multi-fidelity surrogate modelling have been applied. While the Forrester function[162,164,258] is representative of a one-dimensional analytical test case, the Currin function[259–261] allows a verification for multi-dimensional problems. However, in both benchmark cases the correlation between the high- and the low- fidelity functions is linear. Given the non-linear nature of the nacelle aerodynamic optimisation problem, a modified version of these functions with non-linear correlation have been also used to verify the MFNN implementation.

Considering that a random initialization is used for the weight and biases parameters in the training process, it is a common practice[176,177] to perform a set of independent evaluations (N_r) and use the mean (Equation D.2) and standard deviation (Equation D.3) of the relative L2 error (Equation D.1) to quantify the potential variability of the modelling performance. In this work a total of 15 independent evaluations (N_r = 15) have been considered based on previous work[176].

$$L_{2_{error}} = \sqrt{\frac{\sum_n (y - y_{MFNN})^2}{\sum_n y^2}} \tag{D.1}$$

$$\overline{L_{2_{error}}} = \frac{1}{N_r} \sum_{i}^{i=N_r} L_{2_{error,i}} \tag{D.2}$$

$$\sigma\left(L_{2_{error}}\right) = \sqrt{\frac{\sum_i^{i=N_r} \left(\overline{L_{2_{error}}} - L_{2_{error,i}}\right)^2}{N_r}} \tag{D.3}$$

D.1 One-dimensional verification

D.1.1 Linear correlation

The Forrester function (Equations D.4,D.5) is used to verify the MFNN implementation for a one-dimensional case with linear correlation between the low- and high-fidelity data sets. The low-fidelity training data set is composed of 11 data points equi-spaced in the range from 0 to 1. For the high-fidelity level, 4 training points located at $x_{HF} = \{0, 0.4, 0.8, 1\}$ are considered. The network architecture and hyperparameters have been optimized using a full factorial sampling technique to find the best performing model based on the RMSE metric. For the low-fidelity network, 6 hidden layers with 32 neurons per layer, hyperbolic tangent activation function and L2 regularization factor of 10^{-5} have been used (Table D.1). The high-fidelity network is split into the linear and non-linear sub-networks. The linear sub-network is composed of 1 hidden layer with 16 neurons and no activation function and regularization is considered (Table D.1). The non-linear sub-network is built using 2 hidden layers with 16 neurons per layer, hyperbolic tangent activation function and L2 regularization factor of 10^{-6} (Table D.1). This MFNN model provides a good agreement between the prediction and the analytical high-fidelity function (Equation D.4) (Figure D.1). After 15 independent evaluations a mean L2 relative error of 2.9% and a standard deviation of 0.9% are obtained. This equates to an uncertainty of 4.7% for a 2σ confidence level which is below the maximum threshold of 10% commonly used for low-order model uncertainties in preliminary design stages[184,243].

$$y_{HF}(x) = (6x - 2)^2 sin(12x - 4) \tag{D.4}$$

$$y_{LF}(x) = 0.5 y_{HF}(x) + 10(x - 0.5) - 5 \tag{D.5}$$

TABLE D.1: Network architecture and hyperparameters for the MFNN model used to verify the one-dimensional and linear correlation benchmark function.

Neural network	Hidden layers	Neurons/layer	Act. fucntion	L2 reg.
NN_{LF}	6	32	Tanh	10^{-5}
$NN_{HF-linear}$	1	16	None	None
$NN_{HF-nonlinear}$	2	16	Tanh	10^{-6}

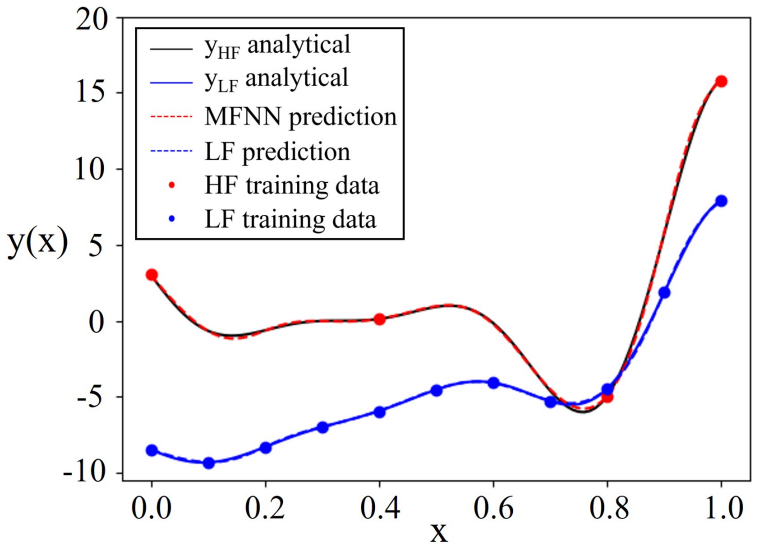

FIGURE D.1: MFNN prediction for the one-dimensional and linear correlation benchmark function.

D.1.2 Non-linear correlation

The Forrester-FSM function is a modified version of the Forrester function and is used to verify the MFNN implementation for the one-dimensional case with non-linear correlation (Equations D.6,D.7). The high-fidelity training datapoints are increased to 6 which are equally spaced from 0 to 1. The same low-fidelity training points are used as in the linear correlation case with 11 points equi-spaced from 0 to 1. A MFNN model have been tuned to predict the high-fidelity analytical function (Figure D.2). The low-fidelity network comprises 6 hidden layers with 32 neurons per layer, hyperbolic tangent function and L2 regularization factor of 10^{-6} (Table D.2). The high-fidelity linear sub-network is built with 1 hidden layer and 16 neurons (Table D.2). The high-fidelity sub-networks has been optimized for 3 hidden layers with 32 neurons per layer, hyperbolic tangent activation function and 10^{-6} as L2 regularization factor (Table D.2). The surrogate model is able to predict the global minimum at around x = 0.75 even when the low-fidelity data set has a local minimum close to that position. After 15 independent evaluations a mean L2 relative error of 3.2% and a standard deviation of 1.4% are obtained. This equates to an uncertainty of 6.0% with a 2σ confidence level.

$$y_{HF}(x) = (6x - 2)sin(12x - 4) + 5 \tag{D.6}$$

$$y_{LF}(x) = y_{HF}(x)^{2/3} + (x+1)^2 - 2 \tag{D.7}$$

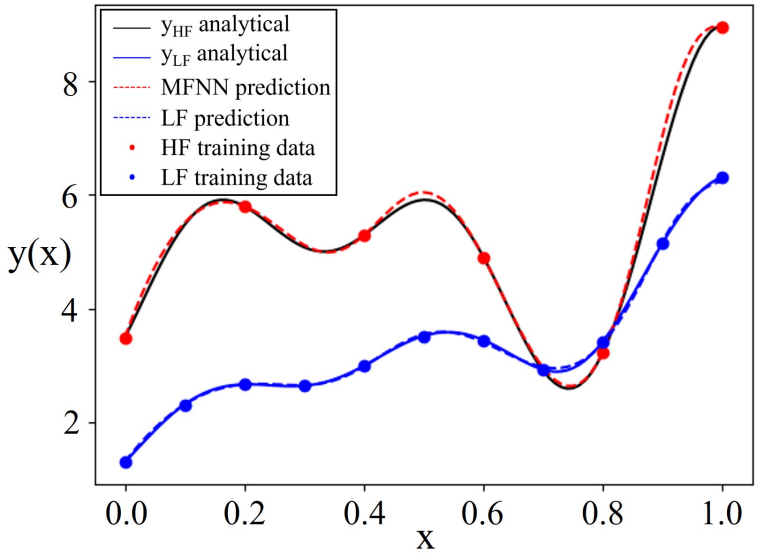

FIGURE D.2: MFNN prediction for the one-dimensional and non-linear correlation benchmark function.

TABLE D.2: Network architecture and hyperparameters for the MFNN model used to verify the one-dimensional and non-linear correlation benchmark function.

Neural network	Hidden layers	Neurons/layer	Act. fucntion	L2 reg.
NN_{LF}	6	32	Tanh	10^{-6}
$NN_{HF-linear}$	1	16	None	None
$NN_{HF-nonlinear}$	3	32	Tanh	10^{-6}

D.2 Multi-dimensional verification

D.2.1 Linear correlation

The MFNN implementation has been verified for a multi-dimensional case using the Currin function (Equations D.8,D.9). It considers a linear correlation between the low- and high-fidelity functions. The training datapoints are equi-spaced in the x_1-x_2 plane following a full factorial sampling technique. The same number of samples for both x_1 and x_2 are considered with a total of 49 points for the low-fidelity and 16 for the high-fidelity case. The hyperparameters of the MFNN have

been optimized to maximize the modelling performances. The low-fidelity network is built with 3 hidden layers and 32 neurons per layer, hyperbolic tangent activation function and 10^{-5} L2 regularization factor (Table D.3). For the linear part of the high-fidelity network 1 hidden layer with 20 neurons is used (Table D.3). The non-linear part of the high-fidelity network has 4 hidden layers with 32 neurons each, hyperbolic tangent activation function and 10^{-6} L2 regularization factor. (Table D.3). The surrogate model predicts the gradients in the x_1-x_2 space and the location of the minimum (Figure D.3b, Figure D.3d). After 15 independent runs, a mean L2 relative error of 2.4% with a standard deviation of 0.5% is obtained. This provides an uncertainty of 3.4% for a 2σ confidence level.

$$y_{HF}(x_1, x_2) = \left(1 - e^{\frac{-1}{2x_2}}\right) \frac{2300x_1^3 + 1900x_1^2 + 2092x_1 + 60}{100x_1^3 + 500x_1^2 + 4x_1 + 20} \tag{D.8}$$

$$\begin{aligned} y_{LF}(x_1, x_2) = & \frac{1}{8}\left[y_{HF}(x_1 + 0.05, x_2 + 0.05) + y_{HF}(x_1 + 0.05, max(0, x_2 - 0.05))\right] + \\ & \frac{1}{8}\left[y_{HF}(x_1 - 0.05, x_2 + 0.05) + y_{HF}(x_1 - 0.05, max(0, x_2 - 0.05))\right] + \\ & \frac{1}{8}\left[-5x_1 - 7x_2^2\right] \end{aligned} \tag{D.9}$$

TABLE D.3: Network architecture and hyperparameters for the MFNN model used to verify the two-dimensional and linear correlation benchmark function.

Neural network	Hidden layers	Neurons/layer	Act. fucntion	L2 reg.
NN_{LF}	3	32	Tanh	10^{-5}
$NN_{HF-linear}$	1	20	None	None
$NN_{HF-nonlinear}$	4	32	Tanh	10^{-6}

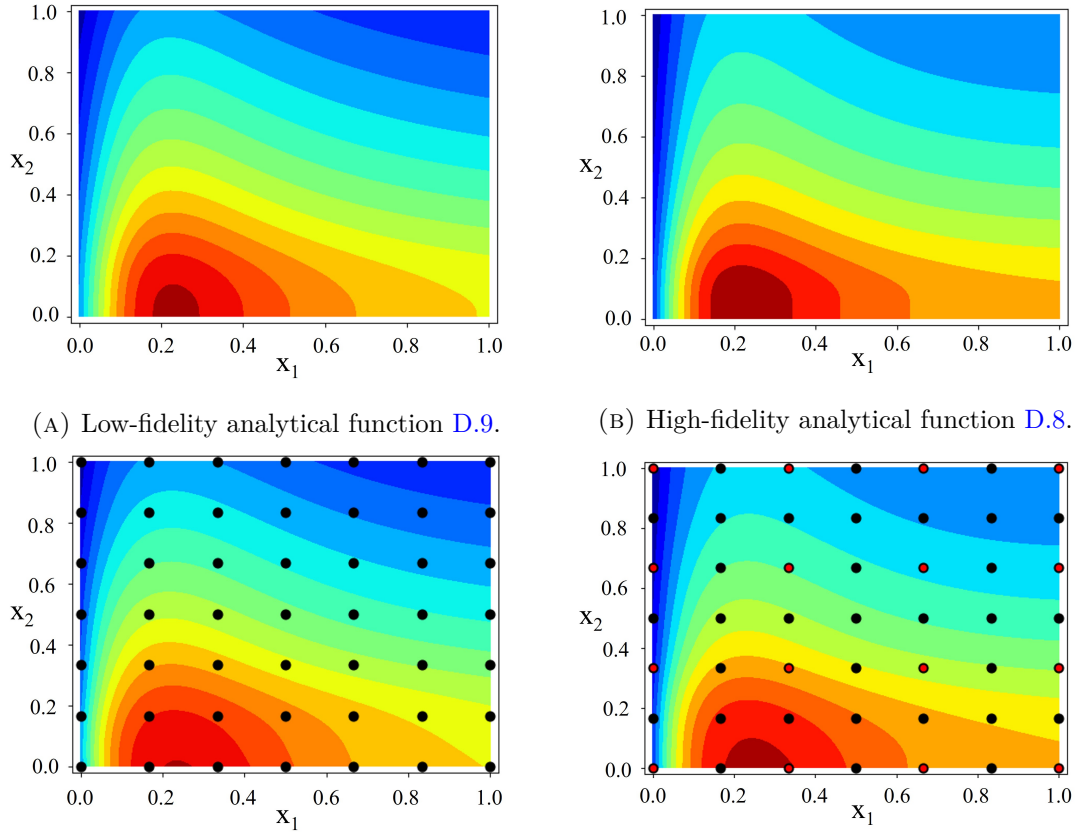

(A) Low-fidelity analytical function D.9.

(B) High-fidelity analytical function D.8.

(C) Low-fidelity prediction.

(D) High-fidelity prediction.

FIGURE D.3: MFNN prediction for the two-dimensional and linear correlation benchmark function. Black dots are low-fidelity training points, red dots are high-fidelity training points.

D.2.2 Non-linear correlation

The Currin-FSM function (Equation D.10) is used to verify the MFNN implementation for a multi-dimensional case with non-linear correlation between fidelities. This function includes the term $-\frac{1}{8}\left[y_{HF}(x_1^2, x_2^2)\right]^{5/3}$ in the low-fidelity part to create a non-linear relationship with the high-fidelity function. The low-fidelity function becomes more complex (Figure D.4a) and more training data points compared to the original Currin function validation case are needed. Therefore, 64 low-fidelity and 25 high-fidelity equi-space points are sampled using the full factorial method. The MFNN has been tuned and the low-fidelity network has been built with 4 hidden layers and 40 neurons per layer, hyperbolic tangent activation function and 10^{-6} L2 regularization factor (Table D.4). For the linear part of the high-fidelity function 1 hidden layer with 20 neurons is used (Table D.4). The non-linear part high-fidelity

sub-network is composed of 4 hidden layers with 40 neurons each, hyperbolic tangent activation function and 10^{-5} L2 regularization factor (Table D.4). In spite of the large non-linear correlation between the low-and high-fidelity functions, the MFNN method predicts the high-fidelity function with a mean L2 error of 4.5% and a standard deviation of 1.8%. This equates to a 2σ confidence level uncertainty of 8.1% which is still below the 10% threshold.

$$\begin{aligned} y_{LF}\left(x_1, x_2\right) = & \frac{1}{8}\left[y_{HF}\left(x_1+0.05, x_2+0.05\right)+y_{HF}\left(x_1+0.05, max\left(0, x_2-0.05\right)\right)\right]+ \\ & \frac{1}{8}\left[y_{HF}\left(x_1-0.05, x_2+0.05\right)+y_{HF}\left(x_1-0.05, max\left(0, x_2-0.05\right)\right)\right]+ \\ & \frac{1}{8}\left[-5x_1-7x_2^2\right]-\frac{1}{8}\left[y_{HF}\left(x_1^2, x_2^2\right)\right]^{5/3} \end{aligned} \tag{D.10}$$

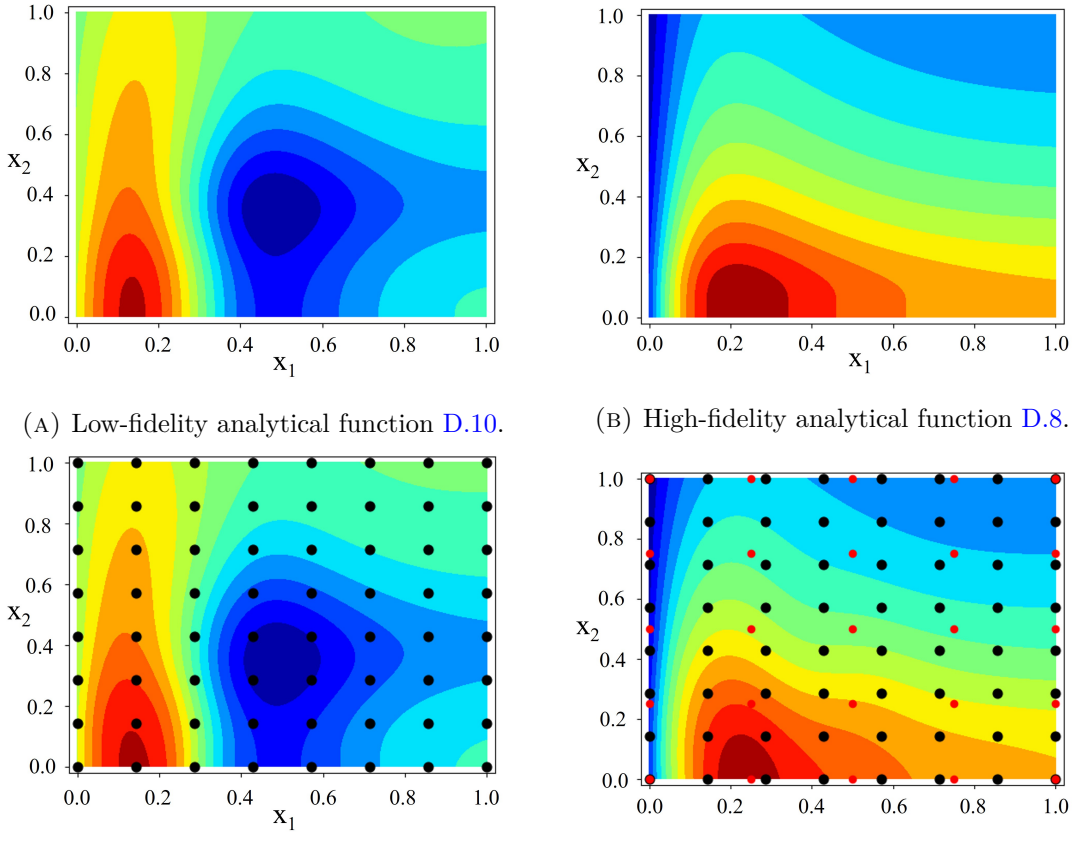

(A) Low-fidelity analytical function D.10.

(B) High-fidelity analytical function D.8.

(C) Low-fidelity prediction.

(D) High-fidelity prediction.

FIGURE D.4: MFNN prediction for the two-dimensional and non-linear correlation benchmark function. Black dots are low-fidelity training points, red dots are high-fidelity training points.

TABLE D.4: Network architecture and hyperparameters for the MFNN model used to verify the two-dimensional and non-linear correlation benchmark function.

Neural network	Hidden layers	Neurons/layer	Act. fucntion	L2 reg.
NN_{LF}	4	40	Tanh	10^{-6}
$NN_{HF-linear}$	1	20	None	None
$NN_{HF-nonlinear}$	4	40	Tanh	10^{-5}

APPENDIX E

Evolutionary algorithms for nacelle optimisations

This appendix addresses a statistical comparison between different Genetic Algorithms (GA) and Particle Swarm Optimisers (PSO) for the transonic aerodynamic optimisation of compact nacelles for the next generation of Ultra-High Bypass Ratio (UHBPR) aero-engines. Based on the best performing algorithms previously found for this optimisation problem by Cheval[50], the non-dominated sorting genetic algorithm II (NSGA-II)[232] and the indicator-based evolutionary algorithm (IBEA)[233] were selected as GA and the Reyes-Coello multi-objective particle swarm optimiser (OMOPSO) was the PSO optimiser considered[234]. The implementation of each optimiser used in this work was verified against a set of optimisation benchmark problems. Zitzler-Deb-Thiele's test function 1 and test function 2 were used for this purpose[262].

For this analysis, RANS CFD-in-the-loop optimisations were performed for a 2D axisymmetric compact nacelle configuration given by $L_{nac}/r_{hi} = 3.1$ and $r_{te}/r_{hi} = 0.95$. The optimisation approach is detailed in Section 4.5.2. Each algorithm was used to drive 16 different optimisations. This enables a statistical comparison of the optimal design space reached by every optimiser and also an analysis of the variability of each algorithm to converge to a certain solution. To purely focus on the impact of the optimiser, every optimisation started from the same Design Space Exploration. This removes the effect of randomness in the population of the design space in the first generation through the Latin Hypercube Sampling technique.

To achieve aerodynamic robust designs, several operating conditions were considered in the optimisation process. In addition to the cruise condition ($C_{D-cruise}$) given by $M = 0.85$ and $MFCR = 0.7$ (Equation 4.39) the sensitivities to an increase in the flight Mach number ($C_{D-\Delta M}$) from 0.85 to 0.87 (Equation 4.40) and a decrease in the aero-engine MFCR from 0.7 to 0.65 (C_{D-EoC}) (Equation 4.41) were also considered.

The minimisation of the nacelle drag at these conditions defines the three objective functions of the optimisation approach.

E.1 Algorithms assessed

E.1.1 NSGA-II

NSGA-II is perhaps the most popular GA for multi-objective optimisations due to an improvement on the spread of the solution and on the convergence near the optimal Pareto front relative to other GAs. This optimiser technique is based on elite-preservation and diversity-preservation. For this purpose, the individuals of a population are sorted based on their elitism rank and on the crowding distance between each other. While the elitism rank keeps the best performing individuals the crowding distance sorting method helps to spread the population on the design space to mitigate local optima. Individuals are selected based on a tournament selection to generate an offspring population (Q_t) (Figure E.1). Out of the parent population (P_t), two individuals are randomly chosen and compared based on the elitism rank. The individual with highest rank is used to reproduce. In case of both individuals having the same rank, the crowding distance factor is used to select Parent 1. This is repeated to find Parent 2. Subsequently, crossover and mutation techniques are applied to generate an offspring individual. The crossover operator randomly chooses certain genes from each parent and combines them (Figure E.2). The mutation operator applies a random change to a gene that is randomly selected out of all of genes (Figure E.2). This is repeated iteratively in each generation until having an offspring population of the same size as the parent population (Figure E.1). In this work a Gaussian mutation operator defined by a standard deviation size of 0.005 and a mutation rate of 0.2 are used[16,27]. A blended (BLX) crossover[263] technique is used to enlarge the range of variability of a certain gene further from the interval defined by both parents (M) which helps to maintain a genetic diversity in the offspring (Figure E.3). For this work, $\alpha = 0.5$ is considered for the BLX crossover which allows the selection of parameters to generate the offspring up to 0.5M on either side of each parent parameter (Figure E.3).

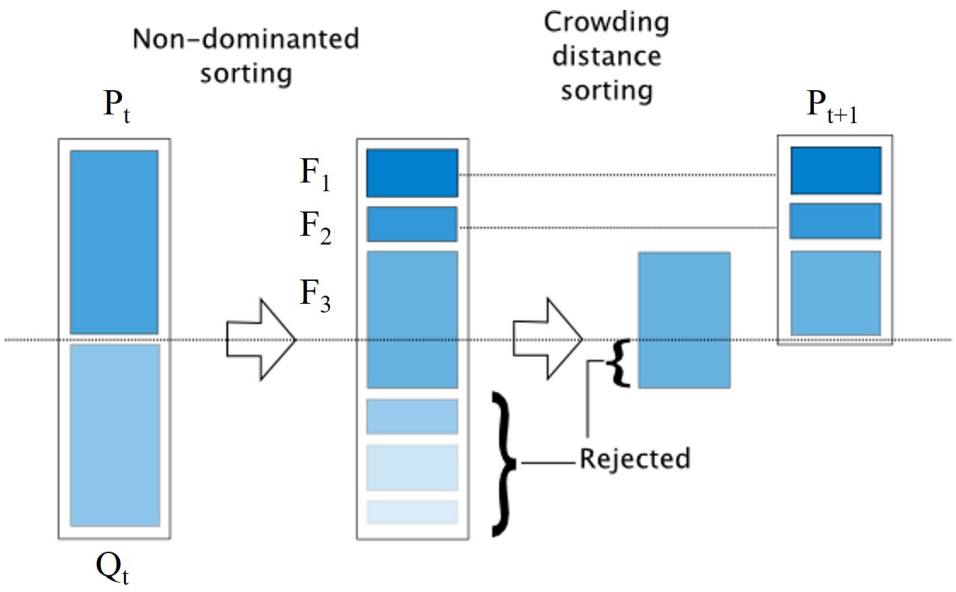

FIGURE E.1: Schematics of NSGA-II. Based on Deb et al.[232].

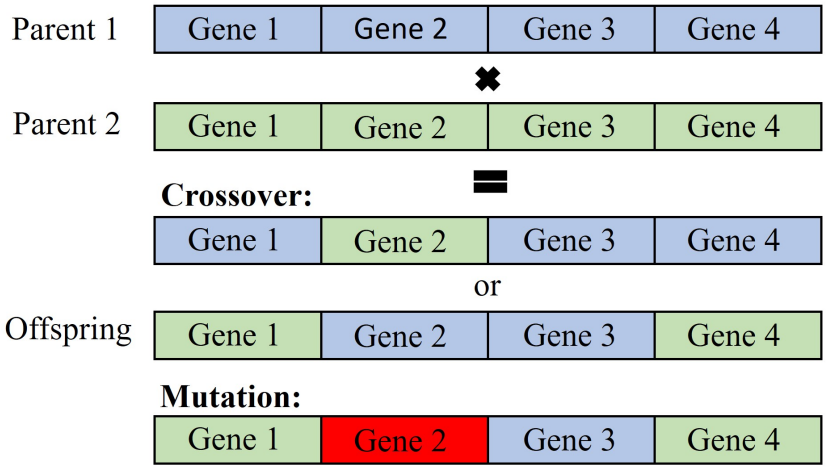

FIGURE E.2: Crossover and mutation operations for the offspring generation.

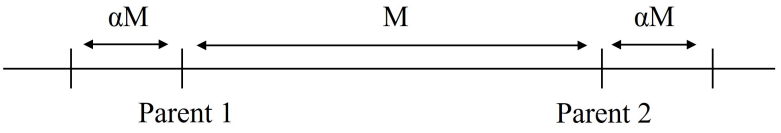

FIGURE E.3: Blended BLX-α crossover operator.

E.1.2 IBEA

In contrast to previous population-based GA, IBEA adapts the search by using the Hypervolume (HV) index in the selection process. Based on an initial population, the fitness value $F(x_i)$ of each individual is calculated. Among many options, one possibility is to sum up the HV values of an individual with respect to the rest of the

population (Equation E.1) where P represent the Pareto data set. As for NSGA-II, a tournament selection is carried out for the parent population members based on a ranking of the corresponding fitness values $F(x_i)$. An offspring is generated from the mating selection through a crossover operator that randomly combine certain genes from each parent and through mutation which randomly picks a gene and modifies it (Figure E.2). This is repeated iteratively until the convergence of the optimisation is reached. In the present study, uniform mutation and binary crossover operators are used.

$$F(x_i) = \sum_{x_j, \varepsilon P \setminus \{x_i\}} HV\left(\{x_j\}, \{x_i\}\right) \tag{E.1}$$

E.1.3 OMOPSO

OMOPSO is the PSO-type of algorithm assessed which was developed by Sierra et al.[234]. OMOPSO is described in Section 4.5.2.1 of the Methodology as it is the selected algorithm for this work.

E.2 Statistical comparison for transonic nacelle optimisations

E.2.1 Optimal design space

In this study, the Pareto data set obtained from a optimisation constitutes a three-dimensional surface of the non-dominated designs. It is presented as a two-dimensional projection on the plane defined by $C_{D-cruise}$ - $C_{D-\Delta M}$ with every data point coloured by C_{D-EoC} (Figure E.4). In a typical Pareto front for this optimisation problem, as $C_{D-\Delta M}$ decreases there is a penalty in C_{D-EoC} which highlights the compromise between these two performance metrics (Figure E.4a). For cruise drag the Pareto is divided into two branches. While in the upper branch a $C_{D-cruise}$ reduction implies a penalty in C_{D-EoC}, a reduction in $C_{D-cruise}$ in the lower branch increases $C_{D-\Delta M}$ (Figure E.4a). However, this layout of the Pareto front changes substantially for some of the optimisations driven by NSGA-II. For example, optimisations 2, 3 and 4 result in different Pareto families with different sensitivities in the trade-off between the objective functions (Figure E.4a). IBEA and OMOPSO show less

variability in the Pareto front with convergence to the same expected Pareto front family composed of two branches (Figure E.4b, Figure E.4c). A statistical comparison was carried out using the designs with minimum drag value for each objective function which provides a sample size of 16 for each operating condition. This allows a quantification of the bounds of the optimal design space reached by each algorithm. This was quantified relative to the NSGA-II results using the mean value ratio ($\mu/\mu_{NSGA-II}$), standard deviation ratio ($\sigma/\sigma_{NSGA-II}$) and amplitude range ratio ($\Delta/\Delta_{NSGA-II}$) where Δ is defined by the difference between the maximum and the minimum value (Table E.1). Using the standard deviation ratio $\sigma/\sigma_{NSGA-II}$ as a measure of the variability of each optimiser to converge to a solution, IBEA and OMOPSO reduce the variability at cruise to 15% and 24% of $\sigma_{NSGA-II}$ (Table E.1). Improvements of the same order of magnitude are obtained for the increased Mach number and end-of-cruise conditions for which OMOPSO outperforms IBEA (Table E.1). Additionally, a comparison of the mean value ratio $\mu/\mu_{NSGA-II}$ and the amplitude range $\Delta/\Delta_{NSGA-II}$ indicate a high similarity based on drag performances in the optimal design space reached by IBEA and OMOPSO. However, a comparison with NSGA-II shows notable differences in the optimal design spaces. Although there is a slight difference between OMOPSO/IBEA and NSGA-II in $\mu/\mu_{NSGA-II}$ of about $\pm 1\%$ which equates to a negligible change in ΔC_D, the amplitude range $\Delta/\Delta_{NSGA-II}$ increases for NSGA-II between 80% and 85% depending on the condition. This indicates a potential low reliability on NSGA-II for this optimisation problem. An assessment of the population level of the Pareto shows an averaged reduction of 64% and 34% for OMOPSO and IBEA relative to NSGA-II (Table E.1). However, the variability in the population size reached by IBEA is higher than OMOPSO by a factor of 2.5. Moreover, OMOPSO shows a good sample resolution in the Pareto front which is the region of interest when down selecting a design (Figure E.4c).

Similarly, the optimal design space is compared based on the design variables (f_{max}, r_{max}, r_{if}, β_{nac}) of the designs contained in the Pareto data set. This data is presented in the format of a box plot for each parameter of each optimisation which compares how the data is distributed in the design space. The box plot extends from the minimum to the maximum value (Figure E.5). Within this range, the median (or second quartile) divides the data set into two halves. Additional split between the median and the ends are shown by the first quartile (Q1) and the third quartile (Q3) (Figure E.5). The range between these first and third quartile is called interquartile range (IQR). This is a key parameter to identify outliers. A datapoint is an outlier if it is either below (Q1-1.5IQR) or above (Q3+1.5Q3). A comparison of the optimal

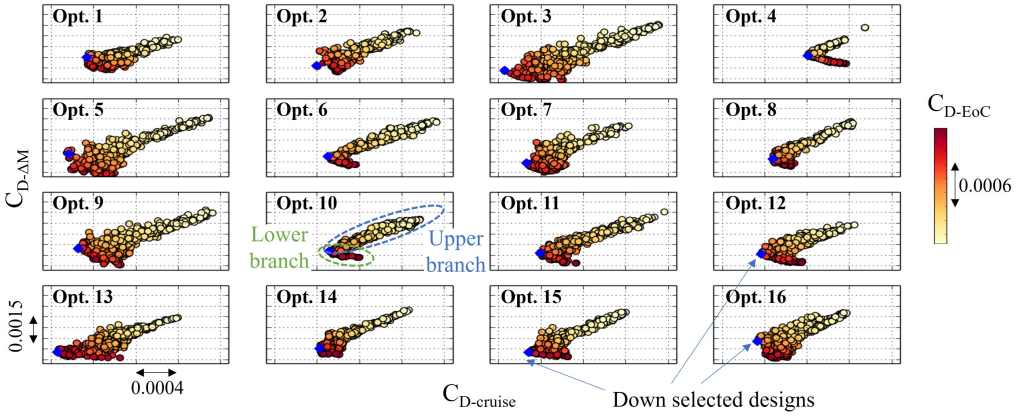

(A) Optimisations with the NSGA-II algorithm.

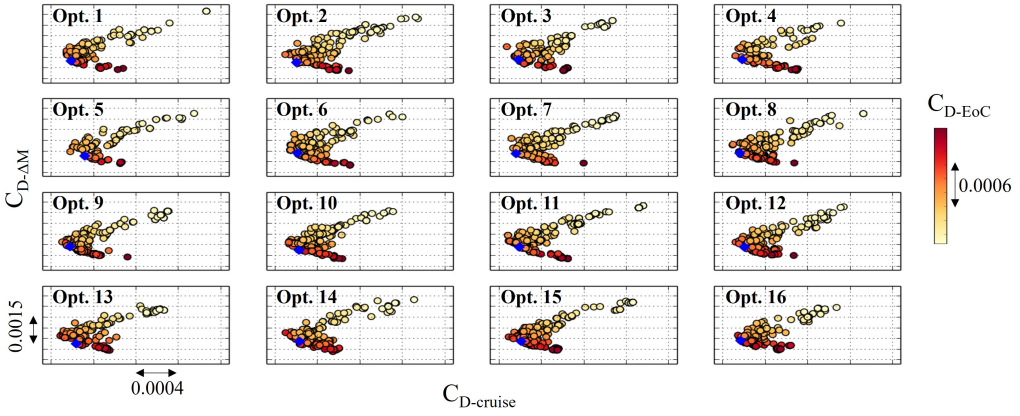

(B) Optimisations with the IBEA algorithm.

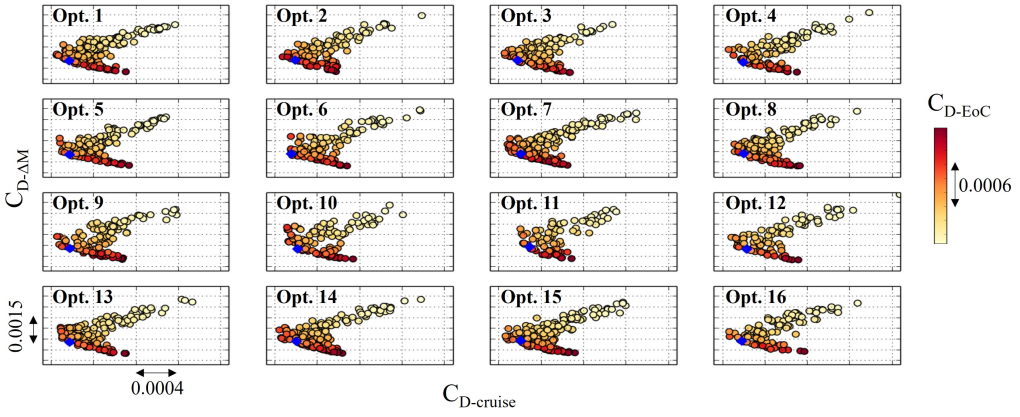

(C) Optimisations with the OMOPSO algorithm.

FIGURE E.4: Pareto fronts for the different optimiser. The blue dot is the down selected design.

design space for each algorithm shows a high similarity for every design variable between IBEA and OMOPSO which is in line with the conclusion drawn based on

the drag performance (Figure E.6). Conversely, NSGA-II converges to a different optimal design space specially for f_{max} and β_{nac} with differences up to $0.03L_{nac}$ and 1.5° respectively (Figure E.6). As was observed in the Pareto plots, the optimisations with NSGA-II have a high variability in the optimal design space whereas OMOPSO and IBEA are very consistent in the solution reached (Figure E.4, Figure E.6).

TABLE E.1: Statistical comparison between IBEA and OMOPSO relative to NSGA-II for the designs with minimum drag at each operating condition.

		IBEA	**OMOPSO**
Min $C_{D-cruise}$ designs	$\mu/\mu_{NSGA-II}$	0.99	0.99
	$\sigma/\sigma_{NSGA-II}$	0.15	0.24
	$\Delta/\Delta_{NSGA-II}$	0.14	0.22
Min $C_{D-\Delta M}$ designs	$\mu/\mu_{NSGA-II}$	1.01	1.01
	$\sigma/\sigma_{NSGA-II}$	0.22	0.14
	$\Delta/\Delta_{NSGA-II}$	0.20	0.14
Min C_{D-EoC} designs	$\mu/\mu_{NSGA-II}$	1.01	1.01
	$\sigma/\sigma_{NSGA-II}$	0.22	0.19
	$\Delta/\Delta_{NSGA-II}$	0.21	0.16
Population	$\mu/\mu_{NSGA-II}$	0.66	0.33
	$\sigma/\sigma_{NSGA-II}$	0.85	0.34
	$\Delta/\Delta_{NSGA-II}$	0.73	0.28

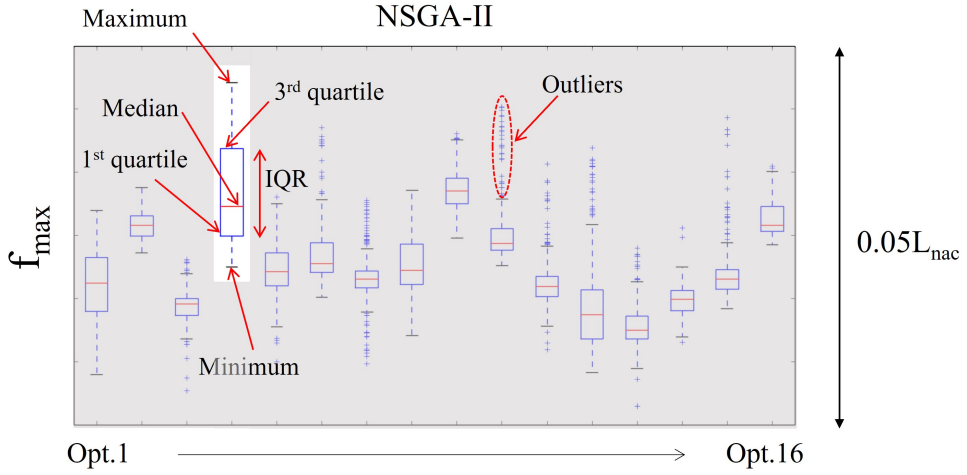

FIGURE E.5: Definition of the box plot used to represent the optimal design space for an optimisation using the designs contained in the Pareto data set. Example for f_{max} and NSGA-II.

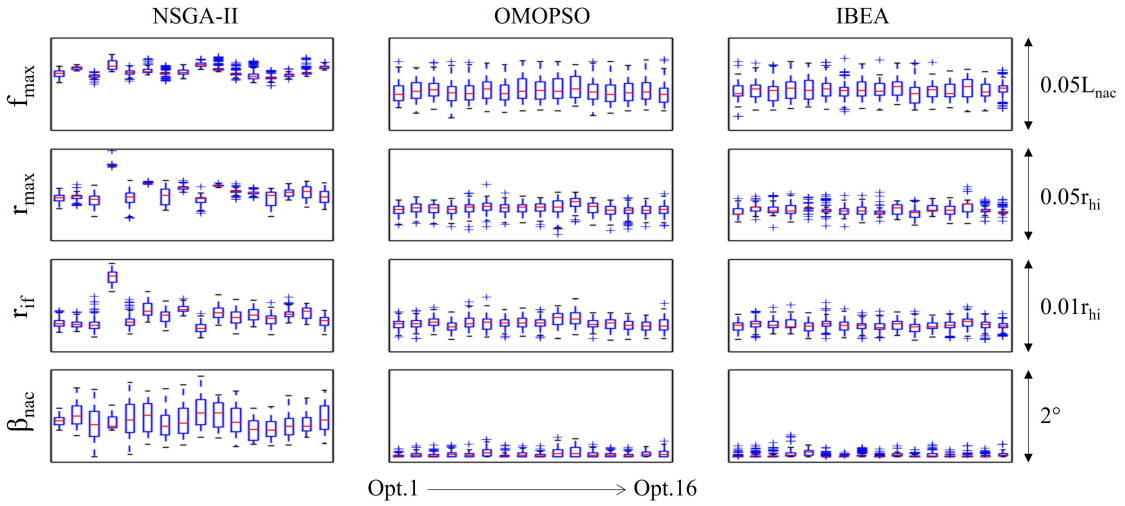

FIGURE E.6: Optimal design space for every optimisation showed by box plots of the designs in the Pareto front.

E.2.2 Down selected designs

The down selection of a design from a Pareto data set is the final outcome from a multi-point optimisation problem. The method detailed in Section 4.5.2.2 for selecting designs was applied for every optimisation with each optimiser to enable a statistical comparison of down selected designs. This provided a population of 16 samples per algorithm. The assessment was based both on the drag performances and the design variables of these selected designs using the standard deviation ratio $\sigma/\sigma_{NSGA-II}$.

For the drag at cruise and increased Mach number condition, IBEA and OMOPSO reduce the variability relative to NSGA-II to below $0.26\sigma_{NSGA-II}$ and $0.17\sigma_{NSGA-II}$ respectively (Table E.2). At end-of-cruise condition, the reduction in variability is around $0.52\sigma_{NSGA-II}$ for IBEA and $0.63\sigma_{NSGA-II}$ for OMOPSO (Table E.2). Substantial improvement for IBEA and OMOPSO are observed in terms of geometry parameters as well. While the reduction in $\sigma/\sigma_{NSGA-II}$ shown by IBEA is between 0.41 for f_{max} and 0.22 for r_{if}, OMOPSO further reduces the variability to 0.30 for f_{max} and 0.13 for r_{if} (Table E.3).

TABLE E.2: Statistical comparison between IBEA and OMOPSO relative to NSGA-II for the variability of the drag performances of the down selected designs.

		IBEA	**OMOPSO**
$\sigma/\sigma_{NSGA-II}$	$C_{D-cruise}$	0.21	0.17
	$C_{D-\Delta M}$	0.26	0.17
	C_{D-EoC}	0.52	0.63

TABLE E.3: Statistical comparison between IBEA and OMOPSO relative to NSGA-II for the variability of the design variables of the down selected designs.

		IBEA	**OMOPSO**
$\sigma/\sigma_{NSGA-II}$	f_{max}	0.41	0.30
	r_{max}/r_{hi}	0.23	0.20
	r_{if}/r_{hi}	0.22	0.13
	β_{nac}	0.25	0.16

E.2.3 Convergence rate

The convergence rate for each optimiser was assessed based on the Hypervolume (HV) index (Figure 4.26) and the associated number of generations of constant number of samples required to achieve convergence. Considering the criteria of a change in the HV index lower than 1% in the last 3 generations, NSGA-II is the fastest algorithm. The optimisations led by NSGA-II converge in average 4 and 6 generations earlier than OMOPSO and IBEA (Figure E.7). It can be inferred that OMOPSO requires 2 generations less than IBEA to meet the convergence criteria (Figure E.7) which provides a 6% reduction in the computation effort.

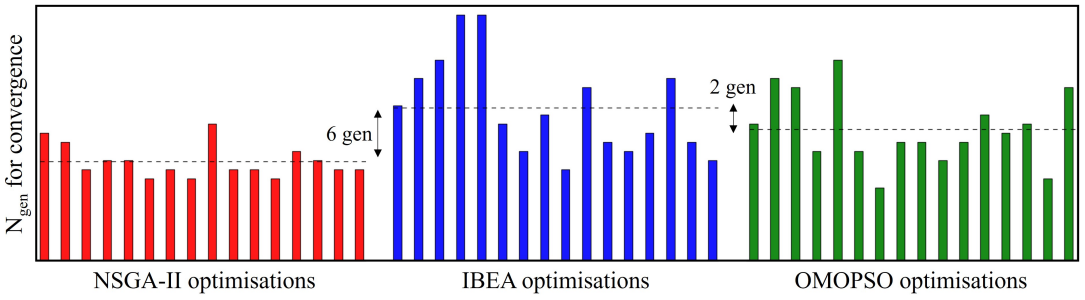

FIGURE E.7: Comparative quantification of the convergence rate for each optimiser to meet the convergence criteria.

E.2.4 Conclusion

Overall, NSGA-II is discarded for this non-linear aerodynamic optimisation problem due to its high variability in the convergence to a solution compared to OMOPSO and IBEA. OMOPSO is selected as the most suitable algorithm for this application due to: (a) the overall lower variability in the convergence to the optimal design space and a down selected design and (b) a reduction of 6% in the computational overhead compared to IBEA.